

Opening the extreme ultraviolet lithography  
source bottleneck: Developing a 13.5-nm  
laser-produced plasma source  
for the semiconductor industry

John White  
B. Sc.

Thesis presented for the degree of  
Doctor of Philosophy

Supervised by Prof. Gerry O'Sullivan.

School of Physics

College of Engineering, Mathematical & Physical Sciences

University College Dublin

February 2006

## Overview

The current semiconductor manufacturing lithographic source wavelength is 193 nm, produced from an ArF excimer laser. A shorter wavelength radiation source is required to extend the proposed Mo/Si manufacturing optics beyond the 32-nm node and continue to manufacture integrated circuits in keeping with past improvements. To this end, the SEMATECH (SEmiconductor MAnufacturing TECHnology) roadmap [1] suggests that a 13.5-nm (92-eV), laser-produced plasma (LPP) or pulsed discharge (PD) source be developed. Various source materials have been suggested, such as Sn, Xe, O, Li, and F ions, which emit in the 13–14-nm region.

At University College Dublin, the School of Physics Spectroscopy group has conducted numerous experiments using laser-produced plasmas in the extreme ultraviolet (EUV) region. From their work with the lanthanides and adjacent related elements (cesium; atomic number  $Z = 55$  to lutetium;  $Z = 71$ ), O'Sullivan and Carroll [2, 3] observed that EUV emission in these elements was dominated by an unresolved transmission array (UTA), whose peak wavelength decreases with increasing atomic number. Further observations, identifying 4d–4f and 4p–4d atomic transitions in the UTA [4], showed that six tin ( $Z = 50$ ) ions ( $\text{Sn}^{7+}$ – $\text{Sn}^{12+}$ ) and one xenon ( $Z = 54$ ) ion ( $\text{Xe}^{10+}$ ) emit at 13.5 nm and are thus of considerable interest as light sources for next generation lithography (NGL) semiconductor manufacturing.

In this thesis, the theoretical analysis and computational methods used to design and create a laser-produced plasma light source at 13.5 nm is discussed, with emphasis on tin as the source target, in varying percentage composition. The Hartree-Fock configuration interaction (HFCI) Cowan code, which calculates transitions between atomic configurations, and the laser parameters and resultant plasma conditions needed to produce a tuned LPP light source are investigated. UTA statistics are calculated to characterise spectra, which result from unresolved in-band (13.5 nm  $\pm 1\%$ ) transitions. A steady-state plasma model is presented, which characterises the plasma by electron temperature, electron density, and average charge state (or ion stage distribution) from input parameters of laser wavelength, pulse energy, pulse length, and focussed spot radius, and the interaction with targets containing various percentage concentrations of tin. A figure of merit is presented, which convolves the in-band emission with ion densities and mirror reflectivity as a function of laser parameters and average electron temperature. Time-dependent, spatially resolved plasmas are analysed with a 1-D, hydrodynamic, laser-plasma interaction code, where level populations are calculated with an energy functional method. A radiation transport model for optically thick plasmas is presented to determine the conversion efficiency of laser energy into useable EUV radiation.

The proposed experimental set-up of an evacuated, 6.60-m grazing incidence spectrometer (GIS) is described, as are the results from tin and other proposed targets in the 13.5-nm wavelength region.

# Contents

<b>1. An introduction to laser-produced plasma spectroscopy.....</b>	<b>1</b>
1.1 Spectroscopy.....	1
1.1.1 Spectroscopy before 1885.....	1
1.1.2 Spectroscopy after 1885.....	2
1.1.3 The spectrometer.....	8
1.1.4 Spectral lines.....	14
1.2. Atomic physics.....	16
1.2.1 The Schrödinger wave equation.....	16
1.2.2 The Cowan code.....	21
1.2.3 The unresolved transition array (UTA).....	24
1.2.4 Tuneable EUV radiation.....	29
1.2.5 Proposed EUV light sources (Sn, Xe).....	33
1.3 Plasma physics.....	36
1.3.1 Plasma.....	36
1.3.2 Nd:YAG laser.....	51
1.4 Next generation lithography (NGL).....	52
1.4.1 Moore's law.....	52
1.4.2 Chip manufacturing.....	55
1.4.3 Multilayer mirrors.....	57
1.5 References.....	60
<b>2. Theoretical Cowan and UTA statistics.....</b>	<b>64</b>
2.1 Sn 4d subshell (Sn V–Sn XIV).....	64
2.2 Sn 4d subshell (4d-4f, 4p-4d, 4d-5p) transition statistics.....	82
2.3. Line broadening.....	98
2.3.1 Doppler broadening.....	98
2.3.2 Electron impact broadening.....	99
2.3.3 Doppler, electronic impact, and other broadening in a plasma.....	100
2.4 UTA reduced broadening survey.....	103
2.5 References.....	113
<b>3. A steady-state plasma model.....</b>	<b>114</b>
3.1 Atomic processes.....	114
3.1.1 Excitation, de-excitation, ionisation, recombination.....	114
3.2 Ionisation model.....	116
3.2.1 Critical density ( $n_{ec}$ ).....	116
3.2.2 Electron temperature, $T_e$ .....	118
3.2.3 Plasma domains (LTE, CE, CR).....	120
3.2.4 CR rate equations.....	123
3.2.5 CR validity.....	127
3.2.6 The ion density rate equation $n_{z+1}/n_z$ .....	129
3.2.7 Average charge in the plasma, $\langle z \rangle$ .....	131
3.2.8 Factors affecting the ion density and average charge.....	132
3.2.8.1 Electron density ( $n_e$ ).....	132
3.2.8.2 Ion model (LTE/CR/CE).....	134
3.2.8.3 Ionisation potential ( $\chi_z$ ).....	135
3.2.8.4 Ionisation potential lowering ( $\Delta\chi_z$ ).....	138
3.2.8.5 Number of open shell electrons ( $\xi_z$ ).....	140
3.2.8.6 Dielectronic recombination.....	141
3.2.8.7 CR rate equations.....	142

3.2.9	$f_z$ using the simultaneous equations method .....	144
3.2.10	Target composition .....	145
3.3	Theoretical source brightness .....	147
3.3.1	Theoretical spectrum.....	147
3.3.2	Intensity figure of merit .....	149
3.4	References.....	156
<b>4.</b>	<b>A spatial and temporal plasma model.....</b>	<b>158</b>
4.1	Laser-produced plasma hydrodynamics .....	158
4.1.1	Medusa LPP hydrodynamics .....	158
4.1.1.1	Medusa control.....	160
4.1.1.2	Medusa input.....	161
4.1.2	Medusa output.....	164
4.1.2.1	The Lagrangian mesh.....	164
4.1.2.2	Hydrodynamic data.....	167
4.1.2.3	Spatial-temporal ion distributions.....	169
4.1.2.4	Medusa mesh size .....	173
4.1.3	Other LPP hydrodynamics .....	174
4.2	Average atom model .....	175
4.2.1	The screened hydrogenic model ( $n$ splitting).....	175
4.2.2	The average atom model (Medusa).....	181
4.2.3	The screened hydrogenic model ( $nl$ subshell splitting) .....	184
4.2.4	The energy functional, $Y_a(E_n)$ versus $E_n$ .....	185
4.2.5	Population number density, $N_i$ and $N_j$ .....	189
4.3	Radiation transport.....	192
4.3.1	LPP velocity gradients .....	195
4.3.2	Aluminium reference case spectra with radiation transport .....	197
4.4	References.....	202
<b>5.</b>	<b>Radiation transport in laser-produced tin plasmas.....</b>	<b>204</b>
5.1	Sn reference case hydrodynamics .....	205
5.1.1	Sn reference case general hydrodynamics .....	205
5.1.2	Sn reference case ion densities and level populations .....	207
5.1.3	Simulated laser pulse .....	211
5.2	Radiation transport and conversion efficiency .....	212
5.2.1	Varying power density .....	212
5.2.2	Varying pulse length .....	220
5.2.3	Pulse shaping .....	222
5.3	References.....	225

Appendix A	Rowland
Appendix B	The Cowan code
Appendix C	PlasMod
Appendix D	Medusa

## List of Figures

Figure 1.1	Newton's Figure 13 from his 1704 <i>Opticks</i> .....	1
Figure 1.2	Hydrogen spectra and related series formula .....	2
Figure 1.3	Rydberg's general series formula .....	2
Figure 1.4	The Bohr quantum model .....	3
Figure 1.5	Moore's tables for Sn I [18] .....	5
Figure 1.6	<i>l</i> -degenerate Grotrian diagram from screened hydrogenic model (Sn I to Sn LI) .....	5
Figure 1.7	Cowan code input file for Sn XI .....	6
Figure 1.8	Calculated <i>gf</i> versus wavelength output from the Cowan code for Sn VI to Sn XIV. ....	6
Figure 1.9	A simple spectroscope in the visible range .....	8
Figure 1.10	Diffraction gratings schematic .....	8
Figure 1.11	The electromagnetic spectrum from 1 $\mu\text{m}$ to .1 nm .....	9
Figure 1.12	Multilayer Mo/Si mirror reflectivity versus wavelength ( $N = 40$ ) .....	10
Figure 1.13	Multi mirror optics set-up for semiconductor manufacturing [28] .....	10
Figure 1.14	Regions of spectral interest (nm) for lithography .....	11
Figure 1.15	The Rowland circle .....	12
Figure 1.16	Wavelength dispersion along the Rowland circle .....	12
Figure 1.17	5% tin in araldite spectra: photographic plate (top) and densitometer trace (bottom) [48] .....	14
Figure 1.18	Spectral lines convolved with Gaussian (left) and Lorentz (right) function .....	15
Figure 1.19	Wavefunction contraction and radial potential as a function of ionisation: Sn I–XIV .....	19
Figure 1.20	Cowan code program control .....	21
Figure 1.21	Discrete Cowan <i>gf</i> versus $\lambda$ convolved with Gaussians of varying width $\sigma$ , where $\text{FWHM} = 2.35\sigma$ .....	22
Figure 1.22	UTA emission with UTA statistics (Sn X and Sn XI) .....	26
Figure 1.23	4d-4f UTA emission with UTA statistics: Sn X (top) and Sn XI (bottom) .....	27
Figure 1.24	Resonant emission versus wavelength (Ba to Er) [48] .....	29
Figure 1.25	UTA peak wavelength versus atomic number [2, 3] .....	30
Figure 1.26	Single configuration weighted average Sn X transitions convolved with a Gaussian of arbitrary width (4p-5d, 4p-5s, 4d-4f, 4p-4d, and 4d-5p) .....	31
Figure 1.27	Multi configuration weighted average Sn X transitions with a Gaussian of arbitrary width (4d-4f, 4p-4d, and 4d-5p) .....	32
Figure 1.28	Densitometer traces of tin at various concentrations (1, 5, 100%) [49] .....	34
Figure 1.29	Variation of spectral emission from pure tin, tin oxide (33%) and a tin doped glass target containing 4% tin by number [62] .....	34
Figure 1.30	Lightning, northern lights, START spherical tokamak .....	36
Figure 1.31	UCD laboratory laser-produced plasma .....	36
Figure 1.32	Electron density ( $\text{cm}^{-3}$ ) versus temperature (eV) [66] .....	37
Figure 1.33	Ideal continuum and line radiation plasma emission spectrum [28] .....	38
Figure 1.34	The Debye length versus density and temperature ( $9.843 \times 10^{20} \text{ cm}^{-3}$ , 32 eV = 1.3 nm) .....	39
Figure 1.35	Plasma model criteria (CE, CR, LTE) .....	40
Figure 1.36	Absorption rate in the plasma by inverse bremsstrahlung .....	42
Figure 1.37	LPP regions (after laser-target interaction) [67] .....	42

Figure 1.38	Average ion state $\langle z \rangle$ versus temperature (eV) for tin ( $n_e = 9.843 \times 10^{20} \text{ cm}^{-3}$ ).....	44
Figure 1.39	Tin ion fraction distribution versus electron temperature ( $n_e = 9.843 \times 10^{20} \text{ cm}^{-3}$ ) .....	45
Figure 1.40	Flow chart to produce theoretical spectrum (intensity, wavelength, temperature).....	46
Figure 1.41	Theoretical UTA (summed oscillator strength versus wavelength at selected electron temperatures).....	47
Figure 1.42	Theoretical UTA (summed oscillator strength versus wavelength versus electron temperature) .....	47
Figure 1.43	Medusa input Gaussian laser pulse.....	48
Figure 1.44	Sample Medusa output showing $n_e$ , $T_e$ , and $\langle z \rangle$ in an aluminium plasma at the peak of the pulse .....	49
Figure 1.45	Nd:YAG laser [62] .....	51
Figure 1.46	Number of components per integrated circuit versus year.....	52
Figure 1.47	Mask and multi-die ICs on silicon wafer [90].....	55
Figure 1.48	Resist profiles of line and space patterns imaged by a 10X camera .....	55
Figure 1.49	Integrated circuit fabrication by lithographic methods .....	56
Figure 1.50	Multilayer mirror construction: alternating Mo and Si layers [28] .....	57
Figure 1.51	Mo/Si multilayer mirror reflectivity versus wavelength ( $n$ reflections).58	
Figure 1.52	Normalised multilayer mirror reflectivity versus wavelength ( $n$ reflections) .....	58
Figure 2.1	Sn VII 4d-5p experimental (top) [6] and Cowan (bottom) (scaling = 56%) .....	65
Figure 2.2	Sn VIII 4d-5p experimental (top) [7] and Cowan (bottom) (scaling = 63%).....	65
Figure 2.3	Sn VI 4d-4f+6p experimental (top) [6] and Cowan (bottom) (scaling = 50%).....	66
Figure 2.4	Sn VII 4d-4f+6p, 4p-4d experimental (top) [7] and Cowan (bottom) (scaling = 56%).....	66
Figure 2.5	Tin spectra with increasing power density from top to bottom (top) and max power density from above (bottom) [12] .....	68
Figure 2.6	Sn XIV (blue), Sn XIII (red), and Sn XII (black, dashed) .....	69
Figure 2.7	Sn V–Sn XIV weighted oscillator strength versus wavelength (5–25 nm) .....	71
Figure 2.8	Sn V–Sn XIV weighted oscillator strength versus wavelength (12.5–14.5 nm) (2 x 7.4%) .....	72
Figure 2.9	Sn V–Sn XIV weighted oscillator strength versus wavelength (13.365–13.635 nm) (2%) .....	73
Figure 2.10	Sn V–Sn XIV in-band $\Sigma gf$ versus ion stage .....	74
Figure 2.11	Sn V–Sn XIV UTA statistics.....	75
Figure 2.12	Sn V–Sn XIV UTA Gaussian: normal (black) and skewed (red) .....	76
Figure 2.13	Sn V–Sn XIV $gf$ versus wavelength.....	76
Figure 2.14	Discrete Cowan (blue), Gaussian (black), and skewed Gaussian (red) (Sn VIII–Sn XIII) .....	77
Figure 2.15	Sn XII $gf$ versus wavelength (nm) convolved with variable width.....	78
Figure 2.16	Sn ions $gf$ versus wavelength (nm) convolved (0.0212 nm, 1000 points) over full spectroscopic range (5–20 nm) (own maxima).....	79

Figure 2.17 Sn ions $gf$ versus wavelength (nm) convolved (0.0212 nm, 1000 points) over full spectroscopic range (5–20 nm) (same maximum) .....	79
Figure 2.18 Sn ions $gf$ versus wavelength (nm) convolved (0.0212 nm, 1000 points) over 2 x 7.4% range (12.5–14.5 nm) (own maxima) .....	80
Figure 2.19 Sn ions $gf$ versus wavelength (nm) convolved (0.0212 nm, 1000 points) over 2 x 7.4% range (12.5–14.5 nm) (same maximum) .....	80
Figure 2.20 Sn ions $gf$ versus wavelength (nm) convolved (0.0212 nm, 1000 points) over 2% range (13.365–13.635 nm) (own maxima) .....	81
Figure 2.21 Sn ions $gf$ versus wavelength (nm) convolved (0.0212 nm, 1000 points) over 2% range (13.365–13.635 nm) (same maximum) .....	81
Figure 2.22 Relative intensity versus wavelength (left: line and right: statistical) for 4d-4f (green), 4p-4d (blue), and 4d-5p (red) transitions .....	82
Figure 2.23 4d-4f statistics (UTA) .....	83
Figure 2.24 4p-4d statistics (UTA) .....	84
Figure 2.25 4d-5p statistics (UTA) .....	85
Figure 2.26 4d-4f, 4p-4d, and 4d-5p transitions: number of lines and $\Sigma gf$ .....	86
Figure 2.27 4d-4f, 4p-4d, and 4d-5p transitions: number of lines and $\Sigma gf$ (ratio) .....	86
Figure 2.28 4d-4f, 4p-4d, and 4d-5p transitions: mean wavelength .....	88
Figure 2.29 4d-4f, 4p-4d, and 4d-4f + 4p-4d transitions: mean wavelength .....	88
Figure 2.30 Eigenvalue energies (together) .....	89
Figure 2.31 Eigenvalue energies: 4p-4d (blue), 4d-4f (green), and 4d-5p (red) .....	89
Figure 2.32 The effect of binning and % $\Sigma gf$ (Sn X 4d-4f and 4p-4d) .....	90
Figure 2.33 Number of transitions and % $\Sigma gf$ less than 10, 1, .1 and 1e-6 (Sn V-Sn XIV 4d-4f and 4p-4d) .....	90
Figure 2.34 $\log_{10} gf$ versus wavelength (4d-4f transitions) .....	91
Figure 2.35 $\log_{10} gf$ versus wavelength (4p-4d transitions) .....	91
Figure 2.36 $\Sigma gf$ for 4d-4f (top), 4p-4d (middle), and 4d-5p (bottom) transitions: full band, 7.4% band, and 2% band .....	93
Figure 2.37 4d-4f transitions convolved with $\Delta\mu_1 = 0.0212$ nm width (red) and 2-parameter UTA (black) with width, $\sigma$ , where $\sigma$ is calculated from the line distribution. ....	94
Figure 2.38 4p-4d transitions convolved with $\Delta\mu_1 = 0.0212$ nm width (red) and 2-parameter UTA (black) with width, $\sigma$ , where $\sigma$ is calculated from the line distribution. ....	95
Figure 2.39 4d-4f transitions convolved with $\Delta\mu_1 = 0.0212$ nm width (red) and 2-parameter UTA (black) with width, $\sigma/2$ , where $\sigma$ is calculated from the line distribution. ....	96
Figure 2.40 4p-4d transitions convolved with $\Delta\mu_1 = 0.0212$ nm width (red) and 2-parameter UTA (black) with width, $\sigma/2$ , where $\sigma$ is calculated from the line distribution. ....	97
Figure 2.41 Doppler broadening versus wavelength and temperature (tin) .....	98
Figure 2.42 Electron impact broadening versus electron density and temperature (tin) .....	99
Figure 2.43 Electron impact (blue) and Doppler broadening (red) (tin, 13.5 nm) versus electron density (from $10^{21}$ to $10^{18}$ $\text{cm}^{-3}$ ) and temperature .....	100
Figure 2.44 Ratio of electron impact ( $\omega$ ) to Doppler broadening ( $\Gamma$ ) versus electron density and temperature .....	101
Figure 2.45 Electron impact ( $\omega$ ) + Doppler broadening ( $\Gamma$ ) versus electron density and temperature .....	101

Figure 2.46	Sn X, 10–20 nm, 4d-4f ( $\sigma/\sigma' = 2.8$ ) .....	103
Figure 2.47	Sn XI, 12.5–14.5 nm, 4p-4d, 40 eV ( $n_{ec}, n_{ec}/10$ ) $\sigma' = 1.2$ .....	104
Figure 2.48	Sn XII, 13.365–13.635 nm, 4d-4f + 4p-4d ( $n_{ec}, n_{ec}/100$ ) $\sigma' = 1.1$ .....	104
Figure 2.49	Reduced broadening ( $n_{ec}, n_{ec}/1000$ ) .....	105
Figure 2.50	Wavelength dependence on spectral region: 4d-4f (top), 4p-4d (bottom) .....	106
Figure 2.51	Sn VIII–Sn XIV 4d-4f (left) 4p-4d (right) (2 x 7.4%: 12.5–14.5 nm) .	108
Figure 2.52	Sn IX–Sn XIII 4d-4f (left) 4p-4d (right) (2%: 13.365–13.635 nm) .....	110
Figure 2.53	Statistically calculated UTA for the main 4d subshell Sn ions: Sn VII–Sn XIV 4d-4f (top) 4p-4d (middle) 4d-4f + 4p-4d (bottom).....	112
Figure 3.1	Atomic processes and their inverses.....	115
Figure 3.2	Electron temperature versus laser flux ( $Z = 50, \lambda = 1.064 \mu\text{m}$ ) .....	118
Figure 3.3	Rate equations versus temperature for tin a) SnV–SnXIV, b) $S, \alpha_r, n_e \alpha_{3b}$ , c) $S, \alpha_r + n_e \alpha_{3b}$ .....	124
Figure 3.4	$n_e \alpha_{3b} / (\alpha_r + n_e \alpha_{3b})$ ratio versus temperature (Sn V–Sn XIV) .....	125
Figure 3.5	$S, \alpha_r$ , and $n_e \alpha_{3b}$ versus ion stage a) 20 eV b) 30 eV c) 40 eV d) 50 eV .	125
Figure 3.6	$n_e \alpha_{3b} / (\alpha_r + n_e \alpha_{3b})$ ratio versus temperature at $n_{ec}, 0.1 n_{ec}, 0.01 n_{ec}$ (Sn XI).....	126
Figure 3.7	LTE and CE plasma boundaries .....	127
Figure 3.8	CR plasma boundaries (LTE, CE criteria) .....	128
Figure 3.9	CR plasma boundaries (CR criteria).....	128
Figure 3.10	$f_z$ versus temperature (tin) linear (top) log (bottom).....	129
Figure 3.11	$f_z$ at 10 eV, 30 eV, 50 eV, and 70 eV (tin).....	130
Figure 3.12	Average charge versus electron temperature: computational and semi- empirical .....	131
Figure 3.13	$\langle z \rangle$ versus $T_e$ (tin) for different densities: $n_e = .01n_{ec}, .1n_{ec}, n_{ec}, 10n_{ec}$ , and $100n_{ec}$ .....	132
Figure 3.14	$\langle z \rangle$ versus $T_e$ (tin) for LTE/CR/CE regions: $n_e = n_{ec}$ (top) $n_e = n_{ec}/10$ (bottom).....	133
Figure 3.15	$\langle z \rangle$ versus $T_e$ for LTE/CR/CE model: 10 eV (top), 30 eV (middle), 50 eV (bottom).....	134
Figure 3.16	Sn ionisation potentials from Table 3.3.....	137
Figure 3.17	$\langle z \rangle$ versus $T_e$ for different ionisation potential data .....	137
Figure 3.18	Ionisation potential lowering in tin ( $n_e = 9.843 \times 10^{20} \text{ cm}^{-3}$ ) using Eq. 3.44 [11].....	139
Figure 3.19	Average charge $\langle z \rangle$ versus $T_e$ (tin) including $\Delta\chi_z$ .....	139
Figure 3.20	$\langle z \rangle$ versus $T_e$ (tin) including DR for $d = 0$ to 5.....	141
Figure 3.21	Comparison of rate equations in CR model of [1] and [16] Sn V (left) Sn XIV (right) .....	143
Figure 3.22	$\langle z \rangle$ versus $T_e$ (tin) for different rate equations [16].....	143
Figure 3.23	Atomic number density versus electron temperature (eV) 99% Sn, 1% O (top) 1% Sn, 99% O (bottom) [28] .....	146
Figure 3.24	Relative intensity versus temperature and wavelength (weighted by fractional ion distribution at 25, 30, 35, 40, 45, and 50 eV).....	148
Figure 3.25	Relative intensity versus wavelength (sum Sn V–Sn XIV).....	148
Figure 3.26	Relative intensity versus wavelength showing contributing ion stages (20, 30, 40, and 50, eV) .....	149

Figure 3.27	Relative intensity versus wavelength showing contributing transitions (30, 40, 50, and 60 eV) .....	150
Figure 3.28	2% figure of merit versus electron temperature for 1, 3, and 10 mirrors .....	151
Figure 3.29	Figure of merit (2%, 7.4% and full spectral range; no mirror).....	151
Figure 3.30	Mirror heating as ratio of figure of merit (7.4%/2%).....	151
Figure 3.31	Relative intensity versus temperature and wavelength .....	152
Figure 3.32	Relative intensity versus temperature and wavelength (normalised) ...	152
Figure 3.33	The 4d-4f, 4p-4d, and 4d-5p transitions (represented statistically by UTA mean wavelength and width) weighted by the fractional ion density as a function of electron temperature compared to experiment [30] (short wavelength edge).....	154
Figure 3.34	The 4d-4f, 4p-4d, and 4d-5p transitions (represented statistically by UTA mean wavelength and width) weighted by the fractional ion density as a function of electron temperature compared to experiment [30] (long wavelength edge).....	154
Figure 3.35	Calculated spectra versus experimental spectra (32 eV).....	155
Figure 3.36	Calculated spectra versus experimental spectra (45 eV).....	155
Figure 4.1	Medusa input/output .....	160
Figure 4.2	Input Medusa laser pulse (from LaserPlot) for aluminium reference case .....	163
Figure 4.3	Cylindrical target geometry .....	163
Figure 4.4	Laser incident on target (N cells = MESH) .....	164
Figure 4.5	Medusa cell map (time step versus distance) to end of simulation.....	165
Figure 4.6	Medusa cell map (time step versus distance) to 180 $\mu\text{m}$ .....	166
Figure 4.7	Time versus cell edge (to 100 $\mu\text{m}$ ).....	166
Figure 4.8	Medusa output versus distance for aluminium reference case at 0.7, 1.5, and 2.3 ns ( $v, n_e, \rho, P, T_e, \langle z \rangle$ ) .....	167
Figure 4.9	Medusa output versus time for aluminium reference case at 1.8, 2.0, and 2.3 ns ( $v, n_e, T_e, \langle z \rangle$ ) .....	168
Figure 4.10	Al ion number densities at peak of pulse (Al I to Al XIV) .....	169
Figure 4.11	Al XIII (left) and Al XIV (right) fractional ion densities at 0.5, 1.0, 1.5, 2.0, 2.5, and 3.0 ns .....	169
Figure 4.12	Al XII to Al XIV ion densities at 0.5, 1.0, 1.5, 2.0, 2.5, and 3.0 ns .....	170
Figure 4.13	Al XII, Al XIII, and Al XIV ion fraction versus time and distance.....	171
Figure 4.14	Al XIII ion fraction versus time and cell number.....	172
Figure 4.15	Aluminium electron temperature profile at 1.0, 1.5, 2.0, 2.5, and 3.0 ns .....	172
Figure 4.16	Aluminium electron and ion temperature at the peak of the pulse (1.5 ns) .....	172
Figure 4.17	Electron temperature versus distance for three mesh sizes (60, 400, 1000) .....	173
Figure 4.18	Average charge versus distance for three mesh sizes (60, 400, 1000). .....	173
Figure 4.19	Electron density (line contours) and temperature (colour) profiles from LASNEX for a $10^{11} \text{ W/cm}^2$ , 1.06 $\mu\text{m}$ , 13-ns pulse, Cu target [20] .....	174
Figure 4.20	SHM ionisation potentials as defined in [23], $Z = 1$ to 29 .....	177
Figure 4.21	$1s^2$ - $1s2p$ transitions for $Z = 1$ to 29 (using SHM) .....	178
Figure 4.22a-c	Aluminium effective charge, energy levels, and ionisation potential .....	179

Figure 4.23a-c	Tin effective charge, energy levels, and ionisation potential .....	180
Figure 4.24	SHM ionisation potentials as defined in [31], $Z = 1$ to 29 .....	181
Figure 4.25	Hydrogenic aluminium level populations a) ( $n = 1$ to 6) versus distance (peak of pulse, 1.5 ns) and b) ( $n = 1$ to 2) versus distance (1.0, 1.5, 2.0, and 2.5 ns).....	183
Figure 4.26	SHM aluminium energy levels: $l$ -degenerate [23] (left) and $nl$ -splitting [22] (right).....	184
Figure 4.27	Aluminium energy functional (zeroed to $n = 2$ ) at 49.8 eV, $n_i = 1.3 \times$ $10^{21} \text{ cm}^{-3}$ .....	185
Figure 4.28	Aluminium energy functional (zeroed to $n = 1$ ) (peak of pulse, outer 80 cells). Each line is a cell and x is marked for each level ( $n = 1$ to 6). .....	186
Figure 4.29	Average atom tin energy functional (middle of simulation, last 6 cells) .....	187
Figure 4.30	Tin energy functional ( $Y_a$ versus $E_n$ ) with Sn X $4p^6 4d^4 4f^1$ interpolation construction (middle of simulation, last cell) .....	188
Figure 4.31	Fractional level populations $4p^6 4d^5$ (black) $4p^6 4d^4 4f^1$ (green), $4p^5 4d^6$ (blue), $4p^6 4d^4 5p^1$ (red) for Sn X (middle of simulation, normalised).....	190
Figure 4.32	$N_i$ and $N_j$ level populations $4p^6 4d^5$ (black) $4p^6 4d^4 4f^1$ (green), $4p^5 4d^6$ (blue), $4p^6 4d^4 5p^1$ (red) for Sn X (middle of simulation, normalised).....	190
Figure 4.33	$\text{Al}^{12+}$ fractional level populations for $n = 1$ , $n = 2$ (dashed) and $nl = 2s_{1/2}$ (red), $2p_{1/2}$ (green), and $2p_{3/2}$ (blue), level (peak of pulse) and comparison from [11].....	191
Figure 4.34	Schematic view of cross-section through cylinder [11] .....	192
Figure 4.35	Aluminium reference case velocity versus time and distance.....	196
Figure 4.36	Aluminium $1s_{1/2} - 2p_{3/2}$ and $1s_{1/2} - 2p_{1/2}$ line profile at 500 eV.....	197
Figure 4.37	Aluminium $1s_{1/2} - 2p_{3/2}$ and $1s_{1/2} - 2p_{1/2}$ line profile and sum at $T_e = 453$ eV, 390 <sup>th</sup> cell (left) and 174 eV, 400 <sup>th</sup> cell (right) at peak of the pulse .....	197
Figure 4.38	Aluminium spectra summed intensity (peak of pulse, no absorption, $y =$ 0) .....	198
Figure 4.39	Aluminium spectra summed intensity (peak of pulse, absorption, $y = 0$ ) .....	198
Figure 4.40	Patel <i>et al.</i> [11] intensity versus wavelength for an optically thin static case (dotted) and with the effects of velocity field on line shape (solid) .....	199
Figure 4.41	Aluminium spectra (relative intensity from cell 400–390 (left) and for all cells (right) at 1.0 ns, 1.5 ns, and 2.0 ns.) .....	200
Figure 4. 42	Maximum intensity as a function of time (top), cell number at maximum emission (middle), and corresponding depth (bottom).....	201
Figure 5.1a-h	Sn reference case hydrodynamic output.....	206
Figure 5.2	Electron and ion temperature at different times (left: 18 ns, 23 ns, and 28 ns; right: 23 ns, 49 ns, and 79 ns) .....	207
Figure 5.3	Ion fractions and ion densities versus distance for Sn V–Sn XIV at the peak of the pulse .....	207
Figure 5.4a	Sn VI (top), Sn X (middle), and Sn XIV (bottom) level populations versus distance before the peak of the pulse (18 ns).....	208
Figure 5.5	Experimental multiple-Gaussian (dashed) and simulated Medusa single- Gaussian (solid) laser pulse .....	211
Figure 5.6	Calculated spectra at different laser power densities ( $0.5\text{--}3.0 \times 10^{11}$ $\text{W}/\text{cm}^2$ for 1064 nm, 15 ns FWHM, cylindrical geometry, 90 $\mu\text{m}$ radius, 20 cell simulation) .....	213

Figure 5.7	Calculated spectra at 0.5, 0.6, 0.7, 0.9 1.0, 1.1, 1.3, 1.5, 2.0, and 3.0 x 10 <sup>11</sup> W/cm <sup>2</sup> (for 1064 nm, 15 ns FWHM, cylindrical geometry, 90 μm radius, 20 cell simulation) .....	214
Figure 5.8	Conversion efficiency versus laser power density (0.5 to 3.0 x 10 <sup>11</sup> W/cm <sup>2</sup> for 1064 nm, 15 ns FWHM, cylindrical geometry, 90 μm radius, 20 cell simulation) .....	215
Figure 5.9	Plasma length (x) and maximum electron temperature (o) versus power density (0.5 to 2.0 x 10 <sup>11</sup> W/cm <sup>2</sup> at 1064 nm, 15 ns FWHM, cylindrical geometry, 90 μm radius, 20 cell simulation) .....	216
Figure 5.10	Calculated 0.9 x 10 <sup>11</sup> W/cm <sup>2</sup> versus experimental 0.82 x 10 <sup>11</sup> (top) and 0.91 x 10 <sup>11</sup> W/cm <sup>2</sup> (bottom) spectra (1064 nm, 15 ns FWHM, cylindrical geometry, 90 μm radius, 20 cell simulation) .....	217
Figure 5.11	Spectra versus selected times (19–31 ns) (0.9 x 10 <sup>11</sup> W/cm <sup>2</sup> at 1064 nm, 15 ns FWHM, cylindrical geometry, 90 μm radius, 20 cell simulation) (top: optically thick including absorption, bottom: no absorption).....	218
Figure 5.12	Calculated spectra versus time at five wavelengths (for 0.9 x 10 <sup>11</sup> W/cm <sup>2</sup> , 1064 nm, 15 ns FWHM, cylindrical geometry, 90 μm radius, 20 cell simulation) .....	219
Figure 5.13	Laser pulse profile for 0.5, 0.6, 0.7, 0.9, 1.0, 1.1, 1.3, 1.5, 2.0, and 3.0 x 10 <sup>11</sup> W/cm <sup>2</sup> (for 1064 nm, 15 ns FWHM, cylindrical geometry, 90 μm radius, 20 cell simulation).....	219
Figure 5.14	Calculated spectra at different pulse lengths (7 to 23 ns (FWHM) for 1064 nm, 0.9 x 10 <sup>11</sup> W/cm <sup>2</sup> , cylindrical geometry, 90 μm radius, 400 cell simulation) .....	220
Figure 5.15	Calculated spectra versus time at five frequencies (for 20 ns FWHM, 1064 nm, 0.9 x 10 <sup>11</sup> W/cm <sup>2</sup> , cylindrical geometry, 90 μm radius, 20 cell simulation) .....	221
Figure 5.16	Laser pulse profile for 7, 10, 15, 20, and 23 ns FWHM (for 1064 nm, 0.9.0 x 10 <sup>11</sup> W/cm <sup>2</sup> , cylindrical geometry, 90 μm radius, 20 cell simulation) ..	221
Figure 5.17	Normalised spectra versus time at five wavelengths: 15 ns FWHM (top) and 10 ns FWHM (bottom) (1064 nm, 0.9 x 10 <sup>11</sup> W/cm <sup>2</sup> , cylindrical geometry, 90 μm radius, 20 cell simulation) .....	222
Figure 5.18	Spectral intensity at 13.5 nm versus power density: survey 1 (top) and survey 2 (bottom) (1064 nm, cylindrical geometry, 90 μm radius, 20 cell simulation) .....	223
Figure 5.19	Calculated spectra at different laser cut-off times (1/4, 1/2, and 3/4, 1064 nm, 0.9 x 10 <sup>11</sup> W/cm <sup>2</sup> , 15 ns FWHM, cylindrical geometry, 90 μm radius, 20 cell simulation) .....	224

## List of Tables

Table 1.1	General regions of spectral interest .....	11
Table 1.2	Orbital occupancy of Sn I to Sn XXIII ions .....	20
Table 1.3	Sn V to Sn XX 4p-4d and 4d-4f transitions.....	31
Table 1.4	Proposed EUVL 13.5-nm sources .....	35
Table 1.5	Nd:YAG laser specifications .....	51
Table 1.6	SEMATECH roadmap metrics [92] .....	53
Table 1.7	Semiconductor manufacturing source and component size.....	53
Table 1.8	Specifications for Mo/Si mirror example in Figure 5.1 (default settings in [27]).....	58
Table 2.1	Initial tin scaling percentages (Sn VI to Sn XIV).....	64
Table 2.2	Experimental line classification for Sn ions (Sn VI to Sn VIII).....	67
Table 2.3	Sn VII line comparisons (Azarov [7] and Cowan) .....	67
Table 2.4	Sn scaling (Sn V–Sn XIV).....	70
Table 2.5	In-band $\Sigma$ gf (*ionised at 92 eV).....	70
Table 2.6	Transition statistics (*total number of configurations = $3n + 2$ , where $n$ is the highest Rydberg series level) .....	70
Table 2.7	4d-4f statistics (UTA) .....	83
Table 2.8	4p-4d statistics (UTA) .....	84
Table 2.9	4d-5p statistics .....	85
Table 2.10	4d-4f, 4p-4d, and 4d-5p UTA statistics .....	87
Table 2.11	Broadening survey .....	103
Table 2.12	Reduced UTA width ratios (flat broadening) .....	104
Table 2.13	Reduced UTA width ratios 7.4% range (Doppler and electron impact broadening) .....	105
Table 2.14	Wavelength dependence on spectral region (full) .....	107
Table 2.15	Wavelength dependence on spectral region (7.4%).....	107
Table 2.16	Wavelength dependence on spectral region (2%).....	107
Table 3.1	Atomic processes and their inverses .....	115
Table 3.2	Fractional ion density versus temperature .....	130
Table 3.3	Tin ( $Z = 50$ ) ionisation potentials .....	136
Table 3.4	Mean wavelength and width for full spectral region .....	147
Table 3.5	Fractional ion density versus temperature .....	147
Table 4.1	Main <b>Medusa</b> input (aluminium reference case).....	161
Table 4.2	Main <b>Medusa</b> input (tin UTA case).....	162
Table 4.3	More’s screening factors $\sigma(n,m)$ [22] .....	176
Table 4.4	Marchand <i>et al.</i> ’s screening factors $\sigma(n,m)$ [24] .....	176
Table 4.5	Au ionisation data (eV), Au I–V.....	178
Table 4.6	Fe XV effective $Z$ data for $Z_1$ – $Z_4$ .....	178
Table 4.7	Tin energy level data, Sn VI–XVI.....	178
Table 4.8	<b>Medusa</b> screening factors $\sigma(n,m)$ BLOCKDATA bdat:sig(10,10) [1–5].....	181
Table 4.9	Aluminium average atom level populations ( $n = 1$ to 6) at 100 $\mu\text{m}$ and edge (peak of pulse).....	182
Table 4.10	Tin populations at middle of simulation for last 6 cells from <b>Medusa</b> .....	187

Table 4.11	Tin UTA mean wavelength and corresponding energies.....	187
Table 4.12	Tin $4d^{N-1} 4f^1$ and $4p^5 4d^{N+1}$ reduced population probability, $Y_a$ (middle of simulation, last cell).....	188
Table 4.13	Tin excited state mean UTA energies ( $E$ ), degeneracies ( $D$ ), and reduced population probabilities $F(C)$ (middle of simulation, last cell) .....	190
Table 5.1	Tin reference case input laser variables .....	205
Table 5.2	Power density survey from $0.5$ to $2.0 \times 10^{11}$ W/cm <sup>2</sup> (1064 nm, 15 ns FWHM, cylindrical geometry, 90 $\mu$ m radius, 400 cell simulation).....	212
Table 5.3	Pulse length survey from 7 to 23 ns (FWHM) (1064 nm, $0.9 \times 10^{11}$ W/cm <sup>2</sup> , cylindrical geometry, 90 $\mu$ m radius, 20 cell simulation) .....	220
Table 5.4	Pulse cut-off survey from 1/4 to 3/4 full length (1064 nm, $0.9 \times 10^{11}$ W/cm <sup>2</sup> , 15 ns (FWHM), cylindrical geometry, 90 $\mu$ m radius, 20 cell simulation) .....	224

# 1. An introduction to laser-produced plasma spectroscopy

## 1.1 Spectroscopy

Spectroscopy is the determination of atomic structure from spectral lines, recorded by the emission or absorption of energy incident on matter. The beginning of modern spectroscopy has been variously attributed to Newton [5], Fraunhofer [6], Kirchhoff and Bunsen [7, 8], Ångström [9], Rydberg [10], and Bohr [8], among others. A brief survey of the major advancements in spectroscopy (theoretical and experimental) follows, divided before and after 1885, the year J. J. Balmer showed that the visible spectrum of hydrogen could be explained by a simple mathematical series [11].

### 1.1.1 Spectroscopy before 1885

In 1666, Isaac Newton separated sunlight into component colours using a prism in a darkened room, observing how light of different wavelengths traveled at different velocities through glass (as the index of refraction of glass increases from red to violet). As Newton wrote in his *Opticks* [12]:

This Image or Spectrum P T was coloured, being red at its least refracted end T, and violet at its most refracted end P, and yellow green and blew in the intermediate spaces. Which agrees with the first Proposition, that Lights which differ in Colour do also differ in Refrangibility.

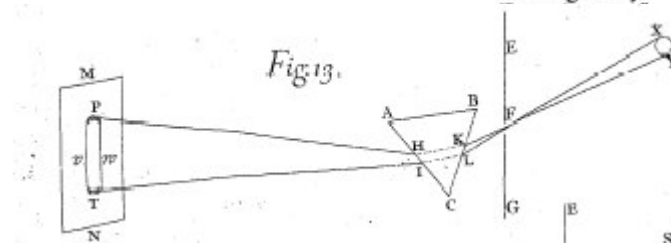


Figure 1.1 Newton's Figure 13 from his 1704 *Opticks*

Building on Wollaston, who in 1802 observed seven dark emission bands in the sun's spectrum [13]<sup>1</sup>, Fraunhofer, in 1814, used a narrow slit instead of a prism [13] and the first diffraction grating (300 lines/cm) [6] to further measure the absorption lines in the sun's spectrum. In 1853, Ångström showed that "some of the lines in the spectrum of an electric spark come from the metal electrodes and others from the gas between them" [14] and also introduced standards in wavelength measurement by interpolating between lines expressed in ten-billionths of a metre ( $10^{-10}$  m), thereafter known as the angström, Å [6]. In 1859, Kirchhoff connected wavelengths to particular atoms; in particular, the sun's spectrum to the emission band of sodium vapour heated in a flame<sup>2</sup> (the yellow doublet Fraunhofer D lines at

<sup>1</sup> Wollaston was testing glass to improve telescope lenses.

<sup>2</sup> In his correspondence with Kelvin, Stokes had already identified sodium.

5896 Å and 5890 Å) [5, 6]. Other spectroscopic advances included the work of Stokes in 1862, who observed the transparency of quartz (using a spark source, quartz optics, and fluorescence detection) [6], thus extending the range of spectral measurement to 1830 Å. Photographic plates, discovered in 1839 by Daguerre, were used to record spectra in the ultraviolet as well as the visible range, further increasing the short wavelength limit of the observed spectral range, as did the concave diffraction grating invented in 1882 by Rowland, which focussed and resolved spectral output, leading to more precise wavelength determination [6].

By 1885, both the prism (developed by Newton) and the diffraction grating (developed by Fraunhofer) were being used to record a wealth of spectral data from numerous sources. The interpretation of such spectra, however, would require further theoretical advances in atomic structure (see Condon and Shortley [15]).

### 1.1.2 Spectroscopy after 1885

In 1885, Balmer made a remarkable mathematical observation about the spectrum of hydrogen [11] that, as such, is my starting point to modern spectroscopy.

Prior to Balmer's discovery, various numerical patterns had been observed in Hartley's zinc spectra [7, 15] (at University College Dublin) and the alkalis and alkaline earth spectra of Liveing and Dewar, when wave numbers (the reciprocal of wavelengths) were used instead of wavelengths [7, 13], but it was Balmer's simplification—connecting the visible hydrogen spectrum to a straightforward mathematical formula—that first suggested an underlying atomic structure, though as yet unknown (Figure 1.2). ( $\lambda$  is wavelength,  $R$  a constant, later the Rydberg constant, and  $n$  an integer  $> 2$ .)

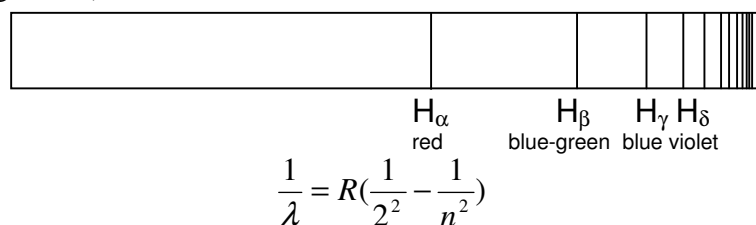


**Figure 1.2** Hydrogen spectra and related series formula

In 1890, Rydberg developed a generalised form of Balmer's formula<sup>3</sup> [9, 10], which explained the series of hydrogen lines later discovered for  $n = 1$  (Lyman series) in the ultraviolet,  $n = 3$  (Paschen series) and  $n = 4$  (Brackett series) in the infrared and also applied to atomic spectra of alkali metals, all of which further supported the empirical observations of Balmer and Rydberg.<sup>4</sup> ( $R$  is the Rydberg constant and  $n_1$  and  $n_2$  are integers with  $n_2 > n_1$ .)

$$\frac{1}{\lambda} = R\left(\frac{1}{n_1^2} - \frac{1}{n_2^2}\right)$$

**Figure 1.3** Rydberg's general series formula

<sup>3</sup> Developed five years after Balmer, Rydberg did not know of Balmer's work [9].

<sup>4</sup> The Balmer ( $n = 2$ ) and higher series ( $n > 2$ ) are, necessarily, for excited hydrogen atoms.

Soon after, the simple representation of observed spectra as a subtraction of terms became known as the Rydberg-Ritz combination principle [10, 13, 15], thus formalising the integral order to the position of spectral lines.<sup>5</sup>

By 1900, however, it was becoming clear that classical mechanics could not explain the various atomic observations; in particular, the blackbody ultraviolet spectrum and the Rydberg-Ritz combination principle. Building on the work of Zeeman, who explained the splitting of spectral lines in a magnetic field<sup>6</sup> [16], Planck, who explained the blackbody spectrum by assuming a discrete or quantized radiation of energy rather than a classical, continuous radiation, and Rutherford's proton-electron atomic model, Neils Bohr was able to make the first detailed theoretical model of the atom (Figure 1.4).

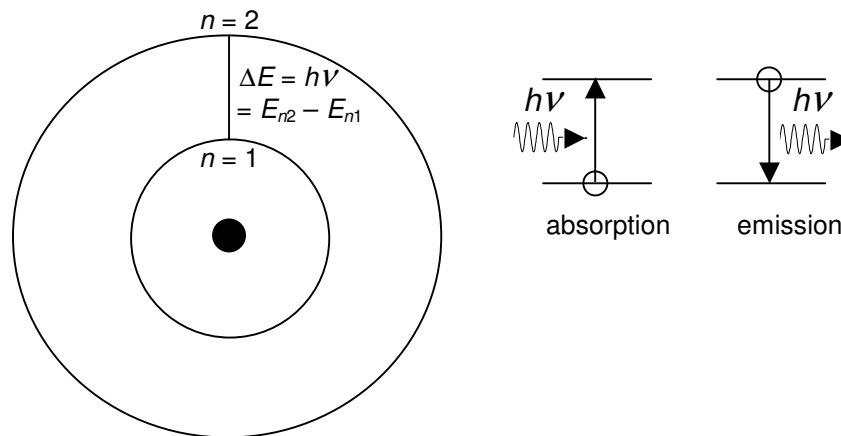


Figure 1.4 The Bohr quantum model

Bohr assumed that an electron moved in discrete orbits and radiated energy only during a transition from one orbit to another, according to the frequency condition:

$$\Delta E = E_{n_2} - E_{n_1} = h\nu \quad (1.1)$$

where  $\Delta E$  is the emitted or absorbed energy,  $n_1$  and  $n_2$  are integers representing the upper and lower orbital shells with corresponding energies ( $n_2 > n_1$ ),  $h$  is Planck's constant and  $\nu$  is the frequency of the emitted or absorbed radiation. Bohr also derived a relation for the energy levels of a one-electron atom (Eq. 1.2) as a function of the Rydberg constant,  $R$ , the atomic number,  $Z$ , and the orbital shell,  $n$ , thereafter identified as the principal quantum number of an electron.

$$E_n = -R_Z \frac{Z^2}{n^2} \quad (1.2)$$

<sup>5</sup> Bohr's quantum model later equated  $n$  to the electron shell number of the one-electron hydrogen atom or one-electron, hydrogen-like (or *hydrogenic*) atoms (e.g.,  $\text{He}^+$ ,  $\text{Li}^{++}$ , . . .). A series formed from hydrogenic atoms is known as a Rydberg series.

<sup>6</sup> The anomalous Zeeman effect was first observed at UCD by Robert Preston.

Bohr's derivation of the hydrogen energy levels (as well as the Rydberg constant) from already determined fundamental constants was a major confirmation of the quantum theory. Although his model has been superseded by the wave mechanics of Schrödinger, Heisenberg, and Dirac, it was a great success in explaining theoretically what Balmer had observed thirty years earlier for the one-electron hydrogen atom. Indeed, not until Bohr's theoretical explanation of Balmer's series did spectroscopy become established as the primary tool for determining atomic structure from spectral lines.

Concurrent to the early theoretical developments in spectroscopy, experimental advancements included Rowland's concave grating (1882), where a grating is ruled onto a concave mirror, in which the entrance slit, grating, and resultant spectrum lie on a circle (known as the Rowland circle), thus collimating as well as dispersing light [8, 17]. Rowland also improved upon the ruling of gratings to as much as 43,000 lines per inch [17].

Schuman extended the UV range to 1200 Å by reducing the absorbing gelatin from photographic plates, conducting experiments under vacuum to eliminate oxygen absorption (1893), and substituting glass and then quartz lenses with fluorite [6, 17]. Lyman's improved fluorite optics further extended the "vacuum ultraviolet" or VUV range to 500 Å [6]. Grazing incidence spectrometers, which overcome high absorption at normal incidence, lowered the observed spectral range to 350 Å. As well, blazed gratings (developed by Wood [17] in 1910), with multiple etchings arranged in a saw tooth (or *echelette*) fashion, magnified the shifted zeroth-order lines at a given blaze angle to increase intensity within a desired range [8].

By the early 20<sup>th</sup> century, spectral measurements ranged from the infrared (IR) to the extreme ultraviolet (EUV) and, thereafter, spectroscopy flourished with the development of the quantum mechanical understanding of spectra, compiling of spectral tables, and faster computers.

Richtmyer *et al.* [7] and Edlén [10] give good historical reviews of the important steps following Balmer's mathematical relation of wavelength to the visible spectrum of hydrogen lines, including Rydberg's more general mathematical explanation and Bohr's quantum interpretation. Edlén also describes the LS coupling scheme and spectral nomenclature of Russell and Saunders, theoretical developments by Condon and Shortley [15], the compiled spectral data of Moore (30,000 energy levels and 482 different spectra of 73 elements [10]), and Grotrian's graphic description of term systems. For reference, Figure 1.5 shows Moore's Table 9 entry [18] for Sn I and Figure 1.6 shows a Grotrian diagram for Sn I to Sn LI created from a screened hydrogenic model (described in Chapter 4).

TABLE 9. PREDICTED TERMS OF THE  $S_n$  I ISOELECTRONIC SEQUENCE<sup>7</sup>

Configuration $1s^2 2s^2 2p^6 3s^2 3p^6 3d^{10}$ $4s^2 4p^6 4d^{10} +$	Predicted Terms				
$5s^2 5p^2$	$\left\{ \begin{array}{l} {}^3P \\ {}^1S \quad {}^1D \end{array} \right.$				
$5s 5p^3$					
	$ns (n \geq 6)$	$np (n \geq 6)$	$nd (n \geq 5)$	$nf (n \geq 4)$	-----
$5s^2 5p(2P^\circ) nx$	$\left\{ \begin{array}{l} {}^3P^\circ \\ {}^1P^\circ \end{array} \right.$	$\begin{array}{l} {}^3S \quad {}^3P \quad {}^3D \\ {}^1S \quad {}^1P \quad {}^1D \end{array}$	$\begin{array}{l} {}^3P^\circ \quad {}^3D^\circ \quad {}^3F^\circ \\ {}^1P^\circ \quad {}^1D^\circ \quad {}^1F^\circ \end{array}$	$\begin{array}{l} {}^3D \quad {}^3F \quad {}^3G \\ {}^1D \quad {}^1F \quad {}^1G \end{array}$	----- -----
$5s 5p^2(4P) nx'$		$\left\{ \begin{array}{l} {}^5P \\ {}^3P \end{array} \right.$	$\begin{array}{l} {}^5S^\circ \quad {}^5P^\circ \quad {}^5D^\circ \\ {}^3S^\circ \quad {}^3P^\circ \quad {}^3D^\circ \end{array}$	$\begin{array}{l} {}^5P \quad {}^5D \quad {}^5F \\ {}^3P \quad {}^3D \quad {}^3F \end{array}$	$\begin{array}{l} {}^5D^\circ \quad {}^5F^\circ \quad {}^5G^\circ \\ {}^3D^\circ \quad {}^3F^\circ \quad {}^3G^\circ \end{array}$

Figure 1.5 Moore's tables for Sn I [18]

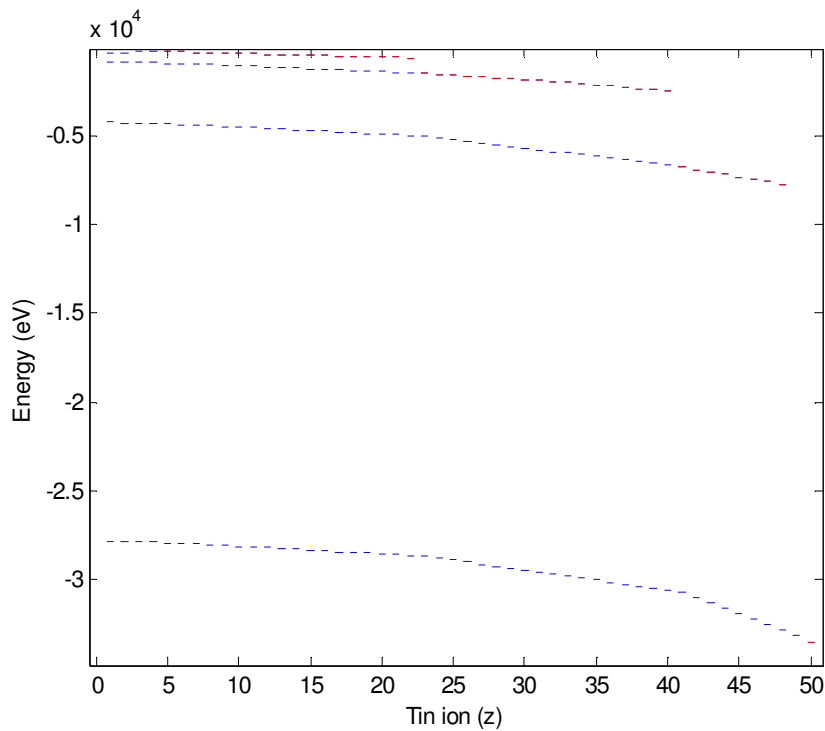


Figure 1.6  $l$ -degenerate Grotrian diagram from screened hydrogenic model (Sn I to Sn LI)

<sup>7</sup> A term label is given as  $^{2S+1}L_J$ , where  $2S+1$  is the multiplicity,  $S$  is the total spin,  $L$  the total orbital momentum, and  $J$  the total angular momentum. For example,  ${}^1S$  is a “singlet S” and  ${}^3P$  is a “triplet P,” etc. By definition, only S terms are singlet.

More recently (in the 1960s), the Cowan code [19] was developed at Los Alamos National Laboratory for multi-electron, Hartree-Fock configuration interaction (HF CI) solutions to the Schrödinger wave equation. Atomic spectra for the neutral atom and successive ion stages are interpreted using the Slater-Condon theory of atomic structure. Figure 1.7 shows a sample Cowan code input file for the tin ion  $\text{Sn}^{10+}$  ( $\text{Sn XI}$  in spectroscopic nomenclature), giving the  $\text{Sn XI}$  ground state ( $[\text{Kr}] 4p^6 4d^4$ ) and three excited configurations ( $4p^5 4d^5$ ,  $4p^6 4d^3 4f^1$ , and  $4p^6 4d^3 5p^1$ ), representing  $\text{Sn XI}$  4p–4d, 4d–4f, and 4d–5p transitions.

Figure 1.8 shows the resultant calculated oscillator strength versus wavelength plots for the ions  $\text{Sn VI}$  to  $\text{Sn XIV}$ , all with transitions of the general form  $4p^6 4d^N \rightarrow 4p^5 4d^{N+1} + 4p^6 4d^{N-1} 4f^1 + 4p^6 4d^{N-1} 5p^1$  over the emission range from 10–20 nm. Here,  $N$  indicates the number of 4d subshell electrons in the ground state.

```

2 -9 2 10 0.2 5.e-08 1.e-11-2 0150 1.0 0.65 0.0 1.0 -6
50 11sn p64d4 4p6 4d4
50 11sn p54d5 4p5 4d5
50 11sn d34f1 4p6 4d3 4f1
50 11sn d35p1 4p6 4d3 5p1
-1

```

ground state  
 4p → 4d  
 4d → 4f  
 4d → 5p

Figure 1.7 Cowan code input file for Sn XI

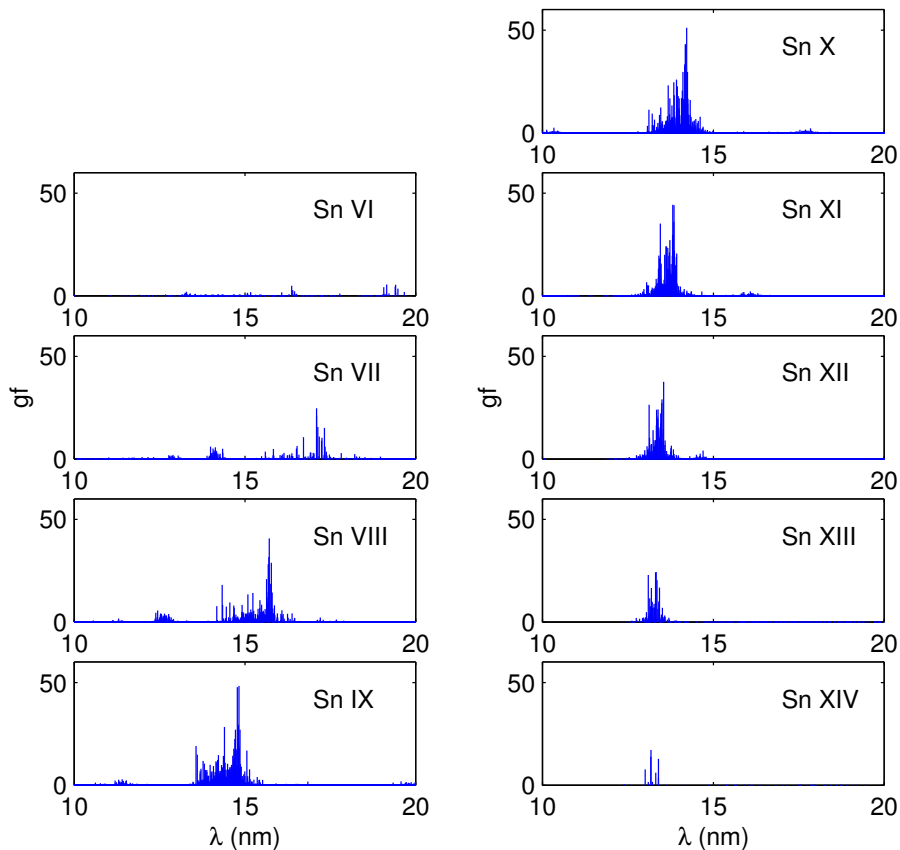


Figure 1.8 Calculated  $gf$  versus wavelength output from the Cowan code for  $\text{Sn VI}$  to  $\text{Sn XIV}$ . (Theoretical spectra of the 4p-4d, 4d-4f, and 4d-5p emission. Each line represents a transition.)

Other Cowan output includes the energy and angular momentum of the initial and final state, wavefunction solutions, and eigenvalues. The Cowan code can also determine ionisation energies for a complete sequence of ions.

Herzberg [20] gives a good outline of the quantum mechanical description required for one-electron atoms and Froese-Fischer [21] for more complex multi-electron and Hartree-Fock numerical solutions. Condon and Odabaşı [13] is an excellent guide to atomic structure calculations. Cowan's *The theory of atomic structure and spectra* [19] and a number of addenda give a comprehensive description of the theory of MCHF calculations and practical use of the Cowan code.

Excellent accounts of the experimental side of atomic spectroscopy are found in Thorne [8] and Samson [17].

### 1.1.3 The spectrometer

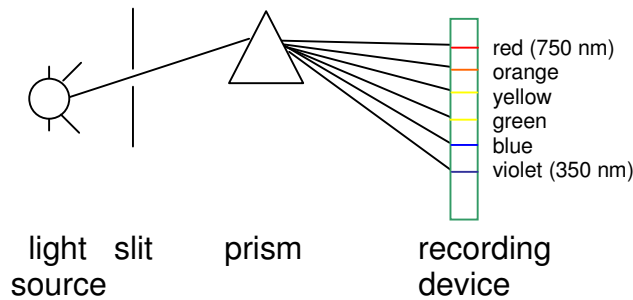


Figure 1.9 A simple spectroscopy in the visible range

Etymologically, one looks through a *spectroscope*, takes a picture with a *spectrograph*, and measures wavelength and intensity with a *spectrometer* [8], although, in practice, *spectrometer* is used to refer to the entire spectroscopic set-up. The basic components are shown in Figure 1.9, where a light source (arc, spark, discharge lamp, laser-produced plasma) is collimated by a slit and dispersed by a prism or diffraction grating, the angle of which is measured by a photographic plate, charge-coupled device (CCD) camera, or micro-channel plate (MCP) detector. Different diffraction gratings (plane, concave, grazing, or blazed) can be used at normal or grazing incidence to record spectra in different wavelength regions (shown schematically in Figure 1.10) and are either transmission or reflection type.

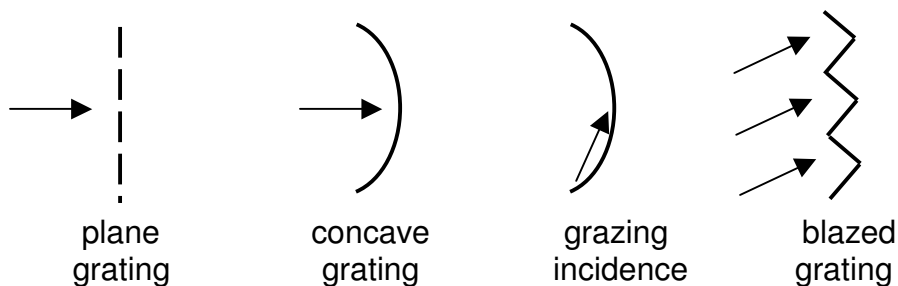


Figure 1.10 Diffraction gratings schematic

#### 1.1.3.1 Spectral range

The spectral range in atomic spectroscopy is typically from 3,000 nm (3  $\mu\text{m}$ ) to 1 nm, although the x-ray range continues to about 0.01 nm, corresponding to the Lyman series of fully stripped, high- $Z$  elements [10]. Figure 1.11 gives the common nomenclature for spectral ranges from the visible (750–350 nm) to the x-ray (0.1 nm). The vacuum ultraviolet range (VUV)<sup>8</sup> is 200–20 nm (2000–200  $\text{\AA}$ ), as defined by Boyce in [20] from the opacity of air.

<sup>8</sup> VUV is a term used by scientists, whereas DUV (deep ultraviolet) is an industry term. Extreme UV is known as XUV by scientists and EUV in industry (hence EUVL for EUV lithography, typically an industry process). There is also an overlap between the VUV and SXR (soft x-ray) regions, corresponding to energy changes in the outer electrons (VUV) or inner electrons (SXR) of an atom or ion [17].

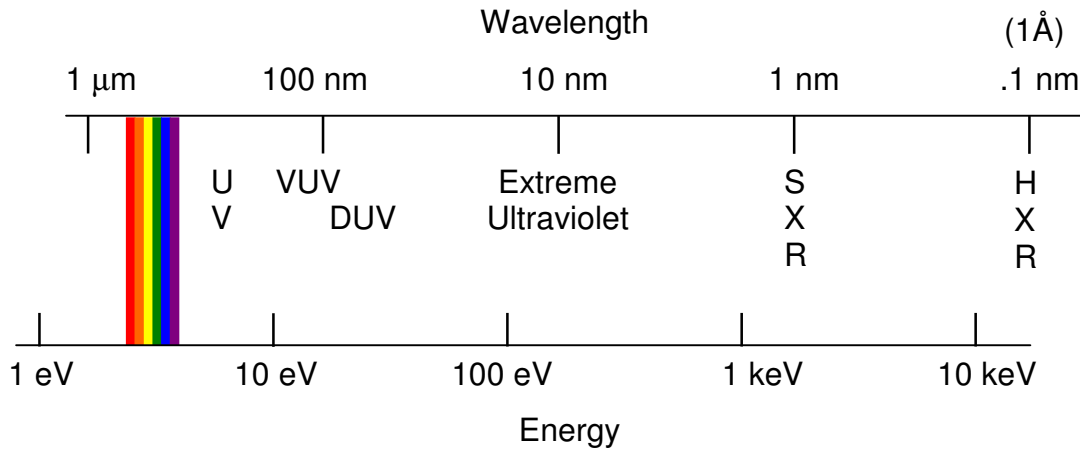


Figure 1.11 The electromagnetic spectrum from 1  $\mu\text{m}$  to .1 nm

The nanometre ( $10^{-9}$  m) is used interchangeably with the electron volt (1 nm wavelength = 1.24 keV energy), although the angström (roughly equal to the diameter of the hydrogen atom) is still popular [22]<sup>9</sup>. One eV equals 11,600 K or about 10,000 K [4] (1 electron volt/Boltzmann constant =  $1.602 \times 10^{-19}$  J/eV /  $1.381 \times 10^{-23}$  J/K = 11,600 K/eV). Wavenumbers (the reciprocal of wavelength in  $\text{cm}^{-1}$ ) are used more in molecular spectroscopy than in atomic spectroscopy.

Many technological advances over the years have improved upon the basic prism spectrometer to lower the observable spectral range. As described by Herzberg [20]; “Lenses, prisms, and windows of glass can be used only in the region from 3  $\mu\text{m}$  to 3600  $\text{\AA}$ . At lower wavelengths, glass absorbs light almost completely and this necessitates the use of quartz or fluorite. Quartz begins to absorb appreciably at 1800  $\text{\AA}$ , and therefore fluorite must be used below this wavelength. Fluorite itself begins to absorb strongly at 1250  $\text{\AA}$ , so that below this wavelength only reflection gratings can be used, with complete exclusion of lenses and windows.”

Below 2000  $\text{\AA}$ , a vacuum is required, because air (or, more precisely, oxygen) absorbs at this wavelength, the same principle as in the ozone ( $\text{O}_3$ ) layer absorbing UV radiation. Quartz (or synthetic fused silica,  $\text{SiO}_2$ ) is replaced below 1800  $\text{\AA}$  by other crystals to 1040  $\text{\AA}$  (the crystal transmission limit)<sup>10</sup> [8], such as lithium fluoride ( $\text{LiF}$ , 1400  $\text{\AA}$ ), fluorite ( $\text{CaF}_2$ , 1300  $\text{\AA}$ ), or magnesium fluoride ( $\text{MgF}_2$ , 1100  $\text{\AA}$ ).

The reflectivity of all materials decreases with wavelength (generally less than 35% at 1000  $\text{\AA}$  and dropping to a few percent at 300  $\text{\AA}$  [23]), thus, below about 350  $\text{\AA}$ , gratings must be used at grazing incidence. At shorter wavelengths, however, the higher energy photons are more easily detected [8, 20]. To focus as well as disperse, a concave grating is used, the theory of which was primarily developed by Rowland [24]. Blazed gratings at a given grazing angle can also be used to amplify first-order spectra. To make diffracted light focus from a concave grating onto a flat focal plane, grooved rules of varied spacing can be used to create a flat field for imaging onto a CCD camera [25].

<sup>9</sup> The hydrogen atom diameter equals  $1.06 \text{ \AA}$  or  $2a_0$ , where  $a_0 = 0.529 \text{ \AA}$  is the Bohr radius, determined from Bohr’s orbital atomic model. In multi-electron atoms, most electronic charge is within  $2a_0$ .

<sup>10</sup> The region above 1040  $\text{\AA}$  is known as the *Schumann* region whereas the region below 1040  $\text{\AA}$  is known as the *Lyman* region [4] (formerly 1250  $\text{\AA}$ , the transmission limit of fluorite [11]), in honour of the two pioneering spectroscopists Schumann and Lyman.

At wavelengths below 300 Å, resolving power decreases from losses in optical performance in the grazing region [22].

As mirror reflectivity decreases even further with decreased wavelength, multilayer mirrors must be used, for example, in semiconductor photolithography [26] to reflect and focus incident radiation. A multilayer mirror is constructed with alternating layers of high- and low- $Z$  elements (*e.g.*,  $N = 40$  layers of Mo/Si, the semiconductor industry choice for 13.5 nm). The theoretical reflectivity versus wavelength is determined from the Fresnel equations as described by Kohn [26]. The theoretical reflectivity for a 40-layer Mo/Si mirror is shown in Figure 1.12 [27]. In an industrial setting, where the light source can be reflected numerous times during semiconductor manufacturing as shown in Figure 1.13 [28], a high minimum reflectivity is required. The theoretical maximum is 75% in a 3.7% band (FWHM) as shown, currently best manufactured to around 70%.

For reference, regions of spectral interest are outlined in Figure 1.14 and Table 1.1.

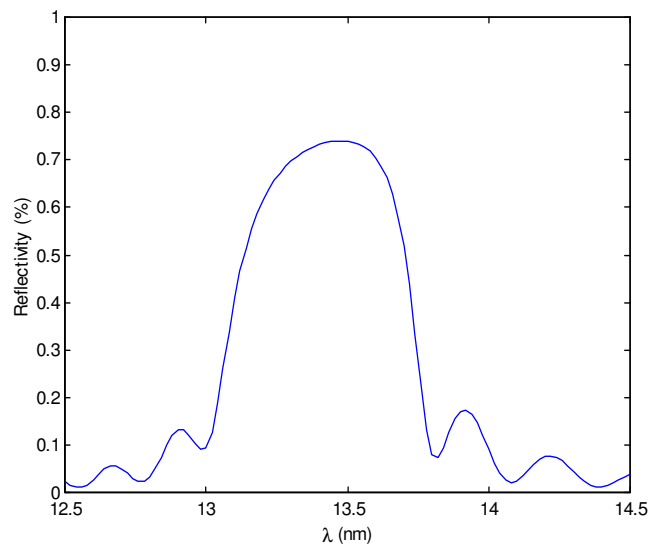


Figure 1.12 Multilayer Mo/Si mirror reflectivity versus wavelength ( $N = 40$ )

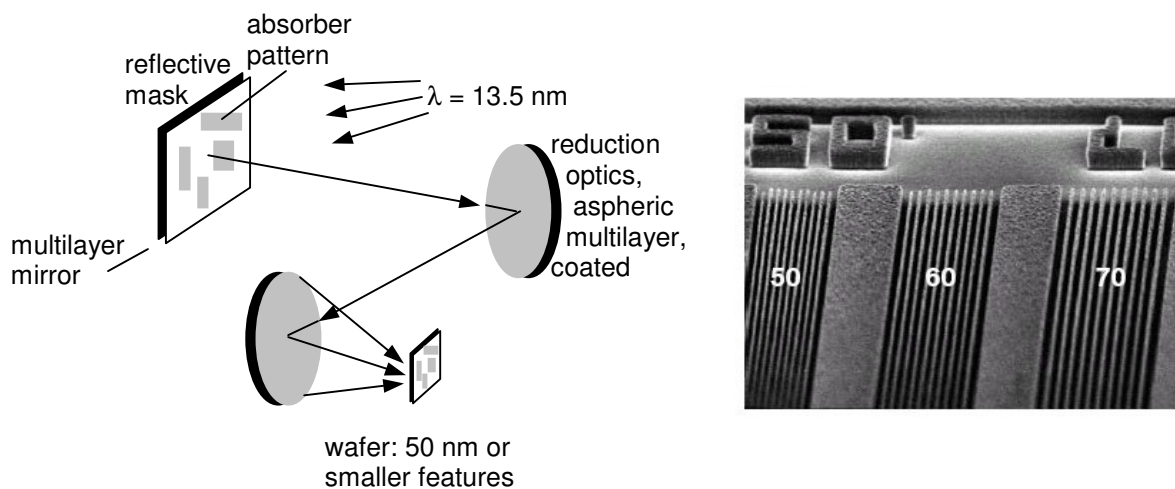
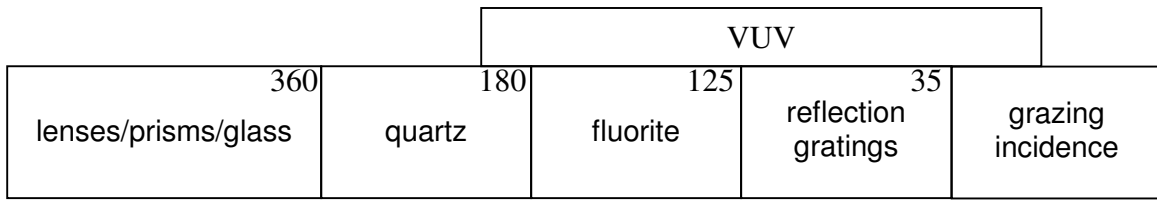


Figure 1.13 Multi mirror optics set-up for semiconductor manufacturing [28]



**Figure 1.14** Regions of spectral interest (nm) for lithography

Range (nm)	
> 700	infrared
750–350	visible range (red to blue)
400–200	ultraviolet
< 360	glass absorbs [20]
200–20	VUV, from the opacity of air as defined by Boyce [20]
< 200	oxygen absorbs
< 180	quartz absorbs appreciably [20]
< 125	fluorite absorbs strongly [20]
121.57	Lyman $\alpha$
< 104	gratings only (crystal transmission limit) [8, 20], no windows transmit
< 35	grazing incidence (reflectivity decreases)
4.38–2.34	water window (oxygen to carbon K-absorption edge)
1.08	shortest optical emission line [17]
1.06	hydrogen atom diameter
0.529	Bohr radius ( $a_0$ )
0.47	shortest x-ray line [17]
0.01	Lyman series of fully stripped high-Z atoms [10]

**Table 1.1** General regions of spectral interest

### 1.1.3.2 The Rowland circle mounting

To diffract and, at the same time, focus radiation at grazing incidence in the VUV, a spectrometer is typically mounted such that the grating (G), entrance slit (S), and detector (D) all lie on a circle, called the Rowland circle [17] (Figure 1.15). The concave grating is mounted tangentially to the Rowland circle and with rulings perpendicular to the Rowland plane, where the radius of curvature of the grating,  $R$ , is equal to the diameter of the Rowland circle. The incident radiation is collimated by the entrance slit at an angle of incidence ( $\alpha$ ), and diffracted, as well as focused, onto the Rowland circle at a resultant angle of diffraction ( $\beta$ ).

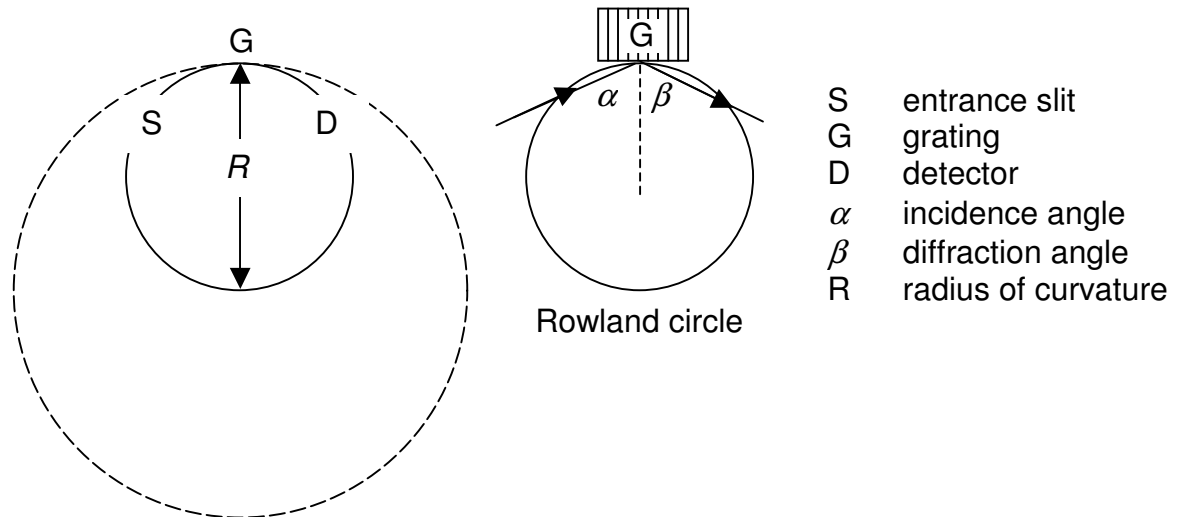


Figure 1.15 The Rowland circle

The angle of diffraction,  $\beta$ , is determined from the grating equation for grazing incidence (Eq. 1.3), the theory of which was primarily developed by Rowland [24].

$$m\lambda = d(\sin(\alpha) + \sin(\beta)) \quad (1.3)$$

$$\therefore \beta = \sin^{-1}\left(\frac{m\lambda}{d} - \sin(\alpha)\right) \quad (1.4)$$

As can be seen in Figure 1.16, longer wavelengths diffract at smaller angles to the normal and, thus, lie at greater distances ( $R \cos(\beta)$ ) along the Rowland circle.

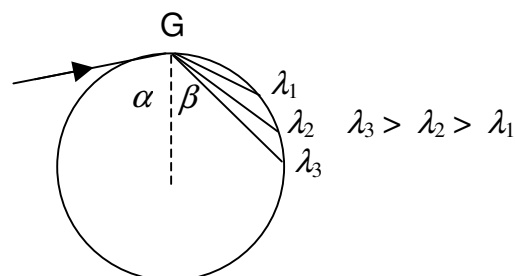


Figure 1.16 Wavelength dispersion along the Rowland circle

Cornu gives the first geometrical treatment of the plane grating with constant groove spacing [29], including first-order errors, while Zernicke uses Fermat's principle of least time [30]. Beutler [31] extended the work of Rowland and Zernicke, although corrections to his work were required and found for resolving power in Mack *et al.* [32], and astigmatism and dispersion in Sai *et al.* [33]. Meijer [34] reported that the Rowland circle is a theoretical, coma-free, first-order approximation and must be corrected for non-constant groove spacing to align spectra onto a self-focussing curve with acceptable coma. For large  $R$ , the focal curve deviates appreciably from the Rowland circle (several centimetres for  $R$  of 6.60 m) [34].

In a concave mirror, the major aberration is astigmatism, where a point on the slit is imaged as a vertical line (*i.e.*, focussed only in the horizontal plane) [17]. Although such astigmatism can be tolerated, it reduces the diffracted intensity and requires precise focussing for maximum resolution [17].

From the principles of geometric and physical optics [24, 29–30, 32–33], the dispersion (angular dispersion,  $d\beta/d\lambda$ , and linear dispersion or plate factor,  $d\lambda/dl$ ), resolving power ( $R_p$ ), and astigmatism ( $z$ ) are determined to a first-order approximation as given below in Eqs. 1.5–1.9. The resolving power is expressed in terms of the optimum grating width,  $W$ , as described by Mack *et al.* [32].

$$\frac{d\beta}{d\lambda} = \frac{m}{d \cos(\beta)} \quad (1.5)$$

$$\frac{d\lambda}{dl} = \frac{\cos(\beta)}{mR \frac{1}{d}} \left[ \times 10^4 \frac{\text{\AA}}{\text{mm}} \right] \quad (1.6)$$

$$R_p = 0.75W \frac{m}{d} \quad (1.7)$$

$$W = 10 \times 1.18 \times \frac{4\lambda R_p^3}{\pi [\tan(\alpha) \sin(\alpha) + \tan(\beta) \sin(\beta)]} \quad (1.8)$$

$$z = l \left[ \frac{\cos(\beta)}{\cos(\alpha)} \right] + L [\sin^2(\beta) + \sin(\alpha) \tan(\alpha) \cos(\beta)] \quad (1.9)$$

where  $m$  is the spectral order,  $d$  is the groove width,  $R$  is the radius of curvature of the grating,  $W$  is the optimum slit width,  $\lambda$  is the incident radiation wavelength,  $l$  is the slit length,  $L$  is the grating length, and  $\alpha$  and  $\beta$  are the incident and diffracted angles.

A comprehensive treatment to VUV spectroscopy, including the theory of concave gratings and the derivations of Eqs. 1.5–1.7 and Eq. 1.9, is given in Samson [17]. Alignment methods for grazing incidence spectrometers, particularly correcting for non-constant groove spacings, are found in Meijer [34, 35].

The location of 13.5 nm (91.84 eV) on the Rowland circle (as well as the dispersion, resolving power, astigmatism, *etc.*) is shown in a snapshot in Appendix A from the program Rowland written for this thesis.

### 1.1.4 Spectral lines

A spectral line is the physical record of the transition of an electron between two energy levels. In Sn X, a spectral line at 13.5 nm (corresponding to a transition of 91.84 eV) identifies an excited 4f electron returning to the 4d ground state (a 4d-4f transition). An absorption spectrum shows the absence of a 4d-4f transition, the corresponding incident radiation having been absorbed.<sup>11</sup>

Spectral lines are recorded by photographic plate (and converted to a densitometer trace, as in Figure 1.17) or by a charge-coupled device (CCD) camera or micro-channel plate (MCP) detector. In Figure 1.17, a number of line transitions can be seen superimposed over a continuum-like transition array.

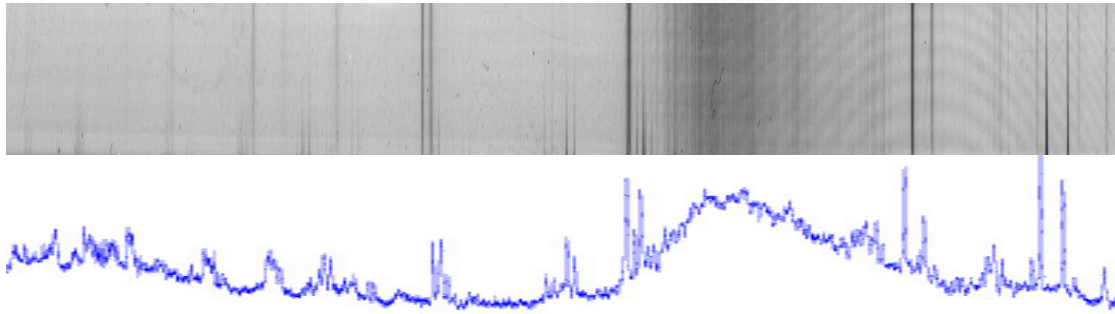


Figure 1.17 5% tin in araldite spectra: photographic plate (top) and densitometer trace (bottom) [48]

Spectral lines are characterized by position (transition wavelength,  $\lambda$ ), intensity (weighted oscillator strength,  $gf$ ) and line width,  $\Gamma$  [10]. The relative intensities depend on the light source and excitation conditions. Natural line widths are proportional to the transition time and are inversely proportional to  $Z^2$  [17].

The width (and shape) of a spectral line is also affected by temperature and pressure. As temperature increases, the number of populated excited states increases and, hence, the number of transitions. To a much lesser degree, as temperature increases, the atomic velocities increase and, thus, line width is broadened, called Doppler broadening. For example, from 300 K to 3000 K, the line width (full width half maximum as defined in [5]) changes from 0.0075 Å to 0.24 Å [5]. As pressure increases, the number of atomic collisions increase, resulting in a shift of energy levels and, hence, line positions (to lower frequencies [5]), called pressure broadening.

As well, external electric (**E**) and magnetic (**B**) fields separate degenerate energy levels, with corresponding “line splitting.” Stark broadening is caused by a fluctuating electric field near a radiating atom [36], and Zeeman broadening by an external magnetic field. In low-density plasma discharges, the “Zeeman effect” produces much greater splitting than the “Stark effect.” In higher-density LPPs, the Stark effect is greater. The Stark effect also exists internally, resulting from the electric field between a proton and electron [5]. For more information on Stark broadening, see O’Reilly [37].

Broadening effects add up, but are generally dominated by one effect only, depending on the temperature and density. Emission and absorption lines can also have different widths.

<sup>11</sup> A transition between an excited state and the ground state is known as a “resonance” line. Satellite lines are transitions between two excited states.

Different functions are used to model the line width: a Gaussian function (Eq. 1.10) for Doppler broadening, a Lorentz function (Eq. 1.11) for pressure broadening, and a Voigt function for mixed Gaussian/Lorentzian.

$$f(x) = \frac{1}{\sigma\sqrt{2\pi}} e^{-\frac{(x-\mu_1)^2}{2\sigma^2}} \quad (1.10)$$

$$f(x) = \frac{1}{1 + \left(\frac{x-c}{w}\right)^2} \quad (1.11)$$

where both the Gaussian and Lorentz functions are characterised by only two parameters (Gaussian: mean,  $\mu_1$ , standard deviation,  $\sigma$ , and Lorentz function: centre,  $c$ , and width,  $w$ ). Broadening is discussed further in Section 2.3, *Line broadening*.

Figure 1.18 shows a spectral line convolved with a Gaussian of standard deviation 2 and a Lorentzian of width 1. The Gaussian is concentrated more in the centre (“rectangular”), whereas a Lorentzian is narrower in the centre and broader in the wings. The Voigt function is Gaussian near the centre and Lorentzian in the wings.

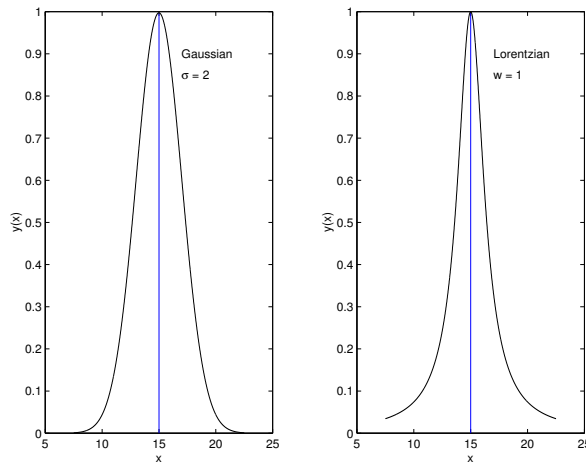


**Figure 1.18** Spectral lines convolved with Gaussian (left) and Lorentz (right) function

Spectra can reveal properties within a plasma, particularly electron temperature and electron density. As reported in Carroll and Kennedy [36], a broadened line shape depends on electron density,  $n_e$ , and, thus, electron density can be determined from line broadening. Although such diagnostics apply more to fusion plasmas, broadening in laser-produced plasmas can be seen at low ion stages.

Furthermore, because line spectra depend on the dominant ion species, knowing the ion distribution in a plasma aids identification of the resultant spectra. The ratio of line to continuum spectra (or bremsstrahlung), which changes with varying percentage target composition, can also be used to identify spectra of a particular ion species. Well-separated transitions and satellite lines are also useful.

The plasma models used to characterise spectra by ion species are discussed further in Section 1.3, *Plasma physics* and in Chapters 3 and 4.

## 1.2. Atomic physics

In this work, the theoretical energy emitted from a radiant source is determined by atomic structure calculations using existing codes, such as the Cowan code [19], a self-consistent, Hartree-Fock method to solve the Schrödinger equation for multi-electron atoms. The Cowan code calculates wavelength,  $\lambda$ , and weighted oscillator strength,  $gf$ , for a transition between two states (*e.g.*, 4d-4f transitions). The theoretical transitions are then convolved with a broadening function and/or an instrument function to match experimental results.

For the tin ions considered in this work (Sn V–Sn XIV), thousands of transitions between bands of near-degenerate energy levels overlap to form an unresolved transition array (UTA), where transitions cannot be individually identified. Statistical methods are introduced to characterise a UTA by peak wavelength and width for a given ion stage.

Proposed light sources in the required EUV range, listing the advantages and disadvantages of atomic sources for next generation lithography (NGL), are also given.

### 1.2.1 The Schrödinger wave equation

Building on Planck’s explanation of the “ultraviolet catastrophe,” where electrons oscillate in discrete energy states rather than continuously within an atom, and Bohr’s atomic model, which accurately predicted the spectra of one-electron atoms when an electron is excited or de-excited between states, the quantum mechanical models of Schrödinger, Heisenberg, and Dirac were developed to explain the experimental results of line spectra for multi-electron atoms.

Eq. 1.12 gives the time-independent Schrödinger equation in the central field approximation<sup>12</sup>, for which the four quantum numbers  $n$ ,  $l$ ,  $m_l$ , and  $m_s$  (principal, angular momentum, orbital momentum, and spin), identify a unique wavefunction,  $\psi$  (Eq. 1.13)<sup>13</sup>. As defined by their wavefunctions ( $\Psi_1$ ,  $\Psi_2$ ), the transition energy between two atomic states is the difference in the energy of each state ( $E_1$ ,  $E_2$ ). Eq. 1.13 shows the separable wavefunction,  $\Psi(r, \theta, \phi)$ , where  $P_{nl}(r)$  is the radial solution,  $Y_l^{ml}$  a spherical harmonic (expressed as an associated Legendre polynomial), and  $\chi_{ms}$  the spin eigenfunction.

$$\frac{-\hbar^2}{2m} \nabla^2 \Psi(r, \theta, \phi) + V(r)\Psi(r, \theta, \phi) = E\Psi(r, \theta, \phi) \quad (1.12)$$

$$\Psi(r, \theta, \phi) = P_{nl}(r)Y_l^{ml}(\theta, \phi)\chi_{ms}(\phi) \quad (1.13)$$

<sup>12</sup> The electrostatic potential  $V(r)$  between the orbital electrons and nuclear protons is spherically symmetric.

<sup>13</sup> For multi-electron atoms,  $n$ ,  $l$ ,  $m_l$ , and  $m_s$  are not “good” quantum numbers (*i.e.*, do not relate to quantities that can be measured) and, so,  $\mathbf{J}^2$ ,  $J_z$ , and  $\Pi$  are used.

Eq. 1.14 [38] gives the energy of a hydrogenic atom, including spin-orbit effects. The spin-orbit interaction, (the interaction of the electron magnetic moment and the magnetic field induced by its motion in an internal electrostatic field), is defined as  $H_{so} = \zeta_i(r_i) \vec{l}_i \cdot \vec{s}_i$ . The total spin is  $\mathbf{j} = \mathbf{l} + \mathbf{s}$ .<sup>14</sup>

$$E = -\frac{RhcZ^2}{n^2} \left[ 1 + \frac{\alpha^2 Z^2}{n^2} \left( \frac{n}{j + \frac{1}{2}} - \frac{3}{4} \right) + \dots \right] \quad (1.14)$$

Other than fundamental constants and the atomic number,  $Z$ , the energy,  $E$ , is a function of  $n$  and  $j$  only.<sup>15</sup> Because the energy levels are degenerate in  $n$  and  $j$ , to zero order, it is sufficient only to determine the radial solution,  $P_n(r)$  to calculate the energy.<sup>16</sup>

However, the Schrödinger equation cannot be solved exactly for anything but a simple hydrogenic atom, and approximate numerical methods are used to determine the energy for more complicated systems (and thus the wavelength and oscillator strengths). The Hartree-Fock method uses a sum of one-electron potentials, representing the Coulomb interaction between an electron and the charge density distribution of the other electrons, to obtain wavefunctions, which give the lowest energy [19]. Here, the Hamiltonian,  $H$ , given in atomic units<sup>17</sup>, is the sum of kinetic, electron-nucleus, electron-electron, and spin-orbit terms (Eq. 1.15).

$$H\Psi(r) = \left[ \sum_{i=1}^N \left( -\frac{1}{2} \nabla_i^2 - \frac{Z}{r_i} \right) + \sum_{i<j} \frac{1}{r_{ij}} + \sum_i \zeta_i(r_i) \vec{l}_i \cdot \vec{s}_i + \right] \Psi(r) = E\Psi(r) \quad (1.15)$$

A resultant transition can have a number of terms, depending on the angular momentum coupling scheme.<sup>18</sup> Eq. 1.15 assumes LS coupling and wavefunctions anti-symmetric with respect to a change of labels (Pauli exclusion principle). Initial estimates of the wavefunctions are given, the energy for each state calculated, and the wavefunctions optimised or iterated until the energy is a minimum (to a given accuracy), the so-called, self-consistent, Hartree-Fock (SCHF) method. Configuration interaction (CI) effects result from using multiple configurations ( $ns$ ,  $np$ ,  $nd$ ,  $nf$ ), giving an increased number of transitions, until at very high  $n$  the oscillator strength contributes a negligible percentage of the average energy from any new configuration.

<sup>14</sup> For multi-electron atoms,  $\mathbf{J} = \mathbf{L} + \mathbf{S}$ . Since inner shells have no angular momentum ( $\mathbf{J} = 0$ ), it is sufficient to determine  $\mathbf{J}$  only for partially filled shells (typically the outer shell, excepting the more complicated lanthanides and transition metals).

<sup>15</sup> Selection rules define allowed or forbidden transitions between states: hydrogenic atoms:  $\Delta l = \pm 1$ ,  $\Delta m_l = 0, \pm 1$ ,  $\Delta j = 0, \pm 1$ , multi-electron atoms:  $\Delta L = 0, \pm 1$ ,  $\Delta S = 0$ ,  $\Delta J = \pm 1$  (all  $J$ ),  $\Delta J = 0$  (all  $J$  except  $J = 0$ ). Selection rules essentially preserve conservation of angular momentum in the atom.

<sup>16</sup> Note that Bohr's atomic shell model is still conceptually useful, because  $\langle r \rangle_{1s} \ll \langle r \rangle_{2s} \cong \langle r \rangle_{2p} \ll \langle r \rangle_{3s}$ .

<sup>17</sup> Atomic units are used to simplify the Hamiltonian and other quantum mechanical operators, where Planck's constant,  $h$ , electron charge,  $e$ , and the reduced mass,  $u$ , are set to unity.

<sup>18</sup> Coupling is typically LS for low- $Z$  atoms and jj for high- $Z$  atoms. As  $Z$  increases, jj coupling is used instead of LS coupling because spin-orbit effects between electrons dominate electrostatic effects between electrons. For highly charged ions, LS coupling is preferred.

Considering the potential,  $V_{eff}(r)$ , explicitly in terms of the attractive Coulomb potential,  $V_c$ , and the repulsive centrifugal potential,  $V_l$ , irregularities in the periodic table (as reported by Goepfert-Meyer in 1941) and wavefunction collapse can be explained (Eq. 1.16; note SI units). Mixed valence and level crossing are also a result of the interplay of  $V_c$  ( $n$ -dependant) and  $V_l$  ( $l$ -dependant).

$$\begin{array}{c} \text{Coulomb} \quad \text{centrifugal} \\ V_{eff}(r) = \frac{Ze^2}{4\pi\epsilon_0 r} - \frac{l(l+1)\hbar^2}{2m_e r^2} \end{array} \quad (1.16)$$

Thus, in the central field approximation (with resultant spherical symmetry), where  $V_{eff}(r)$  is given in Eq. 1.16, the Hamiltonian of Eq. 1.12 is expressed as a function of  $r$  (Eq 1.17).

$$\frac{d^2}{dr^2} P_{nl}(r) + V_{eff}(r)P_{nl}(r) = EP_{nl}(r) \quad (1.17)$$

Since the angular solutions are the same, the only difference is in the radial solution,  $P_{nl}(r)$ , as given in Eq. 1.18,

$$P_{nl}(r) = e^{-Zr/a_0} \left( \frac{Zr}{a_0} \right)^l G_{nl} \left( \frac{Zr}{a_0} \right) \quad (1.18)$$

where  $a_0$  is the Bohr radius and  $G_{nl}$  is a polynomial in  $Zr/a_0$  with different forms for different  $n$  and  $l$ .

The Hartree-Fock method calculates the radial solution using calculus of variations, where  $P_{nl}$  is solved numerically by iteratively changing  $P_{nl}$  until the change between two successive wavefunctions is less than a given tolerance. The average energy of the configuration,  $E_{av}$ , is then determined from a sum of the integrated radial solutions and Coulomb integrals (or Slater integrals),  $F^k$  (direct Coulomb integral for equivalent electrons) and  $G^k$  (direct and exchange Coulomb integral for non-equivalent electrons). From the final wavefunctions,  $E_{av}$ ,  $\zeta$  (spin-orbit integral),  $F^k$ ,  $G^k$ , and  $R^k$  (configuration-interaction Coulomb integral) are determined.

The Hartree-Fock configuration interaction (HFCI) method extends the HF approximation by mixing basis sets, where a new wavefunction is found as a linear combination of Slater determinants as in Eq. 1.19, where  $\phi_i$  are configuration state functions.

$$\Psi(LS) = \sum_{i=1}^M a_i \phi_i(\alpha LS) \quad (1.19)$$

### 1.2.1.1 Wavefunction collapse

Wavefunction collapse explains the sudden transfer of electron filling or stripping from one shell to another (*e.g.*, the 4f, 5s, and 5p shells in the lanthanides or the 5f, 6s, and 6p shells in the actinides) [2, 3]. In the lanthanides, with increasing ionisation, the 4f, 5s, and 5p shells approach near degeneracy,  $l$ -dependence vanishes, and levels regroup according to  $n$ . With further ionisation, the 4f-electron binding energy increases faster than the 5s or 5p electrons, and level crossing occurs at different stages. The same applies in the actinides with 5f, 6s, and 6p shells. With open d and f shells, the resultant spectra are extremely complex, with hundreds of thousands of near degenerate lines.

For tin, level crossing is not as complex, because the 4d electrons are removed in succession. Nonetheless, as electrons are stripped away, the  $\epsilon f$ -wavefunction contracts, transferring continuum oscillator strength (4d- $\epsilon f$ ) to discrete oscillator strength (4d-4f), as reported by O'Sullivan [39] about charge-dependent wavefunction collapse in xenon. As the 4f radius decreases and overlaps with the 4d radius, level crossing occurs and intensity increases, resulting in a continuum-like, transition array of thousands of 4d-4f lines. Figure 1.19 shows the 4f wavefunction contracting (top) and the  $l = 3$  radial potential (bottom) for Sn I through Sn XIV.

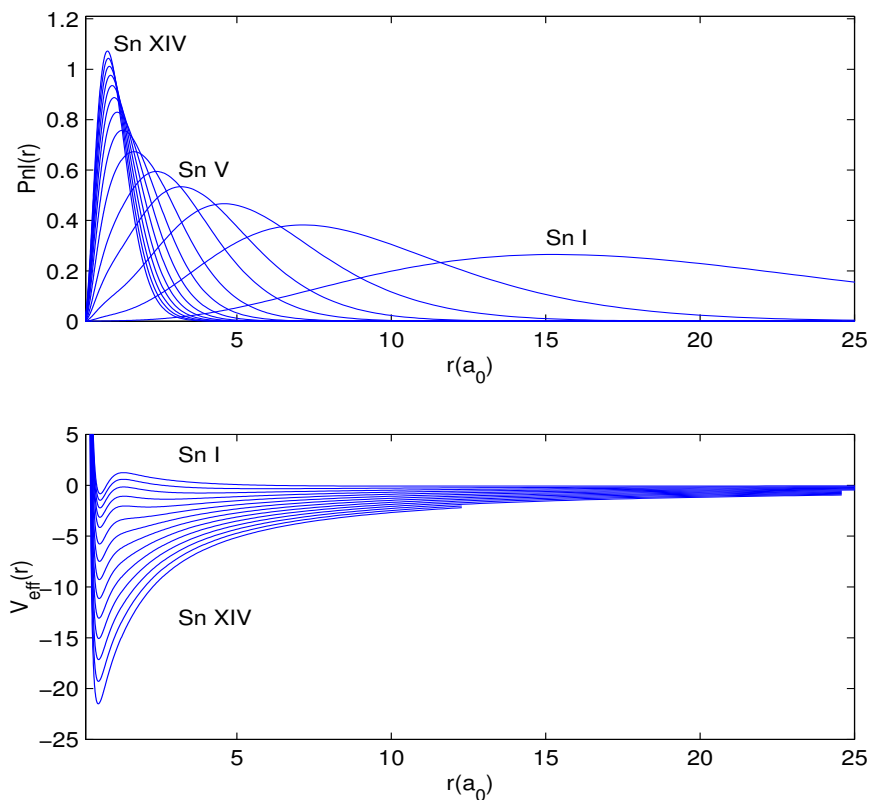


**Figure 1.19** Wavefunction contraction and radial potential as a function of ionisation: Sn I–XIV

For reference, the ground state configuration, LS term label, and orbital occupancy ( $\xi$ ) of the first 22 tin ions are given in Table 1.2.

Ion	Z-like	Configuration*	$^{2S+1}L_J$	$\xi$
Sn I		[Kr] 4d <sup>10</sup> 5s <sup>2</sup> 5p <sup>2</sup>	<sup>3</sup> P <sub>0</sub>	2
Sn II	In	[Kr] 4d <sup>10</sup> 5s <sup>2</sup> 5p <sup>1</sup>	<sup>2</sup> P <sub>0 1/2</sub>	1
Sn III	Cd	[Kr] 4d <sup>10</sup> 5s <sup>2</sup>	<sup>1</sup> S <sub>0</sub>	2
Sn IV	Ag	[Kr] 4d <sup>10</sup> 5s <sup>1</sup>	<sup>2</sup> S <sub>0 1/2</sub>	1
Sn V	Pd	[Kr] 4d <sup>10</sup>	<sup>1</sup> S <sub>0</sub>	10
Sn VI	Rh	[Kr] 4d <sup>9</sup>	<sup>2</sup> D <sub>2 1/2</sub>	9
Sn VII	Ru	[Kr] 4d <sup>8</sup>	<sup>3</sup> F <sub>4</sub>	8
Sn VIII	Tc	[Kr] 4d <sup>7</sup>	<sup>4</sup> F <sub>4 1/2</sub>	7
Sn IX	Mo	[Kr] 4d <sup>6</sup>	<sup>5</sup> D <sub>4</sub>	6
Sn X	Nb	[Kr] 4d <sup>5</sup>	<sup>6</sup> S <sub>2 1/2</sub>	5
Sn XI	Zr	[Kr] 4d <sup>4</sup>	<sup>5</sup> D <sub>0</sub>	4
Sn XII	Y	[Kr] 4d <sup>3</sup>	<sup>4</sup> F <sub>1 1/2</sub>	3
Sn XIII	Sr	[Kr] 4d <sup>2</sup>	<sup>3</sup> F <sub>2</sub>	2
Sn XIV	Rb	[Kr] 4d <sup>1</sup>	<sup>2</sup> D <sub>1 1/2</sub>	1
Sn XV	Kr	[Ar] 3d <sup>10</sup> 4s <sup>2</sup> 4p <sup>6</sup>	<sup>1</sup> S <sub>0</sub>	6
Sn XVI	Br	[Ar] 3d <sup>10</sup> 4s <sup>2</sup> 4p <sup>5</sup>	<sup>2</sup> P <sub>1 1/2</sub>	5
Sn XVII	Se	[Ar] 3d <sup>10</sup> 4s <sup>2</sup> 4p <sup>4</sup>	<sup>3</sup> P <sub>2</sub>	4
Sn XVIII	As	[Ar] 3d <sup>10</sup> 4s <sup>2</sup> 4p <sup>3</sup>	<sup>4</sup> S <sub>1 1/2</sub>	3
Sn XIX	Ge	[Ar] 3d <sup>10</sup> 4s <sup>2</sup> 4p <sup>2</sup>	<sup>3</sup> P <sub>0</sub>	2
Sn XX	Ga	[Ar] 3d <sup>10</sup> 4s <sup>2</sup> 4p <sup>1</sup>	<sup>2</sup> P <sub>0 1/2</sub>	1
Sn XXI	Zn	[Ar] 3d <sup>10</sup> 4s <sup>2</sup>	<sup>1</sup> S <sub>0</sub>	2
Sn XXII	Cu	[Ar] 3d <sup>10</sup> 4s <sup>1</sup>	<sup>2</sup> S <sub>0 1/2</sub>	1
Sn XXIII	Ni	[Ar] 3d <sup>10</sup>	<sup>1</sup> S <sub>0</sub>	10

\* Moore Sn I–Sn VI [18], Cowan code Sn VII–Sn XXIII

**Table 1.2** Orbital occupancy of Sn I to Sn XXIII ions

Orbital shell occupancy ( $\xi$ ) is required for plasma modelling, where the degeneracy is a function of the number of outer shell electrons.

### 1.2.2 The Cowan code

The Cowan code is a FORTRAN program created by Robert Cowan in 1968 [19] to solve the multi-electron, Schrödinger wave equation, and consists of four sub-codes: RCN, RCN2, RCG, and RCE. Program control is shown below in Figure 1.20.

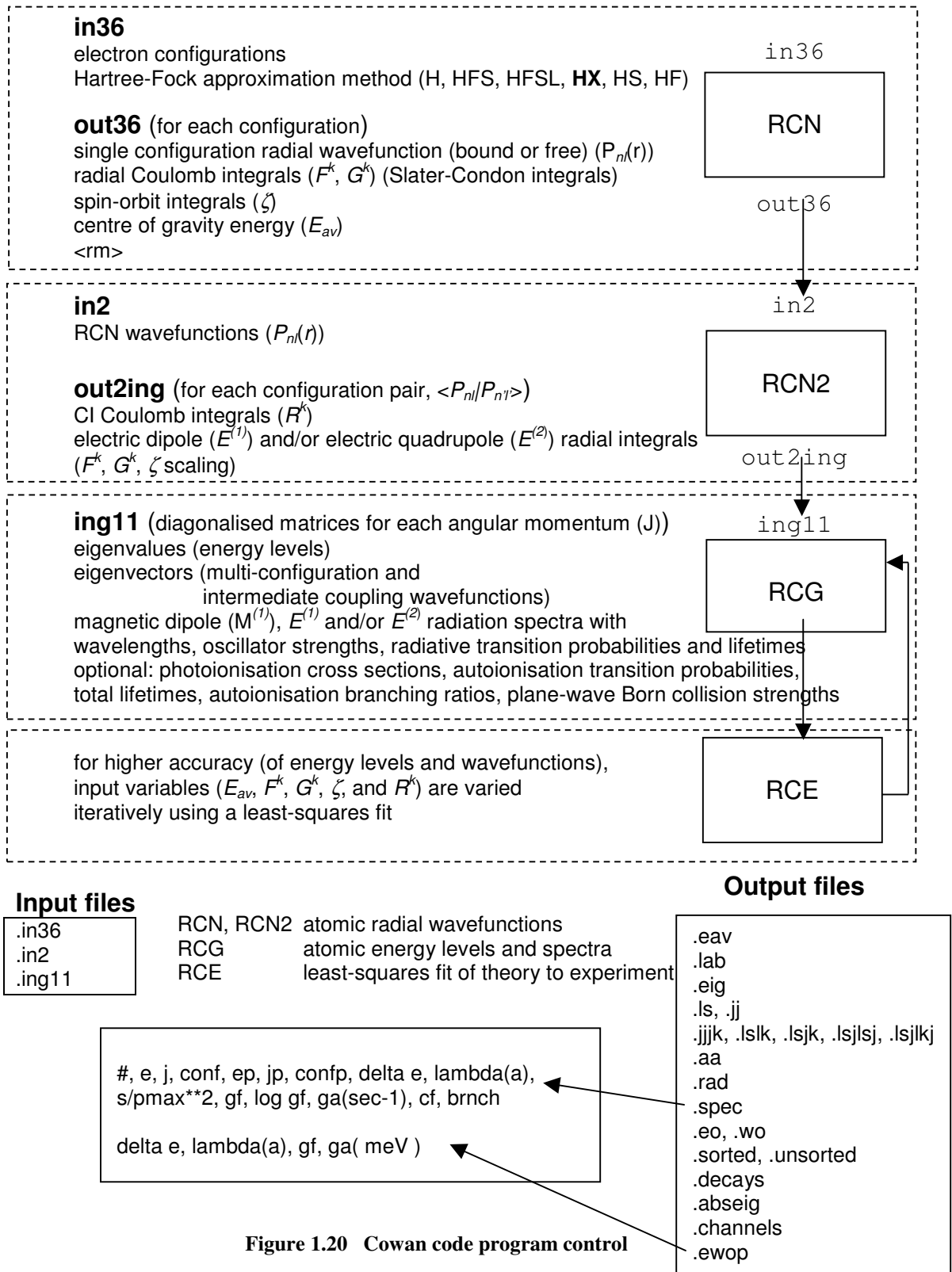
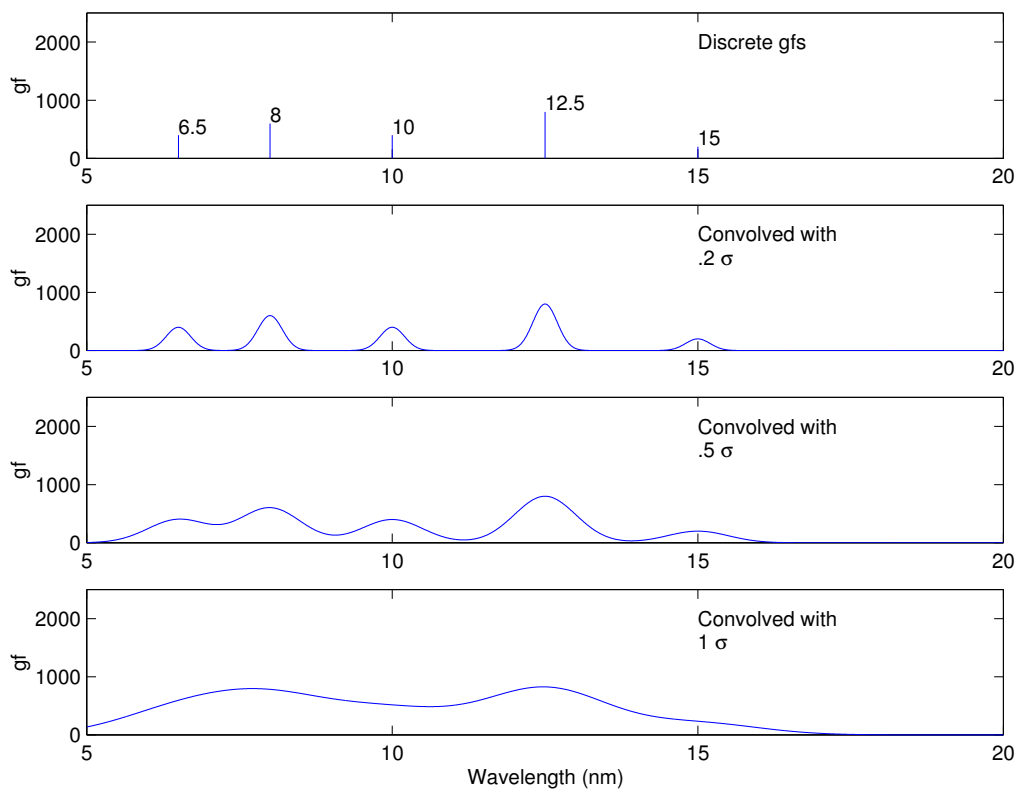


Figure 1.20 Cowan code program control

RCN solves the wavefunctions for each configuration, RCN2 calculates multi-configuration radial integrals and quantities required to calculate energy levels and spectra, which are then calculated in RCG. RCE is a least-squares fit, using Slater scaling factors to match theoretical results to experiment. The Cowan code uses a self-consistent Hartree-Fock (SCHF) method, which starts with an approximate solution for the wavefunction and iterates until the change is less than a given tolerance.

A synthetic spectrum of oscillator strength versus wavelength is produced by convolving the theoretical Cowan “stick” plot (Cowan wavelength data has no width) to model plasma and instrumental broadening, with a Gaussian or Lorentz function of prescribed width. The full width at half maximum (FWHM) is equal to  $2.35\sigma$ , where  $\sigma$  is the standard deviation. For example, Figure 1.21 shows five discrete transitions convolved with Gaussians of increasing widths ( $\sigma = .2, .5, \text{ and } 1$ ). The Gaussians are normalised such that the  $gf$  value is equal to the amplitude.



**Figure 1.21** Discrete Cowan  $gf$  versus  $\lambda$  convolved with Gaussians of varying width  $\sigma$ , where  $\text{FWHM} = 2.35\sigma$

Two files are required as input to Cowan: a single-line (`filename.in2`) and a multi-line configuration file (`filename`). The Cowan code automatically adds electron shells for the highest noble gas with atomic number  $< Z - (\text{spectrum number} - 1)$ . Configurations only beyond the highest noble gas are input by the user. Numerous output files are produced as shown in Figure 1.20, including `filename.wo`, giving weighted oscillator strengths ( $gf$  values) versus energy for allowed transitions, `filename.out36`, from which wavefunctions can be extracted, and `filename.eig`, which lists energy eigenvalues. The output is parsed in post-processing for use as input to a graphics program.

Other atomic structure codes are available, such as the multi-configuration Hartree Fock (MCHF) of Froese-Fischer [21] and Hibbert, the parametric potential method of Klapisch (RELAC), and the fully relativistic method of Grant (GRASP).

For general Cowan code notes and information on all relevant Cowan files used in this thesis, see Appendix B.

### 1.2.2.1 Slater-Condon scaling

Reduction of Slater-Condon parameters of up to 30 percent is typically required to account for the effects of electrostatic interaction with other configurations, and thus calibrate theoretical results to experiment. Five, two-digit, radial integral factors scale the energy-level structure parameters:  $F^k$  (direct Coulomb integral for equivalent electrons),  $\zeta$  (spin-orbit integral),  $F^k$  and  $G^k$  (direct and exchange Coulomb integral for non-equivalent electrons)<sup>19</sup>, and  $R^k$  (configuration-interaction Coulomb integral), where  $k$  is the  $k$ th power of the  $k$ th Legendre polynomial. Since the solutions use the same wavefunctions, the Slater-Condon scaling parameters are not independent of each other and are thus wavefunction dependent.

Cowan [19] recommends decreasing the scaling as ionisation increases. As a rough guide, the scaling factors are closest to unity when electron-correlation effects are smallest (*i.e.*, in highly ionised atoms when the energy levels are more hydrogenic). As reported in his programs addendum [40], “It is known empirically that scaling down of the HF Coulomb radial integral values by 5 to 30 percent will give RCG eigenvalues in better agreement with experimental energy levels, the smaller factors being for neutral or weakly ionised systems, with factors approaching unity for highly ionised systems.”

Breit-Pauli relativistic corrections (where jj coupling is used instead of LS coupling) is included for  $Z > 30$  [39].

---

<sup>19</sup>  $F^k$  and  $G^k$  are also known as the electrostatic-interaction integrals.

### 1.2.3 The unresolved transition array (UTA)

As reported in Bauche and Bauche-Arnoult [41], Condon and Shortley (following Harrison and Johnson in 1931) called a transition array “the totality of lines between the levels of two electronic configurations.” They added that the first published experimental work was by Edlén in 1947, who recorded spectra generated by low inductance vacuum sparks in a band of a few hundred angströms, and that Cowan and co-workers were the first to attempt to interpret unresolved bands as transition arrays. They also stated that the width of a transition array narrows with ionisation since  $\Delta E/E$  is proportional to  $1/Z$  and that a transition array is a superposition of a number of ion stages. Peyrusse [42] reported that broadband line emission features are present in plasma emission for mid- to high- $Z$  elements. Jin and Richardson [43] reported that, “high- $Z$  solid targets, for example, those elements in the vicinity of tin, characteristically emit broadband spectra that come from many excited levels. These energy levels are so close that the radiation they generate in the EUV range can be considered a continuum.” Salzmann [44] stated that, as the number of bound electrons increases, the density of lines in a spectrum increases such that “their spacing is smaller than their width.”

For any given ion stage, a UTA is characterised by spectral position, width, and symmetry (Figure 1.22), and requires statistical methods to measure properly. The statistical approach is relevant because of the extreme complexity of the UTA features [45]. Calculations are not only between levels or lines, but also between groups of levels or lines [45].

The statistical parameters describing a UTA—the theory of which was developed by Cowan [19] and Bauche and Bauche-Arnoult [45]—are the weighted mean,  $\mu_1$ , variance,  $\nu$ , skewness,  $\alpha_3$ , and kurtosis,  $\alpha_4$ ,<sup>20</sup> and are determined from the  $n$ th-order centred moments of the distribution (or moments about the mean),  $\mu_n^c$ . Eq. 1.20 gives the  $n$ th-order, *non-centred* moments, expressed by  $Q_i$ , the energy difference between two levels, and  $w_i$ , the strength of line  $i$  (Eq. 1.21).

$$\mu_n = \frac{\sum_{i=1}^N (Q_i)^n w_i}{\sum_{i=1}^N w_i} \quad (1.20)$$

$$w_i = \left| \langle \alpha J | \mathbf{D}^{(1)} | \alpha' J' \rangle \right|^2 \quad (1.21)$$

where  $\mathbf{D}^{(1)}$  is the electric dipole operator and  $\alpha J$  and  $\alpha' J'$  are the relevant upper and lower levels.

More conveniently, the non-centred moments can be expressed in terms of the energy  $E_i$  (or wavelength,  $\lambda_i$ ) and weighted oscillator strength,  $gf_i$ , for each line  $i$  [4] (Eq. 1.22).  $gf$  values are used instead of intensities, assuming that the level populations in the upper level are proportional to the statistical weight  $2J + 1$  [46].

<sup>20</sup> The lower-order distribution statistics relate to the shape of the distribution. The variance is a measure of width, the skewness coefficient a measure of asymmetry, and the kurtosis coefficient a measure of excess or size of a distribution's tail.

$$\mu_n = \frac{\sum_{i=1}^N (\lambda_i)^n g f_i}{\sum_{i=1}^N g f_i} \quad (1.22)$$

The non-centred moments are centred in Eqs. 1.23–1.26, from which the UTA statistics are calculated in Eqs. 1.27–1.30.

$$\mu_1^c = \mu_1 \quad (1.23)$$

$$\mu_2^c = \mu_2 - \mu_1^2 \quad (1.24)$$

$$\mu_3^c = \mu_3 - 3\mu_1\mu_2^c - \mu_1^3 \quad (1.25)$$

$$\mu_4^c = \mu_4 - 4\mu_1\mu_3^c - 6\mu_1^2\mu_2^c - \mu_1^4 \quad (1.26)$$

$$\mu_1 = \mu_1^c \quad (1.27)$$

$$v = \sigma^2 = \mu_2^c \quad (1.28)$$

$$\alpha_3 = \frac{\mu_3^c}{v^{3/2}} \quad (1.29)$$

$$\alpha_4 = \frac{\mu_4^c}{v^2} \quad (1.30)$$

The full width at half maximum (FWHM) of the distribution can also be used as a measure of width instead of the variance as can the standard deviation,  $\sigma$ , the square root of the variance.

$$FWHM = \Gamma = 2\sqrt{2\log(2)}\sigma = 2.35\sigma \quad (1.31)$$

Skewness is positive ( $\alpha_3 > 0$ ) when the distribution is biased towards the right tail (lower energy or longer wavelength, in this case) and negative towards the left tail (higher energy or shorter wavelength). Kurtosis compares the distribution to a Gaussian (or normal) distribution, where  $\alpha_4 = 3$  for a perfect Gaussian.

Expressed in terms of the mean ( $\mu_1$ ) and standard deviation ( $\sigma$ ) only, a UTA can be represented as a Gaussian (Eq. 1.32) or, including skewness ( $\alpha_3$ ), as a skewed Gaussian (Eq. 1.33), also known as the Edgeworth expansion ( $x$  is replaced with  $(x - \mu_1) / \sigma$ ). Note that if the weighting constant  $c$  in Eq. 1.33 equals the normalisation factor in Eq. 1.32 ( $1/(\sigma\sqrt{2\pi})$ ) and  $x$  is replaced with  $(x - \mu_1) / \sigma$ , the skewed Gaussian reduces to Eq. 1.32 for  $\alpha_3 = 0$ . Note also that highly skewed Gaussians can introduce physical artefacts to the resultant statistical distribution (*i.e.*, negative numbers).

$$f(x) = \frac{1}{\sigma\sqrt{2\pi}} e^{-\frac{(x-\mu_1)^2}{2\sigma^2}} \quad (1.32)$$

$$f(x) = c \left[ 1 - \frac{1}{2}\alpha_3 \left( x - \frac{1}{3}x^3 \right) \right] e^{-\frac{x^2}{2}} \quad (1.33)$$

The weighting constant  $c$  can also be used as a statistical weight of a configuration, as in Eq. 1.34.

$$c = N_s = \prod_{i=1}^q \binom{4l_i + 2}{N_i} \quad (1.34)$$

where  $q$  is the number of open subshells of orbital quantum number  $l_i$  and occupancy  $N_i$ . Configuration weighting is used with extremely complex, multiple  $m_j$  state configurations, resulting in super transition arrays (STA) [45], and in highly ionised atoms, where the spin-orbit integral ( $\propto Z^4$ ) dominates the electrostatic repulsion ( $\propto Z$ ), to create spin-orbit split arrays (SOSA) [41].

Figure 1.22 shows spectral lines (from a typical Cowan code output) for two tin ions (Sn X and Sn XI) with fitted Gaussian and skewed Gaussian, giving UTA statistics for  $\mu_1$ ,  $\sigma$ ,  $\alpha_3$ , and  $\alpha_4$  to quantify peak wavelength, spectral width, and shape. The mean wavelength is seen to decrease with ionisation as is to be expected. Skewness can also be seen on the short wavelength side of the UTA distribution. The number of lines within the output range and the  $\Sigma gf$  are also given. Note that the area under the curve is equal to the summed oscillator strength ( $\Sigma gf$ ), here defined as invariant with width (rather than the amplitude) to facilitate the comparison of different distributions.

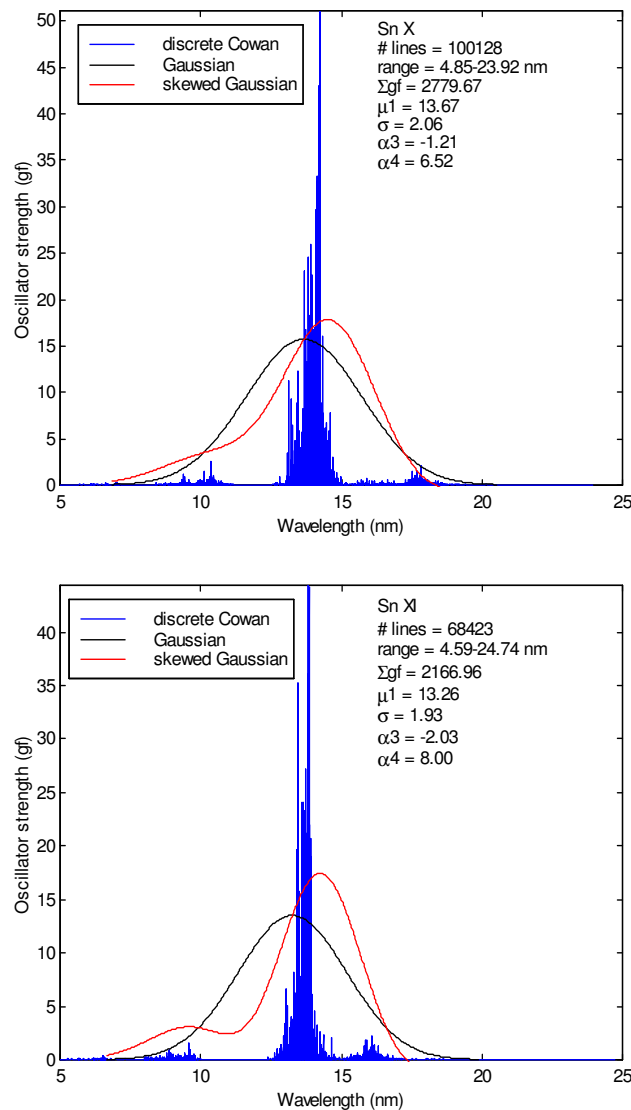


**Figure 1.22** UTA emission with UTA statistics (Sn X and Sn XI)

To calculate configuration interaction, the Cowan data used here includes high  $n$  Rydberg series transitions, which broaden the UTA (to the short wavelength side), but are not part of the UTA. Outlying data is removed by calculating statistics for specific transitions only (*e.g.*,  $\Delta n = 0$  or 4d-4f and 4p-4d transitions), which can shift the average wavelength (and energy) significantly for highly skewed data. As well, strong emission lines are not necessarily at the centre, and the UTA shape may be distorted by strong, off-centre, lines [44]. Furthermore, because weak lines (predominantly at the extremes) are overestimated in the squared variance calculation, the statistical width may be too broad, by as much as a factor of 2 as found in [47]. UTA statistics can be calculated over a limited range, although care should be used in determining the appropriate range.

Figure 1.23 shows the 4d-4f UTA for Sn X and Sn XI, with both a convolution envelope (0.2 Å FWHM width) and as a two-parameter Gaussian. Here it can be seen that the sum of the Gaussians (convolved) are reasonably represented by the Gaussian of the sums (Gaussian). The two-parameter Gaussian representation of the UTA will greatly simplify the numerous atomic calculations required in plasma modelling (see Chapter 4, *A spatial and temporal plasma model*).

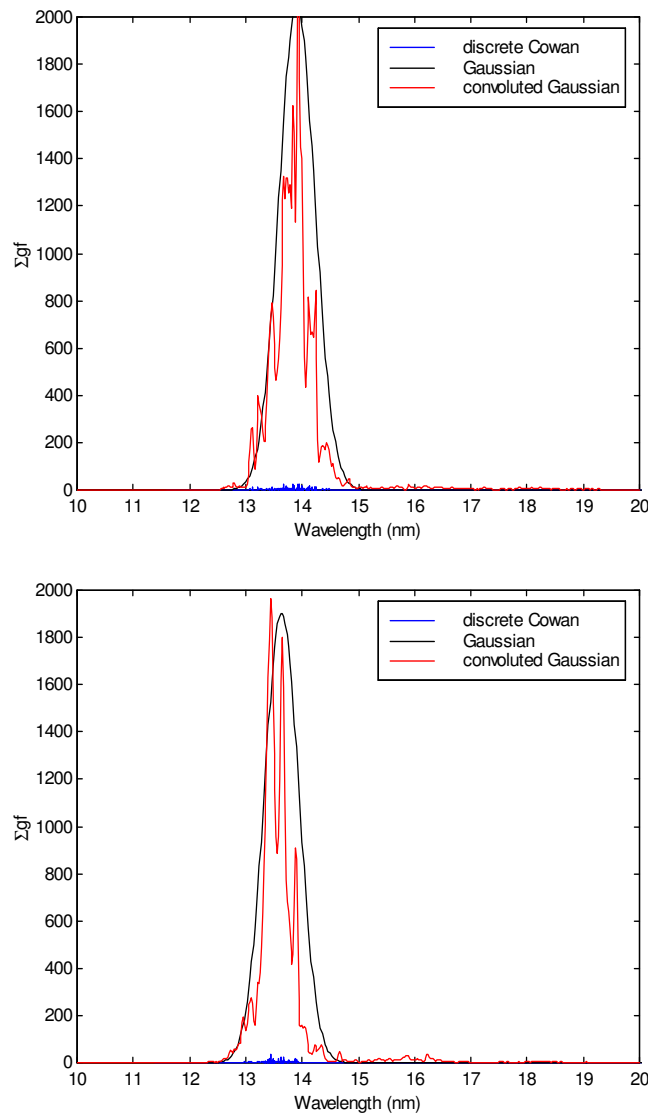


**Figure 1.23** 4d-4f UTA emission with UTA statistics: Sn X (top) and Sn XI (bottom)

As discussed above, in high- $Z$  elements, a gradual transfer of oscillator strength from continuum states to discrete states is observed with ionisation. As an element ionises, the Coulomb force increasingly dominates the  $l$ -dependent centrifugal force, and 4d- $\epsilon f$  continuum oscillator strength ( $\langle 4d|\mathbf{D}|\epsilon f \rangle$ ) transfers to discrete 4d-4f oscillator strength ( $\langle 4d|\mathbf{D}|4f \rangle$ ), resulting in a large number of transition lines that form the UTA [2, 3]. Contributing ion stages in the plasma and, hence, contributing UTAs, adds to spectral complexity. As ionisation increases (with increased laser flux and, hence, plasma temperature), the UTA shifts in position and shape (towards shorter wavelength and narrower width). For ion stages greater than Sn XIV, after all the 4d subshell electrons have been removed, however, the UTA intensity decreases.

From Figure 1.23, it can be seen that a two-parameter Gaussian curve can be used to simplify numerically complex UTA spectral output. A full UTA analysis for tin ions emitting in the 13.5-nm region is given in Section 2.1, *Theoretical Cowan and UTA statistics for Sn V–Sn XIV* and Section 2.2, *Sn 4d shell (4d-4f, 4p-4d, and 4d-5p) transition statistics*.

## 1.2.4 Tuneable EUV radiation

From their work with the lanthanides and adjacent related elements (cesium;  $Z = 55$  to lutetium;  $Z = 71$ ) in the VUV grazing-incidence region from 4 to 20 nm, O'Sullivan and Carroll [2, 3] noticed that the  $\Delta n = 0$  ( $n = 4 \rightarrow n = 4$ ) peak UTA wavelength emission decreased with increasing atomic number (Figure 1.24). Further observations showed that a number of tin ions ( $Z = 50$ ,  $\text{Sn}^{7+}$ – $\text{Sn}^{12+}$ ) and one xenon ion ( $Z = 54$ ,  $\text{Xe}^{10+}$ ) emit at 13.5 nm [4].

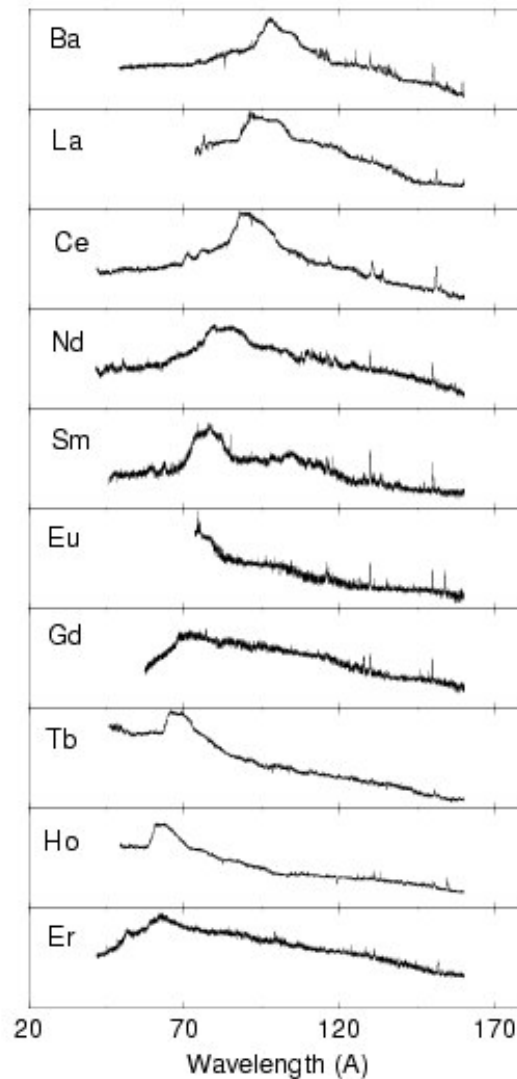


**Figure 1.24 Resonant emission versus wavelength (Ba to Er) [48]**

UTA peak wavelength versus atomic number is shown in Figure 1.25, indicating how the resonance emission transitions (or resonances [2]) move to shorter wavelengths with increasing  $Z$ . Because peak wavelength changes with atomic number ( $50 \leq Z \leq 70$ ), it was reported that “tuneable” radiation could be produced from these sources [49]. The strongest emission is at 8.75 nm from cerium ( $Z = 58$ ). However, no high-reflectivity multilayer mirrors exist at this wavelength.

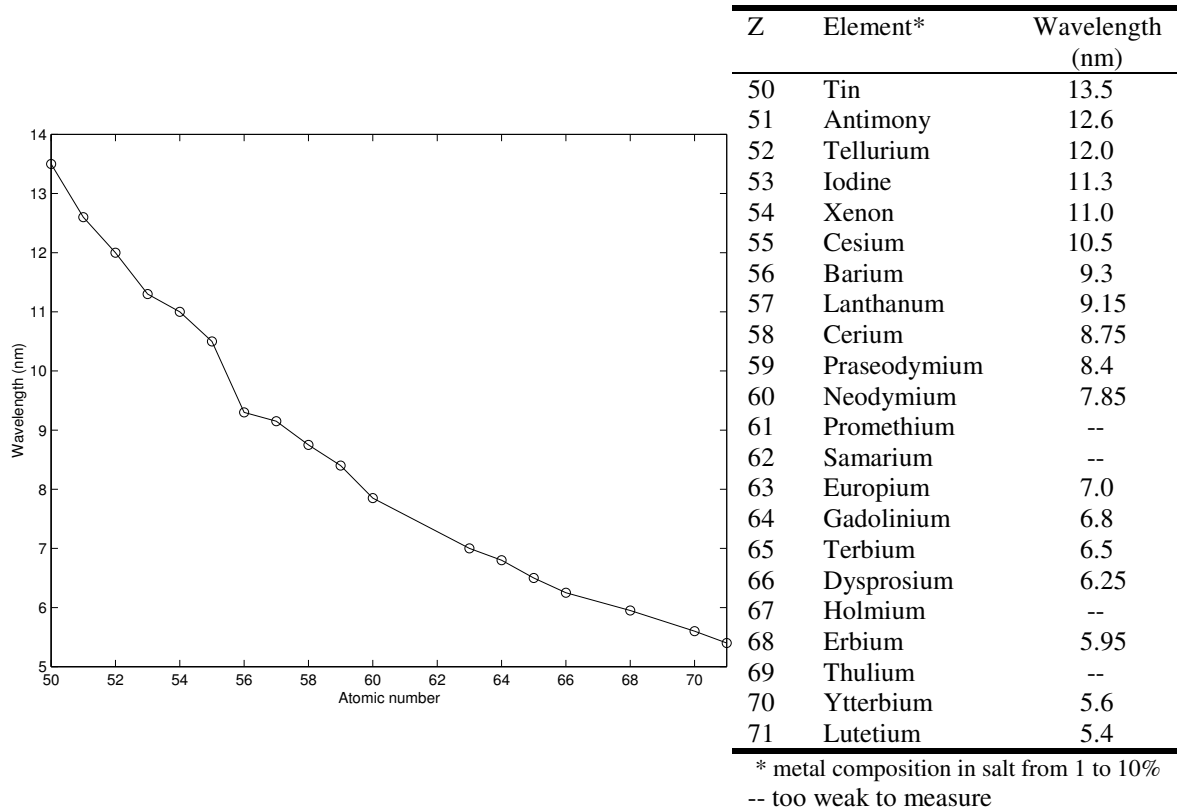


Figure 1.25 UTA peak wavelength versus atomic number [2, 3]

O'Sullivan and Carroll [2] observed that the spectra were characterised by regions of strong resonance-like emission, with typical widths of 9–18 eV and that, with increasing  $Z$ , the resonance line structure tends toward a quasi-continuum [2]. The overall structure consists of tens of thousands of unresolved lines (attributed to overlapping 4d–4f transitions), superimposed over strong well-defined lines. Dunne *et al.* [50] reported that in an optically thin plasma, for a given element concentration, millions of lines overlap in a narrow, 1-nm band and that UTA width as well as central wavelength decreased with increasing  $Z$  [50]. Since the arrays are brighter than any emission lines, the UTA can be used as an excellent narrow-band EUV source for both microscopy and lithography [51].

These UTAs show increased complexity with increasing  $Z$  and spectral width and a profile very sensitive to target concentration [49]. Since solid tin (or high-percentage tin) absorbs too much, introducing a low- $Z$ , optically thin dopant to the tin target (*i.e.*, reducing the tin percentage) can reduce the continuum emission. Furthermore, configuration interaction can result in spectral narrowing to approximately 5 eV [49].

To identify the contributing ion stages as well as the dominant ion stage in the lanthanide targets, a steady-state, collisional-radiative, laser-plasma interaction model [52] is used. Because of level crossing and wavefunction collapse, identifying the ground-state configurations of each ion stage can be difficult, although for targets from  $Z = 49$  to  $Z = 54$  identification of UTA resonances from 4d–4f and 4p–4d transitions is reasonably straightforward.

In tin, two 5p and two 5s electrons are removed first. From Sn V to Sn XIV, the 4d subshell opens up and each 4d electron is ionised in succession with resultant

4p-4d and 4d-4f emission ( $4p^6 4d^n \rightarrow 4p^5 4d^{n+1} + 4d^{n-1} 4f$ ). At higher ion stages (Sn XV–Sn XX), the d subshell is completely ionised and the 4p subshell opens up with resultant 4p-4d transitions ( $4p^n \rightarrow 4p^{n-1} 4d^n$ ) emitting in the 13.5 nm region, although with greatly reduced number of lines and oscillator strength. The tin UTA transitions are summarised in Table 1-3 as the 4d and 4p subshells empty.

Ion stage	Transitions	
Sn V–Sn XIV	$4p^6 4d^n \rightarrow 4p^5 4d^{n+1} + 4d^{n-1} 4f$	4p-4d, 4d-4f
Sn XV–Sn XX	$4p^n \rightarrow 4p^{n-1} 4d^n$	4p-4d

**Table 1.3** Sn V to Sn XX 4p-4d and 4d-4f transitions

Because the overall UTA shape depends on the ion distribution within a laser-produced plasma, which in turn depends on the input parameters (primarily laser flux and target composition), it is possible to create a tuneable, bright, narrow, UTA source from 4d-4f and 4p-4d transitions. Other transitions (4p-5d, 4p-5s, and 4d-5p) are present, of course, but do not emit in the 13.5-nm region. Note, however, that with increasing ionisation, the 4d-5p transitions overlap in the 13.5-nm region (see Section 2.2).

Cowan code results using single configuration calculations (weighted average UTA transitions) are shown in Figure 1.26 (discrete top and convolved bottom) for Sn X, which gives a general idea of the relative position and intensity of the main  $nl-n'l'$  UTA transitions.

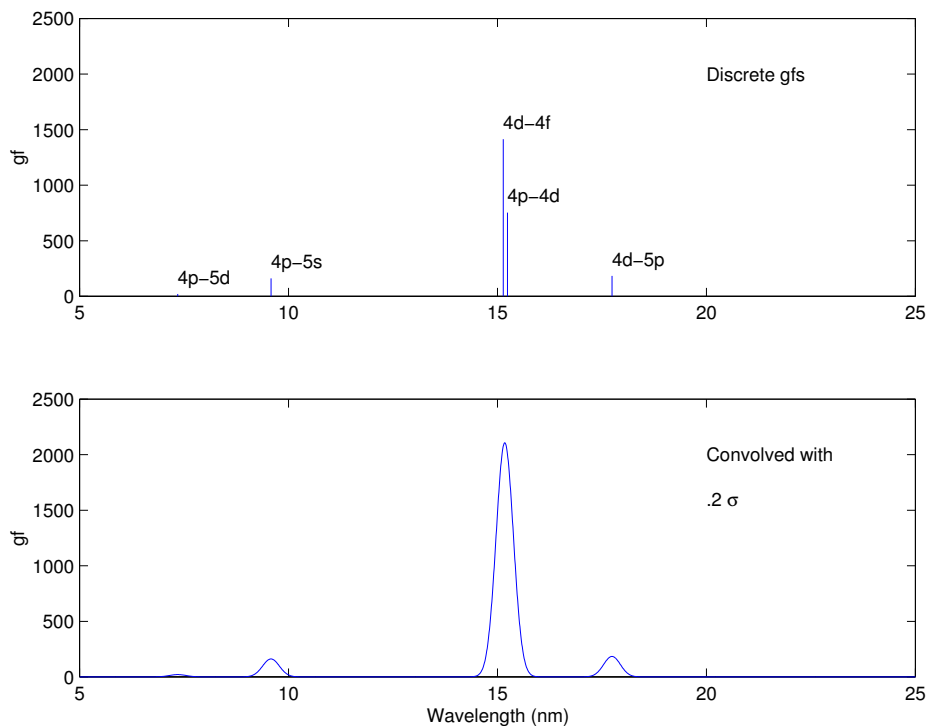


**Figure 1.26** Single configuration weighted average Sn X transitions convolved with a Gaussian of arbitrary width (4p-5d, 4p-5s, 4d-4f, 4p-4d, and 4d-5p)

The multi-configuration results are necessarily different because of configuration interaction and are shown in Figure 1.27 for the 4d-4f, 4p-4d, and 4d-5p transitions. The move to shorter wavelengths for the 4d-4f and 4p-4d UTA is easily seen. As well, the 4p-4d and 4d-4f UTA transitions are of comparable intensity and more separated.

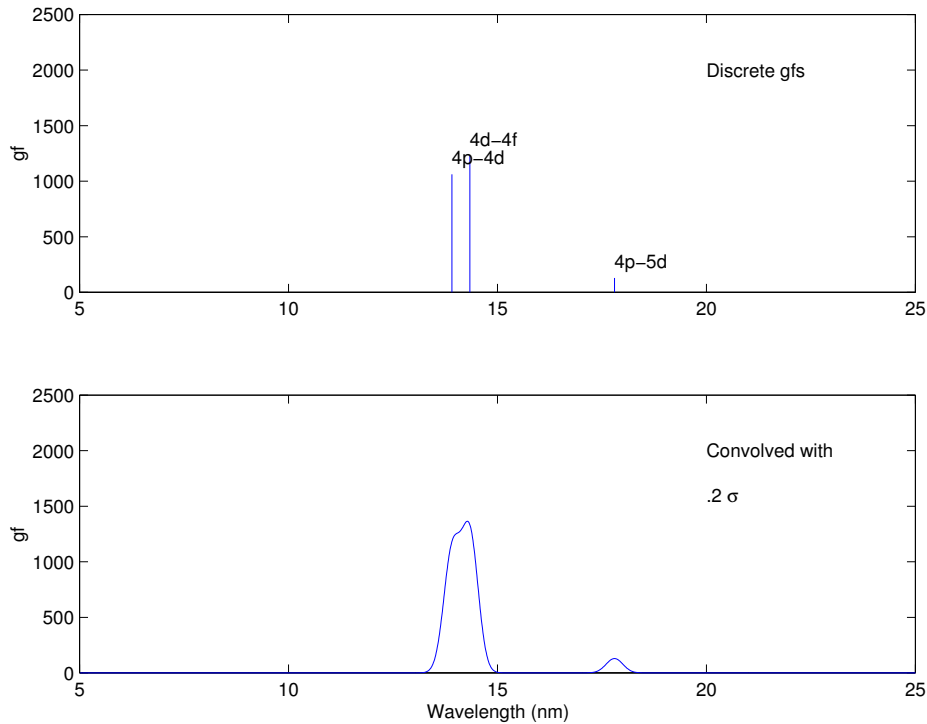


**Figure 1.27** Multi configuration weighted average Sn X transitions with a Gaussian of arbitrary width (4d-4f, 4p-4d, and 4d-5p)

The effect of configuration interaction on UTA shape can be considerable and is discussed further in Chapter 2. Note that the UTA can be used as a plasma diagnostic instead of line ratios. The  $\Sigma gf$  values from a HFCI calculation in a 2% band centred at 13.5 nm gives the ratio of the 4d-4f to 4d-5p relative intensity as 20:1. A full comparison of relative strengths is given in Section 2.2.

For more on determining the charge distribution in a laser-produced plasma, refer to Chapter 3, *A steady-state plasma model* and Chapter 4, *A spatial and temporal plasma model*. An excellent overview of the atomic structure of highly ionised ions created in laser-produced plasmas is given in O'Sullivan [51].

### 1.2.5 Proposed EUV light sources (Sn, Xe)

The current, conventional, lithographic source wavelength is 193 nm, produced by an ArF excimer laser. As source wavelength decreases, however, energy efficiency also decreases and both high-harmonic EUV lasers and excimer lasers do not have enough power. Furthermore, lasers are coherent, which produce problematic diffraction fringes at shorter wavelengths. Diffraction-patterned masks may reduce diffraction problems, but have not been studied. Synchrotrons are not powerful enough and are also too bulky and expensive. Adding wigglers would increase power density, but the integrated power is still not sufficient ( $< 100$  W).

From ongoing work at UCD since the 1970s, 4d-4f and 4p-4d transitions in tin<sup>21</sup> were recognised as bright emitters at 13.5 nm (Sn<sup>7+</sup>-Sn<sup>12+</sup>), but because of debris problems [53], other elements were sought. Xenon was proposed because of its inert nature, although only one ion emits at 13.5 nm (Xe<sup>10+</sup>)<sup>22</sup> and the resultant 4d-5p resonant transition is not as bright. Lithium (Li III 1s-2p resonance doublet) and fluorine (F V 2p-4d resonance doublet, F VI 2sp-2p3p, F VII 2p-3s doublet, and F IX 3-6) were also proposed as clean alternatives, but are also not bright enough. Indium, antimony, tellurium, and iodine, as near-tin elements, emit in the required region, but indium (too soft) and tellurium (too brittle) both splatter excessively. Antimony is harder than tin but is toxic and iodine catalyses oxidation and would be eaten by any oxide. The brightest 4d-4f emitters are in the lanthanides (or rare earths elements), with a maximum at 8.75 nm for cerium ( $Z = 58$ ) [50], but no multilayer mirrors exist at this wavelength.

Today, almost all NGL research involves tin or xenon. Tin is bright, but the associated debris problem has not yet been contained. Xenon is a cleaner source, but is not as bright, and cannot be used at its current lower conversion efficiency of 1% in the industrial lithographic process (up to ten mirror reflections). If the efficiency of the reflecting mirrors was increased, xenon could be bright enough—compare a conversion efficiency for xenon of 1% at 78% mirror reflectivity to 3% at the current 70% for tin (*e.g.*, for ten reflections:  $0.78^{10} / 0.70^{10} = 2.95$ ). As reported by Shields *et al.* [54], “The choice of xenon as the LPP target is primarily based on considerations of minimizing contamination and ease of material handling.”

Methods to reduce debris in tin include low pressure He background gas [55], a rapidly rotating target [56], a mass limited cryogenic target [57], ice droplets [58], and bulk or foil targets. Jin and Richardson [43] used oxygen (in mass-limited water ice targets), but oxidation damaged the optics. Liquid tin and gas puffs are currently being investigated [59] as are shaped tin cavities [60]. Experiments using tin in various compositions and target configurations also attempt to limit debris. Elemental tin targets (or indium and antimony) are also being put into a ceramic to cut down debris. A reduction of 100 has recently been achieved [61].

Interestingly, O’Sullivan and Faulkner [49] observed that brightness increased as the percentage tin composition decreased (*e.g.*, in a doped ceramic target). As well, for low-Z doping, emission is concentrated in a narrower band.

Further analysis is being conducted to optimise emission as a function of target composition and shape, particularly at a low-percentage composition. Research

<sup>21</sup> Tin was known to the ancients, and was used in alloys for early civilizations; bronze (tin and copper), pewter (tin, copper, and antimony).

<sup>22</sup> The xenon 4d-4f emission transition was first identified at UCD.

to improve the brightness of various tin targets (optimum concentration, laser power, target shape) is currently being investigated at UCD.

Figure 1.28 shows densitometer traces of tin at 1%, 5% and 100% concentrations from work done by O'Sullivan and Faulkner [49], while Figure 1.29 shows results from experiments with different tin compositions (4%, 33%, and 100%) as reported by Hayden [62] in 2004. Here, the in-band intensity (2% bandwidth using Mo/Si mirrors, as in Figure 1.13 with 8 reflections) was determined using a calibrated CCD detector housed in a 0.25-m flat-field grazing incidence Jenoptik Microtechnik vacuum spectrometer. The brightness attainable with slab targets at 2% concentration is 45% greater than with a pure tin target, although the optimum concentration is sensitive to laser pulse profile and focusing conditions. For the 2% concentration, the efficiency is estimated to be approximately 1.7% based on the detector calibration and source geometry [62].

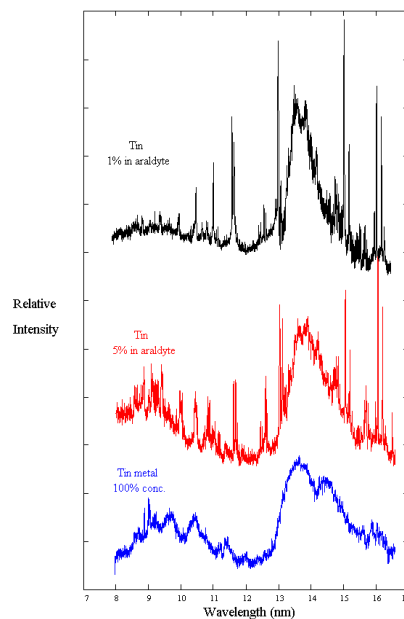


**Figure 1.28** Densitometer traces of tin at various concentrations (1, 5, 100%) [49]

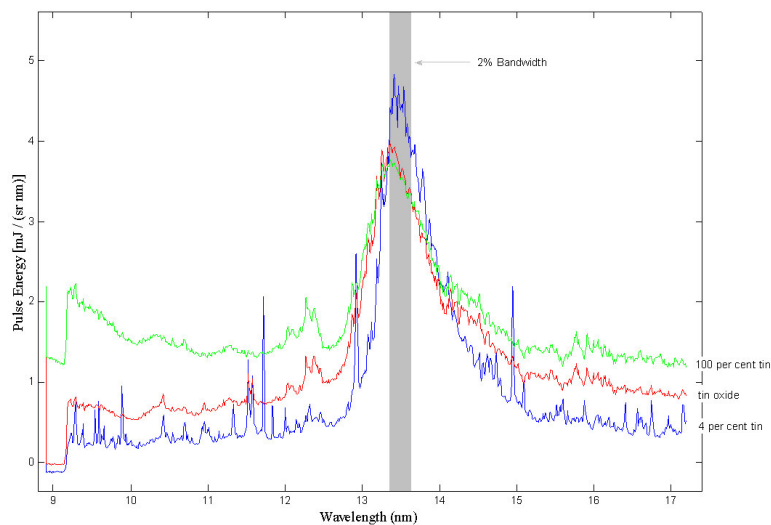


**Figure 1.29** Variation of spectral emission from pure tin, tin oxide (33%) and a tin doped glass target containing 4% tin by number [62]

Table 1.4 summarises the various proposed sources emitting in the 13–14-nm region. Li, O, and F data is from Kelly [63] including reported relative intensities. The relative intensity for the Sn ions, expressed as a percentage of the largest  $\Sigma gf$  Sn UTA (Sn XI:  $\Sigma gf$  value = 2290) is given as a simple measure of brightness; however, a more detailed figure of merit is given in Chapter 3, which includes weighting Cowan code calculations (weighted oscillator strength versus wavelength) by ion percentage in the plasma and multilayer mirror response versus wavelength. As reported in Fahy *et al.* [64], the relative intensity of Xe XI 4d-5p is determined from the relative intensity ratio of 4d-5p to 4-4 transitions in Sn VII, which is isoelectronic to Xe XI.

Element	Ion(s)	Transition(s)	Wavelength (nm)	Intensity
Li	<b>Li III</b>	<b>1s-2p</b>	13.4997, 13.49821	100
O	O V	2s <sup>2</sup> -2s4p	13.55232	300
F	F V	2p-4d	13.4407, 13.4539	400, 500
	F VI	2sp-2p3p	13.5397	300
	F VII	2p-3s	13.4703, 13.4882	100, 200
	F IX	3-6	13.494	--
Sn	Sn VIII	4d-4f, 4p-4d	17.10 ± 0.74*	11.4**
	Sn IX	4d-4f, 4p-4d	15.50 ± 0.72	42.7
	Sn X	4d-4f, 4p-4d	14.59 ± 0.67	84.6
	Sn XI	4d-4f, 4p-4d	14.14 ± 0.71	100.0
	Sn XII	4d-4f, 4p-4d	13.76 ± 0.55	79.9
	Sn XIII	4d-4f, 4p-4d	13.45 ± 0.48	41.7
	Sn XIV	4d-4f, 4p-4d	13.35 ± 0.55	12.6
	Sn XV	4d-4f, 4p-4d	13.32 ± 0.55	2.9
Xe	Xe XI	4d-5p	13.5	< 1

\* mean  $\lambda \pm 1\sigma$  (95% of UTA) \*\*  $\Sigma gf$  (Cowan) 2% in-band relative to Sn XI

**Table 1.4 Proposed EUVL 13.5-nm sources**

## 1.3 Plasma physics

Atomic spectroscopy using radiation from laser-produced plasma (LPP) sources is a well-established experimental method. A plasma is produced when a laser is focussed on an elemental target, resulting in intense emission from many ion stages (*e.g.*,  $\text{Sn}^{7+}$  to  $\text{Sn}^{12+}$  for a 32-eV plasma emitting in the 13.5-nm region). Identifying the ion stages from ion density rate equations and characterising the plasma hydrodynamics (temperature and density in space and time) is necessary to determine the optimum plasma conditions from input laboratory parameters (*e.g.*, laser pulse energy and pulse width).

Steady-state and time-dependent LPPs and the models used to analyze them are briefly discussed. A description of the laser used to produce an LPP is also given. For a more detailed analysis of steady-state plasmas, see Chapter 3, *A steady-state plasma model*. For more about the hydrodynamics within a plasma, see Chapter 4, *A spatial and temporal plasma model*.

Good general plasma physics monographs are given in [65, 66, 67, 68, 69, 70 and 51]. Attwood [28] gives a good mathematical treatment of hot dense plasmas, where the many-bodied problem is represented macroscopically by collective interactions, using charge densities and currents instead of individual charges. Salzmann [44] gives a good monograph on atomic physics in hot plasmas. A general description of the laser-plasma interaction code, *Medusa*, is given in [71].

### 1.3.1 Plasma

Plasmas are found naturally in fluorescent lights, lightning, aurorae, and stars as well as tokamaks and laboratory vacuum arc, spark, and laser-produced plasmas (Figures 1.30–1.31).



Figure 1.30 Lightning, northern lights, START spherical tokamak

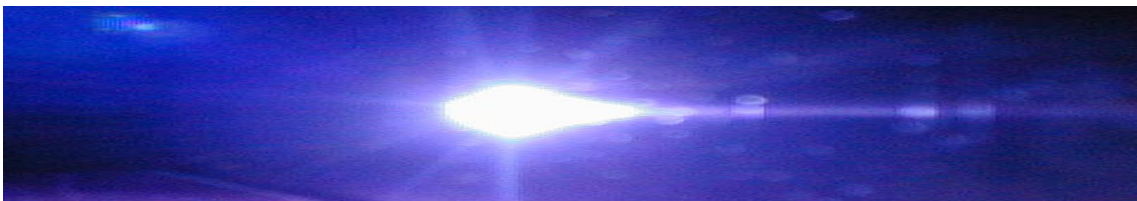
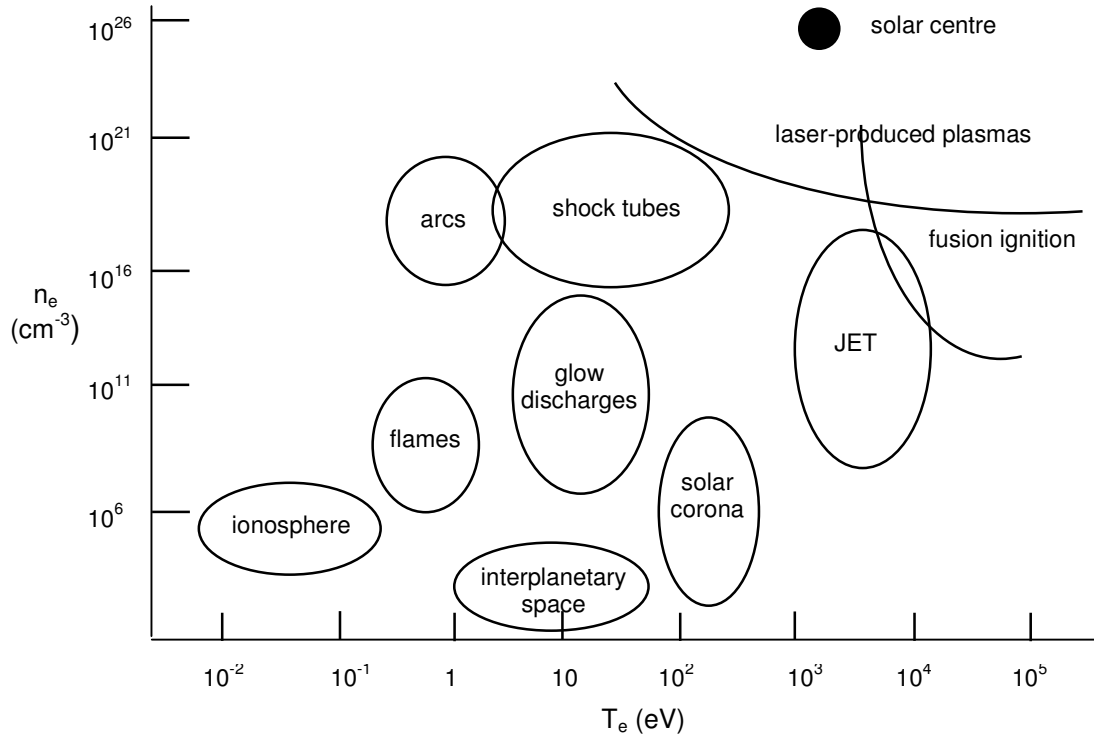


Figure 1.31 UCD laboratory laser-produced plasma

Called the fourth state of matter,<sup>23</sup> plasmas are characterised by electron/ion temperature ( $T_e/T_i$ ) and electron/ion density ( $n_e/n_i$ ) as shown for various plasmas in Figure 1.32, where temperature is given as a measure of plasma energy. A “thermal plasma” is an idealised plasma with one temperature, although plasmas vary greatly by temperature and density both temporally and spatially [28].



**Figure 1.32** Electron density ( $\text{cm}^{-3}$ ) versus temperature (eV) [66]

Intense radiation is emitted from a plasma with a density approaching that of a solid. Emission is both continuum—free-electron-ion interactions (bremsstrahlung or free-free) and free-electron-ion recombination above sharp edges (recombination or free-bound)—and line radiation (bound-bound). Continuum radiation is broad, because of the wide range of incident electron velocities and distances of closest approach, and produces a smooth spectrum characteristic of its temperature or electron velocity distribution (typically Maxwellian), whereas line radiation is characteristically narrow [28]. In hot plasmas, line emission is the most important radiation process [44].

The emission spectrum gives the “local instantaneous” temperature and density of the plasma and is an important diagnostic tool. For short-lived plasmas (nanosecond and femtosecond), it is the only reliable diagnostic to give information about the evolution of a plasma [44]. The relative contributions from bremsstrahlung, recombination, and line radiation depend on the target material, laser pulse power density, and spectral region [66]. An ideal continuum and line radiation emission spectrum is shown in Figure 1.33 from Attwood [28].

<sup>23</sup> The term “plasma” was coined by Langmuir in 1928 to suggest collective electrical behaviour in an ionised gas.

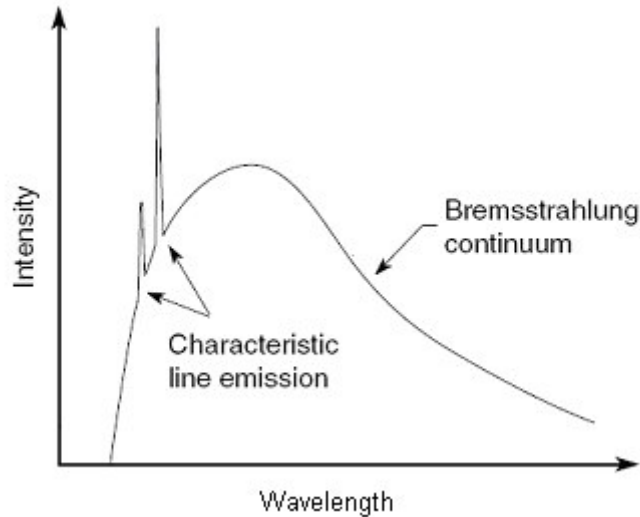


**Figure 1.33** Ideal continuum and line radiation plasma emission spectrum [28]

A plasma is often defined as an ionised gas with linear dimensions much larger than the Debye length,  $\lambda_D$ , [72]<sup>24</sup> where the Debye length (Eq. 1.35) is the distance at which individual ions can no longer be distinguished and electrons in a plasma can be treated collectively. The Debye length is derived from Poisson's equation.

$$\lambda_D = \sqrt{\frac{\epsilon_0 k T_e}{e^2 n_e}} = 69.2 \sqrt{\frac{T_e}{n_e}} \quad (1.35)$$

where  $\epsilon_0$  is the permittivity of free space,  $k$  is Boltzmann's constant,  $e$  is the electron charge. For  $\lambda_D$  in mm,  $T_e$  is the electron temperature in K (1 eV = 11,600 K), and  $n_e$  is the electron density in  $\text{cm}^{-3}$ .

At distances  $< \lambda_D$ , individual Coulomb interactions dominate, whereas at distances  $> \lambda_D$ , collective effects dominate and an overall plasma state exists. For example, for a 32-eV laser-produced plasma of density approximately  $10^{21}$  electrons/ $\text{cm}^3$ ,  $\lambda_D = 1.3$  nm, whereas in a tokamak, where the electron temperature is higher but the electron density lower (10,000 eV,  $10^{13}$   $\text{cm}^{-3}$ ),  $\lambda_D$  is 0.24 mm. In the outer solar corona (at 100 eV,  $10^4$   $\text{cm}^{-3}$ )  $\lambda_D$  is almost a metre long. The Debye length over a range of temperatures and densities is shown in Figure 1.34.

A "Debye sphere" can also be constructed, showing where individual or collective effects dominate as a function of the number of electrons,  $N_D$ , (Eq. 1.36).

$$N_D = \frac{4\pi}{3} \lambda_D^3 n_e \quad (1.36)$$

If  $N_D \gg 1$ , collective effects dominate the plasma. "The influence of the central ion extends out only to ions that are included in the Debye sphere, and, conversely, this ion is influenced only by ions inside this sphere." [44]

<sup>24</sup>  $\rho_D$  is also used interchangeably with  $\lambda_D$ . The Debye length is also known as the Debye screening distance. Note that the Debye length was introduced for electrolyte theory and should be used with caution for laser-produced plasmas [66].

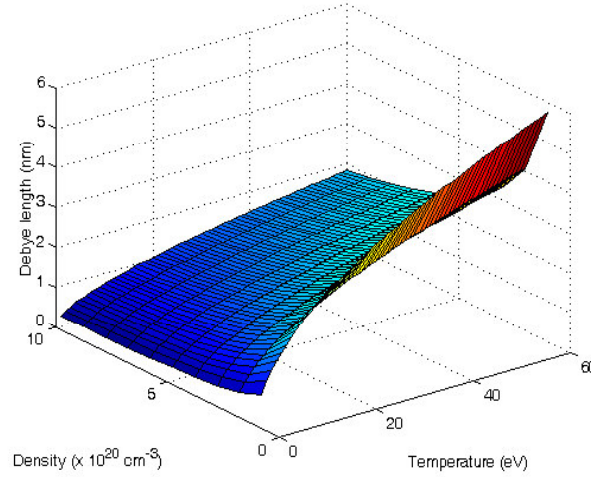


**Figure 1.34** The Debye length versus density and temperature ( $9.843 \times 10^{20} \text{ cm}^{-3}$ ,  $32 \text{ eV} = 1.3 \text{ nm}$ )

Salzmann [44] describes an ion sphere radius,  $R_i$ , where the electrostatic potential and electrostatic field are zero on the ion sphere boundary and beyond. He also derives a relation for the plasma (or ion-ion) coupling constant,  $\Gamma_{ii}$ , a measure of the effects of nearest neighbour ions within the plasma. The ion sphere radius and coupling constant are given in Eq. 1.37 and Eq. 1.38.

$$R_i = \left(\frac{3}{4\pi n_i}\right)^{1/3} \quad (1.37)$$

$$\Gamma_{ii} = \frac{1}{R_i} \frac{\langle z \rangle^2 e^2}{T} \quad (1.38)$$

where  $n_i$  is the ion density in  $\text{cm}^{-3}$ ,  $T$  is the temperature in eV,  $\langle z \rangle$  is the average charge, and  $e^2$  is the electron charge squared (here, in mks units,  $e^2 = 1.44 \times 10^{-7} \text{ eV cm}$ ).  $R_i/\lambda_D$  is approximately 9 for a 10-eV plasma and approximately 3 for a 100-eV plasma. Coupling is weak ( $\Gamma_{ii} \leq 0.1$ ), intermediate ( $0.1 > \Gamma_{ii} > 10$ ), or strong ( $\Gamma_{ii} \geq 10$ ). For a representative LPP plasma ( $T_e = 32 \text{ eV}$ ,  $n_e = 10^{21} \text{ cm}^{-3}$ ),  $\Gamma_{ii} = 0.31$ , and thus the plasma is low intermediately coupled.

The frequency at which the electrons collectively oscillate (*i.e.*, the electron plasma frequency),  $\omega_p$ , and the electron density at this frequency (referred to as the critical density),  $n_{ec}$  (typically in  $\text{cm}^{-3}$ ), is determined from Maxwell's Coulomb equation, assuming simple harmonic motion (Eq. 1.39 and 1.40).

$$\omega_p = \sqrt{\frac{n_{ec} e^2}{m \epsilon_0}} \quad (1.39)$$

$$n_{ec} = \frac{4\pi^2 c^2 m \epsilon_0}{e^2} \frac{1}{\lambda^2} \quad (1.40)$$

where  $c$  is the speed of light,  $m$  is the electron mass,  $\epsilon_0$  is the permittivity of free space,  $e$  is the electron charge, and  $\lambda$  is the wavelength of the incident radiation.

The critical density is the density at which the electrons oscillate as a group in simple harmonic motion. As such, incident radiation is transmitted below the critical density and reflected above the critical density, analogous to the absorption and reflection of AM radio waves by the ionosphere during day and night. From Eq. 1.40, it is seen that the critical density is a function only of the incident laser light frequency. Here it is seen that for a Nd:YAG laser ( $\lambda = 1.064 \mu\text{m}$ ), the critical density is on the order of  $10^{21} \text{ cm}^{-3}$ . Derivations of Eqs. 1.39 and 1.40 are given in Chapter 3.

Salzmann [44] divides plasmas into two regions: low density ( $n_e < 10^{17} \text{ cm}^{-3}$ ) and high density ( $n_e > 10^{19} \text{ cm}^{-3}$ ), where low-density plasmas include astrophysical research areas, tokamaks, and magnetic confinement devices, and high-density plasmas include inertial confinement devices and star interiors. Laser-produced plasmas (LPPs) are on the order of 10–1,000 eV and have electron densities of  $10^{20}$ – $10^{22} \text{ cm}^{-3}$ , and are considered as hot, high-density plasmas. Hot dense plasmas are short lived—on the order of picoseconds—and expand rapidly with sharp density gradients [28].

A plasma is overall electrically neutral; *i.e.*, the number of electrons is exactly equal to the number of ions multiplied by the average charge,  $\langle z \rangle$ , (Eq. 1.41).

$$\langle z \rangle = \frac{n_e}{n_i} \tag{1.41}$$

Of course, within a plasma, charges of one sign will have more opposite sign charges nearby, because of Coulomb interaction, (called plasma polarisation in [63]), and the electron charge will not exactly match the positive charge everywhere, but as a whole, an average charge state can be determined. The average charge state as a function of temperature and density is of prime importance in plasma spectroscopy [44].

The three models used to characterise a plasma, based primarily on electron temperature and density, are coronal equilibrium (CE), collisional-radiative (CR)<sup>25</sup>, and local thermodynamic equilibrium (LTE) as shown in Figure 1.35. The ratio of collisional, C, (or conservative) to radiative, R, (or dissipative) processes within the plasma determines the validity of the model, with CE characterised by radiative processes dominating collisional processes (*i.e.*, in a less dense plasma), and LTE characterised by collisional processes dominating radiative processes (*i.e.*, in a more dense plasma). An LTE plasma is an ionising plasma, whereas a CE plasma is a recombining plasma. The CR model is intermediate between the two, where collisional and radiative processes are balanced. Plasma models can also be characterised by the degree of ionisation [66].

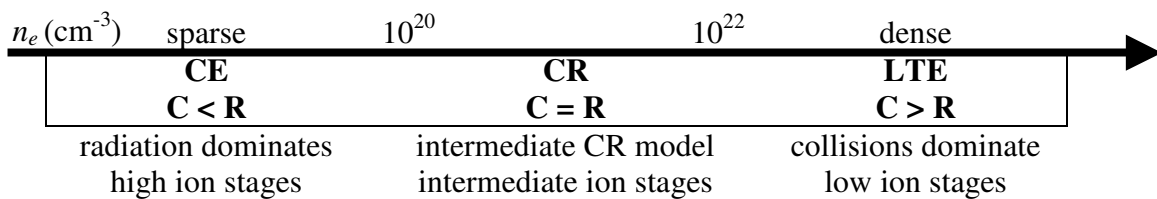


Figure 1.35 Plasma model criteria (CE, CR, LTE)

<sup>25</sup> CR is also referred to as CRM (collisional radiative model), collisional radiative steady state (CRSS), or non-LTE (NLTE).

LTE is closest to complete thermodynamic equilibrium (TE), where the ions and electrons are in equilibrium with themselves, but the photons are not. Three criteria are defined for complete TE: a Maxwell-Boltzmann distribution of ion and electron velocities, a Boltzmann distribution of excited states, and a Planckian distribution of photons. In TE, the mean free path ( $\lambda_p$ ) of the photons  $\gg$  the plasma dimensions  $\gg$  mean free path of the electrons ( $\lambda_e$ ) and ions. According to Salzmann [44],  $\lambda_p/\lambda_e \sim 10^4$ .

In a laboratory LPP, the three models essentially describe the inner, middle and outer regions of the plasma, *i.e.*, inner or core (LTE), middle (CR), and outer (CE). The density and temperature is highest at the core, where there are higher ion stages, with a rapid decrease in density and temperature away from the core [66]. The CR and LTE models are used for emission and absorption, and the CE model for absorption only. Maximum emission is from the core, though opacity is an issue as cooler regions absorb more radiation than hotter regions, thus reducing emission at the periphery as the outer layers absorb. The CR model approaches the LTE model asymptotically for high densities and the CE model for low densities [73]. Validity criteria for the LTE, CE, and CR models are given in Chapter 3.

### 1.3.1.1 Basic hydrodynamics

To fully represent the laser-target interaction, the plasma is characterised in space and time (submicron spatial resolution and picosecond time). Plasma hydrodynamics are quite complicated, particularly for short laser pulses on the order of picoseconds, a time comparable to the electron relaxation time.

Initially, the plasma is heated primarily by inverse bremsstrahlung<sup>26</sup>, which absorbs photons by electron-ion interaction. The classical absorption coefficient is given in Eq. 1.42.

$$K = 5.64 \times 10^{-11} \frac{Z n_e^2 \ln \Lambda}{\omega^2 T_e^{3/2}} \frac{1}{\left(1 - \frac{\omega_p^2}{\omega^2}\right)^{1/2}} \quad (1.42)$$

where  $Z$  is the atomic number,  $n_e$  and  $T_e$  the electron density and electron temperature,  $\omega_p$  the plasma frequency,  $\omega$  the frequency of the incident laser radiation, and  $\ln \Lambda$  is the Coulomb logarithm, a factor related to the electron-ion collisions, which is given in Eq 1.43 [from Spitzer in 65] ( $\ln \Lambda$  is a slowly varying function between 5 and 10 for LPPs).

$$\Lambda = \frac{3}{2Z^2} \left( \frac{T_e^3}{\pi e^6 n_e} \right)^2 \quad (1.43)$$

where  $Z$  is the atomic number,  $n_e$  and  $T_e$  the electron density and electron temperature, and  $e$  is the electron charge.

<sup>26</sup> From Kirchoff's Law, where absorptivity and emissivity of a grey body are equal at any given temperature [69].

Using the plasma frequency and critical density shown in Eqs. 1.39 and 1.40 (and where initially,  $\omega \gg \omega_p$ ), Eq. 1.42 can be simplified as Eq. 1.44. The rate of absorption is shown in Figure 1.36 ( $Z = 50$ ,  $\ln \Lambda = 5$ ,  $\lambda = 1.064 \mu\text{m}$ ) as a function of temperature, showing the decrease in laser absorption as electron temperature increases.

$$K \propto \frac{Z \ln \Lambda}{\lambda^2 T_e^{3/2}} \quad (1.44)$$

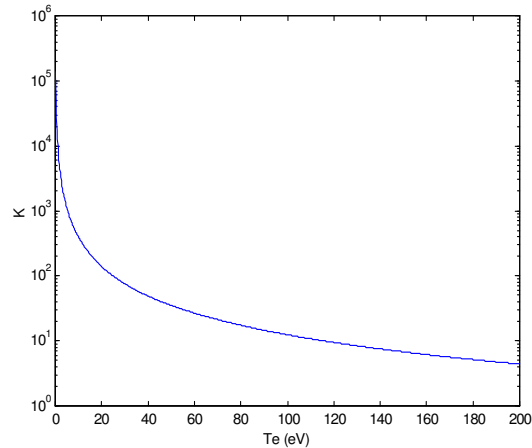


**Figure 1.36** Absorption rate in the plasma by inverse bremsstrahlung

Prior to reaching the critical density, the target breaks down (heating, evaporation, ionisation), and a thin sheet of plasma is formed near the surface [66]. At the critical density ( $n_e = n_{ec}$ ), the plasma becomes opaque to further laser radiation and the incident laser radiation is reflected. The plasma begins to expand, the density decreases, and laser radiation is again incident on the target. Carroll and Kennedy [66] describe the plasma as a self-regulating regime of generation, heating, and expansion over the laser pulse duration. Electrons equilibrate on a time scale very small compared to the laser pulse length, establishing a well-defined temperature. As is to be expected, the average ion charge (and dominant ion) increases with temperature. Furthermore, a longer laser pulse produces a greater range of ion stages [51].

Figure 1.37 shows the plasma divided into regions early on during the laser-target interaction, as per typical plasma nomenclature: the hot electron, pre-heating region, ablation (and deflagration) front, and expansion plume.

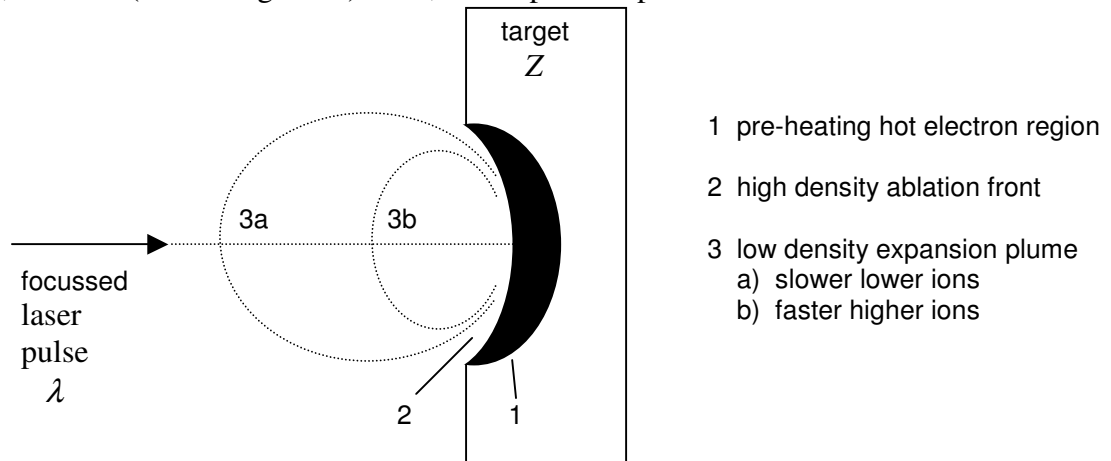


**Figure 1.37** LPI regions (early on after laser-target interaction) [67]

As explained in Key and Hutcheon [67], the initial internal energy is converted to flow kinetic energy in the expansion plume, both axially (in the direction of the laser) and radially, and rapidly cooled by adiabatic expansion in a vacuum. For a solid plane target, the plasma expands in cone-like structures, preferentially normal to the laser pulse [69]. The plasma expansion speed is on the order of  $10^6$  m/s [66]. Attwood [28] derives an expression for plasma expansion velocity,  $v_{\text{exp}}$ , (Eq. 1.45), from conservation of mass and momentum of both ions and electrons, assuming a one-dimensional isothermal expansion of a hot fluid consisting only of ions and electrons:

$$v_{\text{exp}} = 0.28 \left( \frac{Z \kappa T_e}{M} \right)^{\frac{1}{2}} \quad (1.45)$$

where  $Z$  is the atomic number in units of 10,  $\kappa T_e$  is the ion temperature in eV, and  $M$  is the nuclear mass in units of  $20 m_p$ , where  $m_p$  is the mass of the proton. For a 32-eV, tin plasma ( $Z = 5$ ,  $\kappa T_e = 32$  eV, and  $M \approx 6$ ), the plasma expansion velocity is  $0.65 \times 10^6$  m/s (or, using the units of [28], 0.65 microns per picosecond). As reported by Attwood [28], “The rate at which [expansion] occurs determines how fast energy must be supplied to the plasma if it is to reach a high temperature.”

From Eq. 1.45, it is seen that the more highly charged ions have greater velocity [51]. Furthermore, the higher-charge ions are in the inner regions of the expansion plume as is to be expected [67, 69], since the lower-charge ions are ejected earlier (*i.e.*, at lower temperature). The slower-moving, lower-charge ions are in the outer region [67]. As well, the density in the expansion plume is less than the critical density [69].

The ablation front penetrates into the target by thermal conduction heating [69]. From numerical simulations reported in [69], the thermal transport is smaller than classically expected (expressed by a flux inhibition factor). Key and Hutcheon [67] report that thermal conduction increases for shorter wavelengths (as  $\lambda^{-2}$ ) and that the pre-heating region temperature increases substantially with  $Z$  and “depends on the instantaneous irradiance at the critical density more than on hydrodynamic response.” A shockwave travels out from the target ahead of the ablation front [66].

The laser energy is partially converted to the plasma (85%; 50% expansion, 35% enthalpic), the shockwave (10%), and generation of radiation (5%), as reported by Carroll and Kennedy [66] from the work of Fauquignon and Flux on solid deuterium. The conversion to radiation increases with  $Z$ , up to 80% for uranium [66]. The efficiency of laser light absorption is of prime importance in LPP applications, particularly in EUVL semiconductor manufacturing.

The radiative emission is greatest and most intense in the high-density ablation front, which reaches temperatures of 100–1000 eV for irradiances of  $10^{11}$ – $10^{17}$  W/cm<sup>2</sup> [67]. In the expansion plume, the greatest emission is in the higher density inner region, decreasing rapidly from the target surface outward (electron density and temperature decrease outward from the target surface).

For a more detailed description of plasma expansion see De Michelis and Mattioli [69]. Hydrodynamics within the expansion plume are characterised by the laser-plasma interaction code *Medusa*, as discussed below and in more detail in Chapter 4. Attwood [28] gives a good introduction to the linearised techniques used in numerical simulations for both particle in a cell (particle kinetics) and Lagrangian (zone tracking of fluid properties) methods.

### 1.3.1.2 Steady-state laser-produced plasma

For spectroscopic purposes, a laser-produced plasma (LPP) is characterised by its ion distribution,  $f_z$  (or average charge,  $\langle z \rangle$ ), and relaxation time ( $\tau$ ), both spatially and temporally in the plasma. To determine the ion distribution, rate equations for the atomic processes are balanced. As discussed above, three models can be used, depending on plasma temperature and density. For laser-produced plasmas (of moderate average charge) the CR model is typically used.

In the steady-state collisional-radiative (CR) model of Colombant and Tonon [52], collisional and radiative process for each ion state are balanced according to the rate equations originally defined by Bates *et al.*, for optically thin plasmas (emitted radiation not reabsorbed) [74] or optically thick plasmas (emitted radiation reabsorbed) [75] (Eq. 1.46).

$$\frac{dn_{z+1}}{dt} = n_e n_z S(z, T_e) - n_e n_{z+1} [S(z+1, T_e) + \alpha_r(z+1, T_e) + n_e \alpha_{3b}(z+1, T_e)] \quad (1.46)$$

$$+ n_e n_{z+2} [\alpha_r(z+2, T_e) + n_e \alpha_{3b}(z+2, T_e)]$$

where  $n_z$  is the density of ion  $z$ ,  $n_e$  the electron density,  $S$ ,  $\alpha_r$ , and  $n_e \alpha_{3b}$  the collisional ionisation, radiative recombination, and three-body recombination rate coefficients, and  $T_e$  the electron temperature. The temperature is a function of the focused power density (or laser flux  $\phi$ ) and scales as  $\phi^{3/5}$  [49].

For a steady state model,  $dn/dt = 0$ , and thus the ratio of ionisation ( $S$ ) and recombination processes ( $\alpha_r$  and  $\alpha_{3b}$ ) is equal to the steady-state ion density from one ion stage ( $n_{z+1}$ ) to the next ( $n_{z+2}$ ).  $n_{z+2}/n_{z+1}$  is a recursive relation, which when summed to 1 gives the fractional ion density ( $f_z$ ) at each ion stage ( $z$ ) and hence the ion distribution or average charge  $\langle z \rangle$ . Figure 1.38 shows the average ion stage (or charge) and Figure 1.39 shows the fractional ion distribution as a function of temperature for a tin plasma, according to the CR model [52]. A vertical ‘‘slice’’ at any temperature in Figure 1.39 gives the ion distribution at that temperature. The plateau widths for various ion stages (*e.g.*,  $\text{Sn}^{2+}$ : 5–10 eV,  $\text{Sn}^{12+}$ : 50–60 eV,  $\text{Sn}^{18+}$ : 100–200 eV) represent a full electron subshell ( $\text{Sn}^{2+}$ : full 4d subshell,  $\text{Sn}^{12+}$ : full 3p subshell,  $\text{Sn}^{18+}$ : full 3s subshell) and corresponding greater increase in ionisation potential.

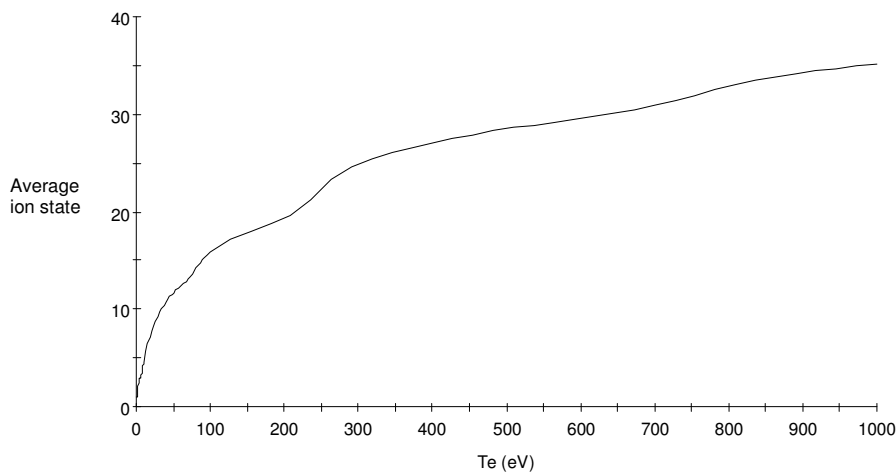
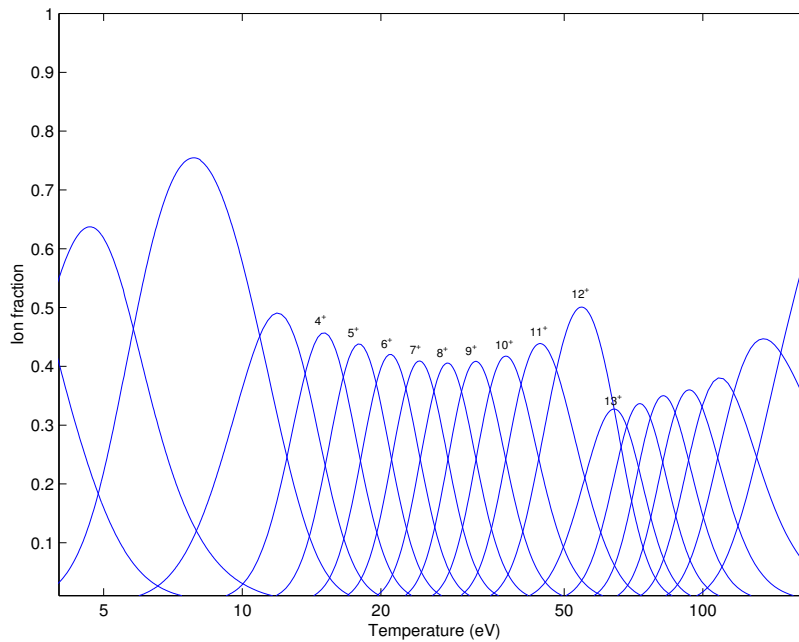


Figure 1.38 Average ion state  $\langle z \rangle$  versus temperature (eV) for tin ( $n_e = 9.843 \times 10^{20} \text{ cm}^{-3}$ )



**Figure 1.39** Tin ion fraction distribution versus electron temperature ( $n_e = 9.843 \times 10^{20} \text{ cm}^{-3}$ )

From Eq. 1.44, it is seen that the three-body recombination rate depends on electron density, and thus for a dense plasma, collisional processes dominate radiative processes, as is to be expected. In a typical CR plasma, however, collisional and radiative rates are comparable, and the ion rate from one stage to the next is small [52].

The CR model of Colombant and Tonon [52] is a semi-empirical approximation, which couples only the ground state of each ion, and does not account for excited states, collisional excitation/de-excitation, photo-ionisation, or dielectronic recombination. It is, nonetheless, a good first model to determine ion stages within a plasma, without using hard-to-get, non-hydrogenic atomic rate equations. Details about the CR model including atomic processes and atomic rate equations are given in Chapter 3.

The LTE<sup>27</sup> model of Eliezer *et al.* [73] includes dielectronic recombination, rate coefficients, and cross-sections, as well as energy levels and transition probabilities. The NLTE model of Peyrusse [43] uses configuration average energies from all atomic processes. Both models are considerably more complicated computationally. An excellent survey [76] of various models with different rate equations, indicating the applicability of atomic processes for different  $T_e$ - $n_e$  regions, is discussed in Chapter 3, for which comparative results are given.

Continuum lowering (or ionisation potential lowering), where the binding energy of an electron is reduced as the plasma density increases, because of increased electrostatic interaction of an ion with nearby charged particles, is included in Chapter 3. Continuum lowering can significantly effect the charge distribution and spectral line positions within a plasma.

<sup>27</sup> LTE models use the Saha equation (derived from conservation of charge and by maximising free energy).

To ultimately determine a theoretical spectrum emitted by a plasma, atomic data from the Cowan Hartree-Fock results is weighted by the ion distribution in the plasma. The spectrum is a function of laser flux (or plasma temperature) and is simplest if an optically thin plasma is assumed (sufficient for low-percentage tin targets). The mean UTA wavelength and width for each transition array is calculated from UTA statistics (see Section 2.2). The effect of the mirror response in the 13.5 nm region can also be included to determine an overall in-band emission figure of merit (see Section 3.3.2). Spatio-temporal results in an optically thick plasma require hydrodynamic output and calculation of level populations (see Chapter 4). A flow chart showing the atomic and plasma physics for a steady-state, optically thin plasma is given in Figure 1.40.

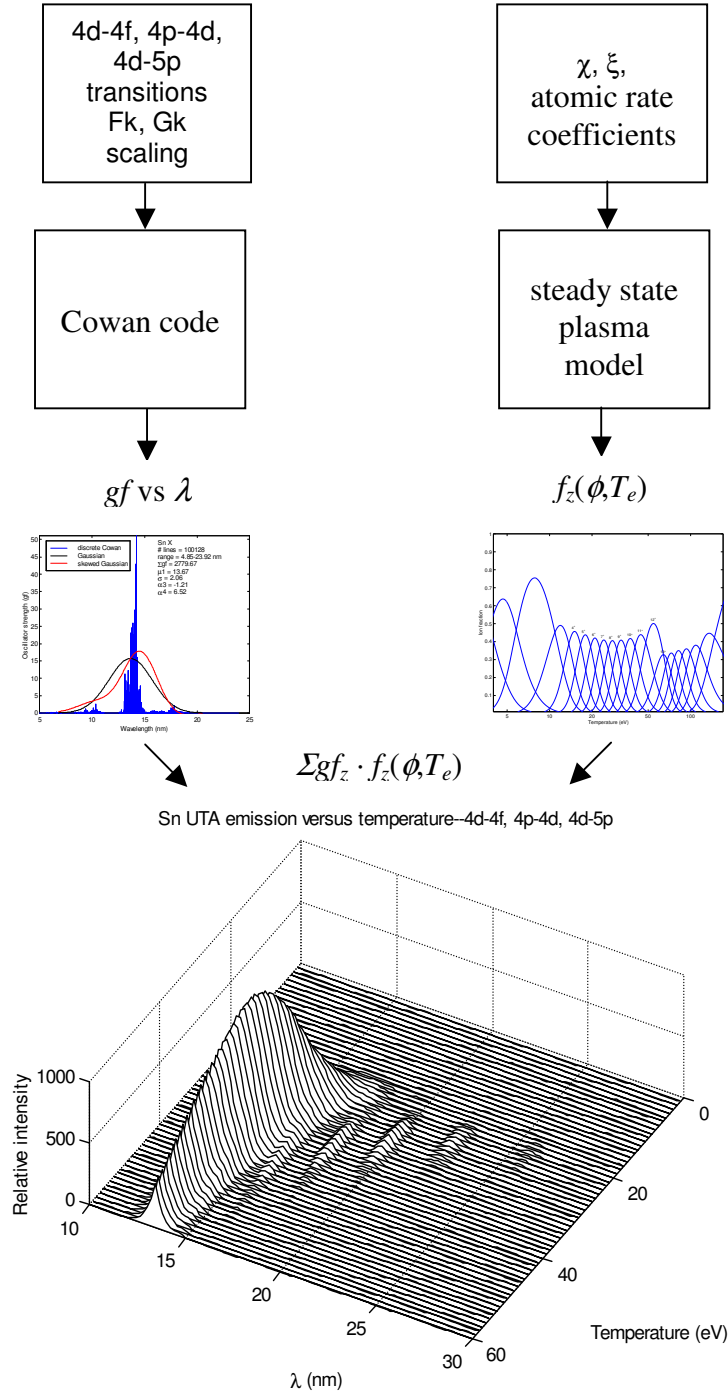
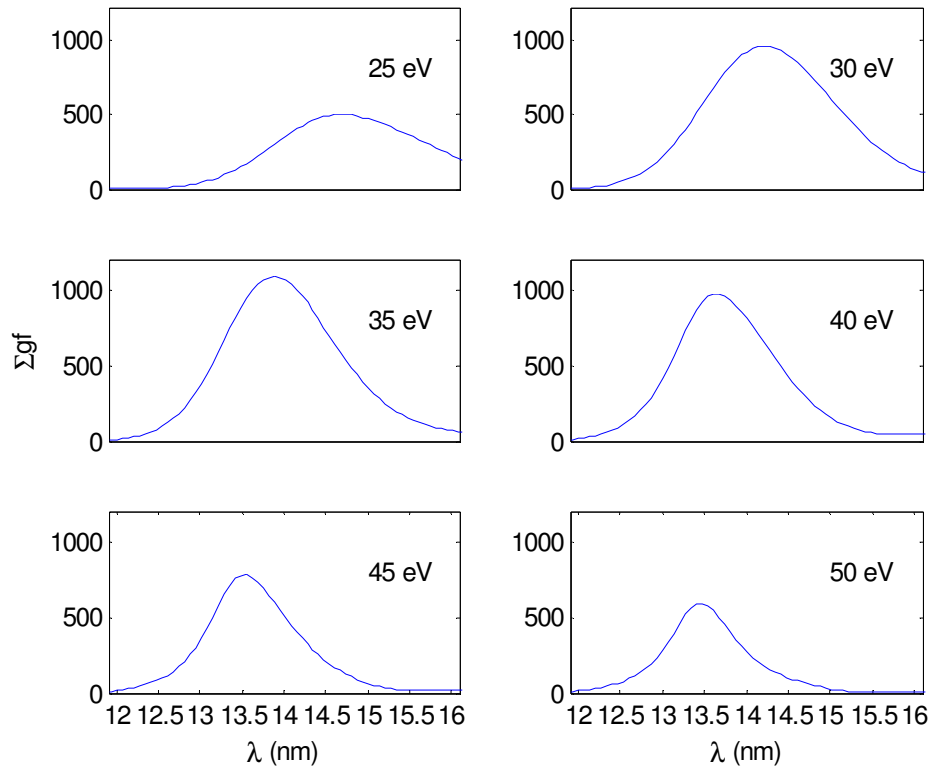
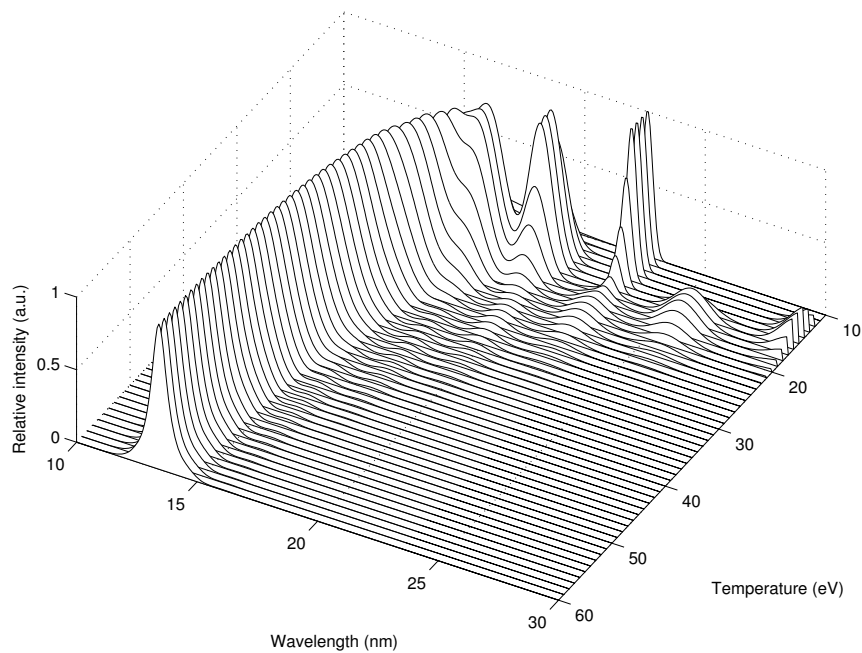


Figure 1.40 Flow chart to produce theoretical spectrum (intensity, wavelength, temperature)

Figure 1.41 shows the theoretical UTA emission at six temperatures for the 4d-4f, 4p-4d, and 4d-5p transitions. Figure 1.42 gives a surface plot (normalised to the maximum at each temperature) over the range 1 to 60 eV.



**Figure 1.41** Theoretical UTA (summed oscillator strength versus wavelength at selected electron temperatures)



**Figure 1.42** Theoretical UTA (summed oscillator strength versus wavelength versus electron temperature)

### 1.3.1.3 Medusa laser-plasma interaction hydrodynamics

**Medusa** [77] is a one-dimensional, Lagrangian, laser-plasma interaction code, developed at UKAEA's Culham Laboratory in 1974 to simulate the hydrodynamic and plasma processes in a laser irradiated pellet. **Medusa** was originally written to determine the feasibility of generating controlled thermonuclear power and is now also used to simulate emission and absorption in a rapidly expanding plasma.

In **Medusa**, the plasma is primarily described by density,  $\rho$ , velocity,  $u$ , ion and electron temperature,  $T_i$  and  $T_e$ , and electron density,  $n_e$ , in time,  $t$ , and a single space variable,  $r$ . A Lagrangian difference mesh is used with an explicit Navier-Stokes hydrodynamics and implicit heat conduction integration scheme. Model geometries are planar, cylindrical, or spherical, for any realistic laser pulse.

The first version of **Medusa** provided a simple laser fusion model, with an accuracy depending on mesh size and convergence criteria. Subsequent versions (**MED101** [78] in 1989 and **MED103** [79] in 1996) were developed to better simulate laser-produced plasmas, including coupling excitation and ionisation energies, in a non-LTE, time-dependent, average atom model, to the free electron energy balance equation.

Modelling a cylindrical aluminium target, Patel *et al.* [80, 81, 82] reported on x-ray line transfer in a rapidly expanding plasma. Line position shifts and line shape changes are attributed to radiation emitted from different regions of the plasma and experimental results are compared to **Medusa** using an escape probability method for radiative transport.

In this thesis, **Medusa** is used on a low  $Z$  target with a small number of transitions (the Al XIII 1s-2p Lyman- $\alpha$  transitions at 7.175 Å and 7.180 Å) and, then, on more complex Sn targets. An input Gaussian laser pulse and sample resultant output ( $n_e$ ,  $T_e$ ,  $\langle z \rangle$ ) for a cylindrical aluminium target is shown in Figure 1.43 and Figure 1.44. Pulse/pre-pulse methods, laser pulses with up to four superimposed Gaussians, and targets of different percentage element concentration, are also available.

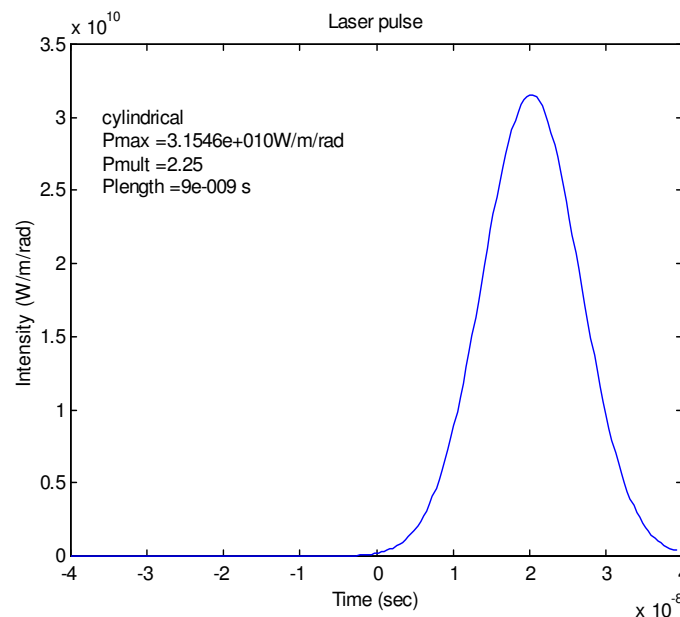


**Figure 1.43 Medusa input Gaussian laser pulse**

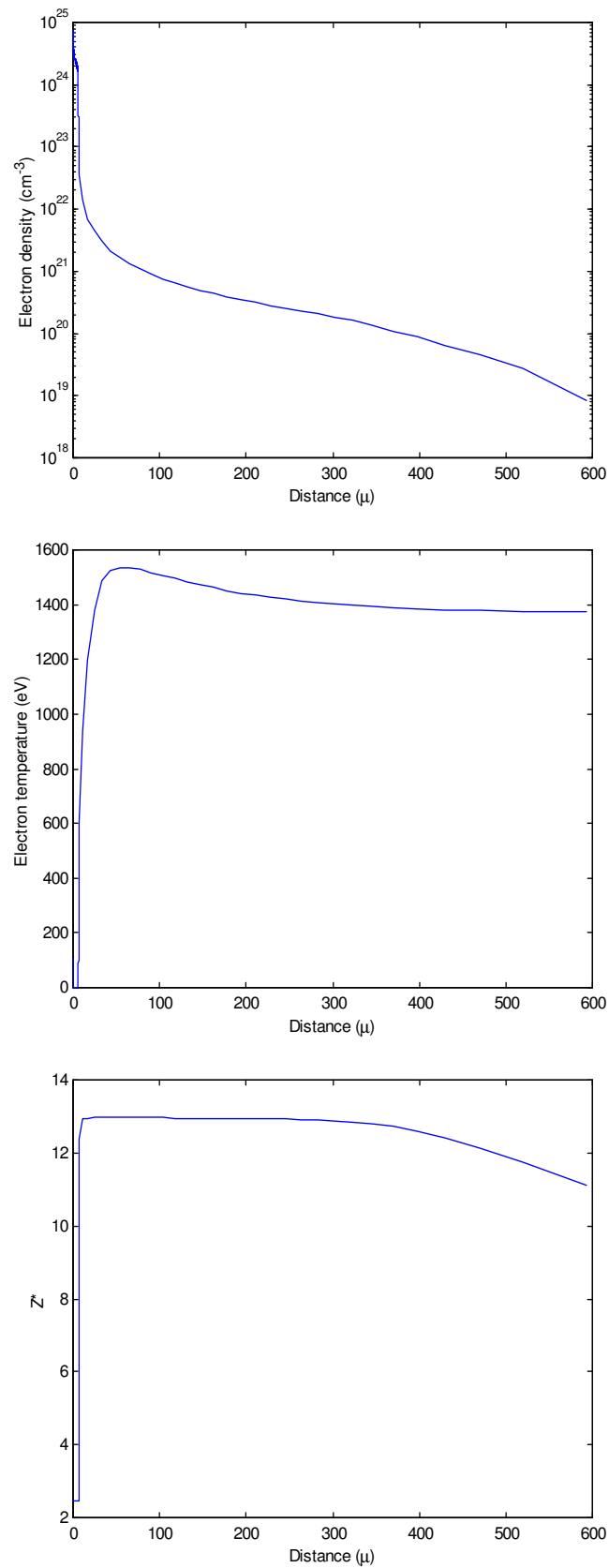


**Figure 1.44** Sample Medusa output showing  $n_e$ ,  $T_e$ , and  $\langle z \rangle$ <sup>28</sup> in an aluminium plasma at the peak of the pulse

<sup>28</sup> Medusa uses  $Z^*$  for average charge (referred to as  $\langle z \rangle$  in this thesis).

Detailed theoretical **Medusa** results are given in Chapter 4 for aluminium and tin targets, where emission is given as a function of space and time within a plasma. Radiation transport and opacity effects are included with different rates for emission and absorption in the plasma, using the Matlab program **RadTran** written for this thesis. As reported in [67], the spectral line intensity and shape is significantly modified by absorption for LPPs. As stated in Greim [65], “If some of the radiation is reabsorbed in the plasma or perhaps even reflected at the plasma boundary, one must also solve the appropriate equations of radiative transfer.”

### 1.3.2 Nd:YAG laser

A pulsed Neodymium Yttrium Aluminum Garnet (Nd:YAG) Spectron laser is used in the experimental work reported in this thesis (Figure 1.45), providing a coherent, collimated, and monochromatic light source. The fundamental wavelength is 1064 nm with maximum pulse energy of 1100 mJ and pulse duration of 15 ns. No harmonics are available. For power densities applicable to the UTAs studied in this thesis (on the order of  $10^{11}$  W/cm<sup>2</sup>), the incident beam is typically focussed to spot sizes on the order of 100  $\mu$ m radius. The standard specifications for the Spectron SL805 model are given in Table 1.5 (reproduced from the Spectron user's manual).

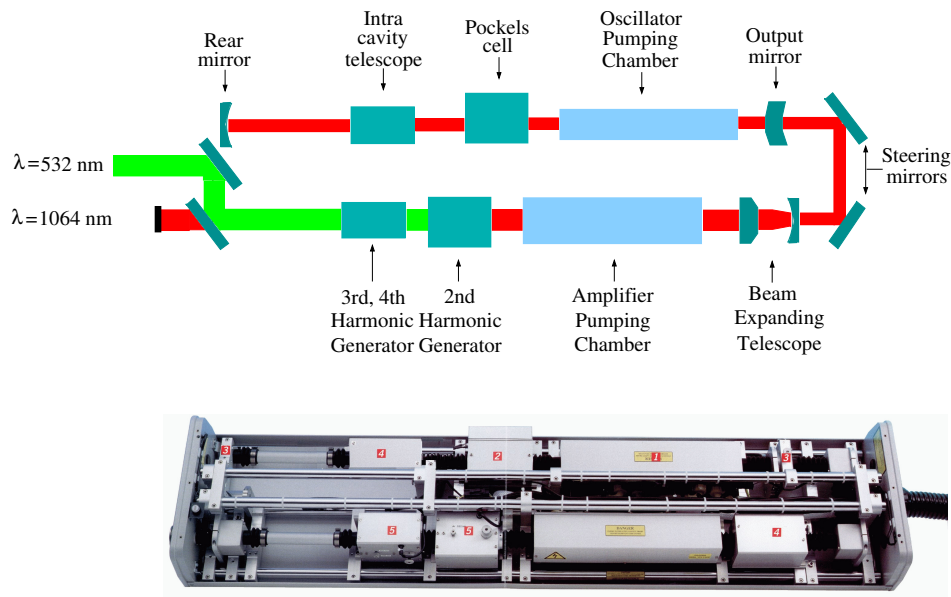


Figure 1.45 Nd:YAG laser [62]

Laser parameter	Specification
Wavelength, nm	1064 nm
Pulse duration, ns	15
Pulse energy, mJ (max)	1100
Pulse energy stability, %	90% (2% rms)
Max. repetition rate, Hz	10
Beam diameter, mm	9.5
Beam divergence $1/e^2$ , mrad	0.8

Table 1.5 Nd:YAG laser specifications

The Pockels cell is a polariser combination that controls transmission of light through the cavity. Fast operation is required to give a single short pulse. Q-switching inhibits normal lasing until an optimum level population inversion is achieved [68]. Good frequency stability of the laser is required.

For a typical 1-joule, 15-ns pulse focussed to about 100-micron radius spot size, an irradiance of  $10^{11}$  W/cm<sup>2</sup> can be achieved.

## 1.4 Next generation lithography (NGL)

A brief overview of the semiconductor industry is given to put laser-produced plasma physics in context with NGL semiconductor manufacturing, with emphasis on EUV lithography (EUVL) and integrated circuit (IC) fabrication. More detailed reports can be found in [83, 84, 85]. For a good introduction to the changing physics of semiconductors and very-large-scale integration (VLSI) chips, see [86, 87]. For a comparison of optical lithography and EUVL with current NGL technologies, see [88].

### 1.4.1 Moore's law

It could be said that modern electronics began with the first working vacuum tube in 1912, which amplified weak electronic signals. Solid-state switches started the process of small-scale manufacturing using transistor technology (1948), and the first integrated circuit (1958) continued the focus on miniaturization. With the microprocessor came optical lithography and etched circuits, and, with each new chip generation, shorter source wavelengths to manufacture higher density chips.

Since the introduction of the integrated circuit<sup>29</sup>, chip fabrication has continued to improve, and component<sup>30</sup> size has substantially decreased, resulting in more components per chip, faster switching speeds, and decreased costs to the consumer. From 1968 to 2000, the number of transistors per chip increased from one thousand to 42 million. In the same period, clock speed increased from 108 kHz to 1.5 GHz and circuit width reduced from 10  $\mu\text{m}$  to 0.25  $\mu\text{m}$ . In 2005, using various industry fabrication techniques, the number of transistors has increased to over 1.5 billion. Improvements have generally followed Moore's Law, a prediction in 1964 by Intel co-founder Gordon Moore, that the number of components per chip would double every eighteen months (a 67% increase in density per year).

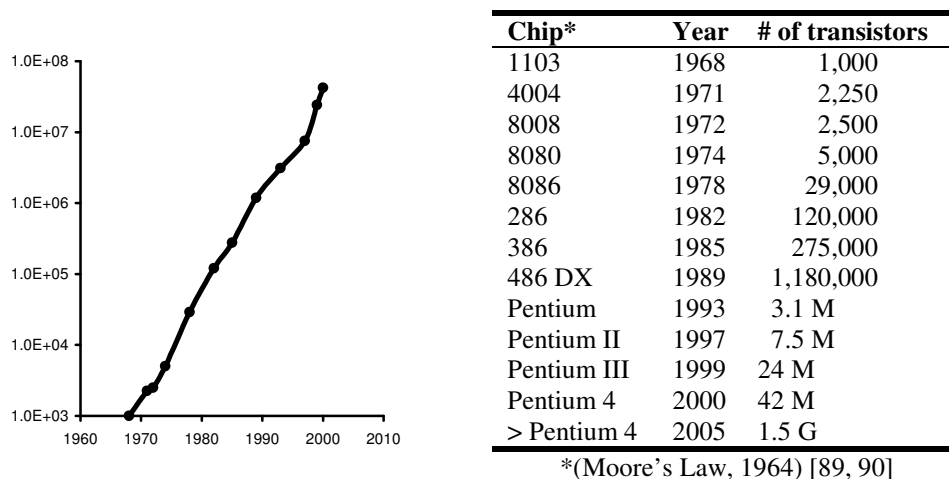


Figure 1.46 Number of components per integrated circuit versus year

<sup>29</sup> The integrated circuit was developed independently by Jack Kilby of Texas Instruments and Robert Noyce of Fairchild Semiconductor (later Intel).

<sup>30</sup> Typically, the number of components refers to the number of transistors, although DRAM (Dynamic RAM) size, MPU (MicroProcessor Unit), and minimum feature size have also been used.

International SEMATECH, a cooperative organisation of 12 firms in the United States, Europe, and Asia, shares developing semiconductor technology. Firms include AMD, Freescale, HP, IBM, Infineon, Intel, Panasonic, Philips, Samsung, Spansion, TSMC, and Texas Instruments. The *International Technology Roadmap for Semiconductors (ITRS)* [1], published by International SEMATECH, aids the development of integrated circuits. Of particular importance is EUVL technology to extend the Mo/Si manufacturing optics to the 32-nm node and beyond by 2010. NGL technology is expected to reduce component size at least five-fold and is considered the most important technological advancement since metal oxide semiconductors (MOS) replaced bipolar transistors in IC manufacturing in 1977 and improved mask technology in the 1980s [91]. Important roadmap metrics for EUV source performance as described by Gabella [92] are summarised in Table 1.6.

•	Central wavelength (nm)	13–14 nm
•	Demonstrated collectable EUV power (2% bandwidth between 13–14 nm)	47–120 W
•	Etendue of source output	$\sim 1.0 \text{ mm}^2 \text{ sr}$
•	Repetition frequency	$> 5000 \text{ Hz}$
•	Pulse-to-pulse repeatability	$\pm 3\% 3\sigma$

**Table 1.6 SEMATECH roadmap metrics [92]**

Past semiconductor manufacturing light sources consisted of Hg discharge lamps and excimer lasers [93]. The current, conventional, leading-edge lithographic source wavelength is 193 nm, produced by an ArF excimer laser. To achieve sub 50-nm minimum feature size,<sup>31</sup> the 193-nm source is to be extended, using the same basic optical lithographic process with improved material technology and immersion lithography.<sup>32</sup> Immersion lithography may also be extended further to the 32-nm node. To manufacture integrated circuits beyond 50 nm with EUVL optics, however, a shorter wavelength radiation source is required to match the proposed Mo/Si multilayer mirrors<sup>33</sup>. The roadmap suggests that a 13.5-nm laser-produced plasma (LPP) or pulsed discharge (PD) source be developed. Possible sources include the resonance transitions of Li, F, Sn, and Xe, which emit at this wavelength [1] as discussed in Section 1.2.5.

Year	Source	Wavelength (nm)	Minimum feature size (nm)
	Hg discharge lamp	248–578	$> 130$
	KrF excimer laser	248	130
2004	ArF excimer laser	193	100
2006	ArF excimer laser with immersion	$< 193$	$< 50$
2009?	LPP	13.5	$< 50$

**Table 1.7 Semiconductor manufacturing source and component size**

<sup>31</sup> One third of the source wavelength is a rule of thumb for minimum feature size.

<sup>32</sup> As such, plans for the 157-nm source with F<sub>2</sub> excimer laser have been discontinued.

<sup>33</sup> Note that shorter wavelength radiation has a lower diffraction limit, which allows smaller minimum feature size.

Original industry ideas to succeed optical lithography included X-ray lithography, ion beam lithography, and electron beam lithography [87], but the preferred NGL technology is now EUVL [88]. Source development includes both laser-produced plasmas and gas discharge pulsed plasmas. The recently proposed immersion lithography [94] will be used to extend 193-nm lithography to the 45 nm node, where the source and wafer are separated by water (refractive index of water,  $n$ , = 1.437). Future development will use other high  $n$  refractive index liquid to further reduce the source wavelength. Double exposures have also been proposed [95].

The Rayleigh-like equation (Eq 1.47) gives the resolution of the minimum feature pitch (or minimum periodic separation between device features). Higher resolution is achieved by decreasing the wavelength or increasing the numerical aperture.

$$res = \frac{k_1 \lambda}{NA} = \frac{k_1 \lambda}{n \sin \theta} \quad (1.47)$$

where  $k_1$  is a photoresist process development factor based on the, illumination characteristics, mask geometries, and manufacturing processes,  $\lambda$  is the source wavelength, and  $NA$  is the numerical aperture.  $k_1$  can be reduced by optical enhancements and process tricks to .3 (0.25 is the theoretical physical limit) [95]. The numerical aperture is a measure of the optical resolution (or lens size) and is equal to the product of the index of refraction,  $n$ , and angle of light incident on the wafer (maximum = 1 at 90°). Thus increasing  $n$  (as in immersion lithography) will increase  $NA$  and decrease the resolution. Note, however, that the depth of field will also decrease.

## 1.4.2 Chip manufacturing

The integrated circuit, silicon “chip” manufacturing process is an advanced lithographic process, using a light source, mask, photo-resist, and a number of silicon-doped or baked layers. A photolithographic process transfers the IC design (mask pattern) to the wafer surface. A number of identical chips (called dies) are manufactured on a single silicon wafer (Figure 1.47.)

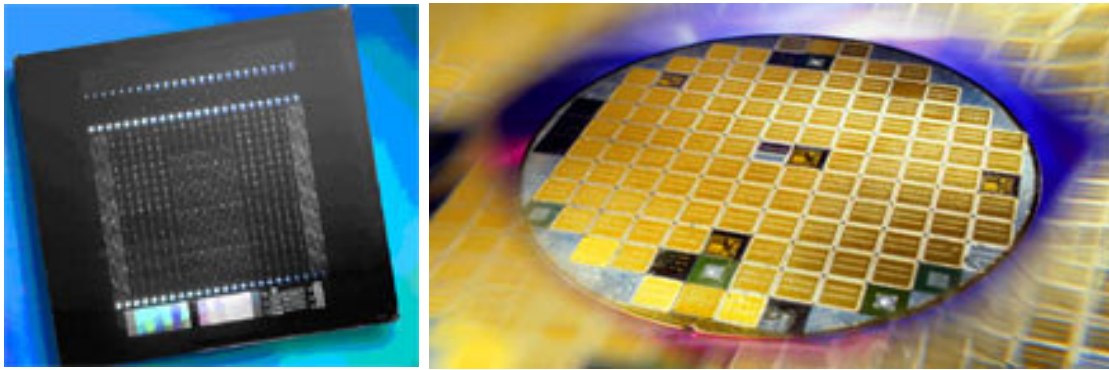


Figure 1.47 Mask and multi-die ICs on silicon wafer [90]

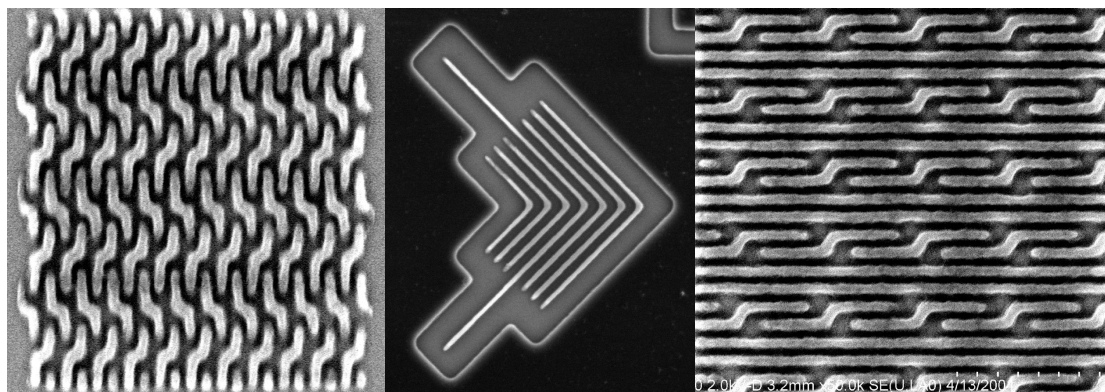
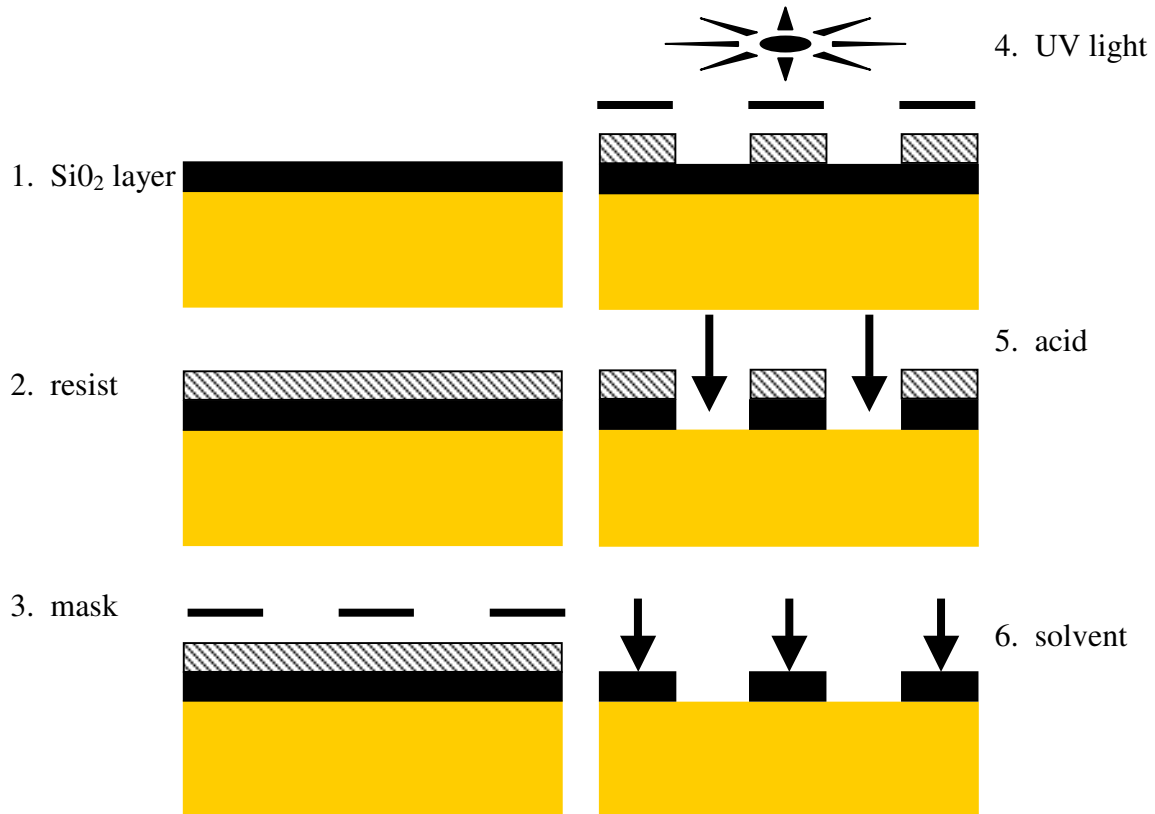


Figure 1.48 Resist profiles of line and space patterns imaged by the ETS at Berkeley (45 nm, 39 nm, and 35 nm) [99]

After designing the circuit logic, the silicon wafer is doped either p- or n-type and baked in an oxygen-rich furnace to create an insulating  $\text{SiO}_2$  layer (see step 1 in Figure 1.49.). A thin, liquid-plastic, radiation -sensitive resist is applied (step 2) and a UV-opaque, patterned glass mask placed over the wafer (step 3). UV light removes the exposed resist (imprinting the IC pattern onto the resist) (step 4). The wafer is then etched with acid, removing the  $\text{SiO}_2$  and leaving the exposed Si and hardened resist (step 5). Finally, an organic solvent removes the resist, leaving the  $\text{SiO}_2$  layer and exposed Si (step 6).

The process is repeated for each layer (new  $\text{SiO}_2$  and resist) with n- or p-doped silicon. Aluminium interconnects (“wires”) are added according to the circuit logic. A single wafer can require up to 250 layers, including etching and implanting. The circuit pattern is then repeated for each die on the wafer and cut into individual chips. Defective dies are discarded.

As described above, the current light source is an excimer laser, ideal for material processing because of the UV wavelength, high peak power and short pulse length. The mask is used as a stencil to etch the IC circuit logic pattern onto the silicon wafer with a feature size smaller than the source wavelength (feature size scaling) [96]. Although EUVL masks can etch features onto a photo-resist at 3:1, traditional optical lithographic methods cannot extend beyond 60 nm, because of the absorption limits of reflecting materials. Multilayer, all-reflective optics are required, although the same basic manufacturing process for optical lithography can be used, with some changes because of the shorter wavelength source and layered reflective optics.



**Figure 1.49** Integrated circuit fabrication by lithographic methods

Physics issues in the NGL process include the limits of conversion efficiency (output intensity at spectral wavelength/input laser power at laser wavelength) and source material emission in the required 13–14 nm range. For an EUVL source, as considered in this work, a conversion efficiency of 3% into a 2% bandwidth is necessary for sufficient throughput (at least 80 wafers/hour [88]).

### 1.4.3 Multilayer mirrors

To image EUV radiation using a multi-mirror optical system, highly reflective, non-absorbing mirrors must be used. Reflectivity must be high, as the proposed industrial lithographic process may require up to ten mirrors for precise beam shaping, delivery, and to correct for aberrations (see Figure 1.13). Depending on the adaptive optics, the expected industry number of mirrors will be 6, 8, or 10.<sup>34</sup> An eight-mirror system, as reported by Stearns *et al.* [97], consists of 3 condenser mirrors, 1 reflective mask, and precision imaging optics with 4 reflecting surfaces to project the reduced mask onto the resist-coated wafer.

All-reflective, multilayer mirrors are made up of a number of alternating high and low Z-layers (Figure 1.50), each about one-quarter of the wavelength of the incident radiation. A 70% peak reflectivity has been achieved in the 13.5-nm range with a 40-layer, molybdenum/silicon (Mo/Si) construction [28].

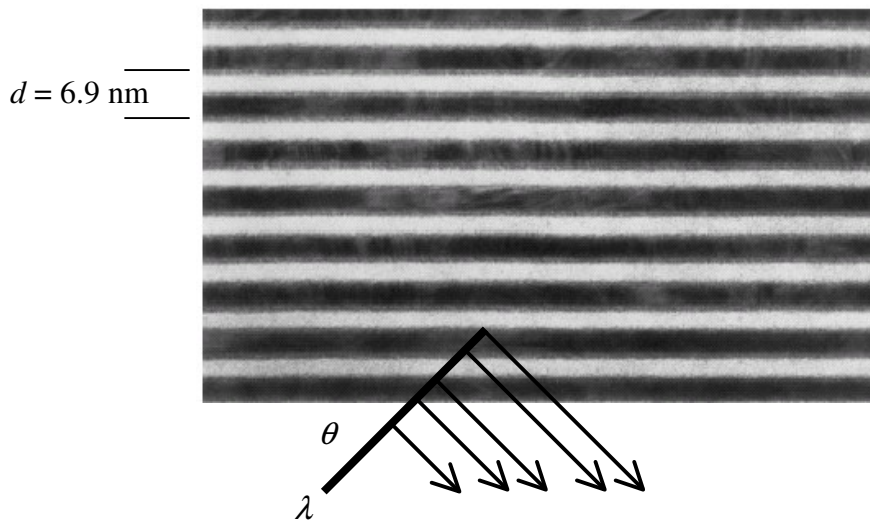


Figure 1.50 Multilayer mirror construction: alternating Mo and Si layers [28]

As described by Attwood [28], multilayer mirrors satisfy the Bragg condition (Eq. 1.48<sup>35</sup>), where incident light is diffracted from each layer, with the reflected waves interfering to give a total superposition reflectivity,  $R$ , as a function of wavelength,  $\lambda$ .

$$m\lambda = 2d \sin(\theta) \quad (1.48)$$

Best reflectivity is from sharp layers, but as the number of layers,  $N$ , exceeds about 40, interdiffusion between layers (called roughness) decreases reflectivity. Original multilayer mirrors were constructed of gold and copper, but the gold and copper reacted and degraded to  $R = 0$  after a month [98]. Design changes, including trying the toxic Rb/Si, resulted in the best reflectivity at 13.5 nm for molybdenum/silicon (Mo/Si) with  $N = 40$  and  $d = 6.9$  nm ( $d$  is the multilayer period).

Molybdenum and silicon are both good materials with high contrast of scattering cross-sections, and are easy to work with. The constructed Mo/Si mirror surface is also durable and strong [28].

<sup>34</sup> An even number of mirrors is needed because of tool symmetry requirements.

<sup>35</sup> To first order.

Table 1.8 gives sample mirror parameters for the proposed NGL Mo/Si mirrors. Figure 1.51 shows the theoretical ideal reflectivity as a function of wavelength for  $n$  reflections, using the Fresnel equations of Kohn [26]. After eight reflections, it can be seen that the reflectivity is reduced to about 10% of the primary optics. The mirror response for  $n$  reflections is normalised in Figure 1.52, showing how the single multilayer mirror reflectivity bandwidth (BW) of 13–14 nm (7.4%) reduces to a multiple mirror bandwidth 13.365–13.635 nm (2%) after 8 reflections.

multilayer period, $d$	6.9 nm
ratio of bottom layer thickness/period, $\Gamma$	0.4
interdiffusion thickness, $s$	0 nm
number of periods, $N$	40
substrate	SiO <sub>2</sub>
fixed angle	90°
polarization	s (1)

**Table 1.8** Specifications for Mo/Si mirror example in Figure 5.1 (default settings in [27])

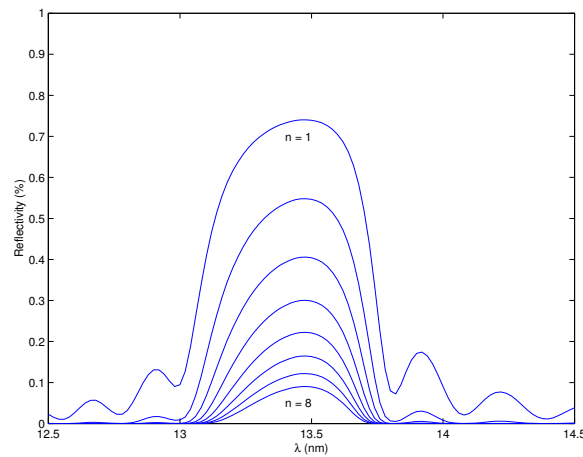


**Figure 1.51** Mo/Si multilayer mirror reflectivity versus wavelength ( $n$  reflections)

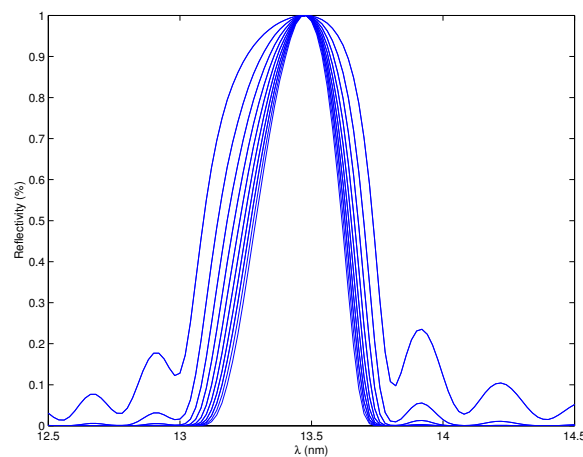


**Figure 1.52** Normalised multilayer mirror reflectivity versus wavelength ( $n$  reflections)

It should be noted that throughput depends on peak reflectivity [97]. The 2% band ( $13.5 \text{ nm} \pm 1\%$  or 13.365–13.635 nm) is suitably monochromatic and is typically given as the industry reference. Out-of-band radiation will produce heating and distortion in the mirrors, but will be reduced by various filters within the optical system. The 7.4% band ( $13.5 \text{ nm} \pm 3.7\%$  or 13.0–14.0 nm) is sometimes given as the in-band limit for one mirror.

## 1.5 References

- 1 SEMATECH: <http://public.itrs.net>.
- 2 O'Sullivan, G. and Carroll, P. K., "4d–4f emission resonances in laser-produced plasmas," *J. Opt. Soc. Am.*, **71** (3), 227–230, 1981.
- 3 Carroll, P. K. and O'Sullivan, G., "Ground-state configurations of ionic species I through XVI for  $Z = 57–74$  and the interpretation of 4d–4f emission resonances in laser-produced plasmas," *Physical Review A: General Physics*, **25** (1), 275–286, 1982.
- 4 Svendsen, W. and O'Sullivan, G., "Statistics and characteristics of xuv transition arrays from laser-produced plasmas of the elements tin through iodine," *Physical Review A: General Physics*, **50** (5), 3710–3718, 1994.
- 5 Harrison, G. R., Lord R. C., and Loofbourow, J. R., *Practical spectroscopy*, Blackie & Son, London, 1949.
- 6 Sawyer, R. A., *Experimental spectroscopy*, Prentice-Hall, 1944.
- 7 Richtmyer, F. K., Kennard, E. H., and Cooper, J. N., *Introduction to modern physics*, Sixth edition, Tata McGraw-Hill Publishing, 1976.
- 8 Thorne, A. P., *Spectrophysics*, Second edition, Chapman and Hall, 1988.
- 9 Schalow, A. L., "Spectroscopy in a new light," Nobel lecture, 1981.
- 10 Edlen, B., "Atomic spectra," in *Encyclopedia of Physics*, S. Flugge, Editor, Vol. 27, Springer-Verlag, Berlin, 1964.
- 11 Balmer, J. J., "Note on the spectral lines of hydrogen," *Ann. Physik Chem.* **25**, 80–85, 1885.
- 12 Newton, I., *Opticks: or a treatise of the reflexions, refractions, inflexions, and colours of light*, Smith and Walford Printers, London, 1704.
- 13 Condon, E. U. and Obadaşı, H., *Atomic structure*, Cambridge University Press, 1980.
- 14 Ångström, A. J., *Kungl. Svenska Vetensk. Akad. Handl.*, 327, 1852.
- 15 Condon, E. U. and Shortley, G. H., *The theory of atomic spectra*, University Press, Cambridge, 1935.
- 16 Weaire, D. and O'Connor, S., *Annals of Science*, **44**, 617–644, 1987.
- 17 Samson, J. A. R., *Techniques of vacuum ultraviolet spectroscopy*, John Wiley & Sons, Inc., New York, 1967.
- 18 Moore, C. E., *Atomic energy levels: as derived from the analyses of optical spectra*, Vols. I–III, Circular of the National Bureau of Standards, 1958.
- 19 Cowan, R. D., *The theory of atomic spectra and structure*, Berkeley, University of California Press, 1981.
- 20 Herzberg, G., *Atomic spectra and atomic structure*, Dover Publications, 1944.
- 21 Froese Fischer, C., Brage, T., and Jönsson, P., *Computational atomic structure—An MCHF approach*, Institute of Physics Publishing, 1997.
- 22 Connerade, J. P., "The non-Rydberg spectroscopy of atoms," *Contemp. Phys.*, Vol. 19, No. 5, 415–448, 1978.
- 23 Kunze, H.-J., "Spectrometer design and laboratory application," in *Astrophysical and laboratory spectroscopy*, R. Brown and J. Lang editors, Proceedings of the thirty-third Scottish summer school in physics, 197–209, St. Andrews, 1987.
- 24 Rowland, H. A., "Preliminary notice of the results accomplished in the manufacture and theory of gratings for optical purposes," *Phil. Mag.* **13**, 469, 1882.
- 25 Namioka, T. and Ito, K., *Physica Scripta*, **37** (4), 673, 1988.
- 26 Kohn, V. G., *Phys., Stat. Sol. (b)*, **187**, 61, 1995.
- 27 Centre for x-ray optics: [http://www-cxro.lbl.gov/optical\\_constants/multi2.html](http://www-cxro.lbl.gov/optical_constants/multi2.html).
- 28 Attwood, D., *Soft x-rays and extreme ultraviolet radiation, principles and applications*, Cambridge University Press, 1999.
- 29 Cornu, M. A., "Mémoires et communications," *Comptes Rendus des Séances de l'Académie des Sciences*, 1215–1222, 1893.
- 30 Zernicke von, F., "Die abbildungsfehler des konkavgitters und ihre hebung," *Zeeman Verhandelingen*, 's-gravenhage, 1935.
- 31 Beutler, H. G., "The theory of the concave grating," *Journal of the Optical Society of America*, **35** (5), 311–350, 1945.
- 32 Mack, J. E., Stehn, J. R., Edlén, B., "On the concave gratings spectograph, especially at large angles of incidence," *Journal of the Optical Society of America*, **22**, 245–264, 1932.

- 33 Sai, T., Seya, M., and Namioka, T., "On Beutler's theory of the concave grating, science of light," *Science of Light*, **17** (1), 11–24, 1968.
- 34 Meijer, F. G., "The use of gratings in the vacuum ultraviolet," *Optica Applicata*, **17** (3), 255–264, 1987.
- 35 Meijer, F. G., "Construction, adjustment and performance of a 6.600 m grazing incidence vacuum spectograph," *J. Phys. E: Sci. Instrum.*, **12**, 129–135, 1979.
- 36 Carroll, P. K. and Kennedy, E. T., "Laser-produced plasmas," *Contemporary Physics*, Vol. 22, 61–96, 1981.
- 37 O'Reilly, F., "Photoabsorption and photoemission spectroscopy of third and fourth row ions," Ph.D. thesis, Appendix 3, University College Dublin, 1998.
- 38 Condon, E. U. and Shortley, G. H., "The theory of atomic spectra," Cambridge University Press, 1970.
- 39 O'Sullivan, G., "Charge-dependent wave-function collapse in ionised xenon," *J. Phys B*, **15** L 765, 1982.
- 40 Cowan, R. D., "Programs RCN/RCN2/RCG/RCE," Addendum to *The theory of atomic spectra and structure*, May 1995.
- 41 Bauche, J. and Bauche-Arnoult, C., "Transition arrays in the spectra of ionised atoms," *Advances in atomic and molecular physics*, Vol. 23, 131–195, 1988.
- 42 Peyrusse, O., "Atomic configuration averages and nonlocal thermodynamical equilibrium plasma spectroscopy calculations," *J. Phys. B: At. Mol. Opt. Phys.* **32**, 683–700, 1999.
- 43 Jin, F. and Richardson, M., "New laser plasma source for extreme-ultraviolet lithography," *Appl. Opt.* **34**, 5750–5760, 1995.
- 44 Salzmann, D., "Atomic physics in hot plasmas," International series of monographs on physics, Oxford University Press, 1998.
- 45 Bauche, J. and Bauche-Arnoult, C., "Statistical approach to the spectra of plasmas," *Physica Scripta*, **T40**, 58–64, 1992.
- 46 Bauche, J. and Bauche-Arnoult, C., "Unresolved transition arrays," *Physica Scripta*, **37**, 659–663, 1988.
- 47 Mandelbaum, P., Finkenthal, M., Schwob, J. L., and Klapisch, M., "Interpretation of the quasicontinuum band emitted by highly ionized rare-earth elements in the 70–100 Å range," *Phys. Rev. A*, **35**(12), 5051–5059, 1987.
- 48 O'Sullivan, G., Carroll, P. K., Dunne, P., Faulkner, R., McGuinness, C. and Murphy, N., "Supercomplex spectra and continuum emission from rare-earth ions: Sm, a case study," *J. Phys. B: At. Mol. Opt. Phys.*, **32** (8), 1893–1922 (1999).
- 49 O'Sullivan, G. and Faulkner, R., "Tunable narrowband soft x-ray source for projection lithography," *Opt. Eng.*, **33**, 3978, 1994.
- 50 Dunne, P., O'Sullivan, G., and O'Reilly, D., "Prepulse-enhanced narrow bandwidth soft x-ray emission from a low debris, subnanosecond, laser plasma source," *Applied Physics Letters*, **76** (1), 2000.
- 51 O'Sullivan, G., "Atomic structure of highly ionised ions," *Comments At. Mol. Phys.*, **28** (3), 143–178, 1992.
- 52 Colombant, D. and Tonon, G. F., "X-ray emission in laser-produced plasmas," *J. Appl. Phys.*, **44** (8), 3524–3537, 1973.
- 53 Bender, H. A., O'Connell, D., and Silfvast, W. T., "Velocity characterization of particulate debris from laser-produced plasmas used for extreme-ultraviolet lithography," *Appl. Opt.*, **34**, 6512, 1995.
- 54 Shields, H., Fornaca, S. W., Petach, M. B., Michaelian, M., McGregor, R. D., Moyer, R. H., and St. Pierre, R., "Xenon target performance characteristics for laser-produced plasma EUV source," Emerging lithographic technologies VI, *Proceedings of SPIE*, **4688**, 2002.
- 55 Bijkerk, F., Shmaenok, L., van Honk, A., Marchand, A., Bastiaensen, R., Platonov, Yu. Ya., Shevelko, A. P., Mitrofanov, A. V., Vob, F., Desor, R., Frowein, H., and Nikolaus, B., "Laser plasma sources for soft x-ray projection lithography," *J. Phys. III France*, **4**, 669–1677, 1994.
- 56 Bijkerk, F., Shmaenok, L. A., Louis, E., Voorma, H.-J., Koster, N. B., Bruineman, C., Bastiaensen, R. K. F. J., van der Drift, E. W. J. M., Romijn, J., de Groot, L. E. M., Rousseeuw, B. A. C., Zijlstra, T., Platonov, Yu. Ya., and Salashchenko, N. N., "Extreme UV lithography: a new laser plasma target concept and fabrication of multilayer reflection masks," *Microelectron. Eng.*, **30**, 183–186, 1996.
- 57 Richardson, M., Torres, D., DePriest, C., Jin, F., and Shimkaveg, G., *Optics Communications*, **145**, 109, 1998.

- 58 Tomie, T., Yashiro, H., Aota, T., Ueno, Y., Lee, D., Niimi, G., Lin, J., Komiyama, K., Yokota, H., and Nishigori, K., "Debris-free EUV plasma source," *Proceedings international symposium on technologies and applications of photoelectron micro-spectroscopy with laser-based VUV sources*, Tsukuba, Japan, 2002.
- 59 Jansson, P. A. C., Hansson, B. A. M., Hemberg, O., Otendal, M., Holmberg, A., de Groot, J., and Hertz, H. M., "Liquid-tin-jet laser-plasma extreme ultraviolet generation," *Applied Physics Letters*, **84** (13), 2004.
- 60 Aota, T., Yashiro, H., Ueno Y., and Tomie, T., "Strong narrowband peak at 13.5-nm generated in a cavity-confined tin plasma," *Emerging lithographic technologies VII, Proceedings of SPIE*, **5037**, 742–749, 2003.
- 61 Van Dijsseldonk, A., "EUV lithographical systems," NANOCMOS-more Moore: Challenges and solutions for sub-45nm technologies," Leuven, Belgium, April 2005.
- 62 Hayden, P., "An investigation of tin based LPPs as a source of radiation at 13.5 nm," M.Sc. thesis, University College Dublin, 2004.
- 63 Kelly, R. L. and Palumbo, L. J., *Atomic and ionic emission lines below 2000 angstroms*, Naval Research Laboratory report 7599, Washington, 1973.
- 64 Fahy, K., Dunne, P., McKinney, L., O'Sullivan, G., Sokell, E., White, J., Aguilar, A., Pomeroy, J. M., Tan, J. N., Blagojevic, B., LeBigot, E.-O. and Gillaspay, J. D., "UTA versus line emissions for EUVL: studies on xenon emission at the NIST EBIT," *J.Phys. D: Applied Physics* **37** (23), 3225-3232 (2004).
- 65 Greim, H. R., *Plasma spectroscopy*, Chapter 6, McGraw-Hill, New York, 1964.
- 66 Carroll, P. K. and Kennedy, E. T., "Laser-produced plasmas," *Contemporary Physics*, Vol. 22, 61–96, 1981.
- 67 Key, M. H. and Hutcheon, R. J., "Spectroscopy of laser-produced plasmas," *Advances in atomic and molecular physics*, Vol. 16, ed. Bates, Sir David, Academic Press, 1980.
- 68 Kennedy, E. T., "Plasmas and intense laser light," *Contemporary Physics*, Vol. 25, 31–58, 1984.
- 69 De Michelis, C. D. and Mattioli, M., "Spectroscopy and impurity behaviour in fusion plasmas," *Report on Progress in Physics*, Vol. 47, 1233–1346, 1984.
- 70 Bell, A. R., "Laser-produced plasmas," in *Plasma physics*, R. Dendy editor, Cambridge University Press, 319–337, 1993.
- 71 Conway, J., "Design and construction of an electronic system for dual laser plasma experiments and its application to photoabsorption studies of medium Z elements," Ph.D. thesis, Chapter 2, University College Dublin, 2000.
- 72 Spitzer, L., *Physics of fully ionized gases*, 2<sup>nd</sup> ed. New York, Interscience, 1962.
- 73 Eliezer, S., Krumbein, A. D., and Salzmann, D., "A generalised validity condition for local thermodynamic equilibrium in a laser-produced plasma," *Phys. D: J. Appl. Phys.* **11**, 1693–1701, 1978.
- 74 Bates, D. R., Kingston, A. E., and McWhirter, R. W. P., "Recombination between electrons and atomic ions. I. Optically thin plasmas," *Proc. Roy. Soc. A*, **267**, 297–312, 1962.
- 75 Bates, D. R., Kingston, A. E., and McWhirter, R. W. P., "Recombination between electrons and atomic ions. II. Optically thick plasmas," *Proc. Roy. Soc. A*, **270**, 152–167, 1962.
- 76 Gupta, G. P. and Sinha, B. K., "Effect of ionization and recombination coefficients on the charge-state distribution of ions in laser-produced aluminium plasmas," *Phys. Rev. E*, **56** (2), 2104–2111, 1997.
- 77 Christiansen, J. P., Ashby, D. E. T. F., and Roberts, K. V., "Medusa: a one-dimensional laser fusion code," *Computer Physics Communications*, **7**, 271–287, 1974.
- 78 Rodgers, A. M., Rogoyski, A. M., and Rose, S. J., "MED101: a laser-plasma simulation code: User guide," Rutherford Appleton Laboratory report: *RAL-89-127*, RAL, Didcot, U.K., 1989.
- 79 Djaoui, A., "A user guide for the laser-plasma simulation code: MED103," Rutherford Appleton Laboratory report: *RAL-TR-96-099*, RAL, Didcot, U.K., 1996.
- 80 Patel, P. K., Wark, J. S., Heading, D. J., Djaoui, A., Rose, S. J., Renner, O., and Hauer, A. "Simulation of x-ray line transfer in a cylindrically expanding plasma," *J. Quant. Spectrosc. Radiat. Transfer*, **57** (5), 683–694, 1997.
- 81 Patel, P. K., Wark, J. S., Renner, O., Djaoui, A., Rose, S. J., Heading, D. J., and Hauer, A. "Experimental and simulated profiles of the Al XIII Ly- $\alpha$  resonance line from a cylindrically expanding plasma," *J. Quant. Spectrosc. Radiat. Transfer*, **58** (4–6), 835–844, 1997.
- 82 Patel, P. K., Wolfrum, E., Renner, O., Loveridge, A., Allott, R., Neely, D., Rose, S. J., and Wark, J. S., "X-ray line reabsorption in a rapidly expanding plasma," *J. Quant. Spectrosc. Radiat. Transfer*, **65**, 429–439, 2000.

- 83 Duffy, G., *Laser-produced plasma: spectroscopy and applications*, Ph.D. thesis, Chapter 4, University College Dublin, 2001.
- 84 O'Reilly, D., *Development of a narrow bandwidth source for projection lithography*, M.Sc. thesis, Chapter 1, University College Dublin, 2000.
- 85 Faulkner, R., *VUV studies of laser-produced plasma emission, application to projection lithography and the collision based studies of selected ions*, Ph.D. thesis, Section 1.3, University College Dublin, 2000.
- 86 Feynman, R. P., *Lectures on computation*, Chapter 7, Penguin Books, 1996.
- 87 Turton, R., *The quantum dot: a journey into the future of microelectronics*, Chapter 4 and 5, W. H. Freeman, Oxford, 1995.
- 88 Bjorkholm, J. E., "EUV lithography—the successor to optical lithography?" *Intel Technology Journal Q3'98*, 1998.
- 89 Moore, G. E., "Cramming more components onto integrated circuits," *Electronics*, **38** (8), 1965.
- 90 Intel: <http://www.intel.com/technology/silicon/sp>.
- 91 O'Sullivan, G., "Opening the extreme ultra-violet lithography source bottleneck: The development of a 13.5 nm plasma based source for the semiconductor industry," *SFI Investigator Programme Grant*, May 15, 2002.
- 92 Gabella, P., "Introduction," *Fifth EUVL source workshop*, Dallas Texas, October 14, 2002.
- 93 Brinkmann, U. (ed.), "193-nm radiation, new resists for submicron lithography," *Lambda Highlights*, **27/28**, April 1991.
- 94 Smith, B., "Under water—immersion techniques carry 193-nm lithography beyond the 65-nm node," *SPIE's oemagazine*, July 2004.
- 95 Wurm, S., "EUVL technology status and challenges," *NanoCMOS/more Moore*, Leuven, Belgium, April 26–27, 2005.
- 96 Hardin, R. W., "Optical lithography gets nod from microchip industry," *OE Reports*, 182, 1999.
- 97 Stearns, D. G., Rosen, R. S., and Vernon, S. P., "Multilayer mirror technology for soft x-ray projection lithography," *Applied Optics*, **32** (34), 1993.
- 98 Underwood, J. H. and Barbee, T. W., "Layered synthetic microstructures as Bragg diffractors for x rays and extreme ultraviolet: theory and predicted performance," *Applied Optics*, **20** (17), 1981.
- 99 Naulleau, P. from Attwood, D., "Imaging at High Spatial Resolution: Soft X-Ray Microscopy and EUV Lithography," Dublin 2006.

## 2. Theoretical Cowan and UTA statistics

The Hartree-Fock configuration-interaction (HFCl) Cowan code [1] (modified for larger dimensions by McGuinness and van Kampen [2, 3]) was used to calculate theoretical spectra for the ten, 4d-subshell tin ions, from Sn V (Pd-like) to Sn XIV (Rb-like)<sup>36</sup>. To determine optimum configuration interaction (CI) and Slater-Condon scaling,  $4p^6 4d^{N-1} 4f^1$ ,  $4p^5 4d^{N+1}$ , and  $4p^6 4d^{N-1} 5p^1$  configurations ( $N = 1$  to 10) were included in the calculation (giving 4d-4f, 4p-4d, and 4d-5p transitions), as were increasingly higher  $n$  configurations (giving 4d- $nf$ , 4d- $np$ , and 4p- $ns$  Rydberg series transitions) in succession for  $n = 5, 6, etc.$  until the Cowan code exceeded its dimensions.

### 2.1 Sn 4d subshell (Sn V–Sn XIV)

In the absence of Sn experimental data for other than Sn V–Sn VIII [4–9] (of which only Sn VI [5] and Sn VII [7] give results for the important 13.5-nm range, 4d-4f and 4p-4d transitions), the Slater-Condon radial integrals were initially scaled to match the experimental 4d-4f  $^1P_1$  line emissions of Churilov *et al.* [10] and Sugar and Kaufman [11] and, as in past analysis, ions isoelectronic to Pd I [10, 11]. Scaling will significantly affect the 2% (13.5 nm  $\pm 1\%$ ) in-band  $\Sigma gf$ , since the positions of the 4d-4f  $^1P_1$  transitions along the isoelectronic sequence are very sensitive to  $G^I(4d,4f)$  in particular. The direct and exchange Coulomb integrals ( $F^k$  and  $G^k$ ) were identically decreased with ionisation stage from 50% for Sn VI to 79% for Sn XIV. The other Slater-Condon scaling factors were unchanged and the same scaling for Sn VI was used for Sn V. Table 2.1 gives the initial scaling used for the ten ions, assumed identical to that obtained for the corresponding stage along the Pd I sequence. Note that the scaling is charge-state dependent rather than configuration dependent.

Sn ion	$F^k_{ii}$	spin-orbit	$F^k_{ij}$	$G^k_{ij}$	$R^k$
Sn VI	85	99	<b>50</b>	<b>50</b>	80
Sn VII	85	99	<b>56</b>	<b>56</b>	80
Sn VIII	85	99	<b>63</b>	<b>63</b>	80
Sn IX	85	99	<b>68</b>	<b>68</b>	80
Sn X	85	99	<b>72</b>	<b>72</b>	80
Sn XI	85	99	<b>75</b>	<b>75</b>	80
Sn XII	85	99	<b>77</b>	<b>77</b>	80
Sn XIII	85	99	<b>78</b>	<b>78</b>	80
Sn XIV	85	99	<b>79</b>	<b>79</b>	80

**Table 2.1 Initial tin scaling percentages (Sn VI to Sn XIV)**

When the theoretical results were compared to the experimental data of Sn VI [5] and Sn VII [7], however, it was apparent that the scaling was incorrect. The 4d-5p transitions of Sn VII in the 23.3–29.0 nm range [6] (Figure 2.1) and of Sn VIII in the 19.7–24.8 nm range [9] (Figure 2.2) matched well, but the 4d-4f transitions did not (Figures 2.3 and 2.4), and are of greater importance for analysing the UTA in higher ion stages. As well, a cursory look showed that large  $gf$  value transitions in the Cowan results did not match any experimental classifications [7]. Table 2.2 lists the experimental data [4–9] by configuration and range.

<sup>36</sup> Note that Sn V is ionised at 13.5 nm (91.84 eV), but is included in some of the 4d subshell analysis for completeness.

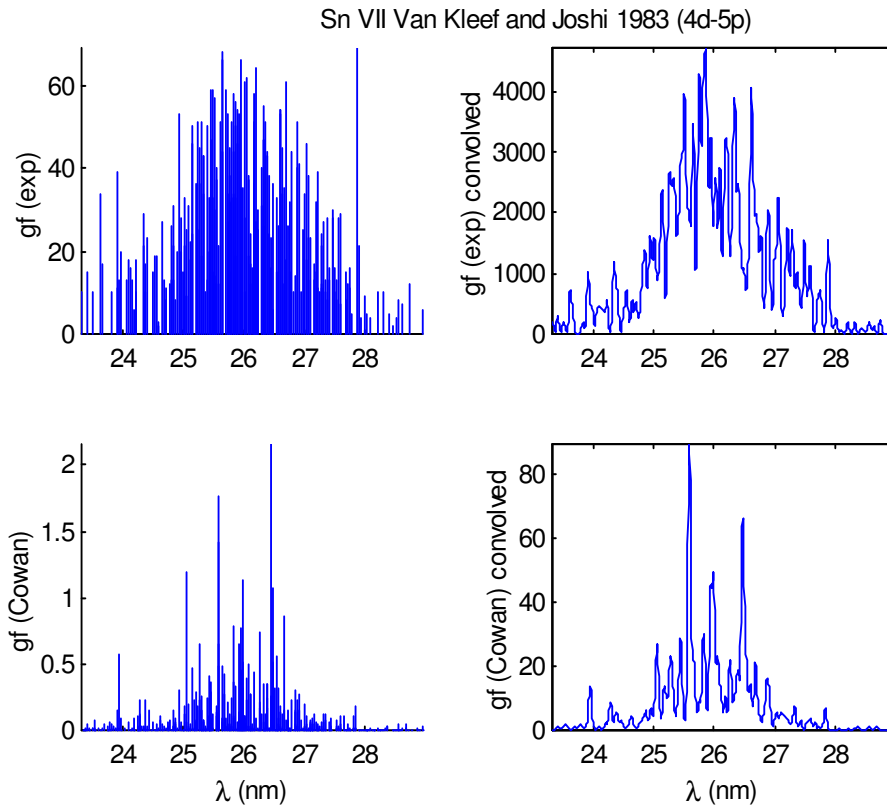


**Figure 2.1** Sn VII 4d-5p experimental (top) [6] and Cowan (bottom) (scaling = 56%)

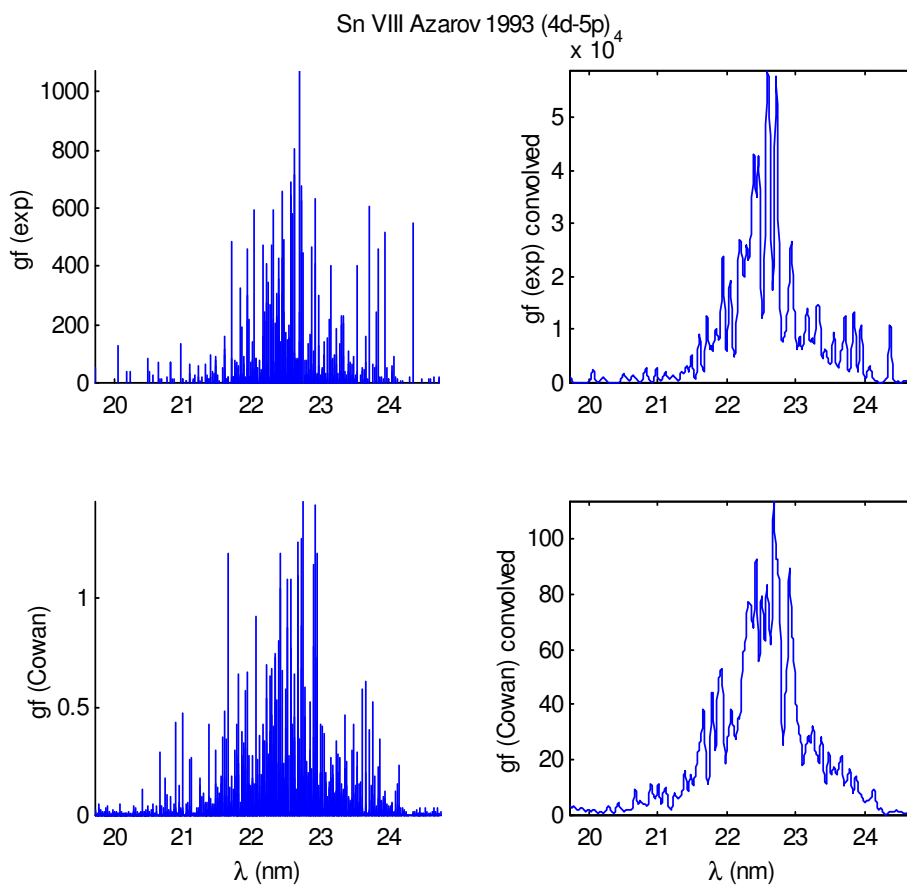


**Figure 2.2** Sn VIII 4d-5p experimental (top) [7] and Cowan (bottom) (scaling = 63%)

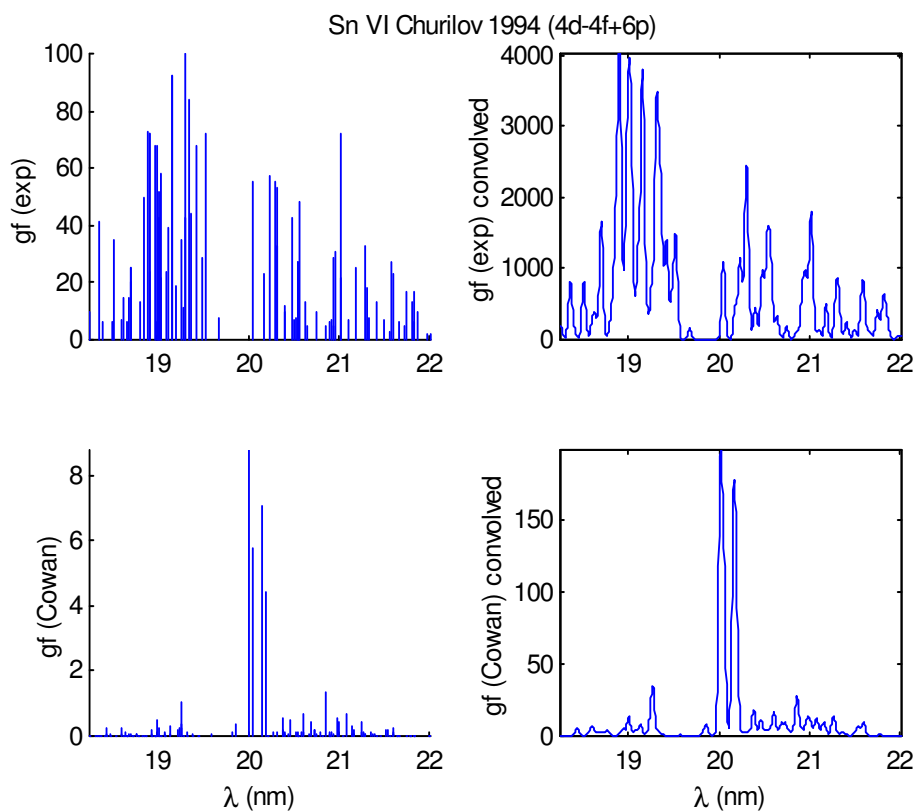


**Figure 2.3** Sn VI 4d-4f+6p experimental (top) [6] and Cowan (bottom) (scaling = 50%)

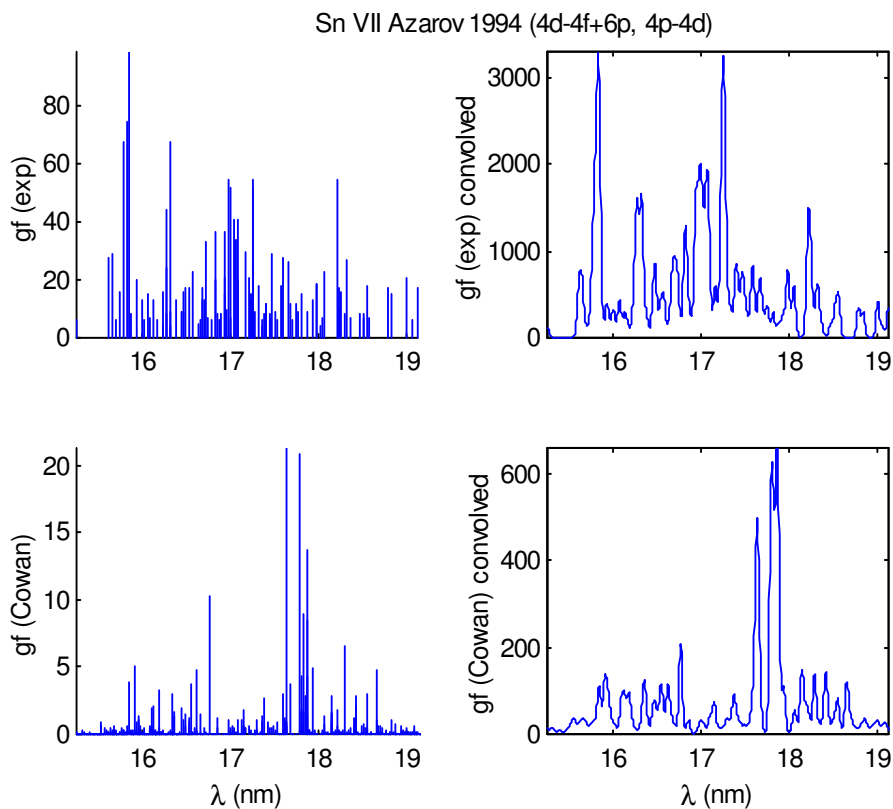


**Figure 2.4** Sn VII 4d-4f+6p, 4p-4d experimental (top) [7] and Cowan (bottom) (scaling = 56%)

Ion	ref.	configurations	range (nm)	# lines
Sn VI	[4] 1997	4d <sup>9</sup> → 4d <sup>8</sup> 5p	4d-5p	
Sn VI	[5] 1994	4d <sup>9</sup> → 4d <sup>8</sup> (4f +6p)	4d-4f 4d-6p	85
Sn VII	[6] 1983	4d <sup>8</sup> → 4d <sup>7</sup> 5p	4d-5p	221
Sn VII	[7] 1994	4d <sup>8</sup> → 4d <sup>7</sup> (4f +6p) + 4p <sup>5</sup> 4d <sup>9</sup>	4d-4f 4d-6p 4p-4d	109
Sn VII	[8] 1993	4d <sup>7</sup> 5s → 4d <sup>7</sup> 5p	5s-5p	863
Sn VIII	[9] 1993	4d <sup>7</sup> → 4d <sup>6</sup> 5p	4d-5p	381

Table 2.2 Experimental line classification for Sn ions (Sn VI to Sn VIII)

Another scaling survey was done to match the strongest Cowan lines to the strongest experimental lines in Sn VII, as classified by Azarov *et al.* [7]. Four such lines were immediately identified (<sup>1</sup>H<sub>5</sub> at 170.155 Å, <sup>3</sup>G<sub>5</sub> at 169.891 Å, <sup>1</sup>G<sub>4</sub> at 172.590 Å, and <sup>3</sup>F<sub>3</sub> at 163.9351 Å), the first three being 4d-4f transitions and the fourth a 4p-4d transition (see Table 2.3). Using these lines, the scaling factors other than the spin-orbit (constant at 99%) were identically changed and only five configurations (4d<sup>8</sup> → 4d<sup>7</sup>(5p + 6p + 4f + 5f) + 4p<sup>5</sup>4d<sup>9</sup>) were included as reported in [7]. The survey showed that a scaling factor of 75 gave the best match. Table 2.3 lists the four lines and their intensities from Azarov *et al.* [7] and from Cowan. The four lines are the eighth, sixth, ninth, and third strongest in Azarov *et al.* [7] and the first, second, fourth and eleventh strongest from Cowan, respectively. The difference in relative strengths and the absence of the strongest experimental lines in the Cowan output is because the Cowan data has not been weighted by level populations as well as the assigning of relative experimental intensities in Azarov *et al.* [7].

line <sup>37</sup>	Azarov (Å)	Azarov (I)	Cowan (Å)	Cowan (gf)
<sup>1</sup> H <sub>5</sub>	170.155	52	169.7145	25.38
<sup>3</sup> G <sub>5</sub>	169.891	55	169.8292	23.59
<sup>1</sup> G <sub>4</sub>	172.590	51	172.0396	14.96
<sup>3</sup> F <sub>3</sub>	163.298	68	163.9351	4.54

Table 2.3 Sn VII line comparisons (Azarov [7] and Cowan)

To determine the required scaling for ions higher than Sn VII, the theoretical results of the initial survey were compared to experimental results recorded at UCD on a Jenoptik spectrometer—a ¼-metre, 1200 lines/mm, variable line spacing grating EUV spectrograph [12]. The results were recorded over increasing power density in the 9.5–18 nm range and are shown in Figure 2.5 [12].

It was noticed that the short-wavelength UTA edge was near 13 nm, comparable to the original Sn XIV theoretical results. A final survey, which varied the scaling between 75% and 90% for Sn XIV, suggested that a scaling factor of 85% was sufficient in the absence of more experimental data.

<sup>37</sup> Labelled in Azarov [7] by lower level: hence <sup>1</sup>H<sub>5</sub> as <sup>1</sup>G<sub>4</sub> and <sup>3</sup>G<sub>5</sub> as <sup>3</sup>F<sub>4</sub>.

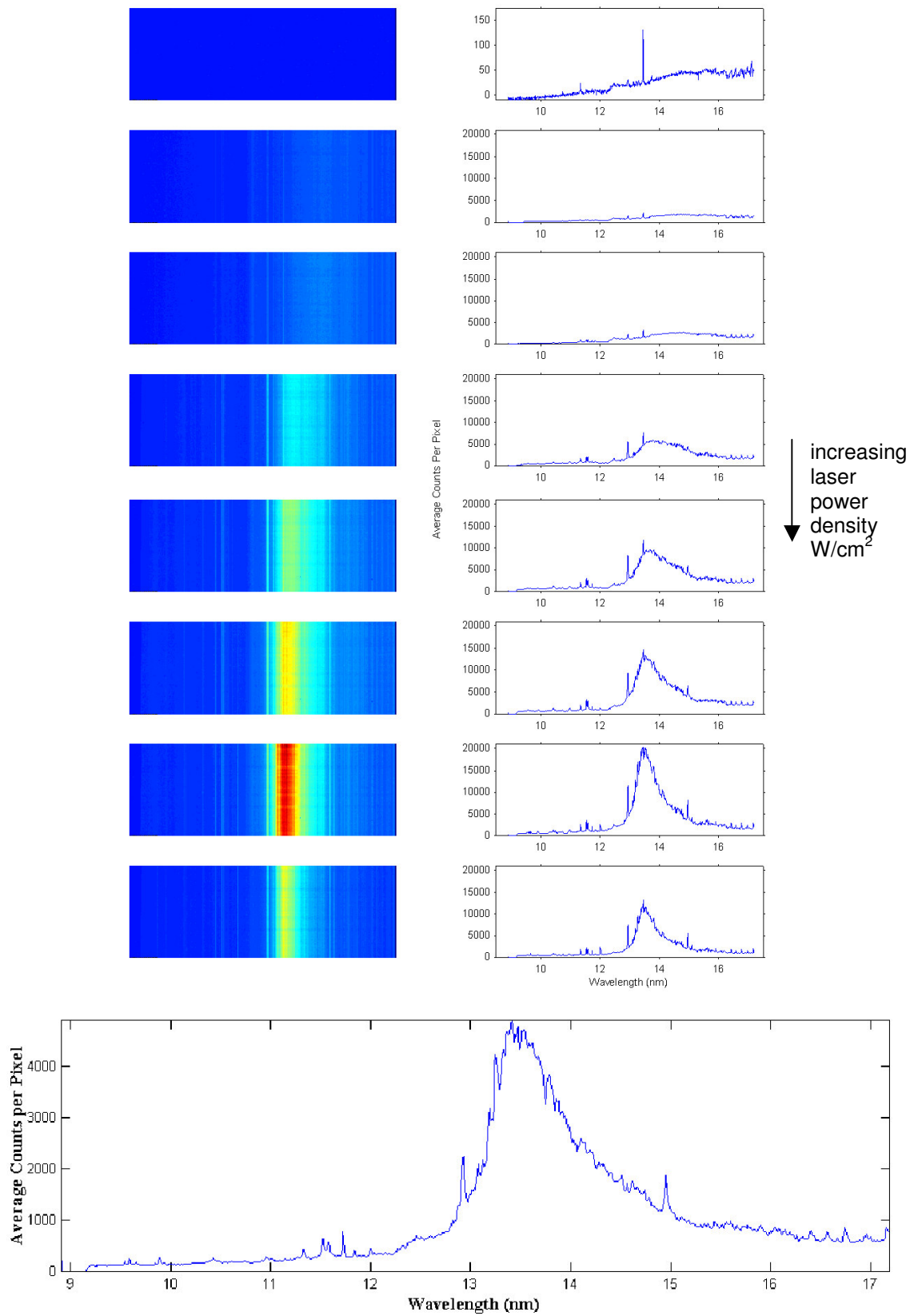
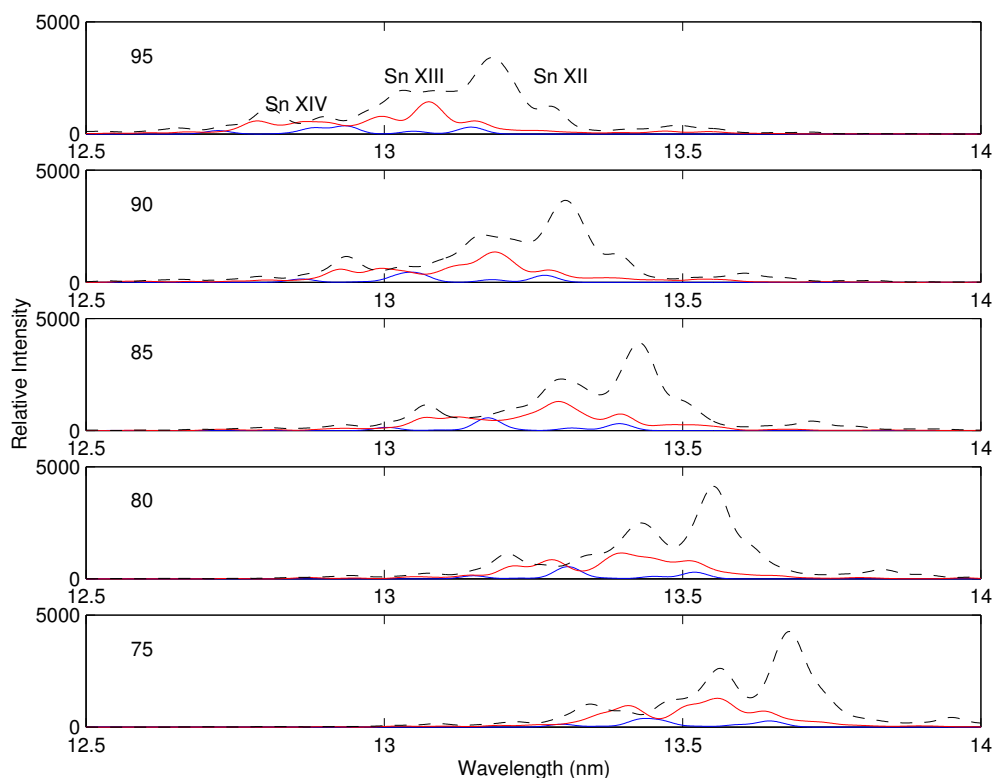


Figure 2.5 Tin spectra with increasing power density from top to bottom (top) and maximum power density from above (bottom) [12]

Figure 2.6 shows the effect of scaling on the theoretical spectrum. Note that, at the short-wavelength edge, the 4p-4d line scales to longer wavelengths by about 0.15 nm for 5% in scaling. Also included for comparison in Figure 2.6 is the theoretical output for Sn XIII and Sn XII, as all three ions overlap in the 13.5-nm region.



**Figure 2.6** Sn XIV (blue), Sn XIII (red), and Sn XII (black, dashed) with scaling varied from 90% (top) to 75% (bottom)

Accordingly, scaling values were interpolated between 75% for Sn VII and 85% for Sn XIV (integer values only in Cowan) and are listed in Table 2.4. The same scaling for Sn VII was used for Sn V and Sn VI. The final Cowan files were generated with the scaling from Table 2.4, using the same number of configurations giving 4d-*nf*, 4d-*np*, and 4p-*ns* transitions as in the initial survey.

The *gf* versus  $\lambda$  plots are shown in Figures 2.7–2.9 over three ranges: 5–25 nm (which contains all Cowan spectral emission for the given configurations), 13.0–14.0 nm or the 7.4% in-band range (representing the full Mo/Si mirror response region), and 13.365–13.635 nm or the 2% in-band range (the industry conversion efficiency standard measure and the only radiation ultimately transmitted through the multi-mirror optics system). Figure 2.10 and Table 2.5 show the sum of the *gf* values in the three regions versus ion stage.

A statistical analysis of the ten ions is shown in Figure 2.11 and Table 2.6 (from the UTA moment statistics in Equations 1.20–1.30 in Section 1.2.3). The mean wavelength, standard deviation, skewness, and kurtosis are the weighted moments of the weighted oscillator strength versus wavelength distribution (*gf* versus  $\lambda$ ), which statistically characterise the total emission. The maximum *gf* value and the wavelength at that maximum are also given.

Sn ion	$F_{ii}^k$	spin-orbit	$F_{ij}^k$	$G_{ij}^k$	$R^k$
Sn V	75	99	75	75	75
Sn VI	75	99	75	75	75
Sn VII	75	99	75	75	75
Sn VIII	77	99	77	77	77
Sn IX	78	99	78	78	78
Sn X	80	99	80	80	80
Sn XI	81	99	81	81	81
Sn XII	83	99	83	83	83
Sn XIII	84	99	84	84	84
Sn XIV	85	99	85	85	85

Table 2.4 Sn scaling (Sn V–Sn XIV)

Sn ion	5-25 nm		12.5-14.5 nm		13.365-13.635 nm	
	# lines	$\Sigma gf$	# lines	$\Sigma gf$	# lines	$\Sigma gf$
Sn V*	91	12.84	1	0.29	0	0
Sn VI	1563	139.47	665	45.91	143	12.59
Sn VII	9919	604.53	1847	194.85	271	6.92
Sn VIII	38084	1593.72	3950	316.93	646	10.13
Sn IX	72073	2557.38	1567	819.34	136	53.05
Sn X	100099	2779.67	1391	2118.13	216	167.08
Sn XI	66802	2165.89	1267	1761.41	187	472.95
Sn XII	22624	1135.10	690	946.94	108	491.52
Sn XIII	4338	388.25	174	334.06	35	84.80
Sn XIV	284	77.65	12	65.26	3	16.61

Table 2.5 In-band  $\Sigma gf$  (\*ionised at 92 eV)

Ion	$n^*$	# lines	$\Sigma gf$	mean $\lambda$	std	skew	kurt	maxgf	peak $\lambda$
				(nm)	(nm)				
Sn V (Sn <sup>4+</sup> )	15	94	13.82	19.63	5.73	1.76	6.10	4.63	16.14
Sn VI	12	1092	145.35	17.33	4.55	1.43	5.25	8.80	20.02
Sn VII	9	10275	633.37	15.93	3.67	1.01	4.57	21.32	17.64
Sn VIII	8	38246	1573.44	15.01	2.90	0.58	4.57	38.97	16.13
Sn IX	7	72089	2535.42	14.33	2.30	-0.07	5.16	47.02	15.11
Sn X	8	100128	2759.33	13.77	2.08	-1.29	6.50	50.42	14.41
Sn XI	8	68422	2152.88	13.34	1.95	-2.07	8.01	43.66	13.93
Sn XII	9	27239	1132.92	12.97	1.99	-2.37	8.44	37.25	13.66
Sn XIII	14	7521	390.7	12.65	2.29	-2.17	7.01	23.64	13.43
Sn XIV	19	816	78.68	12.48	2.50	-1.98	6.05	16.88	13.31

Table 2.6 Transition statistics (\*total number of configurations =  $3n + 2$ , where  $n$  is the highest Rydberg series level)

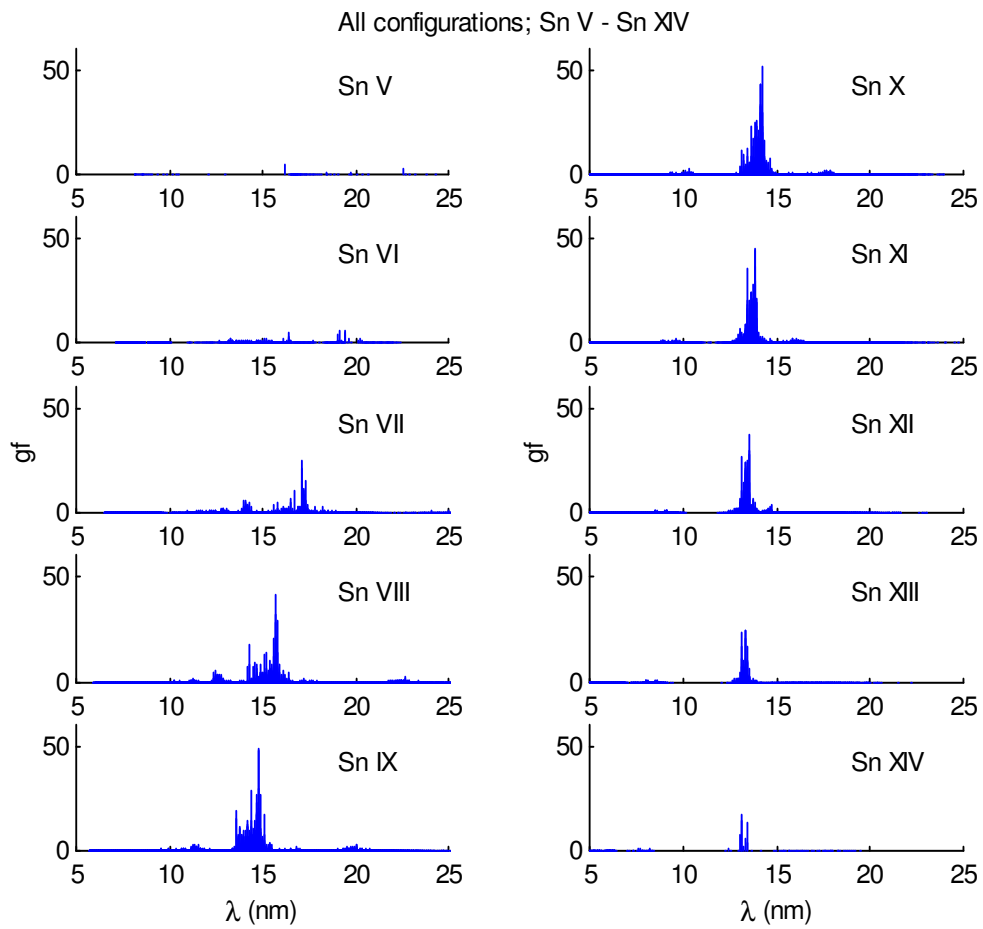


Figure 2.7 Sn V–Sn XIV weighted oscillator strength versus wavelength (5–25 nm)

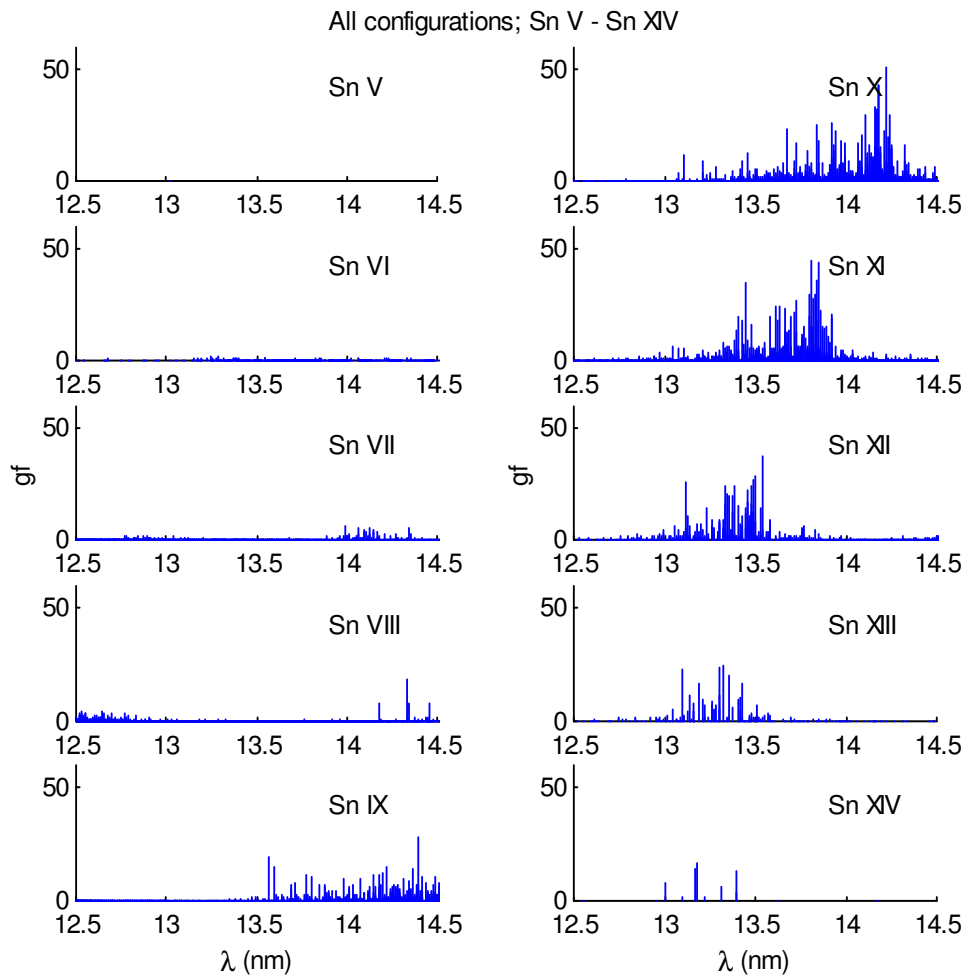


Figure 2.8 Sn V–Sn XIV weighted oscillator strength versus wavelength (12.5–14.5 nm) (2 x 7.4%)

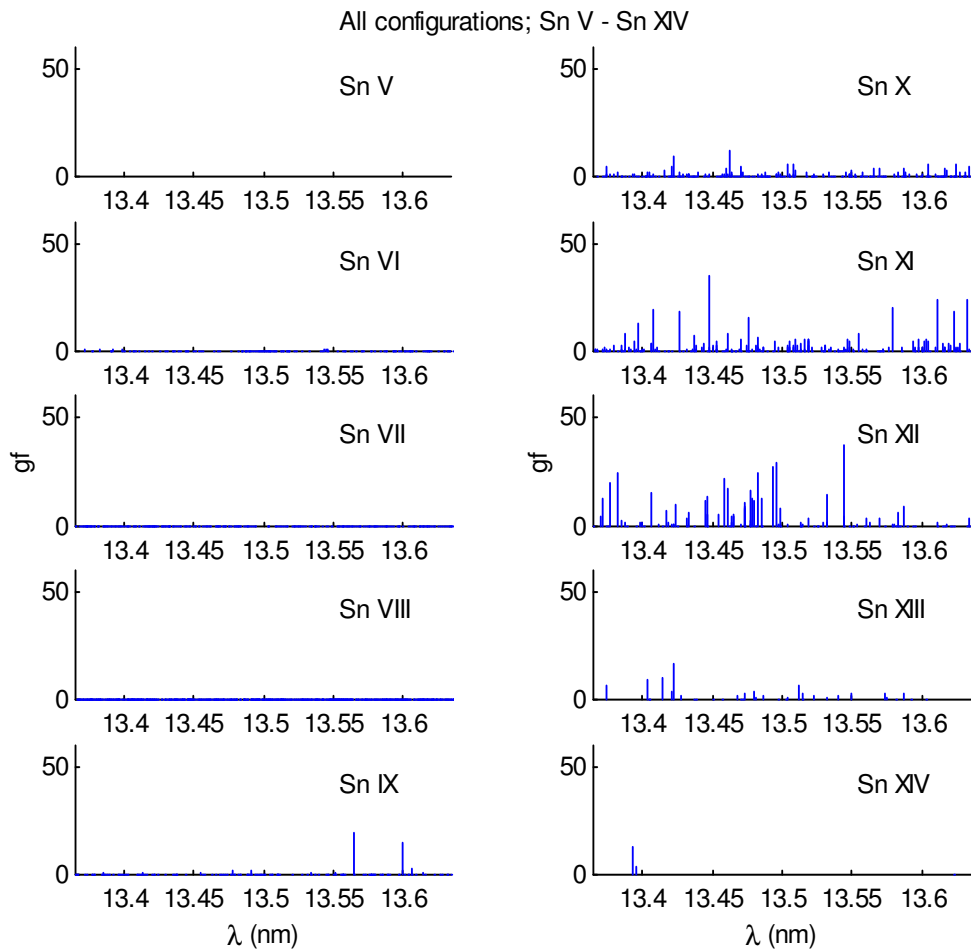


Figure 2.9 Sn V–Sn XIV weighted oscillator strength versus wavelength (13.365–13.635 nm) (2%)

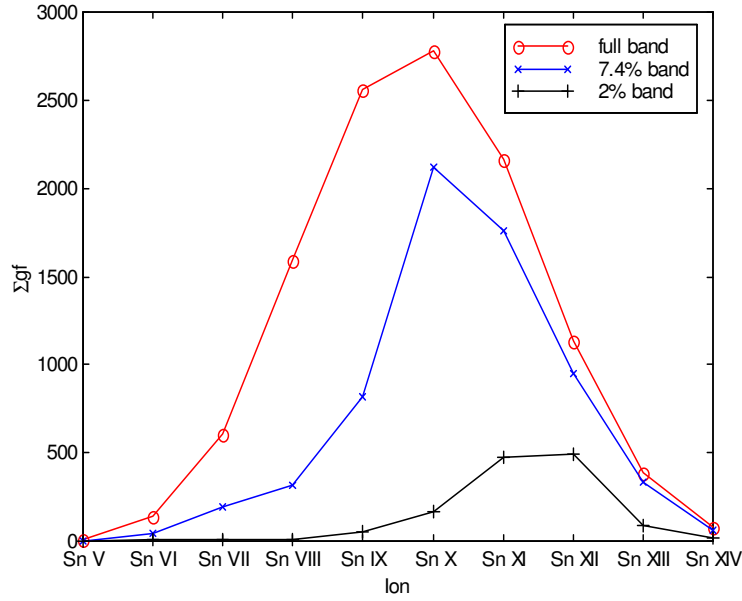


Figure 2.10 Sn V–Sn XIV in-band  $\Sigma gf$  versus ion stage

In Figures 2.7–2.10, it can be seen that nine ions contribute to the 7.4% in-band emission (all but Sn V), while six ions (Sn IX–Sn XIV) contribute to the 2% in-band emission. Only Sn X, Sn XI, Sn XII, and Sn XIII emit significantly in the 2% range (note that the  $\Sigma gf$  for Sn XII exceeds Sn XI in the 2% band but not in the 7.4% band). These ions, weighted by their fractional percentage (determined from the steady-state, optically thin, C-R model [13] or the spatio-temporal *Medusa* model, as described in Chapters 3 and 4, respectively), will contribute to the figure of merit,  $F$ , a measure of the net emission from the plasma ratioed with the Mo/Si mirror response.

From the statistics (see Tables 2.5 and 2.6), some immediate results are seen. With increasing ionisation, both the number of lines and the  $\Sigma gf$  increase and then decrease, proportional to the subshell degeneracy (or statistical weight),  $\binom{2(2l+1)}{w}$ , where  $w$  is the orbital occupancy of the  $l$  subshell for each successive ion. Here,  $l = 2$  for the d subshell and, thus,  $\binom{10}{w}$  is the statistical weight (or binomial coefficient as the

d subshell is stripped from 10 electrons to none). Note that the ions with smaller degeneracy have more configurations (*e.g.*, Sn VI = 39 and Sn XIV 60 configurations, determined by  $n$  in Table 2.6), whereas higher degeneracy ions have fewer configurations (Sn IX has only 24), depending on the matrix dimensions in the Cowan code [1–3]. As such, CI effects may be greater for some ions, and influence the mean wavelength to a greater extent.

As is to be expected, the mean wavelength decreases with increased nuclear charge (*i.e.*, greater Coulombic force). The variance (or standard deviation squared), a measure of emission width, decreases until Sn XI, before increasing slightly. However, it should be noted that the distribution includes high  $n$  Rydberg series transitions, which naturally broaden the distribution width (as discussed further in Section 2.2). Adding more configurations changes the wavelengths because of CI, but also adds more outlying higher energy transitions, which are not part of the UTA emission. Indeed, higher transitions are required for configuration interaction, but should not be included to determine the  $\Delta n = 0$  UTA statistics.

Accordingly, UTA statistics for  $\Delta n = 0$  transitions only (4d-4f and 4p-4d transitions) are given in Section 2.2, where mean, width, skewness, and kurtosis are determined independently for the 4d-4f and 4p-4d UTAs. It is expected that, for  $\Delta n = 0$  transitions, widths will be narrower and that skewness and kurtosis (both measures of distribution shape) will indicate a more symmetric Gaussian probability density distribution. Other so-called “thick-tailed” distributions (lognormal, Lorentzian, and Stable) as well as the effects of restricting data over a limited range to exclude outlying data as suggested in [14] are also discussed.

Using UTA statistics to characterise UTAs (by mean and standard deviation) significantly reduces the tens of thousands of transitions for each ion to two computationally manageable parameters (or three if skewness is included). A graphical representation of the UTA statistics is given in Figure 2.11.

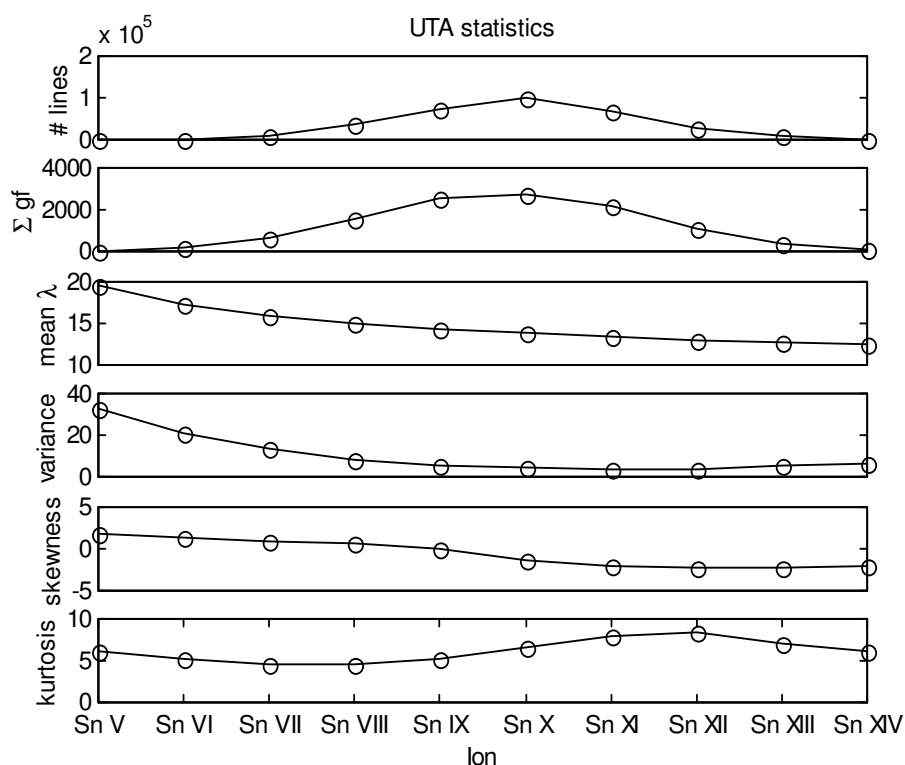


Figure 2.11 Sn V–Sn XIV UTA statistics

Figures 2.12 and 2.13 show the two-parameter Gaussian distribution for each ion over the entire emission range with the full configuration set used, including high- $n$  Rydbergs. Figure 2.12 includes a skewed Gaussian for comparison. Both are normalised to 1. Note that the asymmetric skewed Gaussian shifts the maximum and narrows the distribution, while keeping the same mean [15]. Here,  $\mu_1$  is the mean wavelength and  $\sigma$  the standard deviation of the UTA distribution (in nm). Note that Figure 2.13 uses a normalised amplitude Gaussian, where the maximum is scaled to the  $\Sigma gf$ . From here, it can be inferred that the maximum peak emission in the 5–25-nm range is for Sn X at 14.4 nm.

Figure 2.14 shows detailed statistics for the six main emitting ions, Sn VIII–Sn XIII. Obvious trends can be seen with increasing ionisation, such as the decrease in wavelength and width. The distribution is also more skewed (to the short-wavelength side) because of the higher Rydberg series transitions and is less Gaussian.

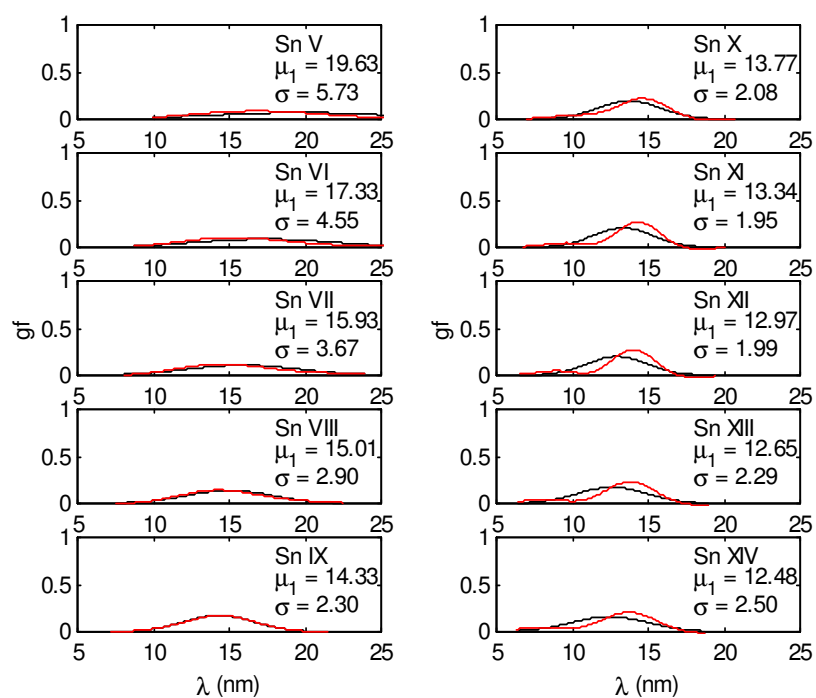


Figure 2.12 Sn V–Sn XIV UTA Gaussian: normal (black) and skewed (red)

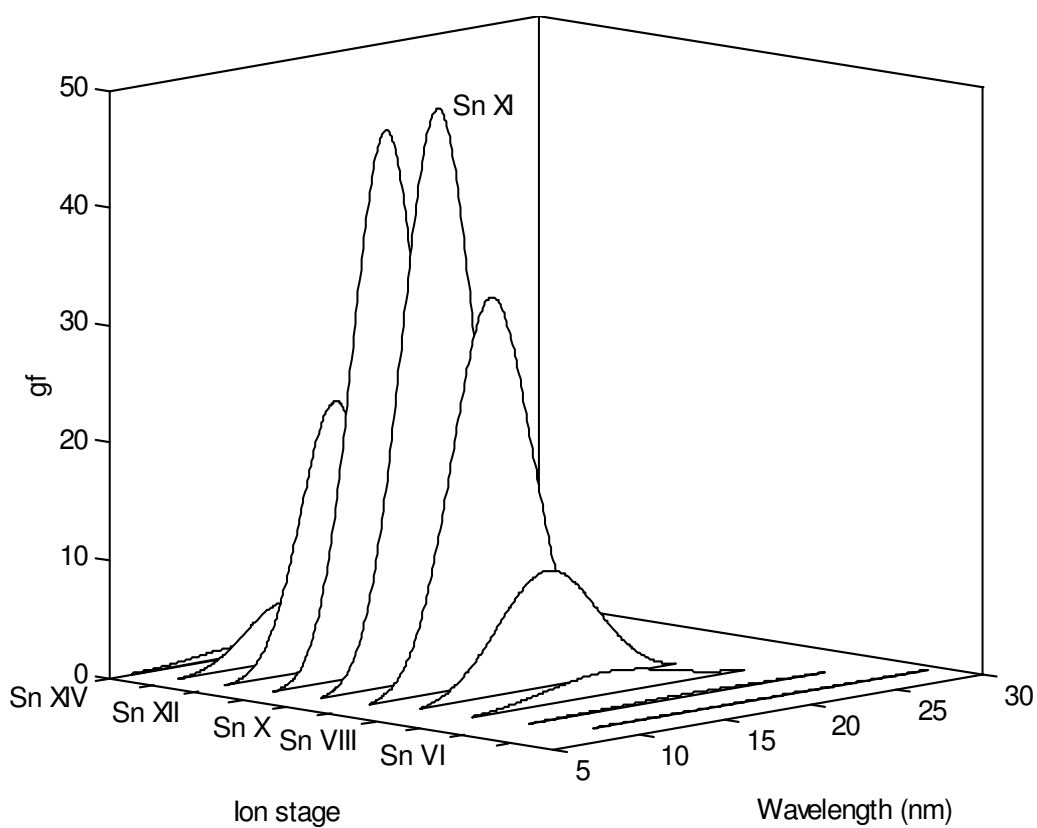


Figure 2.13 Sn V–Sn XIV  $gf$  versus wavelength

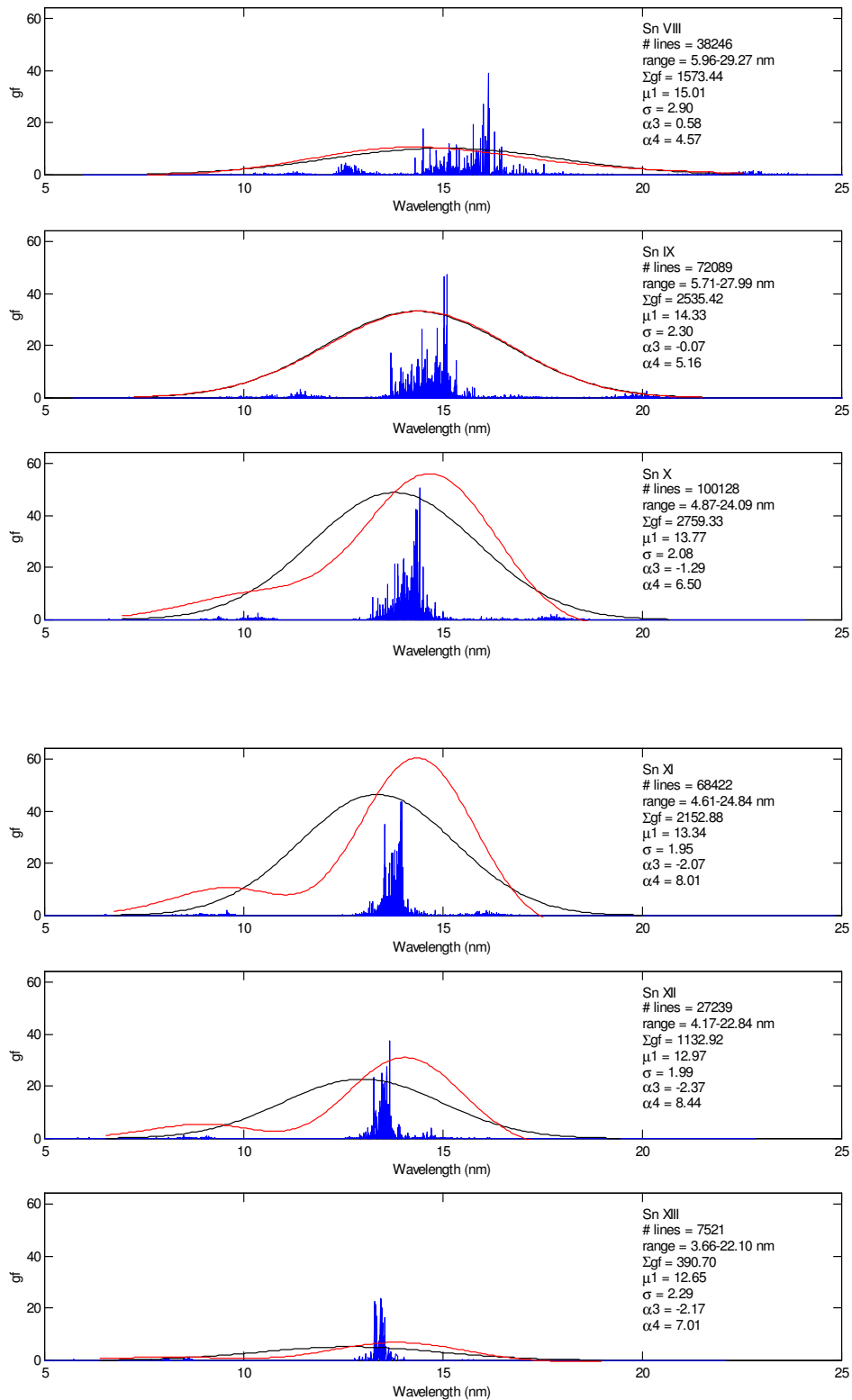
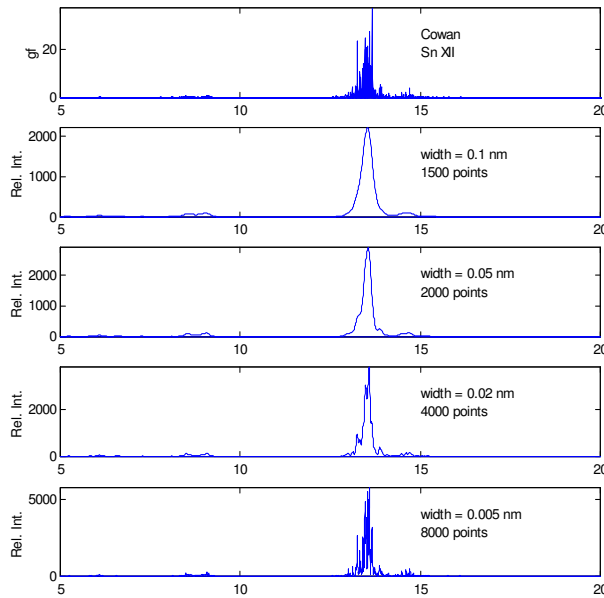


Figure 2.14 Discrete Cowan (blue), Gaussian (black), and skewed Gaussian (red) (Sn VIII–Sn XIII)

It should be noted that Cowan results, represented by line transitions, can be misleading when thousands of lines overlap in a narrow region. Figure 2.15 shows a relative intensity versus wavelength plot of Sn XII (original and convolved with an area Gaussian, such that area = total sum  $gf$ ). The original Cowan output is shown at the top. Proceeding downward, each line is given a width from .1 nm (1500 points) to 0.005 nm (6000 points) and summed (the number of points is increased as the width decreases to match the  $\Sigma gf$  to the area). It is important that the sum  $gf$  value be invariant with a change in broadening to properly reflect oscillator strength statistically for a given ion stage and transition.

Doppler and electron impact broadening (which depend on plasma temperature and density) will also affect the convolved theoretical spectrum, and is discussed further in Section 2.3. The experimental instrument resolution ( $\Delta\lambda$ ) at 13.5 nm (or as a function of wavelength) also affects the broadening. For comparisons to UTA results given here, a 0.5-Å full width at half maximum (FWHM) envelope is used as recommended in [15]. Note that  $\text{FWHM} = 2.355 \sigma$  and thus in terms of a Gaussian width,  $\sigma = 0.212 \text{ \AA}$  or 0.0212 nm.



**Figure 2.15** Sn XII  $gf$  versus wavelength (nm) convolved with variable width

Figures 2.16, 2.18, and 2.20 show all ions, convolved with a Gaussian of 0.212 Å width and 1000 points for the three regions (own maxima). Figures 2.17, 2.19, and 2.21 show the same, scaled to the same relative maximum. In Figure 2.20, the importance of Sn XII in the 2% band is especially seen, as it is both bright and centred on 13.5 nm. The ultimate contribution of the in-band intensity will be quantified at different plasma temperatures by a (steady-state) figure of merit in Chapter 3 and conversion efficiency in Chapter 5.

It should be noted that the theoretical emission is highly dependent on scaling, particularly over a small range (*e.g.*, the 13.5-nm, 2%-band). Note that scaling can be both ion stage dependent and configuration dependent. Note also that to compare the theoretical results to experimental data, the theoretical data will be weighted by the ion fraction distribution (Chapter 3) and the level populations (Chapter 4). For reference, all Cowan input files used in this study are given in Appendix B.

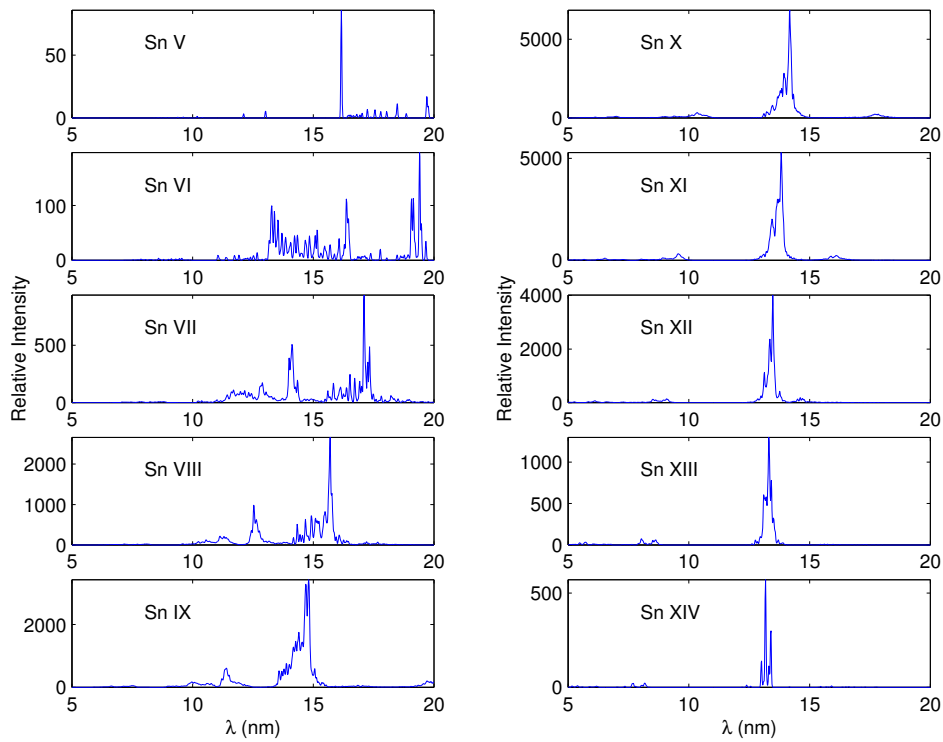


**Figure 2.16** Sn ions *gf* versus wavelength (nm) convolved (0.0212 nm, 1000 points) over full spectroscopic range (5–20 nm) (own maxima)

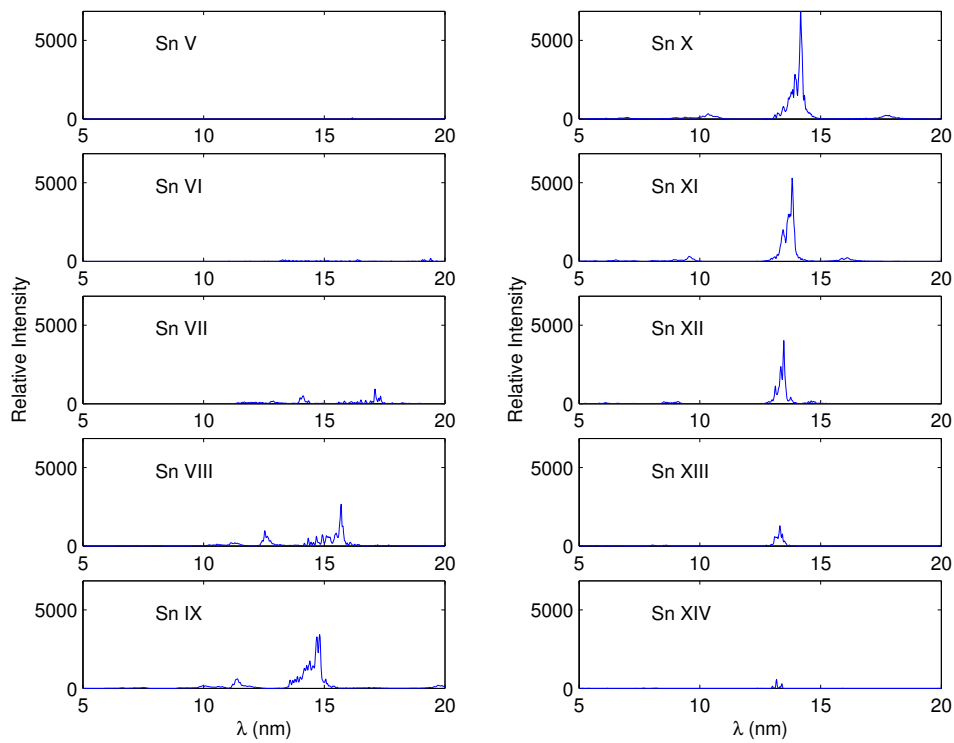


**Figure 2.17** Sn ions *gf* versus wavelength (nm) convolved (0.0212 nm, 1000 points) over full spectroscopic range (5–20 nm) (same maximum)

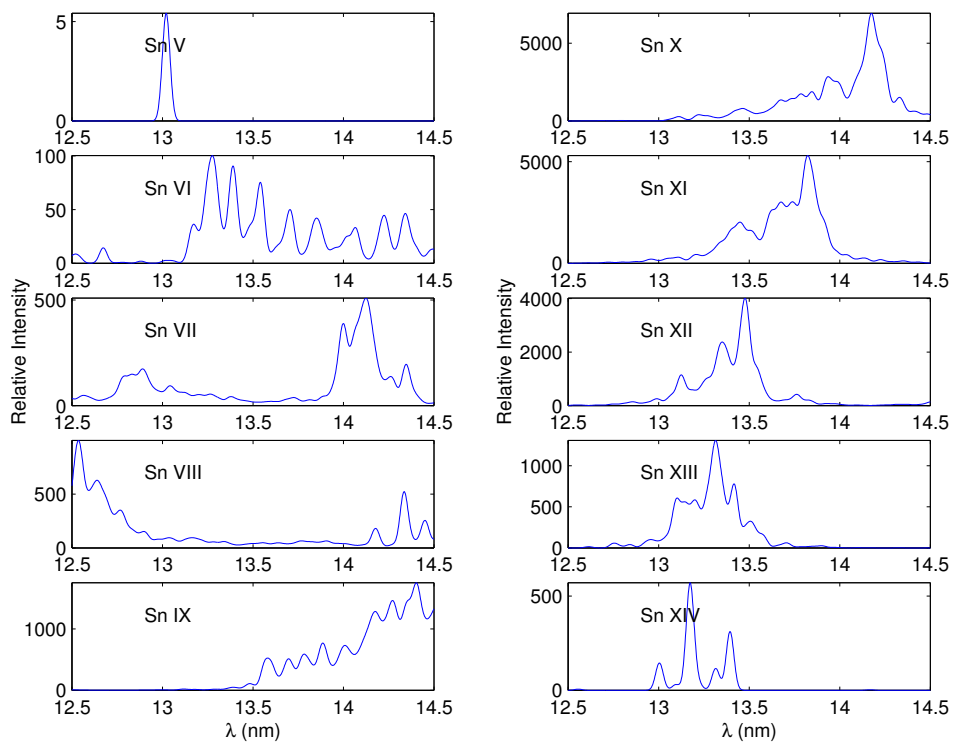


**Figure 2.18** Sn ions *gf* versus wavelength (nm) convolved (0.0212 nm, 1000 points) over 2 x 7.4% range (12.5–14.5 nm) (own maxima)

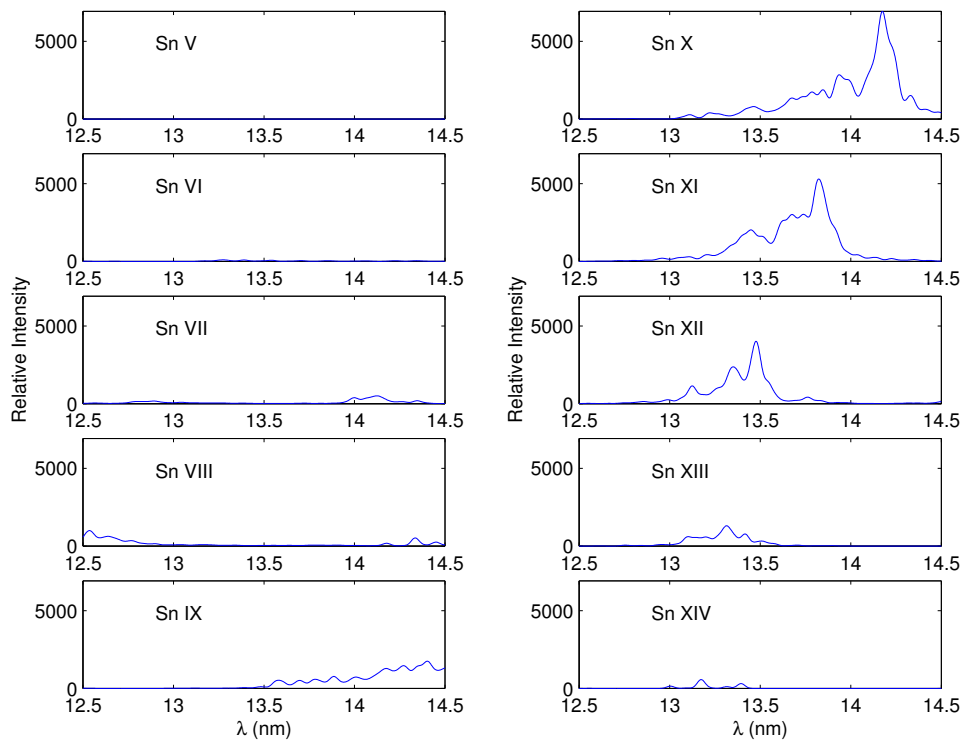


**Figure 2.19** Sn ions *gf* versus wavelength (nm) convolved (0.0212 nm, 1000 points) over 2 x 7.4% range (12.5–14.5 nm) (same maximum)

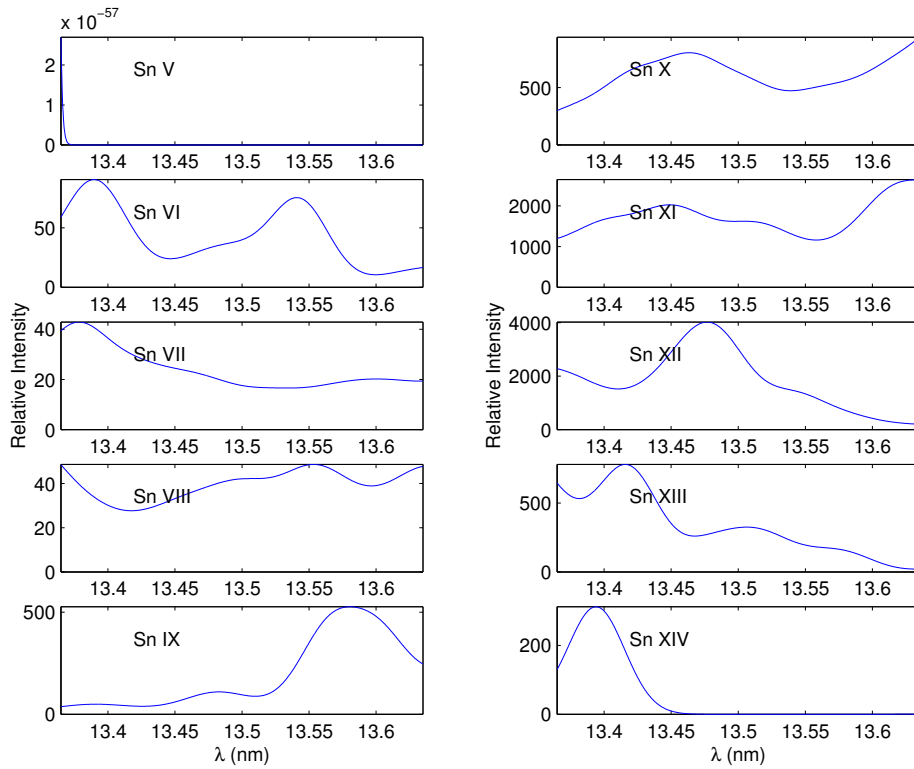


**Figure 2.20** Sn ions *gf* versus wavelength (nm) convolved (0.0212 nm, 1000 points) over 2% range (13.365–13.635 nm) (own maxima)

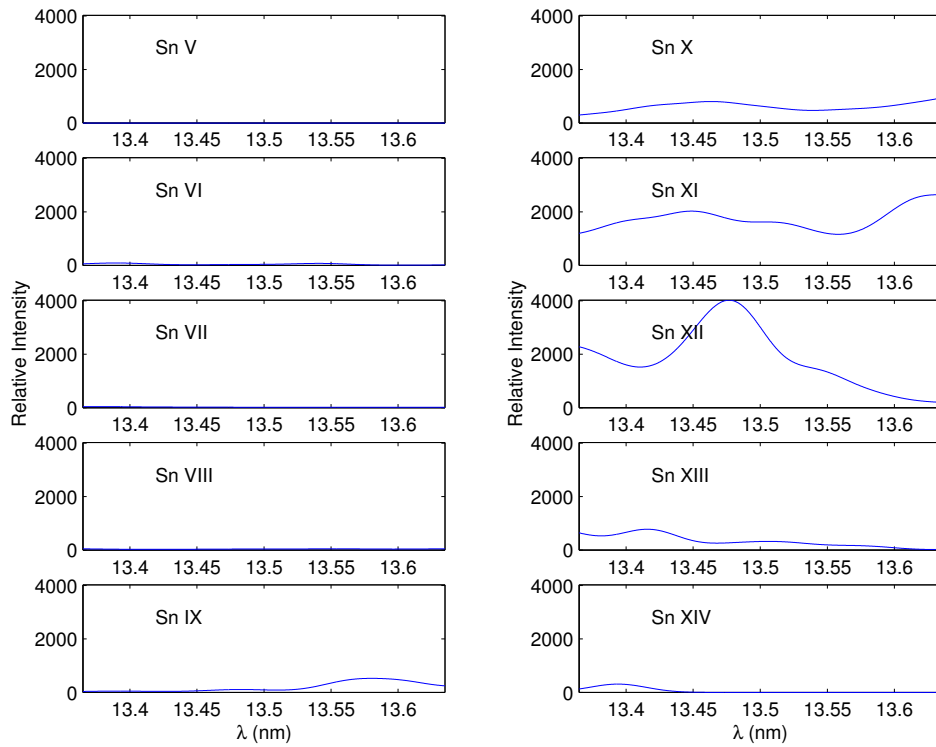


**Figure 2.21** Sn ions *gf* versus wavelength (nm) convolved (0.0212 nm, 1000 points) over 2% range (13.365–13.635 nm) (same maximum)

## 2.2 Sn 4d subshell (4d-4f, 4p-4d, 4d-5p) transition statistics

Transition array statistics are used to simplify numerical calculations involving hundreds of thousands of lines and, thus, more easily interpret unresolved LPP EUV spectra as described in [1, 15–20], as well as for radiation transport for plasma modelling. The first and second order moments ( $\mu_1$  and  $\mu_2$ ) of the weighted distribution of  $gf$  value versus wavelength give the average and width of a “two-parameter” UTA (using the moment equations in Section 1.2.3). The statistical results are convolved with an area Gaussian (mean wavelength as centre, standard deviation as width, and  $\Sigma gf$  equal to the area) to produce a plot of relative intensity versus wavelength. The Cowan code [1–3] output and corresponding statistical data for the 4d-4f, 4p-4d, and 4d-5p transitions<sup>38</sup> are shown below in Figure 2.22. Note that UTA statistics calculated for 4d-4f and 4p-4d transitions are from a full HFCI calculation based on the leading eigenvalue percentages.<sup>39</sup>

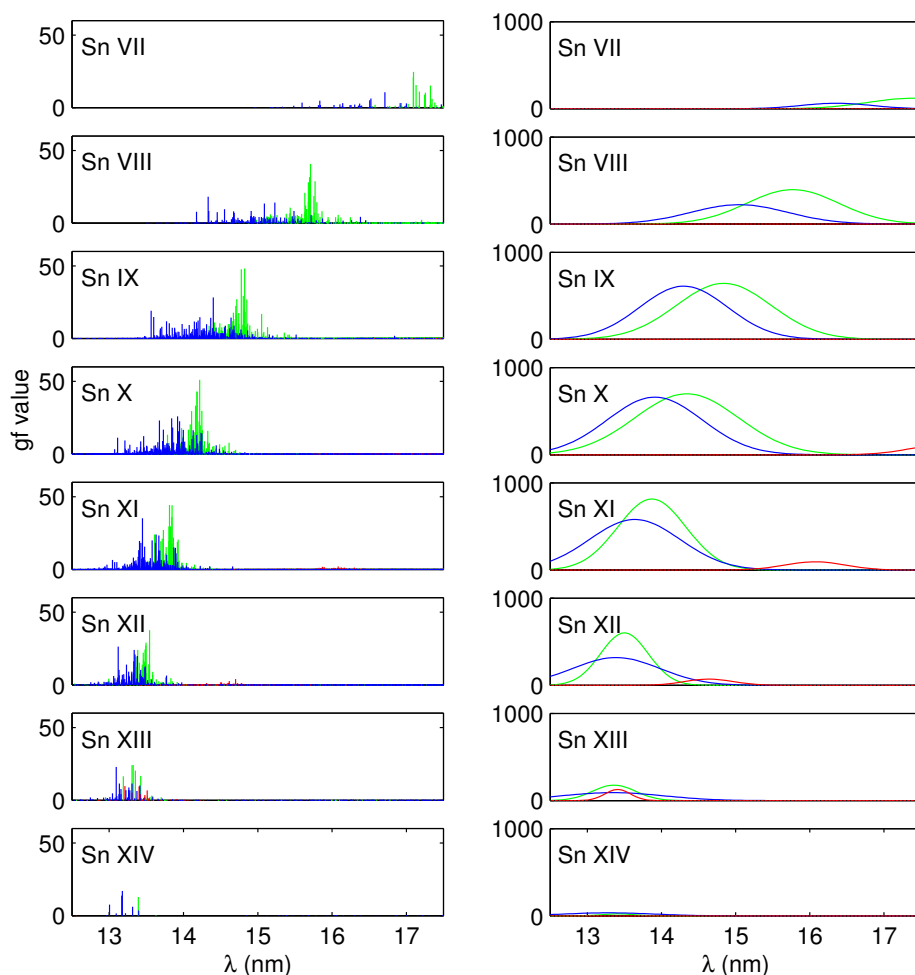


**Figure 2.22** Relative intensity versus wavelength (left: line and right: statistical) for 4d-4f (green), 4p-4d (blue), and 4d-5p (red) transitions

<sup>38</sup> Note that the 4d-5p transitions do not constitute an “unresolved” transition array. However, identical statistical methods can be used to characterise the mean, standard deviation, and higher-order moments.

<sup>39</sup> The label is the highest percentage transition term in the Cowan `.outg11` (or `shrink.ls`) file.

Figures 2.23–2.25 and Tables 2.7–2.9 give the statistical data as calculated from the Cowan results. Note, all transitions are required for configuration interaction, but only 4d-4f, 4p-4d, and 4d-5p transitions overlap in the 13.5-nm range, and are of particular interest to next generation EUV lithography. The dominant configuration interaction is between  $4p^6 4d^{N-1} 4f^1$  and  $4p^5 4d^{N+1}$  configurations ( $N = 1$  to 10). Figures 2.26 and 2.27 give the number of lines and  $\Sigma gf$  (together and as a ratio). Here it can be seen that the 4d-4f and 4p-4d emission is significant for Sn VIII to Sn XII.

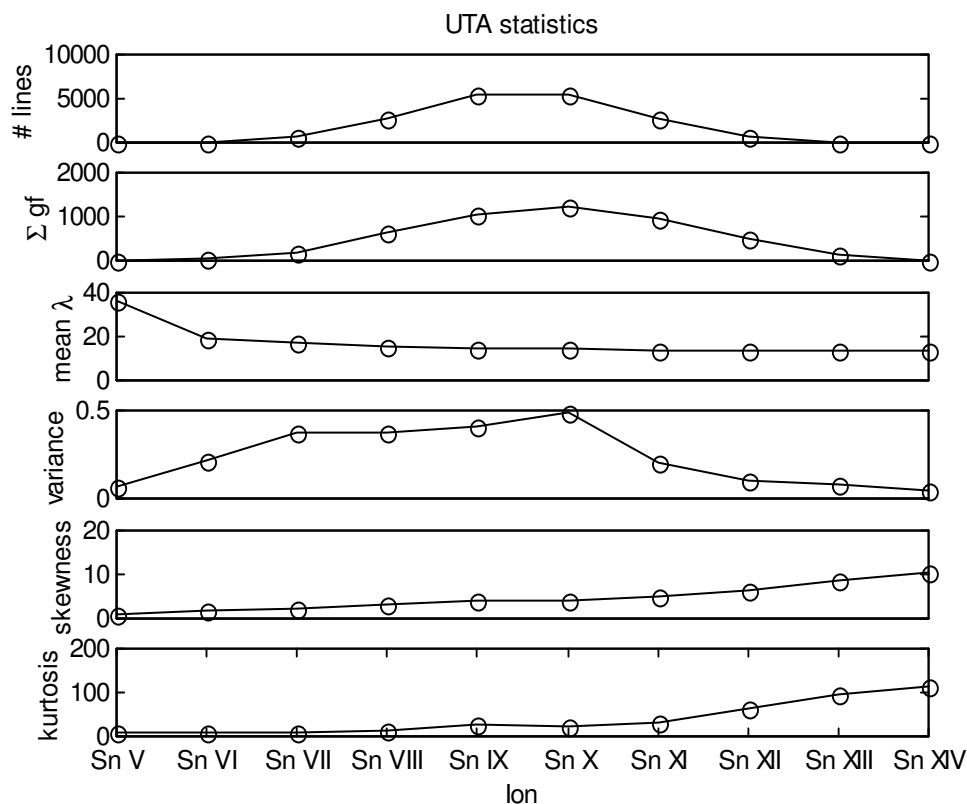


Figure 2.23 4d-4f statistics (UTA)

Ion	# lines	$\Sigma gf$	mean $\lambda$ (nm)	std (nm)	skew	kurt	maxgf	peak $\lambda$ (nm)
Sn V (Sn <sup>4+</sup> )	3	2.63	22.61	0.21	5.54	32.55	2.55	22.58
Sn VI	81	30.43	19.49	0.47	1.92	7.11	5.58	19.15
Sn VII	721	185.54	17.40	0.61	2.22	8.22	24.71	17.10
Sn VIII	2825	614.63	15.77	0.62	3.01	15.22	40.80	15.71
Sn IX	5470	1032.42	14.84	0.64	4.32	26.44	48.30	14.82
Sn X	5346	1227.41	14.34	0.70	4.17	20.50	51.11	14.22
Sn XI	2825	940.50	13.87	0.46	4.81	29.68	44.38	13.81
Sn XII	721	483.43	13.50	0.32	6.21	62.43	37.61	13.54
Sn XIII	81	129.50	13.36	0.29	8.54	93.94	24.38	13.32
Sn XIV	3	13.03	13.41	0.22	10.68	115.16	12.91	13.39

Table 2.7 4d-4f statistics (UTA)

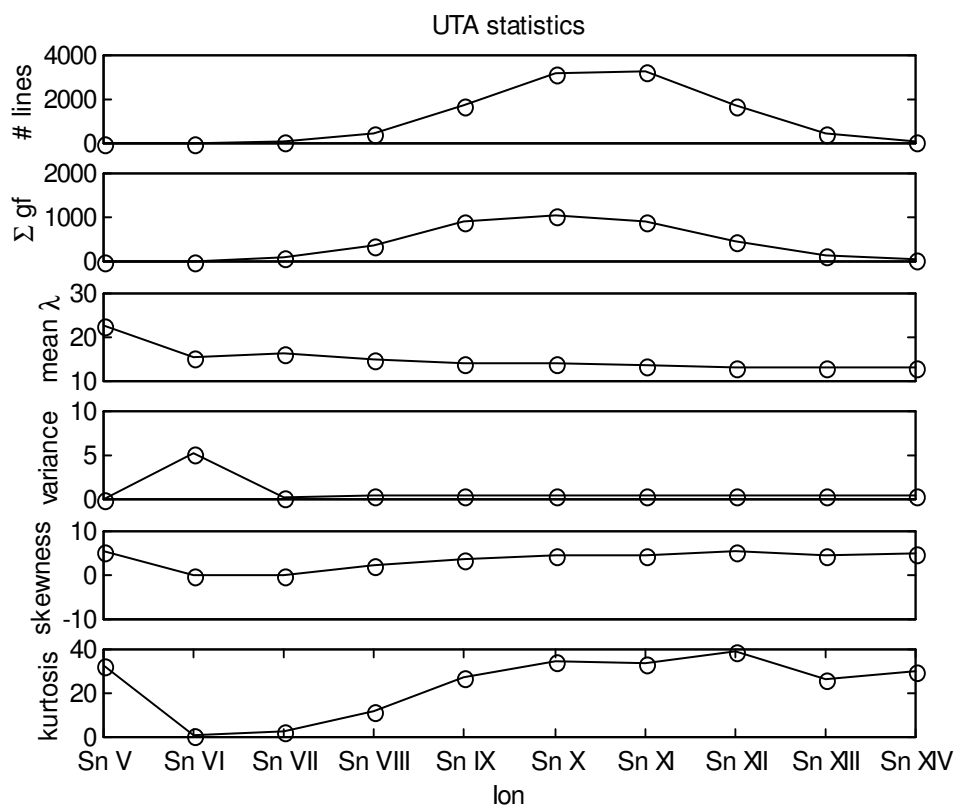


Figure 2.24 4p-4d statistics (UTA)

Ion	# lines	$\Sigma gf$	mean $\lambda$ (nm)	std (nm)	skew	kurt	maxgf	peak $\lambda$ (nm)
Sn V (Sn <sup>4+</sup> )	0							
Sn VI	3	2.88	15.37	2.28	0.15	1.03	1.55	13.25
Sn VII	60	75.20	16.36	0.47	-0.06	2.76	10.61	16.71
Sn VIII	466	362.98	15.05	0.65	2.22	12.26	18.14	14.33
Sn IX	1718	904.94	14.30	0.59	3.50	27.04	28.34	14.40
Sn X	3170	1061.48	13.91	0.64	4.62	34.12	25.95	13.92
Sn XI	3245	888.11	13.64	0.61	4.67	33.33	35.20	13.45
Sn XII	1718	471.46	13.39	0.59	5.41	38.80	26.41	13.12
Sn XIII	466	158.26	13.34	0.69	4.61	26.41	22.99	13.10
Sn XIV	60	53.95	13.29	0.61	5.15	30.24	17.14	13.18

Table 2.8 4p-4d statistics (UTA)

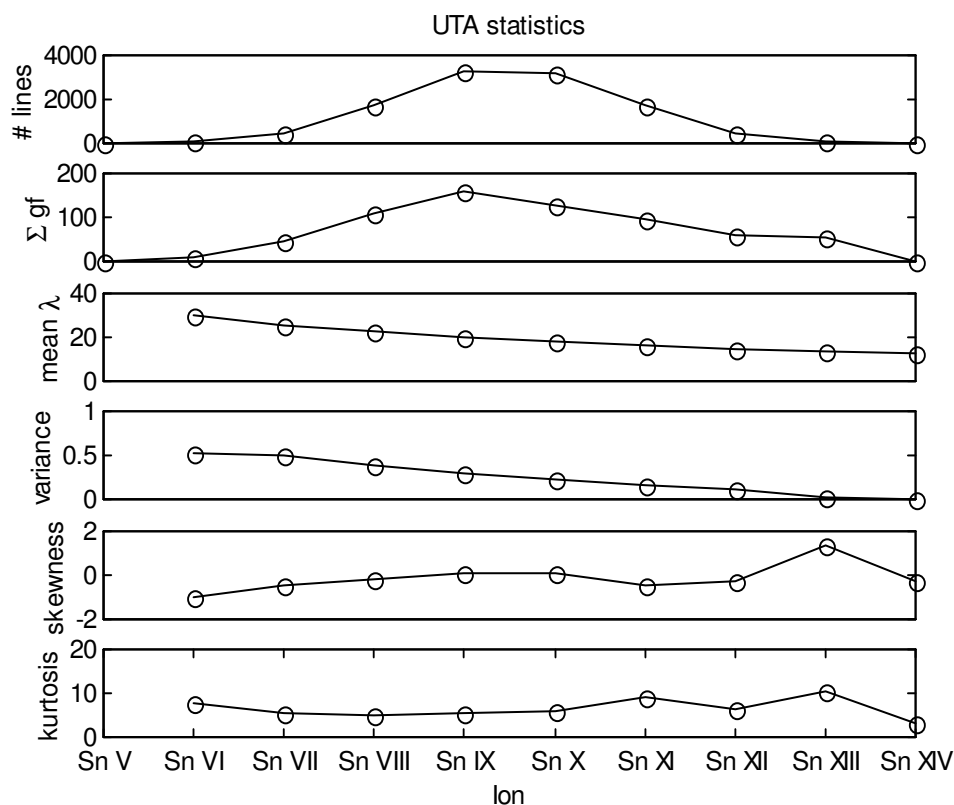


Figure 2.25 4d-5p statistics (UTA)

Ion	# lines	$\Sigma gf$	mean $\lambda$ (nm)	std (nm)	skew	kurt	maxgf	peak $\lambda$ (nm)
Sn V (Sn <sup>4+</sup> )	1	0						
Sn VI	60	10.46	30.19	0.72	-0.97	7.72	1.08	30.04
Sn VII	466	44.24	25.80	0.70	-0.46	5.68	3.25	26.24
Sn VIII	1718	107.17	22.48	0.63	-0.14	5.14	2.62	22.69
Sn IX	3245	158.89	19.90	0.53	0.06	5.46	3.12	20.06
Sn X	3170	129.21	17.80	0.46	0.13	5.90	2.16	17.84
Sn XI	1718	97.46	16.07	0.41	-0.42	9.02	2.19	16.08
Sn XII	466	59.19	14.64	0.33	-0.24	6.49	4.09	14.70
Sn XIII	60	54.73	13.41	0.17	1.36	10.56	9.87	13.21
Sn XIV	3	1.05	12.43	0.10	-0.27	3.01	0.65	12.39

Table 2.9 4d-5p statistics

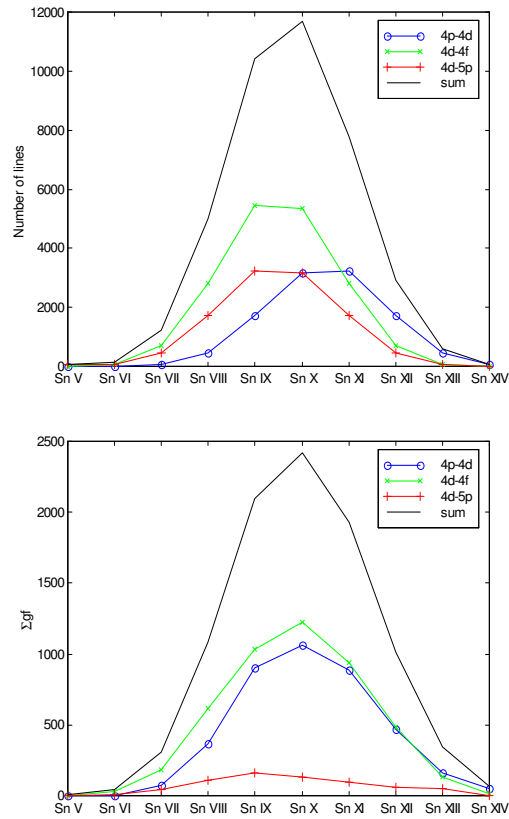


Figure 2.26 4d-4f, 4p-4d, and 4d-5p transitions: number of lines and  $\Sigma gf$

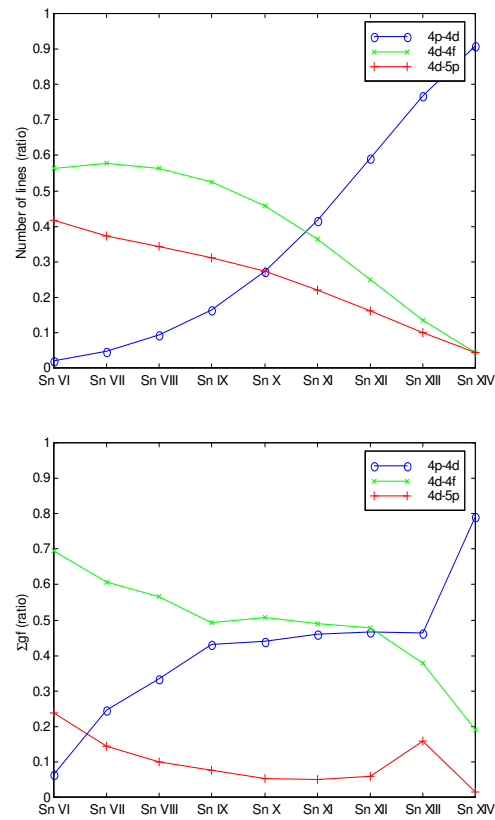


Figure 2.27 4d-4f, 4p-4d, and 4d-5p transitions: number of lines and  $\Sigma gf$  (ratio)

For reference, Table 2.10 lists together the mean and standard deviation of the three transition arrays.

Ion	4d-4f				4p-4d				4d-5p			
	# of lines	$\Sigma gf$	$\lambda$ (nm)	$\sigma$ (nm)	# of lines	$\Sigma gf$	$\lambda$ (nm)	$\sigma$ (nm)	# of lines	$\Sigma gf$	$\lambda$ (nm)	$\sigma$ (nm)
Sn V	3	2.63	22.61	0.21	0				1	0		
Sn VI	81	30.43	19.49	0.47	3	2.88	15.37	2.28	60	10.46	30.19	0.72
Sn VII	721	185.54	17.40	0.61	60	75.2	16.36	0.47	466	44.24	25.80	0.70
Sn VIII	2825	614.63	15.77	0.62	466	362.98	15.05	0.65	1718	107.17	22.48	0.63
Sn IX	5470	1032.42	14.84	0.64	1718	904.94	14.30	0.59	3245	158.89	19.90	0.53
Sn X	5346	1227.41	14.34	0.70	3170	1061.48	13.91	0.64	3170	129.21	17.80	0.46
Sn XI	2825	940.50	13.87	0.46	3245	888.11	13.64	0.61	1718	97.46	16.07	0.41
Sn XII	721	483.43	13.50	0.32	1718	471.46	13.39	0.59	466	59.19	14.64	0.33
Sn XIII	81	129.50	13.36	0.29	466	158.26	13.34	0.69	60	54.73	13.41	0.17
Sn XIV	3	13.03	13.41	0.22	60	53.95	13.29	0.61	3	1.05	12.43	0.10

**Table 2.10** 4d-4f, 4p-4d, and 4d-5p UTA statistics

It is seen that wavelength decreases with ionisation for all three arrays because of increased Coulombic force, as reported above for the statistical distribution of all transitions. The 4p-4d mean wavelengths are less than the 4d-4f mean wavelengths for all ions ( $\lambda_{4p-4d} < \lambda_{4d-4f}$ ), as is to be expected, since  $\Delta E_{4p-4d}$  is greater than  $\Delta E_{4d-4f}$ . The widths are comparable until later ion stages, where  $\sigma_{4p-4d}$  is significantly wider than  $\sigma_{4d-4f}$ , likely because of the greater number of 4p-4d lines past Sn XI. The 4d-4f UTA width decreases with ionisation as reported by O'Sullivan and Carroll [21], though only from Sn IX. However, the 4p-4d UTA width is essentially constant. The 4d-4f  $\Sigma gf$  is greater until Sn XI, where it is almost identical. After Sn XI, the 4p-4d  $\Sigma gf$  is greater, which is to be expected, since the 4d-4f transitions are more dominant for a full d subshell, but as the d subshell empties, the 4p-4d transitions begin to dominate. As reported above for the full Cowan results, the number of lines and the  $\Sigma gf$  increase and decrease in proportion to the subshell degeneracy  $\binom{10}{w}$ , where  $w$  is the orbital occupancy (1–10) of the d subshell for each successive ion.

It should be noted that in this analysis, the configuration labels are notional and caution is required with regards to the purity of labels. Credence, however, is seen from the average energy difference between the two transition arrays ( $\Delta\mu = \mu_1 - \mu_2 = \delta E_{\text{mix}}$ ) and, thus, the method is valid for the purpose of extracting specific transition-type data to calculate array statistics. The levels are highly mixed, yet there is a statistically significant difference between the 4d-4f and 4p-4d UTA data. As such, interesting features about the separate 4d-4f and 4p-4d transitions within the overlapping UTA can be seen. As well, it is noted again that the Cowan output is highly dependent on Slater-Condon scaling parameters (particularly  $G^1(4d,4f)$ ). As discussed above, scaling factors were determined by matching the 4d-4f  $^1P_1$  line in Sn VII [11] and the short-wavelength UTA edge in Sn XIV [12] and interpolating for intermediate ions. As well, the statistics depend on the energy region selected. As a first analysis, all transitions are included in the statistics.

Figure 2.28 shows the mean wavelength versus ion stage (error bars indicate standard deviation). Here, the effect of electron screening is seen with increasing

ionisation. A general idea of the  $4p^6 4d^{N-1} 4f^1$  and  $4p^5 4d^{N+1}$  mixing can also be seen. It is clear that at early ion stages, the mean wavelengths are further apart, suggesting less mixing, but by Sn XII there is a significant overlap. Statistically, the two UTAs could come from the same data set, suggesting that  $4p^6 4d^{N-1} 4f^1$  and  $4p^5 4d^{N+1}$  configurations become more highly mixed with ionisation. The mixing of levels is seen explicitly in the eigenvalues plot in Figures 2.30 and 2.31. Note that the 4d-5p array moves to shorter wavelengths with increasing ionisation and overlaps with the 4d-4f and 4p-4d UTAs in the 13.5-nm region at Sn XIII. Clearly,  $\Delta n = 0$  transitions are less sensitive than  $\Delta n = 1$  transitions to the change in average nuclear charge ( $\langle z \rangle$ ). Figure 2.29 shows the 4d-4f, 4p-4d, and combined 4d-4f + 4p-4d UTA, again highlighting the separate yet overlapping nature of the contributing UTAs.

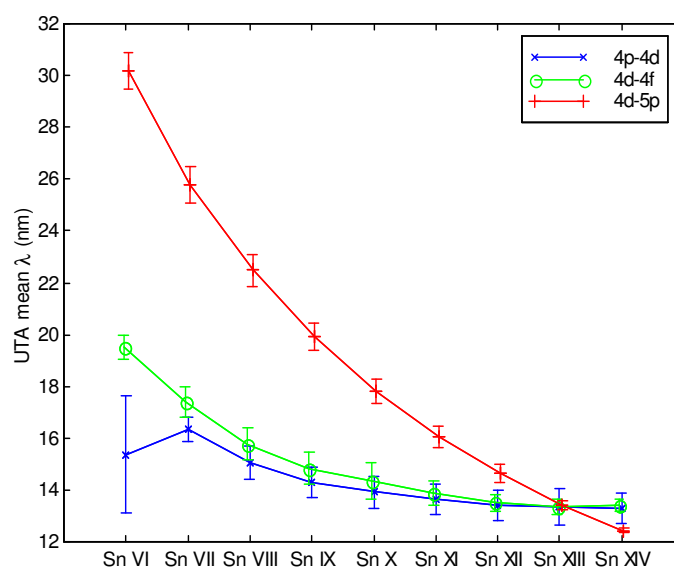


Figure 2.28 4d-4f, 4p-4d, and 4d-5p transitions: mean wavelength

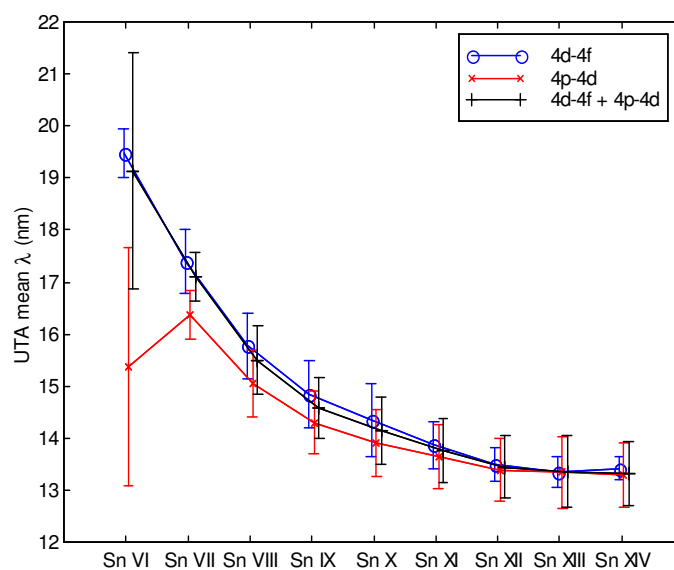
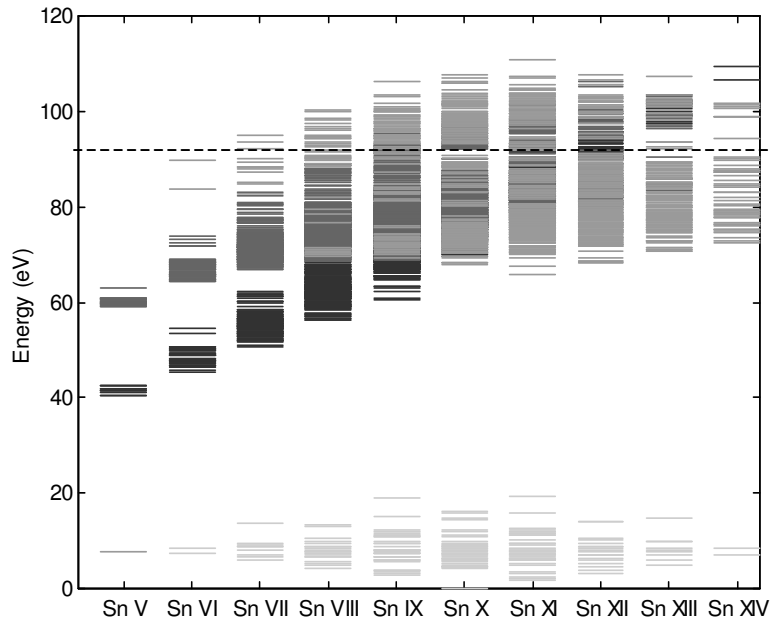
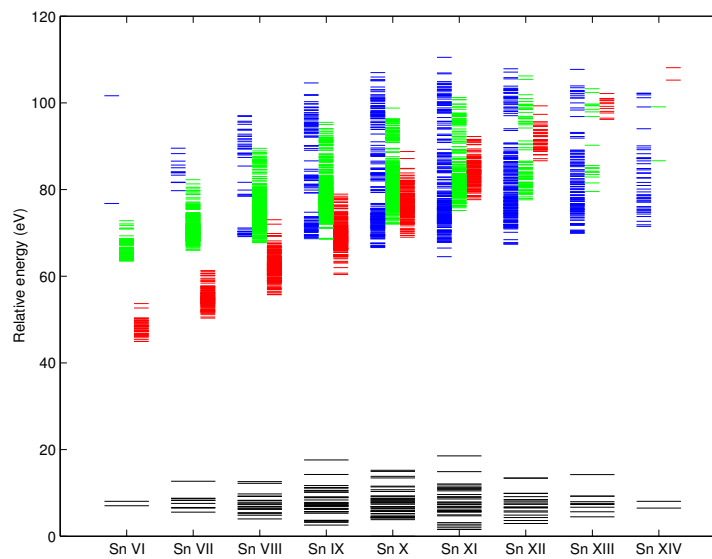


Figure 2.29 4d-4f, 4p-4d, and 4d-4f + 4p-4d transitions: mean wavelength



**Figure 2.30 Eigenvalue energies (together)**



**Figure 2.31 Eigenvalue energies: 4p-4d (blue), 4d-4f (green), and 4d-5p (red)**

Interestingly, the 4d-4f and 4p-4d UTA data is more skewed than the full series spectral output (contrary to what was expected), although to the low energy (long wavelength) side. This is because of the absence of Rydberg series transitions, which balanced the equally outlying 4d-5p transitions. Subsequently, the data is less normal (high kurtosis) than before and increases with ionisation. Indeed, the numerous outlying low  $gf$  lines greatly increase skewness (third moment) and kurtosis (fourth moment) with ionisation. (Note that the 4d-5p data is practically normal.) The effect of skewness on the  $\Delta n = 0$  UTAs is discussed below with regards to broadening and in Chapter 3.

In Figure 2.32, a histogram of 4d-4f and 4p-4d transitions for Sn X shows the effect of discrete binning. Here it is seen that the 4p-4d transitions appear bimodal. Figure 2.33 gives the number of lines and the corresponding percentage  $\Sigma gf$  with  $gf$  values less than 10, 1, 0.1 and 1e-6, highlighting how most of the total oscillator strength comes from relatively few lines or that the  $gfs$  are very small. For example, in Sn X almost 67% of the 4d-4f lines contribute less than 1% of the total  $\Sigma gf$  while more than 88% of 4p-4d lines contribute less than 4% of the total  $\Sigma gf$ .

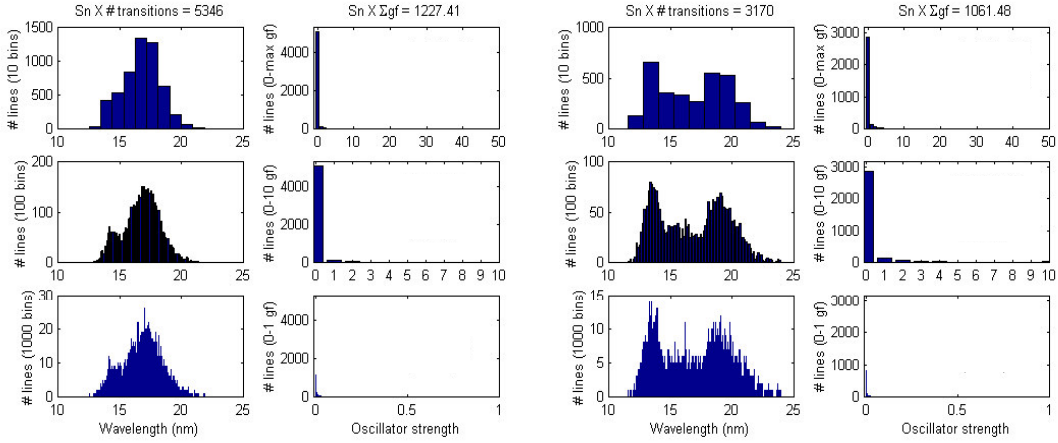


Figure 2.32 The effect of binning and %  $\Sigma gf$  (Sn X 4d-4f and 4p-4d)

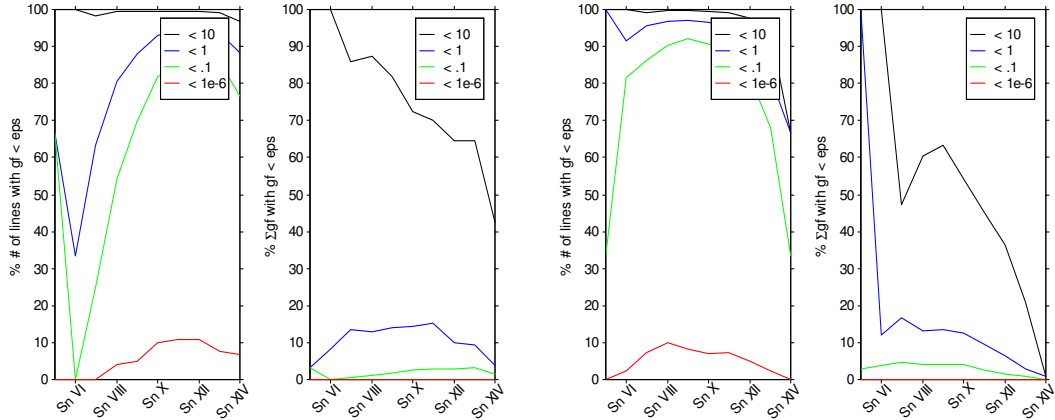


Figure 2.33 Number of transitions and %  $\Sigma gf$  less than 10, 1, .1 and 1e-6 (Sn V-Sn XIV 4d-4f and 4p-4d)

The predicted maximum number of lines is given by Eq 2.1, [14], where  $w_d$  is the 4d subshell occupation number and  $w_p$  is the 4p subshell occupation number.

$$\binom{10}{w_d+1} \binom{14}{1} + \binom{6}{w_p} \binom{10}{w_d-1} \quad (2.1)$$

Figures 2.34 and 2.35 shows a semi-log plot of  $gf$  versus wavelength for all ten ions, highlighting the effect of the numerous small-oscillator outliers on any statistical representation of the theoretical spectrum.

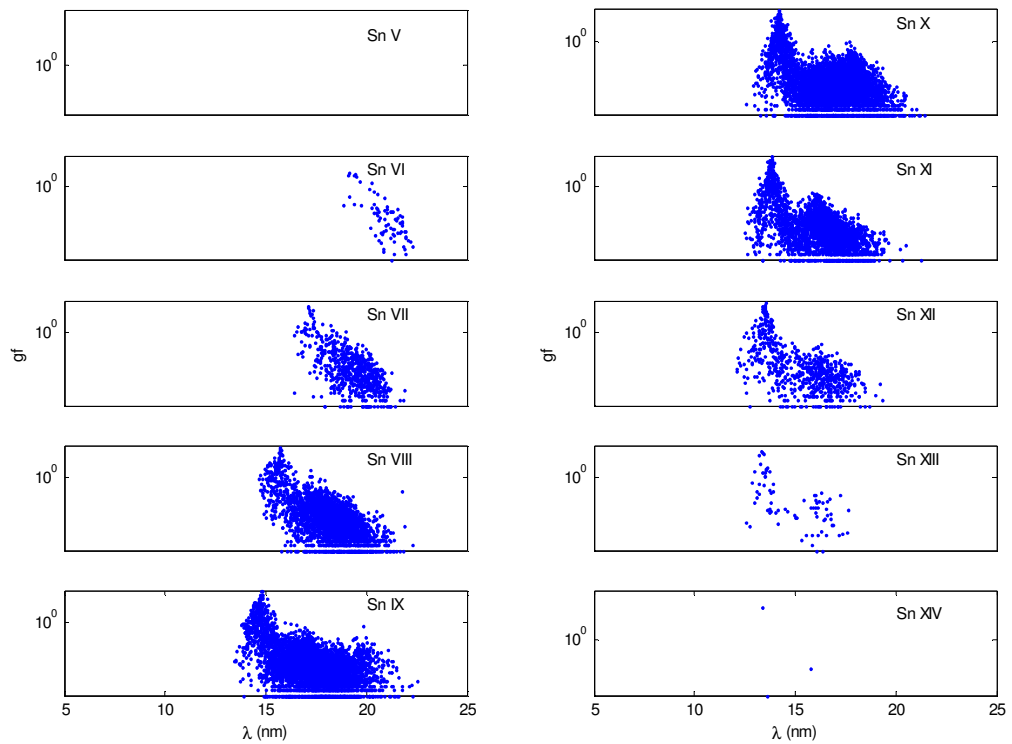


Figure 2.34  $\log_{10} gf$  versus wavelength (4d-4f transitions)

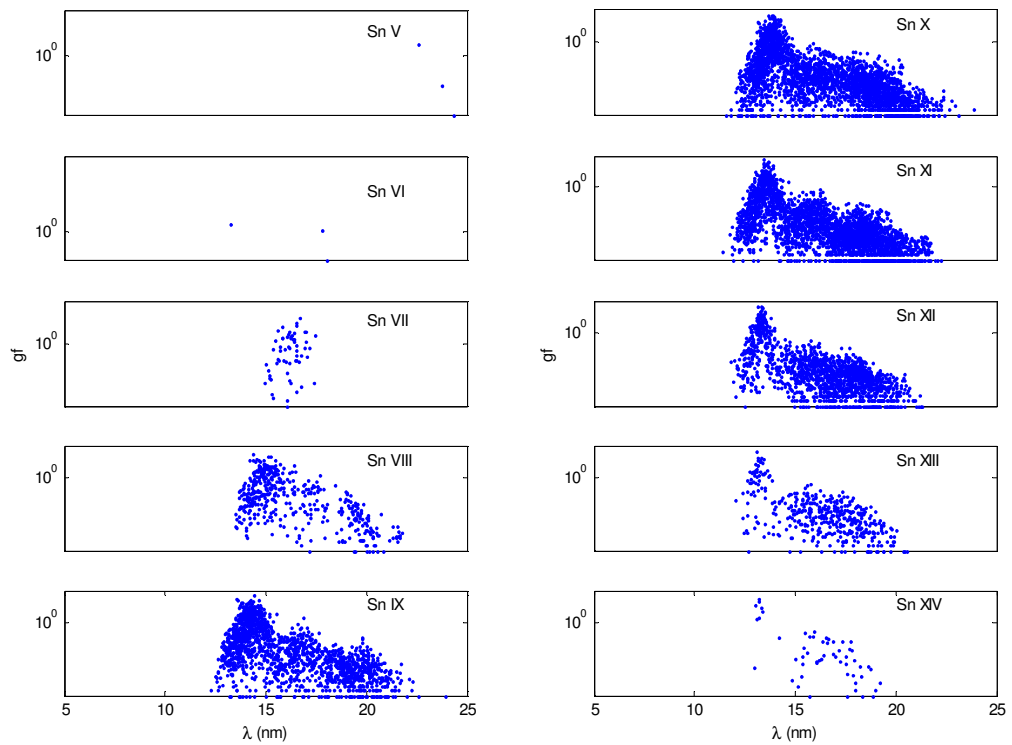


Figure 2.35  $\log_{10} gf$  versus wavelength (4p-4d transitions)

Figure 2.36 shows the full spectral output, 7.4%, and 2% in-band radiation ( $\Sigma gf$ ) for the three transition arrays. Note the different maximum ion stage for each transition type in the 2% band: Sn XI (4d-4f), Sn XII (4p-4d), and Sn XIII (4d-5p). As well, the first contributing ion stage is different: Sn IX (4d-4f), Sn XI (4p-4d), and Sn XIII (4d-5p). However, 4d-4f and 4p-4d  $\Sigma gfs$  are similar and both are about ten times stronger than the 4d-5p  $\Sigma gf$ . From this analysis, it can be seen in Figure 2.10 (see Section 2.1) that the first 2% in-band  $\Sigma gf$  peak at Sn XI results from the 4d-4f UTA, whereas the second peak is from the 4p-4d UTA. The difference between the 7.4% and 2% radiation could be used as a measure of heating, since more than half of the 4d-4f  $\Sigma gf$  at Sn XI (for example) is absorbed by the mirror outside the 2% bandwidth, whereas almost all of the 4p-4d  $\Sigma gf$  at Sn XII lies inside the 2% in-band mirror response.

Figures 2.37 and 2.38 compare the convolved Cowan data (with default width of 0.0212 nm) and the 2-parameter UTA (with width calculated from the line distribution) for the three transition types. Clearly, the 2-parameter UTA is broader, overestimating the convolved results by a factor of 2, as found in [20]. The 4p-4d results overestimate the convolved results by a factor of 4. The UTA width is broader because of the numerous outlying low  $gf$  transitions in the selected region.

Note that comparing the same convolved data and the 2-parameter UTA (with a width equal to half of the calculated UTA standard deviation) gives a much better fit as shown in Figures 2.39 and 2.40. Restricting the statistics to a limited bandwidth will also decrease the width [14, 20]. Matching the convolved data to UTA statistics over selected regions is discussed in Section 2.3, where the effects of Doppler and electron impact broadening are also included.

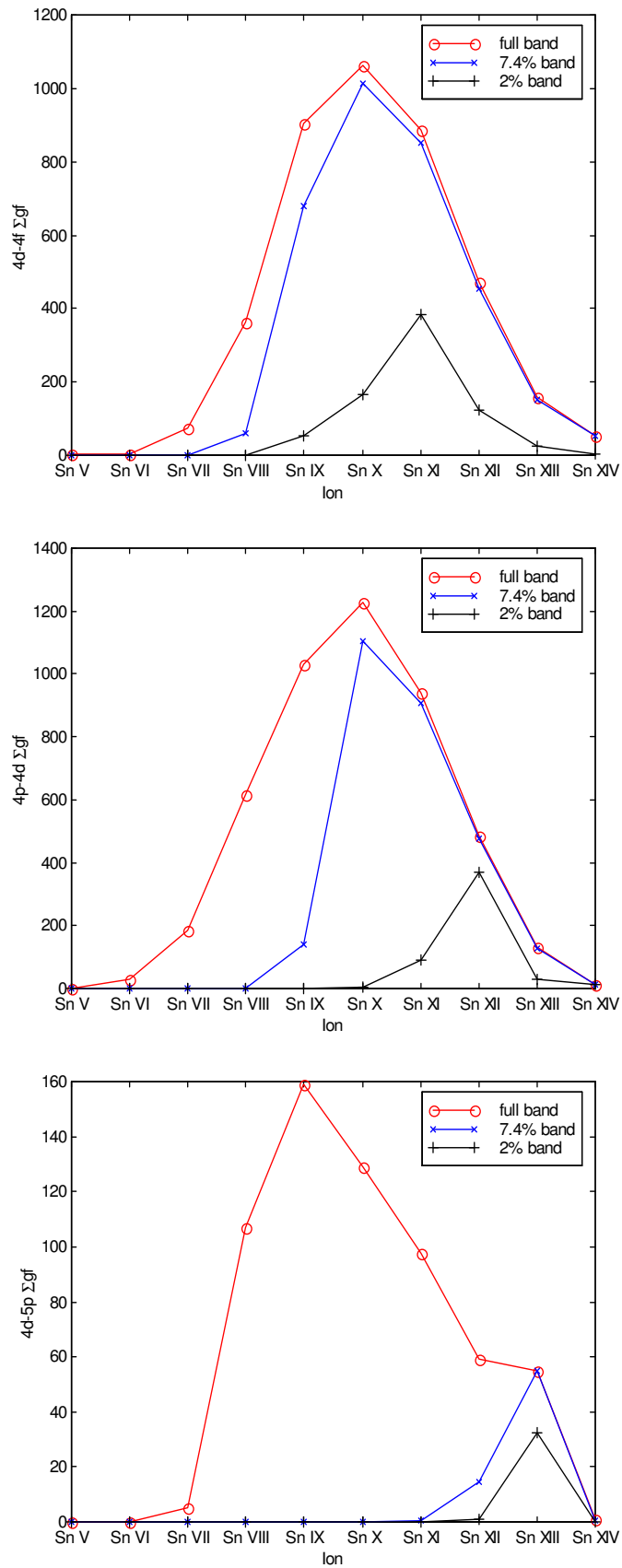
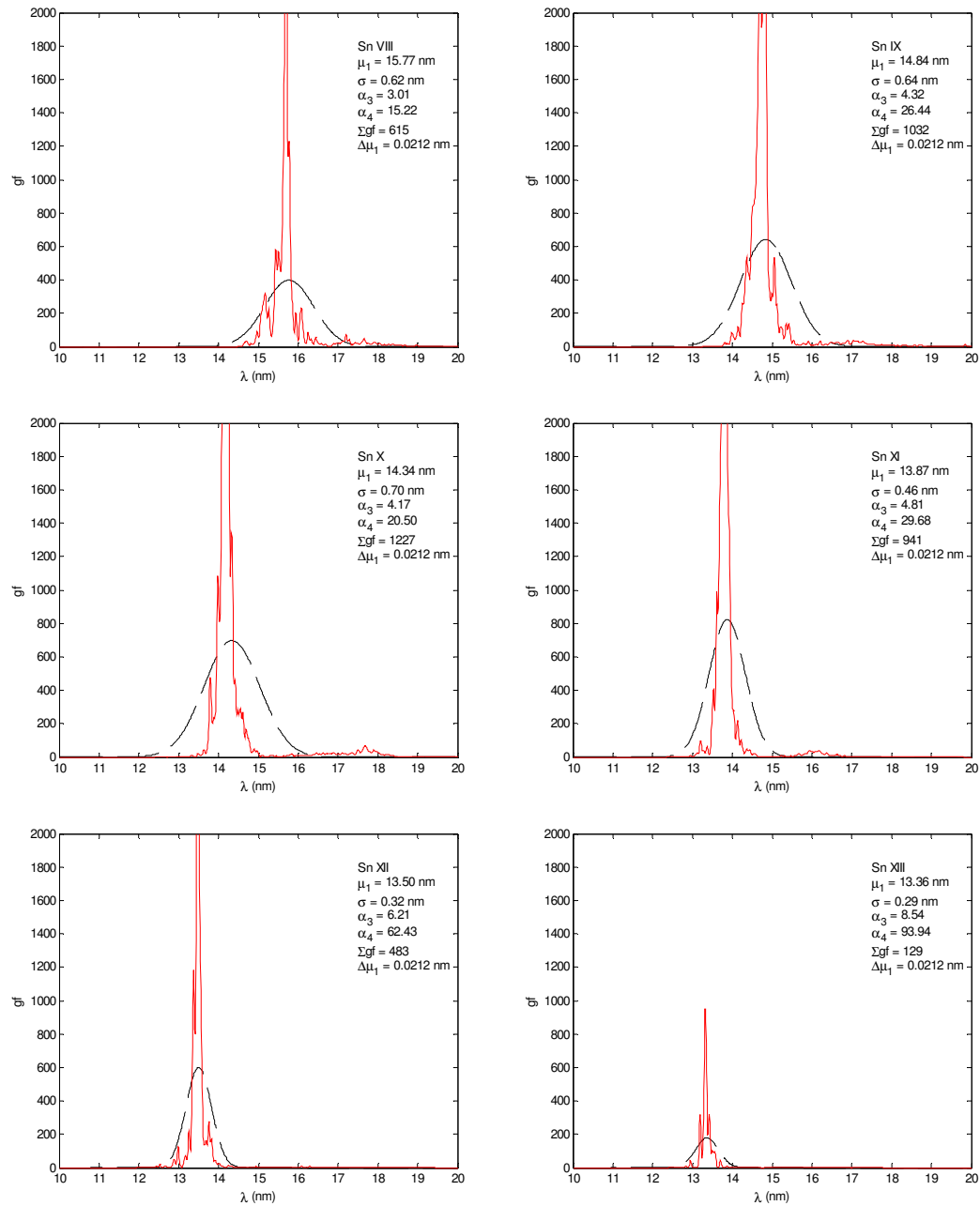
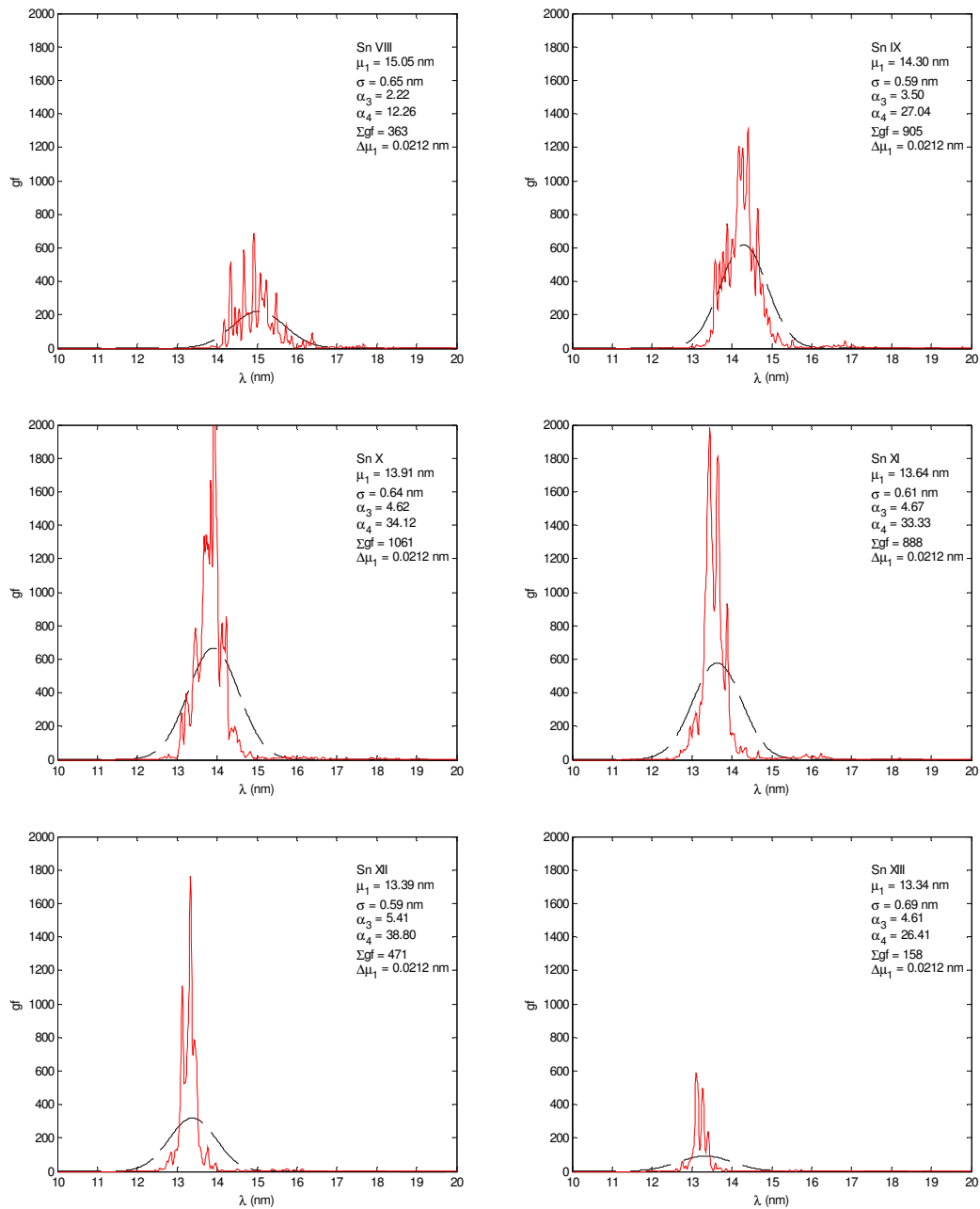


Figure 2.36  $\Sigma gf$  for 4d-4f (top), 4p-4d (middle), and 4d-5p (bottom) transitions: full band, 7.4% band, and 2% band



**Figure 2.37** 4d-4f transitions convolved with  $\Delta\mu_1 = 0.0212$  nm width (red) and 2-parameter UTA (black) with width,  $\sigma$ , where  $\sigma$  is calculated from the line distribution.



**Figure 2.38** 4p-4d transitions convolved with  $\Delta\mu_1 = 0.0212$  nm width (red) and 2-parameter UTA (black) with width,  $\sigma$ , where  $\sigma$  is calculated from the line distribution.

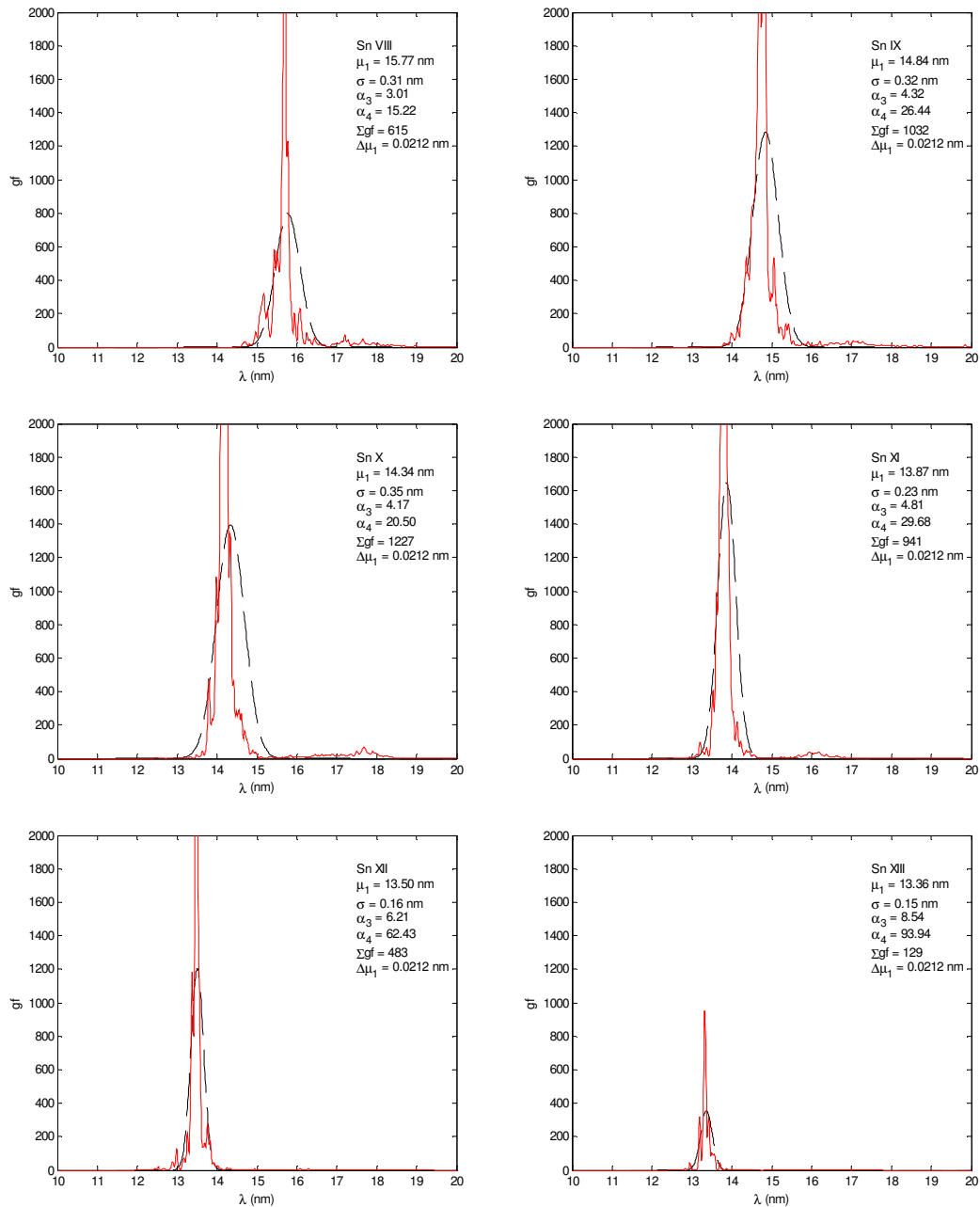


Figure 2.39 4d-4f transitions convolved with  $\Delta\mu_1 = 0.0212$  nm width (red) and 2-parameter UTA (black) with width,  $\sigma/2$ , where  $\sigma$  is calculated from the line distribution.

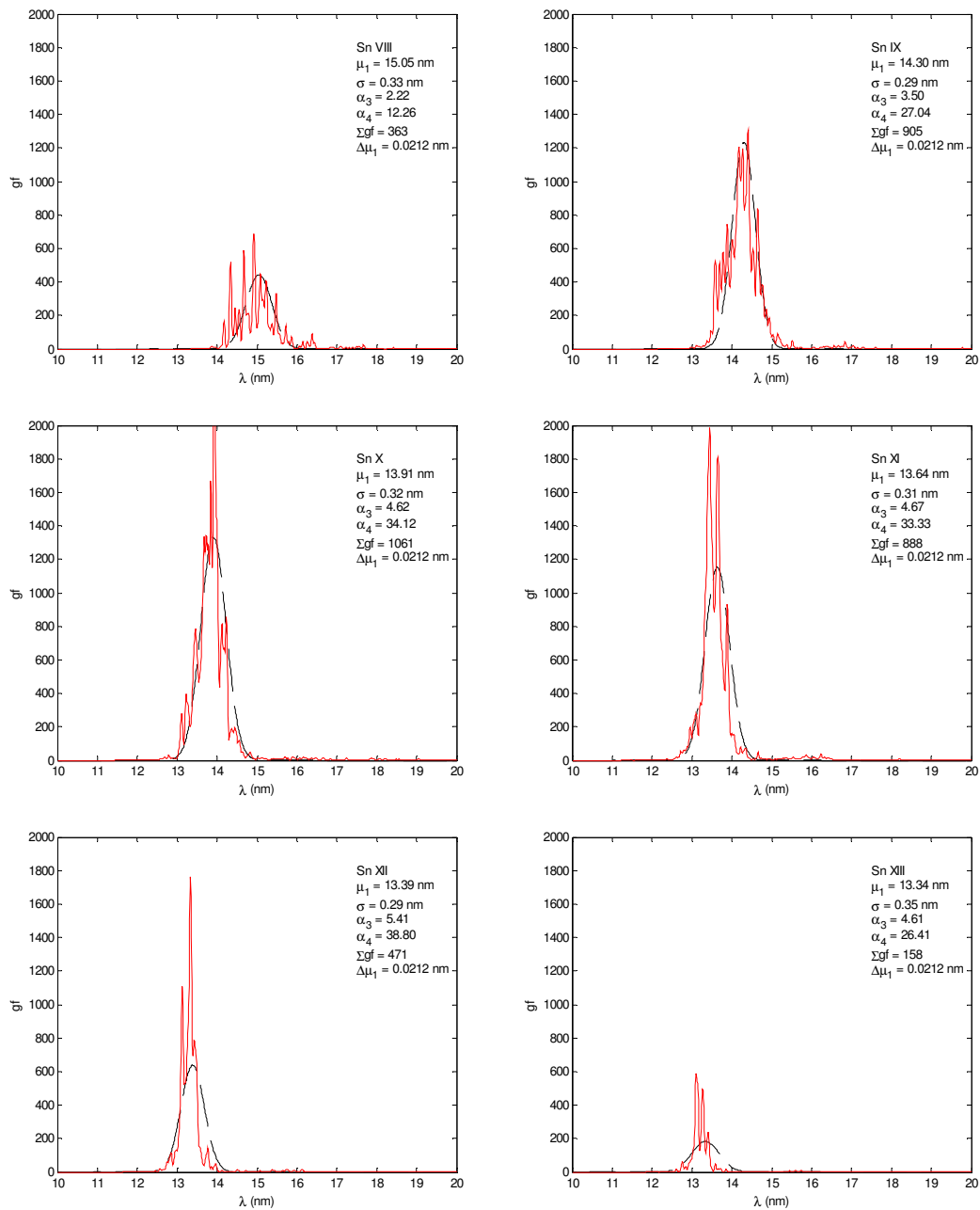


Figure 2.40 4p-4d transitions convolved with  $\Delta\mu_1 = 0.0212$  nm width (red) and 2-parameter UTA (black) with width,  $\sigma/2$ , where  $\sigma$  is calculated from the line distribution.

## 2.3. Line broadening

All lines are broadened depending on how they are created; however, the dominant broadening depends on the conditions. Natural broadening results from the finite lifetime of an excited state, and is generally small compared to Doppler broadening and electron impact broadening.

### 2.3.1 Doppler broadening

Doppler broadening results from the thermal velocity of an emitting ion (or atom), which increases/decreases, depending on the relative motion towards/away from the detector. If the velocity obeys a Maxwell-Boltzmann distribution, the Doppler broadening can be calculated as in Eq. 2.2 as derived in [14].

$$\Delta\lambda = 2\Gamma = 2 \times 3.0414 \times 10^{-7} \sqrt{\frac{T}{A}} \lambda_0 \quad (2.2)$$

where  $T$  is the temperature in K,  $A$  is the atomic weight,  $\lambda_0$  is the unbroadened theoretical wavelength in nanometres, and  $\Gamma$  is the Doppler-broadened width. For a given ion species, the width depends only on temperature and wavelength. For tin ( $A = 118.71$ ) at 40 eV and 13.5 nm,  $\Delta\lambda \sim 0.0005$  nm and thus Doppler broadening is quite small ( $\sim 1/40$  of the envelope width suggested in [15]). Doppler broadening over a range of temperatures and wavelengths in the area of interest for tin LPPs is shown in Figure 2.41, indicating greater broadening at longer wavelengths and temperatures.

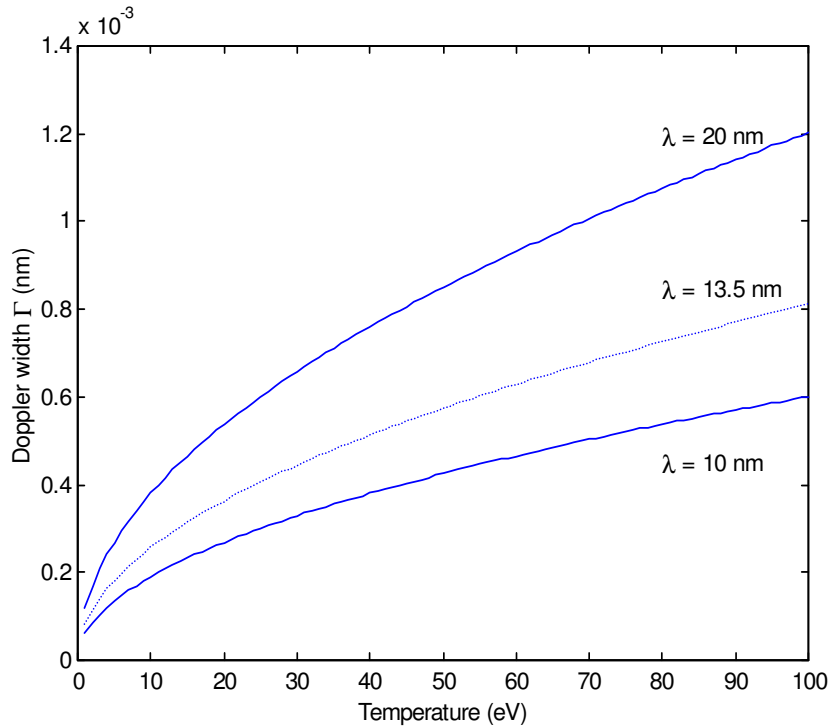


Figure 2.41 Doppler broadening versus wavelength and temperature (tin)

### 2.3.2 Electron impact broadening

Electron impact broadening results from electron collisions and naturally increases as electron density increases. The interaction between an ion and the rapidly moving free electrons in a plasma is a complicated process; however, a general scaling property for electron impact broadening is derived in [14]. The resulting broadening is proportional to electron density and inversely proportional to the square root of the temperature, as in Eqs. 2.3–2.5 [23].

$$\Delta\lambda = \omega = \frac{n_e \pi^3 C_2^2}{\langle v_e \rangle} \left[ 0.923 - \ln \left( \frac{\pi C_2}{\rho_{\max} \langle v_e \rangle} \right) \right] \quad (2.3)$$

$$C_2 = a_0 \frac{Ze^2}{\hbar} \quad (2.4)$$

$$\langle v_e \rangle = \sqrt{\frac{2kT}{m_e}} \quad (2.5)$$

where  $n_e$  and  $T$  are the electron density and temperature in the plasma,  $Z$  is the atomic number,  $\rho_{\max}$  is the Debye length (see Eq 1.35), and  $a_0$ ,  $e$ ,  $\hbar$ ,  $k$ , and  $m_e$  have their usual meanings. For a tin plasma at  $10^{21} \text{ cm}^{-3}$  and 40 eV, the electron impact broadening is about .02 nm, almost three orders of magnitude greater than Doppler broadening at the same temperature and electron density. The electron impact broadening is shown in Figure 2.42 at  $10^{21} \text{ cm}^{-3}$  (critical electron density for 1064-nm laser pulse) and at  $10^{20} \text{ cm}^{-3}$ . Note that in the region of interest for LPP tin plasmas ( $10^{17}$ – $10^{21} \text{ cm}^{-3}$ ), the electronic impact broadening varies significantly as a function of density (four orders of magnitude) and that, at lower densities, Doppler broadening will become more dominant.

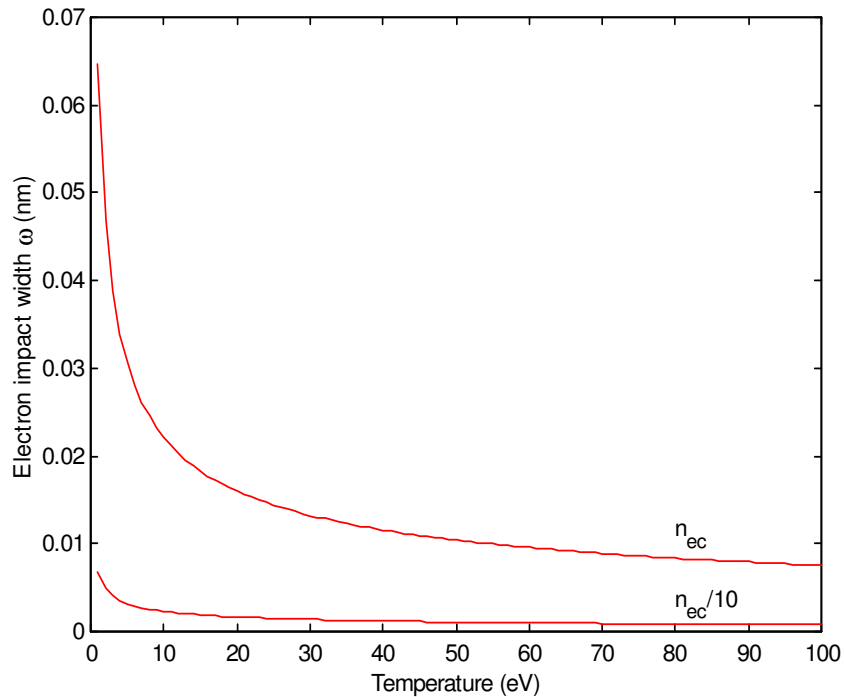
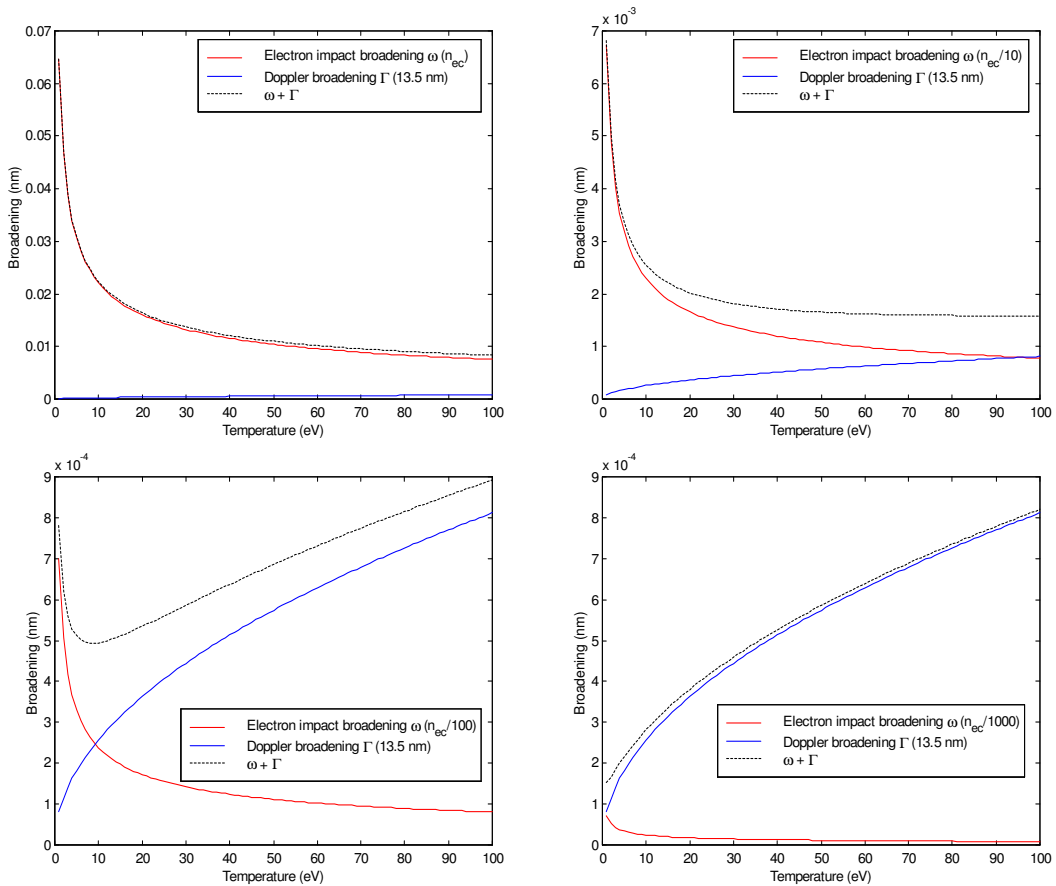


Figure 2.42 Electron impact broadening versus electron density and temperature (tin)

### 2.3.3 Doppler, electronic impact, and other broadening in a plasma

Broadening effects are additive, though generally only one process dominates. Garloff *et al.* neglects Doppler broadening entirely and uses electron impact broadening only [22]. In Figures 2.41 and 2.42 above it was shown that electron impact broadening is the dominant process in a tin LPP plasma at the critical electron density of  $10^{21} \text{ cm}^{-3}$  (Nd:YAG fundamental of  $\lambda = 1064 \text{ nm}$ ).

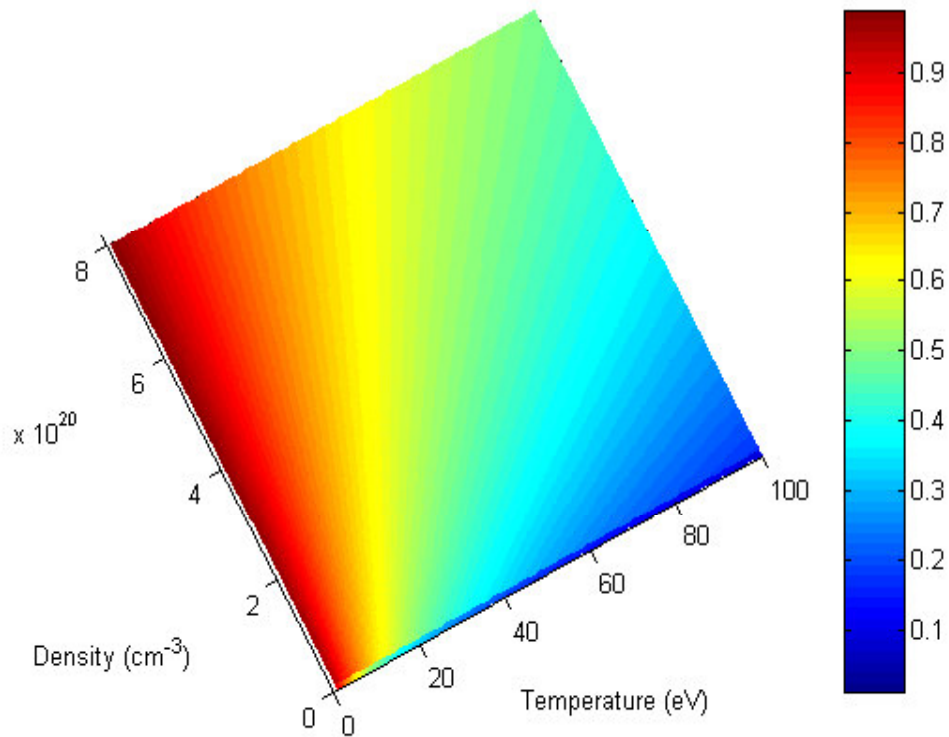
Figures 2.43 show the contribution of both processes versus temperature at four electron densities (from the critical density of  $10^{21} \text{ cm}^{-3}$  to  $10^{18} \text{ cm}^{-3}$ ) and a wavelength of 13.5 nm. In the 10–100 eV temperature range at the critical electron density, the broadening is almost entirely due to electron impact. In the same temperature region at 1/1000 of the critical electron density, Doppler broadening is dominant. Thus it can be seen that as density decreases the dominant broadening mechanism changes from collisional electron impact to thermal Doppler broadening.



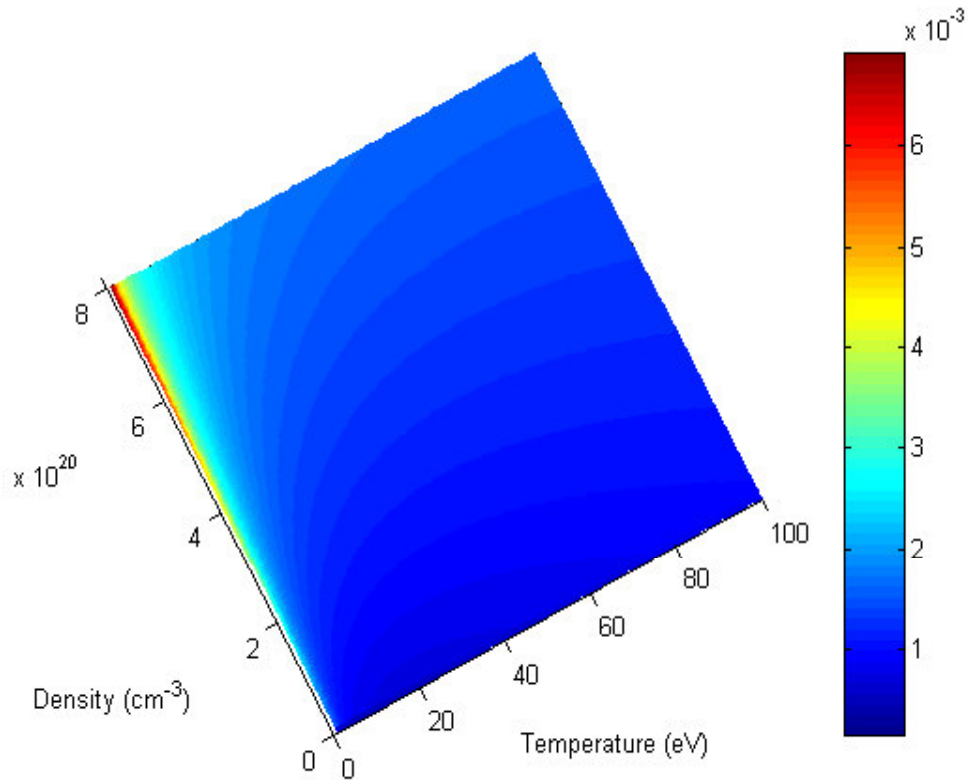
**Figure 2.43** Electron impact (blue) and Doppler broadening (red) (tin, 13.5 nm) versus electron density (from  $10^{21}$  to  $10^{18} \text{ cm}^{-3}$ ) and temperature

Figure 2.44 gives a surface plot of the ratio of the two broadening mechanisms over the expected plasma temperature and electron density region. Figure 2.45 gives the combined effect of Doppler and electron impact broadening in the same region.

For convolving theoretical Cowan data, a Gaussian is used for Doppler broadening and a Lorentz function for electron impact broadening. Where two broadening mechanisms are comparable, a Voigt profile is recommended, however, for computational purposes, convolving with a Gaussian and then a Lorentz function is sufficient as the Voigt profile is computationally considerably more complicated.



**Figure 2.44** Ratio of electron impact ( $\omega$ ) to Doppler broadening ( $\Gamma$ ) versus electron density and temperature



**Figure 2.45** Electron impact ( $\omega$ ) + Doppler broadening ( $\Gamma$ ) versus electron density and temperature

A temperature dependent broadening mechanism is also given in [23], convolved analytically with a Gaussian as shown in Eq. 2.6. The effect is the same as the UTA Gaussian calculated as part of the UTA statistics (Eq. 1.30), ratioed with a decaying exponential temperature-dependent term ( $e^{-1/T}$ ) and an inverse cubic wavelength-dependent term ( $\lambda^{-3}$ ). (The equation has been transformed from an energy variable in [23] to a wavelength variable).

$$f(\lambda) = \frac{1}{\sigma\sqrt{2\pi}} e^{-\frac{(\lambda-\lambda_0)^2}{2\sigma^2} - \frac{hc}{kT\lambda_0} \left(\frac{\lambda}{\lambda-\lambda_0}\right)} \left(\frac{\lambda_0}{\lambda}\right)^3 \quad (2.6)$$

Here,  $\lambda_0$  is the average wavelength,  $\sigma$  is the standard deviation (where FWHM =  $2.355\sigma$ ), and  $T$  is the temperature. The constants  $h$ ,  $c$ , and  $k$  have their usual meanings.

For temperature-dependent Gaussian broadening, the peak wavelength is shifted as given in Eq. 2.7 [23]. The maximum emission is thus at shorter wavelengths as temperature decreases.

$$\lambda_{peak} = \sigma^2 \left( \frac{3\lambda}{c} - \frac{1}{kT} \right) \quad (2.7)$$

The lognormal probability density distribution, which models thick-tailed data in economic finance modelling, can also be used to attempt to better match UTA broadening. The advantage of the lognormal distribution is that it includes a measure of skewness while remaining everywhere positive, unlike the Edgeworth expansion which introduces non-physical negative numbers to the distribution. However, the lognormal distribution is not additive (the sum of two lognormals is not a lognormal). A bimodal Gaussian could also be considered to model the outliers (introducing only two more parameters), although this has the same problem of restricting UTA data to a selected region, namely, how to determine the applicable range.

## 2.4 UTA reduced broadening survey

To determine the appropriate broadening to the statistical UTA theoretical Cowan data for radiation transport modelling (Chapter 5), a survey was conducted using different broadening mechanisms over different temperature and electron densities. The initial survey was conducted by comparing different results to the theoretical data convolved with a flat broadening envelope of 0.0212 nm as recommended in [15]. An arbitrary width of .02 nm is suggested in [20] and it has also been observed experimentally [12] that oxygen lines in a tin laser-produced plasma are broadened by a comparable amount (0.01 nm). Table 2.11 highlights the methods used in the survey.

1.	UTA broadening: width ( $\sigma$ ) calculated from full UTA range (used as a baseline reference)
2.	UTA broadening: reduced width ( $\sigma'$ ) calculated by least squares fit to flat convolved data (0.0212 nm)
3.	UTA broadening over restricted regions (full, 7.4%, and 2%): reduced width ( $\sigma'$ ) calculated as in 2.
4.	UTA broadening: reduced width ( $\sigma'$ ) calculated by least squares fit to Doppler and electron impact broadened convolved data in the 1–100 eV and $10^{17}$ – $10^{21}$ $\text{cm}^{-3}$ range, applicable to EUV tin LPPs.

Table 2.11 Broadening survey

For the flat convolved data, reduced widths ( $\sigma'$ ) were calculated using a least squares fit and expressed as a ratio ( $\sigma/\sigma'$ ), giving the resultant width overestimation or reduction in the calculated UTA width. Figure 2.46 shows the convolved and reduced-width statistical UTA for Sn X 4d-4f transitions over the full spectral range. The reduced width ratio is 2.8. Table 2.12 lists the results as a function of transition type (4d-4f and 4p-4d) and spectral region (full, 7.4%, and 2%). It is seen that the overestimation of 2 suggested by Mandlebaum *et al.* [20] is reasonable. Width overestimations vary from 1.6 for Sn IX (4p-4d) to 3.9 for Sn XII (4d-4f) over the full range and it can be seen that for restricted regions, where outliers have less effect, the reduced width ratio approaches unity. Here, the calculated UTA width is appropriate.

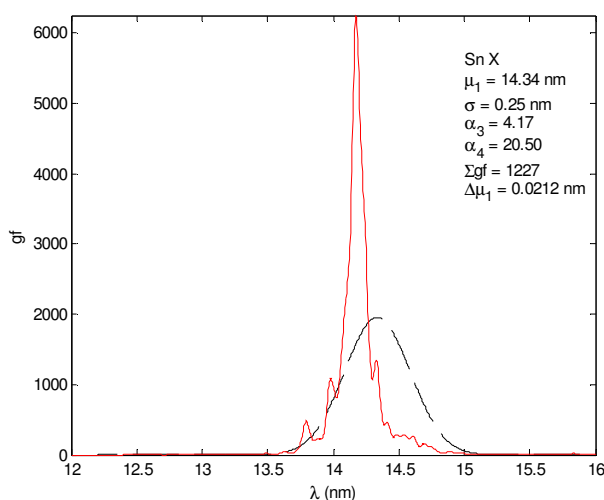
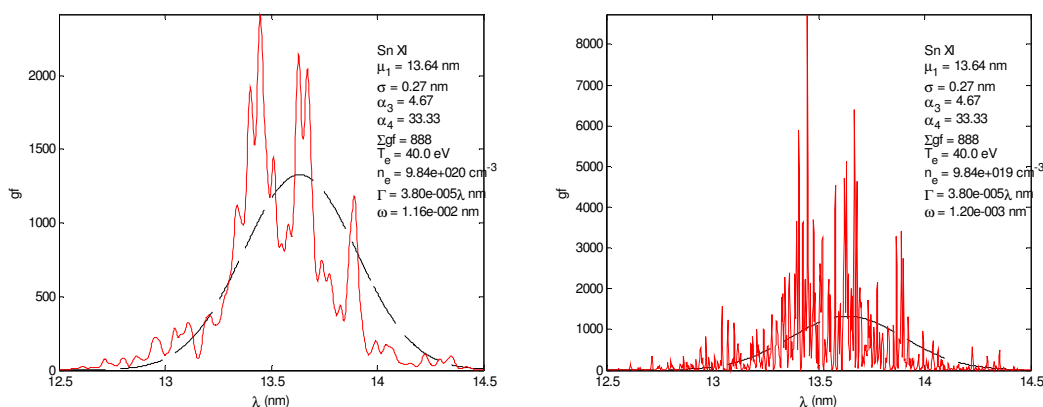


Figure 2.46 Sn X, 10–20 nm, 4d-4f ( $\sigma/\sigma' = 2.8$ )

Ion	full		7.40%		2%	
	4d-4f	4p-4d	4d-4f	4p-4d	4d-4f	4p-4d
Sn IX	2.8	1.6	1.1	0.9	1.1	1.1
Sn X	2.8	2.2	1.6	1.1	0.8	0.8
Sn XI	3.4	2.3	1.6	1.2	0.7	0.8
Sn XII	3.9	3.1	2.3	1.3	1.0	1.0
Sn XIII	3.2	2.9	1.7	1.2	0.9	1.3

**Table 2.12** Reduced UTA width ratios (flat broadening)

A similar survey was done, comparing the effects of using Doppler and electron-impact broadened lines to the calculated UTA width at different electron temperatures and densities. Figure 2.47 (left) shows the convolved and reduced-width statistical UTA for Sn XI 4p-4d transitions over the 7.4% range with broadening determined at 40 eV and  $n_e = 1 \times 10^{-21} \text{ cm}^{-3}$  ( $n_{ec}$ ). The reduced width ratio ( $\sigma/\sigma'$ ) is 1.2. Figure 2.47 (right) shows the same at 40 eV and  $n_e = n_{ec}/10$ . The reduced width is unchanged. Figure 2.48 shows the same for Sn XII 4d-4f + 4p-4d transitions over the 2% range,  $n_e = n_{ec}$  (left) and  $n_e = n_{ec}/100$  (right). The reduced width ratio is 1.1 at both densities. Table 2.13 lists the results as a function of transition type (4d-4f and 4p-4d) in the 7.4% range for three electron densities ( $n_{ec}$ ,  $n_{ec}/100$ , and  $n_{ec}/1000$ ).



**Figure 2.47** Sn XI, 12.5–14.5 nm, 4p-4d, 40 eV ( $n_{ec}$ ,  $n_{ec}/10$ )  $\sigma' = 1.2$

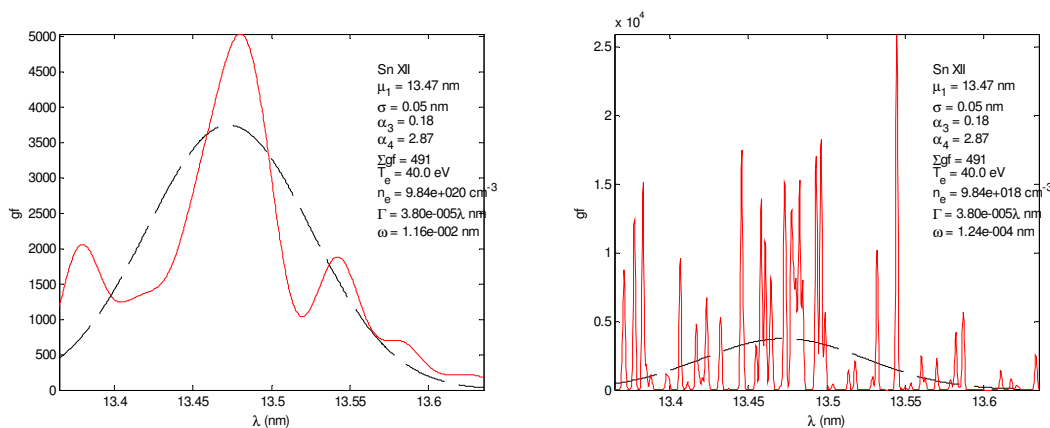


**Figure 2.48** Sn XII, 13.365–13.635 nm, 4d-4f + 4p-4d ( $n_{ec}$ ,  $n_{ec}/100$ )  $\sigma' = 1.1$

Ion	$n_{ec}$		$n_{ec}/100$		$n_{ec}/1000$	
	4d-4f	4p-4d	4d-4f	4p-4d	4d-4f	4p-4d
Sn IX	1.1	0.9	1.1	0.9	1.0	0.9
Sn X	1.6	1.1	1.6	1.0	1.7	1.0
Sn XI	1.6	1.2	1.6	1.1	1.6	1.1
Sn XII	2.4	1.3	2.6	1.3	2.6	1.3
Sn XIII	1.9	1.2	1.6	1.3	1.3	1.3

Table 2.13 Reduced UTA width ratios 7.4% range (Doppler and electron impact broadening)

The most interesting result of this survey is that the reduced width did not depend as expected on temperature and electron density. In fact, only over the full spectral range, did broadening depend on temperature and electron density, likely because of the numerous outliers and the wavelength dependence of the Doppler broadening (at sufficiently high electron densities). In the restricted 7.4% (see Table 2.13) and 2% range, no appreciable electron density dependence was observed, suggesting that the statistical UTA can be reasonably represented by only two parameters at different temperatures and densities. Although the convolved results are more detailed with decreased broadening, the best fit to the single statistical convolution remains essentially the same. As well, in the 2% range, the best-fit broadening is almost the same as the UTA broadening (*i.e.*,  $\sigma/\sigma' = 1$ ). Figure 2.49 shows the 4d-4f and 4p-4d reduced broadening over the 7.4% region at 40 eV for  $n_e$  and  $n_e/1000$ , which shows little difference at the two different electron densities. Note that the narrowing (increased reduced width) does increase with ionisation as already observed. The lack of sufficient temperature dependence on broadening is because of the square root temperature scaling ( $\Gamma \propto T^{1/2}$  and  $\omega \propto T^{1/2}$ ), which is not sensitive enough over the 1–100 eV range.

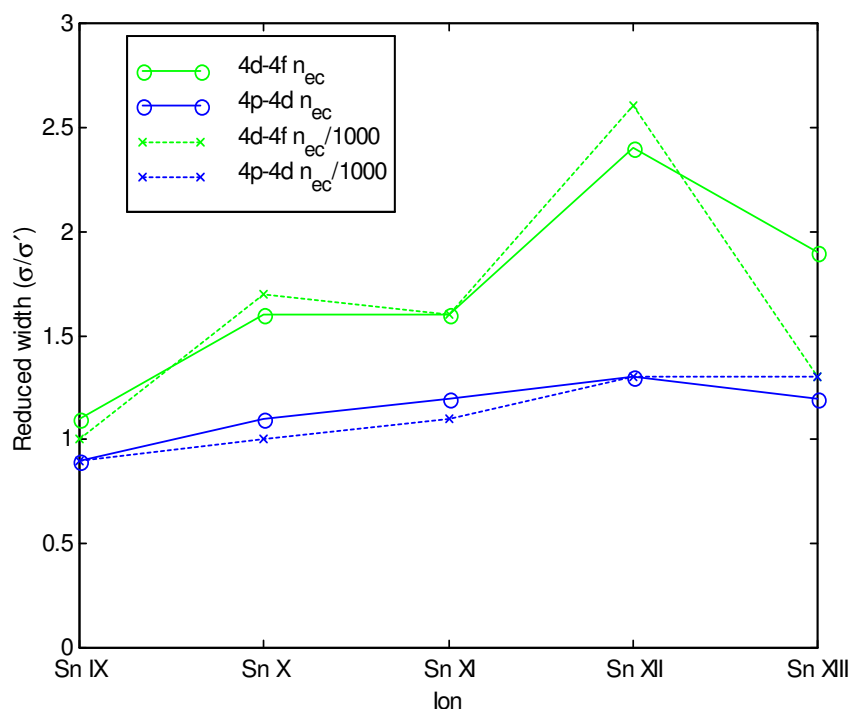


Figure 2.49 Reduced broadening ( $n_{ec}$ ,  $n_{ec}/1000$ )

It should be noted that as the statistical width was changed, the  $\Sigma gf$  (the area under each curve) remained constant so that a comparative analysis could be made. If the peaks were matched, the area would no longer be the same and, although peak emission would match, other regions of the emission array would either be over or underestimated.

Furthermore, the least-squares fit adjusts the UTA width and not the mean, in accordance with the central limit theorem from statistics, which states that the mean of the mean in a line-by-line convolution is equal to the mean in a single statistical convolution. The width, however, is not the same for the two different convolutions, which is why a least-square fit to the line-by-line convolution gives a better width than the calculated UTA width. The results of a numerical fit to the convolved data using a line fitting program gives the same results as the above least-squares UTA reduced-width method.

The average wavelength, however, will change according to the restricted region used, as shown in Figure 2.50 and Tables 2.14–2.16 (the full spectral range is repeated for comparison). In highly ionised rare earths, Mandelbaum *et al.* [20] considered lines only within a range  $\lambda \pm w$  (where  $w$  is a variable parameter), citing that the squared variance over-emphasises weak outlying lines. Three ranges are shown: the full spectral width from the calculated Cowan results, representing the UTA as defined in [15–20], the 7.4% range, and the 2% range. Note that there are no Sn V–Sn VII lines in the restricted ranges and, as is to be expected, the mean wavelengths are comparable for the other emitting ions in the restricted 2% range. Because of the prescribed 7.4% and 2% industry tie-in for NGL EUVL, the problem of restricting the UTA range is less important, though caution should be used whenever UTA data is excluded from a statistical representation.

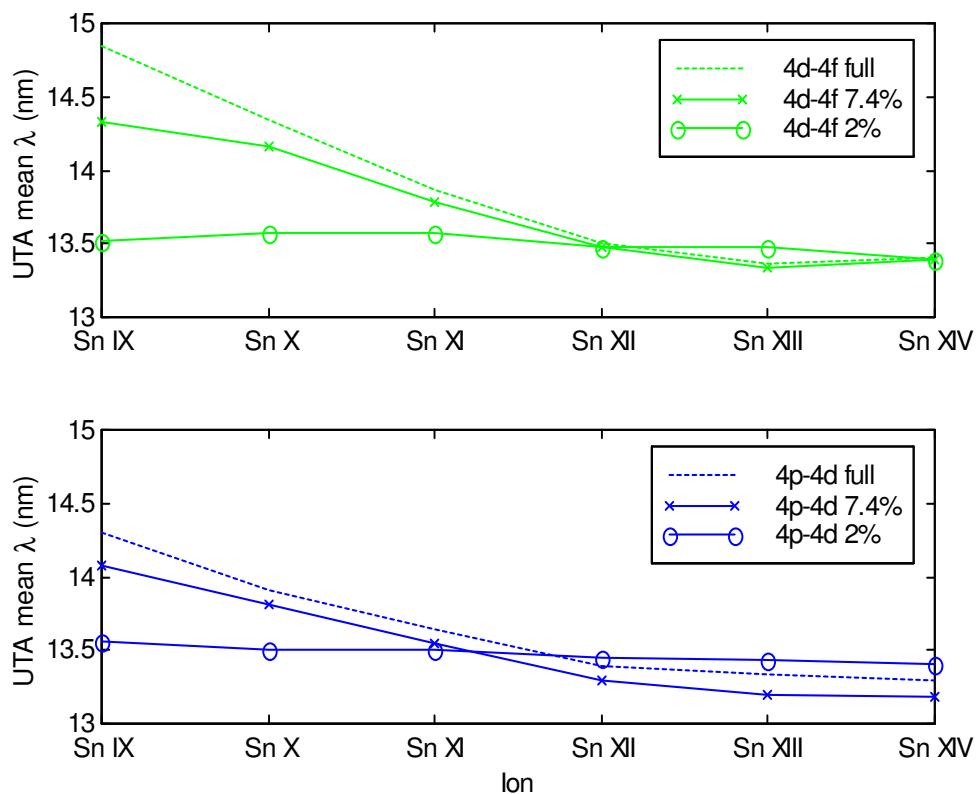


Figure 2.50 Wavelength dependence on spectral region: 4d-4f (top), 4p-4d (bottom)

Ion	4d-4f				4p-4d				4d-4f + 4p-4d			
	# of lines	$\Sigma gf$	$\lambda(\text{nm})$	$\sigma(\text{nm})$	# of lines	$\Sigma gf$	$\lambda(\text{nm})$	$\sigma(\text{nm})$	# of lines	$\Sigma gf$	$\lambda(\text{nm})$	$\sigma(\text{nm})$
Sn V	3	2.63	22.61	0.21	--	--	--	--	3	2.63	22.61	0.21
Sn VI	81	30.43	19.49	0.47	3	2.88	15.37	2.28	84	33.31	19.14	1.41
Sn VII	721	185.54	17.40	0.61	60	75.20	16.36	0.47	781	260.74	17.10	0.74
Sn VIII	2825	614.63	15.77	0.62	466	362.98	15.05	0.65	3291	977.6	15.50	0.72
Sn IX	5470	1032.42	14.84	0.64	1718	904.94	14.30	0.59	7188	1937.37	14.59	0.67
Sn X	5346	1227.41	14.34	0.70	3170	1061.48	13.91	0.64	8516	2288.89	14.14	0.71
Sn XI	2825	940.50	13.87	0.46	3245	888.11	13.64	0.61	6070	1828.61	13.76	0.55
Sn XII	721	483.43	13.50	0.32	1718	471.46	13.39	0.59	2439	954.9	13.45	0.48
Sn XIII	81	129.50	13.36	0.29	466	158.26	13.34	0.69	547	287.75	13.35	0.55
Sn XIV	3	13.03	13.41	0.22	60	53.95	13.29	0.61	63	66.98	13.32	0.55

Table 2.14 Wavelength dependence on spectral region (full)

Ion	4d-4f				4p-4d				4d-4f + 4p-4d			
	# of lines	$\Sigma gf$	$\lambda(\text{nm})$	$\sigma(\text{nm})$	# of lines	$\Sigma gf$	$\lambda(\text{nm})$	$\sigma(\text{nm})$	# of lines	$\Sigma gf$	$\lambda(\text{nm})$	$\sigma(\text{nm})$
Sn VIII	--	--	--	--	90	60.24	14.32	0.13	90	60.24	14.32	0.13
Sn IX	155	139.84	14.33	0.15	574	678.29	14.08	0.28	729	818.13	14.13	0.28
Sn X	506	1106.04	14.16	0.13	884	1012.09	13.81	0.30	1390	2118.13	13.99	0.29
Sn XI	503	907.85	13.79	0.15	717	853.06	13.54	0.26	1220	1760.91	13.67	0.25
Sn XII	233	477.05	13.48	0.17	284	455.51	13.30	0.21	517	932.55	13.39	0.21
Sn XIII	37	128.48	13.34	0.13	78	150.88	13.20	0.18	115	279.36	13.27	0.17
Sn XIV	2	12.92	13.39	0.01	9	52.00	13.18	0.12	11	64.92	13.22	0.13

Table 2.15 Wavelength dependence on spectral region (7.4%)

Ion	4d-4f				4p-4d				4d-4f + 4p-4d			
	# of lines	$\Sigma gf$	$\lambda(\text{nm})$	$\sigma(\text{nm})$	# of lines	$\Sigma gf$	$\lambda(\text{nm})$	$\sigma(\text{nm})$	# of lines	$\Sigma gf$	$\lambda(\text{nm})$	$\sigma(\text{nm})$
Sn VIII	--	--	--	--	4	0.02	13.52	0.02	4	0.02	13.52	0.02
Sn IX	7	0.07	13.52	0.04	95	52.97	13.56	0.06	102	53.05	13.56	0.06
Sn X	45	4.02	13.57	0.06	171	163.78	13.50	0.08	216	167.80	13.51	0.08
Sn XI	62	88.34	13.57	0.06	125	384.62	13.50	0.08	187	472.95	13.51	0.08
Sn XII	49	368.48	13.48	0.05	45	122.11	13.45	0.06	94	490.60	13.47	0.06
Sn XIII	9	29.31	13.47	0.06	10	22.99	13.43	0.06	19	52.30	13.45	0.06
Sn XIV	2	12.92	13.39	0.01	1	3.68	13.40	0.00	3	16.61	13.39	0.01

Table 2.16 Wavelength dependence on spectral region (2%)

Figure 2.51 shows the statistically calculated Cowan UTA Gaussians with best-fit reduced widths for Sn IX–Sn XIII over twice the 7.4% range (own maxima) with the corresponding convolved Doppler and electron impact broadened spectra at 40 eV and  $10^{-20} \text{ cm}^{-3}$ . (Twice the 7.4% bandwidth, 12.5–14.5 nm, is used to show as much as possible of the UTA in the figure.) Figure 2.52 shows the same for Sn IX–Sn XIII in the industry standard 2% region, 13.365–13.635 nm. Figures 2.51 and 2.52 show the appropriateness of using a two-parameter UTA to represent general features within the UTA and, thus, ultimately for use in radiation transport modelling within the plasma.

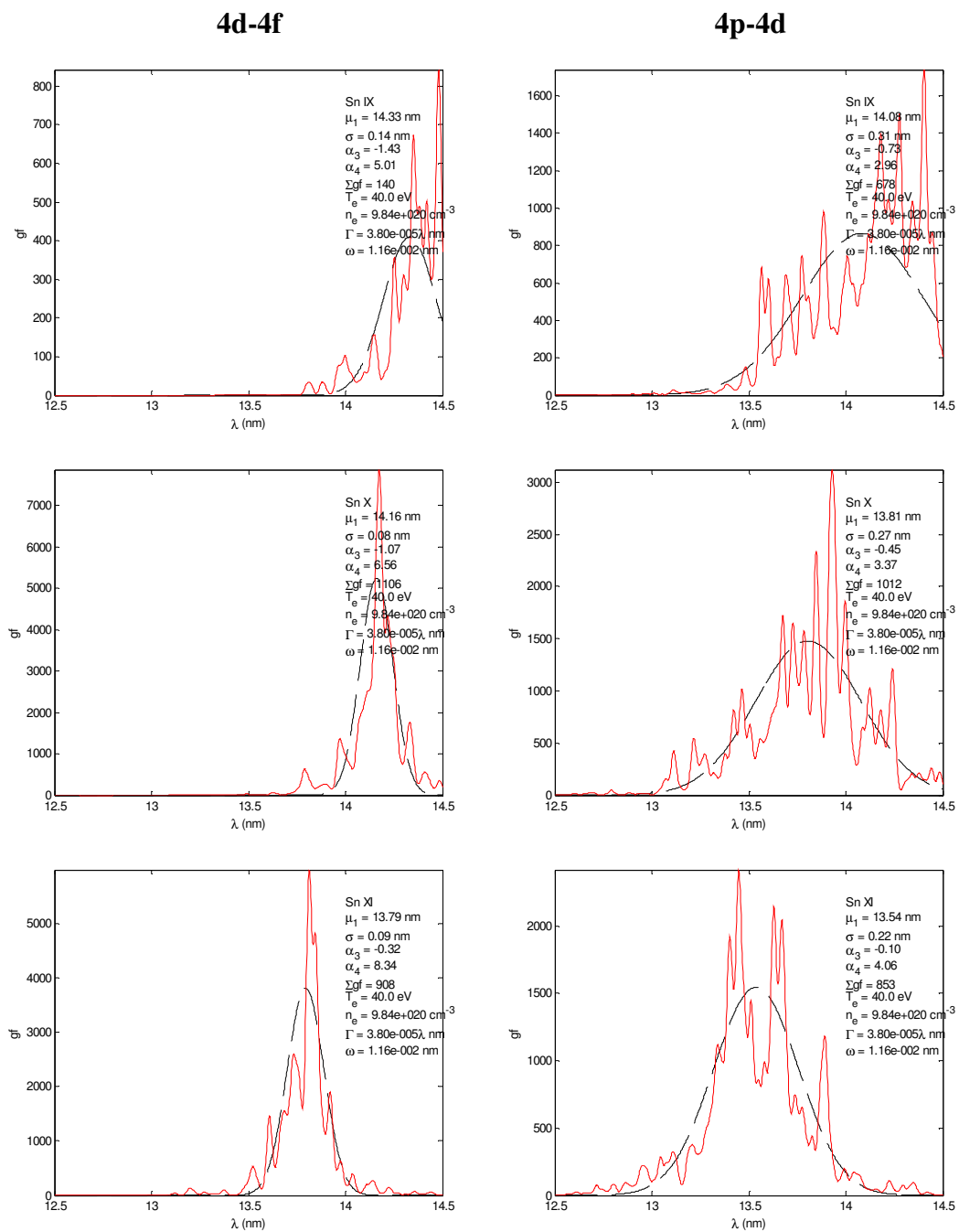


Figure 2.51 Sn VIII–Sn XIV 4d-4f (left) 4p-4d (right) (2 x 7.4%: 12.5–14.5 nm)

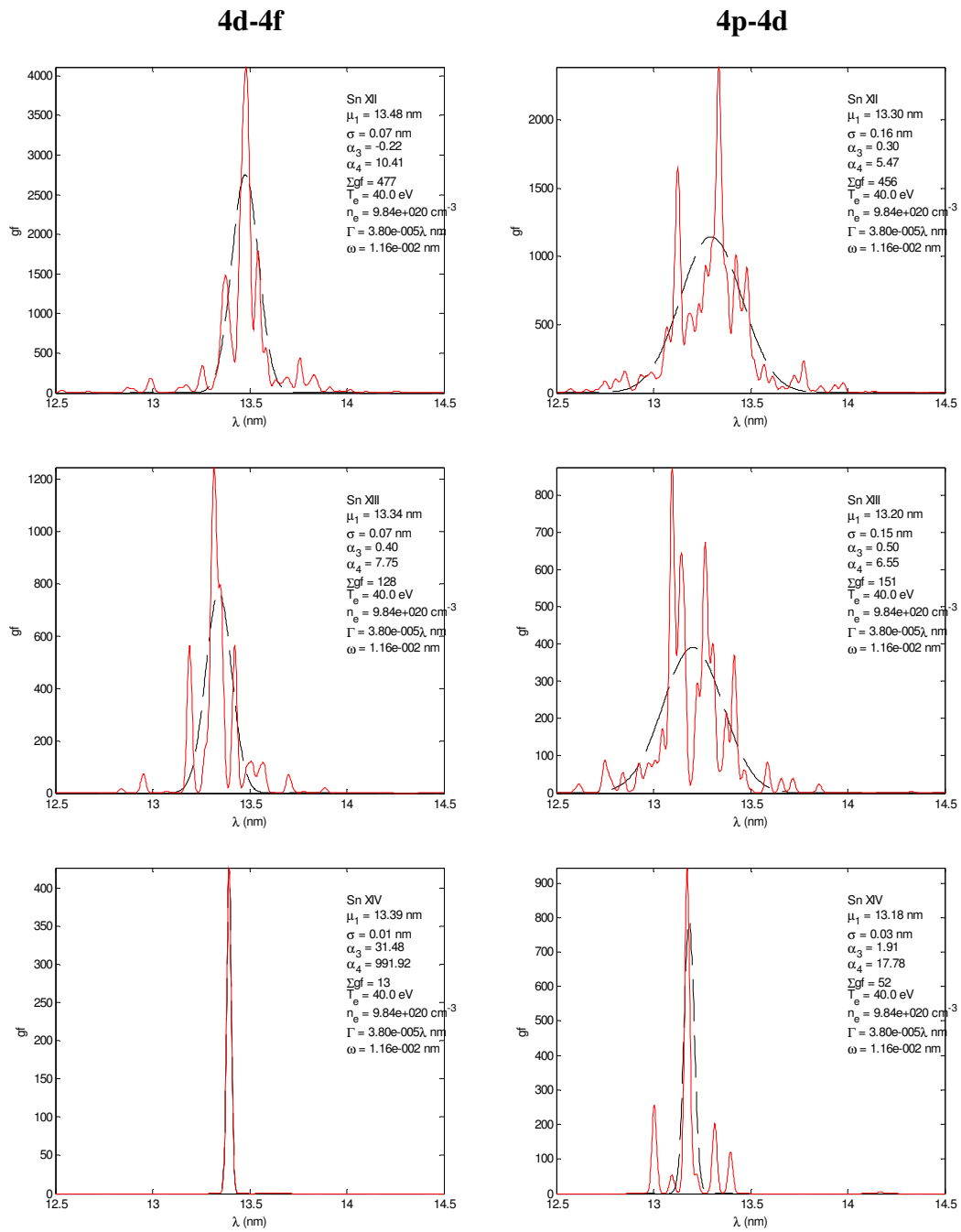


Figure 2.51 (cont) Sn VIII–Sn XIV 4d-4f (left) 4p-4d (right) (2x7.4%: 12.5–14.5 nm)

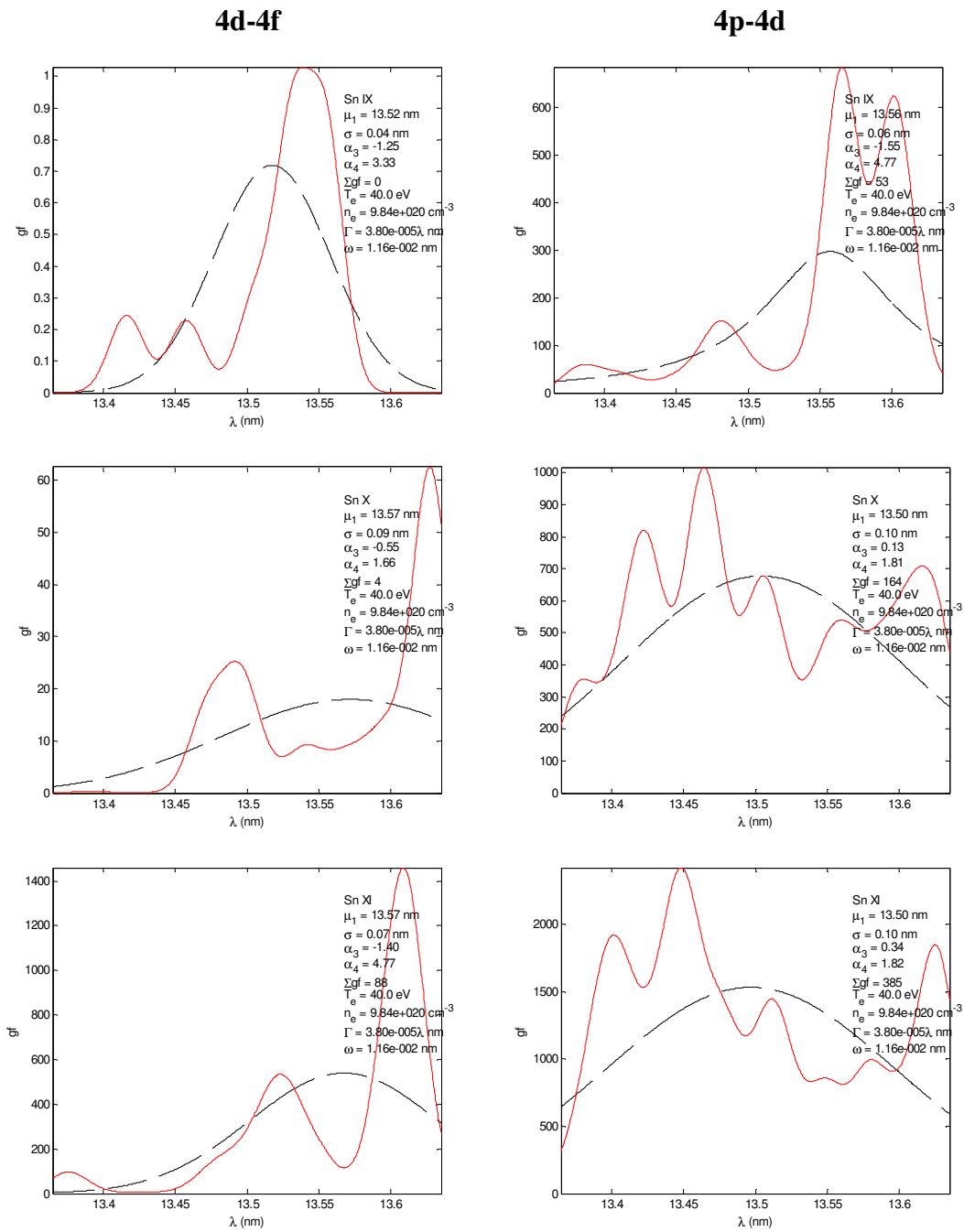


Figure 2.52 Sn IX–Sn XIII 4d-4f (left) 4p-4d (right) (2%: 13.365–13.635 nm)

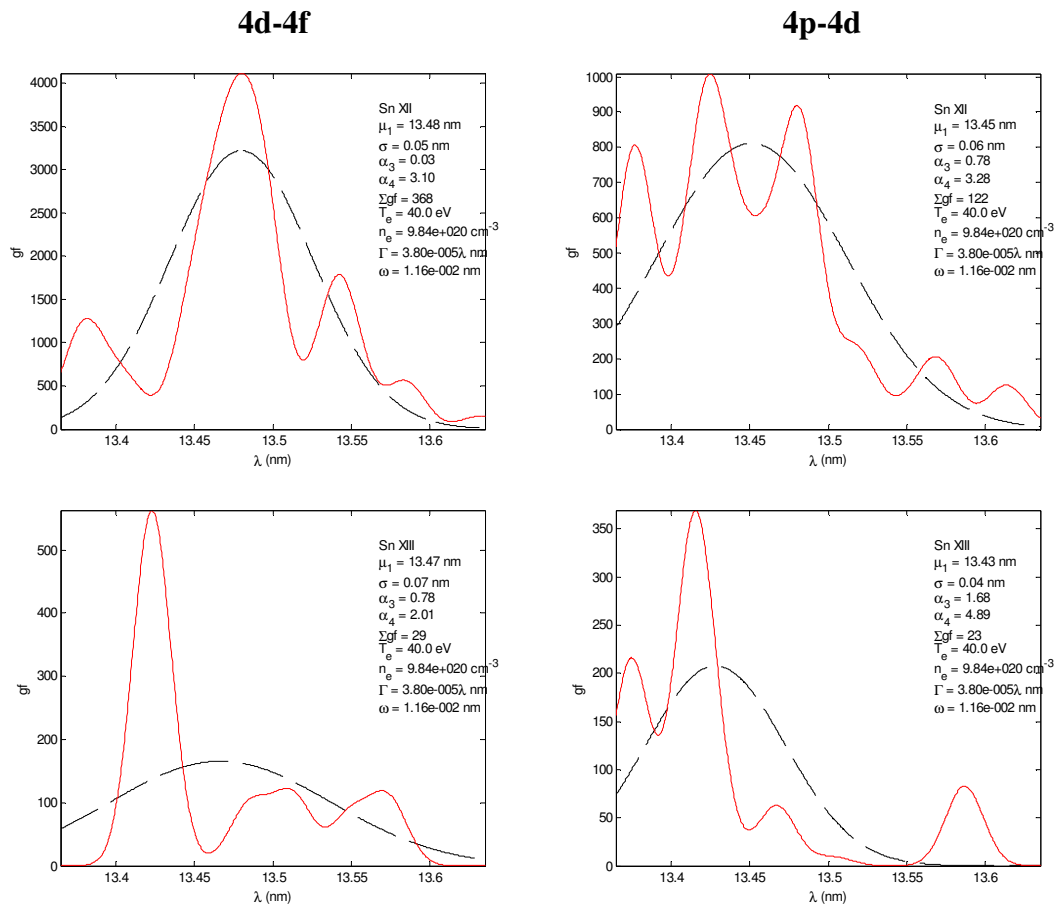
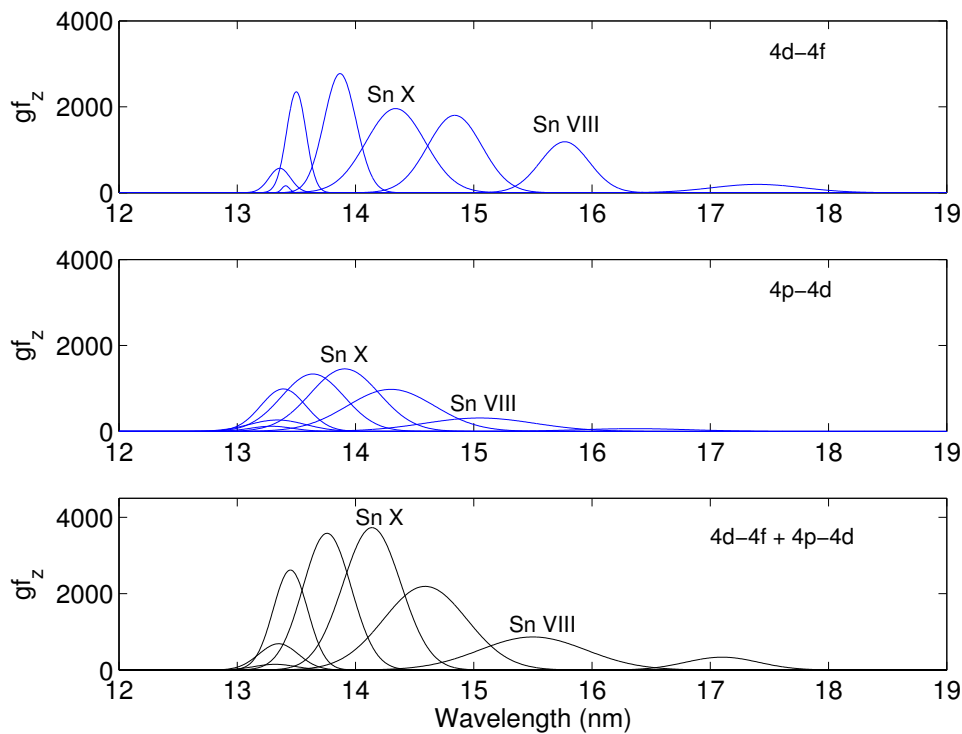


Figure 2.52 (cont) Sn IX–Sn XIII 4d-4f (left) 4p-4d (right) (2%: 13.365–13.635 nm)

A brief survey (not shown) was also undertaken to determine whether a Gaussian, Lorentzian, lognormal, or temperature-dependent Gaussian is a better fit to the calculated UTA distribution. It was seen that the difference between the Gaussian and Lorentzian is minimal. As discussed above, the lognormal is not additive and the temperature-dependent Gaussian shifts the mean.

In conclusion, open 4d and 4f subshell ions produce complex spectra. However, such spectra can be simplified using the UTA statistics methodology [15–20] for use in radiation transport plasma modelling. Such a method does not give detailed spectroscopic information, but does reproduce the essential height and width characteristics of the UTAs within a steady-state tin plasma, thus simplifying radiation transport within a spatially and temporally evolving plasma. Use of transition-specific statistics and a reduced width calculated by a least-squares fit to Doppler and electron impact broadened convolved spectra enhances the above approach. Figure 2.53 shows the statistically calculated UTAs (Sn VII–Sn XIV) plotted together for comparison.



**Figure 2.53** Statistically calculated UTA for the main 4d subshell Sn ions: Sn VII–Sn XIV 4d-4f (top) 4p-4d (middle) 4d-4f + 4p-4d (bottom)

## 2.5 References

- 1 Cowan, R. D., *The theory of atomic structure and spectra*, Berkeley, University of California Press, 1981.
- 2 McGuinness, C., *The XUV Photoabsorption and photoionisation spectra of selected ions: techniques, results, and theory*, Ph.D. thesis, University College Dublin, 1997.
- 3 van Kampen, P., *The outer shell spectra of argon and argon-like ions*, Ph.D. thesis, University College Dublin, 1997.
- 4 Joshi, Y. N. and van Kleef, Th. A. M., “ $4d^9 \rightarrow 4d^8 5p$  transitions in Cd IV, Sn VI, and Sb VII and the resonance lines of Sn V and Sb VI,” *Can. J. Phys.*, **55**, 714–725, 1977.
- 5 Churilov, S. S., Kildiyarova, R. R., Ryabtsev, A. N., and Kramida, A., “Analysis of the  $4d^9 - 4d^8(4f + 6p)$  transition array of Sn VI,” *Physica Scripta*, **50**, 463–468, 1994.
- 6 van Kleef, Th. A. M. and Joshi, Y. N., “Seventh spectrum of tin: Sn VII,” *Can. J. Phys.*, **62**, 167–177, 1983.
- 7 Azarov, V. I., Joshi, Y. N., Churilov, S. S., and Ryabtsev, A. N., “Analysis of the  $4d^7(4f + 6p)$  and  $4p^5 4d^9$  configurations of Sn VII, Sb VIII, and Te IX,” *Physica Scripta*, **50**, 642–653, 1994.
- 8 van het Hof, G. J. and Joshi, Y. N., “The analysis of the  $4d^8$ ,  $4d^7 5s$  and  $4d^7 5p$  configurations of six-times ionized tin: Sn VII,” *Physica Scripta*, **48**, 714–725, 1993.
- 9 Azarov, V. I. and Joshi, Y. N., “Analysis of the  $4d^7 - 4d^6 5p$  transition array of the eighth spectrum of tin: Sn VIII,” *J. Phys. B: At. Mol. Opt. Phys.*, **26**, 3495–3514, 1993.
- 10 Churilov, S. S., Joshi, Y. N., and Ryabtsev, A. N., “The  $4d^{10} 1S_0 - 4d^9 (np + n'f)$  transitions in the Pd I isoelectronic sequence from Cd III to Cs X,” *J. Phys. B, At. Mol. Opt. Phys.*, **27**, 5485–5495, 1994.
- 11 Sugar, J. and Kaufman, V., “Resonance lines in the Pd I isoelectronic sequence: I VIII to XXII,” *Physica Scripta*, **26** (6), 1982.
- 12 Hayden, P., “An investigation of tin based laser produced plasmas as a source of radiation at 13.5 nm,” M.Sc. thesis, University College Dublin, 2004.
- 13 Colombant, D. and Tonon, G. F., “X-ray emission in laser-produced plasmas,” *J. Appl. Phys.*, **44** (8), 3524–3537, 1973.
- 14 Salzmann, D., “*Atomic physics in hot plasmas*,” International series of monographs on physics, Oxford University Press, 1998.
- 15 Bauche-Arnoult, C. and Bauche, J., “Asymmetry of  $l^{N+1} - l^N l'$  transition-array patterns in ionic spectra,” *Phys. Rev. A*, **30** (6), 3026–3032, 1984.
- 16 Bauche, J. and Bauche-Arnoult, C., “Transition arrays in the spectra of ionised atoms,” *Advances in atomic and molecular physics*, Vol. 23, 131–195, 1988.
- 17 Bauche, J. and Bauche-Arnoult, C., “Statistical approach to the spectra of plasmas,” *Physica Scripta*, **T40**, 58–64, 1992.
- 18 Bauche, J. and Bauche-Arnoult, C., “Unresolved transition arrays,” *Physica Scripta*, **37**, 659–663, 1988.
- 19 Svendsen, W. and O’Sullivan, G., “Statistics and characteristics of xuv transition arrays from laser-produced plasmas of the elements tin through iodine,” *Physical Review A: General Physics*, **50** (5), 3710–3718, 1994.
- 20 Mandelbaum, P., Finkenthal, M., Schwob, J. L., and Klapisch, M., “Interpretation of the quasicontinuum band emitted by highly ionized rare-earth elements in the 70–100 Å range,” *Phys. Rev. A*, **35** (12), 5051–5059 (1987).
- 21 O’Sullivan, G. and Carroll, P. K., “4d–4f emission resonances in laser-produced plasmas,” *J. Opt. Soc. Am.*, **71** (3), 227–230, 1981.
- 22 Garloff, K., van den Donker, M., and van der Mullen, J., “Simple model for laser-produced, mass-limited water-droplet plasmas,” *Phys. Rev. E*, **66**, 036403, 1–13, 2002.
- 23 Busquet, M., Klapisch, M., Bar-Shalom, A., “Absorption and emission profiles of unresolved arrays near local thermodynamic equilibrium,” *J. Quant. Spec. & Rad. Tran.*, **81**, 255–263, 2003.

### 3. A steady-state plasma model

A plasma is as an ionised gas with linear dimensions greater than the Debye length, where collective effects dominate. It is overall electrically neutral ( $n_e = \sum n_i Z_i$ ), and is characterized by electron/ion density ( $n_e/n_i$ ), electron/ion temperature ( $T_e/T_i$ ), ion distribution ( $f_z$  or average charge,  $\langle z \rangle$ ), and relaxation time ( $\tau$ ) within the plasma. Three general models describe a plasma, which approximate thermodynamic equilibrium in different temperature and density regions: local thermal equilibrium (LTE), coronal equilibrium (CE), and collisional-radiative (CR) equilibrium.

The following chapter discusses the atomic processes within the plasma and the CR model, typical of laser-produced plasmas ( $10^{10}$ – $10^{12}$  W/cm<sup>2</sup>,  $10^{20}$ – $10^{22}$  cm<sup>-3</sup>, 1–100 eV). The steady-state CR model of Colombant and Tonon [1] (based on the radiative deflagration model of Fauquignon and Floux [2] used to account for solid deuterium laser interaction) is incorporated into a general computer model, giving the ion distribution,  $f_z$  (and average charge,  $\langle z \rangle$ ), within the plasma. A figure of merit for ultimate source brightness ( $F$ ) is derived from multi-configuration Hartree-Fock atomic data calculations (Chapter 2) weighted by the ion distribution determined from the CR model. Theoretical results are compared to tin-doped ceramic (5% Sn by number) experimental spectra.

#### 3.1 Atomic processes

The atomic processes in a plasma, which produce excitation and de-excitation within an atom and ionisation and recombination between adjacent ion stages are discussed below. The ion distribution is determined from the cross sections and rate coefficients from these processes. A steady-state model, which balances the ionising and recombining processes, is derived using a recursive relation and the method of simultaneous equations. The recursive relation is sufficient for the steady-state CR model. The more general simultaneous equations method can be used for mixed atomic species and a time-dependent model. The extent to which these processes radiate within the plasma depends on the population of atomic energy levels.

##### 3.1.1 Excitation, de-excitation, ionisation, recombination

Excitation and de-excitation (collisionally or photon-induced) are between energy levels within an atom species ( $\langle \Psi_{n_l} | \Psi_{n_l} \rangle$ ). Ionisation and recombination are between successive ion stages ( $n_{z-1} \leftrightarrow n_z$ ), leaving the atom species more (or less) ionised. Table 3.1 lists the atomic processes within the atom and Figure 3.1 shows a schematic of these processes. Excitation and de-excitation are not included in the steady-state ionisation model, since the ion stage does not change and, thus, all atoms are considered to be in the ground state. Photo-ionisation is considered negligible, since the number of electrons  $\gg$  the number of photons (*i.e.*, no reabsorption in the assumed optically thin plasma) [3]. Dielectronic (or “two-body”) recombination can be included as a percentage of radiative recombination [4], although a more complete description requires the distribution of excited states within the atom as in Peyrusse [5].

Line emission is from photoabsorption and emission, whereas continuum emission is from radiative and dielectronic recombination and bremsstrahlung. Atomic processes contributing to radiated spectra are also known as free-free (bremsstrahlung), free-bound (radiative recombination), and bound-bound (photon absorption and spontaneous emission).

Process	Inverse
<b>collisional-excitation</b> of an atom species by an electron	<b>collisional-dexcitation</b>
<b>photo-excitation</b> by photon absorption	<b>photo-dexcitation</b> by spontaneous or stimulated emission
<b>S collisional-ionization</b> collision of an atom species by an electron	<b><math>\alpha_{3b}</math> three-body recombination</b> collision of two free electrons resulting in the capture of one
<b>photo-ionization</b> of an atom species by a photon	<b><math>\alpha_r</math> radiative recombination</b> capture of an electron resulting in radiative emission
<b>auto-ionization</b>	<b><math>D_{ij}</math> dielectronic recombination</b> a free electron excites a bound electron and is captured

Process	Reaction	State
collisional excitation	$Z + e_1 \rightarrow Z^* + e_1'$ ( $KE_{e_1'} < KE_{e_1}$ )	$\langle \Psi_{n'l}   \Psi_{n'l'} \rangle$
collisional de-excitation	$Z^* + e_1' \rightarrow Z + e_1$	$\langle \Psi_{n'l'}   \Psi_{n'l} \rangle$
photo-excitation	$Z + h\nu \rightarrow Z^*$	$\langle \Psi_{n'l}   \Psi_{n'l'} \rangle$
photo de-excitation	$Z^* \rightarrow Z + h\nu$	$\langle \Psi_{n'l'}   \Psi_{n'l} \rangle$
collisional ionisation	$Z + e_1 \rightarrow Z^+ + e_1 + e_2$	$Z \rightarrow Z^+$
three-body recombination	$Z^+ + e_1 + e_2 \rightarrow Z + e_1$	$Z^+ \rightarrow Z$
photo-ionisation	$Z + h\nu \rightarrow Z^+ + e$	$Z \rightarrow Z^+$
radiative recombination	$Z^+ + e \rightarrow Z + h\nu$	$Z^+ \rightarrow Z$
auto-ionisation		$Z \rightarrow Z^+$
dielectronic recombination		$Z^+ \rightarrow Z$

Table 3.1 Atomic processes and their inverses

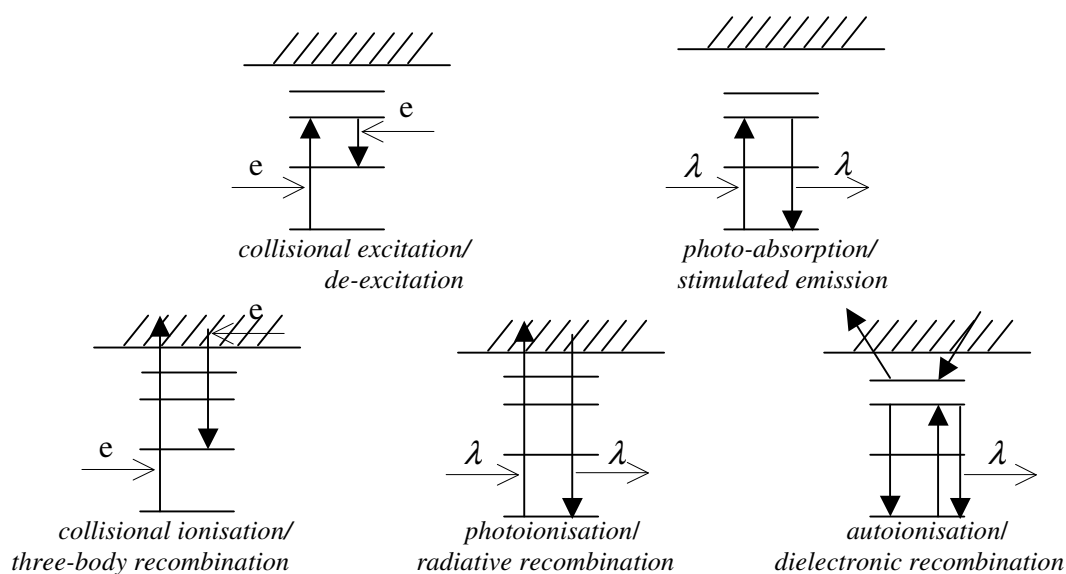


Figure 3.1 Atomic processes and their inverses

## 3.2 Ionisation model

To determine the electron density, electron temperature, and ion state distribution in a steady-state plasma, a model of the interaction between the laser and target is needed [1]. The laser pulse is characterised by wavelength ( $\lambda$ ) and flux ( $\phi$ ) (also known as irradiance or power density), where the flux is calculated from laser pulse energy ( $E$ ), laser pulse duration ( $t$ ), and focussed spot radius ( $r$ ). The target is characterised by atomic number,  $Z$  (more than one element can be considered, expressed in percentage target composition). Note that flux (and not energy or power alone) is the critical factor in generating a plasma [6]. The distribution of ion states is determined from the plasma temperature [7] and target material. A good description of the ionization model is given in Key and Hutcheon [8].

### 3.2.1 Critical density ( $n_{ec}$ )

Below a critical density,  $n_{ec}$ , a plasma is transparent to the incident light source and absorbs energy as it becomes hotter. At the critical density, individual electrons in the plasma behave as a group and oscillate at a characteristic frequency,  $\omega$ . The plasma becomes opaque to the light source and expands outward, thus decreasing its density, and becoming transparent again.

- $n_e < n_{ec}$  transparent
- $n_e = n_{ec}$  electrons oscillate as a group (SHM)
- $n_e > n_{ec}$  opaque (expands, thus decreasing density)

The process of oscillating about a critical density continues during the heating stage. The oscillation frequency is determined from the displacement of the gas a distance  $x$  in an electric field  $E$ . From Maxwell's equations (Gauss's Law),

$$\nabla \cdot \mathbf{E} = \rho / \epsilon_0 \quad (3.1)$$

Considering the  $x$  direction only and letting the charge density equal the product of the electron density and electron charge ( $\rho = n_{ec} e$ ),

$$\frac{dE}{dx} = \frac{n_{ec} e}{\epsilon_0} \quad (3.2)$$

Rearranging and integrating both sides,

$$\int dE = \int \frac{n_{ec} e}{\epsilon_0} dx \quad (3.3)$$

or,

$$E = \left( \frac{n_{ec} e}{\epsilon_0} \right) x \quad (3.4)$$

From Lorentz,

$$\mathbf{F} = e(\mathbf{E} + \mathbf{v} \times \mathbf{B}) \quad (3.5)$$

If the electrostatic force on an electron,  $eE$ , is balanced by its inertia,  $ma$ , (where the electrostatic force is a restoring force set up by the charge separation in the electric field,  $\mathbf{E}$ ) then, assuming no magnetic field,

$$ma = -eE = -e\left(\frac{n_{ec}e}{\epsilon_0}\right)x \quad (3.6)$$

or

$$\frac{d^2x}{dt^2} + \left(\frac{n_{ec}e^2}{m\epsilon_0}\right)x = 0 \quad (3.7)$$

which is the familiar 2<sup>nd</sup>-order differential equation for an oscillator in simple harmonic motion with frequency,

$$\omega = \sqrt{\frac{n_{ec}e^2}{m\epsilon_0}} \quad (3.8)$$

Rearranging and solving for the electron density in terms of frequency,

$$n_{ec} = \frac{\omega^2 m \epsilon_0}{e^2} \quad (3.9)$$

Expressing frequency in terms of wavelength,  $\lambda$ ,

$$\omega = 2\pi \frac{c}{\lambda} \quad (3.10)$$

and, thus,

$$n_{ec} = \left(2\pi \frac{c}{\lambda}\right)^2 \frac{m\epsilon_0}{e^2} \quad (3.11)$$

or

$$n_{ec} = \frac{4\pi^2 c^2 m \epsilon_0}{e^2} \frac{1}{\lambda^2} \quad (3.12)$$

Evaluating for the constants (speed of light,  $c$ , electron mass,  $m$ , permittivity of free space,  $\epsilon_0$ , and electron charge,  $e$ ), and for  $\lambda$  in nm (*e.g.*, 1064 nm for a Nd:YAG),

$$n_{ec} = 1.12 \times 10^{15} \lambda^{-2} \quad [\text{m}^{-3}] \quad (3.13)$$

which gives the critical electron density as a function of incident radiation wavelength. For shorter wavelength radiation, the critical density increases as expected since more energy is incident on the target. Eq. 3.13 is typically approximated by Eq. 3.14, for  $\lambda$  in microns and  $n_{ec}$  in  $\text{cm}^{-3}$ ,

$$n_{ec} \approx 10^{21} \lambda^{-2} \quad [\text{cm}^{-3}] \quad (3.14)$$

Thus, for the Nd:YAG fundamental laser wavelength of 1.064 microns,  $n_{ec} = 9.843 \times 10^{20} \text{ cm}^{-3}$  ( $\sim 10^{21} \text{ cm}^{-3}$ ).

Another derivation of the critical frequency is given in Attwood [9]. For longitudinal waves, the fluid equations (conservation of mass, momentum, and energy) are linearised and the non-linear terms neglected to form a wave equation with the same cut-off frequency, whereas, for transverse waves, Maxwell's first two equations are used to form a wave equation with the same cut-off frequency. For a plane wave of the form in Eq. 3.15, a dispersion relation is derived (Eq. 3.16), from which the cut-off frequency is better understood: if  $\omega > \omega_p$ ,  $k$  is real and the wave propagates, whereas if  $\omega < \omega_p$ ,  $k$  is imaginary, and no wave can propagate.

$$E(r, t) = E_0 e^{-i(\omega t - k \cdot r)} \quad (3.15)$$

$$\omega^2 = \omega_p^2 + k^2 c^2 \quad (3.16)$$

### 3.2.2 Electron temperature, $T_e$

The electron temperature,  $T_e$ , is assumed to be an average temperature within the plasma and is derived in [1] by relating the laser flux to the rate of change of energy in the shocked and expansion (assumed negligible) regions and a radiation term (assumed much smaller than the kinetic and thermal terms) integrated over a distance on the order of the laser focal zone dimension, as in [1, Eq. 12 and further expanded in 1, Eq. 18]. Thus,  $T_e$  is given as

$$T_e \approx 5.2 \times 10^{-6} Z^{\frac{1}{5}} (\lambda^2 \phi)^{\frac{3}{5}} \text{ [eV]} \quad (3.17)$$

where  $Z$  is the atomic number,  $\lambda$  is the wavelength (in microns), and  $\phi$  is the flux (in  $\text{W}/\text{cm}^2$ ). Eq. 3.17 is applicable above a few tens of eV [1]. Figure 3.2 shows the electron temperature for tin ( $Z = 50$ ) irradiated by a 1.064- $\mu\text{m}$  Nd:YAG laser. For upper and lower fluxes of  $10^{10}$  and  $10^{12} \text{ W}/\text{cm}^2$ , typical of the most experimentally explored regions [1], electron temperatures range from 12 to 194 eV.

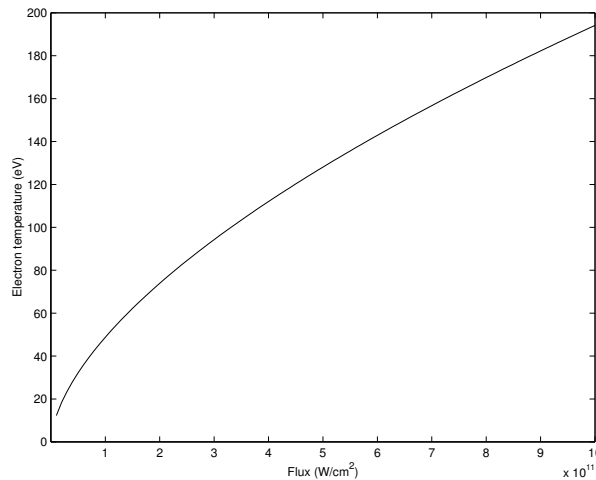


Figure 3.2 Electron temperature versus laser flux ( $Z = 50$ ,  $\lambda = 1.064 \mu\text{m}$ )

Since electron temperature is a function of flux, which in turn depends on laser energy, pulse length, and focussed spot size, and since the dominant ion state depends on electron temperature [7], the ion state distribution within the plasma can be determined from the laser parameters.

Attwood derives the electron temperature from the Stefan-Boltzmann radiation law [9, Eq. 6.143a] (which does not include wavelength or atomic number as in [1]), using a modified Stefan-Boltzmann constant as in Jansson *et al.* [10] to calculate electron temperature in a liquid-tin-jet plasma:

$$T_e = \left( \frac{\phi}{1.027 \times 10^5} \right)^{\frac{1}{4}} \quad (3.18)$$

From Jansson *et al.* [10] ( $Z = 50$ ,  $\lambda = 1064$  nm,  $\phi = 2 \times 10^{11}$  W/cm<sup>2</sup>), an electron temperature of 33 eV is calculated using Eq 3.18 which differs from Eq. 3.17 ( $T_e = 74$  eV) by 55%. By using a modified lower  $Z$  as in a tin/ice droplet (H<sub>2</sub>O 99%, Sn 1%), however, Eq. 3.18 reduces to 44 eV.

### 3.2.3 Plasma domains (LTE, CE, CR)

As stated in Section 1.3.1, three different plasma models are used to determine the ion distribution, depending on the electron density and temperature, and the dominant recombination processes within the plasma:

- local thermodynamic equilibrium (LTE),
- coronal equilibrium (CE),
- collisional-radiative (CR) equilibrium.

In complete thermodynamic equilibrium (TE), ions, electrons, and photons are all in equilibrium. The distribution of electron and ion velocities is Maxwellian (Eq. 3.19), the excited states follow a Boltzmann distribution (Eq. 3.20), and the photons follow a Planck energy distribution (Eq. 3.21).

$$f(v) = \frac{n_e}{(2\pi)^3 v_e^{3/2}} \exp\left(-\frac{v^2}{2v_e^2}\right) \quad (3.19)$$

$$z(T) = V \left( \frac{m_i c^2 T}{2\pi(\hbar c)^2} \right)^2 \sum_n \exp\left(-\frac{E_{z,n}}{T}\right) \quad (3.20)$$

$$E(v) = \frac{2h\nu^3}{c^2} \frac{1}{\exp\left(\frac{h\nu}{kT}\right) - 1} \quad (3.21)$$

where  $v$  is the electron velocity,  $m_i$  is the ion mass,  $E_{z,n}$  is the energy of each state  $n$  within an ion  $z$ ,  $h\nu$  is the incident photon energy, and all other constants have their usual meaning.

In LTE, however, the photons are not in equilibrium, since the mean free paths of the photons are much greater than the electrons and thus travel relatively far within the plasma to escape or be reabsorbed from parts of the plasma at different temperatures and densities [11].

The charge state distribution is calculated from basic principles, where the ion distribution is calculated statistically from thermodynamic equilibrium, as described in Salzmann [11], giving the Saha equation (Eq. 3.22).

$$n_{z+1} = n_z \left( \frac{U_{z+1}}{U_z} \right) \left( \frac{2}{n_e} \frac{(2\pi m_e kT)^{3/2}}{2h^3} \right) \exp\left(\frac{-e\chi_z}{kT}\right) \quad (3.22)$$

where  $U_{z+1}$  and  $U_z$  are the partition functions (Eq. 3.23) of ions  $z+1$  and  $z$ ,  $m_e$  is the electron mass, and  $\chi_z$  is the ionisation potential.

$$U_z = \sum g_{z,n} \exp\left(\frac{-E_{z,n}}{kT}\right) \quad (3.23)$$

where  $g_{z,n}$  is the statistical weight, and  $E_{z,n}$  is the energy of the  $n$ th excited state above the ground state for ion  $z$ . If the ground states are predominant,  $U_{z+1}/U_z$  is about 1.

Eq. 3.22 can be expressed as the ratio of collisional ionisation,  $S(z)$ , and three-body recombination,  $\alpha_{3b}(z+1)$  for high density LTE plasmas (Eq. 3.24), giving another form of the Saha equation,

$$f_z = \frac{n_{z+1}}{n_z} = \frac{S(z)}{n_e \alpha_{3b}(z+1)} \quad (3.24)$$

where  $f_z$  is the ratio of ion densities from one ion stage ( $n_{z+1}$ ) to the next ( $n_z$ ). An important aspect of the Saha equation is that  $f_z$  can be calculated without cross sections and transition probabilities.

For coronal (low-density, optically thin) plasmas, most of the ions are in the ground state and the ion fraction can be expressed as the ratio of collisional ionisation,  $S(z)$ , and radiative recombination,  $\alpha_r(z+1)$ , as in Eq 3.25. In CE, it is seen that the ion distribution is density independent.

$$f_z = \frac{n_{z+1}}{n_z} = \frac{S(z)}{\alpha_r(z+1)} \quad (3.25)$$

Essentially, collisional recombination processes dominates radiative recombination processes in an LTE plasma (as expected in a higher density plasma), whereas recombination processes are primarily radiative in a CE plasma (as expected in a lower density plasma). In between the high- and low-density regimes, the ‘‘collisional-radiative’’ or CR model applies, where collisional recombination and radiative recombination processes are comparably present in the plasma.

The CR model was introduced by Bates *et al.* [12] in 1962 for optically thin plasmas. The plasma flow is assumed plane, one-dimensional, and isothermal [1]. For nanosecond laser-produced plasmas, the atomic processes  $\ll$  plasma formation (*i.e.*, the time to ionise and the time in the heating zone for each ion is less than the time of the laser pulse), and a steady state model applies. The plasma is optically thin to its own radiation (*c.f.* blackbody). Thus, there are three conditions for which the CR model is valid:

- 1) electron velocity distribution is Maxwellian,
- 2)  $f_z$  does not change significantly
- 3) the plasma is optically thin.

The Maxwellian distribution criterion is satisfied if the electron-electron relaxation time is less than the electron heating time (*i.e.*, laser pulse length); that is, if steady state has been reached during laser heating. The relaxation time depends on the slowest process within the atom/ion, *i.e.*, the lowest ionisation and recombination rates, which, for ionisation, is the last to the fully stripped ion ( $Z^{Z-1+}$ – $Z^{Z+}$ ) and, for recombination, the first to the neutral ion ( $Z^{1+}$ – $Z$ ). Thus, from Hinnov [in 1], where  $\tau_z$  is the relaxation time,

$$\tau_z \approx \frac{1}{n_e} \sum_{i=1}^z \frac{1}{S(i-1, T_e)} \quad (3.26)$$

Only collisions with electrons are considered because they are more efficient than heavier particles [1]. Dielectronic recombination is not considered in [1], but can be included as a percentage of the radiative recombination as given in [3].

The rate equation for the  $z$  coupled equations for each ion is given in Eq. 3.27, which includes both collisional and radiative recombination terms [12].

$$\begin{aligned} \frac{dn_{z+1}}{dt} = & n_e n_z S(z, T_e) - n_e n_{z+1} [S(z+1, T_e) + \alpha_r(z+1, T_e) + n_e \alpha_{3b}(z+1, T_e)] \\ & + n_e n_{z+2} [\alpha_r(z+2, T_e) + n_e \alpha_{3b}(z+2, T_e)] \end{aligned} \quad (3.27)$$

The rate equations are determined from cross sections averaged over a free electron distribution function (assumed to be Maxwellian). That is  $S = \langle \sigma v \rangle$ , where  $\sigma$  is the cross section and  $v$  is the velocity. In 1912, Thomson estimated the ionisation cross section by equating the binary collision cross section to the ionisation cross section between two free electrons as described in [13, section 6.2]. Ionisation cross sections and rate coefficients of atoms in the ground state can be measured experimentally (crossed-beams or ion-trap experiments) although ionisation from excited states requires a theoretical approach [13, pg. 167].

For steady state,  $dn_{z+1}/dt = 0$ , and thus Eq. 3.27 reduces to Eq. 3.28.

$$f_z = \frac{n_{z+1}}{n_z} = \frac{S(z)}{\alpha_r(z+1) + n_e \alpha_{3b}(z+1)} \quad (3.28)$$

The CR model is intermediate between LTE and CE with electron densities around  $10^{21} \text{ cm}^{-3}$  and temperatures in the range 10–100 eV. As reported in [6], “the collisional-radiative model is applicable for most laser-produced plasmas in moderate stages of ionisation.” Sub-nanosecond laser pulses are also better described by the CR model as 87% of the emitted radiation is from the CR domain [14]. It should be noted, however, that the CR model under-predicts the charge distribution, because only ground states are considered. The CR model also does not take into account conservation of total number of ions/electrons per unit volume.

It can be seen from Eqs. 3.24, 3.25, and 3.28 that as  $n_e$  increases, CR approaches LTE ( $n_e \alpha_{3b} \gg \alpha_r$ ) and, as  $n_e$  decreases, CR approaches CE ( $\alpha_r \gg n_e \alpha_{3b}$ ) [11]. Derivations of LTE validity and CE validity and, thus, CR validity are discussed below (Section 3.3.2).

### 3.2.4 CR rate equations

The semi-empirical rate equations from [1] are given below in Eqs. 3-29 to 3-31. Dielectronic recombination is included from [3]:

$$S(z) = \frac{9 \times 10^{-6} \xi_z \left( \frac{T_e}{\chi_z} \right)^{1/2}}{\chi_z^{3/2} \left( 4.88 + \frac{T_e}{\chi_z} \right)} \quad (3.29)$$

$$\alpha_r(z) = 5.2 \times 10^{-14} \left( \frac{\chi_z}{T_e} \right)^{1/2} (z) \left[ 0.429 + \frac{1}{2} \log \left( \frac{\chi_z}{T_e} \right) + .469 \left( \frac{T_e}{\chi_z} \right)^{1/2} \right] \quad (3.30)$$

$$n_e \alpha_{3b}(z) = n_e \frac{2.97 \times 10^{-27} \xi_z}{T_e \chi_z^2 \left( 4.88 + \frac{T_e}{\chi_z} \right)} \quad (3.31)$$

$$D_{ij}(z) = d \alpha_r(z) \quad (3.32)$$

where  $T_e$  is the electron temperature,  $n_e$  the electron density,  $z$  the charge,  $\chi_z$  the ionisation potential and  $\xi_z$  the number of open shell electrons.  $D_{ij}(z)$  is the dielectronic recombination from which radiation is emitted between two states  $i$  and  $j$ , expressed as a percentage,  $d$ , of the radiative recombination. The ionisation potential ( $\chi_z$ ) and number of outer shell electrons ( $\xi_z$ ) are determined from references or from theory. Ionisation applies to the lower ion stage ( $z$ ) whereas recombination applies to the higher ion stage ( $z+1$ ). The ratio measures the change in ion density from one stage to the next.

The rate equations are shown in Figure 3.3a (semi-log) for the 4d subshell electrons (Sn V–Sn XIV) to 100 eV. It is seen that the collisional processes ( $S$  and  $n_e \alpha_{3b}$ ) both decrease with ionisation whereas the radiative process ( $\alpha_r$ ) increases, as is to be expected since less bound electrons are available for collisional ionisation and three-body recombination, but more free electrons are available for radiative recombination. The processes are shown together for Sn V and Sn XIV in Figure 3.3b and Figure 3.3c, where the trends are more easily seen. Figure 3.3c shows  $S$  and  $\alpha_r + n_e \alpha_{3b}$  combined. Note that collisional ionisation is very slow at low temperatures.

In Figure 3.3c, it is seen that for Sn V, collisional processes balance recombination processes at about 10 eV, and for Sn XIV at about 50 eV. Furthermore, in earlier ion stages, collisional processes dominate ( $n_e \alpha_{3b} > \alpha_r$ ) and the plasma is in LTE. In the later stages, recombination processes dominate ( $\alpha_r > n_e \alpha_{3b}$ ) and the plasma is in CE. Comparing Figure 3.3b to Figure 3.3c, it is seen that the plasma becomes more coronal with ionisation as radiative recombination exceeds three-body recombination from Sn V to Sn XIV. Indeed, beyond a certain temperature (or ion stage) density effects are minimal and the plasma becomes highly coronal. Figure 3.4 shows the ratio of three-body to radiative recombination, where Sn V is almost entirely LTE and Sn XIV almost entirely coronal.

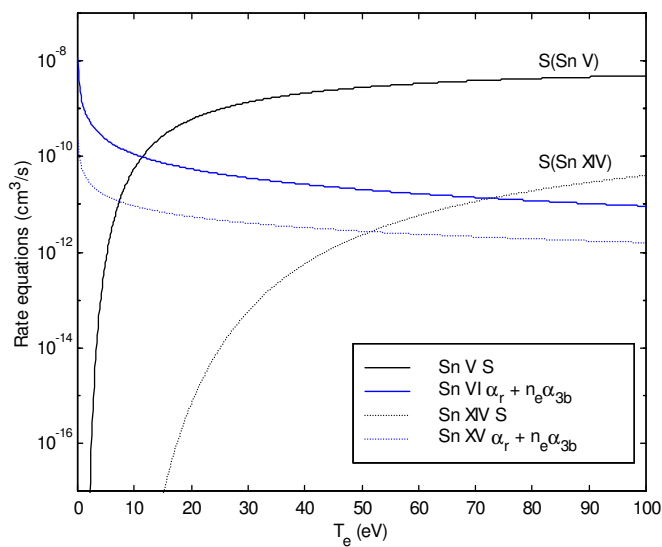
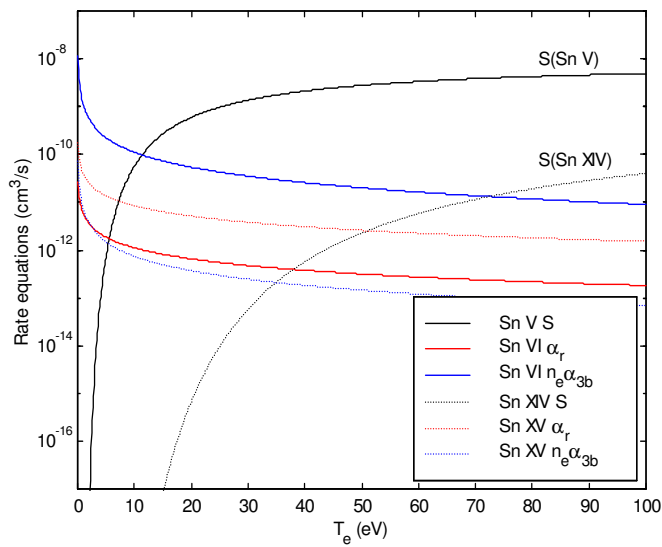
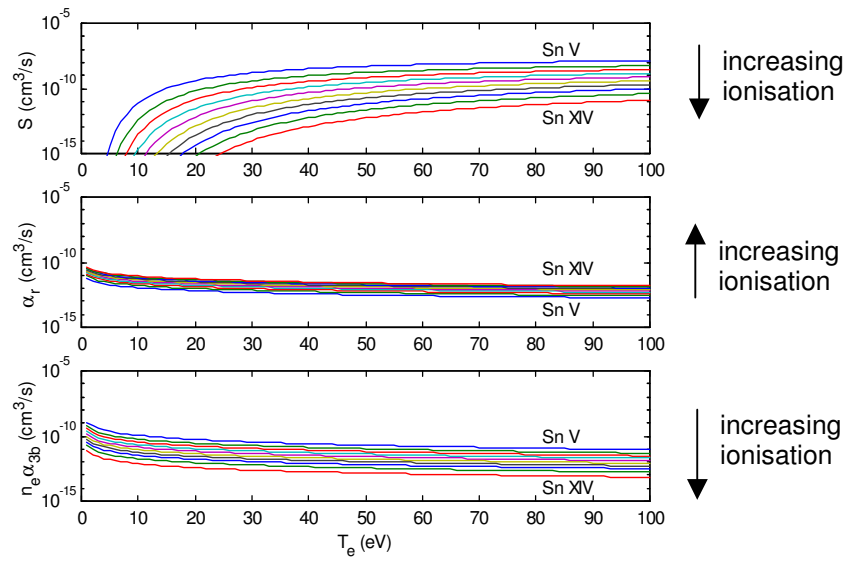


**Figure 3.3** Rate equations versus temperature for tin a) SnV–SnXIV, b)  $S$ ,  $\alpha_r$ ,  $n_e \alpha_{3b}$ , c)  $S$ ,  $\alpha_r + n_e \alpha_{3b}$

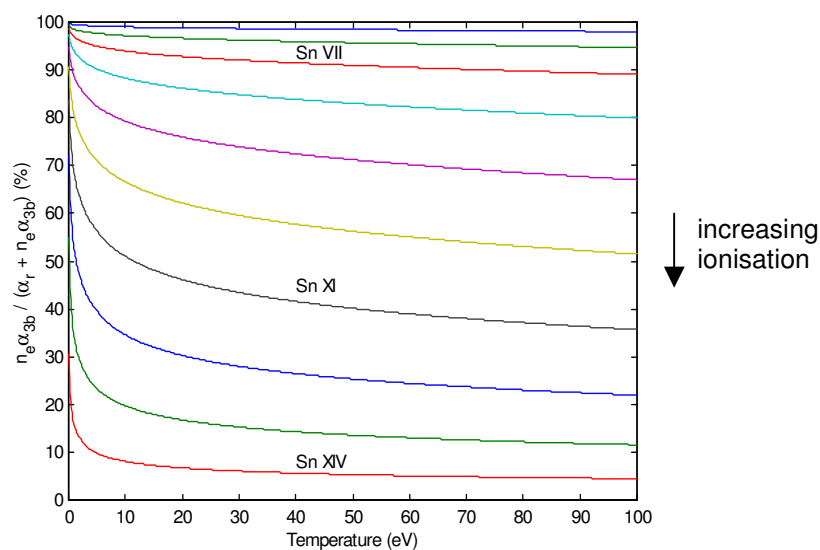


Figure 3.4  $n_e \alpha_{3b} / (\alpha_r + n_e \alpha_{3b})$  ratio versus temperature (Sn V–Sn XIV)

As can be seen in Figure 3.5, which shows the rate equations versus ion stage for a given temperature, collisional ionisation and three-body recombination decrease with ionisation whereas radiative recombination increases with ionisation. The rate equations are shown at four temperatures: 20, 30, 40, and 50 eV.

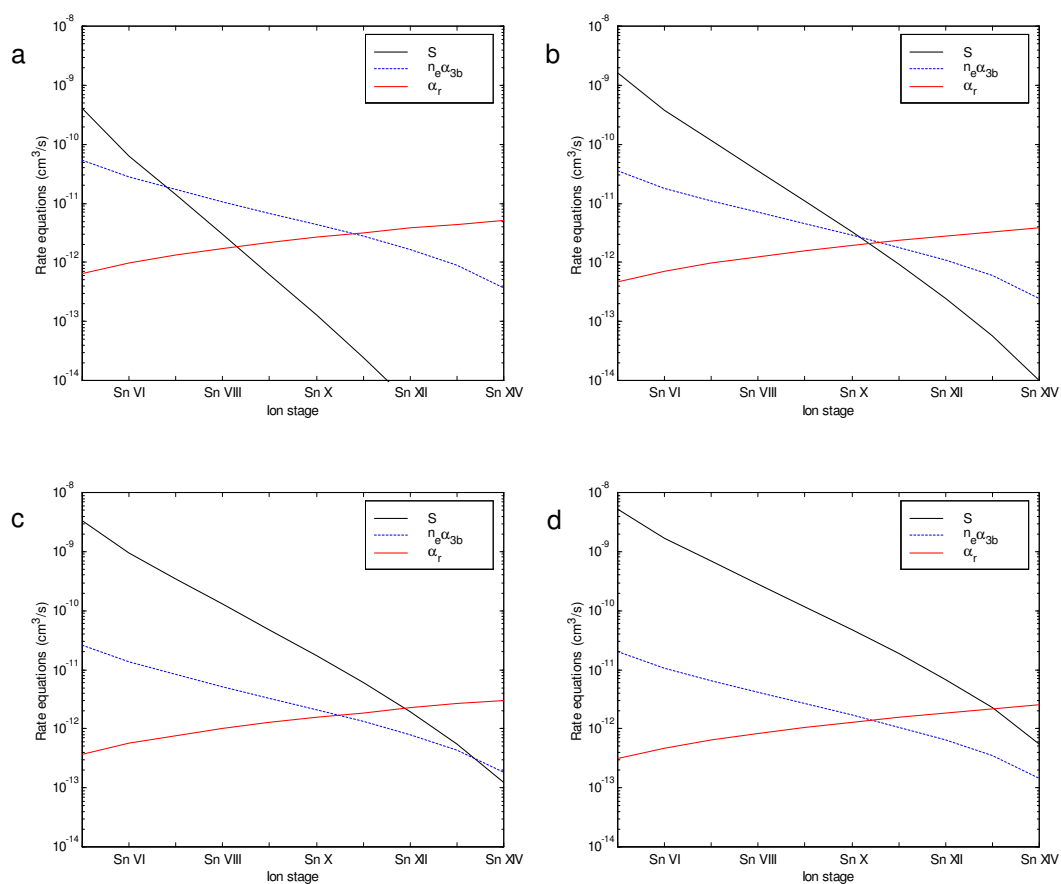


Figure 3.5  $S$ ,  $\alpha_r$ , and  $n_e \alpha_{3b}$  versus ion stage a) 20 eV b) 30 eV c) 40 eV d) 50 eV

Plasma density must also be considered in the rate equations. As stated in [11], “Since three-body recombination requires the presence of two electrons inside the ionic volume, its rate is higher in high density plasmas.” Figure 3.6 shows the ratio of three-body to radiative recombination at the critical density, and at 10% and 1% of the critical density for Sn XI. Here, it is seen that for densities less than the critical density, a plasma is more coronal. As density decreases, the plasma becomes coronal at much lower temperatures.

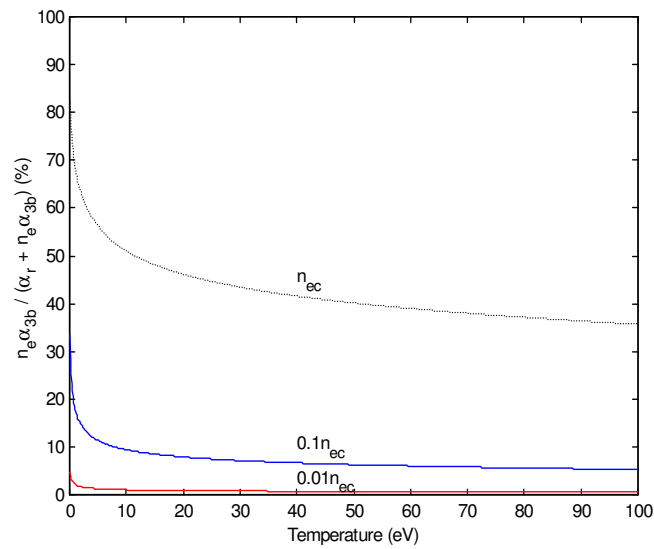


Figure 3.6  $n_e \alpha_{3b} / (\alpha_r + n_e \alpha_{3b})$  ratio versus temperature at  $n_{ec}$ ,  $0.1 n_{ec}$ ,  $0.01 n_{ec}$  (Sn XI)

### 3.2.5 CR validity

Validity criteria for the LTE and CE models were originally given by McWhirter [in 11] as functions of electron temperature and ionisation potential (and, hence, ion stage). The LTE criterion requires that the collisional rate be 10% greater than the radiative rate ( $C > 1.1 \times R$ , Eq. 3.33). Since this condition is not sufficient for LTE, a further criterion requires that the excited states follow a Boltzmann distribution, which leads to a further limiting criterion (originally from [15, Eq. 3.34]). The CE criteria follows in Eq. 3.35, such that the collisional rate is 10% less than the radiative rate ( $C < 1.1 \times R$ ).

$$\text{LTE} : n_e \geq 1.6 \cdot 10^{12} T_e^{1/2} \chi^3 \quad (3.33)$$

$$\text{LTE: (excited states)} \quad n_e \geq 9 \cdot 10^{17} \left( \frac{E_{z,1} - E_{z,0}}{E_H} \right) \left( \frac{T_e}{E_H} \right)^{1/2} \quad (3.34)$$

$$\text{CE: } n_e \leq 1.6 \cdot 10^{10} T_e^{1/2} \chi^3 \quad (3.35)$$

where  $n_e$  and  $T_e$  are the electron density and temperature,  $\chi$  is the ionisation potential,  $E_{z,1} - E_{z,0}$  is the energy of the first excited state above the ground state, and  $E_H$  is 13.6 eV, the ionisation potential of hydrogen (potentials are in eV and  $n_e$  is in  $\text{cm}^{-3}$ ).

Figure 3.7 shows a graph of the LTE and CE criteria for tin, where vertical lines represent the CR region for successive ions, from Sn I to Sn XX (every other ion is shown for clarity). The ion stages were determined from the CR model of [1], using the dominant ion stage.

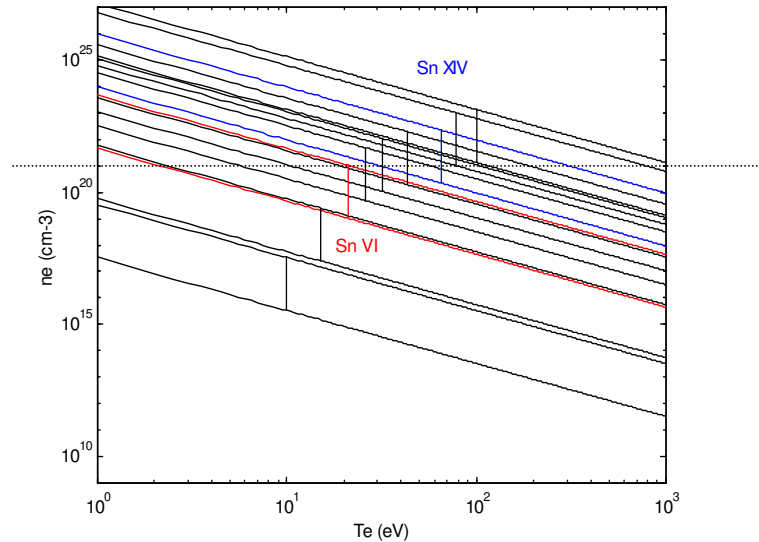
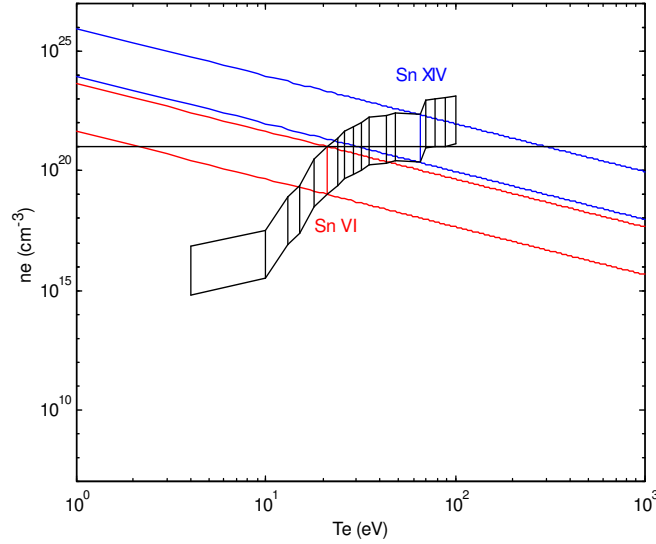


Figure 3.7 LTE and CE plasma boundaries

The CR region can be shown on an  $n_e$ - $T_e$  graph as a function of the upper and lower intersections as shown in Figure 3.8. At a given density, the validity of the LTE, CR, or CE regions can be determined from the point of intersection of the density and the ion stage. For example, for the density indicated ( $n_e \sim 10^{21} \text{ cm}^{-3}$ ), LTE

is valid up to the first five ion stages, followed by CR for the next 11, and then CE for all ion stages thereafter. The electron density can, of course, be less in much of the plasma, but  $n_e = n_{ec}$  is used here as an upper limit. For example, at  $n_e = n_{ec}/1000$  ( $10^{17} \text{ cm}^{-3}$ ), the plasma would be entirely CE.



**Figure 3.8** CR plasma boundaries (LTE, CE criteria)

A comparable CR validity criterion can be determined directly from Eq. 3.28, where radiative and recombination processes are balanced (Eq. 3.36) and is shown in Figure 3.9 for comparison.

$$n_e = \frac{S(z) - \alpha_r(z+1)}{\alpha_{3b}(z+1)} \quad (3.36)$$

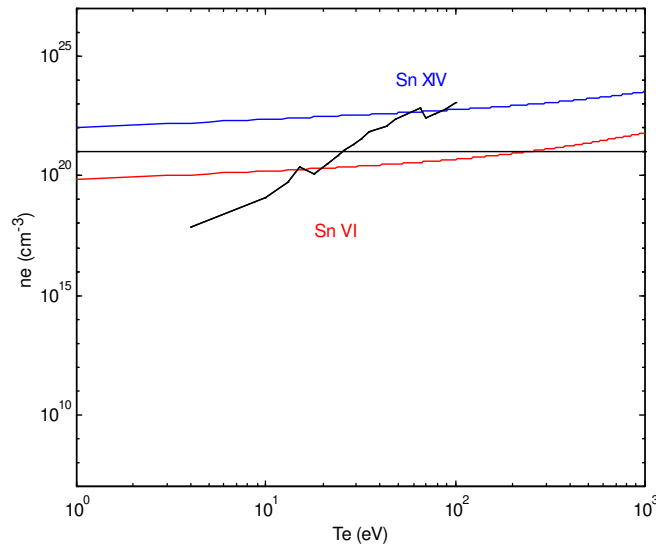


**Figure 3.9** CR plasma boundaries (CR criteria)

Note that if the average ion stage is used instead of the dominant ion stage, the CR (and CE) region would begin at a lower temperature.

### 3.2.6 The ion density rate equation $n_{z+1}/n_z$

$n_{z+1}/n_z$  is a recursive relation, summed to determine the ion distribution,  $f_z$ , at each ion stage within the plasma. Since the total number of ions  $n_T = \sum n_z$ , and  $f_z = n_z/n_T$  is the fractional number density for ion  $z$ , applying the recursive relation over all ion stages gives the distribution of ion densities in the plasma. Figure 3.10 (top) shows the ion densities versus electron temperature to 100 eV. The open 4d subshell ions are indicated and are present from 9–100 eV in fractions as given in Table 3.2. Figure 3.10 (bottom) shows the same with a log temperature scale. In the linear plot, the Kr-like Sn XIV ( $\text{Sn}^{13+}$ ) is especially seen as the dominant species from about 50–70 eV.

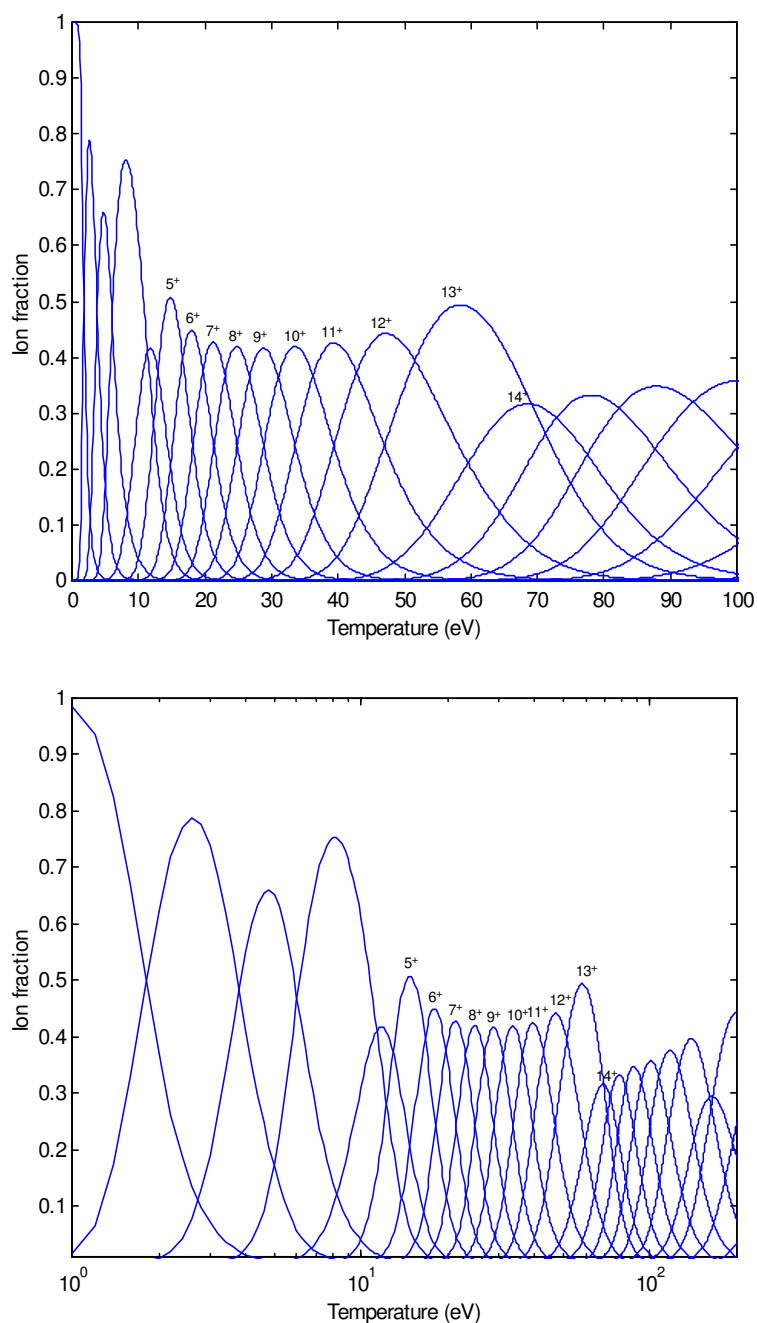


Figure 3.10  $f_z$  versus temperature (tin) linear (top) log (bottom)

The extended ion stages and/or large changes in ion density from one stage to the next correspond to abrupt changes in ionisation potential and/or number of outer shell electrons: for example  $\text{Sn}^{3+}$  (Ag-like  $[\text{Kr}] 4d^{10}$  with ten 4d electrons) to  $\text{Sn}^{4+}$  (Pd-like  $[\text{Kr}] 4d^9$ ), and similarly for  $\text{Sn}^{13+}$  to  $\text{Sn}^{14+}$  (Kr-like and Br-like). Especially long plateaus correspond to noble gas like species. The values used for the ionisation potential,  $\chi$ , in Eqs. 3.29–3.31 and their effect on the ion density distribution is explained in Section 3.2.8.

From Sn V–Sn XIV, each ion comprises a maximum of 40% to 50% at a given temperature and up to five ions can be present. At any temperature, the sum of the densities is 1, as is seen more easily in Figure 3.11 for 10, 30, 50, and 70 eV and in Table 3.2. Here, the ion distribution is easily seen as a function of temperature within the plasma (and thus of laser flux).

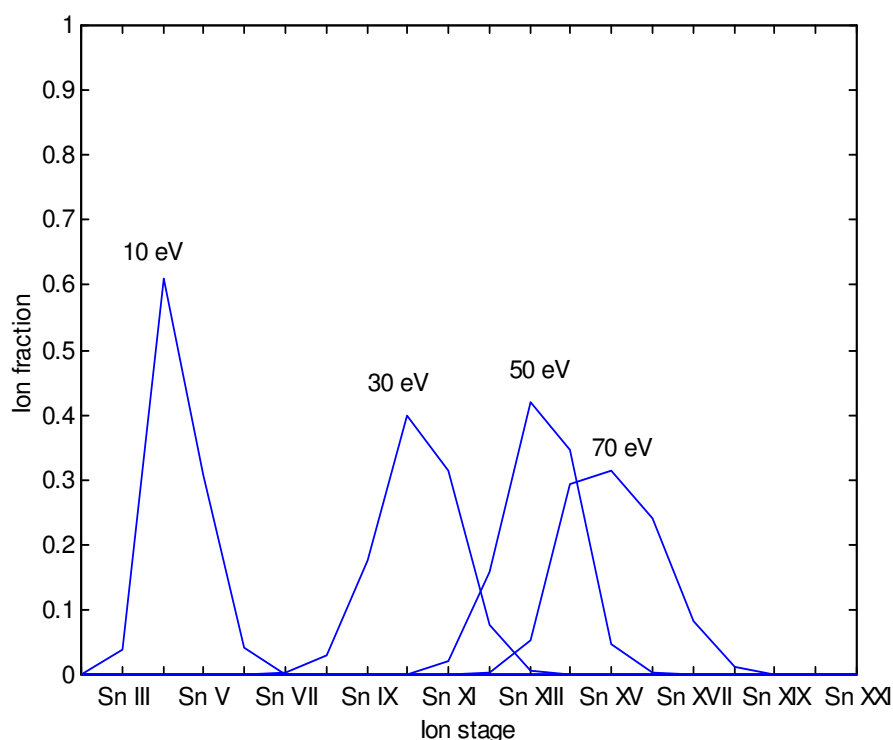


Figure 3.11  $f_z$  at 10 eV, 30 eV, 50 eV, and 70 eV (tin)

Temp (eV)	Sn V	Sn VI	Sn VII	Sn VIII	Sn IX	Sn X	Sn XI	Sn XII	Sn XIII	Sn XIV
10	0.04									
20	0.10	0.35	0.39	0.13	0.01					
30				0.18	0.40	0.31	0.07			
40					0.04	0.22	0.42	0.27	0.05	
50						0.02	0.16	0.42	0.35	0.05
60							0.03	0.20	0.49	0.22
70								0.05	0.29	0.31

Table 3.2 Fractional ion density versus temperature

### 3.2.7 Average charge in the plasma, $\langle z \rangle$

The average charge within the plasma increases with temperature and decreases with density [2]. Colombant and Tonon [1] use a semi-empirical formula to determine average charge within the plasma,  $\langle z \rangle$ , which is applicable above 30 eV in the coronal limit ( $\alpha_r \gg n_e \alpha_{3b}$ ) and applies better to heavier than light elements, where the ionisation potentials vary almost continuously.

$$\langle z \rangle = \frac{2}{3} Z T_e^{\frac{1}{3}} \quad (3.37)$$

where  $Z$  is the atomic number and  $T_e$  is the electron temperature (in eV).

However, the average charge can also be calculated computationally from the ion distribution, as in Eq. 3.38,

$$\langle z \rangle = \sum_{z=1}^N f_z z \quad (3.38)$$

Figure 3.12 shows both calculations. Clearly, the semi-empirical formula (Eq. 3.37) over-predicts the average charge at low temperatures, and under-predicts at higher temperatures, but can be used as a simple first measure of average charge from atomic number and electron temperature. Equation 3.38 is used throughout this work.

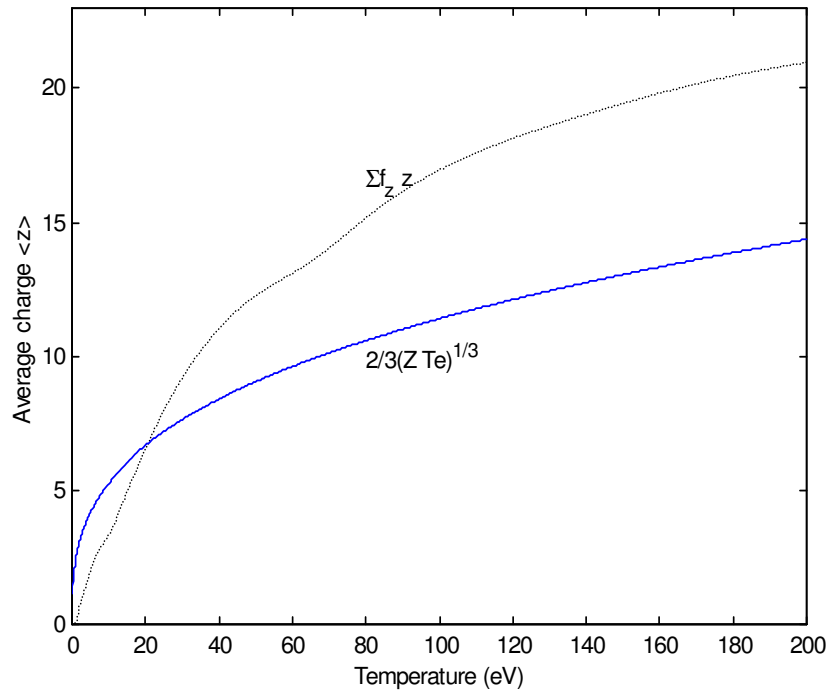


Figure 3.12 Average charge versus electron temperature: computational and semi-empirical

### 3.2.8 Factors affecting the ion density and average charge

For a given element ( $Z$ ) and laser profile ( $\lambda, \phi$ ), the ion distribution is a function of the atomic rate equations for  $S$ ,  $n_e\alpha_{3b}$ ,  $\alpha_r$ , and  $D_{ij}$ , which in turn are functions of electron temperature ( $T_e$ ) and two atomic parameters: ionisation potential ( $\chi_z$ ) and number of open shell electrons ( $\xi_z$ ) (as well as charge state ( $z+1$ ) for radiative recombination and electron density ( $n_e$ ) for three-body recombination). The effect of electron density on the CR model and the boundaries of the CR model to the LTE and CE model are discussed. The effect of ionisation potential (determined from reference tables or, in their absence, from theoretical calculations) and the number of outer shell electrons on ion distribution are discussed, as are ionisation potential (or continuum) lowering and dielectronic recombination. Various authors' rate equations and their effects are also shown. To quantify the effects, changes are compared to the reference computational average charge (Eq. 3.38) from the CR model of Colombant and Tonon [1].

#### 3.2.8.1 Electron density ( $n_e$ )

The average charge within the plasma decreases with increasing electron density, because collisional recombination is more dominant at higher densities. Figure 3.13 shows the effect of electron density on average charge ( $\langle z \rangle$ ) above and below the critical density (the dashed curve is the reference Colombant and Tonon curve). It is seen here that the plasma regions below critical density contribute a higher average charge to the resultant emission. Note, however, that reducing the density below critical density has an effect only below about 40 eV and that  $\langle z \rangle$  for  $0.1 n_{ec}$  and  $0.01 n_{ec}$  are almost identical.

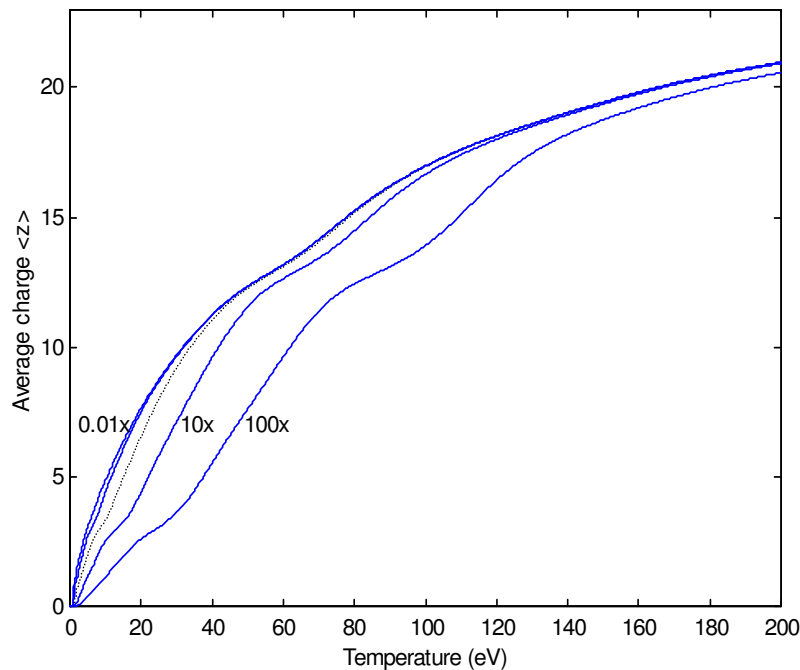
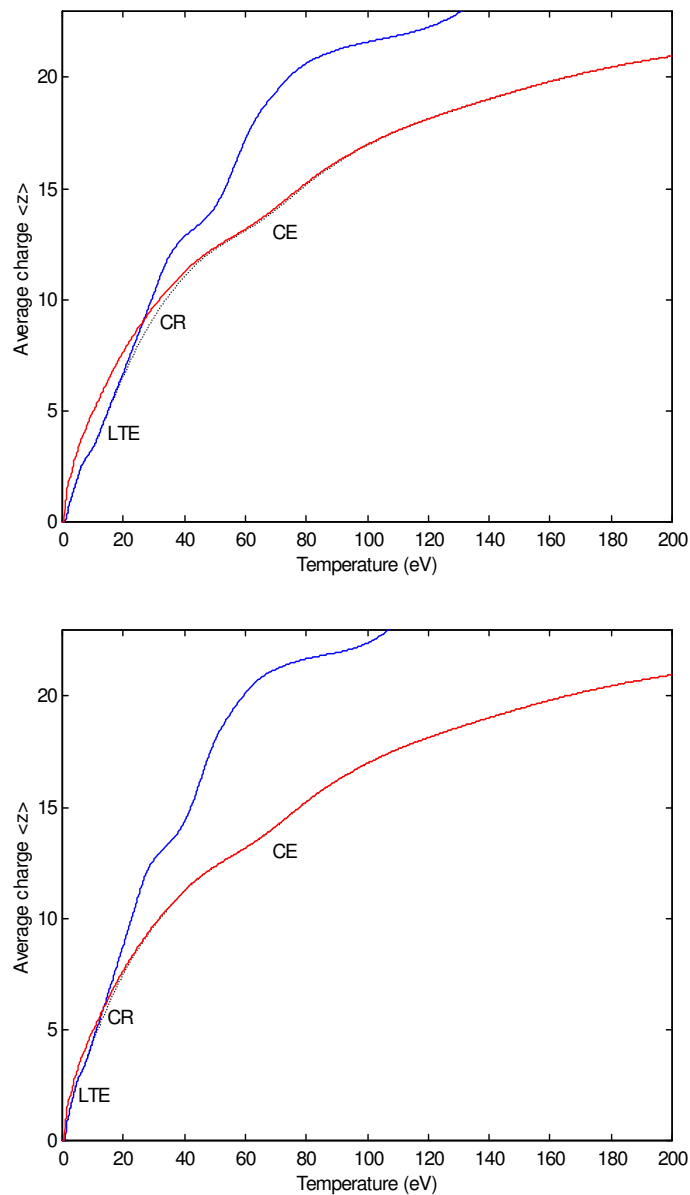


Figure 3.13  $\langle z \rangle$  versus  $T_e$  (tin) for different densities:  $n_e = .01n_{ec}, .1n_{ec}, n_{ec}, 10n_{ec},$  and  $100n_{ec}$

To better understand density effects on a plasma, consider the limits of the CR model ( $\alpha_r = 0$  in the LTE limit and  $n_e \alpha_{3b} = 0$  in the CE limit). In Figure 3.14 (top), the LTE/CR boundary is seen at about 20 eV and the CR/CE boundary at about 60 eV, giving a CR range between about 20 and 60 eV (corresponding flux between  $2.2$  and  $7.2 \times 10^{10} \text{ W/cm}^2$ ) with a resultant  $\langle z \rangle$  between 6 and 13.

In Figure 3.14 (bottom), the density has been decreased by a factor of 10, decreasing the CR range to between 10 and 30 eV. Given that some of the plasma will be below the critical density, a tin plasma above 30 eV at this density can be considered highly coronal. Gupta and Sinha [16] state that “the coronal equilibrium model can safely be applied to laser plasmas with electron densities less than or equal to  $10^{22} \text{ cm}^{-3}$  for estimating the abundance of high-charge ions.” Indeed, with decreasing density, the CR region becomes smaller and applies at lower temperatures.



**Figure 3.14**  $\langle z \rangle$  versus  $T_e$  (tin) for LTE/CR/CE regions:  $n_e = n_{ec}$  (top)  $n_e = n_{ec}/10$  (bottom)

### 3.2.8.2 Ion model (LTE/CR/CE)

Figure 3.15 shows the ion distribution for the LTE, CR, and CE models at 10, 30, and 50 eV. Note that at 10 eV (top), the LTE and CR distributions are identical, whereas at 50 eV (bottom), the CR and CE distributions are almost identical, showing the asymptotic limits of the CR model for  $C > R$  and  $R > C$ . At 30 eV (in the middle of the CR region), a lower charge distribution is predicted for the CR model than either the CE or LTE models and, thus, the charge distribution depends on which model is used and care should be taken to use the CR model in the appropriate region.

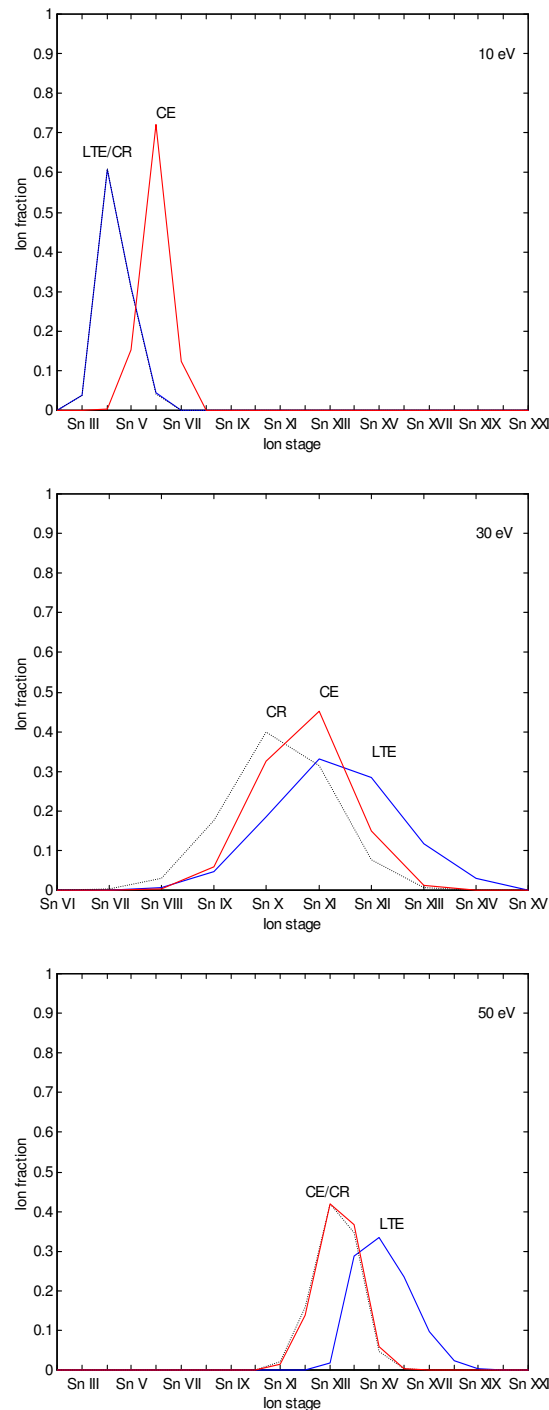


Figure 3.15  $\langle z \rangle$  versus  $T_e$  for LTE/CR/CE model: 10 eV (top), 30 eV (middle), 50 eV (bottom)

### 3.2.8.3 Ionisation potential ( $\chi_z$ )

The ionisation potential of an element or ion stage is the energy required to remove the least-bound electron from the atom and is typically given in eV. Ionisation potentials are determined from reference tables of known experimental data or determined from theory. The *CRC Handbook of Chemistry and Physics* [17] gives experimentally determined ionisation potentials for all ions to copper ( $Z = 29$ ); thereafter, only some ionisation potentials are listed—the first three ionisation potentials are listed for tin and the first five for xenon. Moore [18] also lists data for the first five tin ion stages. Some data can be obtained as well by EBIT. For example, xenon data up to  $\text{Xe}^{26+}$  are known to at least 3% from EBIT experiments at NIST [19]. Further xenon data can be found in [20].

In the absence of experimental data, ionisation potentials are determined from theory, either by polynomial fit or Hartree-Fock methods. Carlson [in 21] uses a simple semi-empirical shell model, Edlén [in 21] an isoelectronic formula to fit successive unknown ion stages, and Fraga *et al.* [22] the Hartree-Fock method. The Cowan code [23] also uses the Hartree-Fock method. The average atom model (discussed in Chapter 4) uses an empirically fitted lookup table derived from a large number of known ionisation potentials.

Colombant and Tonon [1] derive a simple approximation, which can be used if no experimental or easily derived theoretical data is available (Eq. 3.39).

$$\chi_z \approx \frac{45z^2}{A^{2/3}} [eV] \quad (3.39)$$

where  $z$  is the ionic charge and  $A$  is the atomic mass<sup>40</sup>. The Colombant and Tonon approximation is good only to about  $z = 35$ , the limit of the 3d subshell.

Another approximation derived from the Thomas-Fermi model in Salzmann [11] is given in Eq. 3.40.

$$\chi_z = \left(\frac{2}{3}\right)^{2/3} E_H Z^{4/3} \left[ \frac{(z/Z)^2}{1 - (z/Z)^{2/3}} \right] [eV] \quad (3.40)$$

where  $E_H$  is the ionisation potential of hydrogen (13.6 eV) and  $Z$  is the atomic number. Both approximations are essentially  $z^2$  fits.

To calculate ionisation potentials from the Cowan code [23], the ground state configuration is determined from the lowest average energy from a sequence of configurations as each electron is removed<sup>41</sup>. This also determines the correct number of outer-shell electrons as the atom is ionised, which is not always shell by shell as in tin and xenon.

Table 3.3 gives the tin ionisation potentials from Moore [18], the *CRC Handbook* [17], [www.chemsoc.org](http://www.chemsoc.org) [24], the Cowan code [23], and Colombant and Tonon's approximation [1], Eq. 3.39. Figure 3.16 shows the ionisation potentials from chemsoc, Cowan, Colombant and Tonon, and Salzmann.

<sup>40</sup> Note that atomic mass gives a better fit than atomic number as used in [1].

<sup>41</sup> The accuracy can be improved by using ground state to ground state rather than average energies.

Z	Z-like	$\xi$	Ionisation potential (eV)				
			Moore	CRC	chemsoc	Cowan	C and T
Sn I	Sn	2	7.342	7.34381	7.34	7.085	1.86
Sn II	In	1	14.628	14.63225	14.60	14.401	7.45
Sn III	Cd	2	30.49	30.50260	30.54	29.364	16.77
Sn IV	Ag	1	40.72	40.73502	40.70	40.070	29.81
Sn V <sup>42</sup>	Pd	10	72.3	72.28	72.30	76.508	46.58
Sn VI	Rh	9			102.75	96.023	67.07
Sn VII	Ru	8			126.62	116.484	91.29
Sn VIII	Tc	7			151.53	137.832	119.23
Sn IX	Mo	6			176.44	160.022	150.91
Sn X	Nb	5			213.80	183.017	186.30
Sn XI	Zr	4				206.792	225.43
Sn XII	Y	3				231.331	268.28
Sn XIII	Sr	2				256.589	314.85
Sn XIV	Rb	1				282.582	365.15
Sn XV	Kr	6				383.782	419.18
Sn XVI	Br	5				412.215	476.94
Sn XVII	Se	4				441.186	538.42
Sn XVIII	As	3				470.667	603.62
Sn XIX	Ge	2				500.582	672.56
Sn XX	Ga	1				531.143	745.21
Sn XXI	Zn	2				608.549	821.60
Sn XXII	Cu	10				642.242	901.71
Sn XXIII	Ni	9				1132.715	985.55
Sn XXIV	Co	8				1204.830	1073.11
Sn XXV	Fe	7				1278.541	1164.40
Sn XXVI	Mn	6				1353.842	1259.41
Sn XXVII	Cr	5				1430.708	1358.15
Sn XXVIII	V	4				1509.197	1460.62
Sn XXIX	Ti	3				1589.236	1566.81
Sn XXX	Sc	2				1670.838	1676.73
Sn XXXI	Ca	1				1754.000	1790.38

Table 3.3 Tin ( $Z = 50$ ) ionisation potentials

Note that the ionisation potential effects the duration of each ion stage in the plasma as temperature increases, shown as a plateau in the fractional ion density versus temperature plot. Furthermore, as electrons are stripped, the atom becomes more hydrogenic and Bohr's hydrogenic atomic model ( $\chi_Z = E_H Z^2$ ) can be used for the last ion: *e.g.*, Sn<sup>50+</sup>,  $\chi_z = 34000$  eV.

Using experimental data instead of the Cowan data for the first five ion stages can effect the percentage distribution (*e.g.*, the ratio of Sn<sup>4+</sup>/Sn<sup>5+</sup> decreases by about 10%), although no change is observed in the average charge. Figure 3.17 shows the effect on average charge for  $\chi_z$  data from both Cowan (Hartree-Fock) and Colombant and Tonon (semi-empirical  $z^2$  fit) in Table 3.3. Note that Colombant and Tonon's approximation fits reasonably well up to the 3d subshell and that the  $\langle z \rangle$  comparison to the Cowan code is quite good over the 1–100 eV range. In the absence of better data, Colombant and Tonon's approximation can be used as a first attempt for computational purposes. The Cowan code potentials are used throughout this work, where experimental values are not available.

<sup>42</sup> For EUV lithography purposes, note that Sn I–Sn V are auto-ionised at 92 eV.

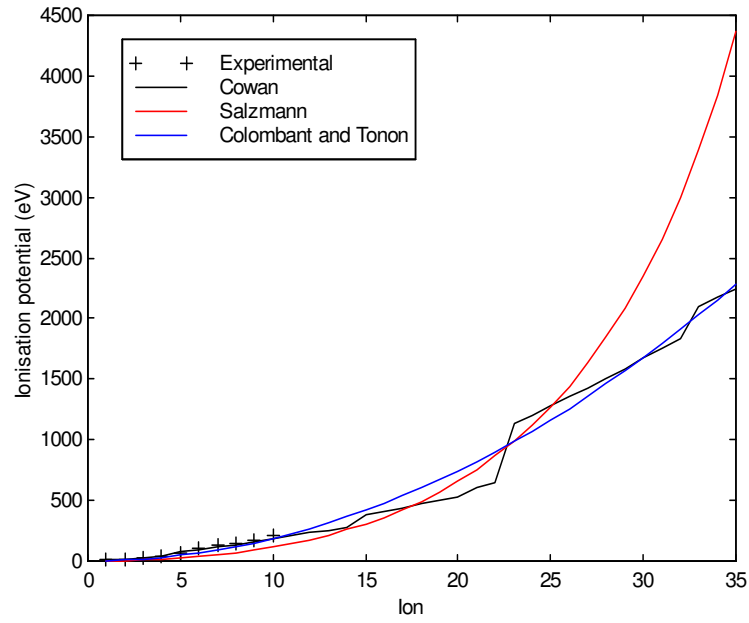


Figure 3.16 Sn ionisation potentials from Table 3.3

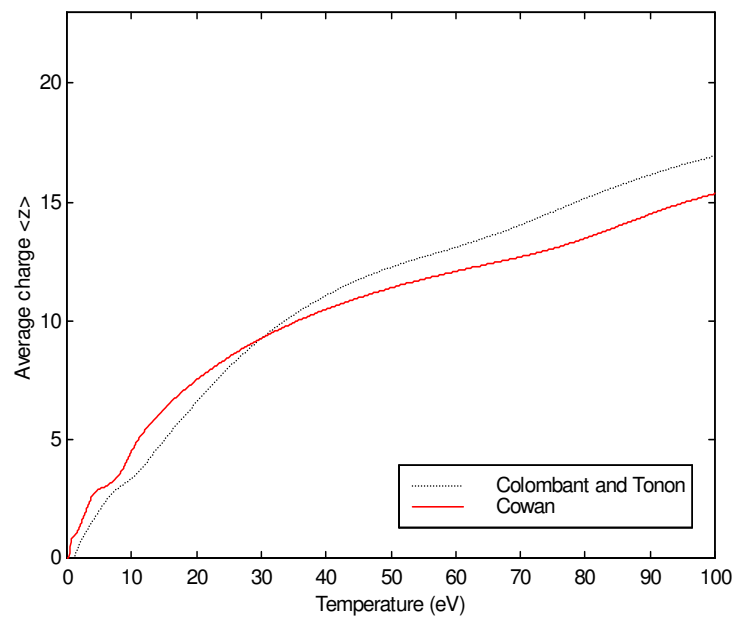


Figure 3.17  $\langle z \rangle$  versus  $T_e$  for different ionisation potential data

### 3.2.8.4 Ionisation potential lowering ( $\Delta\chi_z$ )

Ionisation potential (or continuum) lowering,  $\Delta\chi_z$ , is the reduction of the ionisation potential because of electrostatic fields created by local separation of charge in the plasma [15]. At large electron densities, ionisation potential lowering can be quite significant, even exceeding the ionisation potential ( $\Delta\chi_z > \chi_z$ ) [2], and is more important for highly charged ions. Salzmann states that it is the main atomic phenomenon unique to plasmas and notes that because of ionisation potential lowering an ion cannot have an infinite number of excited states [11].

Greim [15] defines ionisation potential lowering as in Eq. 3.41,

$$\Delta\chi_z = \frac{ze^2}{\lambda_D} \quad (3.41)$$

where  $\lambda_D$  is the Debye length in Eq. 3.42 (see derivation in Section 1.3.1),

$$\lambda_D = \sqrt{\frac{\epsilon_0 k T_e}{e^2 n_e}} \quad (3.42)$$

Thus,

$$\Delta\chi_z = ze \sqrt{\frac{n_e}{\epsilon_0 k T_e}} \quad (3.43)$$

where  $z$  is the ion charge,  $\epsilon_0$  is the permittivity of free space,  $k$  is the Boltzmann constant,  $e$  is the electron charge,  $T_e$  is the electron temperature (in K), and  $n_e$  is the electron density (in  $\text{m}^{-3}$ ). Ionisation potential lowering increases as the Debye length decreases (*i.e.*, as the electrostatic field increases) and scales as the square root of electron density over electron temperature.

Salzmann [11] defines ionisation potential lowering in Eq. 3.44,

$$\Delta\chi_z = 3.48z \left( \frac{n_i}{10^{21}} \right)^{1/3} \quad (3.44)$$

where  $n_i$  is the ion density (in  $\text{cm}^{-3}$ ). Here, ionisation potential lowering scales as the cube root of ion density and is independent of temperature. Both equations increase linearly with ion charge.

For LPPs, on the order of  $n_e = n_{ec} = 10^{21} \text{ cm}^{-3}$ , Greim's  $\Delta\chi_z$  is almost negligible (0.06 eV for  $z = 1$ , 1.3 eV for  $z = 20$  at 32 eV). Indeed, he states that, "in laboratory applications,  $\Delta\chi_z$  rarely becomes larger than 0.2 [%], and uncertainties in the exponential of the Saha equation should accordingly stay below about 4 per cent." On the other hand, Salzmann's  $\Delta\chi_z$  can be appreciable for large enough densities (3.5 eV or 49% for  $z = 1$ , to 69.2 eV or 13% for  $z = 20$ , at  $n_e = n_{ec}$ ). For densities less than  $n_{ec}$ ,  $\Delta\chi_z$  is of course lower than this, although Salzmann also suggests a greater  $\Delta\chi_z$  for more weakly coupled-plasmas.

It should be noted that although there is extensive literature on the subject, there is little experimental evidence [11].

The difference between the results of Greim (Eq. 3.43) and Salzman (Eq. 3.44) is primarily because Greim considers an electron to be bound within the Debye length ( $\lambda_D$ ) and Salzman within the ion sphere radius ( $R_i$ ), where the higher excited states are no longer bound to a particular ion, but are better regarded as bound to the plasma as a whole, *i.e.*, as negative energy continuum electrons [11]. Salzman [11] (citing More) suggests that  $R_i$  should be used for lower density plasmas ( $\lambda_D/R_i \sim 1.1$  at 10 eV,  $\sim 2.0$  at 32 eV, and  $\sim 3.5$  at 100 eV). Salzman further suggests that a probabilistic  $\Delta\chi$  could be used since all ions experience different micro electric fields within the plasma.

The ionisation potentials and corresponding ionisation potential lowering from Eq. 3.44 versus ion stage are shown in Figure 3.18 ( $Z = 50$ ,  $n_e = 9.843 \times 10^{20} \text{ cm}^{-3}$ ). At densities lower than the critical density, the reduction would lie within the two. Note that the reduction from Eq. 3.43 is negligible.

As shown in Figure 3.19, the effect of ionisation potential lowering (Eq. 3.44) in the CR model can increase the average charge in the plasma significantly (by about 20% at 32 eV).

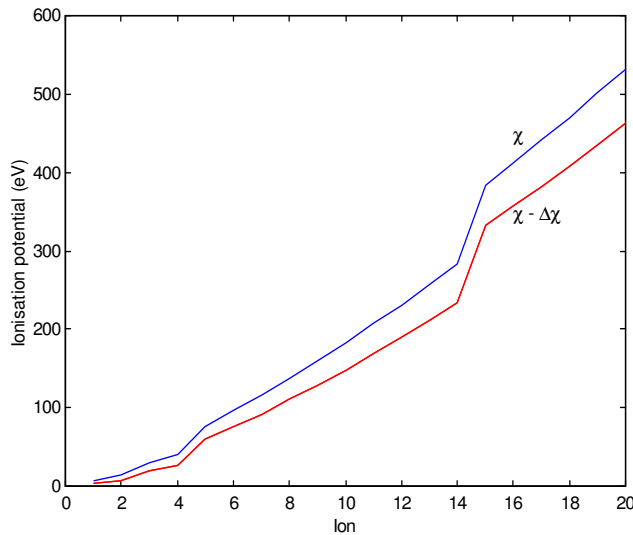


Figure 3.18 Ionisation potential lowering in tin ( $n_e = 9.843 \times 10^{20} \text{ cm}^{-3}$ ) using Eq. 3.44 [11]

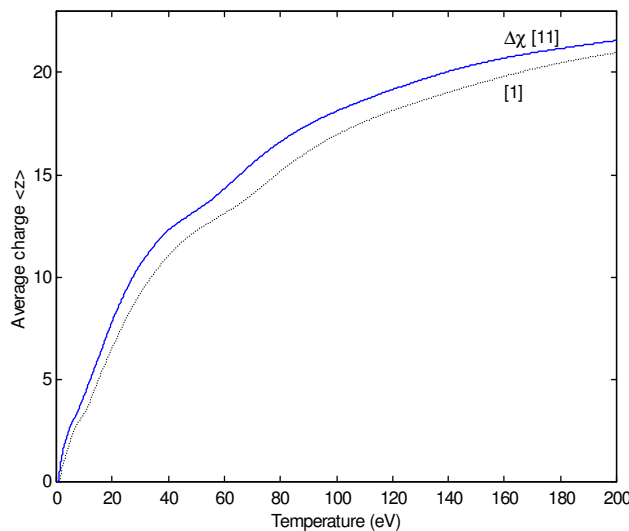


Figure 3.19 Average charge  $\langle z \rangle$  versus  $T_e$  (tin) including  $\Delta\chi_z$

### 3.2.8.5 Number of open shell electrons ( $\xi_z$ )

The number of open shell electrons is required in both the CR and LTE models. In the CR model, collisional ionisation and three-body recombination both depend on  $\xi_z$ , whereas in the LTE model, the Saha equation is a function of ground state degeneracy  $(2J + 1)$ , which in turn depends on  $\xi_z$ .

The number of open shell electrons is determined from an element's isoelectronic sequence, using the reverse *aufbau* principle. For example, the number of outer shell electrons for a particular ion stage of an element is the same as that for the next lower stage of the next lower element. There are many exceptions: for example, at chromium ( $Z = 24$ ), level crossing occurs between the 4s and 3d subshells. For  $Z > 23$ , at higher ion stages, level crossing can occur unexpectedly and  $\xi_z$  must be determined from tables of isoelectronic data or from theoretical atomic calculations (as in the Cowan code). For a more detailed description on level crossing and irregularities in the periodic table, see Section 1.2.1.

Typically, the number of *open* shell electrons is identical to the number of *outer* shell electrons for any element or ion species. For some isoelectronic sequences, (*e.g.*, in the lanthanides and actinides), however, an inner shell is opened before all of the outer shell electrons are removed, and thus two shells are open in an ion stage at the same time, from which the next electron is removed. In this case, it is not immediately obvious how many electrons should be considered as outer shell electrons: the *outer*-shell electrons, the *open*-shell electrons, the *highest-energy*-shell electrons, or combinations thereof.

In the case of tin and xenon, however, the reverse *aufbau* principle can be used and thus the number of open shell electrons is easily determined for each ion stage and is equal to the number of outer ( $n, l$ ) subshell electrons, where  $n$  is the principal quantum number and  $l$  is the azimuthal quantum number.

The extent to which  $\xi_z$  can effect the rate equations is more pronounced at changes from shell to shell, for example from Sn V ( $\xi_z = 1$ ) to Sn VI ( $\xi_z = 10$ ).  $\xi_z$  is given along with the ionisation potential for tin in Table 3.3.

### 3.2.8.6 Dielectronic recombination

Dielectronic recombination (DR) occurs when a free electron excites a bound electron and falls into a bound level, and one of these two excited electrons (dielectronic) de-excites within the atom [25]. The sum of the two excited states must be greater than the ionisation potential. Dielectronic recombination is the inverse of autoionisation and can occur in all ions except the fully stripped ion where the process is not possible. Dielectronic recombination requires atomic rate coefficients and is difficult to calculate because of the two excited states [16]. In LPPs, dielectronic recombination probably takes place during the plasma cooling phase [26].

As the atomic charge increases, dielectronic recombination decreases: for  $z = 10\text{--}15$ , dielectronic recombination (DR) is approximately equal to radiative recombination ( $\alpha_r$ ), but with increasing ionisation DR becomes less than  $\alpha_r$  [8]. Dielectronic recombination is more significant at higher temperatures and lower electron densities: DR = 75% at  $n_e = 10^{18} \text{ cm}^{-3}$ , 10% at  $10^{20} \text{ cm}^{-3}$ , and is completely negligible at  $10^{24}$  ( $T_e > 100 \text{ eV}$ ) as reported in [2].

At  $n_e = n_{ec} = 10^{21} \text{ cm}^{-3}$ , it is reasonable to exclude DR from the ion distribution calculation. However, for lower densities within the plasma, DR could be significant.

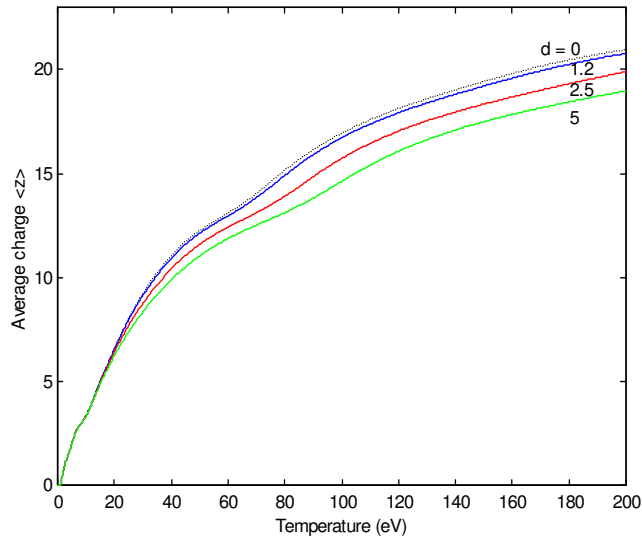


Figure 3.20  $\langle z \rangle$  versus  $T_e$  (tin) including DR for  $d = 0$  to 5

Dielectronic recombination is considered in this study only as a percentage of radiative recombination (Eq. 3.32). The effect of DR on the average charge for 1.2, 2.5, and 5% of radiative recombination is shown in Figure 3.20. Clearly, increasing DR decreases the average charge, as is to be expected for an increased recombination process, though the effect is less so at lower electron temperatures.

### 3.2.8.7 CR rate equations

Gupta and Sinha [16] reported that the ion distribution in a laser-produced plasma varies considerably with ion model and rate equations used for collisional ionisation and radiative and three-body recombination. They state that, “the adequacy of an ionisation model depends on the accuracy of the available rate coefficients” adding that there are no universally accepted expressions. The models reported by them included those of Colombant and Tonon, Eliezer *et al.*, and Brunner and John, and the rate equations of Landshoff and Perez, Bates *et al.*, McWhirter, Seaton, Greim, Salzmann and Krumbein, and Pert [all referred to in 16].

Different approximations in the theoretical evaluation of the ionisation cross section were studied for collisional ionisation. Formulae derived from H-like ions and applied to all ions regardless of the number of bound electrons were studied for radiative recombination. Three-body recombination rates were determined from those that lead to the Saha equation. (Note that the results apply to aluminium plasmas in the 500–700 eV region.)

Their results show that at  $T_e = 500$  eV, the fractional density,  $f_z$ , for Al XII ions varied from 60% to 90% with different collisional ionisation rate equations (Landshoff and Perez the lowest, Bates *et al.* the highest). At  $T_e = 700$  eV,  $f_z$  varied from 75% to 25% with different radiative recombination rate equations for the same ion (Greim the highest, Pert the lowest). Percentages for different three-body recombination rate equations were not given. From comparisons of the ion distribution for the CE, LTE, and CR models, they stated that the most suitable expressions for rate equations were those of Bates *et al.* ( $S$ ), Seaton ( $\alpha_r$ ), and Salzmann and Krumbein ( $\alpha_{3b}$ ). These expressions are reproduced below:

$$S(z) = \frac{1.64 \times 10^{-6} \xi_z}{T_e^{3/2}} \left[ \frac{\exp(\frac{\chi_z}{T_e})}{\frac{\chi_z}{T_e}} \right] \quad (3.45)$$

$$\alpha_r(z) = 5.2 \times 10^{-14} \left(\frac{\chi_z}{T_e}\right)^{1/2} z \left[ 0.429 + \frac{1}{2} \log\left(\frac{\chi_z}{T_e}\right) + .469 \left(\frac{T_e}{\chi_z}\right)^{1/3} \right] \quad (3.46)$$

$$n_e \alpha_{3b}(z) = n_e 8.05 \times 10^{-28} \xi_z \frac{g(z)}{2g(z-1)} \frac{1}{T_e \chi_z^2} \quad (3.47)$$

where all variables are as above and  $g$  is the degeneracy ( $2J + 1$ ), evaluated as the maximum number of outer shell electrons choose the number of outer shell electrons (*e.g.*, for  $4d^5$ ,  $g = 10$  choose 5, or 252).

The rate equations are shown for Sn V (left) and Sn XIV (right) in Figure 3.21. Clearly, the collisional ionisation and three-body recombination rates are different from those of Colombant and Tonon [1] and that the radiative recombination rate is essentially the same (the only difference between Colombant and Tonon’s Eq. 3.29 and Seaton’s Eq. 3.46 is the exponent in the final term ( $^{1/2}$  instead of  $^{1/3}$ )).

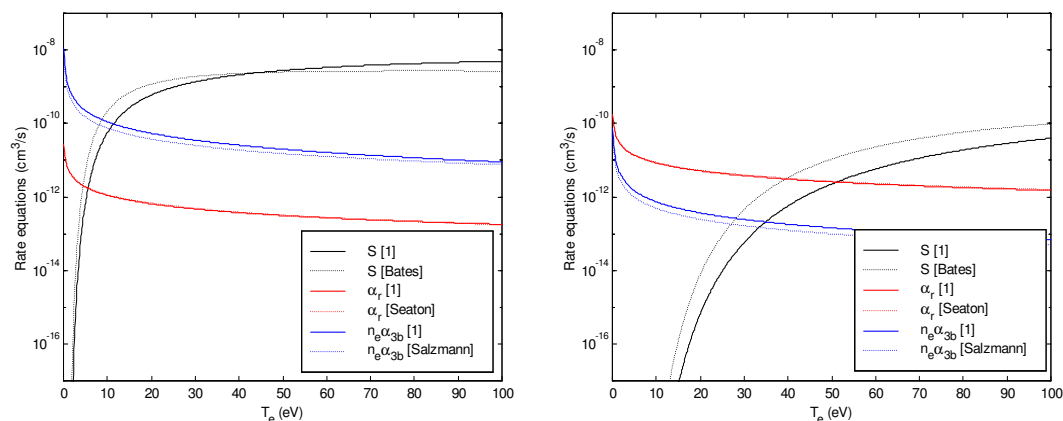


Figure 3.21 Comparison of rate equations in CR model of [1] and [16] Sn V (left) Sn XIV (right)

The effect on the average charge of using Gupta and Sinha's [16] recommended rate equations is shown in Figure 3.22. The effect of  $\alpha_{3b}$  alone is almost negligible, and thus it can be seen that the change in the average charge is almost entirely because of the different collisional ionisation rate equations,  $S$ , used from Bates.

Using these equations in the CR plasma model would increase the average charge at a given temperature, and thus lowers the temperature for maximum tin ion emission (Sn IX–Sn XII) at 13.5 nm, a result which agrees with observation [27].

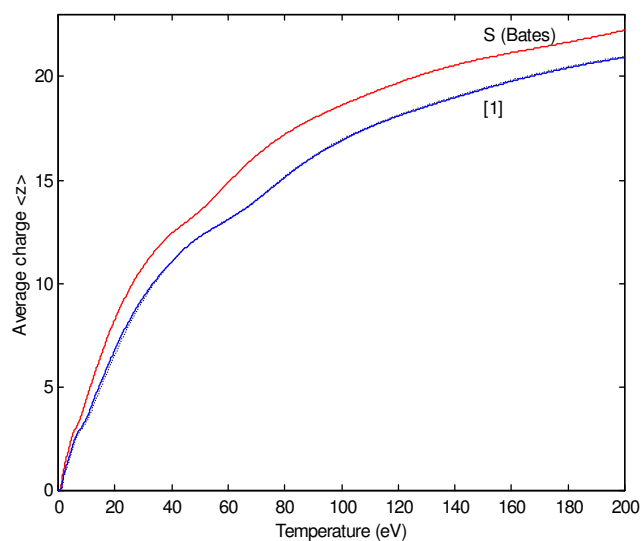


Figure 3.22  $\langle z \rangle$  versus  $T_e$  (tin) for different rate equations [16]



$$\mathbf{F} = \begin{bmatrix} f_0 \\ f_1 \\ \vdots \\ f_j \\ \vdots \\ f_z \end{bmatrix} \quad (3.51)$$

Note that  $R_{z+1}$  is the sum of the radiative and three-body recombination of ion  $z+1$ .

Considering the time-independent case,

$$\mathbf{0} = \mathbf{A} \cdot \mathbf{F} \quad (3.52)$$

where  $\mathbf{0}$  is the zero column vector, Eq. 3.52 can be solved numerically by Gaussian elimination with partial pivoting. To obtain a non-trivial solution to the time-independent case, the following condition is used as in [29]:

$$\sum_{z=1}^N f_z = 1 \quad (3.53)$$

which is applied numerically by replacing all of the elements of the last row of  $\mathbf{A}$  by 1s and the last element of  $\mathbf{0}$  by 1.  $\mathbf{F}$  is then found by inversion:

$$\mathbf{F} = \mathbf{A}^{-1} \mathbf{0} \quad (3.54)$$

### 3.2.10 Target composition

The effect of target percentage (or tin concentration) on the ion distribution  $f_z$  in the plasma as a function of electron temperature and electron density was calculated by Cummings *et al.* [28] and found to be negligible at atomic number densities below  $10^{19.5} \text{ cm}^{-3}$ . The algorithm employed is described in [28]. Figure 3.23 from [28] shows the atomic number density and electron temperature dependence on the ion distributions for Sn IX to Sn XII at mixtures of 99% Sn and 1% O (top) and 1% Sn and 99% O (bottom). The ion distributions are essentially the same for both mixtures. It should be noted, however, that at an electron density approaching  $10^{19.5} \text{ cm}^{-3}$  there is an appreciable difference between the binary mixture of Sn and O.

In Figure 3.23, it can be seen that for Sn IX to Sn XII, ion distributions have a similar shape and begin to curve at around  $10^{19.5} \text{ cm}^{-3}$ , because of the influence of three-body recombination. Other tin mixtures (Sm, Li) show that ion populations can be displaced by as much as 10–15 eV for higher atomic number densities [28].

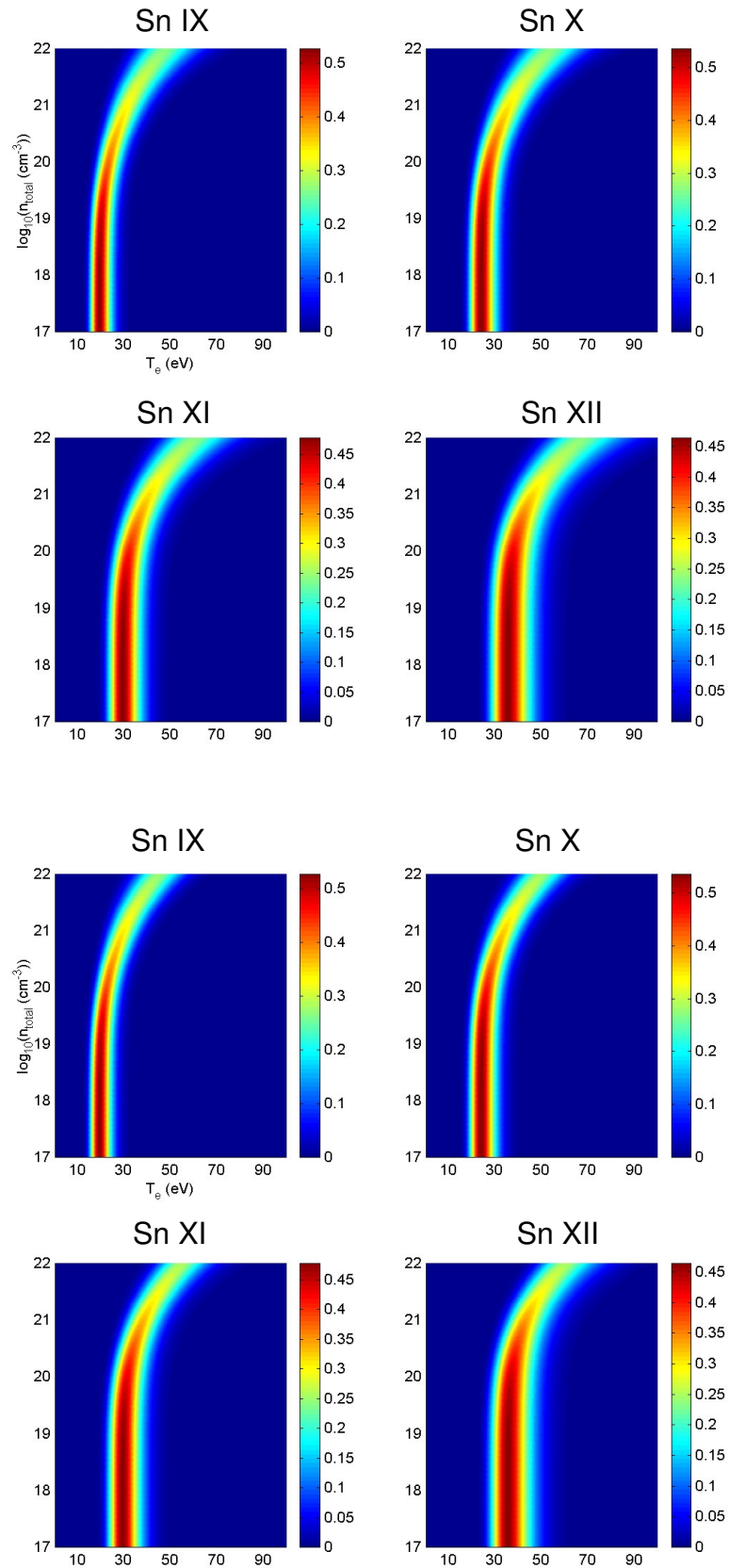


**Figure 3.23** Atomic number density versus electron temperature (eV)  
 99% Sn, 1% O (top) 1% Sn, 99% O (bottom) [28]

### 3.3 Theoretical source brightness

A theoretical spectrum can be obtained versus temperature and wavelength using the two-parameter UTA mean wavelength and standard deviation (as calculated in Chapter 3 and described in White *et al.* [30]) and the contributing ion stages based on laser power density (or temperature within the plasma) for the 4d-4f, 4p-4d, and 4d-5p transitions in the ten 4d-subshell tin ions. Furthermore, an overall in-band intensity figure of merit can be calculated to quantify the total in-band oscillator strength within the NGL Mo/Si mirror 13.5-nm bandwidth.

#### 3.3.1 Theoretical spectrum

The theoretical atomic data was calculated in Chapter 2 (Tables 2.14–2.16) and is summarised below in Table 3.4. Note that the inter-shell  $\Delta n = 1$  transitions are more sensitive to ionisation than the intra-shell  $\Delta n = 0$  transitions. As such, the 4d-5p transitions are well separated and more easily identified in the spectra, until Sn XIII, where the 4d-4f, 4p-4d, and 4d-5p transitions all overlap. The steady-state fractional ion density versus temperature for tin was shown above in Figure 3.10 and Table 3.2 and is reproduced below in Table 3.5 for a selected range of temperatures.

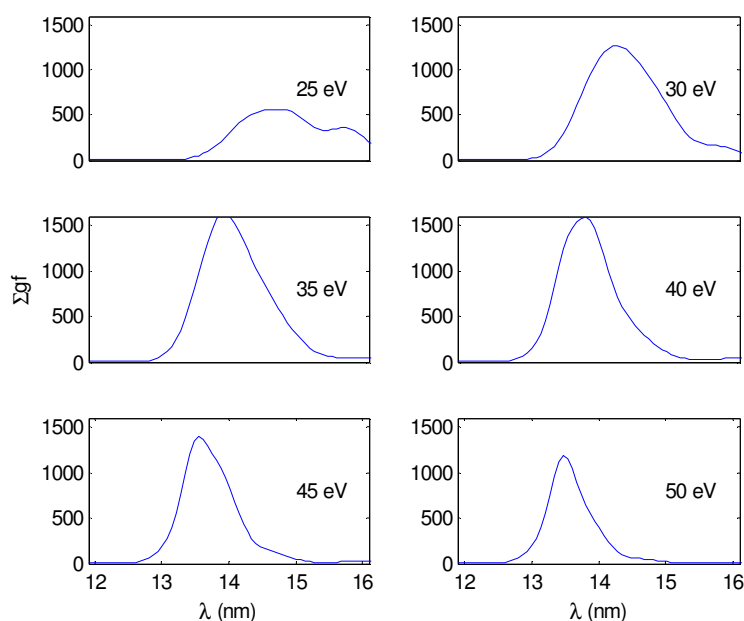
Ion	4d-4f			4p-4d			4p-5d		
	$\Sigma gf$	$\lambda(\text{nm})$	$\sigma(\text{nm})$	$\Sigma gf$	$\lambda(\text{nm})$	$\sigma(\text{nm})$	$\Sigma gf$	$\lambda(\text{nm})$	$\sigma(\text{nm})$
Sn VI	30.43	19.49	0.47	2.88	15.37	2.28	10.46	30.45	1.28
Sn VII	185.54	17.40	0.61	75.20	16.36	0.47	44.24	26.10	1.56
Sn VIII	614.63	15.77	0.62	362.98	15.05	0.65	107.17	22.78	1.64
Sn IX	1032.42	14.84	0.64	904.94	14.30	0.59	158.89	20.17	1.50
Sn X	1227.41	14.34	0.70	1061.48	13.91	0.64	129.21	18.02	1.25
Sn XI	940.50	13.87	0.46	888.11	13.64	0.61	97.46	16.25	1.01
Sn XII	483.43	13.50	0.32	471.46	13.39	0.59	59.19	14.79	0.72
Sn XIII	129.50	13.36	0.29	158.26	13.34	0.69	54.73	13.54	0.43
Sn XIV	13.03	13.41	0.22	53.95	13.29	0.61	1.05	12.38	0.18

Table 3.4 Mean wavelength and width for full spectral region

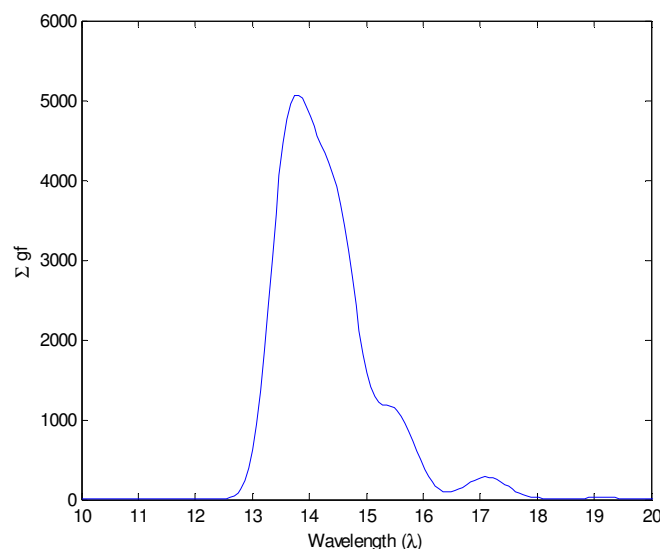
Ion	10 eV	20 eV	30 eV	40 eV	50 eV	60 eV	70 eV
Sn VI		0.35					
Sn VII		0.39					
Sn VIII		0.13	0.18				
Sn IX		0.01	0.40	0.04			
Sn X			0.31	0.22	0.02		
Sn XI			0.07	0.42	0.16	0.03	
Sn XII				0.27	0.42	0.20	0.05
Sn XIII				0.05	0.35	0.49	0.29
Sn XIV					0.05	0.22	0.31

Table 3.5 Fractional ion density versus temperature

To show the in-band radiative characteristics, a theoretical spectrum (relative intensity versus wavelength and temperature) is calculated by weighting the atomic data by the fractional ion distribution. The summed 4d-4f, 4p-4d, and 4d-5p transitions for all ion stages (statistically represented by the UTA mean wavelengths and widths) are weighted by the fractional ion density as a function of electron temperature and are shown in Figure 3.24 for 25, 30, 35, 40, 45, and 50 eV. (Note that the rate equations used are those from Colombant and Tonon [1]). As is to be expected, the overall emission moves to shorter wavelengths with temperature because of the inclusion of higher contributing ion stages, which emit at higher energies (shorter wavelengths). Furthermore, as the 4d subshell becomes fully stripped with increasing temperature, the UTA diminishes. The unweighted sum is shown in Figure 3.25 to highlight the effect of temperature on the spectrum.



**Figure 3.24** Relative intensity versus temperature and wavelength (weighted by fractional ion distribution at 25, 30, 35, 40, 45, and 50 eV)



**Figure 3.25** Relative intensity versus wavelength (sum Sn V–Sn XIV)

### 3.3.2 Intensity figure of merit

A figure of merit,  $F$ , is defined to quantify the theoretical in-band radiation. The figure of merit is taken as the product of the summed  $gf$  values for transitions within each ion stage, weighted according to their distribution as a function of electron temperature with the multilayer mirror reflectivity.

$$F = \sum_{\lambda} \sum_z R_{\lambda}^n f_z gf_{\lambda,z} \quad (1.5)$$

where  $R_{\lambda}$  is the wavelength-dependent reflectivity of the Mo/Si multilayer mirror,  $n$  is the number of mirrors,  $f_z$  is the fractional weighting of an ion of charge  $z$ , and  $gf_{\lambda,z}$  is the weighted oscillator strength for that ion stage at a wavelength  $\lambda$ . For plasma modelling purposes, the figure of merit can be considered without the mirror reflectivity (*i.e.*,  $n = 0$ ).

The figure of merit is calculated over a given wavelength range  $\Sigma_{\lambda}$  and temperature, and shown in Figure 3.26 for the 2% bandwidth at six temperatures. The contributing ion stages are shown individually as statistical UTAs, and the temperature, power density, and figure of merit are indicated. Note that the relative in-band contribution increases and then decreases with temperature. Figures 3.27 shows the relative contributions of the 4d-4f, 4p-4d, and 4d-5p transition arrays at four temperatures. Note, especially, the increasing 2% in-band contribution of the 4d-5p transition array with temperature.

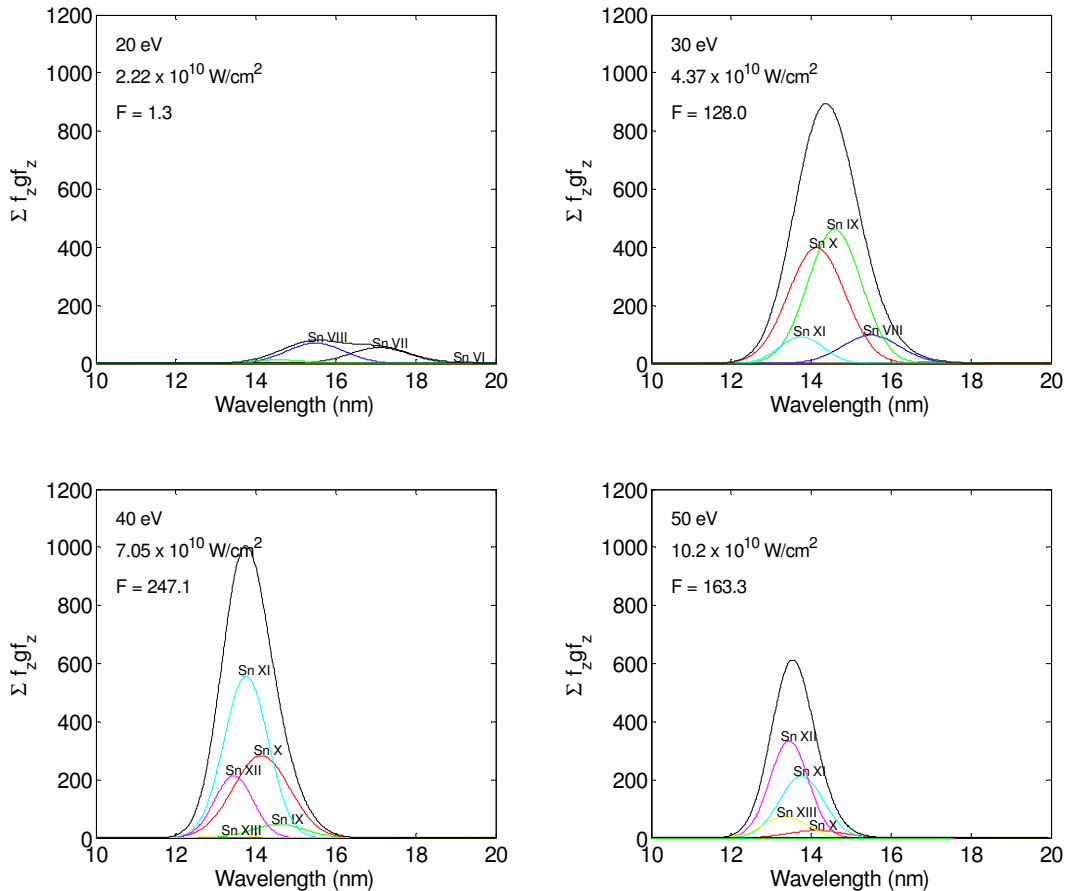
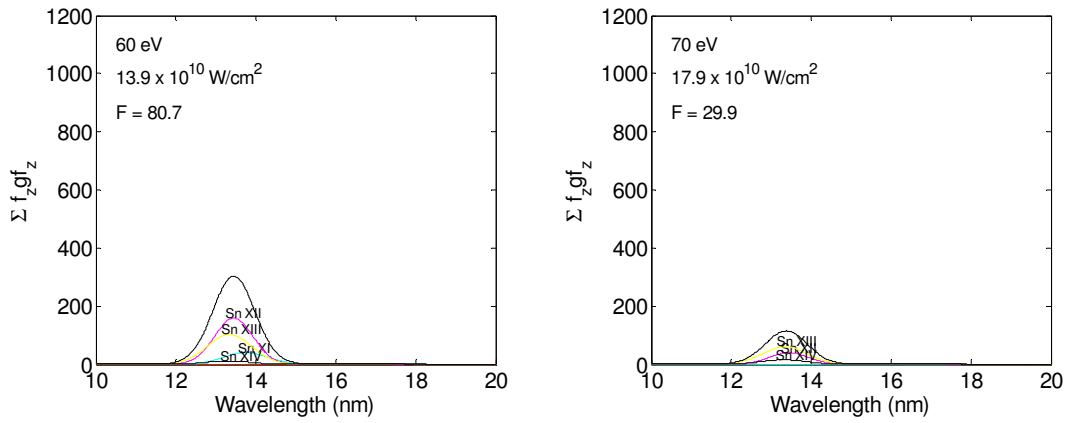
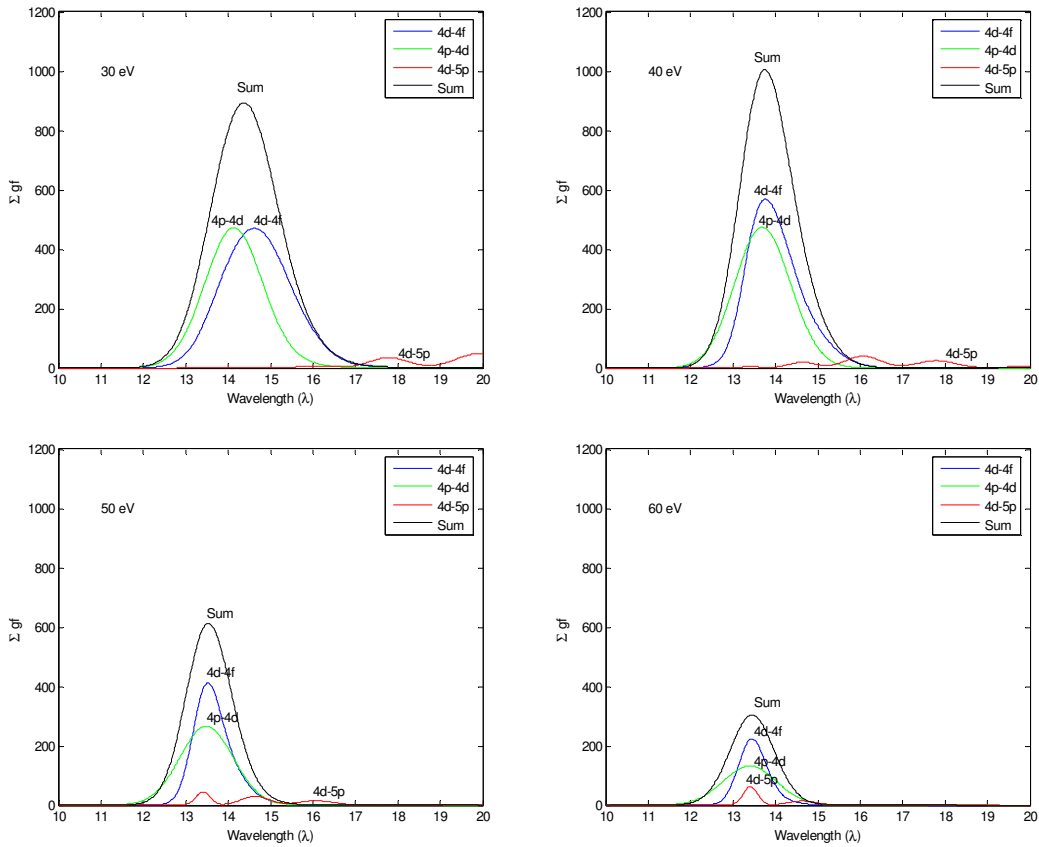


Figure 3.26 Relative intensity versus wavelength showing contributing ion stages (20, 30, 40, and 50, eV)



**Figure 3.26 (cont.) Relative intensity versus wavelength showing contributing ion stages (60 and 70 eV)**



**Figure 3.27 Relative intensity versus wavelength showing contributing transitions (30, 40, 50, and 60 eV)**

An overall figure of merit versus temperature is given in Figure 3.28, which includes the effect of the number of mirrors on  $F$ . A 2% and 7.4% figure of merit is given in Figure 3.29 along with the full spectral range. The 2%  $F$  represents the ultimate brightness seen by the Mo/Si mirror system. The temperature at the maximum in-band contribution increases as the band narrows (as more higher ions contribute exclusively) and is approximately 40 eV for the 2% band.

A simple measure of mirror heating can be given as the ratio of the 7.4%/2%  $F$ , since the 7.4%  $F$  represents emission seen but not imaged by the mirrors. (Note that the first mirror will see the full spectral range and heating will be greater.) The ratio is given in Figure 3.30 and shows a sharp increase to 20 eV with a steady decline thereafter.

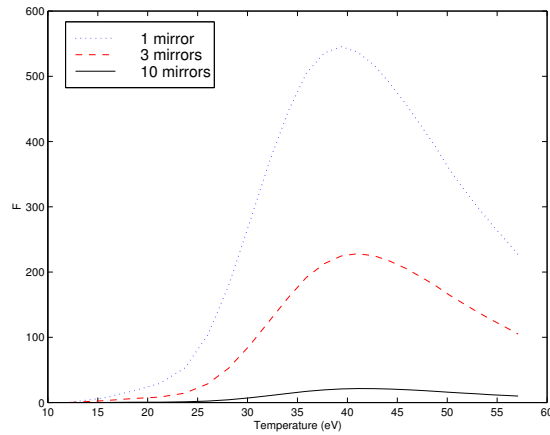


Figure 3.28 2% figure of merit versus electron temperature for 1, 3, and 10 mirrors

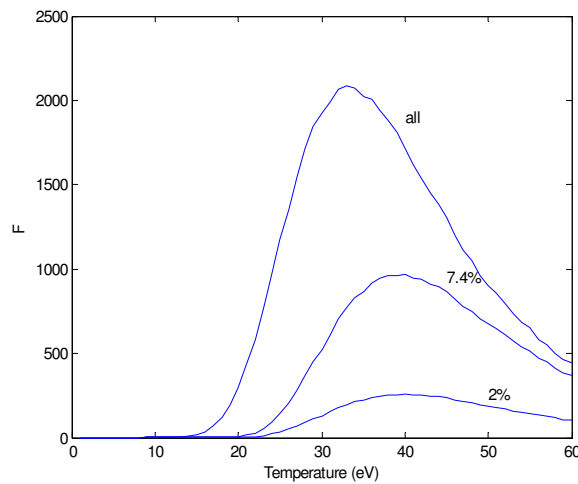


Figure 3.29 Figure of merit (2%, 7.4% and full spectral range; no mirror)

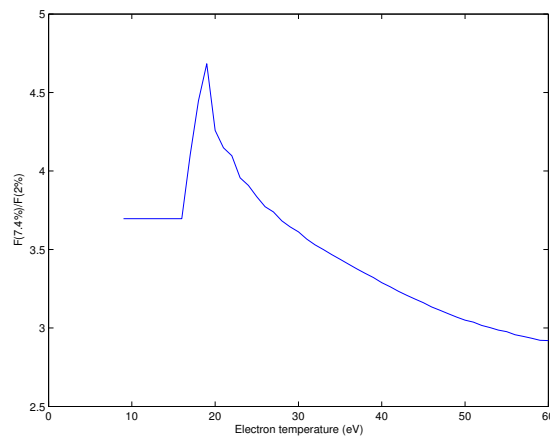
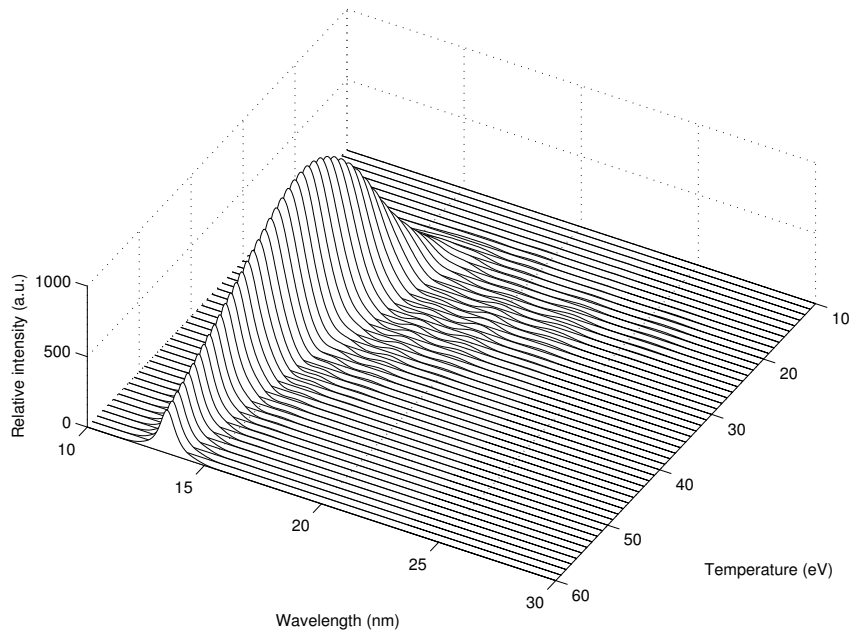
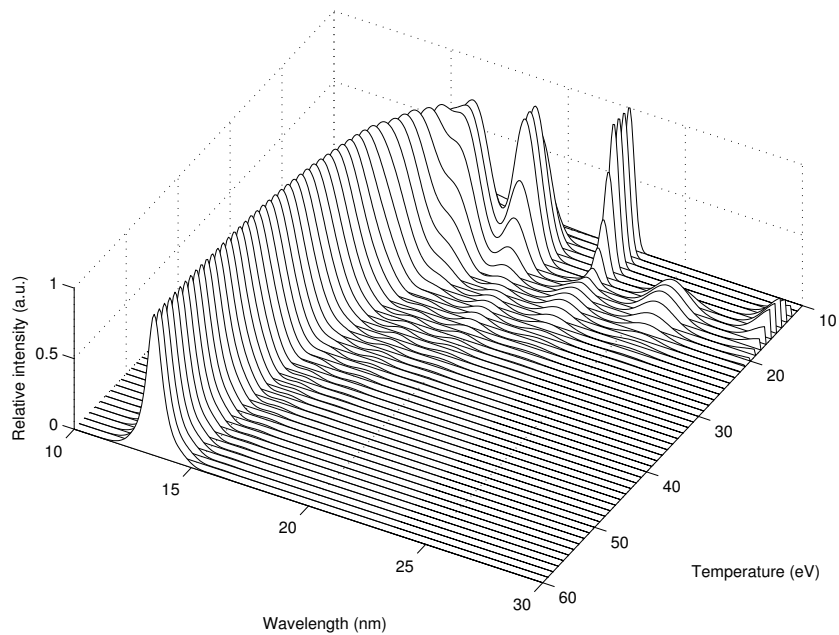


Figure 3.30 Mirror heating as ratio of figure of merit (7.4%/2%)

Figure 3.31 gives a continuous surface plot versus temperature and Figure 3.32 the same scaled to 1 for each temperature, as presented by Böwering [31] for xenon. Here, it is seen that the 4d-4f and 4p-4d transitions overlap to give broad UTA emission, which narrows with increasing temperature. The 4d-5p transitions are also seen at higher energies. In an optically thick plasma (radiation reabsorbed), the 4d-5p lines will be relatively strong compared to the 4d-4f and 4p-4d lines which self absorb [30].



**Figure 3.31** Relative intensity versus temperature and wavelength



**Figure 3.32** Relative intensity versus temperature and wavelength (normalised)

The theoretical results are compared to experimental results conducted at UCD [32]. The experimental setup (described in [30]) consisted of a target chamber of diameter 700 mm, with a ceramic target doped with 5% tin (by number), containing spectroflux ® (80% LiBO<sub>2</sub>, 20% Li<sub>2</sub>B<sub>4</sub>O<sub>7</sub>), and silica, doped with tin(IV) oxide. A Nd:YAG laser was used to produce the tin plasmas, delivering up to 800 mJ in 15 ns. The fundamental wavelength, 1064 nm, was focused via a plano-convex lens to spotsize of  $\approx 200 \mu\text{m}$ . The range of power densities were obtained by varying the energy of the incident laser pulse, while maintaining the same focusing conditions to keep the emitting volume constant.

The spectra were recorded on a Jenoptik 0.25-m grazing incidence, flatfield spectrograph, fitted with an absolutely calibrated backside illuminated x-ray CCD, covering the spectral range 9.5–18 nm. The spectrograph viewed the plasma at an angle of 45° to the incident laser pulse, as the plasma expanded along the horizontal entrance slit to the spectrograph. The spectra were recorded at power densities from  $1.2 \times 10^{11}$  to  $1.9 \times 10^{11} \text{ W/cm}^2$ .

The theoretical and experimental spectra are shown together in Figure 3.33 and Figure 3.34, where the temperature is chosen to match the theoretical spectra to the corresponding experimental spectra. The statistical UTA data is weighted by the steady-state fractional ion distribution. An arbitrary background was added to the theoretical spectra to account for continuum emission (such as bremsstrahlung), which was not calculated, and the theoretical maxima have been fitted to the experimental maxima for comparison. The 4d-4f and 4p-4d statistical UTA widths were reduced by factors from 1.6–3.9 as in Table 2.12. Self-absorption is not included in the calculated spectra.

Matching of the long wavelength edge is achieved at lower electron temperatures and thus lower tin ion stages within the plasma. The short wavelength edge is matched at higher electron temperatures and thus higher tin ion stages within the plasma. Note that oxygen lines can be identified as can the Li III 1s-2p line at the 13.5 nm peak. Figures 3.35 and 3.36 show the same spectra enlarged at 32 eV and 45 eV.

In conclusion, it is seen that a range of ion stages are present in a plasma at a given electron temperature, where higher temperatures produce higher ion stages. For example, Sn IX comprises 41% of the plasma at 31 eV and Sn XII 43% at 44 eV. It is seen that the optimum 2% bandwidth emission at 13.5 nm is at 40 eV, where the dominant ions are Sn XI, Sn XII, and Sn XIII.

However, for a range of temperatures, a time-averaged snapshot is required, requiring a time-dependent plasma model. A spatio-temporal model (Chapter 4) will further explore radiation transport in the plasma, where both absorption and emission is modelled.

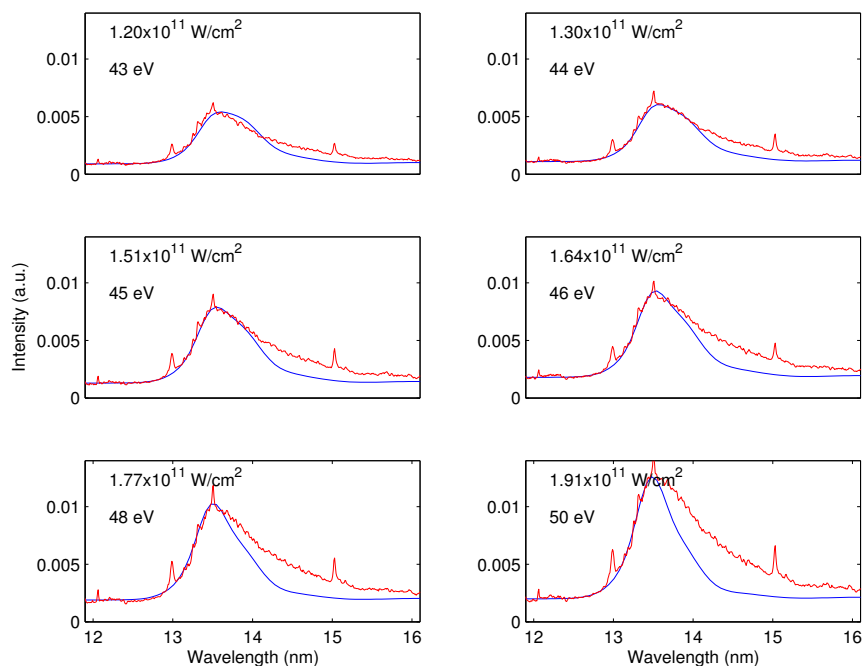


**Figure 3.33** The 4d-4f, 4p-4d, and 4d-5p transitions (represented statistically by UTA mean wavelength and width) weighted by the fractional ion density as a function of electron temperature compared to experiment [30] (short wavelength edge)

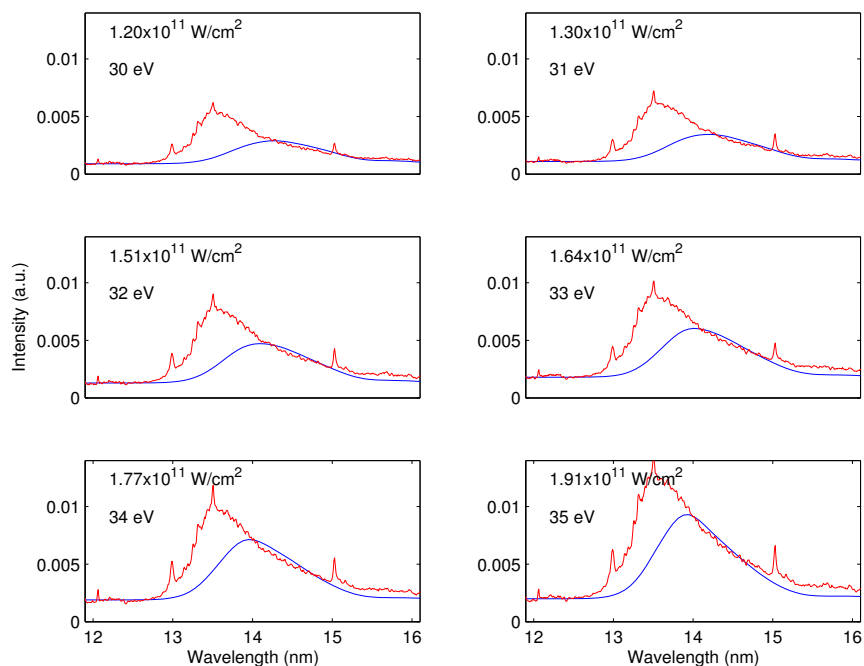


**Figure 3.34** The 4d-4f, 4p-4d, and 4d-5p transitions (represented statistically by UTA mean wavelength and width) weighted by the fractional ion density as a function of electron temperature compared to experiment [30] (long wavelength edge)

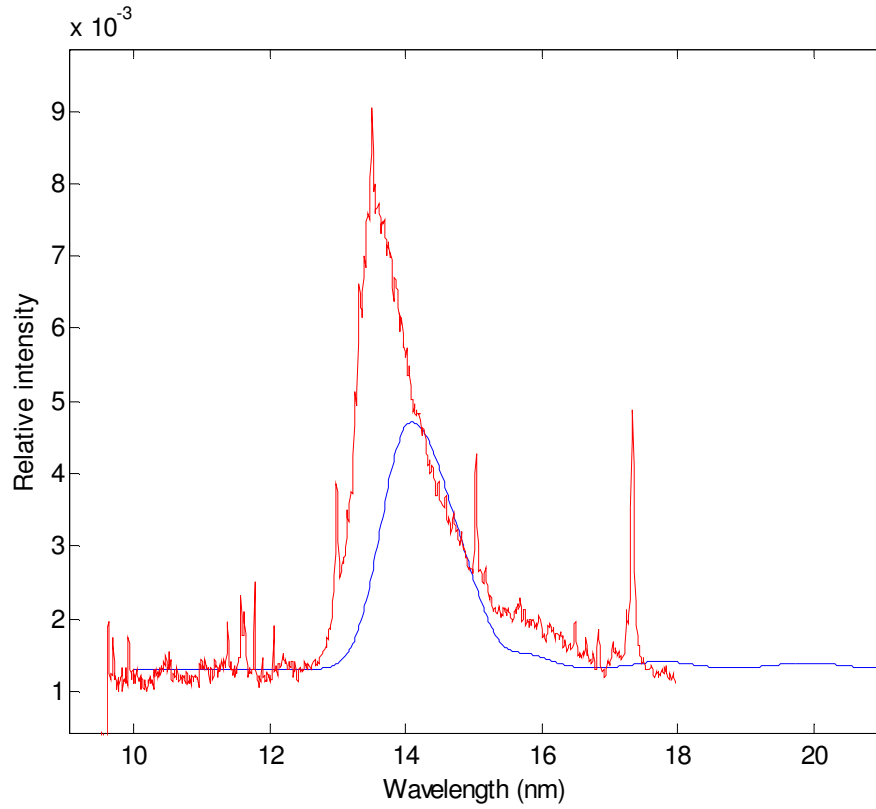


Figure 3.35 Calculated spectra versus experimental spectra (32 eV)

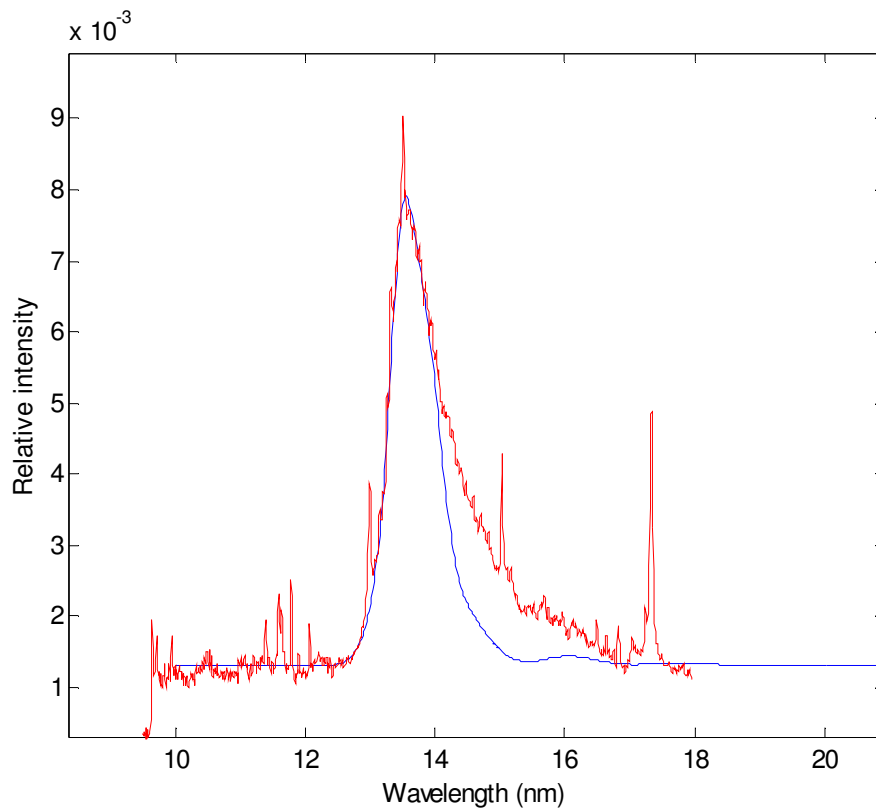


Figure 3.36 Calculated spectra versus experimental spectra (45 eV)

### 3.4 References

- 1 Colombant, D. and Tonon, G. F., "X-ray emission in laser-produced plasmas," *J. Appl. Phys.*, **44** (8), 3524–3537, 1973.
- 2 Fauquignon, C. and Floux, F., "Hydrodynamic behavior of solid deuterium under laser heating," *Phys. Fluids*, **13** (2), 386–391, 1970.
- 3 Salzmann, D. and Krumbein, A., "Calculation of x-ray production rate and ionization-state density in hot aluminium plasma," *J. Appl. Phys.*, **49** (6), 3229–3238, 1978.
- 4 Eidmann, K., "Radiation transport and atomic physics modelling in high-energy-density laser-produced plasmas," *Laser and Particle Beams*, Vol. 12, 223–244, 1994.
- 5 Peyrusse, O., "Atomic configuration averages and nonlocal thermodynamical equilibrium plasma spectroscopy calculations," *J. Phys. B: At. Mol. Opt. Phys.*, **32**, 683–700, 1999.
- 6 Carroll, P. K. and Kennedy, E. T., "Laser-produced plasmas," *Contemporary Physics*, Vol. 22, 61–96, 1981.
- 7 O'Sullivan, G. and Carroll, P. K., "4d–4f emission resonances in laser-produced plasmas," *J. Opt. Soc. Am.*, **71** (3), 227–230, 1981.
- 8 Key, M. H. and Hutcheon, R. J., "Spectroscopy of laser-produced plasmas," *Advances in atomic and molecular physics*, Vol. 16, ed. Bates, Sir David, Academic Press, 1980.
- 9 Attwood, D., "Soft x-rays and extreme ultraviolet radiation, principles and applications," Cambridge University Press, 1999.
- 10 Jansson, P. A. C., Hansson, B. A. M., Hemberg, O., Otendal, M., Holmberg, A., de Groot, J., and Hertz, H. M., "Liquid-tin-jet laser-plasma extreme ultraviolet generation," *Applied Physics Letters*, **84** (13), 2004.
- 11 Salzmann, D., "Atomic physics in hot plasmas," International series of monographs on physics, Oxford University Press, 1998.
- 12 Bates, R. D., Kingston, A. E., and McWhirter, R. W. P., "Recombination between electrons and atomic ions. I. Optically thin plasmas," *Proc. Roy. Soc. A*, **267**, 297–312, 1962.
- 13 Greim, H. R., *Principles of plasma spectroscopy*, Cambridge University Press, 1997.
- 14 Eliezer, S., Krumbein, A. D., and Salzmann, D., "A generalised validity condition for local thermodynamic equilibrium in a laser-produced plasma," *J. Phys. D: Appl. Phys.*, Vol. 11, 1978.
- 15 Greim, H. R., *Plasma spectroscopy*, Chapter 6, McGraw-Hill, New York, 1964.
- 16 Gupta, G. P. and Sinha, B. K., "Effect of ionisation and recombination coefficients on the charge-state distribution of ions in laser-produced plasmas," *Phys. Rev. E.*, **56** (2), 1997.
- 17 *CRC Handbook of Chemistry and Physics*, 73<sup>rd</sup> Edition, D. R. Lide editor-in-chief, CRC press, Boca Raton, 1992.
- 18 Moore, C. E., *Atomic energy levels: as derived from the analyses of optical spectra*, Vols. I–III, Circular of the National Bureau of Standards, 1958.
- 19 Gillaspay, J. D., "EUV source fundamental data requirements," Sematech fundamental data working group, EUV source workshop, February 23, 2003.
- 20 Saloman E. B., "Energy levels and observed spectral lines of xenon, Xe I through Xe LIV," *J. Phys. Chem. Ref. Data*, Vol. 33 (3), 2004.
- 21 O'Sullivan, G., "A spectroscopic study of laser-produced plasmas of the rare-earth and related elements," Ph.D. thesis, University College Dublin, 1980.
- 22 Fraga, S., Karwowski, J., and Saxena, K. M. S., *Handbook of atomic data*, Elsevier, N.Y., 1976.
- 23 Cowan, R. D., *The theory of atomic structure and spectra*, Berkeley, University of California Press, 1981.
- 24 Chemsoc: <http://www.chemsoc.org>.
- 25 Landshoff, R. K. and Perez, J. D., "Determination of plasma parameters of laser-produced aluminium plasma from x-ray line radiation," *Phys. Rev A.*, **13** (4), 1619–1632, 1976.
- 26 Doron, R., Behar, E., Mandelbaum, P. Schwob, J. L., Fiedorowicz, H., Bartnik, A., Jarocki, R., Szczyrek, M., and Wilhein, T., "Spectroscopic signature of strong dielectronic recombination in highly ionized xenon produced by irradiating a gas puff with laser," *Phys. Rev. A.*, **59** (1), 188–194, 1999.
- 27 Nishihara, K., *et al.*, 3<sup>rd</sup> Int. Sematech EUVL Symp., Miyazaki, Japan, November 2004.
- 28 Cummings, A., O'Sullivan, G., Dunne, P., Sokell, E., Murphy, N., White, J., Fahy, K., Fitzpatrick, A., Gaynor, L., Hayden, P., Kedzierski, D., Kilbane, D., Lysaght, M., McKinney,

- L., and Sheridan, P., "Variable composition laser-produced Sn plasmas—a study of their time-independent ion distributions," *J. Phys. D: Appl. Phys.*, **37**, 2376–2384, 2004.
- 29 Zhou, Z. Y., Pan, S. F., and Ding, P. Z., "Asynchronous non-iterative algorithm for time-dependent atomic dynamics in laser-plasma simulations," *J. Phys. D.: Appl Phys.*, **31** (4), 410–417, 1998.
- 30 White, J., Hayden, P., Dunne, P., Cummings, A., Murphy, N., Sheridan, P., and O'Sullivan, G., "Simplified modeling of 13.5 nm unresolved transition array emission of a Sn plasma and comparison with experiment," *J. Appl. Phys.*, **98**, 113301, 1–12, 2005.
- 31 Böwering, N., Martins, M., Partlo, W. N., Fomenkov, I. V., "Extreme ultraviolet emission spectra of highly ionized xenon and their comparison with model calculations," *Journal of Applied Physics*, **95** (1), 2004.
- 32 Hayden, P. B., Sheridan, P., O'Sullivan, G. D., Dunne, P., Murphy, N., "EUV laser produced plasma source development for lithography," *Proceedings of SPIE*, Opto Ireland, 5826A, April 2005.

## 4. A spatial and temporal plasma model

The spatial and temporal hydrodynamics within a laser-produced plasma are calculated using the laser-matter interaction program MED103 (an updated version of Medusa)<sup>43</sup>. Electron density, electron temperature, ion distribution, and other hydrodynamic data are given in this chapter for an aluminium reference case and a tin reference case. Energy levels are determined using an average atom (or average ion) model in Medusa and the corresponding level populations determined for  $l$ -degenerate levels. An energy functional method is used to derive populations for the distribution of states with different  $nl$  levels ( $nl$  splitting for  $\Delta n = 0$  transitions). Radiation transport within the plasma is then modelled, using a Matlab program written for this thesis, from the spatial and temporal ion densities, calculated level populations, and emission and absorption profiles, as well as the emitting and absorbing path lengths and velocities for two reference cases (Al XIII:  $Ly_{\alpha}$  1s-2p line emission and Sn V–Sn XIV: 4d-4f + 4p-4d + 4d-5p UTA emission). In Chapter 5, the radiation transport model described here is used to determine the laser power density for optimum 13.5 nm emission (and corresponding conversion efficiency).

### 4.1 Laser-produced plasma hydrodynamics

Numerical hydrodynamic calculations are required to determine the spatial and temporal velocity, pressure, temperature, and ion distribution within a LPP. As in a steady-state LPP, emission depends on the ion stages present; however, time-dependent hydrodynamics will affect the spectral intensity and line shape. Time-dependent rate equations are required when the relaxation time for atomic processes is on the order or greater than the hydrodynamic timescale. The hydrodynamics from the 1-D laser-plasma interaction code Medusa, coupled to an average atom atomic model, is discussed below.

#### 4.1.1 Medusa LPP hydrodynamics

Plasma hydrodynamics are modelled using the FORTRAN laser-plasma interaction code MED103, an updated version of Medusa [1]. Medusa was created in 1974 by Christiansen *et al.* [1] for the UKAEA research group at Culham Laboratory and was originally designed to simulate inertial confinement fusion in a target compressed by laser irradiation to investigate controlled thermonuclear power generation.

As described in [1], the hydrodynamics and plasma processes are represented by four main dependent variables: density ( $\rho$ ), velocity ( $v$ ), ion temperature ( $T_i$ ), and electron temperature ( $T_e$ ) as a function of space ( $r$ ) and time ( $t$ ). Navier-Stokes hydrodynamics equations are supplemented by separate heat conduction equations for  $T_i$  and  $T_e$ . A one-dimensional Lagrangian difference mesh is used in planar, cylindrical, or spherical geometry, with an explicit integration scheme for the hydrodynamics and an implicit integration scheme for heat conduction [1]. Any realistic laser pulse can be modelled. The accuracy of the results depends on the mesh size and convergence criteria [1].

---

<sup>43</sup> Medusa refers generically to Medusa and all subsequent updates, except where explicitly referring to an updated version, *e.g.*, Med103.

In 1980, new equations of state were added as an option to **Medusa**, based on the Thomas-Fermi model [2]. In 1983, radiation transport by x-ray photons was added for comparison with spectroscopic results, including details of line shape and line intensity ratios [3]. Subsequent versions of **Medusa** (MED101 [4] in 1989 and MED103 [5] in 1996) were developed to better simulate laser-produced plasmas, including coupling excitation and ionisation energies in a non-LTE (or CR), time-dependent, average atom model. The average atom model can produce non-integer shell occupation,  $\{P_n\}$ . Levels are  $l$ -degenerate (no  $nl$  splitting).

As stated in Eidmann [6], “the radiation hydrodynamics of plasmas heated by high-power lasers is quite complex, because a wide range of density and temperature with different characteristic regimes is covered.” Rate equations for the ion distribution and excited level populations are solved together with the hydrodynamics at each step. If emission and absorption coefficients are calculated independently in opacity tables from the density and temperature, the physics is somewhat simplified [6]. In this case, the plasma must be close to steady state, *i.e.*, ionisation and recombination processes are short enough compared to the hydrodynamics, a reasonable assumption in laser-produced plasmas [7]. Opacity tables in **Medusa** are determined using the average atom model (discussed below in Section 4.2.1).

The physics in **Medusa** is described in [1]. Charge neutrality in each cell is assumed. Electrons and ions are coupled by their common velocity and energy exchange from electron-ion (or electron-atom) collisions. The electron density changes because of hydrodynamic expansion/contraction of each fluid element (Lagrangian cell).

A brief description of the hydrodynamics is given below, including the equations of state for hydrodynamic flow and heat conduction (Eqs. 4.1–4.3). The motion of the plasma is determined by the Navier-Stokes equation, a 2nd-order non-linear partial differential equation describing fluid flow in terms of conservation of mass and momentum transport:

$$\rho \frac{\partial u}{\partial t} = -\nabla p \quad (4.1)$$

where  $\rho$  is the mass density,  $p$  is hydrodynamic pressure, and  $u$  is the plasma velocity as defined in Eq. 4.2,

$$u(r, t) = \frac{\partial r}{\partial t} \quad (4.2)$$

and  $r$  is the Lagrangian coordinate.

Heat conduction for both ions and electrons is described as

$$H = \frac{1}{\rho} \nabla \cdot k \nabla T \quad (4.3)$$

where  $k$  is the thermal conductivity and  $T$  is the temperature.

As stated in [1], the **Medusa** mesh integration scheme solves the equation of motion explicitly and the energy equation implicitly. Thus the coordinates and volumes are calculated one time step ahead of the temperatures and pressure. More detailed descriptions of the energy equation, heat conduction, thermal conductivity, energy exchange, and shock region are given in [1].

### 4.1.1.1 Medusa control

Medusa input/output is shown below in Figure 4.1. MED103 data is read from a single input data file (`ZIn.txt`) and written to a single output file (`ZOut`).

`ZOut` is post-processed in a gawk scripting file, `BatchOut`, written by A. Cummings, and generates four files: `ZOut1.dat`, `ZOut2.dat`, `ZOut3.dat`, and `ZOut4.dat`. The first output file, `ZOut1.dat`, gives cell edge, velocity, electron density, density, pressure, electron temperature, ion temperature, and average charge state. `ZOut2.dat` gives occupation numbers  $\{P_n\}$  for the K- to P-shell (default  $n = 1$  to 6)<sup>44</sup> and the average charge,  $Z^*$ <sup>45</sup>. Data for all cells is output for each time step for the duration of the simulation. `ZOut3.dat` gives the times for all time steps and `ZOut4.dat` gives either the LTE or non-LTE ion distribution, if requested. A restricted number of time steps can be output (as selected in `ZIn.txt`).

The four output files are then input to the Matlab program `MedOut` written for this thesis for general `Medusa` data analysis.

`Medusa` and `BatchOut` are run in Cygwin, a Unix-like environment for Windows. For more on running `Medusa`, `BatchOut`, and `MedOut`, see Appendix D.

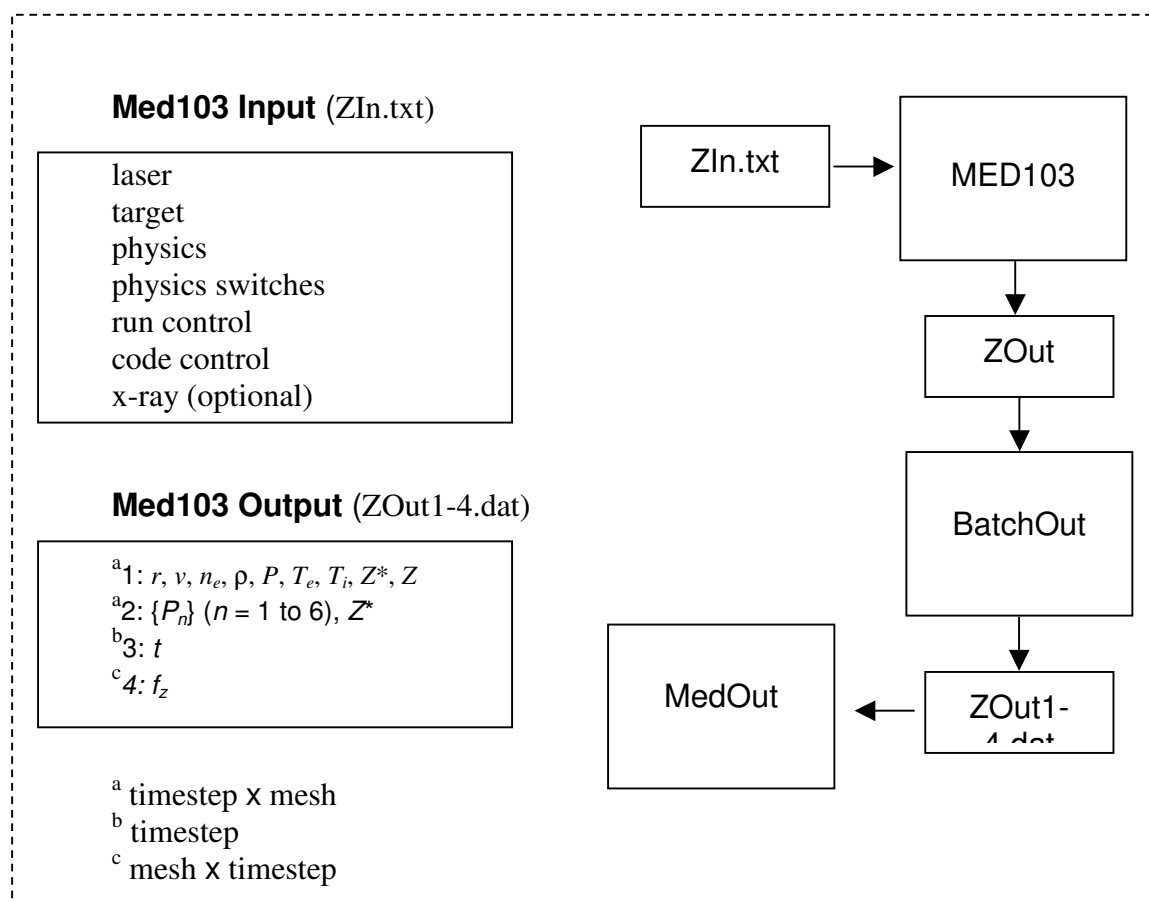


Figure 4.1 Medusa input/output

<sup>44</sup> The default 6 shells in `Medusa` can be changed in code (e.g., `nmax = 10`). For code changes in `Medusa`, see Appendix D.

<sup>45</sup> `Medusa` uses  $Z^*$  for average charge (referred to as  $\langle z \rangle$  in this thesis)

### 4.1.1.2 Medusa input

Medusa input data is divided into seven areas: laser, target, physics, physics switches, run control, code control, and x-ray. The main variables for an aluminium reference case are given in Table 4.1. The aluminium reference case (two 1.0-ns (FWHM), 0.53- $\mu\text{m}$  laser pulses with peak irradiance of  $4 \times 10^{14} \text{ W/cm}^2$  coincident in opposite directions on a solid aluminium wire at the Trident Laser Facility in Los Alamos) is used to introduce Medusa by comparing output to existing literature [8–13], and to illustrate the radiation transport model written for this thesis.

**Aluminium line reference case** (for  $\text{Al}^{12+}$  1s-2p line emission)  
 laser: 0.53  $\mu\text{m}$ , 1.0 ns (FWHM), Gaussian,  $P_{\text{equiv}}$  for planar =  $4 \times 10^{14} \text{ W/cm}^2$   
 target: solid aluminium, 50- $\mu\text{m}$  diameter wire  
 simulation: 400 cells, 3.0 ns (60 time steps), cylindrical geometry

	variable	value	unit	meaning	comment
<b>Laser</b>	XAMDA1	0.53E-6	m	Wavelength	Nd:YAG 2nd harmonic
	GAUSS	1.0		pulse shape	Gaussian
	PLENTH <sup>46</sup>	0.6E-9	s	pulse length	0.6 x FWHM
	PMAX	1E+14	W/m/rad	Peak power*	$P_{\text{equiv}} = 4 \times 10^{14} \text{ W/cm}^2$
	PMULT	2.55		# of PLENTHS <sup>47</sup>	
<b>Target</b>	NGEOM	2		geometry	cylindrical
	MESH	400		# of cells	
	RINI	25.0E-6	m	target radius**	initial cell width
	rhogas	2700.0	kg/m <sup>3</sup>	density	aluminium
	XZ	13.0		atomic #	aluminium
	XMASS	26.98		Mass #	aluminium
	piq(55)	0.0		boundary	left fixed, right free
<b>Physics</b>	default <sup>48</sup>	values		Note: ANABS = 0.2 (% inverse bremsstrahlung absorption)	
<b>Switches</b>	default	values			
<b>Run</b>	TSTOP	3.0E-9	s	simulation time	0–3 ns
	NRUN	50000		max # time steps	
	NPRNT	-50 <sup>***</sup>	ps	time of print out	+ time step, - time
<b>Code</b>	DELTAT	1.0E-12	s	initial time step <sup>****</sup>	
<b>X-ray</b>	ILOSTA	1		ground configuration ion distribution	all Al ions
	IHISTA <sup>*****</sup>	13		from 1–Z	

**Table 4.1 Main Medusa input (aluminium reference case)**

\*  $P_{\text{max}}$  is in  $\text{W/m}^2$  for planar,  $\text{W/m/rad}$  for cylindrical and  $\text{W/ster}$  for spherical geometry.

\*\* Initial cell width =  $r_{\text{ini}}/\text{mesh}$ .

\*\*\* -1 = 1 ps  $\therefore$  -50 = 50 ps (and 3.0 ns/50 ps = 60 time steps)

\*\*\*\* Default value. Medusa will choose its own time step after a few time steps. Medout outputs Medusa data at specified time steps for easier data analysis (including graphing). 60 equal time steps from 0–3.0 ns were chosen as in [12].

\*\*\*\*\* LOWest STAge = H-Like, HIest STAge = Z-like. (ILOSTA = IHISTA to suppress)

<sup>46</sup> PLENTH is the time from the peak of the pulse to  $e^{-1}$  of the maximum value (in s) and is approximated as  $\text{PLENTH} = 0.6 \times \text{FWHM}$  [5].

<sup>47</sup> Note: called PLENTH in Medusa.

<sup>48</sup> If not declared in the input file, the default coded Medusa value is used.

The main input variables for the tin reference case are shown in Table 4.2. A Gaussian laser pulse is used here for comparison to the aluminium reference case (in particular, the method of calculating level populations using the energy functional method in Section 4.2.4). An 1100-mJ, 15-ns (FWHM) pulse with focussed spot radius of 132  $\mu\text{m}$  is used as in [14]. A multi-mode longitudinal pulse can also be used to model experiments at UCD.

**Tin UTA reference case** (for SnV–Sn XIV 4d-4f + 4p-4d UTA emission)  
laser: 1.064  $\mu\text{m}$ , 15.0 ns (FWHM), Gaussian,  $P_{\text{equiv}}$  for planar =  $1.3 \times 10^{11}$  W/cm<sup>2</sup>  
target: solid tin, 50  $\mu\text{m}$ -diameter wire  
simulation: 400 cells, 100.0 ns (100 time steps), cylindrical geometry

	variable	value	unit	meaning	comment
<b>Laser</b>	XAMDA1	1.064E-6	m	wavelength	Nd:YAG fundamental
	GAUSS	1.0		pulse shape	gaussian
	PLENTH	9.0e-9	s	pulse length	0.6 x FWHM
	PMAX	3.8E+10	W/m/rad	peak power	$P_{\text{equiv}} = 1.3 \times 10^{11}$ W/cm <sup>2</sup>
	PMULT	2.55		# of PLENTHS	
<b>Target</b>	NGEOM	2		geometry	cylindrical
	MESH	400		# of cells	
	RINI	25.0E-6	m	target radius	initial cell width
	rhogas	7280.0	kg/m <sup>3</sup>	density	tin
	XZ	50.0		atomic #	tin
	XMASS	118.71		mass #	tin
	piq(55)	0.0		boundary	left fixed, right free
<b>Physics</b>	default	values			
<b>Switches</b>	default	values			
<b>Run</b>	TSTOP	100.0E-9	s	simulation time	0–100 ns
	NRUN	50000		max # time steps	
	NPRNT	-1000	ps	time of print out	+ time step, - time
<b>Code</b>	DELTAT	1.0E-12	s	initial time step	
<b>X-ray</b>	ILOSTA	30		ground configuration ion distribution	first 20 Sn ions
	IHISTA	50		from 1-Z	

**Table 4.2 Main Medusa input (tin UTA case)**

The Matlab program LaserPlot, written for this thesis, models the laser pulse in Medusa as shown in Figure 4.2. The laser pulse is modelled as a single Gaussian. The power as a function of time  $P(t)$  is given in equation 4.4. The maximum power,  $P_{\text{max}}$ , depends on the incident laser energy,  $E_{\text{tot}}$ , and the target geometry and is given in Equation 4.5 for cylindrical geometry.

$$P(t) = P_{\text{max}} \exp\left(-\left(\frac{t - P_{\text{mult}} P_{\text{length}}}{P_{\text{length}}}\right)^2\right) \quad (4.4)$$

$$P_{\text{max}} = \frac{E_{\text{tot}}}{P_{\text{length}} \frac{\sqrt{\pi}}{2} \cdot \text{erf}\left(\frac{t - P_{\text{mult}} P_{\text{length}}}{P_{\text{length}}}\right) + \text{erf}(P_{\text{mult}}) \cdot r} \quad (4.5)$$

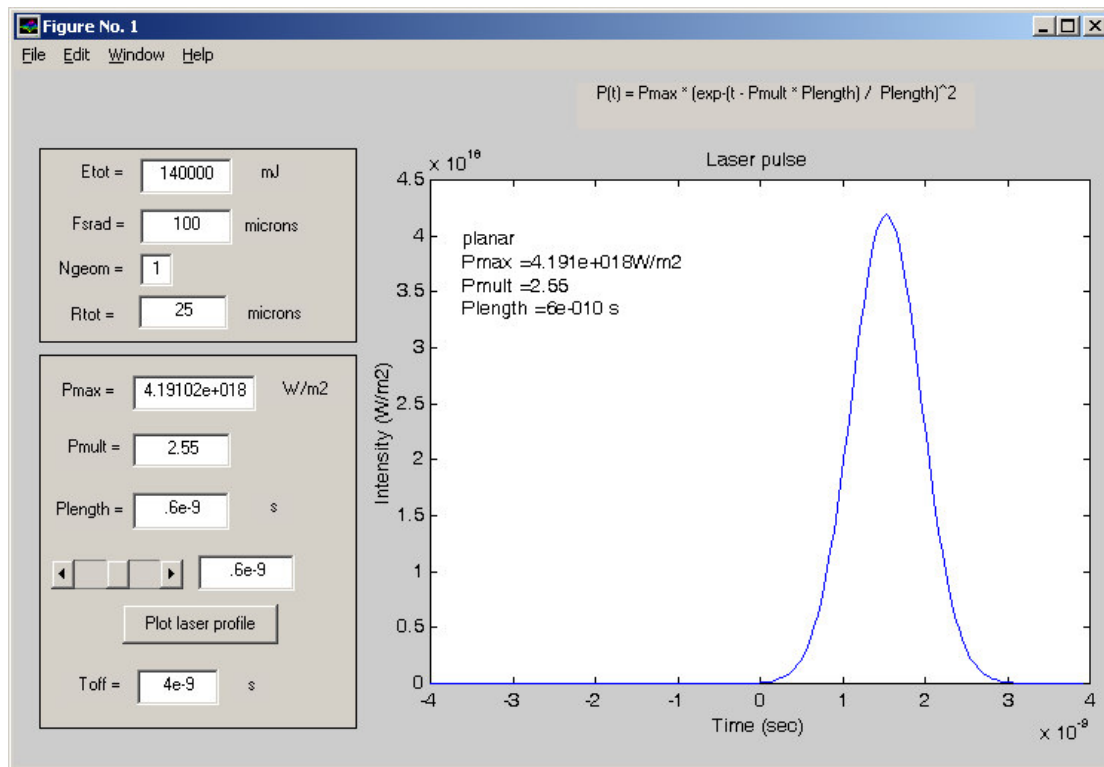


Figure 4.2 Input Medusa laser pulse (from LaserPlot) for aluminium reference case

The variables are as given in Tables 4.1 and 4.2, and  $erf(t)$  is the error function used to integrate the Gaussian function. The symmetrical laser pulse begins at a time specified by  $P_{mult}$  (in Medusa, the time at  $P_{max} - P_{mult} \times P_{length}$ ).

From Figure 4.2, it can be seen that the peak of the pulse is at 1.5 ns for the aluminium reference case. (For the tin reference case, the peak is at 23 ns.) For more about modelling the laser pulse in Medusa using LaserPlot, including the derivation of  $P_{max}$ , see Appendix D.

The target considered here is cylindrical, of unit height, and one radian in angle as shown in Figure 4.3 [10]. Only the coordinate  $r$  is used. Flow is modelled by an angle perpendicular to the cylindrical axis. In the simulation, the laser pulse is incident on  $2\pi$ , but is shown incident in only one direction for the 1-D model. In the general radiation transport model, output data can be rated as a function of angle,  $\theta$ . In the normal plane,  $\theta = 0^\circ$  is towards the laser,  $\theta = 90^\circ$  is perpendicular to the laser, and  $\theta = 180^\circ$  is in the direction of the laser behind the target.

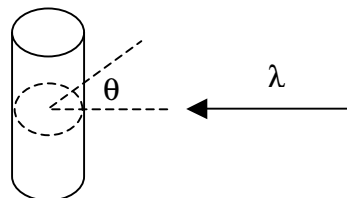


Figure 4.3 Cylindrical target geometry

Tallents [15] shows a geometrical set-up for a spherical (microballoon), cylindrical (wire), and a conical plasma (solid slab) target.

### 4.1.2 Medusa output

Medusa gives hydrodynamic output within the plasma for velocity, electron density, density, pressure, electron temperature, ion temperature, and average charge versus cell edge and time. Lagrangian cells expand in time, although each time step is of equal length. The compression region, conversion layer (optically thin), and reemission zone (optically thick) can be seen in a plot of cell edge versus time. Much of the interesting cell dynamics occurs in the conversion layer.

Aluminium is used as a reference case to compare results to existing literature [8–13] and has an electronic structure of  $[\text{Ne}] 3s^2 3p$ . The hydrodynamic output data is coupled with hydrogen-like  $1s-2p$  atomic data ( $\text{Al}^{12+}$ , Lyman- $\alpha$  doublet  $1s-2p_{3/2}$  at  $7.175 \text{ \AA}$  and  $1s-2p_{1/2}$  at  $7.180 \text{ \AA}$ ) to model the time-dependent spectral profile, including radiation transport. Results are then given for tin with corresponding statistical UTA atomic data calculated in Chapter 2.

#### 4.1.2.1 The Lagrangian mesh

As stated in Attwood [16], sharp density profiles, rapid thermal expansion, and largely non-thermal particle and radiation energy distributions cannot generally be linearised and, thus, require numerical solutions. A Lagrangian moving cell simulation (where a cell of specified mass moves as an element) models fluid flow better than a Eulerian fixed grid simulation (where velocity is calculated at fixed points), because Lagrangian methods are more efficient in the fluid domain [17]. As well, conservation laws are inherently Lagrangian since they apply to material elements rather than points in space (although Lagrangian equations of motion are more difficult when applied to a continuum) [17].

The total number of cells remains the same in a Lagrangian simulation, while the cell (represented by the cell centre) expands in time, depending on the plasma hydrodynamics. Each cell represents the hydrodynamic flow in space and time. Larger cells indicate the plasma expanding into vacuum as well as having a lower density, whereas smaller cells indicate contraction and an increased density.

In Figure 4.4, the laser pulse is incident on the target from the right. The Lagrangian mesh is numbered from the left (cell #1) to the right (cell #N = MESH), and thus the highest cell number indicates the expanding plasma edge. The left edge is fixed while the right edge is free to move. The hydrodynamic calculations are evaluated at the cell centres, although edge values can be calculated by averaging adjacent cells, *e.g.*,  $(r_i + r_{i+1})/2$ .

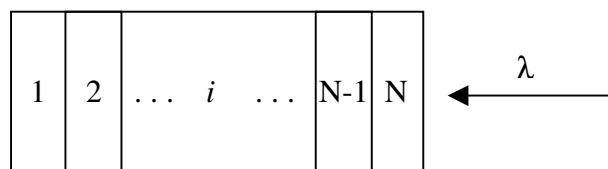
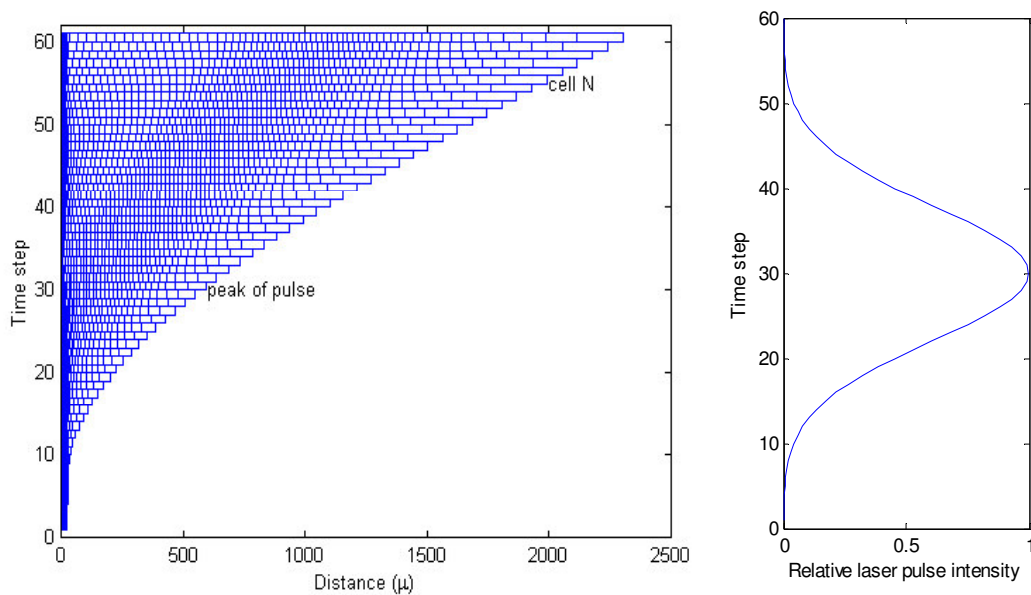


Figure 4.4 Laser incident on target (N cells = MESH)

The cell map in Figure 4.5 shows the cell radius versus time for the aluminium reference case, from an initial cell radius of  $0.0625 \mu\text{m}$  ( $25\mu\text{m}/400$ , all cells, time step = 1) to  $74 \mu\text{m}$  at the peak of the laser pulse (last cell, time step = 30) and  $190 \mu\text{m}$  at the end of the simulation (last cell, time step = 60)<sup>49</sup>. The plasma edge is also seen expanding from the initial  $25 \mu\text{m}$  solid radius to  $592 \mu\text{m}$  at the peak of the laser pulse (time step = 30 = 1.5 ns) to  $2300 \mu\text{m}$  by the end of the simulation (time step = 60 = 3.0 ns). Clearly, the greatest cell expansion is at the plasma edge. The simulated Gaussian laser pulse is shown for comparison. (Time steps are used to highlight the generic nature of the expanding plasma from a Gaussian pulse.)

Note that the plasma expands after the peak of the pulse, though at a lesser rate (expansion appears to scale non-linearly until maximum loading and then linearly thereafter as loading decreases). More than 75% of the plasma expansion occurs after peak loading. Furthermore, the plasma is still expanding after the end of the simulation.



**Figure 4.5 Medusa cell map (time step versus distance) to end of simulation**

The zoomed-in cell map in Figure 4.6 shows the cell width increasing with time more clearly. As in Figure 4.5, at  $t = 0$  ns (time step 1), the mesh length is equal to the original target size ( $25 \mu\text{m}$ ), where the target is divided into equal-length cells, ( $25\mu\text{m}/400 = .0625 \mu\text{m}$ ). It can be seen in Figure 4.6 that a number of cells have decreased in width (distance at the peak of the pulse is less than the original target radius at 0 ns). While the plasma is clearly expanding away from the target, the laser is also compressing the target inwards behind the ablation front. The original, unablated target width is represented by a solid line at  $25 \mu\text{m}$ .

The undisturbed solid (shown at this magnification as solid below  $25 \mu\text{m}$ ) and the shockwave region (compression into the target) can also be seen in a plot of time versus cell edge (Figure 4.7), as previously shown in Eidmann [6]. Here, the conversion layer and reemission zone (as well as the undisturbed solid and shockwave region) can also be seen.

<sup>49</sup> Cell width =  $\Delta z_i = r_i - r_{i-1}$ , where  $r$  is the expanding right cell edge. Note that the last cell width is thus  $r_N - r_{N-1}$ .

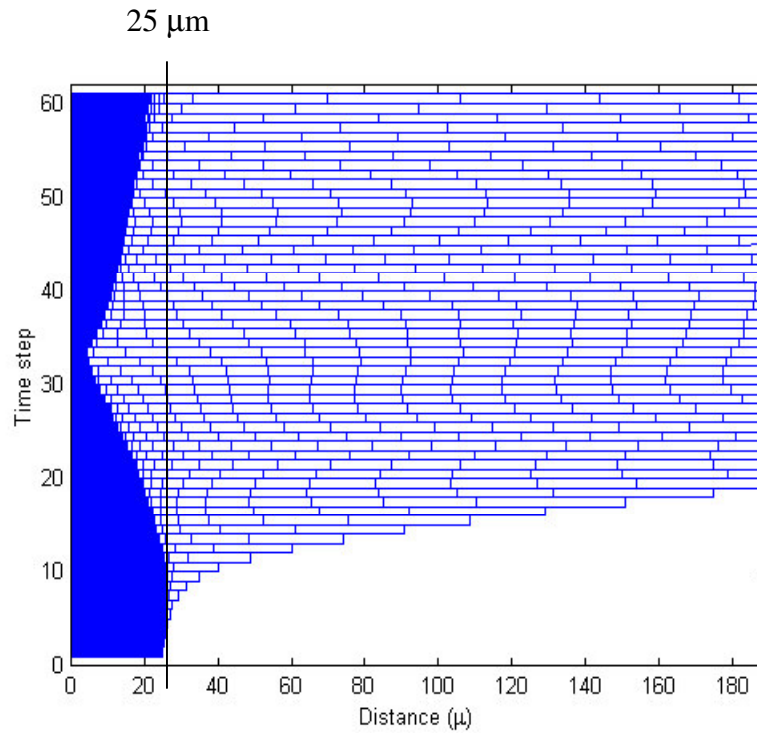


Figure 4.6 Medusa cell map (time step versus distance) to 180  $\mu\text{m}$

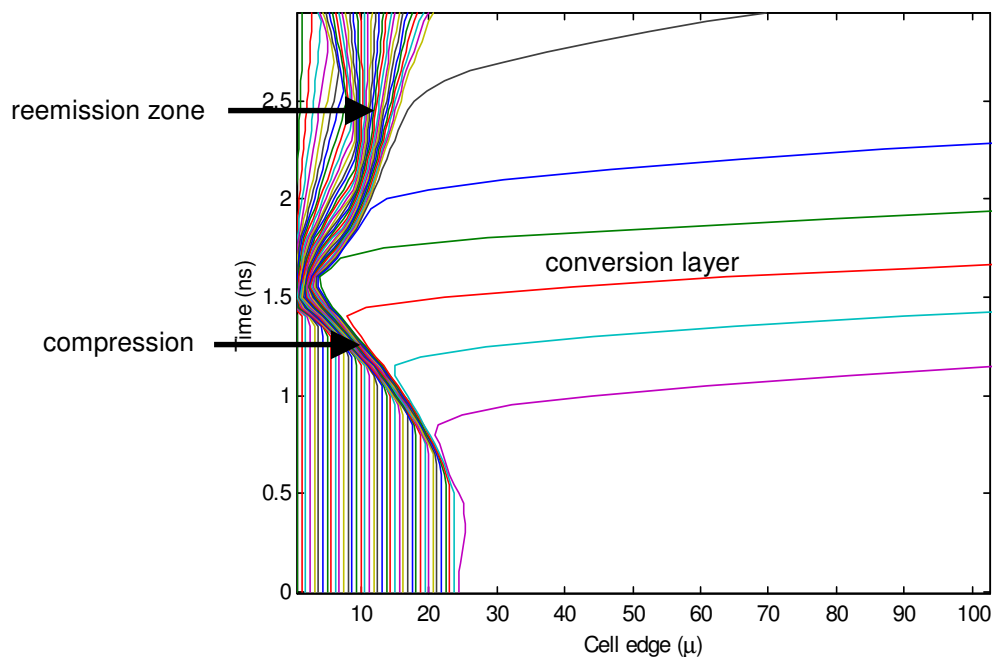


Figure 4.7 Time versus cell edge (to 100  $\mu\text{m}$ )

Large temperature fluctuations and fast plasma expansion create the shockwave in the target (as well as recoil from the expanding plasma) as described in [16] and seen below in the hydrodynamic plots of Figure 4.8. The temperature is approximately the same as the solid, but the density is much greater. In the conversion layer, temperatures can be  $\sim 10^7$  K ( $\sim 1000$  eV) [18].

### 4.1.2.2 Hydrodynamic data

Visualisation of multi-dimensional hydrodynamic data represents a significant challenge in plasma analysis. Here, results are shown versus time and then space as a general introduction to *Medusa* output. Where applicable, further graphical output will show more complete results.

Data for the aluminium reference case is shown in Figure 4.8. Velocity, electron density, mass density, pressure, electron temperature, and average charge are plotted versus distance at three times (0.7 ns, 1.5 ns (peak of the pulse), and 2.3 ns). Data is deemed to be at the cell centre (considered uniform over the entire cell [1]) except for velocity, which is at the cell edge.

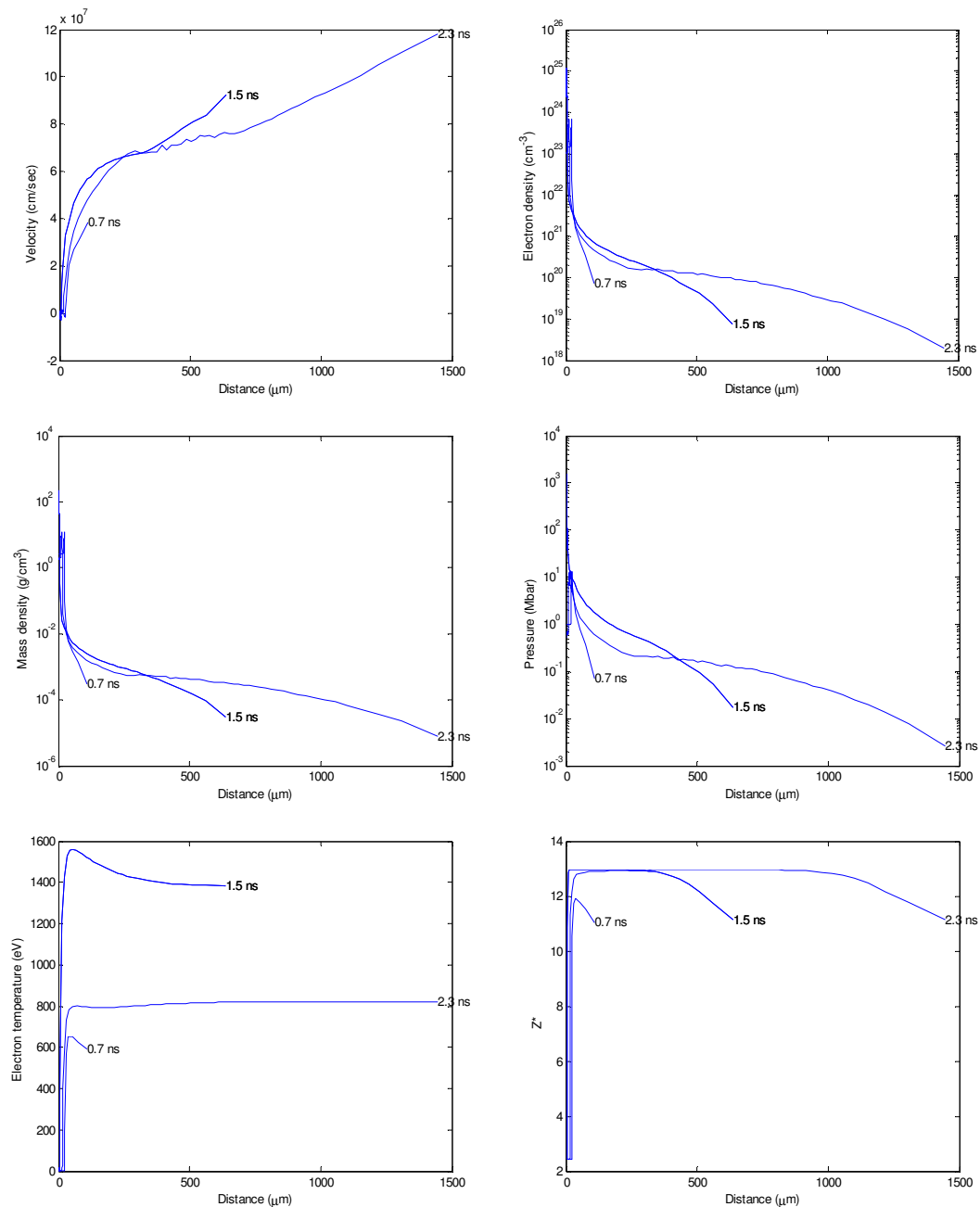
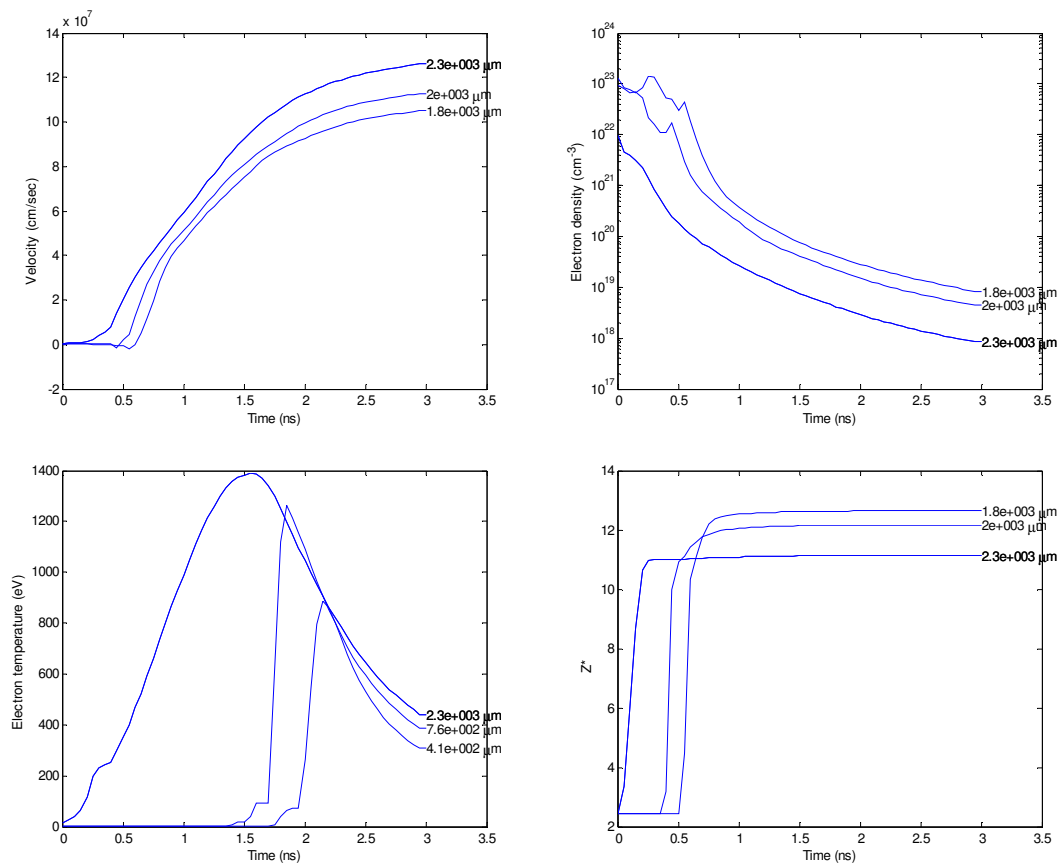


Figure 4.8 *Medusa* output versus distance for aluminium reference case at 0.7, 1.5, and 2.3 ns  
 $(v, n_e, \rho, P, T_e, \langle Z \rangle)$

Note that the velocity is still increasing significantly ( $\sim 10^8$  cm/s) after the peak of the pulse. At the same time, the density has decreased by 6 orders of magnitude from the ablation front to the plasma edge. Furthermore, it can be seen that, at the peak of the pulse, the electron temperature profile ranges from 0–1600 eV in the overdense region, decreasing to  $\sim 1400$  eV at the plasma edge.

Note that the average charge freezes (at about  $12^+$  for the outer cell). The plasma is too dilute for three-body recombination, because of the fast plasma expansion (and resultant decrease in electron density;  $n_e \alpha_{3b} = f(n_e)$ ) and additionally the radiative recombination rate is too low ( $\alpha_r = f(T_e)$ ). As such, although no further ionisation occurs, the plasma cannot recombine and the charge “freezes”. As stated in Cummings *et al.* [14], “This ‘freezing’ phenomenon of  $\langle z \rangle$  appears to be generic within these laser-produced plasmas which have rapidly varying temperature, density, and velocity gradients both temporally and spatially.” A contribution to the charge freezing may also result from full-shell ionisation potential “plateaus” (a large change in ionisation potential from He-like Al<sup>11+</sup> to H-like Al<sup>12+</sup>), comparable to the steady-state case, where the average charge versus temperature plot flattens (Section 3.2.6).

Figure 4.9 shows Medusa output for velocity, electron density, electron temperature, and average charge versus time at the plasma edge for the fifth last, third last, and last cell of the Lagrangian mesh (1.8, 2.0, and 2.3 mm). (The temperature profile is almost identical for these cells and is shown at 0.41 (350th cell), 0.76 (360th cell), and 2.3 mm (last cell).) Note that the temperature (and average charge) increases as a function of depth in the plasma as time increases, highlighting the heating at the ablation front with laser pulse absorption.



**Figure 4.9** Medusa output versus time for aluminium reference case at 1.8, 2.0, and 2.3 mm ( $v$ ,  $n_e$ ,  $T_e$ ,  $\langle z \rangle$ )

### 4.1.2.3 Spatial-temporal ion distributions

Spatial and temporal plots of ion density are shown below for the reference aluminium case. Figure 4.10 shows the ion density versus distance for all 13 aluminium ions (and the neutral atom) at the peak of the pulse. Note that the dominant ion stage during loading is fully stripped  $\text{Al}^{13+}$  until about  $500 \mu\text{m}$ . Because of the large laser power density ( $4 \times 10^{14} \text{ W/cm}^2$ ), only  $\text{Al}^{11+}$ ,  $\text{Al}^{12+}$ , and  $\text{Al}^{13+}$  are present in any appreciable amounts.

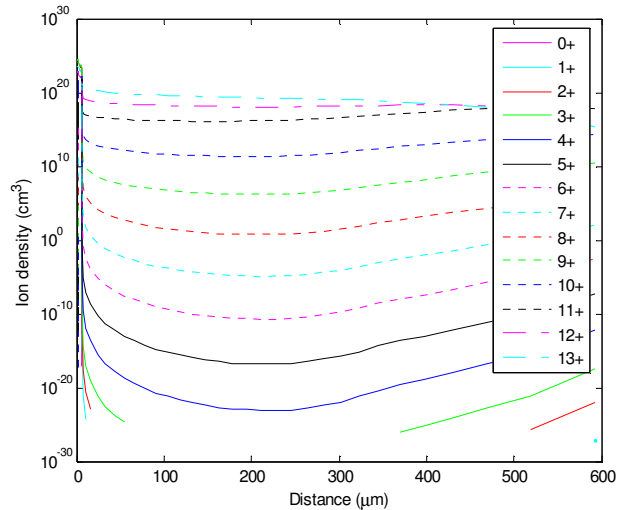


Figure 4.10 Al ion number densities at peak of pulse (Al I to Al XIV)

Figure 4.11 (left) shows the fractional ion density temporal evolution of a single ion (H-like  $\text{Al}^{12+}$ ) plotted at equal time intervals (red dashed is before the peak, solid black at the peak, and dotted blue after the peak) to  $1000 \mu\text{m}$ . Figure 4.11 (right) shows the same for fully stripped  $\text{Al}^{13+}$ . Note that, at the peak of the pulse (solid black), the plasma cools from fully stripped to H-like aluminium at about  $500 \mu\text{m}$ . The plasma is being heated from the outside in as the Al XIII ions move out from the ablation front. Note that at any time and space in the plasma, the sum of the fractional ion densities equals one.

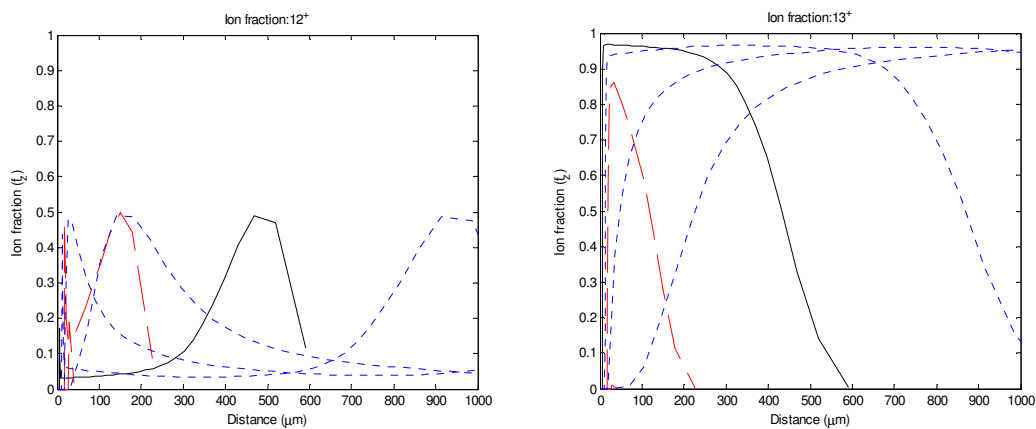
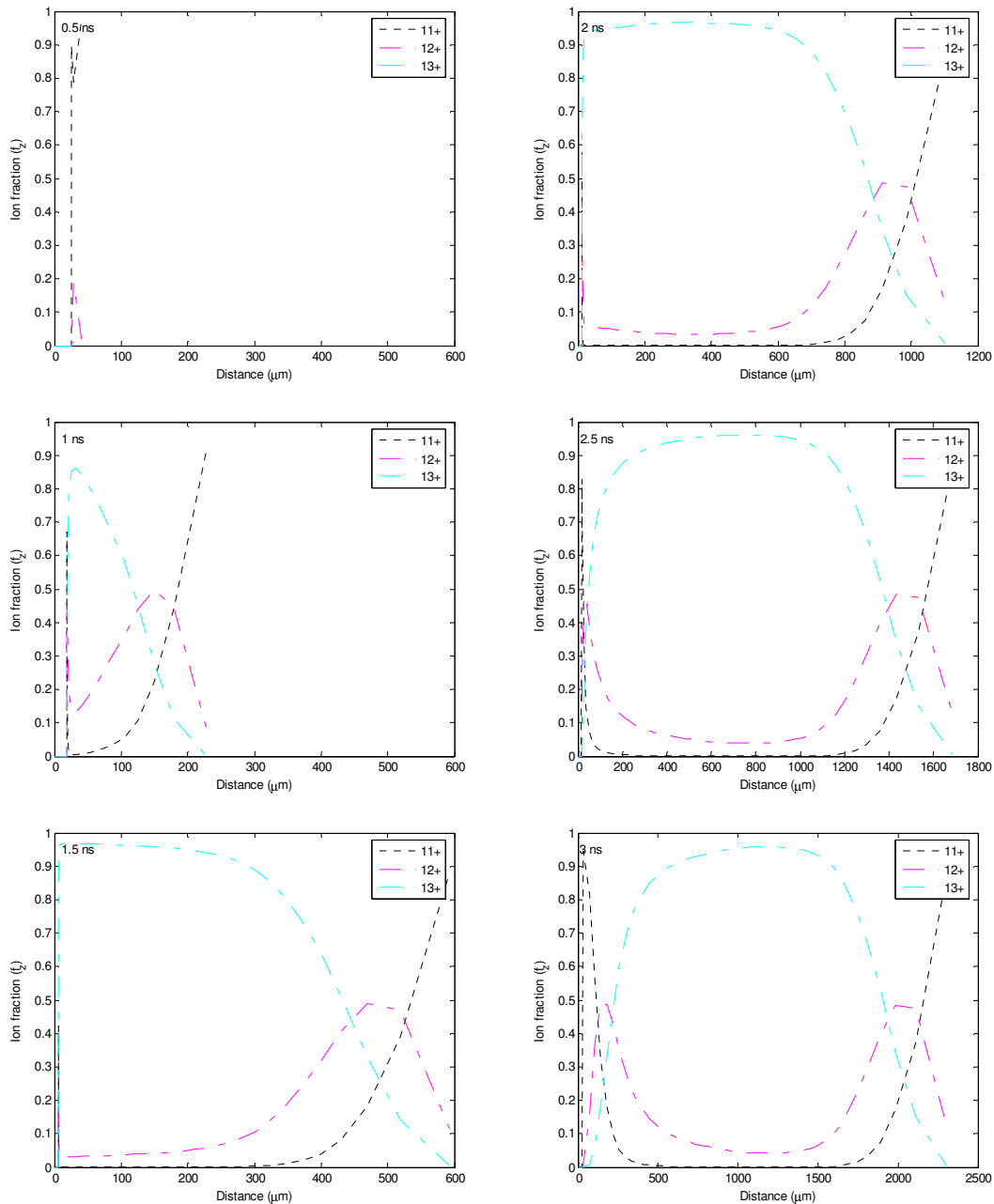


Figure 4.11 Al XIII (left) and Al XIV (right) fractional ion densities at 0.5, 1.0, 1.5, 2.0, 2.5, and 3.0 ns

Figure 4.12 shows the ion fraction for  $\text{Al}^{11+}$ ,  $\text{Al}^{12+}$ , and  $\text{Al}^{13+}$  on the same plot at the six times (0.5, 1.0, 1.5, 2.0, 2.5, and 3.0 ns).

Here the temporal evolution of hydrogenic and fully stripped aluminium is more easily seen as the plasma expands (note the change in distance scale after the peak of the pulse). For radiation transport modelling, the emission from Al XIII (1s-2p) will be calculated over all times (Section 4.3).



**Figure 4.12** Al XII to Al XIV ion densities at 0.5, 1.0, 1.5, 2.0, 2.5, and 3.0 ns

A surface plot shows the ion distribution for Al XII, Al XIII, and Al XIV versus time and space (Figure 4.13). The same surface plot versus cell number instead of cell distance for Al XIII shows that only the outer cells ( $\sim 10$ ) ultimately contribute to the simulation (Figure 4.14). With such high velocities, the outer cells show the most expansion in a Lagrangian mesh, with resultant decreased density.

The corresponding temperature profile at the six times is shown (Figure 4.15). In Figure 4.16, the non-LTE behaviour of the plasma is seen, where a one-temperature model overestimates the ion temperature ( $T_e$  not equal to  $T_i$ ) [9]. At the greatest electron temperature,  $T_e$  is  $\sim 2.5 T_i$ .

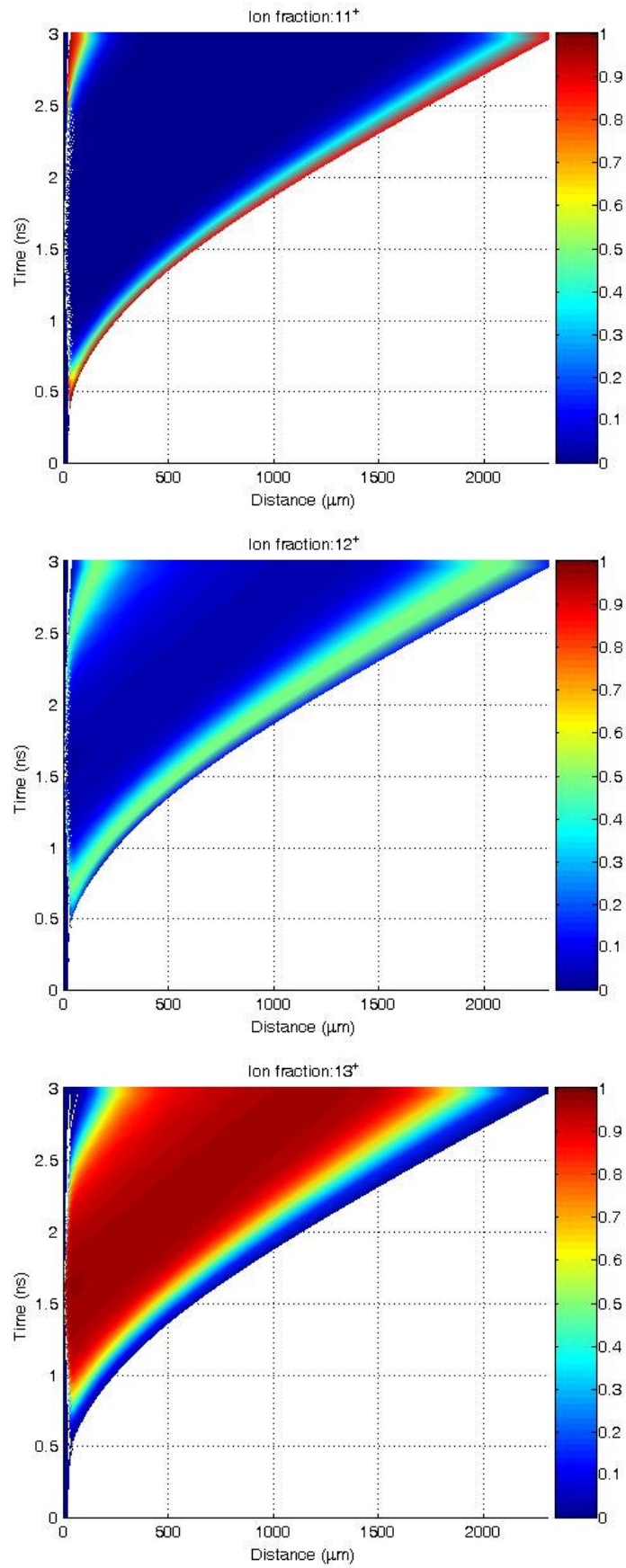
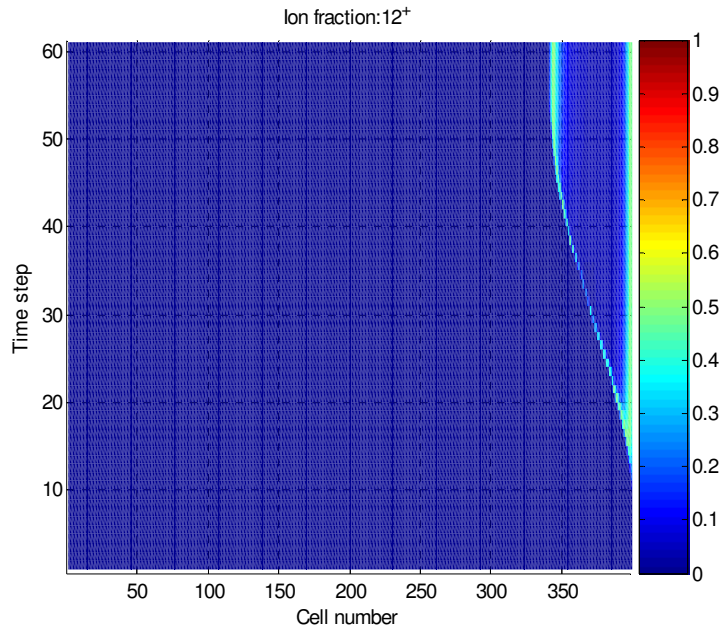
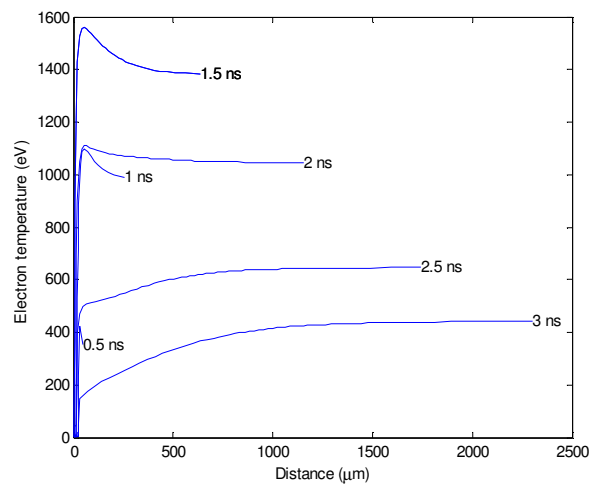


Figure 4.13 Al XII, Al XIII, and Al XIV ion fraction versus time and distance



**Figure 4.14** Al XIII ion fraction versus time and cell number



**Figure 4.15** Aluminium electron temperature profile at 1.0, 1.5, 2.0, 2.5 , and 3.0 ns

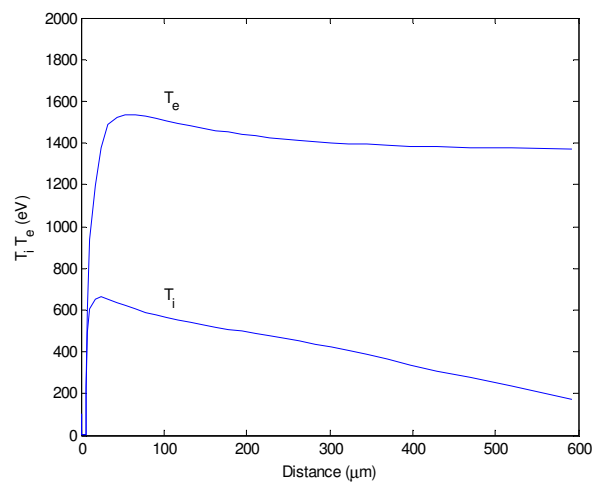


**Figure 4.16** Aluminium electron and ion temperature at the peak of the pulse (1.5 ns)

#### 4.1.2.4 Medusa mesh size

Hydrodynamic results can depend on the number of cells used in a simulation. It is not a simple matter to determine the optimal mesh size. The maximum mesh size is ultimately determined by the available computer RAM, but simulation time will also increase dramatically with an increased number of cells (MESH).

The effect of mesh size on the hydrodynamic variables for three mesh sizes (60, 400, 1000) is shown below for electron temperature and average charge versus distance (at the peak of the pulse). Calculation times increased 7 fold from MESH = 60 to 400 and 4 fold from 400 to 1000.<sup>50</sup> Note that a small mesh size (60) produces a lower electron temperature and significantly smaller expansion (bigger cells are harder to heat). Here it can be seen that a mesh size of 400 is comparable to that of 1000 with considerable savings in computation time. A logarithmic mesh, giving finer detail at the surface, can also be used.

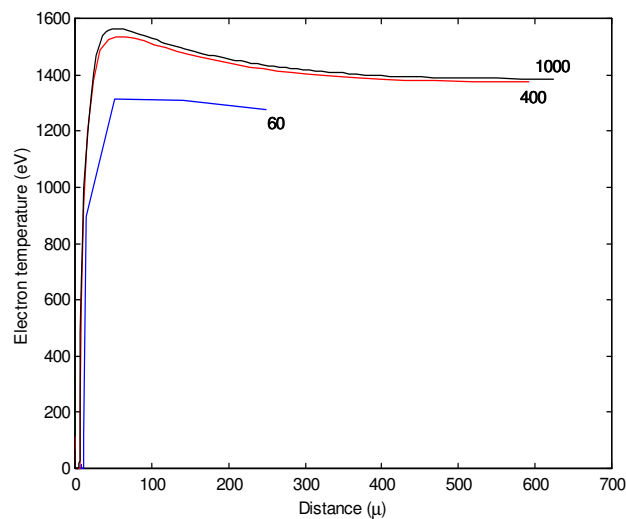


Figure 4.17 Electron temperature versus distance for three mesh sizes (60, 400, 1000)

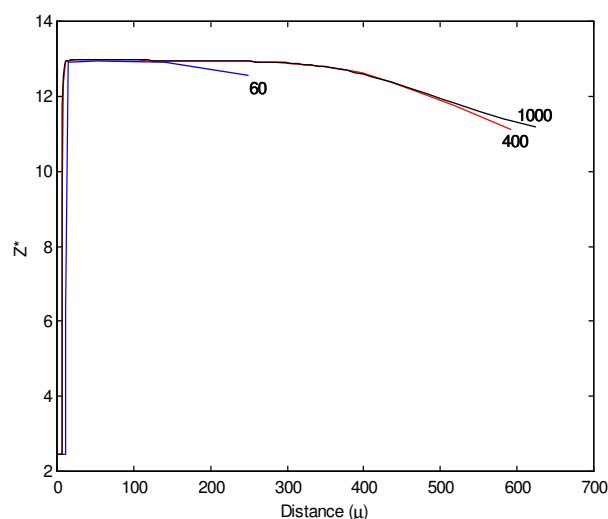


Figure 4.18 Average charge versus distance for three mesh sizes (60, 400, 1000)

<sup>50</sup> For a 2.5 GHz, 1 GB RAM, Pentium IV processor, Med103 compiled with Force 2.0 and run in cygwin Linux emulator for Windows, mesh size = 1000 = 85 minutes (real time).

### 4.1.3 Other LPP hydrodynamics

The two-dimensional hydrodynamic code LASNEX was originally developed at Lawrence Livermore National Laboratory in the 1970s to model laser fusion and has been adapted to model laser-produced plasmas [19]. Some general results are shown here to illustrate two-dimensional effects in a laser-produced plasma.

Simulation results for a  $10^{11}$  W/cm<sup>2</sup>, 1.06  $\mu$ m, 13-ns (FWHM) Nd:YAG pulse incident on a solid planar copper target are shown in Figure 4.19 [20], where two high density lobes and an on-axis density depression are seen. Strong pressure gradients drive lateral expansion and the laterally moving material cools rapidly and slows down. The build-up of density from radiative heating and thermal conduction forms the side lobes and the on-axis density depression. The spatial distribution is shown at 3, 6, 9, and 12 ns [20]. The laser is incident from the right.

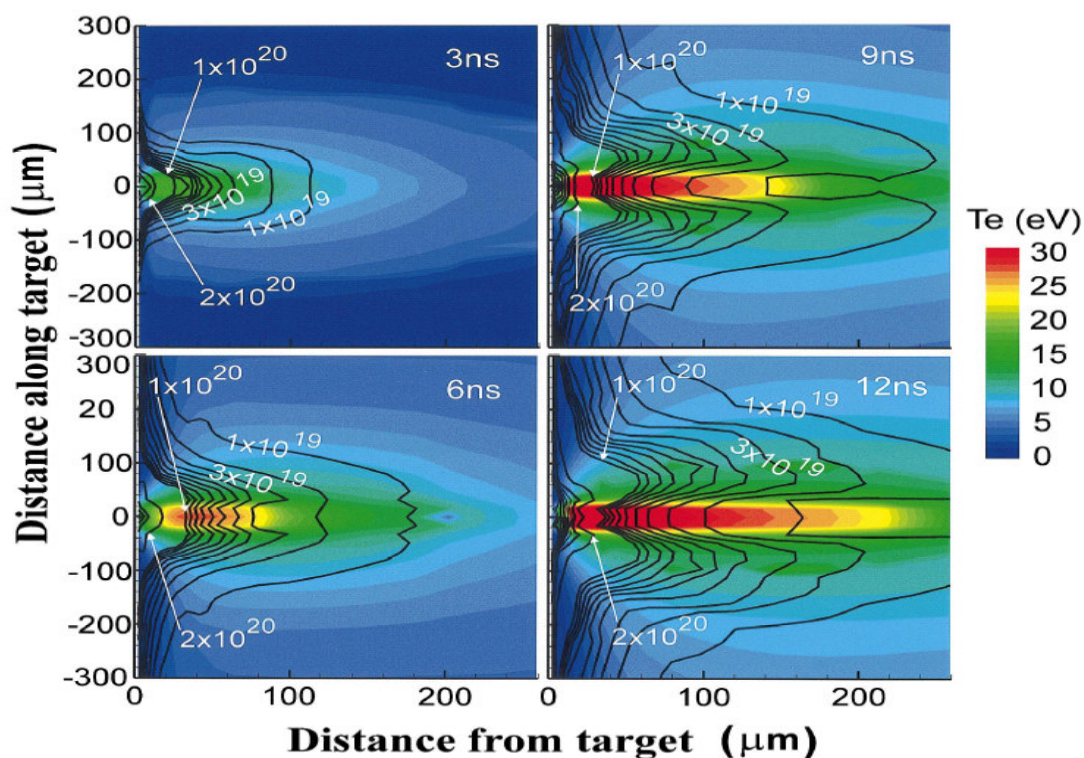


Figure 4.19 Electron density (line contours) and temperature (colour) profiles from LASNEX for a  $10^{11}$  W/cm<sup>2</sup>, 1.06  $\mu$ m, 13-ns pulse, Cu target [20]

Note that the temperature is hottest along the laser axis, and thus lower ions are found in the plasma at the edge in 2-D slab targets (though not so much in spherical targets). This result is less pronounced for higher atomic number, because of less lateral expansion. Nonetheless, in tin-based targets, absorption by neutral tin and Sn II to Sn IV ions will be greater at  $45^\circ$  than at near normal incidence. The plasma is anisotropic and any experimental spectra will depend on the observation angle. Interferometry, which can be used as a plasma diagnostic to compare electron density as a function of time [21], verifies that the lobe volume increases in time.

Despite the two-dimensional effects caused by the pondermotive force, 1-D codes qualitatively reproduce the central region of plasma expansion [20].

## 4.2 Average atom model

The computational nature of radiation transport modelling requires extensive calculations. To reduce the numerous atomic calculations for coupling to a hydrodynamics code, an average atom model is used, based on a screened hydrogenic model (SHM), where the excited levels are represented by one atom in the rate equations. As stated in Perrot [22], “[SHM models] allow a fast computation of total energy, one-electron energies, ionisation potentials . . . for any ionic configuration.” Reasonable comparisons to Hartree-Fock data can be made. Note, however, that the average atom model can overestimate the binding of the outer levels [22].

The screened hydrogenic model of More [23], modifications by Marchand *et al.* [24], and that used in *Medusa* [1–5] are described below ( $n$  splitting only). To extend the SHM model to include intra-shell energy levels ( $\Delta n = 0$  transitions) for Sn 4d-4f and 4p-4d transitions,  $nl$ -splitting is considered in Perrot [22] and Rickert and Meyer-ter-Vehn [25]. The energy functional method of Itoh *et al.* [26] is discussed and used here to calculate  $\Delta n = 0$  level populations.

### 4.2.1 The screened hydrogenic model ( $n$ splitting)

The screened hydrogenic model was first used by Mayer [27] in 1947 to calculate approximate energy levels within a multi-electron atom and was modified by Lokke and Grassberger [28] in 1977 and by More [23] in 1985. As reported by More [23], “[the] model provides a useful description of atomic ionisation and emission properties which can be adapted to a more complete simulation of plasma dynamics.”

Faussier *et al.* [29] state that, “[the screened hydrogenic model] is based on the independent particle approximation where each bound electron is taken to move in an effective central potential representing the Coulomb interaction with the nucleus and the  $N-1$  other electrons.” From Bohr, the energy levels,  $E_n$ , are given in Eq. 4.6 for a hydrogenic atom as

$$E_n = -E_H \frac{Z^2}{n^2} \text{ [eV]} \quad (4.6)$$

where  $E_H$  is the hydrogen ground state energy (13.6 eV),  $Z$  is the atomic charge, and  $n$  is the principal quantum number. For a given atom or ion, the energy level depends only on  $n$ .

To model multi-electron atoms, the shells are populated with  $P_n \leq 2n^2$  electrons (2, 8, 18, 32, 50, 72 for  $n = 1$  to 6), where  $Z = \Sigma P_n$  in the ground configuration (and  $\langle z \rangle = Z - \Sigma P_n$ ), where  $\langle z \rangle$  is the average charge state. The energy levels are also described by the Bohr model, but with a reduced (or effective) atomic number,  $Z_n$ , to account for electron screening at each level [23]. Eq. 4.6, thus, becomes:

$$E_n = -E_H \frac{Z_n^2}{n^2} \text{ [eV]} \quad (4.7)$$

and the potential energy is given as

$$V(r) = -\frac{Z_n e}{r} \quad (4.8)$$

where

$$Z_n = Z - \frac{1}{2}\sigma(n,n)P_n - \sum_{m<n}\sigma(n,m)P_m \quad (4.9)$$

$\sigma$  is the screening factor (*a.k.a.* constant or coefficient), determined from Scofield's least-squares linear fit over a large number of Hartree-Fock calculated potentials (800 ionisation potentials for 30 elements [24]).  $P_m$  is the population of level  $m$ , and is assumed to lie inside the  $n$ th level, for which the screening is determined. The screening factors ( $n = 1$  to 10 levels) from More [23] are reproduced in Table 4.3 below (note that both inner and outer shell screening is given).

$m \backslash n$	1	2	3	4	5	6	7	8	9	10
1	0.3125	0.9380	0.9840	0.9954	0.9970	0.9970	0.9990	0.9999	0.9999	0.9999
2	0.2345	0.6038	0.9040	0.9722	0.9979	0.9880	0.9900	0.9990	0.9999	0.9999
3	0.1093	0.4018	0.6800	0.9155	0.9796	0.9820	0.9860	0.9900	0.9920	0.9999
4	0.0622	0.2430	0.5150	0.7100	0.9200	0.9600	0.9750	0.9830	0.9860	0.9900
5	0.0399	0.1597	0.3527	0.5888	0.7320	0.8300	0.9000	0.9500	0.9700	0.9800
6	0.0277	0.1098	0.2455	0.4267	0.5764	0.7248	0.8300	0.9000	0.9500	0.9700
7	0.0204	0.0808	0.1811	0.3184	0.4592	0.6098	0.7374	0.8300	0.9000	0.9500
8	0.0156	0.0624	0.1392	0.2457	0.3711	0.5062	0.6355	0.7441	0.8300	0.9000
9	0.0123	0.0493	0.1102	0.1948	0.2994	0.4222	0.5444	0.6558	0.7553	0.8300
10	0.0100	0.0400	0.0900	0.1584	0.2450	0.3492	0.4655	0.5760	0.6723	0.7612

**Table 4.3** More's screening factors  $\sigma(n,m)$  [22]

The screening factors are more accurate for highly ionised than nearly neutral atoms [23]. In Eq. 4.9, the nuclear charge is reduced by two terms: screening by same-shell electrons ( $n,n$ ) and screening by the sum of all inner-shell electrons ( $m < n$ ). The ionisation energy is the energy of the outermost occupied energy level and the total energy of the atom or ion is given by:

$$E_{tot} = \sum_n E_n P_n \quad (4.10)$$

The energy levels,  $\epsilon_n$ , satisfy Koopman's theorem [23], such that

$$\epsilon_n = \frac{\partial E_{tot}}{\partial P_n} = -E_H \frac{Z_n^2}{n^2} + E_H \frac{Z_n}{n^2} \sigma(n,n)P_n + 2E_H \sum_{m>n} \frac{Z_m}{m^2} \sigma(m,n)P_m \quad (4.11)$$

Marchand *et al.* [24] calculated improved screening factors over a larger distribution of ionisation and excitation stages, which minimised the maximum relative error instead of using Scofield's least squares fit. Experimental data was used wherever possible. Their screening factors for  $n = 1$  to 5 are shown in Table 4.4. Marchand *et al.* reported that their improved screening factors produce less relative error than More's for all  $Z$  except  $42 \leq Z \leq 65$ , where the error is practically the same [24].

$m \backslash n$	1	2	3	4	5
1	0.5966	0.8597	0.9923	0.9800	0.9725
2		0.6888	0.8877	0.9640	1.0000
3			0.7322	0.9415	0.9897
4				0.6986	0.8590
5					0.8502

**Table 4.4** Marchand *et al.*'s screening factors  $\sigma(n,m)$  [24]

$Z_n$  is given in Eq. 4.12, where the only difference to Eq. 4.9 is that the maximum of 0 and  $P_n - 1$  is used instead of  $P_n$  to insure exact energy levels for truly hydrogenic ions (*e.g.*, no self-screening in the  $n = 1$  shell, where  $Z_n = Z$ ). Self-screening is significant for H-like (5%) and Li-like (30%), but of little consequence otherwise [24].

$$Z_n = Z - \frac{1}{2} \sigma(n, n) \max(0, P_n - 1) - \sum_{m < n} \sigma(n, m) P_m \quad (4.12)$$

The matrix elements in Tables 4.3 and 4.4 are smooth monotone functions of  $m$  and  $n$ , reflecting a greater screening with increasing shells; *e.g.*,  $\sigma(2,1) = .8597$  is the screening factor for the L shell by the K shell and  $\sigma(3,1) = .9923$  for the M shell by the K shell. More's data obeys the symmetry property  $n^2 \sigma(n, m) = m^2 \sigma(m, n)$ .

Note that subshell ( $nl$ ) splitting from quantum defects and spin-orbit interaction is not included. Without subshell splitting,  $\Delta n = 0$  transitions cannot be calculated. Excitation energies (for low  $Z$  elements) and neutral atom K and L edges, however, can be predicted, although large error exists in some excitation energies [24]. For improved accuracy, Perrot [22] and Rickert and Meyer-ter-Vehn [25] include  $l$  splitting as does Faussier *et al.* [29], who also calculate screening factors from a database of 15,636 data points. A subshell  $nl$ -splitting model is briefly described in Section 4.2.3.

General descriptions of the screened hydrogenic model are given in Eidmann [6] and Salzmann [30]. Eidmann also includes an estimate of continuum lowering.

Using the screened hydrogenic model (SHM), implemented for this thesis in Matlab, ionisation potentials versus atomic number for  $Z = 1$  to 29 are shown in Figure 4.20. Note that More uses a regular electronic configuration (essentially, the *aufbau* principle) to populate shells (*e.g.*,  $P_n = 2, 8, 9$  instead of 2, 8, 8, 1 for potassium) [23], and thus greatly over predicts the N shell atoms ( $Z = 19$  to 30). Marchand *et al.*'s modified screening factors fit the K, L, and M shells better, but do not match the N shell. A non-regular building up is a better match, but under predicts the N shell. The experimental data is from the *CRC Handbook* [31].

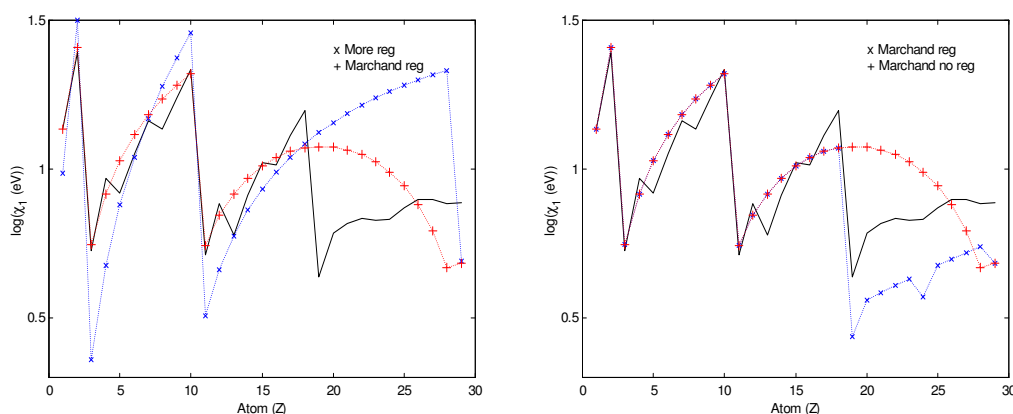


Figure 4.20 SHM ionisation potentials as defined in [23],  $Z = 1$  to 29

Ionisation potentials for gold (Table 4.5) and effective  $Z$  values for iron (Fe XV) at 200 eV (Table 4.6) are shown, which match the results reported in [24] to a good approximation. The SHM results are given using methods from both More [23] and Marchand *et al.* [24].

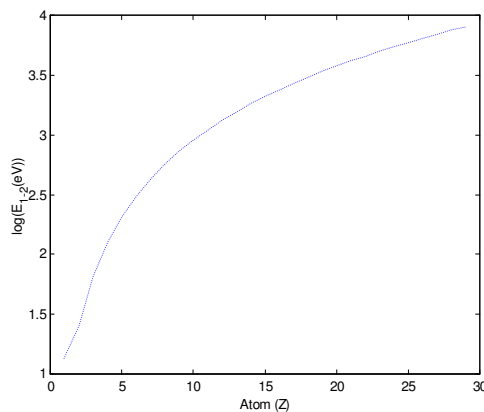
Ion stage	Cowan [32]	More [22]	SHM [22]	SHM [23]
0	9.2	13.4	14.9	7.0
1	20.5	23.0	24.4	18.6
2	32.3	33.1	34.4	30.9
3	46.2	43.6	44.8	43.7
4	61.1	54.6	55.6	57.1

Table 4.5 Au ionisation data (eV), Au I–V

Energy level	More [22]	SHM [22]	SHM [23]
K shell	25.7	25.7	25.7
L shell	21.9	21.7	21.9
M shell	16.7	16.5	16.9
N shell	15.3	15.3	15.4

Table 4.6 Fe XV effective Z data for  $Z_I$ – $Z_4$ 

1s-2p He-like transitions are shown in Figure 4.21 for atomic number 1 to 29, which match the experimental data given in [24] almost exactly. Calculated energy level values for Sn V to Sn XIV are given in Table 4.7 with the average Hartree-Fock values from Cowan [32] (see Chapter 2). Because of the hydrogenic SHM nature, the SHM  $E_4$  compares well to the Hartree-Fock  $E_{4s}$ , but less so for the higher  $4l$  levels. Figures 4.22a–c show the effective charge, energy levels versus ion (occupied levels only), and ionisation potential for aluminium. Figures 4.23a–c show the same for tin. Note that in Figures 4.22a and 4.23a  $Z_{eff}$  changes little beyond  $n = 6$ . The ionisation values (in Figures 4.21c and 4.22c) compare almost exactly with the CRC data [31].

Figure 4.21  $1s^2$ - $1s2p$  transitions for  $Z = 1$  to 29 (using SHM)

Ion stage	Hartree Fock (eV)					SHM (eV)	
	$E_{4s}$	$E_{4p}$	$E_{4d}$	$E_{4f}$	$E_{5p}$	$E_4$	$E_5$
Sn VI	230	178	103	37	56	242	25
Sn VII	249	197	122	53	69	262	32
Sn VIII	269	218	143	69	83	282	40
Sn IX	292	239	165	88	98	301	49
Sn X	314	261	186	108	113	321	59
Sn XI	339	284	209	131	129	340	70
Sn XII	363	309	234	152	147	359	82
Sn XIII	389	333	258	177	165	378	95
Sn XIV	415	359	--	200	182	395	108

Table 4.7 Tin energy level data, Sn VI–XVI

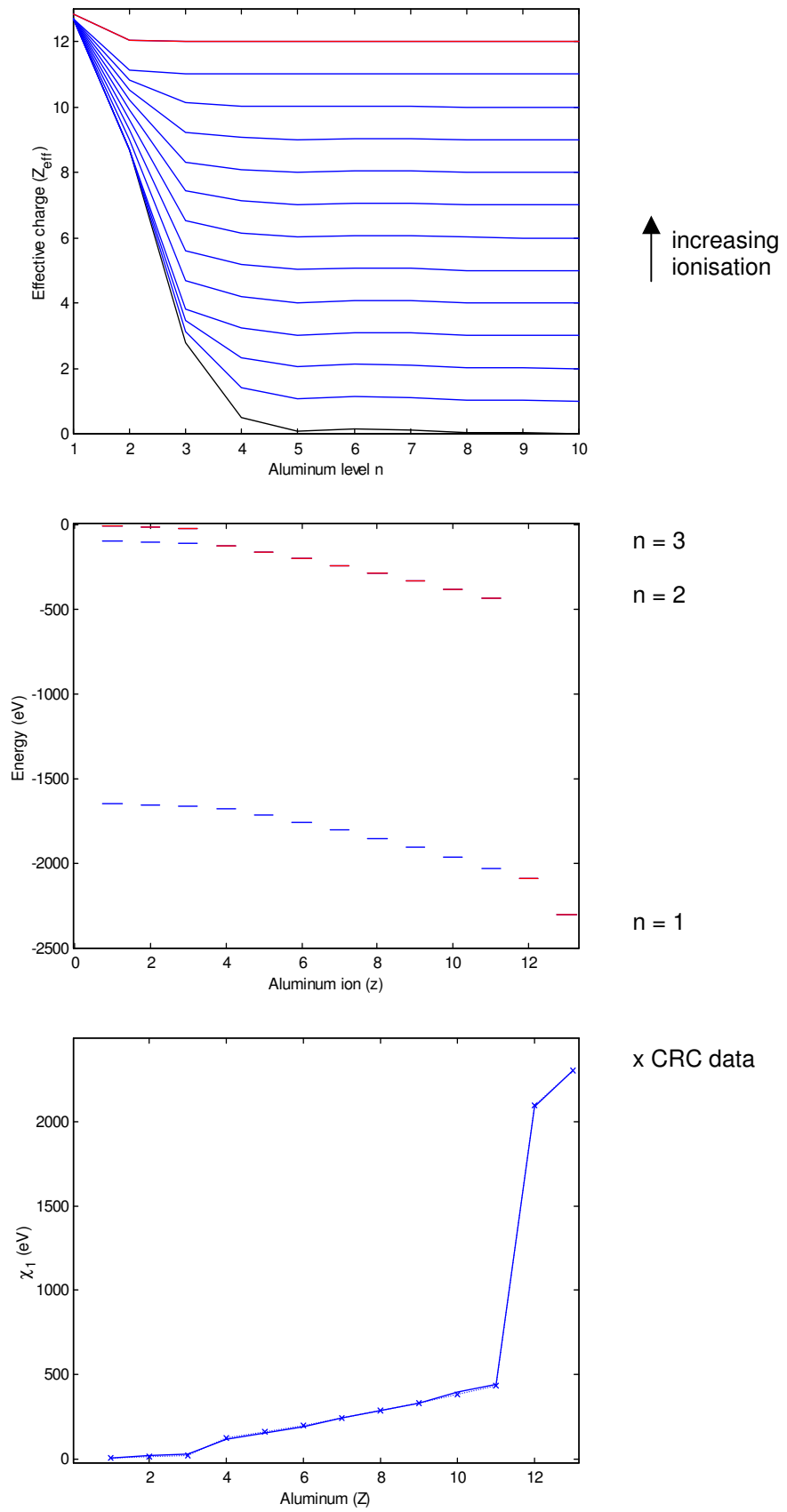


Figure 4.22a-c Aluminium effective charge, energy levels, and ionisation potential

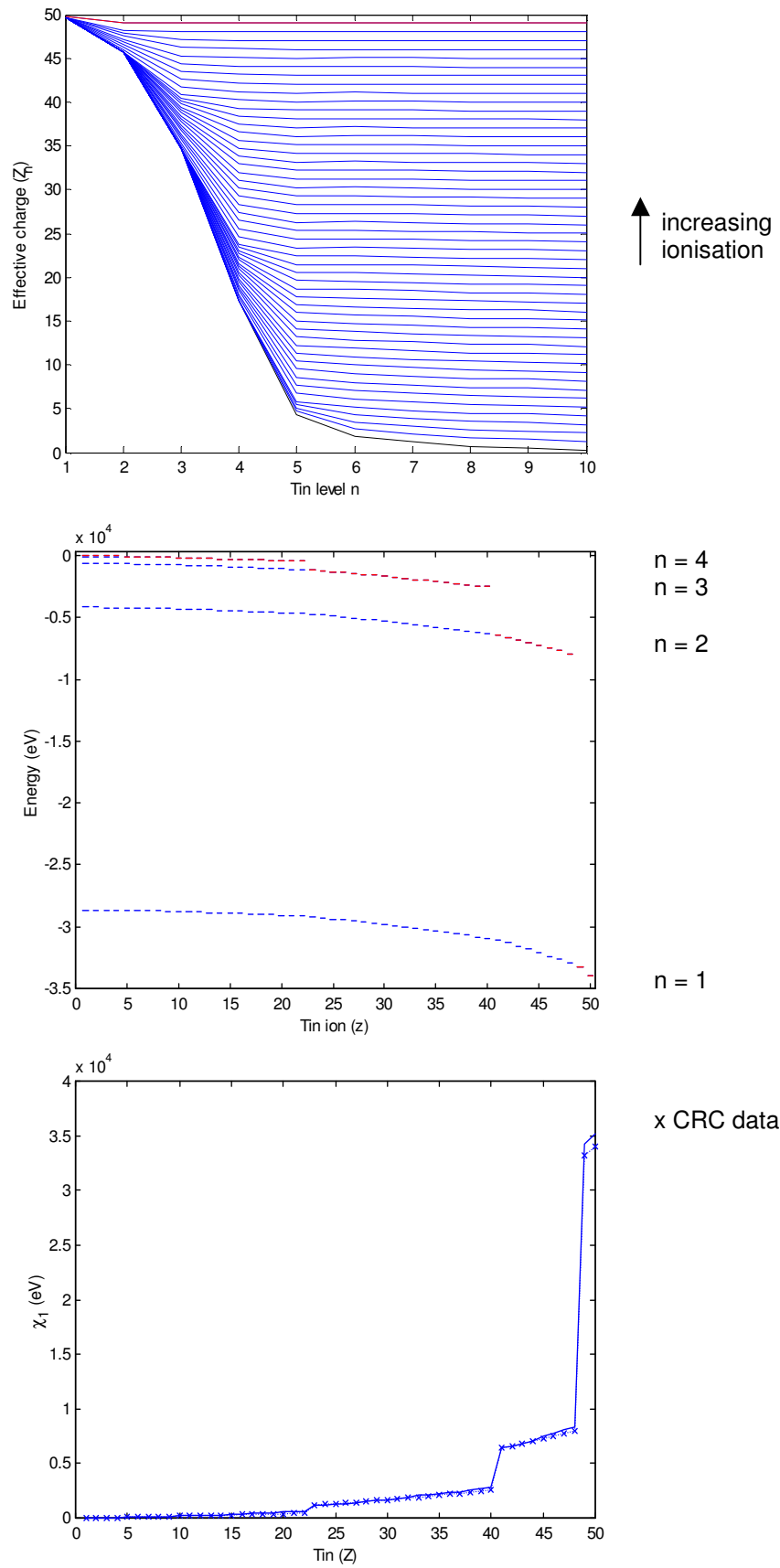


Figure 4.23a-c Tin effective charge, energy levels, and ionisation potential

### 4.2.2 The average atom model (Medusa)

Medusa uses a similar screened hydrogenic model as described above, where Eq. 4.13 gives the effective charge and Eq. 4.14 the energy levels [33]. The energy levels include relativistic corrections. The screening factors used in Medusa [1–5] are shown in Table 4.8, which are essentially those of More with minor differences. Note that Medusa includes outer electron screening ( $m > n$ ) as well as inner electron screening ( $m < n$ ) directly in Eq. 4.13 (from  $m \neq n$ ) ( $\alpha =$  fine structure constant).

$$Z_{eff} = Z - \sigma(n,n)P_n \left(1 - \frac{1}{2n^2}\right) - \sum_{m \neq n} \sigma(n,m)P_m \quad (4.13)$$

$$E_n = E_H \frac{Z_n^2}{n^2} \left[ 1 + \frac{(\alpha Z_n)^2}{2n} \left(1 - \frac{1}{2n}\right) \right] \text{ [eV]} \quad (4.14)$$

$m \backslash n$	1	2	3	4	5	6	7	8	9	10
1	0.6250	0.9380	0.9810	0.9870	0.9940	0.9970	0.9990	1.0000	1.0000	1.0000
2	0.2350	0.6900	0.8930	0.9400	0.9700	0.9840	0.9900	0.9930	0.9950	1.0000
3	0.1090	0.3970	0.7020	0.8500	0.9200	0.9550	0.9700	0.9800	0.9900	1.0000
4	0.0617	0.2350	0.4780	0.7050	0.8300	0.9000	0.9500	0.9700	0.9800	0.9900
5	0.0398	0.1550	0.3310	0.5310	0.7200	0.8300	0.9000	0.9500	0.9700	0.9800
6	0.0277	0.1090	0.2390	0.4000	0.4800	0.7350	0.8300	0.9000	0.9500	0.9700
7	0.0204	0.0808	0.1780	0.3100	0.4590	0.6100	0.7450	0.8300	0.9000	0.9500
8	0.0156	0.0625	0.1380	0.2430	0.3710	0.5060	0.6350	0.7500	0.8300	0.9000
9	0.0123	0.0494	0.1110	0.1940	0.2990	0.4310	0.5440	0.6560	0.7000	0.8300
10	0.0100	0.0400	0.0900	0.1580	0.2450	0.3530	0.4600	0.5760	0.6700	0.7650

Table 4.8 Medusa screening factors  $\sigma(n,m)$  BLOCKDATA bdat:sig(10,10) [1–5]

The SHM calculated ionisation potentials using Eq. 4.13 and Eq. 4.14 are shown in Figure 4.24. Note that the N shell is much better approximated in Medusa than in both [23] and [24].

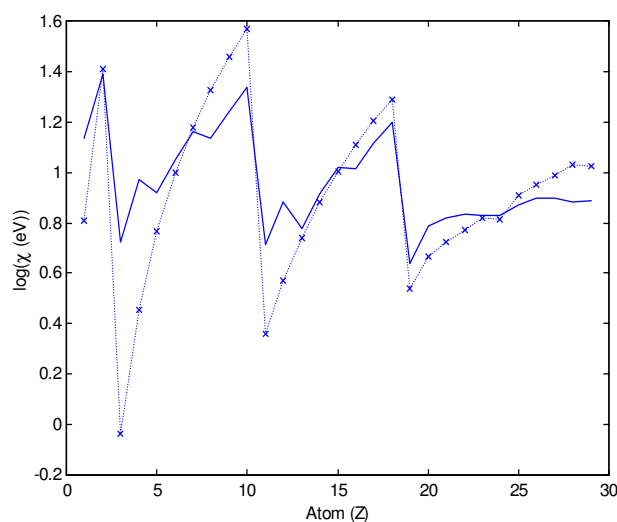


Figure 4.24 SHM ionisation potentials as defined in [31],  $Z = 1$  to 29

In conjunction with the screened hydrogenic model, **Medusa** uses the average atom model, where level populations are calculated for a single ‘fictitious’ atom in the plasma from the rate equations for the average atom [33]. The fractional level populations,  $f(C)$ , for an ion can then be calculated for any configuration from Eq. 4.15 [33, Eq. 18].

$$f(C) = \prod_{n=1}^{n_{\max}} \left[ \frac{P_n}{2n^2} \right]^{k_n} \frac{2n^2!}{(2n^2 - k_n)! k_n!} \left[ 1 - \frac{P_n}{2n^2} \right]^{2n^2 - k_n} \quad (4.15)$$

$P_n$  is calculated in **Medusa** using the time-dependent non-LTE rate equations, where  $P_n$  is the level population (not necessarily integer) of the  $n$ th shell in the average atom and  $k_n$  is the integer occupation number in the configuration  $C = [k_1, k_2, \dots, k_n]$ . As stated in [33], “the first term in the product represents the probability that  $k_n$  electrons occupy level  $n$ , the second term is the number of ways of arranging  $k_n$  (indistinguishable) electrons in level  $n$  of degeneracy  $2n^2$ , the third term is the probability that  $2n^2 - k_n$  vacancies exist in level  $n$ .” As stated in [34], “the factor  $1 - P_n/2n^2$  represents the probability that  $n$  is empty.” All  $\Delta n = 0$  levels are assumed statistically equilibrated [10, 11, 35], which is valid at high densities, but increasingly inaccurate at lower densities [35].

For hydrogenic  $\text{Al}^{12+}$ , there is only one electron and thus  $C_i = [1\ 0\ 0\ 0\ 0\ 0]$  for the ground state  $i$  (K shell occupancy = 1),  $C_j = [0\ 1\ 0\ 0\ 0\ 0]$  for the first excited state  $j$  (L shell occupancy = 1), and  $C_j = [0\ 0\ 1\ 0\ 0\ 0]$  for the second excited state  $j$  (M shell occupancy = 1), *etc.*

In the average atom model, the level populations (or electron occupation numbers) can be non-integer (for example, as shown in Table 4.9 for aluminium). Table 4.9 shows the level populations,  $P_n$ , and fractional populations,  $f(C)$ , for each level at 100  $\mu\text{m}$  and at the edge of the plasma (at the peak of the pulse), for  $n = 1$  to 6. From Table 4.9, it can be seen that the target is not as ionised at 600  $\mu\text{m}$  (peak of pulse) as the lower  $\langle z \rangle$  indicates, which is primarily because of the more occupied  $n = 1$  shell (larger  $P_1$ , and thus larger  $f(C)$ ).

Level ( $n$ )	$C$	100 $\mu\text{m}$		600 $\mu\text{m}$	
		$P_n$	$f(C)$	$P_n$	$f(C)$
1	[1 0 0 0 0 0]	.03547	0.0348	1.87590	0.116
2	[0 1 0 0 0 0]	.00004	3.858e-005	0.00031	1.193e-006
3	[0 0 1 0 0 0]	.00003	2.894e-005	0.00003	1.155e-007
4	[0 0 0 1 0 0]	.00006	5.787e-005	0.00002	7.697e-008
5	[0 0 0 0 1 0]	.00009	8.681e-005	0.00002	7.697e-008
6	[0 0 0 0 0 1]	.00013	1.254e-004	0.00003	1.155e-007
$\langle z \rangle$ or $\Sigma f(C)$		12.964	0.035138	11.124	0.116002

**Table 4.9** Aluminium average atom level populations ( $n = 1$  to 6) at 100  $\mu\text{m}$  and edge (peak of pulse)

Figure 4.25a shows the hydrogen-like level populations (for  $n = 1$  to 6) as a function of distance at the peak of the pulse, which are almost identical to the results given in [11] for  $n = 1$  and  $n = 2$ .<sup>51</sup> Note that the  $n = 3, 4,$  and  $5$  populations exceed that of the  $n = 2$  populations to about 400  $\mu\text{m}$ , reflecting the increased ionisation (see Figure 4.8).

<sup>51</sup> The format accuracy in **Medusa** was changed in the code to include populations  $< 10^{-5}$ .

Figure 4.25b gives the same for  $n = 1$  and  $n = 2$  at four times in the plasma (1.0, 1.5, 2.0, and 2.5 ns), from which the population number densities will be calculated for radiation transport modelling. (The energy functional method can also be used as discussed in Section 4.2.4.)

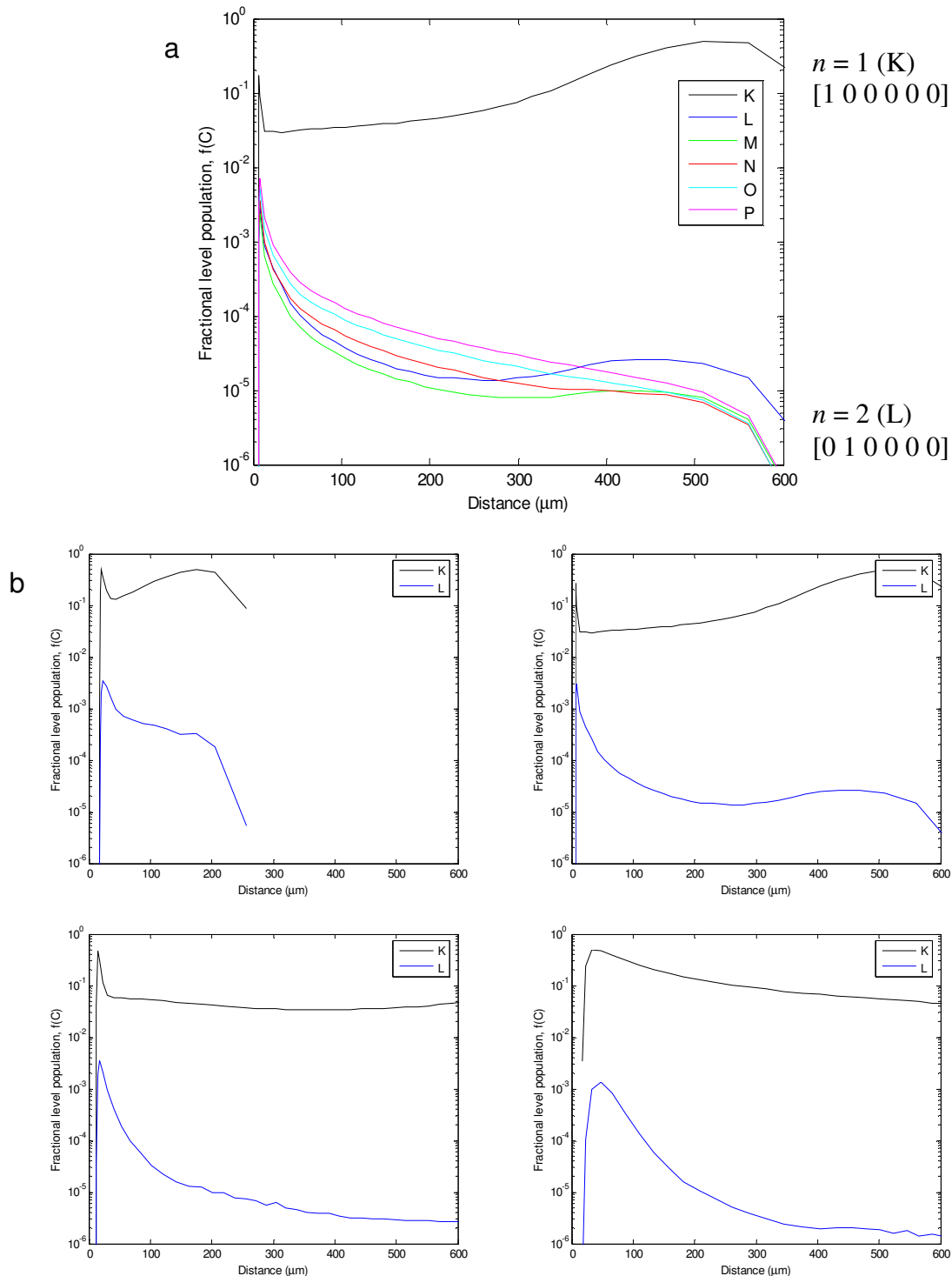


**Figure 4.25** Hydrogenic aluminium level populations a) ( $n = 1$  to 6) versus distance (peak of pulse, 1.5 ns) and b) ( $n = 1$  to 2) versus distance (1.0, 1.5, 2.0, and 2.5 ns)

### 4.2.3 The screened hydrogenic model ( $nl$ subshell splitting)

More's model [23] was derived intuitively from the idea of inner and outer screening. The screened hydrogenic model can also be derived from variational properties of the total energy, by neglecting  $l$ -splitting (average density) and letting the screening functions equal constants [22]. First order perturbation of the total energy as in Perrot [22, Eq. 19] gives  $l$ -splitting, although an adjustment of some screening parameters is also required to match results [22].

In  $nl$ -splitting, energy levels with orbital angular momentum quantum number  $l$  are calculated. In addition, better opacity tables can be calculated for hydrodynamics simulations.  $l$ -splitting can give significant differences in  $nl$  energy levels for  $\Delta n = 0$  configurations, *e.g.*, as large as 500 eV between the 4f and 4s levels in neutral gold [36]. Note that for  $nl$ -splitting, the occupation number is  $P_{nl}$  (*e.g.*, for neon or neon-like ions,  $P_{10} = 2$ ,  $P_{20} = 2$ ,  $P_{21} = 6$ , . . .) instead of  $P_n$  (2, 8, . . .).

Figure 4.26 (right) shows the results of  $nl$ -splitting for aluminium, using the screened hydrogenic model of Perrot [22]. The  $l$ -degenerate model of More [23] is shown for comparison (left).

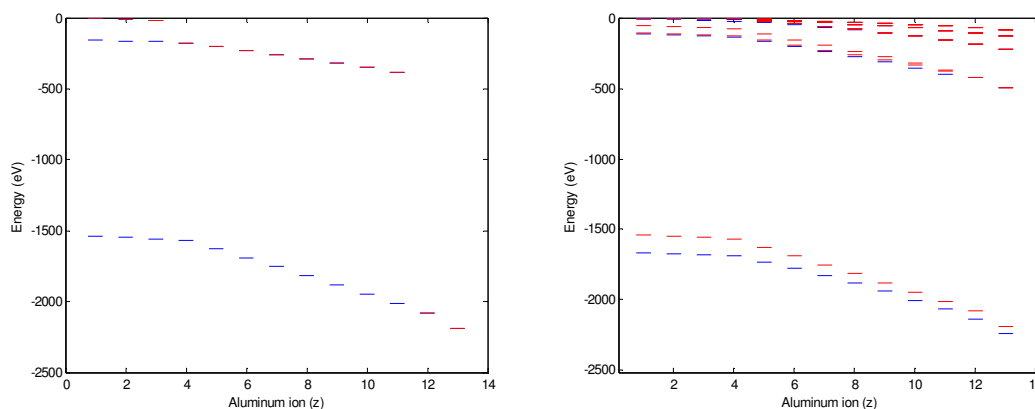


**Figure 4.26** SHM aluminium energy levels:  $l$ -degenerate [23] (left) and  $nl$ -splitting [22] (right)

Perrot [22] comments that for  $10 < Z < 60$ , “the accuracy [of the  $nl$ -splitting screened hydrogenic model] remains better than 1.2%, but approaches that of the  $l$ -degenerate model, because the “splitting-energy” is a decreasing fraction of the difference between the Hartree-Fock and SHM energies.” The accuracy could be improved by optimising the screening factors. However, Scofield’s data is not available as noted in [22].

As discussed in the next section, the energy functional method of Itoh *et al.* [26] is used to determine level populations for  $\Delta n = 0$  configurations (*e.g.*, for the Sn 4d-4f and 4p-4d UTA). However, it may be possible in future to incorporate an  $nl$ -splitting model directly in *Medusa* to calculate the level populations for  $\Delta n = 0$  configurations.

#### 4.2.4 The energy functional, $Y_a(E_n)$ versus $E_n$

To calculate the  $nl$  level populations of an ion, the average atom energy functional form of the reduced population probability ( $Y_a(E_n)$  versus  $E_n$ ) [26] can be used, rather than explicitly determining levels and their corresponding populations.

The energy functional uses occupation numbers from the average atom model in **Medusa** and the level energies calculated from the  $l$ -degenerate screened hydrogenic model. No changes are required in the hydrodynamics code and results are immediately available for post-processing. As stated in [26], because there are fewer rates to calculate, the results can be coupled to a hydrodynamics code with a significantly reduced computation time. Furthermore, the CR model is impracticable for high- $Z$  plasmas [26].

The reduced population probability,  $Y_a(E_n)$ , is calculated from the average atom occupation numbers,  $P_n$ , and shell degeneracy,  $g_n = 2n^2$  ( $n = 1, 2, n_{max}$ ), as in Eq. 4.16. As stated in [26], because the excited level populations for different charge state ions have common level dynamics, the average atom  $P_n$  can be used to calculate level populations. Note that  $\Sigma P_n$  is the summation taken over all *ionising* shells and that 0 eV is the energy of the ground level [26].  $E_n$  is calculated using the SHM from Eq. 4.14.

$$Y_a(E_n) = \frac{P_n}{g_n \sum_n P_n} \quad (4.16)$$

To compare results given in [26] (where the energy functional was calculated for aluminium for  $T_e = 50$  eV and  $n_i = 10^{20}$  cm $^{-3}$ ), the nearest results in **Medusa** were used ( $T_e = 49.8$  eV and  $n_i = 1.3 \times 10^{21}$  cm $^{-3}$ ) and are shown in Figure 4.27 (non-LTE,  $P_n = \{2, 3.01924, 0.30009, 0.23684, 0.26469, 0.32127\}$ ; LTE,  $P_n = \{2, 3.85272, 0.39649, 0.28545, 0.30479, 0.36086\}$ ). It is seen that from  $n = 2$  onwards, the shells are ionised and therefore  $E = E_n - E_2$  for this particular example. Note that the maximum laser pulse power in the aluminium reference case is too high for an exact comparison. Nonetheless, the energy functional is satisfactorily reproduced for  $n_i \sim 10^{20}$  cm $^{-3}$ , from which any  $n = 2$  shell ion (Al $^{3+}$ -Al $^{10+}$ ;  $2s^N 2p^M$ ) level population can be exponentially interpolated. Figure 4.27 shows both the non-LTE and LTE energy functional for comparison, which compares well with that given in [26].

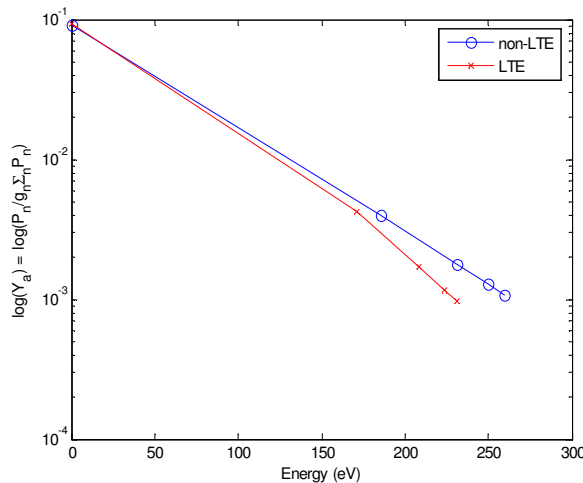


Figure 4.27 Aluminium energy functional (zeroed to  $n = 2$ ) at 49.8 eV,  $n_i = 1.3 \times 10^{21}$  cm $^{-3}$

The average atom energy functional is weighted by the degeneracy ( $g_k$ ) of an ion to get the population probability,  $W_a$ , for a specific ion, either above (less ionised) or below (more ionised) the average atom energy functional. The population probability,  $W_a(E_n)$ , is then given as

$$W_a(E_n) = Y_a g_k \quad (4.17)$$

where  $g_k$  is the level degeneracy  $2J+1$ , where  $J$  is the total angular momentum of the required state for a given ion. (The configuration degeneracy,  $D$ , is used in the UTA model, as seen in Section 4.2.5). For hydrogenic aluminium  $\text{Al}^{12+}$ ,  $g_k(2s_{1/2}) = 2$ ,  $g_k(2p_{1/2}) = 2$ , and  $g_k(2p_{3/2}) = 4$ .

Note that an appropriately zeroed energy functional must be used for the  $n = 1$  shell for the  $\text{Al}^{12+}$   $2p_{1/2}$  and  $2p_{3/2}$  energy levels at 1727 and 1728 eV. A sample interpolation of  $Y_a$  using the energy functional is shown for the  $2p_{3/2}$  level in Figure 4.28. The reduced population probability (non-LTE, peak of pulse, last cell; 1380 eV,  $n_i = 7.6 \times 10^{18} \text{ cm}^{-3}$ ) for the  $2p_{3/2}$  level (1728 eV) is  $9.560 \times 10^{-6}$ . Including the level degeneracy (4), the population probability is thus  $3.82 \times 10^{-5}$ . (For the  $2p_{1/2}$  level (1727 eV),  $Y_a = 9.750 \times 10^{-6}$ ,  $g_k = 2$ , and  $W_a = 1.95 \times 10^{-5}$ .) For presentation purposes, only the  $n = 2$  and 3 points are used in the interpolation fit.

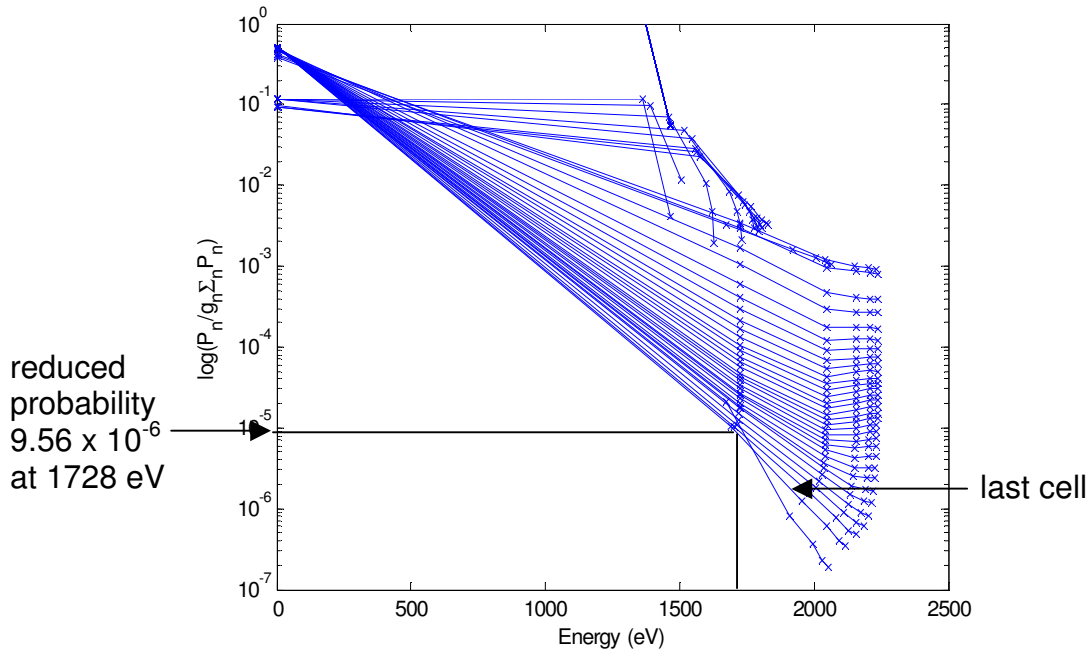


**Figure 4.28** Aluminium energy functional (zeroed to  $n=1$ ) (peak of pulse, outer 80 cells). Each line is a cell and x is marked for each level ( $n = 1$  to 6).

In Figures 4.27 and 4.28, the ion density,  $n_i$ , was calculated according to Eq. 4.18, where  $\rho$  is the mass density (in  $\text{kg/cm}^3$ ) from Medusa,  $A$  is the atomic mass (26.98 for Al), and  $m_p$  is the mass of the proton.<sup>52</sup>

$$n_i = \frac{\rho}{A m_p} \quad (4.18)$$

<sup>52</sup> Note  $m_p \approx m_n$  and thus  $Z m_p + (A-Z) m_n \approx A m_p$ .

Figure 4.29 shows the energy functional for tin ( $A = 118.710$ ) in the middle of the simulation<sup>53</sup> for the last six cells (where  $\langle z \rangle$  varies from 15.2 to 5.5). The  $P_n$  from Medusa are given in Table 4.10. Note that, in this case, the energy functional is zeroed to the  $4p^6 4d^N$  ground configuration ( $E_n - E_4$ ).

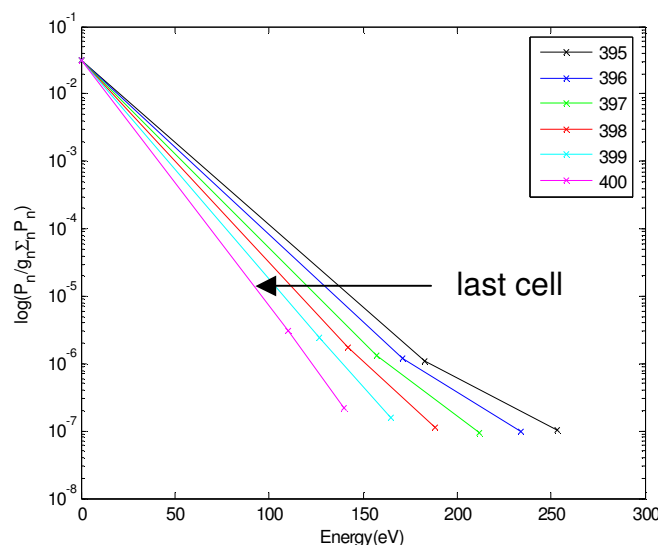


**Figure 4.29** Average atom tin energy functional (middle of simulation, last 6 cells)

$T_e$ (eV)	$n_e$ (cm <sup>-3</sup> )	cell	1	2	3	4	5	6	$\langle z \rangle$
12.60	3.18E+18	395	2	8	18	6.82355	0.00037	0.00005	15.2
12.24	2.98E+18	396	2	8	18	8.36578	0.00049	0.00006	13.6
12.05	2.67E+18	397	2	8	18	10.16654	0.00068	0.00007	11.8
11.79	2.25E+18	398	2	8	18	12.21725	0.00106	0.00010	9.8
11.20	1.63E+18	399	2	8	18	14.29705	0.00172	0.00016	7.7
10.28	6.51E+17	400	2	8	18	16.54770	0.00254	0.00026	5.5

**Table 4.10** Tin populations at middle of simulation for last 6 cells from Medusa

For intermediate  $nl$  levels,  $Y_a(E_n)$  is interpolated from the energy of the excited  $nl$  level. The ten Sn 4d subshell ions are listed in Table 4.11 using the mean UTA wavelengths (and corresponding mean UTA energies) as calculated in Chapter 2.

Ion	4d-4f		4p-4d		4d-5p	
	$\mu_1$ (nm)	E(eV)	$\mu_1$ (nm)	E(eV)	$\mu_1$ (nm)	E(eV)
Sn VI	19.49	63.62	15.37	80.68	30.19	41.07
Sn VII	17.40	71.26	16.36	75.79	25.80	48.06
Sn VIII	15.77	78.63	15.05	82.39	22.48	55.15
Sn IX	14.84	83.56	14.30	86.71	19.90	62.30
Sn X	14.34	86.47	13.91	89.14	17.80	69.65
Sn XI	13.87	89.40	13.64	90.91	16.07	77.15
Sn XII	13.50	91.85	13.39	92.60	14.64	84.69
Sn XIII	13.36	92.81	13.34	92.95	13.41	92.46
Sn XIV	13.41	92.47	13.29	93.30	12.43	99.75

**Table 4.11** Tin UTA mean wavelength and corresponding energies

<sup>53</sup> To show a larger plasma volume for the tin reference case, the middle of the simulation is used (which is after the peak of the pulse).

A sample construction is shown in Figure 4.30 for the  $4p^6 4d^4 4f^1$  configuration of Sn X at 84.67 eV (middle of simulation, last cell). The ground state configuration (at 0 eV) is  $4p^6 4d^5$ . The interpolated reduced probabilities,  $Y_a$ , between  $n = 4$  and  $n = 5$  are given in Table 4.12 (e.g., the reduced probability for the Sn X  $4d^4 4f^1$  configuration is given as  $3.31 \times 10^{-5}$ ). The population probabilities,  $W_a$ , are then calculated from the configuration degeneracy (as described in Section 4.2.5) and normalised for the transitions involved.

Ion	Ground configuration	Excited configuration	UTA		Ground configuration	Excited configuration	UTA	
	( $4d^N$ )	$4d^{N-1} 4f^1$	mean E (eV)	$Y_a$	( $4p^6 4d^N$ )	$4p^5 4d^{N+1}$	mean E (eV)	$Y_a$
Sn VI	$[4p^6] 4d^9$	$[4p^6] 4d^8 4f^1$	63.62	$2.02e-4$	$4p^6 4d^9$	$4p^5 4d^{10}$	80.68	$5.24e-5$
Sn VII	$[4p^6] 4d^8$	$[4p^6] 4d^7 4f^1$	71.26	$1.10e-4$	$4p^6 4d^8$	$4p^5 4d^9$	75.79	$7.72e-5$
Sn VIII	$[4p^6] 4d^7$	$[4p^6] 4d^6 4f^1$	78.63	$6.16e-5$	$4p^6 4d^7$	$4p^5 4d^8$	82.39	$4.58e-5$
Sn IX	$[4p^6] 4d^6$	$[4p^6] 4d^5 4f^1$	83.56	$4.17e-5$	$4p^6 4d^6$	$4p^5 4d^7$	86.71	$3.25e-5$
Sn X	$[4p^6] 4d^5$	$[4p^6] 4d^4 4f^1$	86.47	$3.31e-5$	$4p^6 4d^5$	$4p^5 4d^6$	89.14	$2.68e-5$
Sn XI	$[4p^6] 4d^4$	$[4p^6] 4d^3 4f^1$	89.40	$2.63e-5$	$4p^6 4d^4$	$4p^5 4d^5$	90.91	$2.33e-5$
Sn XII	$[4p^6] 4d^3$	$[4p^6] 4d^2 4f^1$	91.85	$2.16e-5$	$4p^6 4d^3$	$4p^5 4d^4$	92.60	$2.04e-5$
Sn XIII	$[4p^6] 4d^2$	$[4p^6] 4d^1 4f^1$	92.81	$2.00e-5$	$4p^6 4d^2$	$4p^5 4d^3$	92.95	$1.98e-5$
Sn XIV	$[4p^6] 4d^1$	$[4p^6] 4d^0 4f^1$	92.47	$2.06e-5$	$4p^6 4d^1$	$4p^5 4d^2$	93.30	$1.93e-5$

Table 4.12 Tin  $4d^{N-1} 4f^1$  and  $4p^5 4d^{N+1}$  reduced population probability,  $Y_a$  (middle of simulation, last cell)

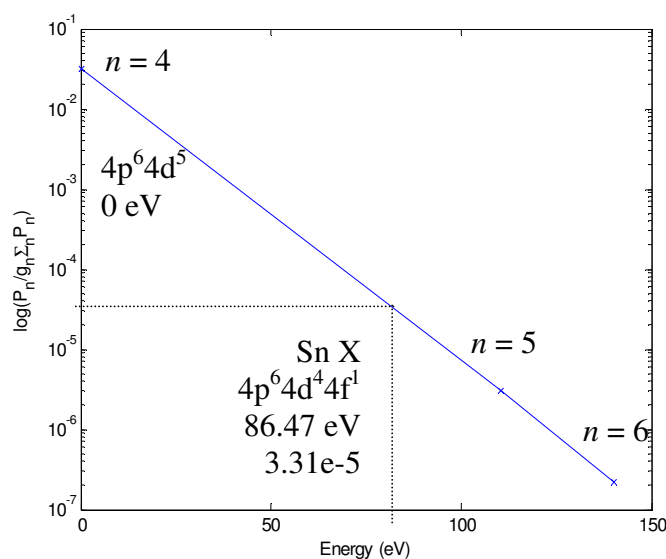


Figure 4.30 Tin energy functional ( $Y_a$  versus  $E_n$ ) with Sn X  $4p^6 4d^4 4f^1$  interpolation construction (middle of simulation, last cell)

In Figure 4.30, the interpolation is shown between the  $n = 4$  and  $n = 5$  levels. Since a straight line is expected, data can be fitted for all three levels ( $n = 4, 5$ , and  $6$ ) or up to 7 levels (for  $n = 4$  to  $10$ , if 10 points are used). However, it can be seen in Figure 4.29 (in the tin case) and in Figure 4.28 (in the aluminium case) that the energy functional is not always a straight line (on a semi-log y plot). In the tin case, using all points would raise the level populations (for the cells shown), though this effect will be minimised after normalisation (relative degeneracies must also be considered).

It should be remembered that the number of fitting points can effect the level populations, though less so for straighter fits and that interpolating between two points will reflect an increased population for a higher shell.

### 4.2.5 Population number density, $N_i$ and $N_j$

The population number densities ( $N_i$  and  $N_j$ ) required in radiation transport modelling are calculated from the average atom model. The ground state ( $N_i$ ) is given in *Medusa*. However, the excited state ( $N_j$ ) must be calculated as in Eq. 4.19 ( $\rho$ ,  $A$ , and  $m_p$  are as in Eq. 4.18).

$$N = f(C) \frac{\rho}{Am_p} \quad (4.19)$$

where the ion fraction  $f(C)$  is as above in Eq. 4.15 for the corresponding configuration (*e.g.*, in  $\text{Al}^{12+}$ ,  $C_i = [1\ 0\ 0\ 0\ 0\ 0]$  for the ground state and  $C_j = [0\ 1\ 0\ 0\ 0\ 0]$  for the first excited state.) The energy functional method [26] can also be used to calculate the excited population number density, where  $f(C) = W_a$ .

For the UTA model, however,  $f(C)$  can only be calculated using the energy functional method as in Eq. 4.20 (here called  $F(C)$ ).

$$F(C) = Y_a(E_n)D \quad (4.20)$$

where  $D$  is the *configuration* degeneracy as described below.

The statistical weight or degeneracy of a subshell is given in Eq. 4.21 by Greim [37],

$$g(l^w) = \frac{(4l+2)!}{w!(4l+2-w)!} \quad (4.21)$$

where  $l = 1, 2,$  and  $3,$  for the p, d, and f shells respectively, and  $w$  is the subshell occupancy.

For example, for the ground state of Sn IX,  $4p^64d^6$ ,  $w = 6$  and  $g(d^6) = 10!/6!/4! = 210$ . For shells with two open subshells, the degeneracy of each subshell is multiplied as in Eq. 4.22 [38].

$$D = \prod_i g_i \quad (4.22)$$

where  $i$  is taken over all open subshells. (Note that a full subshell has degeneracy = 1.)

For example, for the excited state of Sn IX  $4p^64d^54f^1$ ,  $w = 5$  (d-shell) and  $w = 1$  (f shell), giving  $g(d^5) = 10!/5!/5! = 252$  and  $g(f^1) = 14!/13!/1! = 14$ , and thus  $D = 3528$ . The ground state ( $4p^64d^N$ ) and excited states' ( $4p^64d^{N-1}4f^1$  and  $4p^54d^{N+1}$ ) degeneracies for all ten 4d subshell Sn ions are given in Table 4.13 as calculated from Eq. 4.21 and Eq. 4.22.

$F(C)$  is then calculated using the reduced population probability from the energy functional method and the level degeneracy. The unnormalised fractional level populations are included in Table 4.13. The corresponding  $4d^N5p$  levels are also calculated accordingly.

From the data in Table 4.13, Figure 4.31 shows the fractional level populations for Sn X: the  $4p^64d^5$  ground state and  $4p^64d^44f^1$ ,  $4p^54d^6$ ,  $4p^64d^45p^1$  excited states. **Note that the level populations are normalized such that  $\Sigma F(C) = 1$ .** Figure 4.32 shows the normalised population number densities for the four configurations shown,  $N_i$  ( $4p^64d^5$ ) and  $N_j$  ( $4p^64d^44f^1$ ,  $4p^54d^6$ , and  $4p^64d^45p^1$ ) using Eq. 4.19 ( $f(C) = F(c)$ ). A full presentation of the level populations and ion densities for all 4d subshell tin ions is given in Chapter 5 (as well as all relevant tin hydrodynamic data).

Ion	Ground configuration ( $4d^N$ )		Excited configuration ( $4p^6 4d^{N-1} 4f^1$ )		UTA mean E (eV)		Excited configuration ( $4p^5 4d^{N+1}$ )		UTA mean E (eV)	
		D				D	$F(C)$		D	$F(C)$
Sn VI	$4p^6 4d^9$	10	$4p^6 4d^8 4f^1$	63.62	630	$1.27e-1$	$4p^5 4d^{10}$	80.68	6	$3.14e-4$
Sn VII	$4p^6 4d^8$	45	$4p^6 4d^7 4f^1$	71.26	1680	$1.85e-1$	$4p^5 4d^9$	75.79	60	$4.63e-3$
Sn VIII	$4p^6 4d^7$	120	$4p^6 4d^6 4f^1$	78.63	2940	$1.81e-1$	$4p^5 4d^8$	82.39	270	$1.24e-2$
Sn IX	$4p^6 4d^6$	210	$4p^6 4d^5 4f^1$	83.56	3528	$1.47e-1$	$4p^5 4d^7$	86.71	720	$2.34e-2$
Sn X	$4p^6 4d^5$	252	$4p^6 4d^4 4f^1$	86.47	2940	$9.73e-2$	$4p^5 4d^6$	89.14	1260	$3.38e-2$
Sn XI	$4p^6 4d^4$	210	$4p^6 4d^3 4f^1$	89.40	1680	$4.42e-2$	$4p^5 4d^5$	90.91	1512	$3.52e-2$
Sn XII	$4p^6 4d^3$	120	$4p^6 4d^2 4f^1$	91.85	630	$1.36e-2$	$4p^5 4d^4$	92.60	1260	$2.57e-2$
Sn XIII	$4p^6 4d^2$	45	$4p^6 4d^1 4f^1$	92.81	140	$1.40e-3$	$4p^5 4d^3$	92.95	720	$1.43e-2$
Sn XIV	$4p^6 4d^1$	10	$4p^6 4d^0 4f^1$	92.47	14	$1.48e-4$	$4p^5 4d^2$	93.30	270	$5.21e-3$

Table 4.13 Tin excited state mean UTA energies (E), degeneracies (D), and reduced population probabilities  $F(C)$  (middle of simulation, last cell)

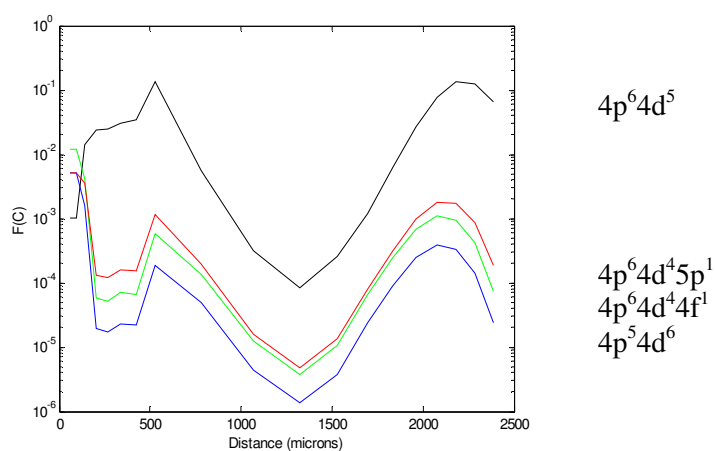


Figure 4.31 Fractional level populations  $4p^6 4d^5$  (black)  $4p^6 4d^4 4f^1$  (green),  $4p^5 4d^6$  (blue),  $4p^6 4d^4 5p^1$  (red) for Sn X (middle of simulation, normalised)

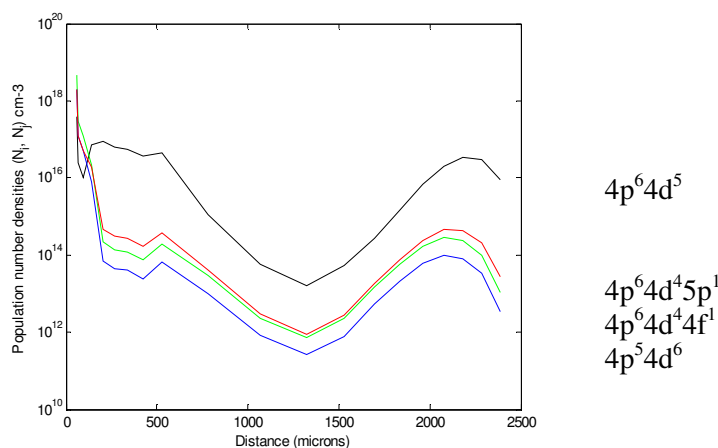
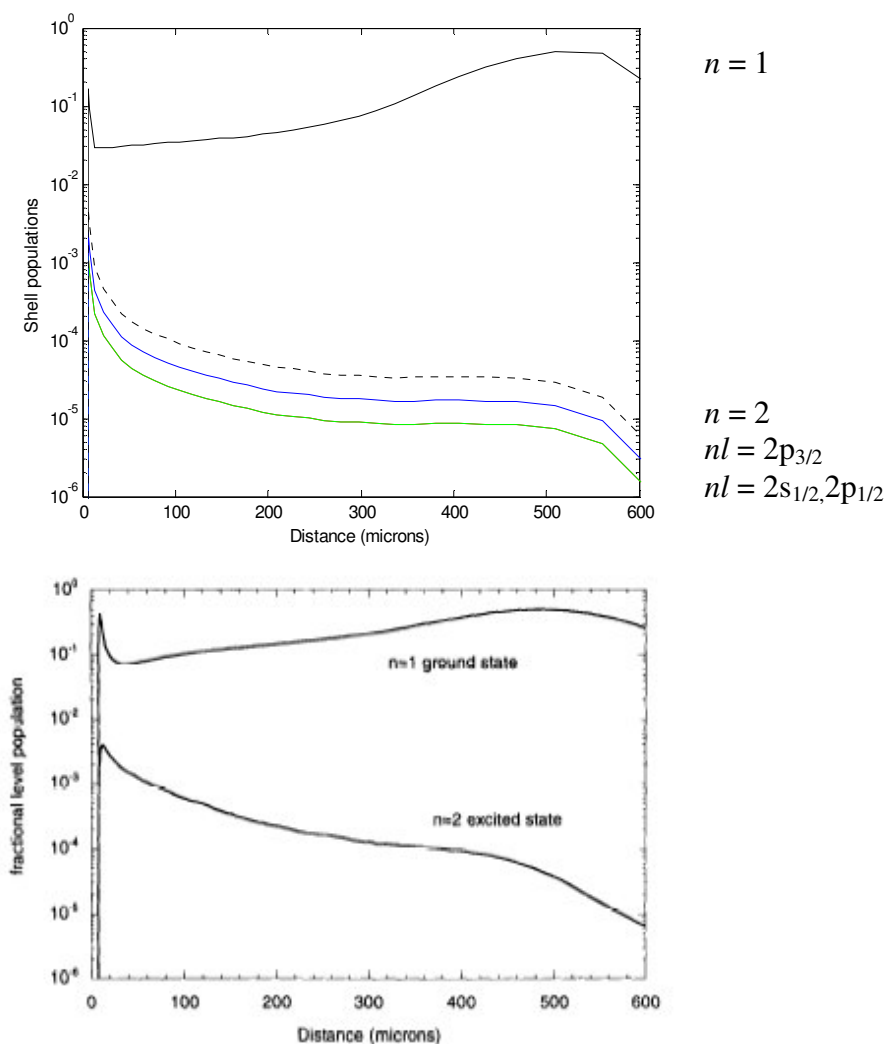


Figure 4.32  $N_i$  and  $N_j$  level populations  $4p^6 4d^5$  (black)  $4p^6 4d^4 4f^1$  (green),  $4p^5 4d^6$  (blue),  $4p^6 4d^4 5p^1$  (red) for Sn X (middle of simulation, normalised)

Note the decreased level populations from 500 to 2000  $\mu\text{m}$  because of the decreased Sn X ion fraction. From a similar plot of level populations over a range of ions (see Chapter 5), it will be seen that higher ions stages are dominant in this region.

To illustrate  $nl$ -splitting (as well as verify the energy functional method for aluminium), a comparison is made between the population levels calculated in *Medusa* for the  $n = 2$  level and by the energy functional method for the  $nl = 2s_{1/2}$ ,  $2p_{1/2}$ , and  $2p_{3/2}$  levels. Figure 4.33 (top) shows the shell populations using the energy functional method (the  $2s_{1/2}$  and  $2p_{1/2}$  levels are degenerate and are thus shown on top of each other), which compares almost exactly with that of *Medusa* in [11]. The  $nl$  levels are summed (dashed line) and Figure 2c from [11] is reproduced in Figure 4.33 (bottom) for comparison. Six levels ( $n = 1$  to 6) have been used in the interpolation fit and the populations have been normalised such that  $\Sigma W_a = 1$  (or  $\Sigma f(C) = 1$ ), however, a better fit was achieved using only three levels ( $n = 1$  to 3).



**Figure 4.33**  $\text{Al}^{12+}$  fractional level populations for  $n = 1$ ,  $n = 2$  (dashed) and  $nl = 2s_{1/2}$  (red),  $2p_{1/2}$  (green), and  $2p_{3/2}$  (blue), level (peak of pulse) and comparison from [11]

From Figure 4.33, it is thus seen that the energy functional method is equivalent to using Eq. 4.15 (as in *Medusa*) to calculate  $l$ -degenerate fractional level populations for  $\text{Al}^{12+}$  ( $n = 1, 2$ ). However, the  $nl$  levels can also be determined ( $1s_{1/2}$ ,  $2s_{1/2}$ ,  $2p_{1/2}$ , and  $2p_{3/2}$ ) using this method and, as seen in Figure 4.32, the fractional level populations for the ground and excited configurations ( $4p^6 4d^N$ ,  $4p^6 4d^{N-1} 4f^1$ , and  $4p^5 4d^{N+1}$ ) for the Sn UTA emitting ions can then be determined. (Note that to calculate the population number densities, the level populations are multiplied by the fractional ion density as given in *Medusa*.)

### 4.3 Radiation transport

The relative intensities of spectral lines depend on the light source and excitation conditions. As reported by Djaoui *et al.* [9], “An understanding of radiative energy transfer in astrophysical and laser-produced plasmas is important for the prediction of plasma behaviour and for the interpretation of spectroscopic diagnostics.”

The emission intensity in a plasma with negligible radiation absorption (an optically thin plasma) is given by integrating the emissivity over the line of sight as in Eq. 4.23 [38].

$$I = \int E dz \quad (4.23)$$

where  $I$  is the intensity,  $E$  the emissivity, and  $z$  the distance.

Spectral intensity is reduced, however, in a plasma with non-negligible absorption (an optically thick plasma), where radiation from the core may be absorbed and re-emitted several times [12]. As well, for an anisotropic plasma, the intensity strongly depends on observation angle [8]. As stated in [10], spectral intensity and shape [of the hydrogenic aluminium 1s-2p resonance line] varies dramatically as a function of observation angle, because at different observation angles, “the x-rays . . . traverse different space-dependent profiles of emissivity, opacity, temperature (which determines the local thermal Doppler width of the line) and velocity.” Furthermore, Doppler shifts from large velocity gradients in the plasma can broaden and shift the peak of optically thick lines [10]. Position is less shifted and the width more narrow as the observation angle increases from the angle of laser pulse incidence, consistent with decreased velocity relative to the observer [10].

Following the treatment in [9–11], the methodology for calculating radiation transport in an optically thick plasma is described below (Eqs. 4.24–4.30). A schematic of the cross section through a cylinder as used in [11] is shown in Figure 4.34. The laser pulse is incident on the target from the right.

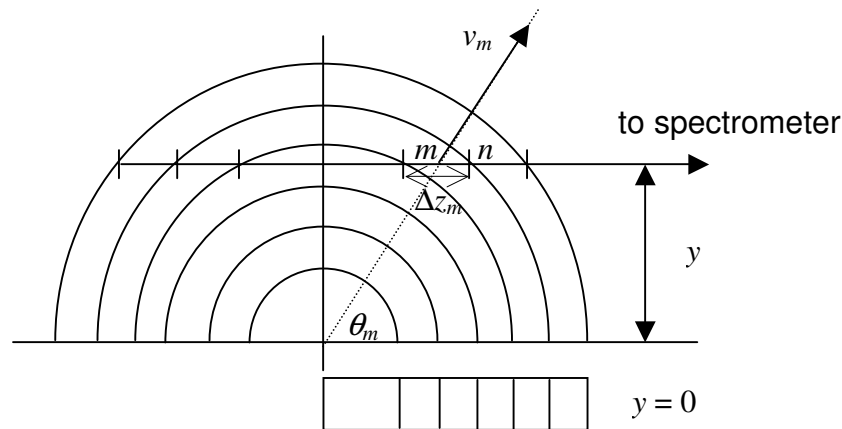


Figure 4.34 Schematic view of cross-section through cylinder [11]

$\Delta z_m$  is the cell width,  $v_m$  the velocity, and  $\theta_m$  the angle to the incident laser pulse for cell  $m$ . In this thesis, spectra will be calculated for  $\theta_m$  (and thus  $y$ ) equal to zero only.

The radiative transfer equation from [39] is

$$\frac{\partial I_\nu}{\partial z} = K_\nu I_\nu + E_\nu \quad (4.24)$$

where  $K_\nu$  is the absorption coefficient,  $I_\nu$  is the intensity,  $E_\nu$  is the total emissivity (all a function of frequency  $\nu$ ), and  $z$  is the distance.

Eq 4.24 can be solved for a range of frequencies at all positions and angles in the plasma, but is computationally very intensive [39]. Instead, an optical thickness,  $\tau_\nu$ , over the distance from the point of emission to the plasma boundary [9] is defined to simplify the solution. The radiative transfer equation is then given in Eq 4.25.

$$\frac{\partial I_\nu}{\partial \tau_\nu} = I_\nu - S_\nu \quad (4.25)$$

where  $I_\nu$  is the radiation intensity,  $\tau_\nu$  the optical depth, and  $S_\nu$  the source function (ratio of total emissivity to total opacity of the material [11];  $S_\nu = E_\nu/K_\nu$ ).

The solution to the radiative transfer equation [11] is then given as

$$I_\nu(\tau_\nu) = I_\nu^0 e^{-\tau_\nu} + \int_0^{\tau_\nu} S_\nu(t) e^{-t} dt \quad (4.26)$$

where the integral is evaluated from  $\tau_\nu$  to the edge of the material and  $I_\nu^0$  is the incident radiation intensity at  $\tau_\nu$ .

For a homogeneous plasma with no incident radiation, the intensity is thus

$$I_m(\nu) = \sum_l S_m^l(\nu) [1 - \exp(-\chi_m^l(\nu) \Delta z_m)] \quad (4.27)$$

where  $S_m^l(\nu)$  is the source function and  $\chi_m^l(\nu)$  is the opacity of line  $l$  and cell  $m$  and  $\Delta z_m$  the length of cell  $m$ . The sum is taken over each line.<sup>54</sup> Note that Eq. 4.27 assumes no line interaction in the emission cell.

The source function at a given frequency,  $\nu$ , for line  $l$  and cell  $m$  is

$$S_m^l(\nu) = \frac{2h\nu^3}{c^2} \frac{1}{\left[ \frac{N_i g_j}{N_j g_i} - 1 \right]} \quad (4.28)$$

where  $S$  is in  $\text{W/m}^2/\text{sr}/[\text{Hz/s}]$ ,  $N_i$  and  $N_j$  are the population number densities in  $\text{cm}^{-3}$ ,  $g_i$  and  $g_j$  are the degeneracies of the  $i$ th and  $j$ th levels ( $i$  is the lower level and  $j$  the higher level), and  $h$  and  $c$  have their usual meaning. ( $N_i$  and  $N_j$  are calculated as in Section 4.2.5, where for the tin UTA the degeneracy,  $D$ , is used (instead of  $g$ ) as in Table 4.13).

<sup>54</sup> In [11],  $\chi_m^l$  is given as  $\chi_m$ .

The opacity for line  $l$  and cell  $m$  is

$$\chi_m^l(\nu) = \frac{\pi e^2}{4\pi\epsilon_0 m_e c} f_{ij} N_i \left[ 1 - \frac{N_j g_i}{N_i g_j} \right] \phi_m^l(\nu) \quad (4.29)$$

where  $f_{ij}$  is the absorption oscillator strength for an  $i$ - $j$  transition; ( $f_{ij} = gf/(2J_i+1)$ ).  $2J_i + 1$  is the degeneracy and  $J_i$  is the total angular momentum of the lower configuration. (For tin UTA, the degeneracy is  $D$ .)  $\phi_m^l(\nu)$  is the area normalised line profile assumed to be the same in emission and absorption [9]. (Note that  $1/4\pi\epsilon_0$  is included for SI units.) A Doppler broadened width as a function of electron temperature is used for aluminium (see Section 2.3.1, Eq. 2.2). For the tin UTA, lines are not Doppler broadened; instead, the UTA reduced width is used (see Section 2.3.4). Stark broadening (which includes electron collision effects) is considered negligible in this particular example [8], but is not necessarily negligible in Sn plasmas. (It is assumed that  $N_j \ll N_i$  (no population inversion) and thus stimulated emission can be neglected.)

The emission profile is then recursively attenuated through successive cells, where the observed emission from cell  $m$  is given in Eq. 4.30:

$$I_m^{obs}(\nu) = I_m(\nu) \exp\left(\sum -\chi_n(\nu)\Delta z_n\right) \quad (4.30)$$

with the opacity summed over  $n$  cells (from the  $m+1$ th cell to the last cell). Note that the sum in Eq. 4.30 is the attenuation ( $e^{-\chi_m\Delta z_m} \cdot e^{-\chi_{m-1}\Delta z_{m-1}} \dots \cdot e^{-\chi_1\Delta z_1}$ ).

The emission as a function of time,  $I_{out}$ , is then calculated by summing up the attenuated cell emission over all  $m$  cells. The number of photons at a given frequency (used in [11] for the aluminium reference case) is  $I_{out}/h\nu$  [9]. To see the effect of absorption,  $I_{out}$  can be compared to  $I_{out}$  with  $\chi_n(\nu)\Delta z_n = 0$  in Eq. 4.30.

### 4.3.1 LPP velocity gradients

The spectral profile from a laser-produced plasma is affected by density, temperature, and velocity gradients. As stated in Djaoui *et al.* [9], “inclusion of velocity gradients is found to be critical in determining the intensity and shape of emitted spectral lines.” In hydrogenic aluminium, the Doppler shift caused by velocity gradients in a plasma ( $\sim 12 \text{ m\AA}$ ) can be greater than both the Doppler broadening ( $\sim 3 \text{ m\AA}$ ) and the  $1s-2p_{3/2}$ ,  $1s-2p_{1/2}$  line separation ( $\sim 5 \text{ m\AA}$ ) [9]. Large velocity gradients reduce reabsorption of a photon beyond a distance from the point of emission (known as the Doppler-decoupling distance), where the Doppler shift is less than the line width [9].<sup>55</sup>

Note that in hydrogenic aluminium, power densities are high, producing significant plasma expansion and resultant Doppler shift. At lower power densities (*e.g.*, for 5–14 times ionised tin UTAs), velocity gradients will not significantly affect total emission.

The absorption profiles of the absorbing ions are Doppler shifted relative to the emission profiles as given in Eqs. 4.31 and 4.32 [11].

$$v_m = v \left( 1 - \frac{V_m \cos \theta_m}{c} \right) \quad (4.31)$$

$$v_{mn} = v_m \left( 1 + \frac{V_m \cos \theta_m - V_n \cos \theta_n}{c} \right) \quad (4.32)$$

where  $\theta_m$  is as in Figure 4.34 ( $\theta_m = 0$  is the laser incidence direction),  $c$  is the speed of light in m/s,  $v_m$  is the velocity of cell  $m$  and  $v_{mn}$  is the relative velocity of cell  $m$  with respect to cell  $n$ .

The maximum velocity and, thus, greatest spectral shift, is at  $y = 0 \text{ }\mu\text{m}$  (see Figure 4.34), both decreasing with increasing  $y$  (as  $\theta$  increases,  $\cos(\theta)$  decreases) [11].

As stated in [12], at greater velocities, the Doppler shift increases and “shorter wavelength photons . . . experience an increased probability of being absorbed in the plasma,” which, for hydrogenic aluminium, can result in a greater contribution from the longer wavelength doublet line ( $1s-2p_{1/2}$ ), even though it is the weaker of the two. The shorter wavelength line ( $1s-2p_{3/2}$ ) is red-shifted and absorbed by the longer wavelength line, resulting in a preferential trapping of the  $1s-2p_{3/2}$  line [11]. At lower velocities, the shorter wavelength line contributes more and is comparable to the static ( $v_m = 0$ ) case.

The effect of absorption through the plasma and of velocity gradients for  $\text{Al}^{12+}$  in the aluminium reference case is shown in Section 4.3.2. As seen in Figure 4.35, the highest velocity gradients and thus largest Doppler decoupling is expected at the edge of the plasma. The outer cell is indicated (2.3 mm at the end of the simulation).

<sup>55</sup> Note that velocity gradients are also important for XUV lasers because resonance line reabsorption will pump the lower laser level, thus reducing the population inversion [8, 9].

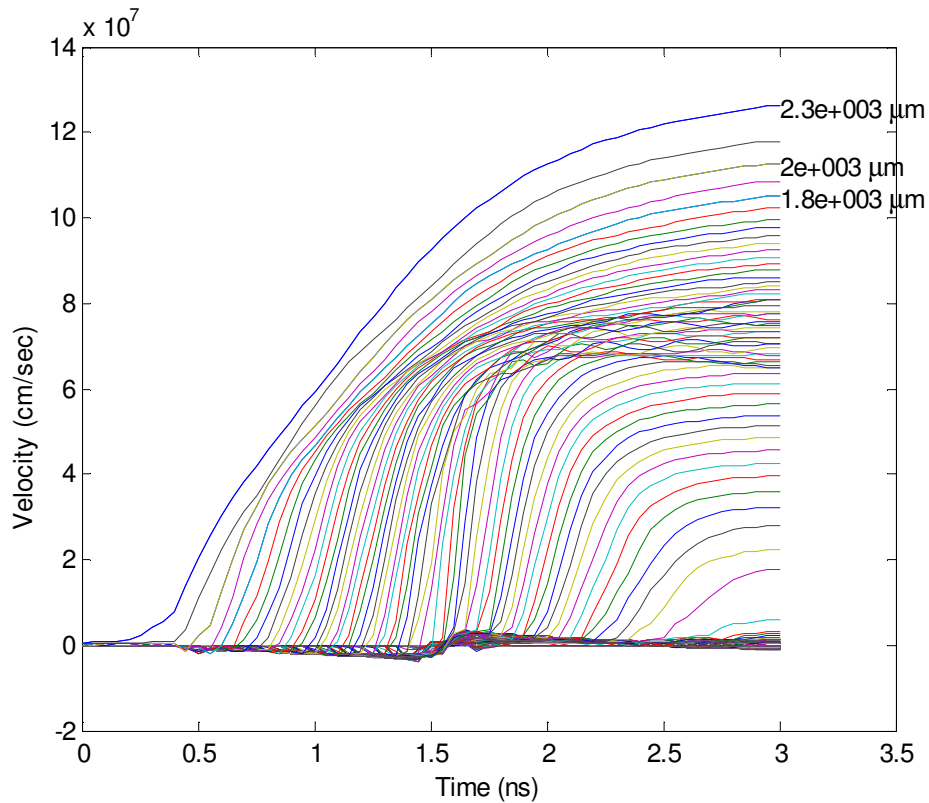


Figure 4.35 Aluminium reference case velocity versus time and distance

As stated in Chambers *et al.* [40], “The emission profile of the  $2p_{3/2}-1s_{1/2}$  transition, when emitted from the slowly moving plasma region close to the target surface, was Doppler shifted into resonance with the absorption profile of the  $2p_{3/2}-1s_{1/2}$  transition further out in the plasma where the plasma velocity was much higher. Simulations also showed that the single line recorded was therefore emitted by the supposedly weaker  $2p_{3/2}-1s_{1/2}$  transition.” Large velocity gradients are important, because the relative motions of different parts of the plasma can create spectral overlaps.

### 4.3.2 Aluminium reference case spectra with radiation transport

Table 4.14 gives the relevant data used for the hydrogenic aluminium 1s-2p doublet at 7.175 Å and 7.180 Å [8–13]. The  $gf$  values of the two lines (labelled 1B:  $1s_{1/2} - 2p_{3/2}$  and 2R:  $1s_{1/2} - 2p_{1/2}$ ) are in the ratio of 2:1, as theoretically determined, where  $g_j = 2J_j + 1$  and  $J_j$  is the upper level angular momentum. The  $gf$  values used were determined by an atomic code as stated in [11]. The reference Gaussian line profile for each line and their sum (dashed), calculated from this data, is shown in Figure 4.36 at  $T_e = 500$  eV to compare with [9] (the broadening is as in Section 2.3.1, Eq. 2.2). (Line width is calculated from the ion temperature in Medusa at all cells and times.) Note that the densities are sufficiently low enough that Doppler broadening dominates [9]. The individual lines are shown superimposed for reference.

Line	$\lambda_{i-j}$	$E_{i-j}$	$gf_{i-j}$	$n_i J_i - n_j J_j$	$g_j$
1B	7.175 Å	1728 eV	0.2775	$1s_{1/2} - 2p_{3/2}$	4
2R	7.180 Å	1727 eV	0.1387	$1s_{1/2} - 2p_{1/2}$	2

Table 4.14 Al XIII 1s-2p line characteristics

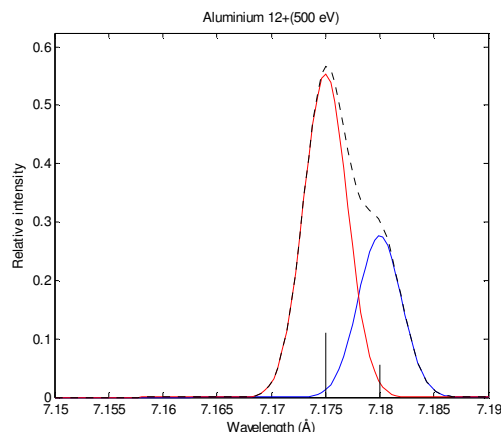


Figure 4.36 Aluminium  $1s_{1/2} - 2p_{3/2}$  and  $1s_{1/2} - 2p_{1/2}$  line profile at 500 eV

The profiles for the 390<sup>th</sup> cell ( $T_e = 453$  eV) and the 400<sup>th</sup> cell ( $T_e = 174$  eV) at the peak of the pulse are shown in Figure 4.37, where the decreased broadening with decreasing electron temperature toward the edge of the plasma can easily be seen.

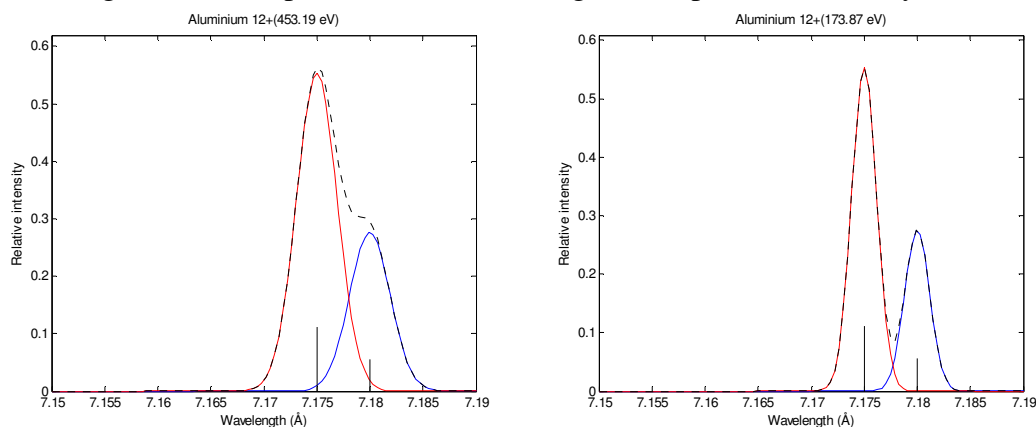
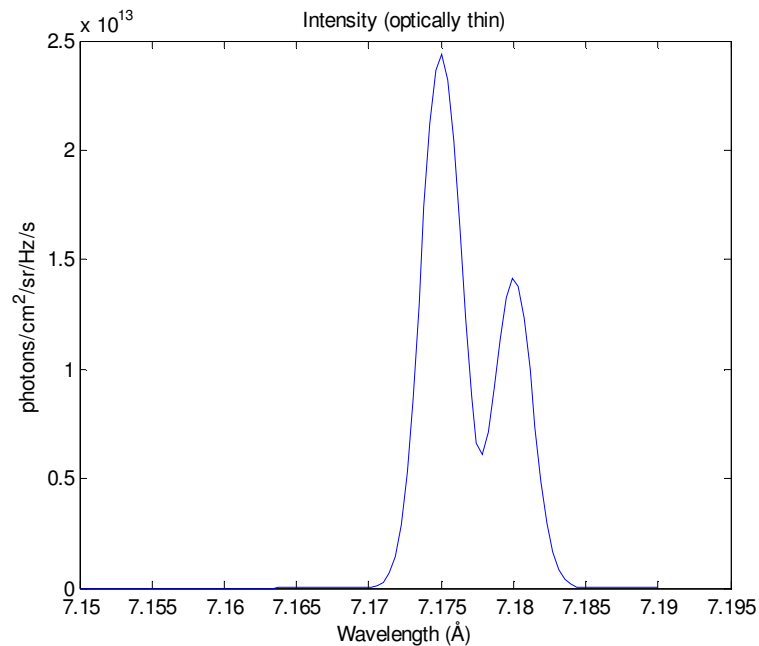
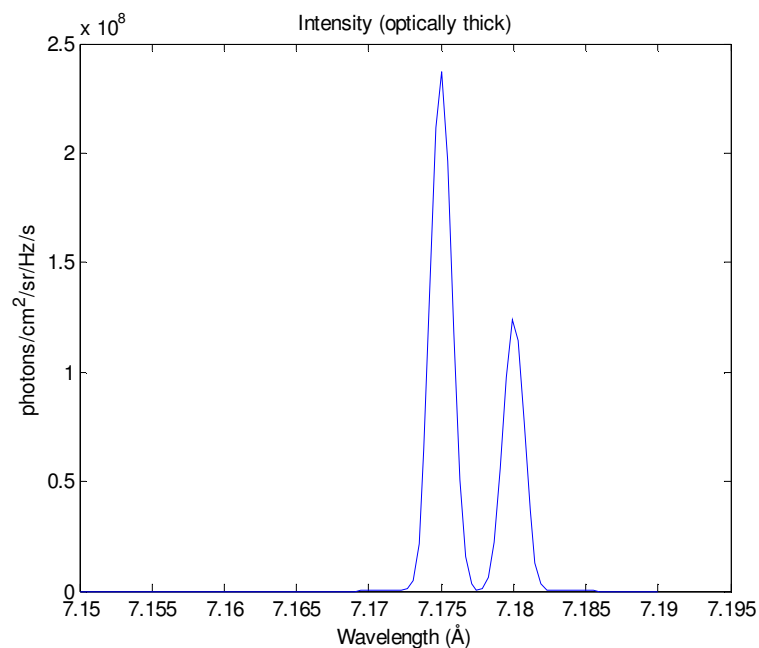


Figure 4.37 Aluminium  $1s_{1/2} - 2p_{3/2}$  and  $1s_{1/2} - 2p_{1/2}$  line profile and sum at  $T_e = 453$  eV, 390<sup>th</sup> cell (left) and 174 eV, 400<sup>th</sup> cell (right) at peak of the pulse

Figure 4.38 shows the optically thin spectrum at  $y = 0$  and Figure 4.39 shows the same with absorption included where the effect of absorption in the middle of the doublet can be seen. The intensity is in photons/cm<sup>2</sup>/sr/Hz/s as in [11] at the peak of the pulse (1.5 ns), for a maximum ion temperature of 647 eV.



**Figure 4.38** Aluminium spectra summed intensity (peak of pulse, no absorption,  $y = 0$ )



**Figure 4.39** Aluminium spectra summed intensity (peak of pulse, absorption,  $y = 0$ )

The results from Patel *et al.* [11] for the optically thin static case are reproduced in Figure 4.40 for comparison, showing good agreement. Note that the figure in [11] includes the effect of velocity gradients which are not reported on here. Furthermore, Doppler broadening is that from [30].

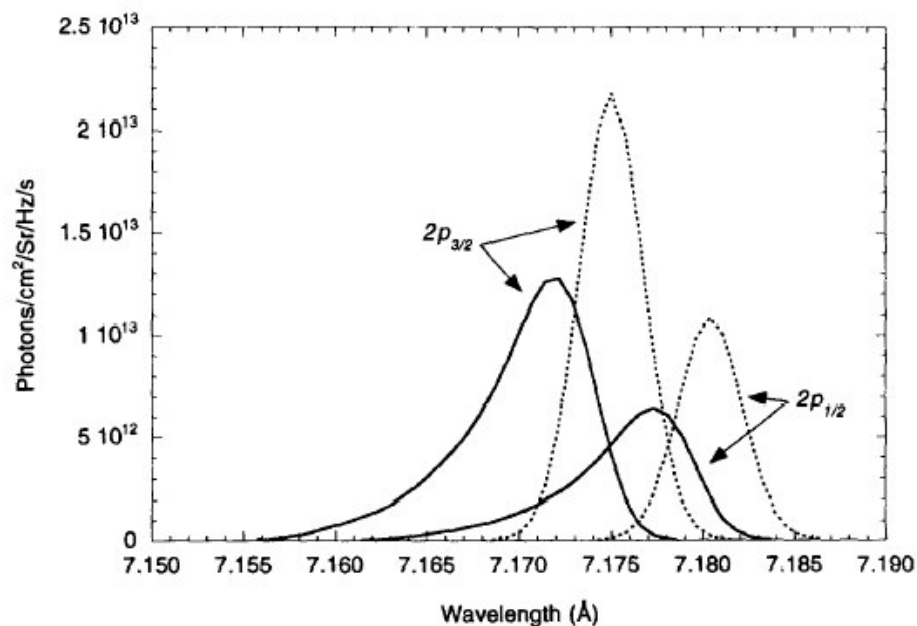


Figure 4.40 Patel *et al.* [11] intensity versus wavelength for an optically thin static case (dotted) and with the effects of velocity field on line shape (solid)

Note that the effect of using the energy functional instead of the statistically equilibrated  $n = 2$  levels is minimal in the aluminium reference case, because only  $\Delta n = 1$  (1s-2p) transitions were considered, but will be essential for the 4d-4f and 4p-4d UTAs (see Chapter 5). Furthermore, the simulations are for the static case, *i.e.*, no velocity gradients are included.

Figure 4.41 (left) show the increasing relative intensity with cell from the last cell inward (from cell 400 to cell 390) and Figure 4.41 (right) shows the same for all cells. Snapshots at three times are shown: before (1.0 ns), at (1.5 ns), and after (2.0 ns) the peak of the pulse. It can be seen that intensity increases with cell to a maximum depth and that the broadened profile changes with depth as a function of temperature.

Because the 2p level population is high with increasing radius, significant radiation occurs at the edge of the plasma [11], but for  $\text{Al}^{12+}$ , the bulk of the  $\text{Ly}\alpha$  radiation is close to the wire surface (low cell numbers in *Medusa*) [11]. In the aluminium reference case it was seen that because of recombination the  $n = 2$  excited state population falls off more rapidly with distance. Furthermore, longer wavelength lines can also absorb nearby shorter wavelength lines (blue shifted), although lines with higher oscillator strength have greater absorption.

In the tin case (see Chapter 5), absorption by lower tin ion discrete transitions (Sn I–Sn IV) are not included in the opacity calculations (Eq. 4.27), because the density of lower ions is lower at  $y = 0$  (toward the laser pulse) [20, 41, 42]. At other angles, absorption from shape resonances in the lower tin ions can reduce the radiant output [42]. However, further simulations are required to quantify the actual reduction.

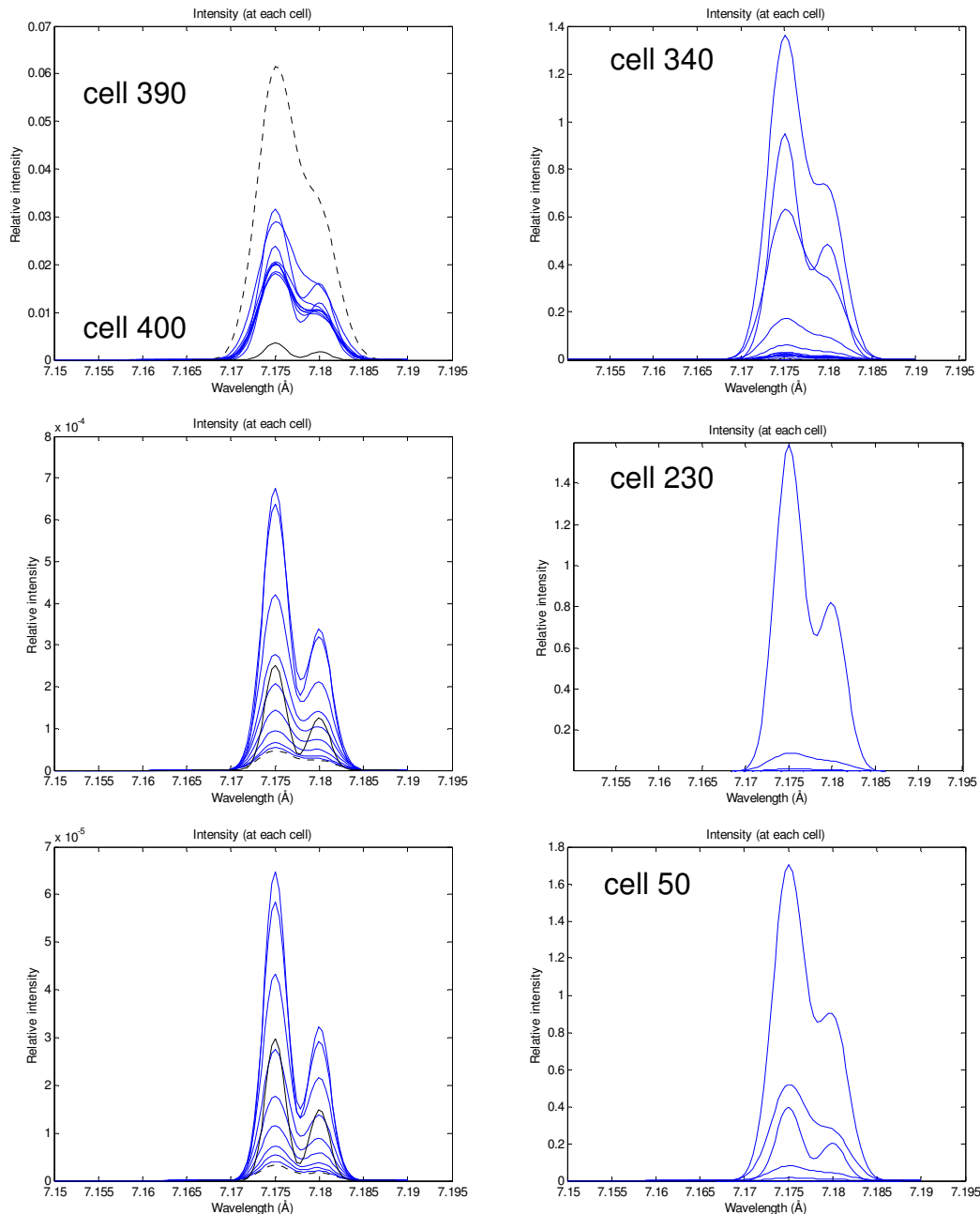


**Figure 4.41** Aluminium spectra (relative intensity from cell 400–390 (left) and for all cells (right) at 1.0 ns, 1.5 ns, and 2.0 ns.)

Figure 4.42 (top) shows the maximum intensity as a function of time. Here it can be seen that the maximum intensity is before the peak of the pulse and that a sharp drop occurs around the peak of the pulse. Figure 4.42 (middle) gives the Medusa cell number at which the maximum intensity occurs and Figure 4.42 (bottom) gives the corresponding distance for maximum emission. The oscillating nature of the plasma can be seen and the depth at which radiation penetrates. The penetration also increases in time. Note that the depth is given as negative to correspond to the cell number plot where cell number 400 is the outer edge. For the bottom two graphs, the laser can be thought of as incident from above.

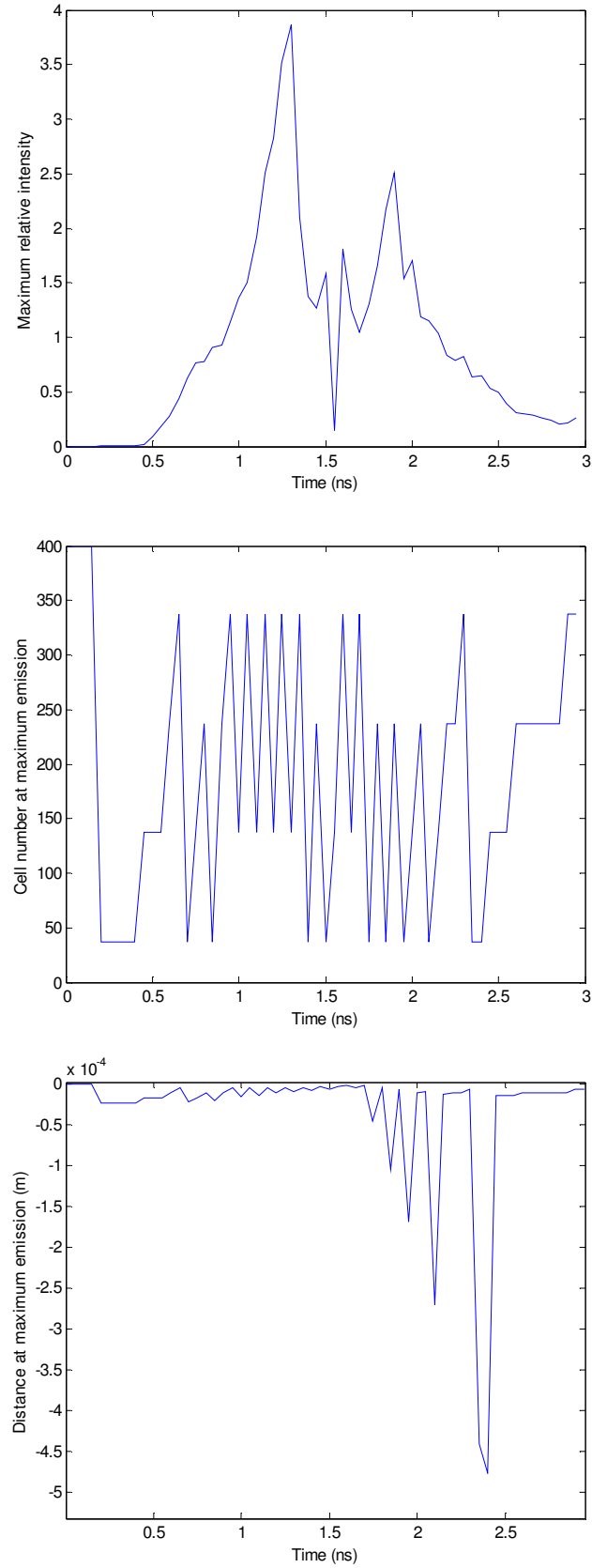


**Figure 4. 42** Maximum intensity as a function of time (top), cell number at maximum emission (middle), and corresponding depth (bottom).

## 4.4 References

- 1 Christiansen, J. P., Ashby, D. E. T. F., and Roberts, K. V., "Medusa: a one-dimensional laser fusion code," *Computer Physics Communications*, **7**, 271–287, 1974.
- 2 Bell, A. R., "New equations of state for medusa," Rutherford Appleton Laboratory report: *RAL-80-091*, RAL, Didcot, U.K., 1980.
- 3 Rose, S. J. and Evans, R. G., "Radiation transport in Medusa," Rutherford Appleton Laboratory report: *RL-83-040*, RAL, Didcot, U.K., 1983.
- 4 Rodgers, A. M., Rogoyski, A. M., and Rose, S. J., "MED101: a laser-plasma simulation code. User guide," Rutherford Appleton Laboratory report: *RAL-89-127*, RAL, Didcot, U.K., 1989.
- 5 Djaoui, A., "A user guide for the laser-plasma simulation code. MED103," Rutherford Appleton Laboratory report: *RAL-TR-96-099*, RAL, Didcot, U.K., 1996.
- 6 Eidmann, K., "Radiation transport and atomic physics modelling in high-energy-density laser-produced plasmas," *Laser and Particle Beams*, **12** (2), 223–244, 1994.
- 7 Colombant, D. and Tonon, G. F., "X-ray emission in laser-produced plasmas," *J. Appl. Phys.*, **44** (8), 3524–3537, 1973.
- 8 Wark, J. S., Djaoui, A., Rose, S. J., He, H., Renner, O., Missalla, T., and Foerster, E., "Effects of velocity gradients on x-ray line transfer in laser-produced plasmas," *Phys. Rev. Letters*, Vol. 72, No. 12, 1826–1829, 1994.
- 9 Djaoui, A., Rose, S. J., and Wark, J. S., "Calculation of the effects of velocity gradients and opacity on line transfer in laser-produced plasmas," *J. Quant. Spectrosc. Radiat. Transfer*, Vol. 52, No. 5, 531–544, 1994.
- 10 Wark, J. S., Renner, O., Djaoui, A., Rose, S. J., Missalla, T., Neely, D., Foerster, E., and Hauer, A., "Measurements and simulation of the intensity and shape of the hydrogenic Al resonance line ( $1s^2S-2p^2P$ ) in laser-produced plasmas," *J. Quant. Spectrosc. Radiat. Transfer*, Vol. 54, No. 1/2, 419–425, 1995.
- 11 Patel, P. K., Wark, J. S., Heading, D. J., Djaoui, A., Rose, S. J., Renner, O., and Hauer, A., "Simulation of x-ray line transfer in a cylindrically expanding plasma," *J. Quant. Spectrosc. Radiat. Transfer*, Vol. 57, No. 5, 683–694, 1997.
- 12 Patel, P. K., Wark, J. S., Renner, O., Djaoui, A., Rose, S. J., Heading, D. J., and Hauer, A., "Experimental and simulated profiles of the Al XIII Ly- $\alpha$  resonance line from a cylindrically expanding plasma," *J. Quant. Spectrosc. Radiat. Transfer*, Vol. 58, No. 4–6, 835–844, 1997.
- 13 Patel, P. K., Renner, O., Rose, S. J., and Wark, J. S., "Effect of large velocity gradients on x-ray lineshapes," Science high power laser programme, *CFL Annual Report*, 1996/7.
- 14 Cummings, A., O'Sullivan, G., Dunne, P., Sokell, E., Murphy, N., and White, J., "Conversion efficiency of a laser-produced Sn plasma at 13.5 nm, simulated with a one-dimensional hydrodynamic model and treated as a multi-component blackbody," *J. Phys. D: Appl. Phys.*, **38**, 604–616, 2005.
- 15 Tallents, G. J., "An investigation into the potential of optically thick line profiles for determining laser-produced plasma parameters," *J. Atom. Molec. Phys.* **13**, 3057–3072, 1980.
- 16 Attwood, D., "Soft x-rays and extreme ultraviolet radiation, principles and applications," Cambridge University Press, 1999.
- 17 Price, J. F., "Lagrangian and Eulerian representations of fluid flow: Part I, kinematics and the equations of motion," Version 7.4, [www.who.edu](http://www.who.edu).
- 18 Conway, J. "Design and construction of an electronic system for dual laser plasma experiments and its application to photoabsorption studies of medium Z elements," M.Sc. thesis, University College Dublin, 2000.
- 19 Zimmerman, G. D. and Kruer, W. L., Comments Plasma Physics, *Controlled Fusion*, **2**, 51, 1975.
- 20 Filevich, J., Rocca, J. J., Jankowska, E., Hammarsten, E. C., Kanizay, K., and Marconi, M. C., "Two-dimensional effects in laser-created plasmas measured with soft-x-ray laser interferometry," *Phys. Rev. E*, **67**, 056409, 1–6, 2003.
- 21 George, S., Koay, C.-S., Takenoshita, K., Bernath, R., Al-Rabban, M., Keyser, C., Bakshi, V., Scott, H., and Richardson, M., "EUV spectroscopy of mass-limited Sn-doped laser microplasmas," in *Emerging Lithographic Technologies IX*, Mackay, R.S., editor; SPIE-Int Society Optical Engineering: Bellingham, Vol. 5751, Chapter Pt 1-2, 779–788, 2005.
- 22 Perrot, F., "Fast calculation of electronic structure in plasmas: the screened hydrogenic model with  $l$ -splitting," *Physica Scripta*, Vol. 39, 332–337, 1989.

- 23 More, R. M., "Electronic energy-levels in dense plasmas," *J. Quant. Spectrosc. Radiat. Transfer*, Vol. 27, No. 3, 345–357, 1982.
- 24 Marchand, R., Caillé, S., and Lee, Y. T., "Improved screening coefficients for the hydrogenic ion model," *J. Quant. Spectrosc. Radiat. Transfer*, Vol. 43, No. 2, 149–154, 1990.
- 25 Rickert, A. and Meyer-ter-Vehn, J. "Frequency-dependent opacity calculations for high-Z plasma including *l*-splitting," *Laser and Particle Beams*, Vol. 8, No. 4, 715–727, 1990.
- 26 Itoh, M., Yabe, T., and Kiyokawa, S., "Collisional-radiative and average-ion hybrid models for atomic processes in high-Z plasmas," *Phys. Rev. A*, **35** (1), 233–241, 1987.
- 27 Mayer, H., unpublished report LA-647, Los Alamos Scientific Laboratory, Los Alamos, NM, 1947.
- 28 Lokke, W. A. and Grassberger, W. H., unpublished report UCRL-52276, Lawrence Livermore Laboratory, Livermore, CA, 1977.
- 29 Faussier, G., Blancard, C., and Decoster, A., "New screening coefficients for the hydrogenic ion model including *l*-splitting for fast calculations of atomic structure in plasmas," *J. Quant. Spectrosc. Radiat. Transfer*, Vol. 58, No. 2, 233–260, 1997.
- 30 Salzmann, D., "Atomic physics in hot plasmas," International series of monographs on physics, Oxford University Press, 1998.
- 31 *CRC Handbook of Chemistry and Physics*, 73<sup>rd</sup> Edition, D. R. Lide editor-in-chief, CRC press, Boca Raton, 1992.
- 32 Cowan, R. D., *The theory of atomic structure and spectra*, Berkeley, University of California Press, 1981.
- 33 Djaoui, A. and Rose, S. J., "Calculation of the time-dependent excitation and ionisation in a laser-produced plasma," *J. Phys. B: At. Mol. Opt. Phys.*, **25**, 2745–2762, 1992.
- 34 Pei, W. and Chang, T., "Improved calculation for ion configuration distribution from the average-atom model," *J. Quant. Spectrosc. Radiat. Transfer*, **64**, 15–23, 2000.
- 35 Patel, P. K., Wolfrum, E., Renner, O., Loveridge, A., Allott, R. Neely, D., Rose, S. J., and Wark, J. S., "X-ray line reabsorption in a rapidly expanding plasma," *J. Quant. Spectrosc. Radiat. Transfer*, **65**, 429–439, 2000.
- 36 Nishikawa, T., Takabe, H., and Mima, K., "Atomic modelling and radiation transport in laser produced plasmas," *Technology Reports of the Osaka University*, Vol. 41, No. 2059, 253–266, 1991.
- 37 Greim, H. R., *Principles of plasma spectroscopy*, Cambridge University Press, 1997.
- 38 Rose, S. J., "Atomic and radiation physics of hot dense plasmas," *Proceedings of 45<sup>th</sup> Scottish Universities Summer School in Physics—Laser-Plasma Interactions*, ed. M. B. Hooper, IOP, Bristol, 1995.
- 39 Tallents, G., "Atomic processes in high density plasmas," QuAMP II, Summer School, Open University, Milton Keynes, September 19–22, 2005.
- 40 Chambers, D. M., Glenzer, S. H., Hawreliak, J., Wolfrum, E., Gouveia, A., Lee, R. W., Marjoribanks, R. S., Renner, O., Sondhauss, P. Topping, S., Young, P. E., Pinto, P. A., and Wark, J. S., "Detailed hydrodynamic and x-ray spectroscopic analysis of a laser-produced rapidly-expanding aluminium plasma," *J. Quant. Spectrosc. Radiat. Transfer*, **71**, 237–247, 2001.
- 41 Hayden, P., Cummings, A., Murphy, N., O'Sullivan, G., Sheridan, P., White, J., and Dunne, P., "13.5 nm EUV emission from tin based laser produced plasma source," submitted for publication to *J. Appl. Phys.*, 2006.
- 42 Lysaght, M., Kilbane, D., Murphy, N., Cummings, A., Dunne, P., and O'Sullivan, G., *Phys. Rev. A* **72**, 014502, 2005.

## 5. Radiation transport in laser-produced tin plasmas

Next generation lithography (NGL) schemes for the semiconductor industry are currently based on a 13.5-nm (91.8-eV) tin plasma light source [1], where hundreds of thousands of near degenerate 4d-4f, 4p-4d, and 4d-5p transitions (from  $\text{Sn}^{5+}$ – $\text{Sn}^{13+}$  ions) overlap to form an unresolved transition array (UTA) [2, 3]. Such plasmas are optically thick, and radiation transport must be considered to calculate spatially-resolved, time-dependent spectra.

A radiation transport model is computationally intensive for any atomic system with more than a few lines. The UTAs are thus treated statistically as described in Chapter 2. The plasma hydrodynamics are simulated using the 1-D Lagrangian fluid hydrodynamic code **Med103** (an updated version of **Medusa**) [4–6] as described in Chapter 4. In this chapter, the hydrodynamics for a tin reference case (see Chapter 4) and spectra for tin plasmas under different laser power densities (*a.k.a.* irradiance), pulse widths, and pulse shapes are presented. The theoretical results are compared to experiment at UCD and the available literature. A conversion efficiency (CE), defined as the percentage of laser energy converted to in-band radiation, is given to quantify the optimum laser parameters within a 2% bandwidth (13.5 nm  $\pm$  1%).

The atomic model profiles the UTA statistically for each ion stage, characterising hundreds of thousands of lines by three parameters (mean wavelength, width, and sum  $gf$ ) [7–10], from spectral data as calculated using the Cowan code [11]. The average atom model in **Medusa** calculates the bound electron states, based on the screened hydrogenic model of More [12], and assumes an average of all possible ionisation states to reduce the number of rate equations in the hydrodynamic simulation. Rate equations in the calculation are for electron collisional excitation and de-excitation, electron ionisation, three-body recombination, spontaneous emission, and radiative recombination [4].  $nl$  splitting for  $\Delta n = 0$  (and 4d-5p) transitions is determined using the energy functional method of Itoh *et al.* [13] (see Chapter 4), from which the  $4p^6 4d^N$ ,  $4p^6 4d^{N-1} 4f^1$ ,  $4p^5 4d^{N+1}$ , and  $4p^6 4d^{N-1} 5p^1$  ( $1 \leq N \leq 9$ ) level populations are calculated. In **Medusa**, non-LTE equations are coupled to the free electron equation [14] giving hydrodynamic output for electron temperature and free electron density at each cell and time step, from which the ion fraction and  $l$ -degenerate level populations are determined [14, 15]. From the calculated  $nl$  level populations of the contributing UTA ions, emissivities and opacities of the fluid cells are then calculated to determine the multi-frequency radiation transport through the plasma, resulting in a spatially and temporally resolved spectrum and conversion efficiency in the 13.5-nm range.

1-D spatial output in the direction of the laser pulse (normal incidence) is reported here. Absorption from neutral and lower tin ion discrete transitions (Sn I–Sn IV) is not included in the opacity calculations, since absorption from these ions is considerably lower at normal incidence [16–18]. Doppler shift absorption from high-velocity gradients in the plasma is also not included, as the plasma expansion velocities are not observed to be high enough. Spatially-dependent laser absorption is from inverse bremsstrahlung [19] and is modelled as 20%, the default value in **Medusa** [5]. The laser pulse is modelled as a Gaussian of a given input maximum power density and pulse width (FWHM).

## 5.1 Sn reference case hydrodynamics

Theoretical data for the tin reference case (outlined in Chapter 4) is shown in Table 5.1. Only the variables in this table are changed during the surveys presented in this chapter (Section 5.2).

Variable	Unit	Value
laser wavelength	$\mu\text{m}$	1.064
laser irradiance	$\text{W}/\text{cm}^2$	$1.3 \times 10^{11}$
pulse width (FWHM)	ns	15
target diameter	$\mu\text{m}$	50

**Table 5.1** Tin reference case input laser variables

### 5.1.1 Sn reference case general hydrodynamics

Figures 5.1a-h show the output hydrodynamic data from the tin reference case, firstly (a-d) versus distance at three times near the peak of the pulse (23 ns,  $\pm 5$  ns) and, then (e-h) versus time for various cells, and is shown on one page for comparison.

The electron temperature ranges from 0–50 eV (c) and the electron density is mostly from  $10^{20}$  to  $10^{22}$   $\text{cm}^{-3}$  (b), indicating that the plasma is predominantly in the non-LTE range. The maximum temperature of the plasma is 52.3 eV.

From the velocity versus distance plot (a), it is clear that the expansion velocity (and thus plasma volume) increases with “loading” and continues after the peak of the pulse (laser “loading” is here defined as the laser pulse profile versus time). The velocity at the edge of the plasma increases the most (a and e), showing the change from a non-LTE to the less dense CE plasma model. This effect can also be seen in the electron density plots (b and f), where a non-LTE model is generally considered valid for LPPs from  $10^{20}$  to  $10^{22}$   $\text{cm}^{-3}$ . Most of the plasma can be classified as non-LTE (f). However, the hot inner core is in LTE, whereas the outer edge is in CE. A reduction in density corresponds to lower opacity and thus the plasma edge does not absorb as significantly. Conversely, the hot inner core after the peak of the pulse shows a marked increase in density and is highly self-absorbing. (Opacity is analysed further with spectral plots in Section 5.2.) Note that the maximum velocity at the edge of the plasma (e) is less than .01% the speed of light and thus any Doppler shift absorption due to velocity gradients at this laser intensity is not significant.

The average charge rises rapidly as the target absorbs radiation and slowly decreases after the end of the pulse from the inner core out (d). It can be seen (c and d) that the average charge distribution ( $\langle z \rangle$ ) closely resembles that of the electron temperature distribution, clearly showing the strong dependence of  $\langle z \rangle$  on temperature.<sup>56</sup> However, on the down side of the pulse, the average charge decreases more slowly than the temperature as a result of charge freezing ([14] and as discussed in Chapter 4). The maximum  $T_e$  and  $\langle z \rangle$  occurs after the peak of the pulse, indicating that energy is still being absorbed. In (h), note the charge freezing versus time. Note also that the average charge starts at 3.8 in the *Medusa* simulation, because of the average atom representation at room temperature (effectively the valence of the neutral  $[\text{Kr } 4d^{10}] 5s^2 5p^2$  atom at low temperature).

<sup>56</sup> Such a large dependence greatly aids the heuristic analysis of the multi-dimensional data set.

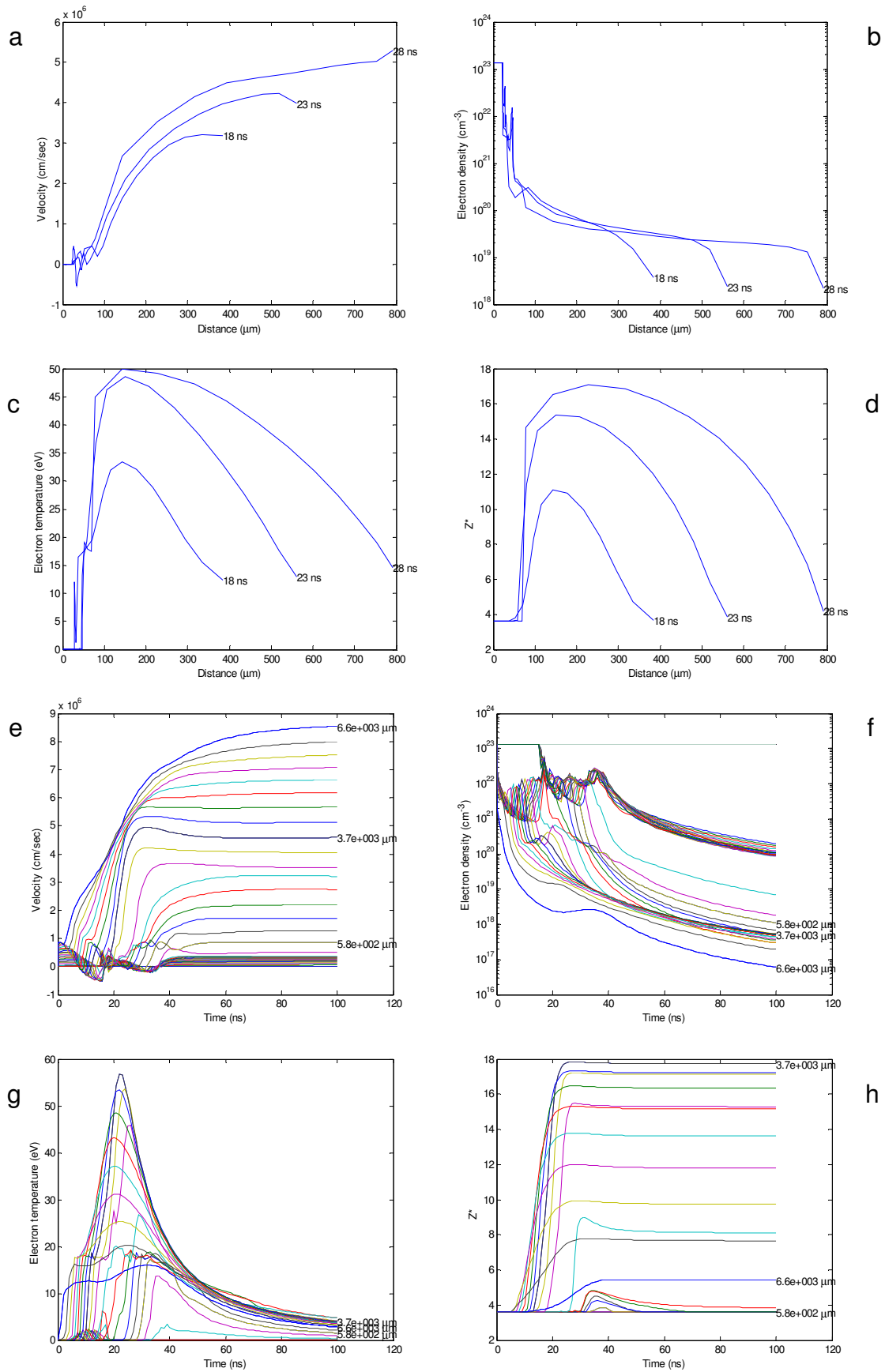
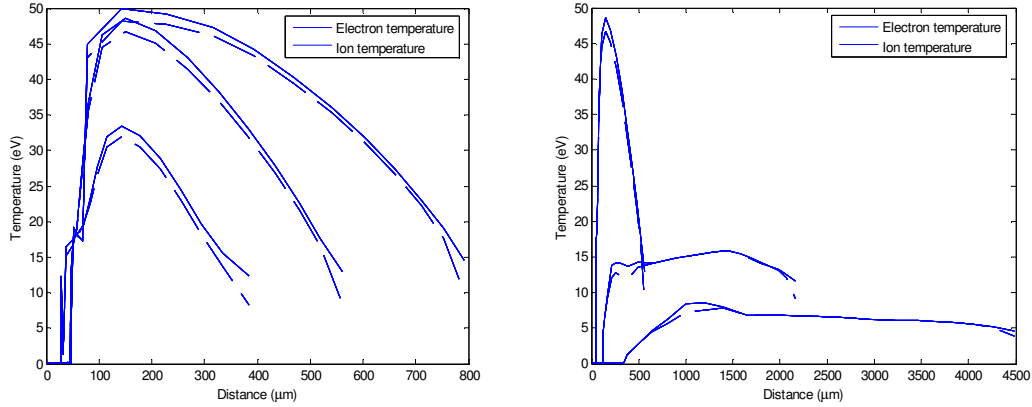


Figure 5.1a-h Sn reference case hydrodynamic output



**Figure 5.2** Electron and ion temperature at different times (left: 18 ns, 23 ns, and 28 ns; right: 23 ns, 49 ns, and 79 ns)

Figure 5.2 shows the electron and ion temperatures together versus distance at different times within the plasma. Note that the ion temperature and electron temperature are different, but not nearly as much as in the aluminium reference case (see Chapter 4), because of the much smaller incident laser power density. The difference between  $T_e$  and  $T_i$  can help quantify the validity of a steady-state plasma model, which is based on one temperature only. Here, it can be seen that because the temperatures are almost the same, a steady-state model (such as that of Colombant and Tonon [20]) can reasonably quantify in-band ion contribution, as shown in [10].

### 5.1.2 Sn reference case ion densities and level populations

The fractional and total ion densities for the 4d subshell ions (Sn V–Sn XIV) at the peak of the pulse are shown in Figure 5.3. Here it is seen that in the middle of the reference plasma, Sn VIII is in greatest abundance (to about 350  $\mu\text{m}$ ) and that Sn IV is dominant at the edge of the plasma. Note that all of the 4d subshell ions rise, fall, and rise with distance, showing the coupling to the laser pulse on the ablation plume.

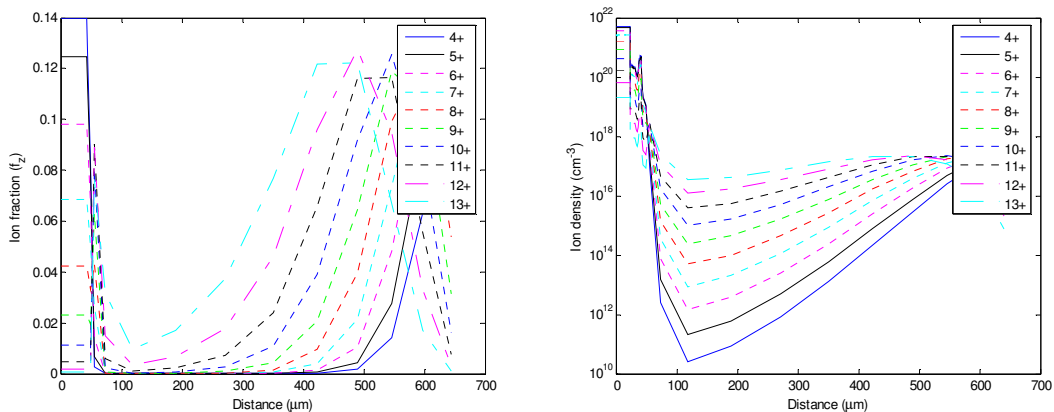


**Figure 5.3** Ion fractions and ion densities versus distance for Sn V–Sn XIV at the peak of the pulse

The population levels versus distance for three representative 4d subshell ions (Sn VI, Sn X, and Sn XIV) are shown before, at, and after the peak of the pulse in Figures 5.4a-c.

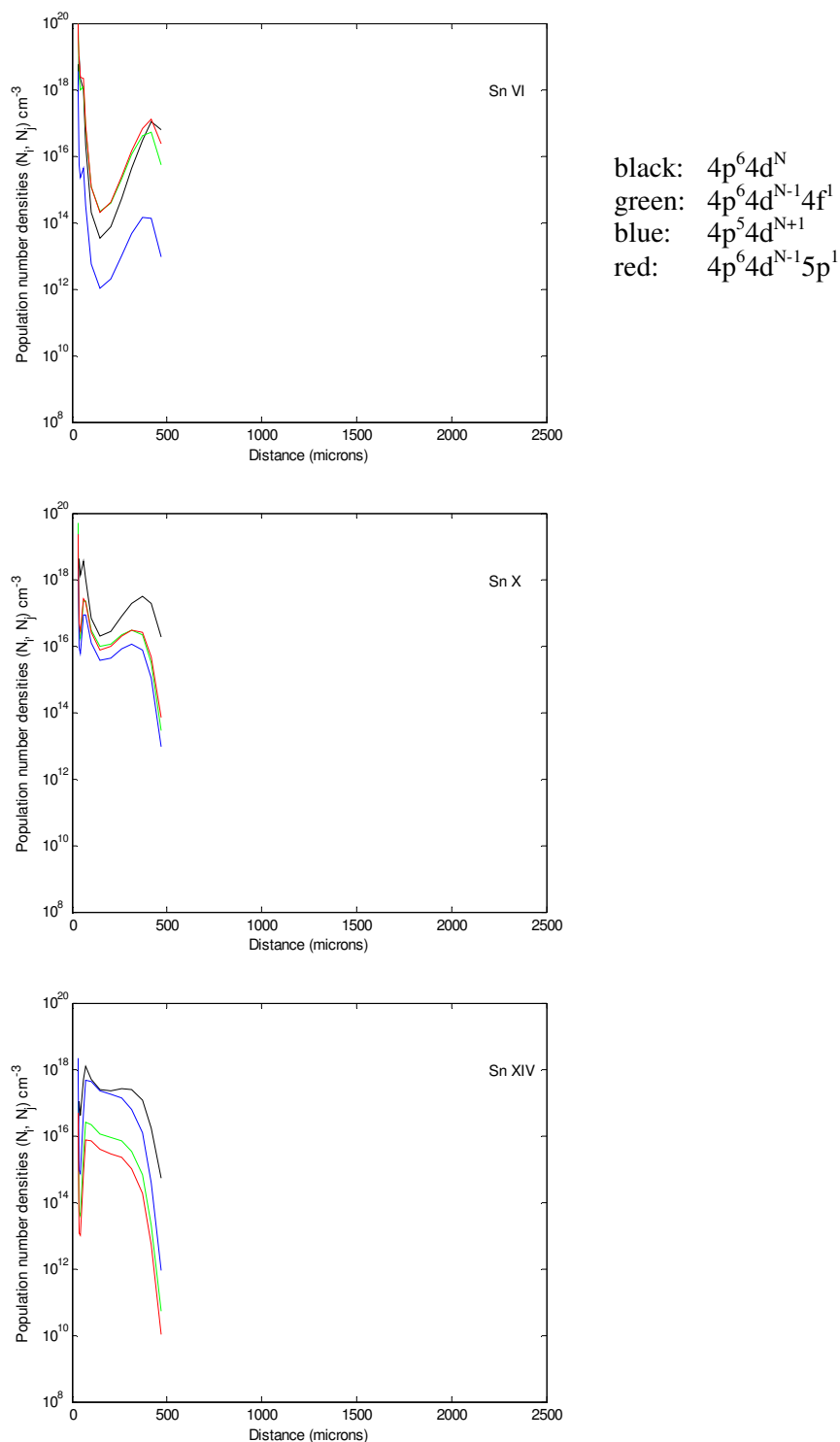


**Figure 5.4a** Sn VI (top), Sn X (middle), and Sn XIV (bottom) level populations versus distance before the peak of the pulse (18 ns)

Here, the increased  $4p^5 4d^{N+1}$  (blue) and decreased  $4p^6 4d^{N-1} 5p^1$  (red) populations are seen with increased ionisation, indicating the increased 4p-4d and decreased 4d-5p contributions to the UTA. Furthermore, the rise, fall and rise of the level populations (primarily a function of ion fraction) is more pronounced at the peak of the pulse as expected with increased coupling to the laser pulse. Note the significant population decrease at the edge of the plasma (last cells).

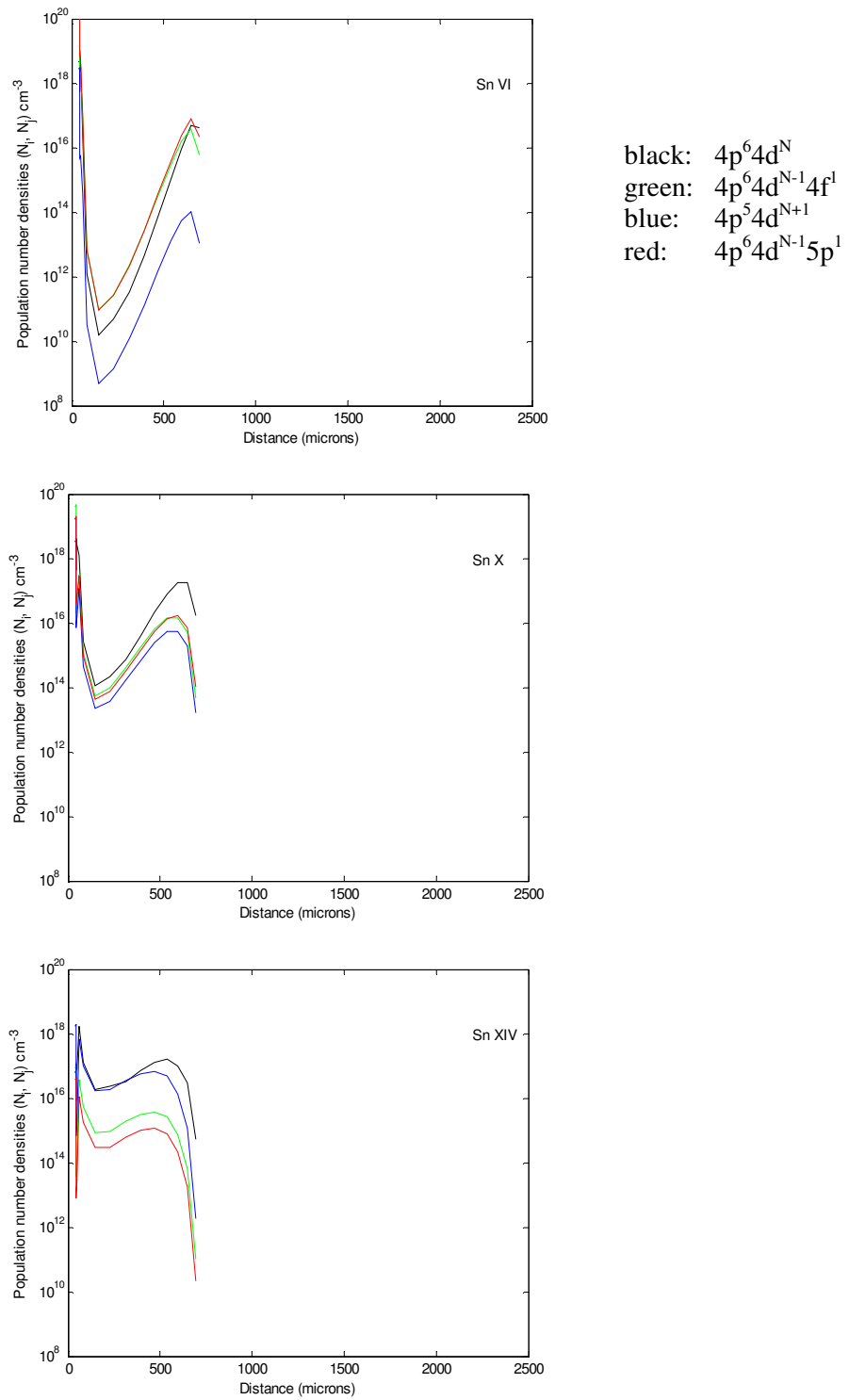


**Figure 5.4b** Sn VI (top), Sn X (middle), and Sn XIV (bottom) level populations versus distance at the peak of the pulse (23 ns)

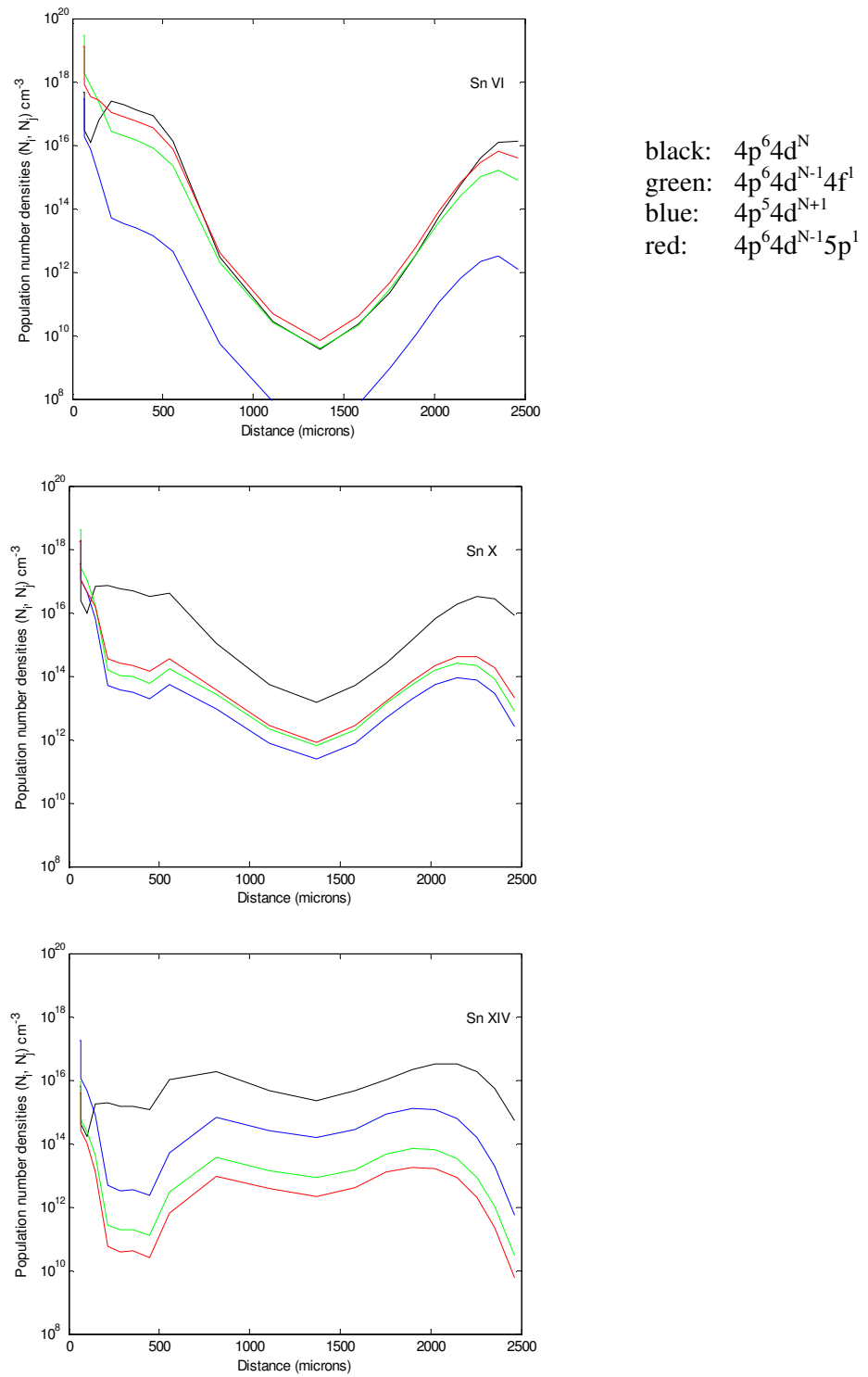
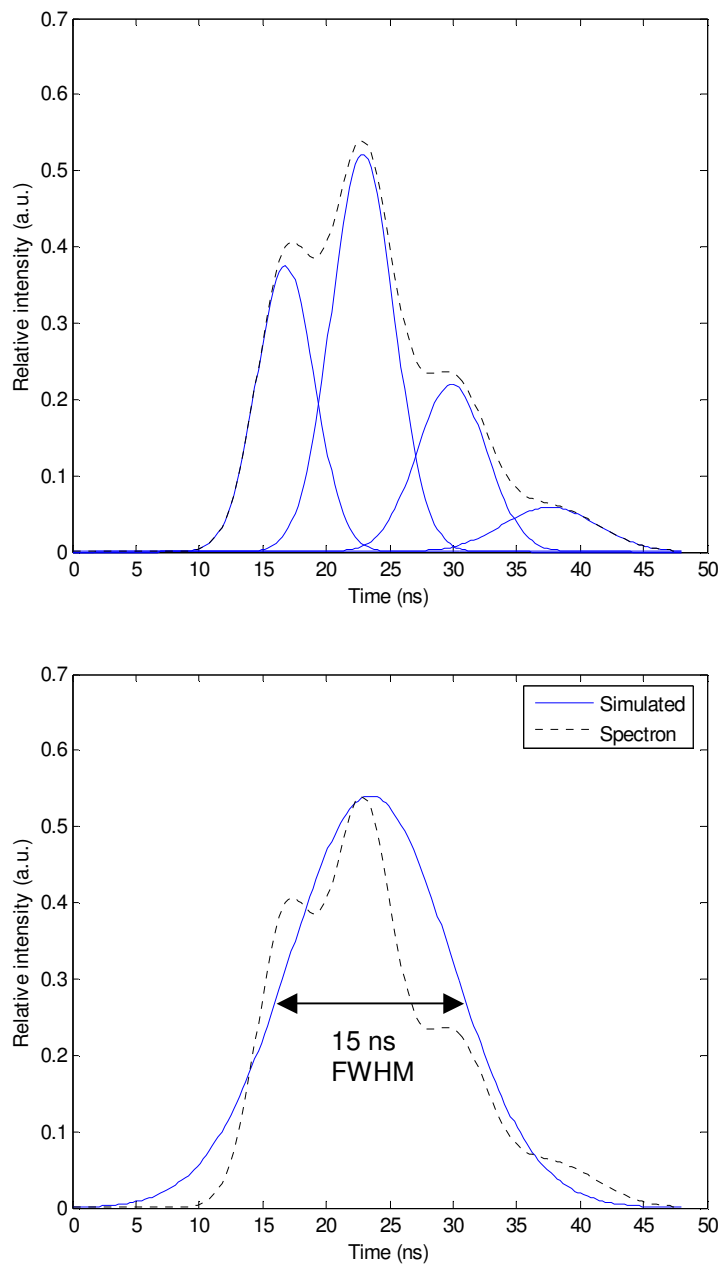


Figure 5.4c Sn VI (top), Sn X (middle), and Sn XIV (bottom) level populations versus distance after the peak of the pulse (49 ns)

### 5.1.3 Simulated laser pulse

The laser pulse is simulated as a single Gaussian in the *Medusa* hydrodynamic calculations. The 1100 mJ, Spectron Nd:YAG laser used in experiments at UCD [18], however, is more realistically represented as a sum of four Gaussians. The experimental pulse (normalised) is shown in Figure 5.5 (top) with individual pulses. The experimental and simulated pulses are shown in Figure 5.5 (bottom).

For the simulated runs in the analysis in this chapter, a single Gaussian is used, which matches the peak and minimises excess pre and post loading. The laser was thus given a width of 15 ns (FWHM) to best compare to the laser used in experiments. It is intended in a future study to input a multiple-Gaussian laser pulse into *Medusa*.



**Figure 5.5** Experimental multiple-Gaussian (dashed) and simulated *Medusa* single-Gaussian (solid) laser pulse

## 5.2 Radiation transport and conversion efficiency

Three surveys are presented which independently vary power density, pulse width, and pulse shape. A cylindrical target of 90  $\mu\text{m}$  radius is assumed in all simulations as described in Chapter 4. An equivalent power is given in *Medusa* to convert from cylindrical geometry to planar geometry to compare to experimental planar targets used at UCD [18]. Power density is varied from 0.5 to  $3.0 \times 10^{11} \text{ W/cm}^2$ , with a 15-ns pulse width (FWHM) at a wavelength of 1064 nm (Nd:YAG). Using the power density with the maximum conversion efficiency (CE) from the first survey, the pulse width is then varied from 7 to 20 ns (FWHM). Finally, results are presented for different pulse cut-off lengths to investigate the effects of pulse shaping. The theoretical spectra with radiation transport and a conversion efficiency are calculated for each case and results compared to experiments at UCD.

### 5.2.1 Varying power density

In the first survey, power density was varied from 0.5 to  $3.0 \times 10^{11} \text{ W/cm}^2$ . The relevant data is shown in Table 5.2 along with some general results (laser energy, CE into  $2\pi$  sr, plasma length, maximum  $T_e$  and  $\langle z \rangle$ ). Results are reported for a simulation over the outer 20 cells. (A survey of cell number was conducted and the results were almost identical for simulations greater than 20 cells.) As observed in [14], only the outer cells of the plasma contribute to the in-band emission. The hot inner core is self-absorbing and does not contribute to the net EUV emission [14]. (Note that the number of cells in the hydrodynamics simulation was 400 cells.)

Run	Wave-length (nm)	Width (ns) 0.6 FWHM	Pmax ( $\times 10^{11}$ W/m <sup>2</sup> )	Pequiv ( $\times 10^{11}$ W/cm <sup>2</sup> )	Etot (mJ) Eq 5.1	Elaser (mJ) Eq 5.4	CE (%)	Plasma length (mm)	$\max T_e$ (eV)	$\max \langle z \rangle$
A1	1064	9	0.45	0.5	72	191	2.57	2.90	21.9	8.6
A2	1064	9	0.54	0.6	86	229	3.90	3.11	24.8	9.9
A3	1064	9	0.63	0.7	100	267	4.83	3.26	28.0	11.1
A4	1064	9	0.81	0.9	129	344	4.84	3.68	34.3	13.2
A5	1064	9	0.90	1.0	143	382	3.83	3.81	37.8	14.2
A6	1064	9	0.99	1.1	157	420	2.77	3.89	41.4	15.1
A7	1064	9	1.17	1.3	186	496	1.41	4.20	48.4	16.7
A8	1064	9	1.35	1.5	215	573	0.78	4.78	60.4	18.7
A9	1064	9	1.80	2.0	286	763	0.46	5.50	70.5	20.0
A10	1064	9	2.70	3.0	429	1145	0.20	8.63	106.3	22.9

**Table 5.2 Power density survey from  $0.5$  to  $2.0 \times 10^{11} \text{ W/cm}^2$  (1064 nm, 15 ns FWHM, cylindrical geometry, 90  $\mu\text{m}$  radius, 400 cell simulation)**

The laser energy was calculated using Eqs. 5.1 and 5.2. The *Medusa* input variables are as described in Section 4.1.1.2 and Appendix D. (Note that  $P_{\max}$  is the maximum power,  $P_{\text{length}}$  is the pulse length, and  $r$  is the focussed spot radius.)

Conversion efficiency is given in Eq. 5.3.  $I_{\text{out}}$  is in  $\text{W/m}^2/\text{sr}/[\text{Hz/s}]$  and is converted to energy by integrating over the simulation time ( $t_{\text{stop}}$ ) and the 2% in-

band frequency range (calculated over 20 frequency points between 13.365–13.635 nm) and multiplying by the focussed spot radius surface area,  $\pi r^2$ , and  $2\pi$  sr. A constant surface area at the end of the simulation is used here.

The laser energy was calculated in Eq. 5.4 to compare to experimental values. The ratio of the experimental to theoretical laser energy is  $4\log(2)$  (2.77), where the difference is due to using  $P_{max}$  (theoretical) or  $P_{equiv}$  (experimental), an input pulse length of 0.6 x FWHM (e.g., 9-ns in *Medusa* for a 15-ns FWHM pulse), and from integrating a Gaussian in the theoretical calculation. The ratio of  $P_{max}$  to  $P_{equiv}$  (to convert from cylindrical to planar geometry) is given in Eq. 5.5.

The plasma length was determined from the length of the last cell at each time step in *Medusa*.

$$E_{tot} = P_{max} P_{length} \frac{\sqrt{\pi}}{2} \cdot \xi \cdot r \quad (5.1)$$

$$\xi = erf\left(\frac{t - P_{mult} P_{length}}{P_{length}}\right) + erf(P_{mult}) \quad (5.2)$$

$$CE = \frac{2\pi \int_{13.5-1\%}^{13.5+1\%} \int_0^{t_{stop}} I_{out}(\lambda, t) dt d\lambda dA}{E_{tot}} \quad (5.3)$$

$$E_{laser} = P_{equiv} P_{length} \pi r^2 \quad (5.4)$$

$$P_{max} = \frac{P_{equiv} r}{100} [r \text{ in } \mu\text{m}] \quad (5.5)$$

The calculated spectra are shown on one graph in Figure 5.6. The calculated spectra at each power density are shown individually in Figures 5.7a-j.

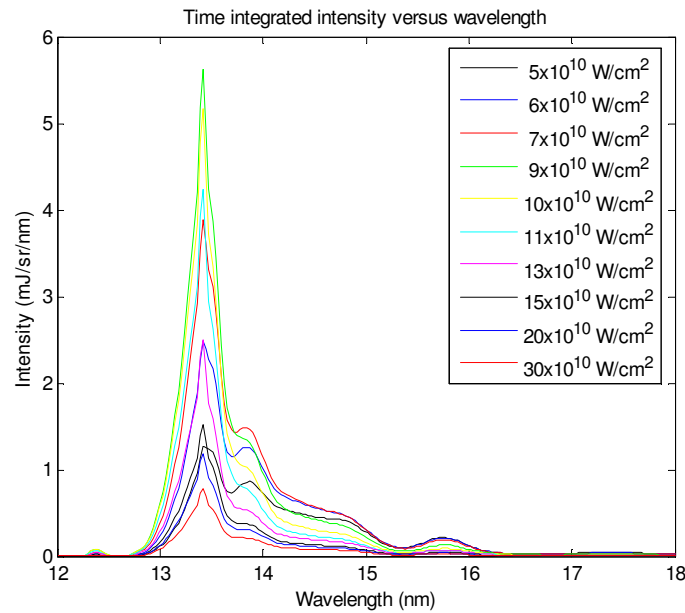


**Figure 5.6** Calculated spectra at different laser power densities ( $0.5\text{--}3.0 \times 10^{11}$  W/cm<sup>2</sup> for 1064 nm, 15 ns FWHM, cylindrical geometry, 90  $\mu\text{m}$  radius, 20 cell simulation)

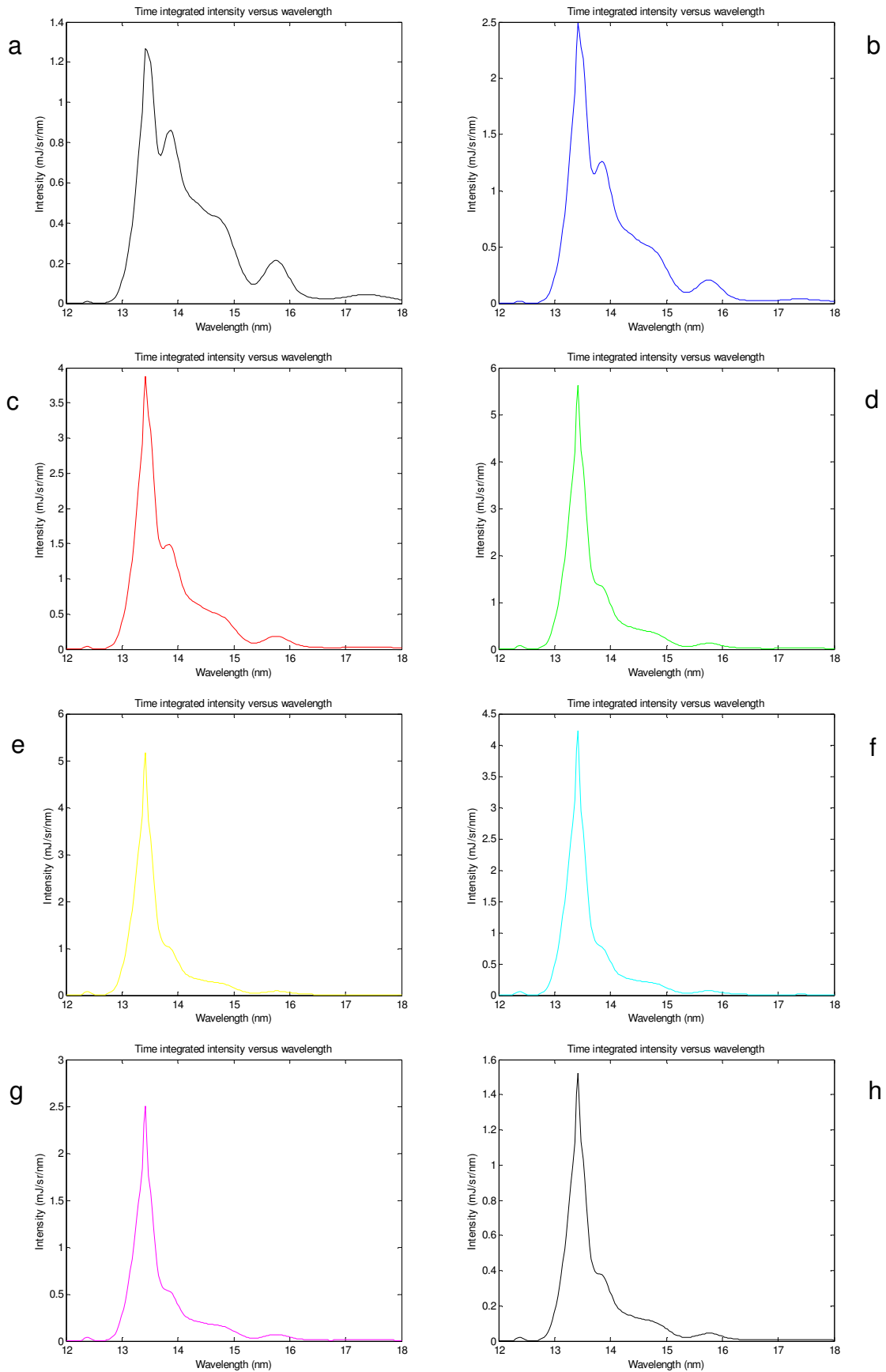


**Figure 5.7** Calculated spectra at  $0.5, 0.6, 0.7, 0.9, 1.0, 1.1, 1.3, 1.5, 2.0,$  and  $3.0 \times 10^{11} \text{ W/cm}^2$  (for 1064 nm, 15 ns FWHM, cylindrical geometry, 90  $\mu\text{m}$  radius, 20 cell simulation)

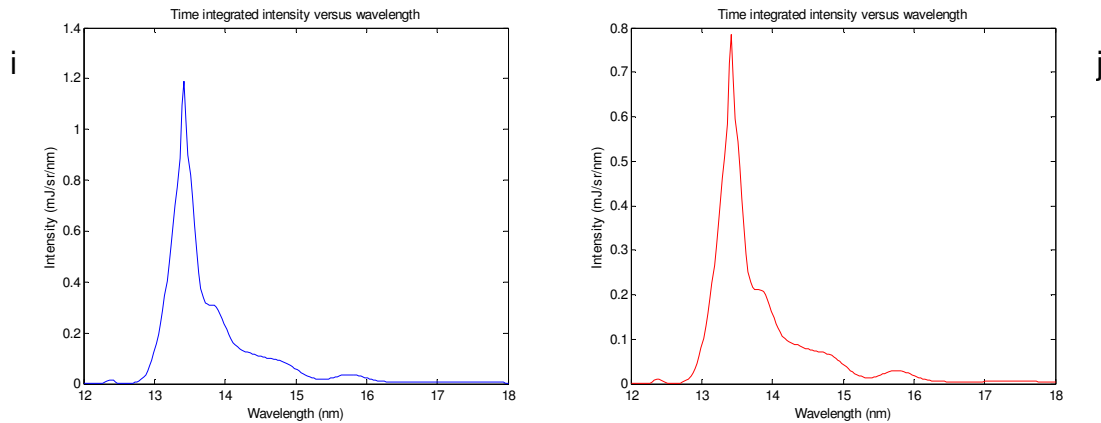


**Figure 5.7 (cont)** Calculated spectra at  $0.5, 0.6, 0.7, 0.9, 1.0, 1.1, 1.3, 1.5, 2.0,$  and  $3.0 \times 10^{11} \text{ W/cm}^2$  (for 1064 nm, 15 ns FWHM, cylindrical geometry, 90  $\mu\text{m}$  radius, 20 cell simulation)

Some general results can be observed in the spectra as power density increases. The emission increases and then decreases with increased laser intensity as the UTA contributing ions move in- and then out-of-band, as was seen in the steady-state case using the model of Colombant and Tonon [20], where an average temperature and density was assumed over the whole plasma. As a result the spectra narrows as power density increases and the narrowing continues as net emission decreases. Furthermore, the wavelength at peak emission decreases as power density increases, as seen experimentally by Hayden *et al.* [18] and in the steady-state analysis in [10].

The corresponding plot of CE versus power density is given in Figure 5.8, where a maximum CE of 4.8% is seen at  $0.9 \times 10^{11} \text{ W/cm}^2$ . Hayden *et al.* [18] observed a maximum CE of 2.3% at  $1.6 \times 10^{11} \text{ W/cm}^2$  for experimental results at  $45^\circ$ .

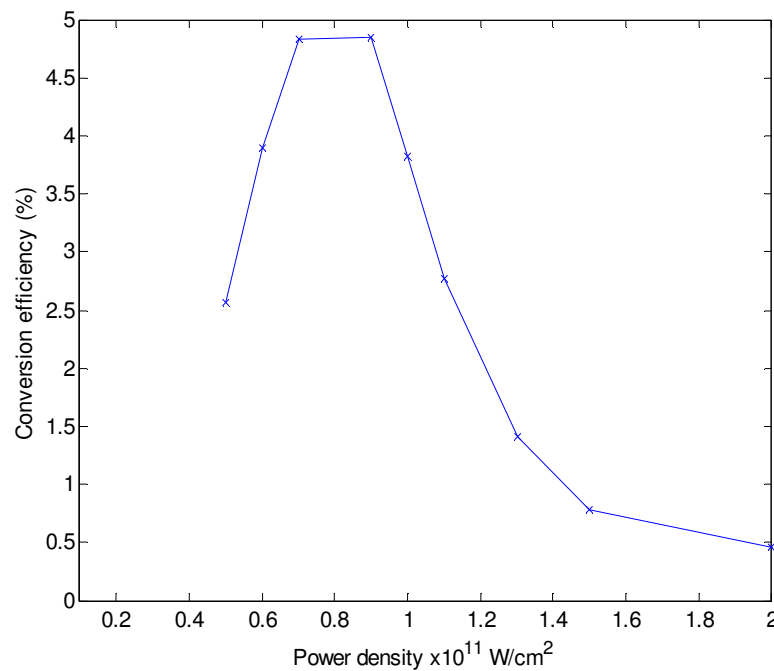


**Figure 5.8** Conversion efficiency versus laser power density ( $0.5$  to  $3.0 \times 10^{11} \text{ W/cm}^2$  for 1064 nm, 15 ns FWHM, cylindrical geometry, 90  $\mu\text{m}$  radius, 20 cell simulation)

It should be noted that a real plasma is anisotropic and thus the calculated CE would be greater than that obtained from a 2-D or 3-D plasma. As noticed by Wark *et al.* [21], emission is strongly dependent on observation angle. Fujioka *et al.* [22] report experimental CEs 70% of the simulated CEs, because non normal incidence radiation travels  $1/\cos(\theta)$  longer (where  $\theta$  is the angle between laser incidence and the detector) and thus absorption is greater, and also that the simulated plasma does not consider lateral heat transfer or plasma expansion along the target [22]. Hayden *et al.* [18] give a  $\cos^{0.18}(\theta)$  dependence on CE. Furthermore, for the simulated spectra, the spot size was kept constant and the energy varied, but it should be noted that the spot sizes in [18] were calculated  $\pm 10\%$ . As well, only 4d-4f, 4p-4d, and 4d-5p UTAs are considered here and that satellite transitions and absorption from lower ion stages are not included.

Plasma length (at the end of the simulation) and maximum electron temperature versus the surveyed power densities are shown in Figure 5.9 (to  $2 \times 10^{11}$  W/cm<sup>2</sup>), where it is seen that both depend linearly on laser intensity. As stated in [23], expansion velocity depends on laser intensity and increases with ionisation. Figure 5.9 gives a straightforward indication of the dependence of plasma length (and thus the velocity of expansion) and maximum electron temperature (and thus average charge) on laser intensity. A simple estimate of the optimum power density near  $1 \times 10^{11}$  W/cm<sup>2</sup> can be seen since optimum 13.5-nm emission is between 35 and 40 eV, as reported in the steady-state analysis [10].

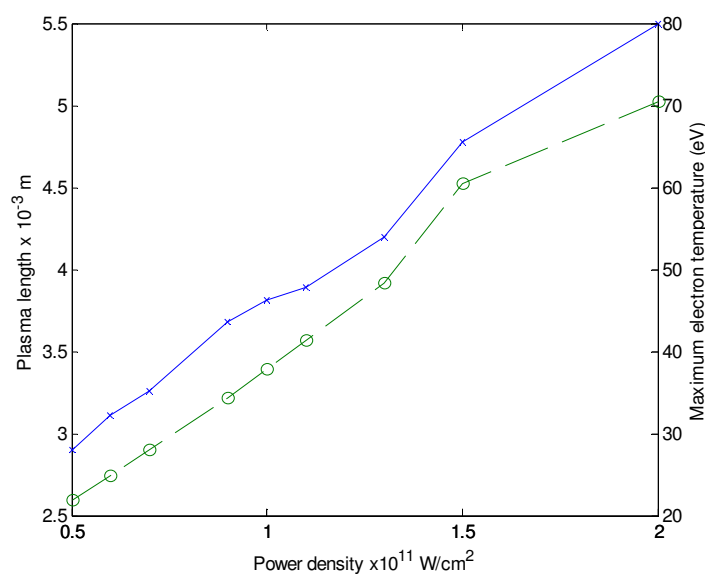


**Figure 5.9** Plasma length (x) and maximum electron temperature (o) versus power density ( $0.5$  to  $2.0 \times 10^{11}$  W/cm<sup>2</sup> at 1064 nm, 15 ns FWHM, cylindrical geometry, 90  $\mu$ m radius, 20 cell simulation)

A comparison between calculated and experimental spectra in [18] is shown in Figure 5.10 for a calculated power density of  $0.9 \times 10^{11}$  W/cm<sup>2</sup> and two experimental power densities:  $0.82 \times 10^{11}$  W/cm<sup>2</sup> and  $9.10 \times 10^{11}$  W/cm<sup>2</sup>. A constant background has been added to the calculated spectrum to account for the continuum and the calculated spectrum was multiplied by  $0.94 (\cos(45)^{18})$  to account for the detector angle. It can be seen that the spectra are well matched on both the short and long wavelength sides of the UTA using the non-LTE population levels calculated by the energy functional method. The difference in the peaks can be attributed to absorption from Sn I–Sn V ions, especially Sn IV and Sn V.

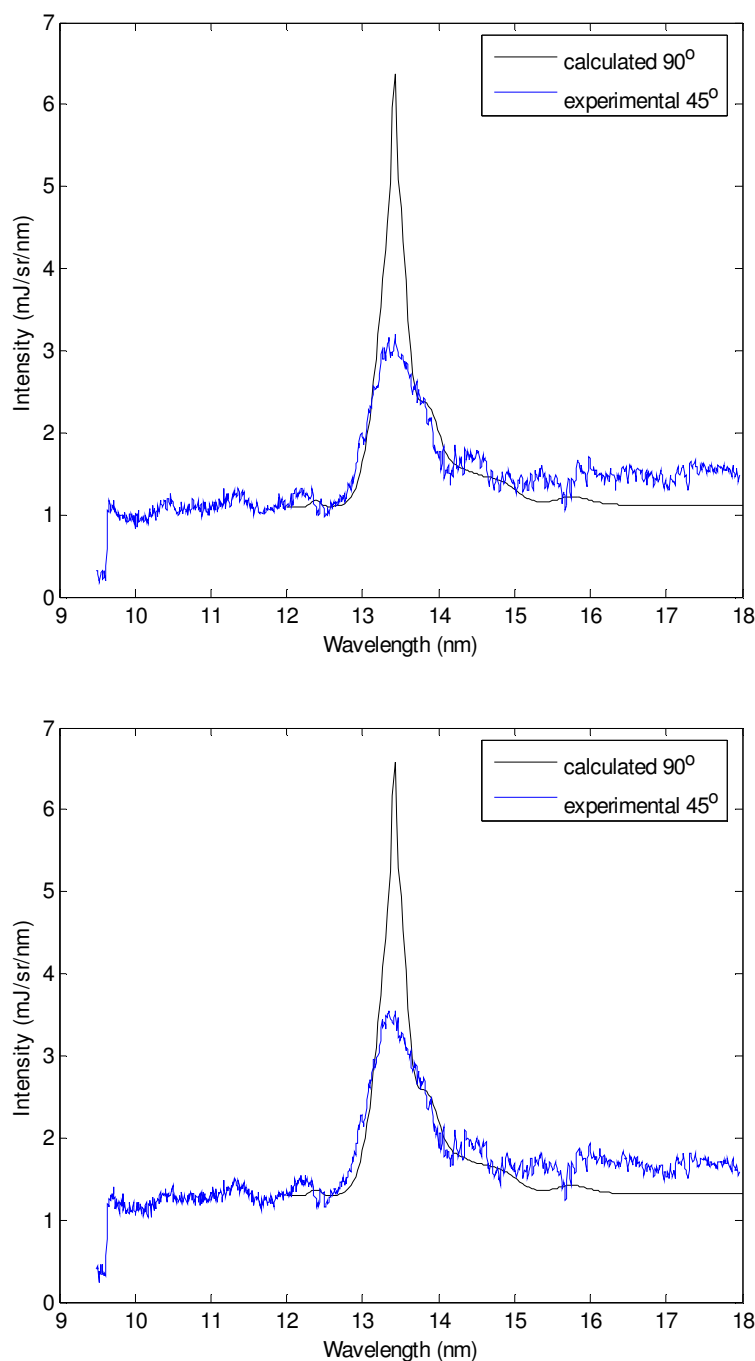


**Figure 5.10** Calculated  $0.9 \times 10^{11} \text{ W/cm}^2$  versus experimental  $0.82 \times 10^{11}$  (top) and  $0.91 \times 10^{11} \text{ W/cm}^2$  (bottom) spectra (1064 nm, 15 ns FWHM, cylindrical geometry, 90  $\mu\text{m}$  radius, 20 cell simulation)

Calculated spectra at selected times near the peak of the pulse (19–31 ns) are shown in Figure 5.11 (top) for a power density of  $0.9 \times 10^{11} \text{ W/cm}^2$ , where the maximum emission is seen at the peak of the pulse. The same spectra are shown in Figure 5.11 (bottom) with absorption equal to 0 in the calculation. Note that the spectra are more blackbody like as is to be expected. However, it should be noted that the same hydrodynamic data was used for both calculations (*i.e.*, a no absorption radiation transfer here is not necessarily the same as optically thin).

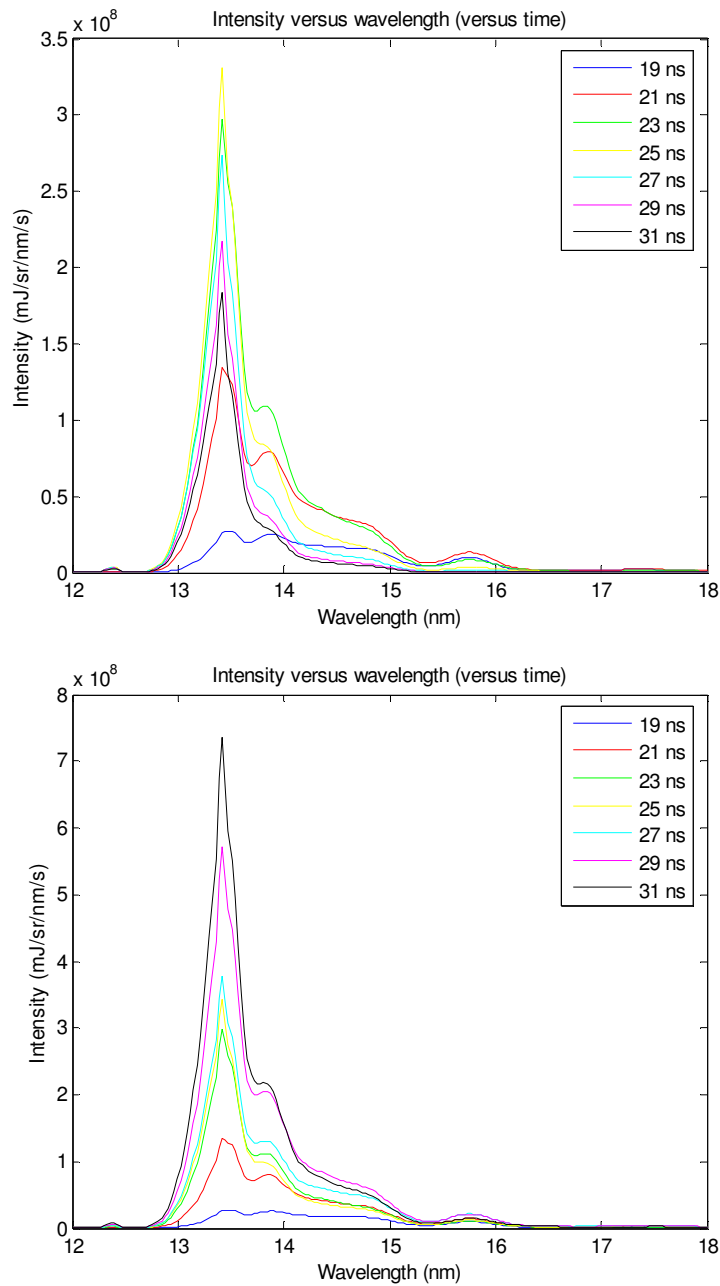


**Figure 5.11 Spectra versus selected times (19–31 ns) ( $0.9 \times 10^{11} \text{ W/cm}^2$  at 1064 nm, 15 ns FWHM, cylindrical geometry, 90  $\mu\text{m}$  radius, 20 cell simulation) (top: optically thick including absorption, bottom: no absorption)**

Note the increased emission and narrowing of the UTA with time up to the peak of the pulse for the optically thick calculation. In the previous graphs (which showed a time-integrated spectra), the broader emission could not be seen as easily because the absorption features were averaged out by the dominant peak emission.

The time resolved spectra in the 2% bandwidth are shown in Figure 5.12. Here, it can be seen again that the peak of the in-band emission occurs approximately at the peak of the pulse, and depends on time and wavelength. The shape is not symmetric about 13.5 nm, showing the increased UTA overlap of lower ion stages at higher wavelengths.

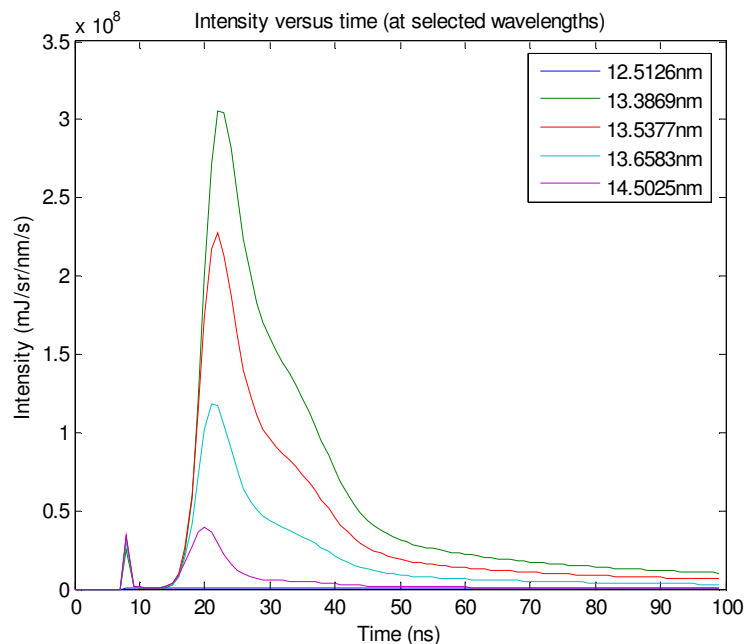


**Figure 5.12** Calculated spectra versus time at five wavelengths (for  $0.9 \times 10^{11} \text{ W/cm}^2$ , 1064 nm, 15 ns FWHM, cylindrical geometry, 90  $\mu\text{m}$  radius, 20 cell simulation)

The effect of matching the laser pulse exactly to spectral output for a specific wavelength (or optimised over a wavelength range) is examined more closely in Section 5.2.3, where the “macro” atomic system is compared to a classical system, which moves in and out of resonance at 13.5 nm as a function of the laser pulse loading. It will be seen below that matching the spectral output to the peak of the pulse achieves the best spectral response. The laser pulse profiles for the surveyed power densities are shown in Figure 5.13 for reference.

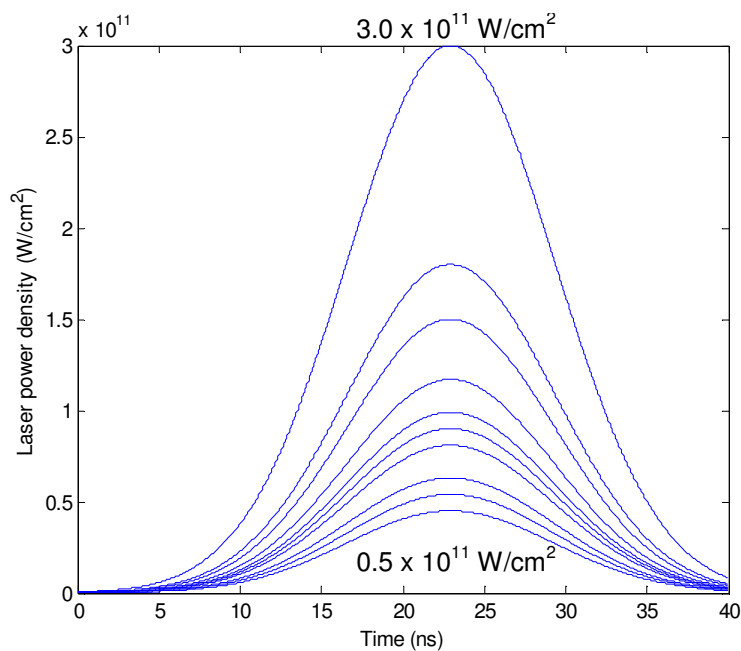


**Figure 5.13** Laser pulse profile for 0.5, 0.6, 0.7, 0.9, 1.0, 1.1, 1.3, 1.5, 2.0, and  $3.0 \times 10^{11} \text{ W/cm}^2$  (for 1064 nm, 15 ns FWHM, cylindrical geometry, 90  $\mu\text{m}$  radius, 20 cell simulation)

### 5.2.2 Varying pulse length

In the second survey, the laser pulse length was varied from 7 to 23 ns (FWHM), using the power density with the maximum CE from the first survey ( $0.9 \times 10^{11}$  W/cm<sup>2</sup>). The relevant data is shown in Table 5.3 along with general results (laser energy, CE into  $2\pi$  sr, plasma length, *etc.*). As in the first survey, the results are reported for a simulation over the outer 20 cells, laser energy was calculated using the Medusa laser input variables, the 2% in-band energy was calculated over 20 frequency points, and the plasma length was determined from the length of the last cell in Medusa.

Run	Wave-length (nm)	Width (ns) FWHM	Width (ns) 0.6 FWHM	Pequiv (W/cm <sup>2</sup> ) $\times 10^{11}$ W/cm <sup>2</sup>	Etot (mJ) Eq 5.1	Elaser (mJ) Eq 5.4	CE (%)	Plasma length (mm)	$max T_e$ (eV)	$max \langle z \rangle$
B1	1064	7	4.2	0.9	60	160	4.09	1.66	22.4	12.0
B2	1064	10	6.0	0.9	86	229	5.18	2.21	36.4	13.4
<b>B3</b>	1064	15	9.0	0.9	129	344	4.84	3.68	34.3	13.2
B4	1064	20	12.0	0.9	172	458	4.68	4.35	41.8	15.3
B5	1064	23	13.8	0.9	198	527	3.45	4.40	42.8	15.7

**Table 5.3 Pulse length survey from 7 to 23 ns (FWHM) (1064 nm,  $0.9 \times 10^{11}$  W/cm<sup>2</sup>, cylindrical geometry, 90  $\mu$ m radius, 20 cell simulation)**

The calculated spectra are shown in Figure 5.14. Clearly, the in-band emission increases with pulse width to a maximum and decreases again as the UTA contributing population increases and decreases. The maximum intensity and CE was calculated at a pulse width of 10 ns, where the CE was 8% higher than that at 15 ns. Note that the intensity increases with increased pulse width, although the conversion efficiency decreases because of the greater energy required. The plasma length also increases with longer pulse widths as is to be expected and reported in [22, 24, 25].

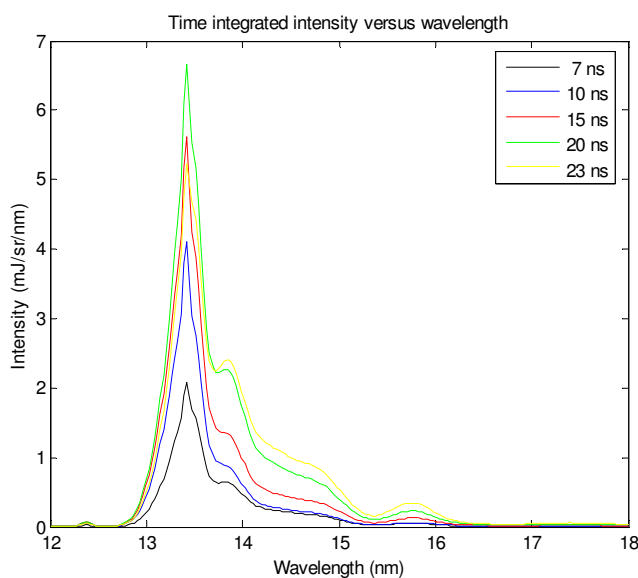


**Figure 5.14 Calculated spectra at different pulse lengths (7 to 23 ns (FWHM) for 1064 nm,  $0.9 \times 10^{11}$  W/cm<sup>2</sup>, cylindrical geometry, 90  $\mu$ m radius, 400 cell simulation)**

Furthermore, in an experiment on a 500- $\mu\text{m}$ , spherical, mass-limited microballoon target, an increase in CE was obtained as the pulse length decreased [22, 26]. It is not clear from that study, however, whether the power density remained constant, and it is likely that the pulse energy was kept constant, *i.e.*, the power density and pulse width were changed together. Here, a shorter pulse width produced a greater CE with the power density kept constant.

It should be noted that the original width of 15 ns was chosen to compare to the Nd:YAG laser available for experiment at UCD [18]. A further survey, varying both power density and pulse width, is required to determine optimum loading.

The time resolved spectra for the largest CE pulse width surveyed (10 ns) is shown in Figure 5.15, showing a greater intensity over a shorter time than for the optimum 15-ns pulse in the first survey. The laser pulse profiles for the surveyed pulse lengths are shown in Figure 5.16, again for reference.

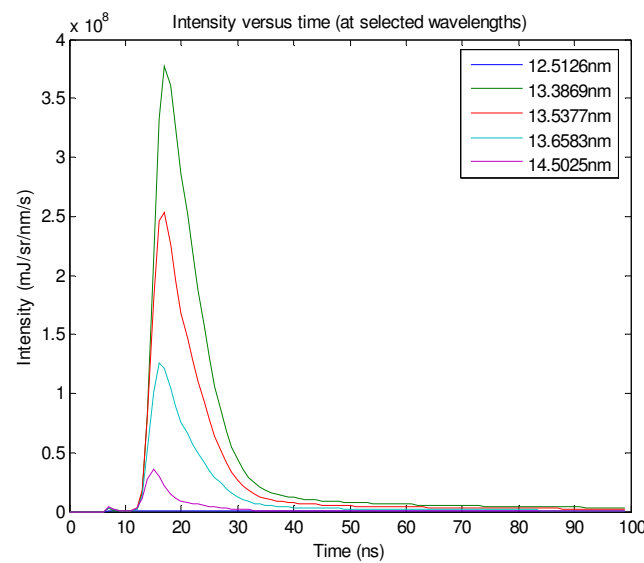


**Figure 5.15** Calculated spectra versus time at five frequencies (for 20 ns FWHM, 1064 nm,  $0.9 \times 10^{11}$  W/cm<sup>2</sup>, cylindrical geometry, 90  $\mu\text{m}$  radius, 20 cell simulation)

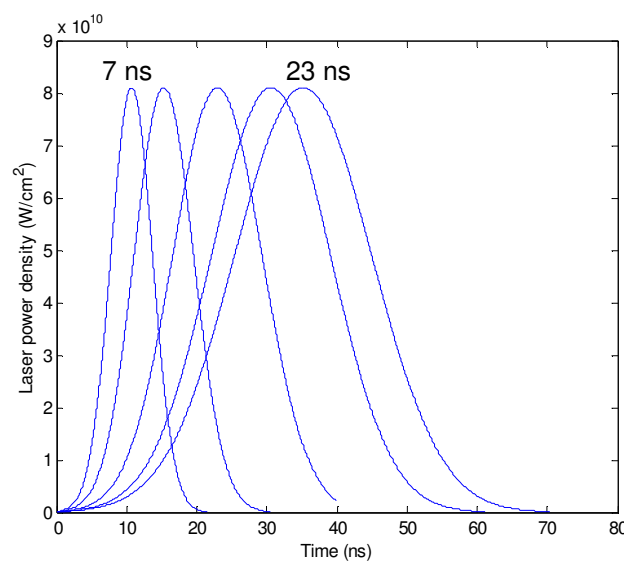


**Figure 5.16** Laser pulse profile for 7, 10, 15, 20, and 23 ns FWHM (for 1064 nm,  $0.9.0 \times 10^{11}$  W/cm<sup>2</sup>, cylindrical geometry, 90  $\mu\text{m}$  radius, 20 cell simulation)

### 5.2.3 Pulse shaping

From the results of the first survey, optimum emission occurred when the input laser pulse profile and output spectral emission matched temporally, suggesting a spectral tuning. Maximum UTA emission occurs at the laser energy where the temperature and density of the plasma give the required charge distribution. However, as loading increases, in-band emission passes through the optimum range: at lower power densities, maximum emission is after the peak of the pulse where the trailing edge of the pulse produces more emission and at higher power densities, maximum emission is before the peak, where more emission results from the leading edge of the pulse. If the loading could be maintained in the optimum range longer, such as for a flat top or oscillating pulse, the in-band emission could be increased.

Figure 5.17 (top) shows the laser pulse (dashed line) superimposed over the 2% bandwidth emission ( $0.9 \times 10^{11} \text{ W/cm}^2$ , 15 ns FWHM). The laser pulse and emission are normalised to highlight the temporal matching. Figure 5.17 (bottom) shows the same for a 10-ns pulse length. More spectral matching can be seen in the shorter, higher CE pulse.

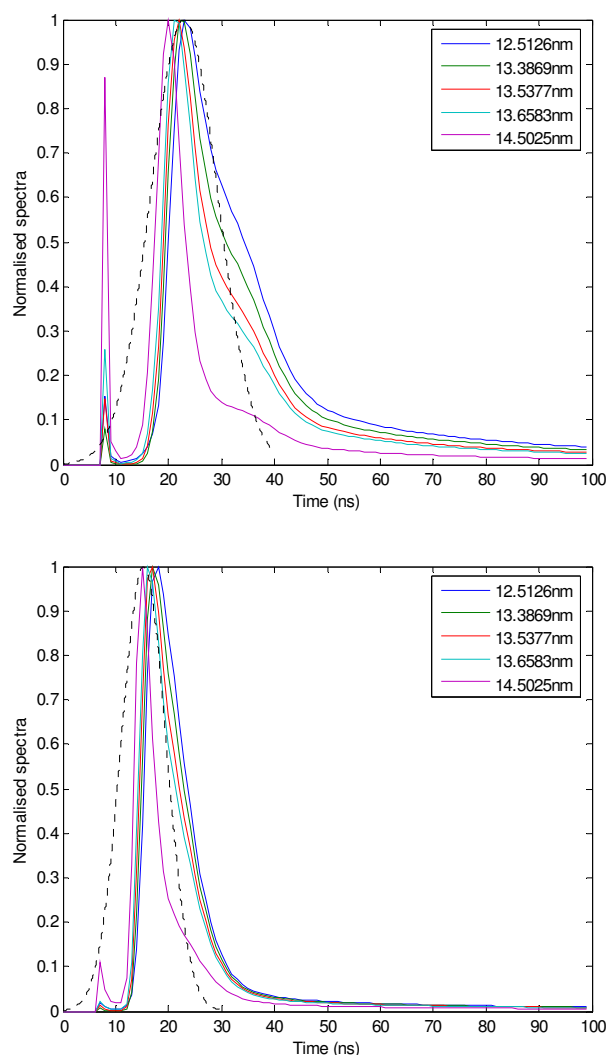


**Figure 5.17** Normalised spectra versus time at five wavelengths: 15 ns FWHM (top) and 10 ns FWHM (bottom) ( $1064 \text{ nm}$ ,  $0.9 \times 10^{11} \text{ W/cm}^2$ , cylindrical geometry,  $90 \mu\text{m}$  radius, 20 cell simulation)

Figure 5.18 (top) shows a “load-intensity” plot as the power density increases as in the first survey from  $0.5\text{--}3.0 \times 10^{11} \text{ W/cm}^2$  (for a constant 15-ns FWHM pulse length). Figure 5.18 (bottom) shows the same as the pulse width is increased from 7 to 23 ns (for a constant  $0.9 \times 10^{11} \text{ W/cm}^2$  power density). In all cases, the spectral response begins approximately at the peak loading, but for higher CEs the spectral response decreases more slowly or continues to increase with “unloading.”

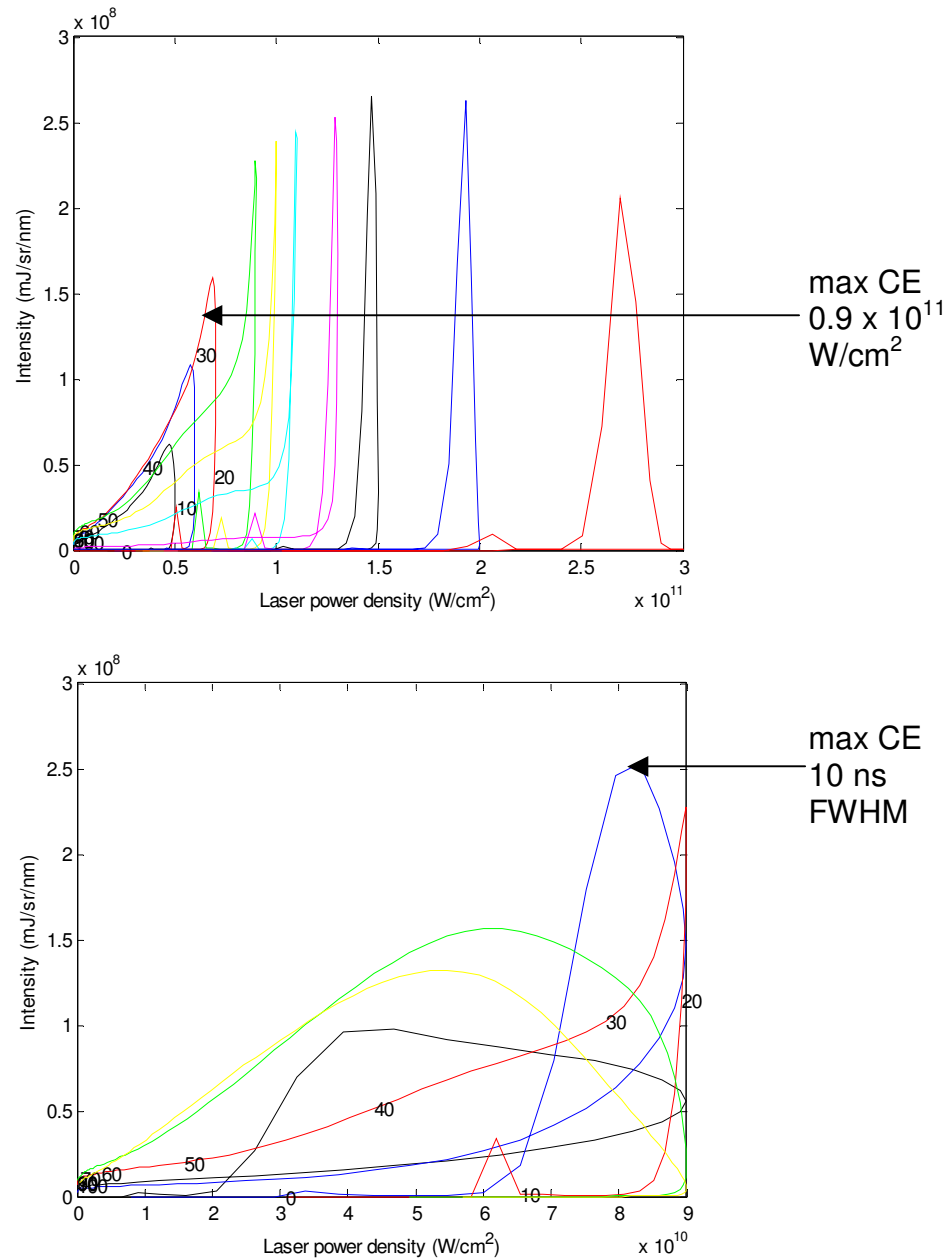
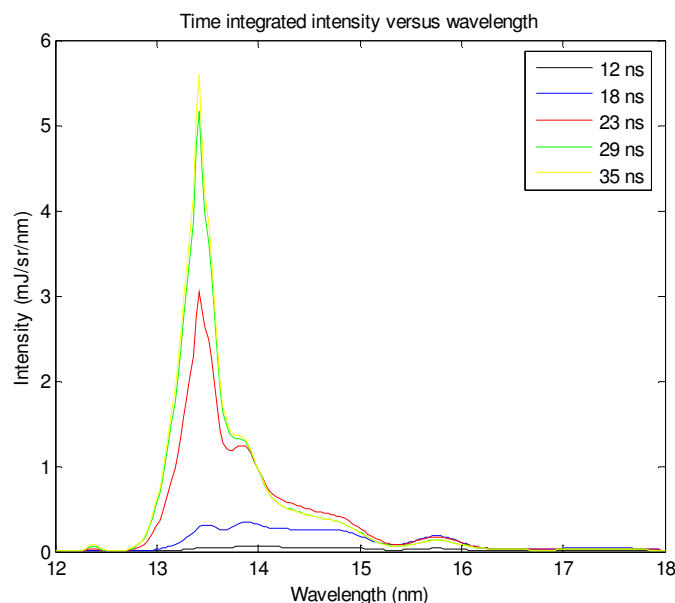


Figure 5.18 Spectral intensity at 13.5 nm versus power density: survey 1 (top) and survey 2 (bottom) (1064 nm, cylindrical geometry,  $90 \mu\text{m}$  radius, 20 cell simulation)

It is seen that pulse shaping can effect the conversion efficiency. As such, a number of loading schemes were considered, including multiple short pulses (as in pre-pulse-pulse loading). For this thesis, the effect of cutting off the loading was considered as suggested in [14], where the pulse was cut off at  $1/4$ ,  $3/8$ ,  $1/2$ ,  $5/8$ , and  $3/4$  of the full length, the results of which are shown in Table 5.4 and Figure 5.19.

Run	Wave-length (nm)	Width (ns) FWHM	Pequiv ( $\text{W}/\text{cm}^2$ ) $\times 10^{11}$ $\text{W}/\text{cm}^2$	Cut-off (ns)	Etot (mJ) Eq 5.1	Elaser (mJ) Eq 5.4	CE (%)	Plasma length (mm)	$\max T_e$ (eV)	$\max \langle z \rangle$
C1	1064	15	0.9	12	6	344	1.38	0.91	16.6	3.7
C2	1064	15	0.9	18	28	344	1.73	1.82	19.4	6.3
C3	1064	15	0.9	23	65	344	5.94	2.28	30.6	11.0
C4	1064	15	0.9	29	107	344	5.43	3.29	34.3	13.1
C5	1064	15	0.9	35	125	344	4.93	3.63	34.3	13.2
<b>C6</b>	1064	15	0.9	40	129	344	4.84	3.68	34.3	13.2

**Table 5.4 Pulse cut-off survey from 1/4 to 3/4 full length (1064 nm,  $0.9 \times 10^{11} \text{ W}/\text{cm}^2$ , 15 ns (FWHM), cylindrical geometry, 90  $\mu\text{m}$  radius, 20 cell simulation)**



**Figure 5.19 Calculated spectra at different laser cut-off times (1/4, 1/2, and 3/4, 1064 nm,  $0.9 \times 10^{11} \text{ W}/\text{cm}^2$ , 15 ns FWHM, cylindrical geometry, 90  $\mu\text{m}$  radius, 20 cell simulation)**

A 23% increase in conversion efficiency was observed for the 23-ns or 1/2-pulse cut-off. It should be noted, however, that it is not a simple task to turn off a laser in mid pulse and is of no value for improving CE in semiconductor manufacturing if the laser energy is still output.

In conclusion, the statistically calculated UTA showed greatest 13.5-nm oscillator strength for the 4d-subshell tin ions from Sn IX–Sn XIV. To determine emission from a doped-tin target, the oscillator strengths were weighted by the fractional ion density calculated from an optically thin, steady-state plasma model and showed a maximum emission at 40 eV. To determine emission from a pure tin target, the oscillator strengths were weighted by the ion density as a function of time and distance calculated from a 1-D Lagrangian hydrodynamic code and a multi-frequency radiation transport model. Conversion efficiency of in-band emission to laser energy was determined from two independent parametric studies and the maximum efficiency was obtained for a laser power density of  $0.9 \times 10^{11} \text{ W}/\text{cm}^2$  and a pulse width of 10 ns.

### 5.3 References

- 1 Derra, G., Zink, P., Krücken, T., Weber, A. and Pankert, J., “Tin Delivery Systems for Gas Discharge Sources,” *EUV Source Workshop*, San Jose, CA, USA, 2005.
- 2 O’Sullivan, G. and Carroll, P. K., “4d–4f emission resonances in laser-produced plasmas,” *J. Opt. Soc. Am.*, **71** (3), 227–230, 1981.
- 3 Carroll, P. K. and O’Sullivan, G., “Ground-state configurations of ionic species I through XVI for  $Z = 57–74$  and the interpretation of 4d–4f emission resonances in laser-produced plasmas,” *Physical Review A: General Physics*, **25** (1), 275–286, 1982.
- 4 Patel, P. K., Wark, J. S., Heading, D. J., Djaoui, A., Rose, S. J., Renner, O., and Hauer, A., “Simulation of x-ray line transfer in a cylindrically expanding plasma,” *J. Quant. Spectrosc. Radiat. Transfer*, **57** (5), 683–694, 1997.
- 5 Christiansen, J. P., Ashby, D. E. T. F., and Roberts, K. V., “Medusa: a one-dimensional laser fusion code,” *Computer Physics Communications*, **7**, 271–287, 1974.
- 6 Djaoui, A., “A user guide for the laser-plasma simulation code: MED103,” Technical Report *RAL-TR-96-099*, Central Laser Facility, Rutherford Appleton Library, 1996.
- 7 Mandelbaum, P., Finkenthal, M., Schwob, J. L., and Klapisch, M., “Interpretation of the quasicontinuum band emitted by highly ionized rare-earth elements in the 70–100 Å range,” *Phys. Rev. A*, **35**(12), 5051–5059 (1987).
- 8 Bauche, J. and Bauche-Arnoult, C., “Unresolved transition arrays,” *Physica Scripta*, **37**, 659–663, 1988.
- 9 Bauche, J. and Bauche-Arnoult, C., “Statistical approach to the spectra of plasmas,” *Physica Scripta*, **T40**, 58–64, 1992.
- 10 White, J., Hayden, P., Dunne, P., Cummings, A., Murphy, N., Sheridan, P., and O’Sullivan, G., “Simplified modeling of 13.5 nm unresolved transition array emission of a Sn plasma and comparison with experiment,” *J. Appl. Phys.*, **98**, 113301, 2005.
- 11 Cowan, R. D., *The theory of atomic spectra and structure*, Berkeley, University of California Press, 1981.
- 12 More, R. M., “Electronic energy-levels in dense plasmas,” *J. Quant. Spectrosc. Radiat. Transfer*, Vol. 27, No. 3, 345–357, 1982.
- 13 Itoh, M., Yabe, T., and Kiyokawa, S., “Collisional-radiative and average-ion hybrid models for atomic processes in high- $Z$  plasmas,” *Phys. Rev. A*, **35** (1), 233–241, 1987.
- 14 Cummings, A., O’Sullivan, G., Dunne, P., Sokell, E., Murphy, N., and White, J., “Conversion efficiency of a laser-produced Sn plasma at 13.5 nm, simulated with a one-dimensional hydrodynamic model and treated as a multi-component blackbody,” *J. Phys. D: Appl. Phys.*, **38**, 604–616, 2005.
- 15 Cummings, A., O’Sullivan, G., Dunne, P., Sokell, E., Murphy, N., White, J., Fahy, K., Fitzpatrick, A., Gaynor, L., Hayden, P., Kedzierski, D., Kilbane, D., Lysaght, M., McKinney, L., and Sheridan, P., “Variable composition laser-produced Sn plasmas—a study of their time-independent ion distributions,” *J. Phys. D*, **37** (17), 2376–2384, 2004.
- 16 O’Sullivan, G., “The spectra of laser produced plasmas with lanthanide targets,” in *Giant Resonances in Atoms, Molecules and Solids*, eds. Connerade, J. P., Esteva, J. M., and Karnatak, R. C., Plenum New York and London, 505–532, 1987.
- 17 Lysaght, M., Kilbane, D., Murphy, N., Cummings, A., Dunne, P., and O’Sullivan, G., *Phys. Rev. A* **72** 014502, 2005.
- 18 Hayden, P., Cummings, A., Murphy, N., O’Sullivan, G., Sheridan, P., White, J., and Dunne, P., “13.5 nm EUV emission from tin based laser produced plasma source,” submitted for publication to *J. Appl. Phys.*, 2006.
- 19 Patel, P. K., Wolfrum, E., Renner, O., Loveridge, A., Allott, R. Neely, D., Rose, S. J., and Wark, J. S., “X-ray line reabsorption in a rapidly expanding plasma,” *J. Quant. Spectrosc. Radiat. Transfer*, **65**, 429–439, 2000.
- 20 Colombant, D. and Tonon, G. F., “X-ray emission in laser-produced plasmas,” *J. Appl. Phys.*, **44** (8), 3524–3537, 1973.
- 21 Wark, J. S., Renner, O., Djaoui, A., Rose, S. J., Missalla, T., Neely, D., Foerster, E., and Hauer, A., “Measurements and simulation of the intensity and shape of the hydrogenic Al resonance line ( $1s^2S-2p^2P$ ) in laser-produced plasmas,” *J. Quant. Spectrosc. Radiat. Transfer*, Vol. 54, No. 1/2, 419–425, 1995.

- 22 Fujioka, S., Nishimura, H., Nishihara, K., Sasaki, A., Sunahara, A., Okuno, T., Ueda, N., Ando, T., Tao, Y., Shimada, Y., Hashimoto, K., Yamaura, M., Shigemori, K., Nakai, M., Nagai, K., Norimatsu, T., Nishikawa, T., Miyanaga, N., Izawa, Y., and Mima, K., "Opacity effect on extreme ultraviolet radiation from laser-produced tin plasmas," *Phys. Rev. Lett.*, **95**, 235004, 2005.
- 23 Goldsmith, S., Moreno, J. C., and Griem, H. R., "Relative ion expansion velocity in laser-produced plasmas," *J. Appl. Phys.*, **64** (2), 1988.
- 24 Fujioka, S., Nishimura, H., Nishihara, K., Murakami, M., Kang, G-Y., Gu, Q., Nagai, K., Norimatsu, T., Miyanaga, N., Izawa, Y., and Mima, K., "Properties of ion debris emitted from laser-produced mass-limited tin plasmas for extreme ultraviolet light source applications," *Appl. Phys. Lett.*, **87**, 241503, 2005.
- 25 Tao, Y., Nishimura, H., Okuno, T., Fujioka, S., Ueda, N., Nakai, M., Nagai, K., Norimatsu, T., Miyanaga, N., Nishihara, K., Izawa, Y., and Izawa, Y., "Dynamic imaging of 13.5 nm extreme ultraviolet emission from laser-produced Sn plasmas," *Appl. Phys. Lett.*, **87**, 241502, 2005.
- 26 MacFarlane, J. J., Rettig, C. L., Wang, P., Golovkin, I. E., and Woodruff, P. R., "Radiation-hydrodynamics, spectral, and atomic physics modelling of laser-produced plasma euv lithography light sources," in *Emerging Lithographic Technologies IX*, Mackay, R.S., editor; SPIE-Int Society Optical Engineering: Bellingham, Vol. 5751, 588–600, 2005.
- 27 Djaoui, A., Rose, S. J., and Wark, J. S., "Calculation of the effects of velocity gradients and opacity on line transfer in laser-produced plasmas," *J. Quant. Spectrosc. Radiat. Transfer*, Vol. 52, No. 5, 531–544, 1994.

## Appendix A Rowland

The Windows program Rowland was created to calculate the location of the 13.5-nm region on a Rowland circle mounting for a grazing incidence spectrometer (or GIS) currently being refurbished at UCD and is briefly described below. Rowland.exe is available for download at [www.ucd.ie/physics/speclab](http://www.ucd.ie/physics/speclab).

An evacuated spectrometer with a concave grating at grazing incidence and a CCD camera is used to collect data in the 13.5-nm region. Meijer [1, 2] describes one such grazing incidence spectrometer. The characteristics of the UCD GIS with 6.6 m Rowland circle, 1200 grooves, and angle of incidence  $85^\circ$  is shown in Table A.1. Of particular note with regards to Rowland circle mountings are the corrections from the Rowland circle to the self-focussing curve.

Slit length, $l$ , (mm)	40
Grating length, $L$ , x width, $w$ , (mm x mm)	20 x 80
Radius of curvature, $R$ , (m)	6.6
Number of grooves, $N = 1/d$ , ( $\text{mm}^{-1}$ )	1200
Incidence angle, $\alpha$ , (deg)	<b>85</b>
Order number, $m$	1

Wavelength, $\lambda$ , (nm)	10	20	30	40	50	60
Diffraction angle, $\beta$ , (deg)	-79.8	-76.5	-73.8	-71.5	-69.4	-67.6
Plate factor, $d\lambda/dl$ , (nm/mm)	.0224	.0296	.0353	.0401	.0444	.0482
Astigmatism, $z$ , (mm)	141.0	179.7	210.3	236.1	258.9	279.3
Optimum grating width, $W$ , (mm)	51.0	62.0	69.5	75.3	80.1	84.2
Theoretical resolving power, $R$	45907	55820	62535	67747	72064	75778

**Table A.1** GIS spectrometer characteristics [2]

The resultant 13.5-nm spectral position on the Rowland circle can be calculated by solving for the intersection of the Rowland circle and the equation of the line of diffracted radiation at angle  $\beta$  from the grating, using the centre of the grating as the origin.

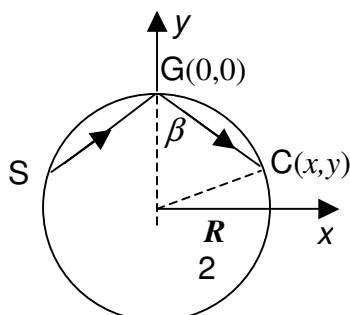


**Figure A.1** Coordinates of diffracted radiation on the Rowland circle

The equation of the Rowland circle is given in Eq. A.1 and the equation of the diffracted radiation line is in Eq. A.2.

$$x^2 + y^2 = \left(\frac{R}{2}\right)^2 \quad (\text{A.1})$$

$$y = -\frac{1}{\tan(\beta)}x + \frac{R}{2} \quad (\text{A.2})$$

where the slope =  $-\frac{1}{\tan(\beta)}$  and  $y$ -intercept =  $\frac{R}{2}$ . Solving for  $x$  and  $y$  in Eqs. A.1 and A.2 gives

$$x = \frac{R \tan(\beta)}{\tan^2(\beta) + 1} \quad (\text{A.3})$$

$$y = \pm \sqrt{\frac{R^2}{4} - x^2} \quad (\text{A.4})$$

The origin is at the centre of the grating and  $d$  is the distance from the centre of the grating. Using the data in Table A.1, the resultant position on the Rowland circle for a wavelength range centred on 13.5 nm is calculated for the first order. Figure A.2 shows the output from Rowland for the set-up described in Table A.1. For an input of  $\lambda = 13.5$  nm and  $\beta = -78.5$ ,  $x = 1.29$  m,  $y = 0.26$  m, and  $d = 1.31$  m. Coordinates of diffracted radiation can be determined for any angle, wavelength, or groove spacing in Rowland as can the angular dispersion, linear dispersion, resolving power, and astigmatism (see Chapter 1, Eqs. 1.5–1.9). The segment number along a 2-m track arc on the Rowland circle can also be determined, where the track consists of 100 2-cm segments, shifted from the grating origin (0,0). The track segments serve to calibrate movement of the camera along the Rowland circle.

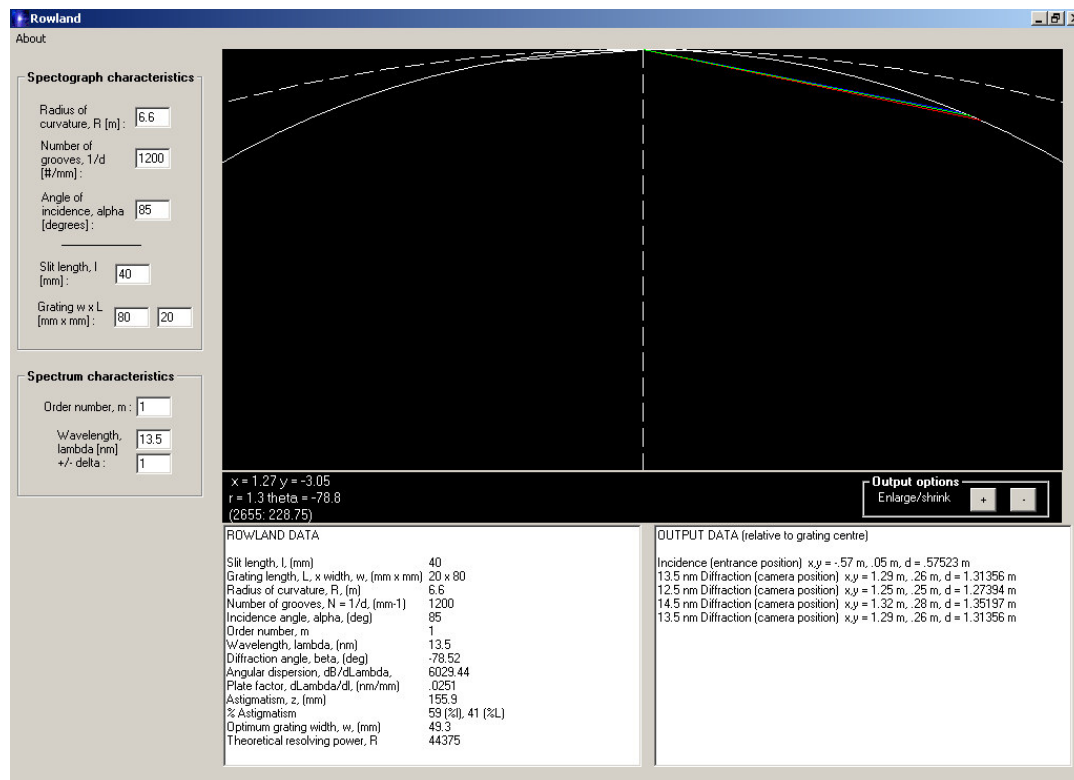


Figure A.2 Rowland output for set-up in Table A.1

## Appendix B The Cowan code

Appendix B.1 gives general notes to the Cowan code. The Windows program MyPsi was created to plot Cowan wavefunctions and is shown in Appendix B.2. All Cowan code input files used in this thesis for Sn V–Sn XIV are given in Appendix B.3.

### Appendix B.1 General Cowan code notes

Two input files are required to run the Cowan code (`filename` and `filename.in2`). To run the Cowan code in the UCD Spectroscopy UNIX speclab environment, type

```
user@speclab7:dir>cowan.sh filename
```

The following shell script commands can be used.

```
user@speclab7:dir>cowan.sh -flag [option]
```

Command	Shell script flag
Help	-h
Run Rcn/Rcn2	-m rcn
Run Rcg	-m rcg
Run Rce	-m rce
Run Shrink	-m shrink
Remove temporary files	-m clean
Run Rcg using large dimensions	-d l
Run Rcg using extra large dimensions	-d xl
Run Rcg using extremely large dimensions	-d xxl

**Table B.1** Cowan script commands

Separate files are automatically created when running `cowan.sh` (which uses the `shrink` program of McGuinness and van Klampen [3, 4]). Numerous files are generated after parsing. Table B.2 lists those files used in this thesis.

File	Description
.out36	wavefunctions
.spec	radiation spectra
.eav	average energies
.eig	energy levels
.wo	gf and wavelengths

**Table B.2** `shrink` output files used in this thesis

Slater-Condon parametric reduction of up to 30 percent is typically required to calibrate theoretical results with experiment. The five, two-digit, radial integral scale factors (or ‘‘Slater scaling’’) scale the energy-level structure parameters  $F^k$  (direct Coulomb integral for equivalent electrons),  $\zeta$  (spin-orbit integral),  $F^k$  and  $G^k$  (direct and exchange Coulomb integral for non-equivalent electrons), and  $R^k$  (configuration-interaction Coulomb integral).  $k$  is the  $k$ th power of the  $k$ th Legendre polynomial. Cowan recommends decreasing the scaling as ionisation increases [5].

Table B.3 shows the Slater scaling parameters. The radial integral scale factors are input as IFACT(5) to Cowan in columns 51–60 of the in2 file. The two-digit scale factors are expressed in percent (99=99%). For example, a factor of 69 scales down the results by 31 percent. A factor less than 50 scales greater than 1 (e.g., 45 = 1.45). 01 = 0.1. If no values are input, the default is 8595858585. Cowan recommends 9099909090 for HF calculations, 5–10 times ionised. Values for  $R^k$  are less than or equal to  $F^k$  and  $G^k$ .

IFACT (i)	Scale factor		
1	$F^k(l_i, l_i)$	direct Coulomb integrals	equivalent electrons
2	$\zeta$	spin-orbit integral	
3	$F^k(l_i, l_j)$	direct Coulomb integrals	non-equivalent electrons
4	$G^k(l_i, l_j)$	exchange Coulomb integrals	non-equivalent electrons
5	$R^k(l_i l_j, l_i l_j)$	configuration interaction Coulomb integrals	

**Table B.3** Slater scaling parameters

Unless otherwise specified, the Cowan code uses units as given in Table B.4.

Quantity	Unit	Value
length	Bohr Unit	5.3E-11 m
energy	Rydberg	13.6 eV
energy radial integrals	kiloKayser (kK)	1000 cm <sup>-1</sup>

**Table B.4** Cowan code internal units

A sample Cowan code input for the two input files is given in Table B.5 to highlight specific data: RCN (1 control card, followed by  $n$  configuration card(s)) and RCN2 (1 control card, followed by one input card). -1 ends input. Note that the spectrum number is one more than ionisation stage. The element/spectrum ID and configuration label are for label purposes only. A wavefunction is calculated for each configuration (as given on the input card) and  $\Delta E$  is calculated between two configurations.

**Sample RCN Input**

	1	2	3	4	5	6	7
12345678901234567890123456789012345678901234567890123456789012345							
2	-9	2 10	0.2	5.e-08	1.e-11-2 0150	1.0 0.65 0.0 0.0	-6
52	1Te	d10s2p4		4d10 5s2 5p4			
52	1Te	d10s2p4		4d10 5s2 5p2 5d2			
52	1Te	d9s2p5		4d9 5s2 5p5			
-1							

**RCN configuration card(s)**

column	format	name	e.g.
3-5	3n	atomic number (Z)	52
9-10	2n	spectrum number (SN)	1
11-16	6a	element/spectrum ID	Te
17-28	10a	configuration label	d10s2p4
free +3		electron orbital specification	4d10 5s2 5p4

**Sample RCN2 Input**

	1	2	3	4	5	6	7
12345678901234567890123456789012345678901234567890123456789012345							
g5inp	000	0.0000	00	7	7899787878	0.00	001108229
-1							

**RCN2 control card**

column	format	name	e.g.
51-60	5(2n)	2-digit scaling factors	78

**Table B.5** Selected control card fields

Table B.6 and Table B.7 gives descriptions of all control card fields for the two input files as originally described in Cowan addendum notes [6].

Column	Name	Description
1-9	varied	For output displayed on screen during calculations
10	IHF	0 – RCN calculation only 1 – RCN output to HF8 instead of RCN2 2 – HF calculation within RCN
11-13	IBB	Not debugged, do not use
14-15	TOLSTB	
16-20	TOLKM2	
21-30	TOLEND	Maximum value of DELTA (change in value of RU) allowed to end self-consistent field (SCF) iteration
31-40	THRESH	Maximum fractional change in energy eigenvalue allowed to end eigenvalue calculation iterations
41-42	KUTD	
42-44	KUT1	
45	IVINTI	Calculate Vinti Integrals : 0 on 1 off
46	IREL	0 – Nonrelativistic calculations 1 – Relativistic 2 – Relativistic + Briet magnetic retardation energies (inaccurate, don't use)
47-48	MAXIT	Maximum number of SCF iterations to be performed. (If convergence of solutions is not achieved in this number, 4 extra cycles with diagnostics are performed)
49-50	NPR	
51-55	EXF10	Coefficient for Slater exchange term for Hartree-Fock-Slater calculation. Originally 1.5, revised to 1.0 by Kohn & Sham.
56-60	EXFM1	
61-65	EMX	
66-70	CORRF	Coefficient for theoretical correlation potential
71-75	IW6	Set negative to send more output to screen.

**Table B.6** Control card for filename (no suffix)

Column	Name	Description
1-5		Specifies routine for code – this is the only option for this!
6-7	NCK	Blank (or for RCG input, if used)
8	IOVFACT	Multiplies product of overlap integrals for spectator electrons into 0 – nothing 1 – Rk 2 – radial multipole values >2 – both
9-10	NOCET	Set <>0 to produce specific input for RCE
11	NSCONF(3,1)	0 (or for RCG input)
12-13	NSCONF(3,2)	0 (or for RCG input)
14-20	EAV11	Energy of first configuration (which all others are measured relative to) – a way of moving the scale.
21	IABG	>0, specifies extra parameters to be incorporated by hand into RCG I/P
22-49	OPTION	Blank (or for RCG input)
50	IQUAD	0 (non-zero for E2 spectra)
51-60	IFACT	Slater scalings
61-65	DMIN	Blank (or for RCG input)
66-70	IPRINT	Blank (or for RCG input)
71-72		Input for RCG
73	ICON	2
74	ISLI	2 (0 for more printout)
75	IDP	5-8 for photoionisation calculations 0 for plane-wave Born calculation

**Table B.7** Control card for .in2 file

## Appendix B.2 Wavefunction plotter (MyPsi)

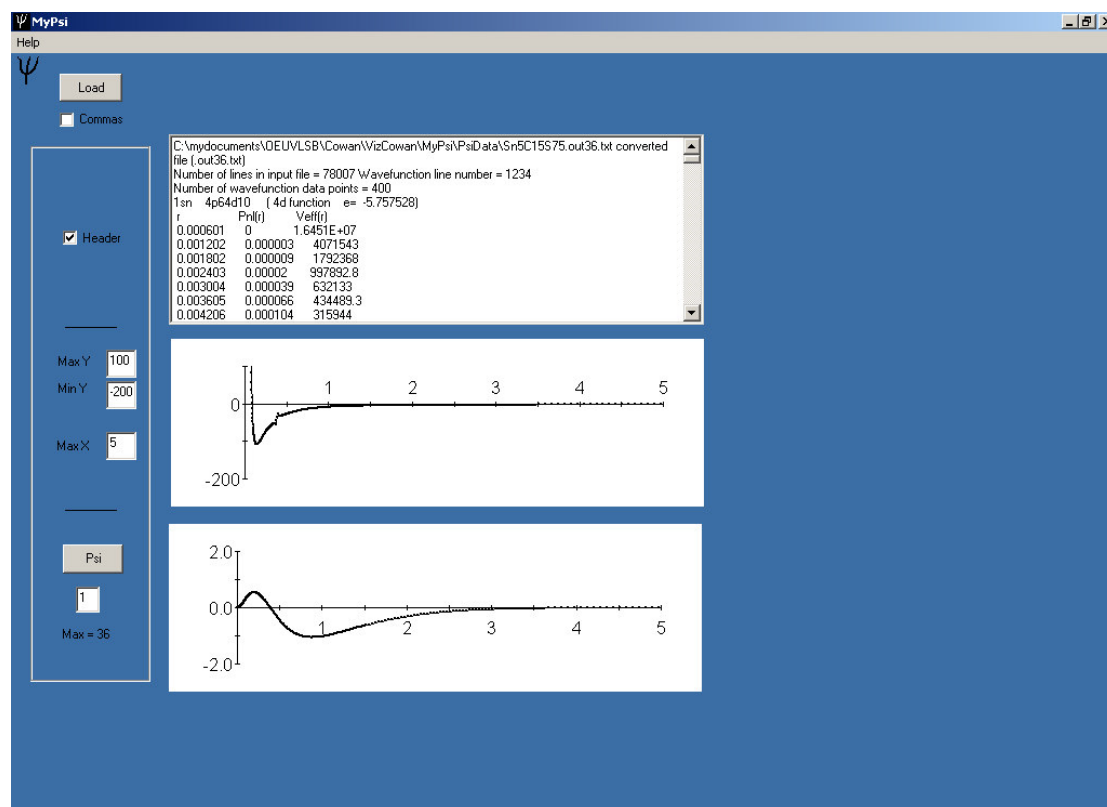
The Windows program MyPsi was created to plot Cowan code wavefunctions more easily in a graphical environment and then create data files for use in other plotting packages. MyPsi.exe is available for download at [www.ucd.ie/physics/speclab](http://www.ucd.ie/physics/speclab).

Figure B.1 shows a sample output from MyPsi for Sn I from which the wavefunction files are created. Note that MyPsi uses the .out36 file to get the wavefunction data. Header information can be included in the output data files as shown in Table B.8.

Figure B.2 shows the 4d radial potential and wavefunction for the Sn V to Sn XIV ions.

C:\mydocuments\OEUVLSB\Cowan\VizCowan\MyPsi\PsiData\Sn5C15S75.out36.txt converted file (.out36.txt)  
 Number of lines in input file = 78007 Wavefunction line number = 1234  
 Number of wavefunction data points = 400  
 1sn 4p64d10 (4d function e= -5.757528)

**Table B.8** MyPsi header data (Sn I)



**Figure B.1** MyPsi wavefunction output (Sn I)

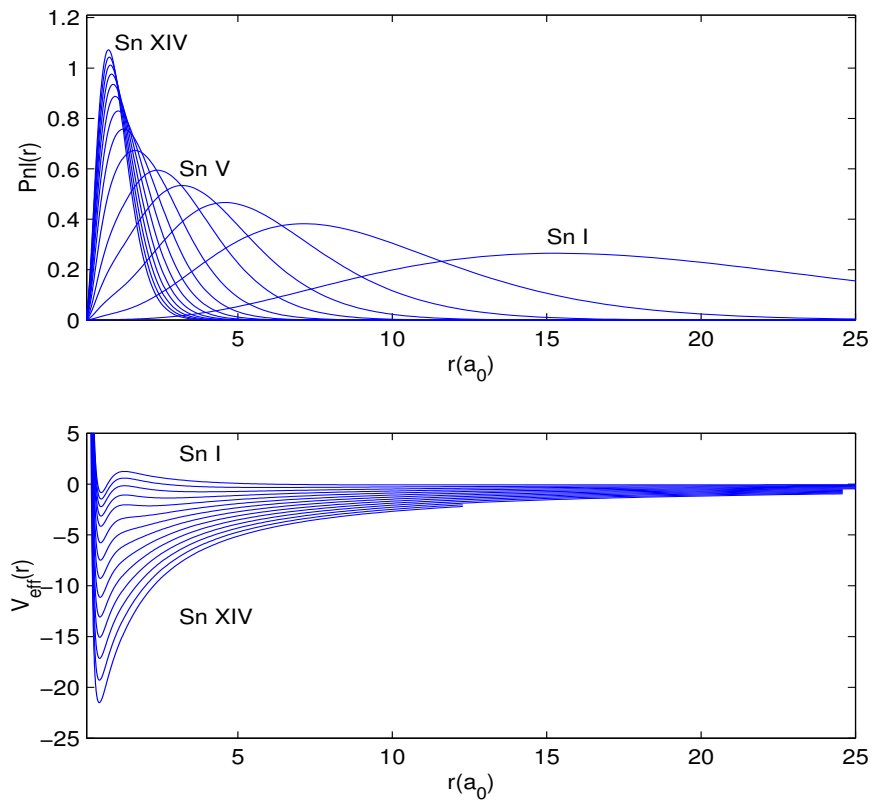


**Figure B.2** 4d radial wavefunctions for Sn I to Sn XIV

### B.3 Statistical UTA Cowan input files Sn V – Sn XIV

```

g5inp      000 0.0000      00      7      7599757575 0.00 001104229
26 -9      2 10 0.2 5.e-08 1.e-11-2 0150 1.0 0.65 0.0 1.0 -6
50 5sn 4p64d10 4p6 4d10
50 5sn 4p54d95d 4p5 4d10 5d1
50 5sn 4d84f1 4p6 4d9 4f1
50 5sn 4d95f1 4p6 4d9 5f1
50 5sn 4d95p1 4p6 4d9 5p1
50 5sn 4p54d105s 4p5 4d10 5s1
50 5sn 4d96f1 4p6 4d9 6f1
50 5sn 4d96p1 4p6 4d9 6p1
50 5sn 4p54d106s 4p5 4d10 6s1
50 5sn 4d97f1 4p6 4d9 7f1
50 5sn 4d97p1 4p6 4d9 7p1
50 5sn 4p54d107s 4p5 4d10 7s1
50 5sn 4d98f1 4p6 4d9 8f1
50 5sn 4d98p1 4p6 4d9 8p1
50 5sn 4p54d108s 4p5 4d10 8s1
50 5sn 4d99f1 4p6 4d9 9f1
50 5sn 4d99p1 4p6 4d9 9p1
50 5sn 4p54d109s 4p5 4d10 9s1
50 5sn 4d910f1 4p6 4d9 10f1
50 5sn 4d910p1 4p6 4d9 10p1
50 5sn 4p54d109s 4p5 4d10 10s1
50 5sn 4d911f1 4p6 4d9 11f1
50 5sn 4d911p1 4p6 4d9 11p1
50 5sn 4p54d911s 4p5 4d10 11s1
50 5sn 4d912f1 4p6 4d9 12f1
50 5sn 4d912p1 4p6 4d9 12p1
50 5sn 4p54d912s 4p5 4d10 12s1
50 5sn 4d913f1 4p6 4d9 13f1
50 5sn 4d913p1 4p6 4d9 13p1
50 5sn 4p54d913s 4p5 4d10 13s1
50 5sn 4d914f1 4p6 4d9 14f1
50 5sn 4d914p1 4p6 4d9 14p1
50 5sn 4p54d914s 4p5 4d10 14s1
50 5sn 4d915f1 4p6 4d9 15f1
50 5sn 4d915p1 4p6 4d9 15p1
50 5sn 4p54d915s 4p5 4d10 15s1

```

```

g5inp      000 0.0000      00      7      7599757575 0.00 001104229
26 -9      2 10 0.2 5.e-08 1.e-11-2 0150 1.0 0.65 0.0 1.0 -6
50 6sn 4p64d9 4p6 4d9
50 6sn 4p54d10 4p5 4d10
50 6sn 4p54d95d 4p5 4d9 5d1
50 6sn 4d84f1 4p6 4d8 4f1
50 6sn 4d85f1 4p6 4d8 5f1
50 6sn 4d85p1 4p6 4d8 5p1
50 6sn 4p54d95s 4p5 4d9 5s1
50 6sn 4d86f1 4p6 4d8 6f1
50 6sn 4d86p1 4p6 4d8 6p1
50 6sn 4p54d96s 4p5 4d9 6s1
50 6sn 4d87f1 4p6 4d8 7f1
50 6sn 4d87p1 4p6 4d8 7p1
50 6sn 4p54d97s 4p5 4d9 7s1
50 6sn 4d88f1 4p6 4d8 8f1
50 6sn 4d88p1 4p6 4d8 8p1
50 6sn 4p54d89s 4p5 4d9 8s1
50 6sn 4d89f1 4p6 4d8 9f1
50 6sn 4d89p1 4p6 4d8 9p1
50 6sn 4p54d99s 4p5 4d9 9s1
50 6sn 4d810f1 4p6 4d8 10f1
50 6sn 4d810p1 4p6 4d8 10p1
50 6sn 4p54d109s 4p5 4d9 10s1
50 6sn 4d811f1 4p6 4d8 11f1
50 6sn 4d811p1 4p6 4d8 11p1
50 6sn 4p54d119s 4p5 4d9 11s1
50 6sn 4d812f1 4p6 4d8 12f1
50 6sn 4d812p1 4p6 4d8 12p1
50 6sn 4p54d129s 4p5 4d9 12s1

```

```

g5inp      000 0.0000      00      7      7599757575 0.00 001104229
26 -9      2 10 0.2 5.e-08 1.e-11-2 0150 1.0 0.65 0.0 1.0 -6
50      7sn 4p64d8      4p6 4d8
50      7sn 4p54d9      4p5 4d9
50      7sn 4p54d85d      4p5 4d8 5d1
50      7sn 4d74f1      4p6 4d7 4f1
50      7sn 4d75f1      4p6 4d7 5f1
50      7sn 4d75p1      4p6 4d7 5p1
50      7sn 4p54d85s      4p5 4d8 5s1
50      7sn 4d76f1      4p6 4d7 6f1
50      7sn 4d76p1      4p6 4d7 6p1
50      7sn 4p54d86s      4p5 4d8 6s1
50      7sn 4d77f1      4p6 4d7 7f1
50      7sn 4d77p1      4p6 4d7 7p1
50      7sn 4p54d87s      4p5 4d8 7s1
50      7sn 4d78f1      4p6 4d7 8f1
50      7sn 4d78p1      4p6 4d7 8p1
50      7sn 4p54d88s      4p5 4d8 8s1
50      7sn 4d79f1      4p6 4d7 9f1
50      7sn 4d79p1      4p6 4d7 9p1
50      7sn 4p54d89s      4p5 4d8 9s1

```

```

g5inp      000 0.0000      00      7      7799777777 0.00 001104229
26 -9      2 10 0.2 5.e-08 1.e-11-2 0150 1.0 0.65 0.0 1.0 -6
50      8sn 4p64d7      4p6 4d7
50      8sn 4p54d8      4p5 4d8
50      8sn 4p54d75d      4p5 4d7 5d1
50      8sn 4d64f1      4p6 4d6 4f1
50      8sn 4d65f1      4p6 4d6 5f1
50      8sn 4d65p1      4p6 4d6 5p1
50      8sn 4p54d75s      4p5 4d7 5s1
50      8sn 4d66f1      4p6 4d6 6f1
50      8sn 4d66p1      4p6 4d6 6p1
50      8sn 4p54d76s      4p5 4d7 6s1
50      8sn 4d67f1      4p6 4d6 7f1
50      8sn 4d67p1      4p6 4d6 7p1
50      8sn 4p54d77s      4p5 4d7 7s1
50      8sn 4d68f1      4p6 4d6 8f1
50      8sn 4d68p1      4p6 4d6 8p1
50      8sn 4p54d78s      4p5 4d7 8s1

```

```

g5inp      000 0.0000      00      7      7899787878 0.00 001104229
26 -9      2 10 0.2 5.e-08 1.e-11-2 0150 1.0 0.65 0.0 1.0 -6
50      9sn 4p64d6      4p6 4d6
50      9sn 4p54d7      4p5 4d7
50      9sn 4p54d65d      4p5 4d6 5d1
50      9sn 4d54f1      4p6 4d5 4f1
50      9sn 4d55f1      4p6 4d5 5f1
50      9sn 4d55p1      4p6 4d5 5p1
50      9sn 4p54d65s      4p5 4d6 5s1
50      9sn 4d56f1      4p6 4d5 6f1
50      9sn 4d56p1      4p6 4d5 6p1
50      9sn 4p54d66s      4p5 4d6 6s1
50      9sn 4d57f1      4p6 4d5 7f1
50      9sn 4d57p1      4p6 4d5 7p1
50      9sn 4p54d67s      4p5 4d6 7s1

```

```

g5inp      000 0.0000      00      7      8099808080 0.00 001104229
26 -9      2 10 0.2 5.e-08 1.e-11-2 0150 1.0 0.65 0.0 1.0 -6
50      10sn 4p64d5      4p6 4d5
50      10sn 4p54d6      4p5 4d6
50      10sn 4p54d55d      4p5 4d5 5d1
50      10sn 4d44f1      4p6 4d4 4f1
50      10sn 4d45f1      4p6 4d4 5f1
50      10sn 4d45p1      4p6 4d4 5p1
50      10sn 4p54d55s      4p5 4d5 5s1
50      10sn 4d46f1      4p6 4d4 6f1
50      10sn 4d46p1      4p6 4d4 6p1
50      10sn 4p54d56s      4p5 4d5 6s1
50      10sn 4d47f1      4p6 4d4 7f1
50      10sn 4d47p1      4p6 4d4 7p1
50      10sn 4p54d57s      4p5 4d5 7s1
50      10sn 4d48f1      4p6 4d4 8f1
50      10sn 4d48p1      4p6 4d4 8p1
50      10sn 4p54d58s      4p5 4d5 8s1

```

```

g5inp      000 0.0000      00      7      8199818181 0.00 001104229
26 -9      2 10 0.2 5.e-08 1.e-11-2 0150 1.0 0.65 0.0 1.0 -6
50 11sn 4p64d4 4p6 4d4
50 11sn 4p54d5 4p5 4d5
50 11sn 4p54d45d 4p5 4d4 5d1
50 11sn 4d34f1 4p6 4d3 4f1
50 11sn 4d35f1 4p6 4d3 5f1
50 11sn 4d35p1 4p6 4d3 5p1
50 11sn 4p54d45s 4p5 4d4 5s1
50 11sn 4d36f1 4p6 4d3 6f1
50 11sn 4d36p1 4p6 4d3 6p1
50 11sn 4p54d46s 4p5 4d4 6s1
50 11sn 4d37f1 4p6 4d3 7f1
50 11sn 4d37p1 4p6 4d3 7p1
50 11sn 4p54d47s 4p5 4d4 7s1
50 11sn 4d38f1 4p6 4d3 8f1
50 11sn 4d38p1 4p6 4d3 8p1
50 11sn 4p54d48s 4p5 4d4 8s1

```

```

g5inp      000 0.0000      00      7      8399838383 0.00 001104229
26 -9      2 10 0.2 5.e-08 1.e-11-2 0150 1.0 0.65 0.0 1.0 -6
50 12sn 4p64d3 4p6 4d3
50 12sn 4p54d4 4p5 4d4
50 12sn 4p54d35d 4p5 4d3 5d1
50 12sn 4d24f1 4p6 4d2 4f1
50 12sn 4d25f1 4p6 4d2 5f1
50 12sn 4d25p1 4p6 4d2 5p1
50 12sn 4p54d35s 4p5 4d3 5s1
50 12sn 4d26f1 4p6 4d2 6f1
50 12sn 4d26p1 4p6 4d2 6p1
50 12sn 4p54d36s 4p5 4d3 6s1
50 12sn 4d27f1 4p6 4d2 7f1
50 12sn 4d27p1 4p6 4d2 7p1
50 12sn 4p54d37s 4p5 4d3 7s1
50 12sn 4d28f1 4p6 4d2 8f1
50 12sn 4d28p1 4p6 4d2 8p1
50 12sn 4p54d38s 4p5 4d3 8s1
50 12sn 4d29f1 4p6 4d2 9f1
50 12sn 4d29p1 4p6 4d2 9p1
50 12sn 4p54d39s 4p5 4d3 9s1

```

```

g5inp      000 0.0000      00      7      8499848484 0.00 001104229
26 -9      2 10 0.2 5.e-08 1.e-11-2 0150 1.0 0.65 0.0 1.0 -6
50 13sn 4p64d2 4p6 4d2
50 13sn 4p54d3 4p5 4d3
50 13sn 4p54d25d 4p5 4d2 5d1
50 13sn 4d14f1 4p6 4d1 4f1
50 13sn 4d15f1 4p6 4d1 5f1
50 13sn 4d15p1 4p6 4d1 5p1
50 13sn 4p54d25s 4p5 4d2 5s1
50 13sn 4d16f1 4p6 4d1 6f1
50 13sn 4d16p1 4p6 4d1 6p1
50 13sn 4p54d26s 4p5 4d2 6s1
50 13sn 4d17f1 4p6 4d1 7f1
50 13sn 4d17p1 4p6 4d1 7p1
50 13sn 4p54d27s 4p5 4d2 7s1
50 13sn 4d18f1 4p6 4d1 8f1
50 13sn 4d18p1 4p6 4d1 8p1
50 13sn 4p54d28s 4p5 4d2 8s1
50 13sn 4d19f1 4p6 4d1 9f1
50 13sn 4d19p1 4p6 4d1 9p1
50 13sn 4p54d29s 4p5 4d2 9s1
50 13sn 4d101f1 4p6 4d1 10f1
50 13sn 4d101p1 4p6 4d1 10p1
50 13sn 4p54d210s 4p5 4d2 10s1
50 13sn 4d111f1 4p6 4d1 11f1
50 13sn 4d111p1 4p6 4d1 11p1
50 13sn 4p54d211s 4p5 4d2 11s1
50 13sn 4d112f1 4p6 4d1 12f1
50 13sn 4d112p1 4p6 4d1 12p1
50 13sn 4p54d212s 4p5 4d2 12s1
50 13sn 4d113f1 4p6 4d1 13f1
50 13sn 4d113p1 4p6 4d1 13p1
50 13sn 4p54d213s 4p5 4d2 13s1
50 13sn 4d114f1 4p6 4d1 14f1
50 13sn 4d114p1 4p6 4d1 14p1
50 13sn 4p54d214s 4p5 4d2 14s1

```

```

g5inp      000 0.0000      00      7      8599858585 0.00 001104229
26 -9      2 10 0.2 5.e-08 1.e-11-2 0150 1.0 0.65 0.0 1.0 -6
50 14sn 4p64d1 4p6 4d1
50 14sn 4p54d2 4p5 4d2
50 14sn 4p54d15d 4p5 4d1 5d1
50 14sn 4d04f1 4p6 4d0 4f1
50 14sn 4d05f1 4p6 4d0 5f1
50 14sn 4d05p1 4p6 4d0 5p1
50 14sn 4p54d15s 4p5 4d1 5s1
50 14sn 4d06f1 4p6 4d0 6f1
50 14sn 4d06p1 4p6 4d0 6p1
50 14sn 4p54d16s 4p5 4d1 6s1
50 14sn 4d07f1 4p6 4d0 7f1
50 14sn 4d07p1 4p6 4d0 7p1
50 14sn 4p54d17s 4p5 4d1 7s1
50 14sn 4d08f1 4p6 4d0 8f1
50 14sn 4d08p1 4p6 4d0 8p1
50 14sn 4p54d18s 4p5 4d1 8s1
50 14sn 4d09f1 4p6 4d0 9f1
50 14sn 4d09p1 4p6 4d0 9p1
50 14sn 4p54d19s 4p5 4d1 9s1
50 14sn 4d010f1 4p6 4d0 10f1
50 14sn 4d010p1 4p6 4d0 10p1
50 14sn 4p54d110s 4p5 4d1 10s1
50 14sn 4d011f1 4p6 4d0 11f1
50 14sn 4d011p1 4p6 4d0 11p1
50 14sn 4p54d111s 4p5 4d1 11s1
50 14sn 4d012f1 4p6 4d0 12f1
50 14sn 4d012p1 4p6 4d0 12p1
50 14sn 4p54d112s 4p5 4d1 12s1
50 14sn 4d013f1 4p6 4d0 13f1
50 14sn 4d013p1 4p6 4d0 13p1
50 14sn 4p54d113s 4p5 4d1 13s1
50 14sn 4d014f1 4p6 4d0 14f1
50 14sn 4d014p1 4p6 4d0 14p1
50 14sn 4p54d114s 4p5 4d1 14s1
50 14sn 4d015f1 4p6 4d0 15f1
50 14sn 4d015p1 4p6 4d0 15p1
50 14sn 4p54d115s 4p5 4d1 15s1
50 14sn 4d016f1 4p6 4d0 16f1
50 14sn 4d016p1 4p6 4d0 16p1
50 14sn 4p54d116s 4p5 4d1 16s1
50 14sn 4d017f1 4p6 4d0 17f1
50 14sn 4d017p1 4p6 4d0 17p1
50 14sn 4p54d117s 4p5 4d1 17s1
50 14sn 4d018f1 4p6 4d0 18f1
50 14sn 4d018p1 4p6 4d0 18p1
50 14sn 4p54d118s 4p5 4d1 18s1
50 14sn 4d019f1 4p6 4d0 19f1
50 14sn 4d019p1 4p6 4d0 19p1
50 14sn 4p54d119s 4p5 4d1 19s1

```

## B.4 Cowan input file for Sn ionisation data

50	1Sn	5p	3d10	4s2	4p6	4d10	5s2	5p2
50	2Sn	5p	3d10	4s2	4p6	4d10	5s2	5p1
50	3Sn	5s	3d10	4s2	4p6	4d10	5s2	
50	4Sn	5s	3d10	4s2	4p6	4d10	5s1	
50	5Sn	4d	3d10	4s2	4p6	4d10		
50	6Sn	4d	3d10	4s2	4p6	4d9		
50	7Sn	4d	3d10	4s2	4p6	4d8		
50	8Sn	4d	3d10	4s2	4p6	4d7		
50	9Sn	4d	3d10	4s2	4p6	4d6		
50	10Sn	4d	3d10	4s2	4p6	4d5		
50	11Sn	4d	3d10	4s2	4p6	4d4		
50	12Sn	4d	3d10	4s2	4p6	4d3		
50	13Sn	4d	3d10	4s2	4p6	4d2		
50	14Sn	4d	3d10	4s2	4p6	4d1		
50	15Sn	4p	3d10	4s2	4p6			
50	16Sn	4p	3d10	4s2	4p5			
50	17Sn	4p	3d10	4s2	4p4			
50	18Sn	4p	3d10	4s2	4p3			
50	19Sn	4p	3d10	4s2	4p2			
50	20Sn	4p	3d10	4s2	4p1			
50	21Sn	4s	3d10	4s2				
50	22Sn	4s	3d10	4s1				
50	23Sn	3d	3d10					
50	24Sn	3d	3d9					
50	25Sn	3d	3d8					
50	26Sn	3d	3d7					
50	27Sn	3d	3d6					
50	28Sn	3d	3d5					
50	29Sn	3d	3d4					
50	30Sn	3d	3d3					

**Table B.9** Cowan file to determine lowest energy ionisation sequence in tin

Note that it is necessary to include the 3d shell in the Cowan input file for output to Sn XXX.

## Appendix C PlasMod (a steady state plasma model)

The Windows program PlasMod was created to calculate the ion distribution in a steady state plasma according to the theoretical model of Colombant and Tonon [7]. The basic input, output, and installation for PlasMod are described below. PlasMod.exe is available for download at [www.ucd.ie/physics/speclab](http://www.ucd.ie/physics/speclab).

Figure C.1 shows the main output window (default on execution). Note that an input .txt file (PMInDef.txt) can be used to create a specific initial set-up (e.g., tin ions Sn I–Sn XX at  $6 \times 10^{10}$  W/cm<sup>2</sup> laser power density). Table C.1 gives the input file for the output shown in Figure C.1.

Output tables can be toggled on screen (summarised in Table C.2) as can output plots (summarised in Table C.3). There are eight table windows and 5 plot windows (in groups of six). Individual plots can be expanded on screen and saved. Selected table and plot data is shown in Tables C.4 and C.5 and Figures C.2 and C.3. General output data is automatically generated for each PlasMod run in the PMOUT folder.

A theoretical spectrum can be plotted, by weighting Cowan data with the steady state ion fraction calculated by PlasMod. The required .wo files must be in the PMIN folder. A weighted spectrum at 36 eV is shown in Figure C.4. The in-band sum  $gf$  contribution is calculated for each ion and for the weighted total (CXRO weighting can be included as well if desired). The four main emitting ions at 36 eV (Sn X, Sn XI, Sn XII, and Sn XIII) are shown in Figure C.5.

The PlasMod readme.txt file, giving all installation notes, is reproduced in Appendix C.2

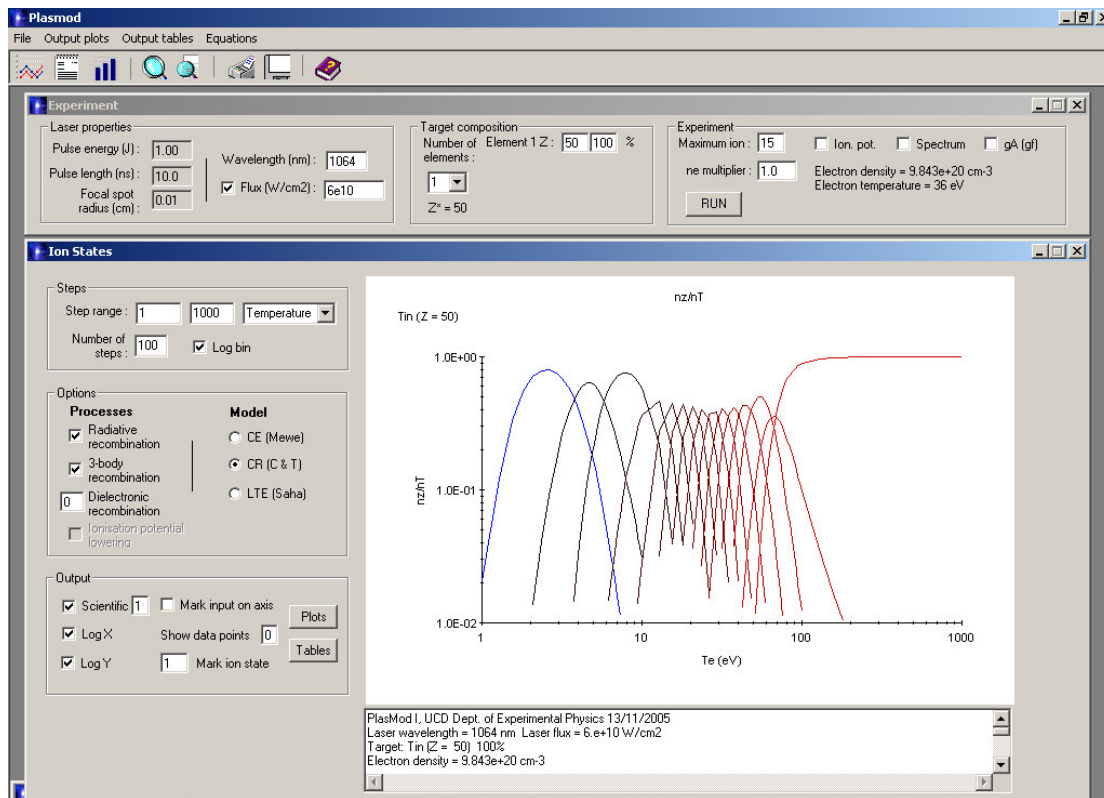


Figure C.1 PlasMod main output window

1	Number of outer shell electrons
2-4	Ion distribution (3 files)
5	Wilson CE and McWhirter LTE criteria
6	Log file
7	Atomic processes percentage
8	PMInIP.dat ionisation potentials (C&T where no input data)

**Table C.1** PlasMod tables

1 Collisional ionisation Radiative recombination Three-body recombination Nz Nz/nT C-R	2 Hinnov tau McWhirter tau Ready tau Hinnov tau sum McWhirter tau sum Nz/nT	3 Lowest ion state Highest ion state Dominant ion state Average ion state Low, max, and average ion state Average (approx and calculated)	4 Saha nz vs Te Saha fn vs Te Nz/nT	5 Ion fraction vs charge state
--	---	---	--	-----------------------------------

**Table C.2** PlasMod plots

```

PlasMod 0.9 UCD Dept. of Experimental Physics
Sn 50-28 with Cowan chis
---LASER
1.00,      Pulse energy (j)
10.0,     Pulse length (ns)
0.01,     Focal spot radius (cm)
1064,     Wavelength (nm)
6e10,     Flux (W/cm^2)
1,        Use flux calculation (0/1)?
---TARGET (1 line for each element; max 4)
1,        Number of elements
50, 100,  Element atomic number; Percentage
---EXPERIMENT
15,       Maximum ion state
0,        Show IP graph (0/1)?
0,        Show spectrum (0/1)?
---OPTIONS
0,        ne approximate calculation (0/1)?
0,        Show last ion state (0/1)?
1,        IP method (Input; Cowan; C&T 0/1/2)?
0,        NOSE file (Override input ground state
          configuration 0/1)?
---SPECTRUM
.01,     bin size
1,       line/scatter plot (0/1)?

```

**Table C.3** PlasMod input .txt file (PMInDef.txt)

Laser wavelength = 1.064 microns, electron density (ne) = 9.84E+20 cm <sup>-3</sup> Tin					
Ion	# outer shell	Ionisation potential (eV)	f <sub>nz</sub> (35.89 eV)	n <sub>z+1</sub> /n <sub>z</sub> (cm <sup>-3</sup> )	n <sub>z</sub>
Sn I	2	7.08	0	3340	0
Sn II	1	14.41	0	760	0
Sn III	2	29.36	0	1010	0
Sn IV	1	40.06	0	72.5	0
Sn V	10	76.52	0	132	0
Sn VI	9	96.02	0	70.6	0
Sn VII	8	116.48	0	36.6	0
Sn VIII	7	137.84	0.0105	18.1	1.03E+19
Sn IX	6	160.02	0.0872	8.33	8.58E+19
Sn X	5	183.02	0.306	3.51	3.01E+20
Sn XI	4	206.8	0.402	1.32	3.96E+20
Sn XII	3	231.33	0.173	0.431	1.71E+20
Sn XIII	2	256.59	0.0203	0.117	2E+19
Sn XIV	1	282.58	0	0.0158	0
Sn XV	6	383.78	0	0	0
Sn XVI	5	412.22	0	0	0

**Table C.4** PlasMod ion distribution

---

PlasMod I, UCD School of Physics 13/11/2005  
 Laser wavelength = 1064 nm Laser flux = 6.e+10 W/cm<sup>2</sup>  
 Target: Tin (Z = 50) 100%  
 Electron density = 9.843e+20 cm<sup>-3</sup>  
 Sn Electron temperature = 36 eV  
 Sn Average charge (C&T approx.) = 8.1 : Sn IX is Mo-like  
 Sn Heat transfer relaxation time (Ready 1971) = 6.687e-13 s  
 Sn Relaxation time/Laser pulse length = .01 %  
 Debye length = 2.507e+0 m Debye criterion: 6.5e+22 cm<sup>-3</sup> >>  
 1 (1 electron per 2.55e-21 cm<sup>3</sup>)  
 Wilson CE criteria: CE valid: NO  
 McWhirter LTE criteria: LTE valid: YES  
 Greim LTE criteria : LTE valid: YES

---

**Table C.5** PlasMod log file

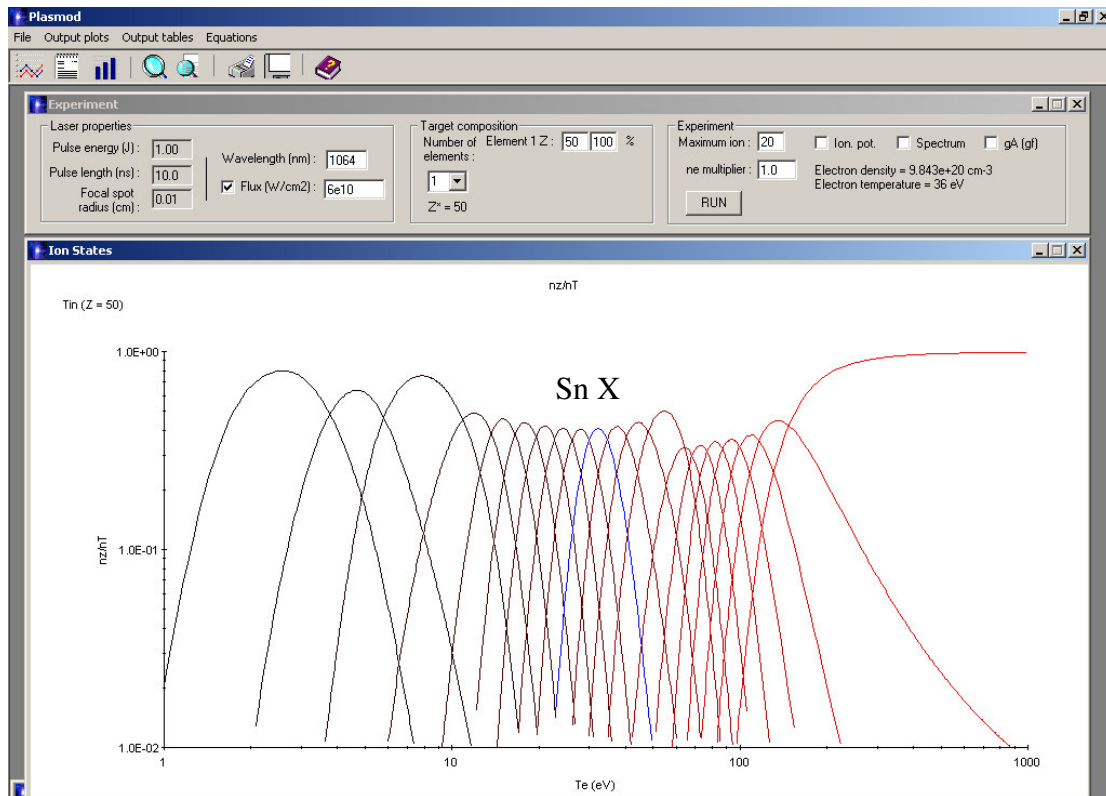


**Figure C.2** PlasMod ion distribution : Sn I–Sn XX (500 steps :1–1000 eV)  
Sn X is marked in blue

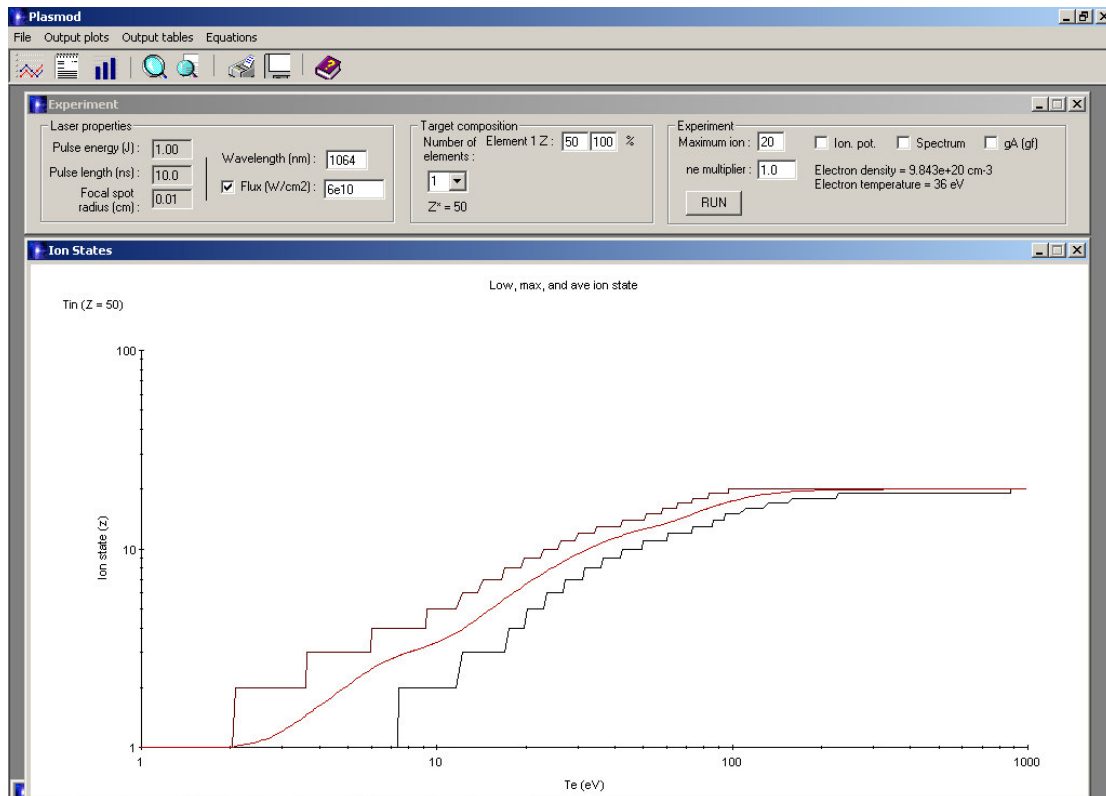


**Figure C.3** PlasMod low, max, and ave. ion : Sn I–Sn XX (500 steps :1–1000 eV)

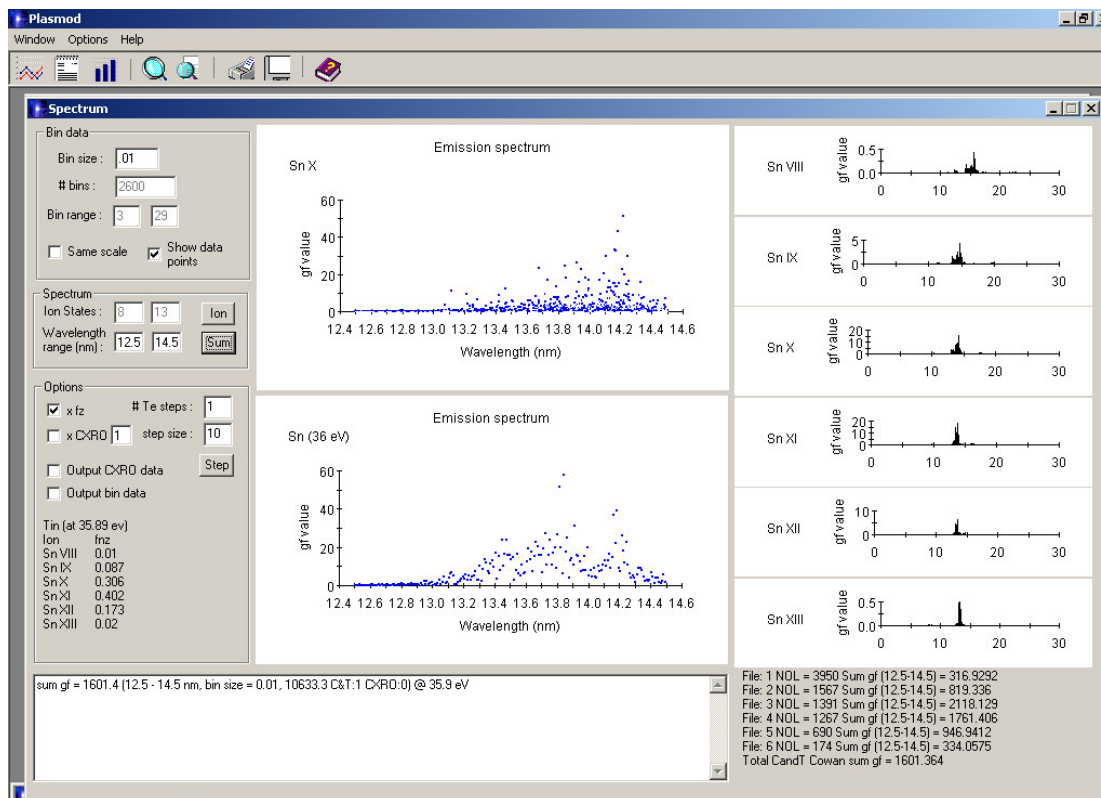


Figure C.4 PlasMod weighted spectrum at 36 eV : Sn VIII–Sn XIII

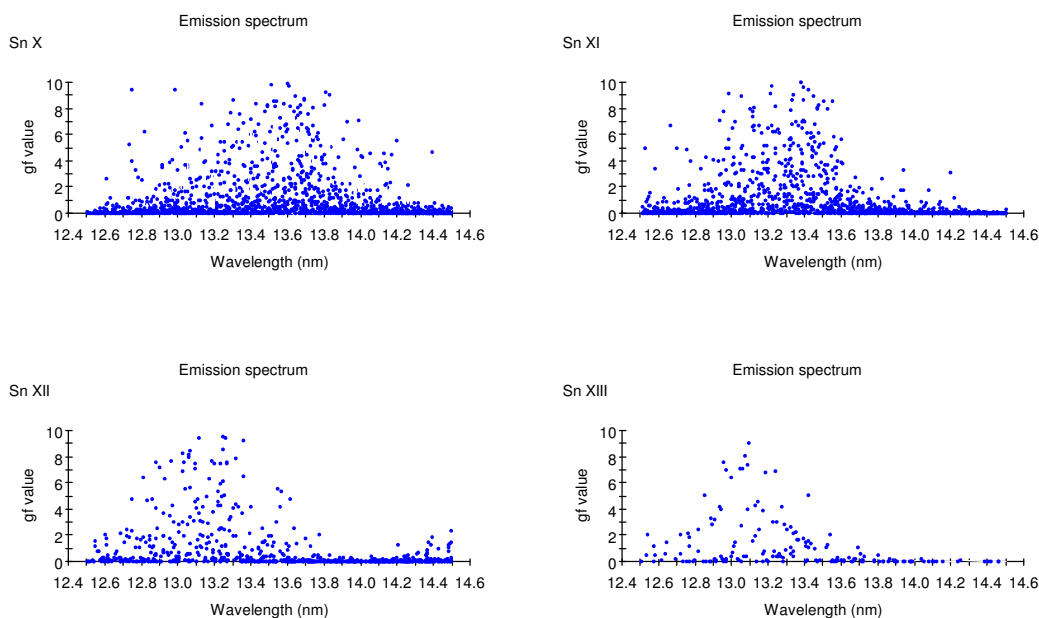


Figure C.5 PlasMod spectrum at 36 eV (Sn X, Sn XI, Sn XII, and Sn XIII)

## Appendix C.1 PlasMod (installation)

### readme.txt for PlasMod (PM) V0.9 December 2005

#### 1.0 Setup notes

=====

copy plasmod.exe and the .ocx and .dll files (Active X plot components) to any folder.

Create PMIN folder under .exe folder and copy zip files.

Create PMOUT folder (can be renamed in code).

In DOS prompt, register both .ocx files: regsvr32 [file.ocx]

#### 2.0 Input data (in PMIN folder)

=====

- PMInIP.dat (Ionisation potential data)

Default file complete to  $Z = 29$  (CRC/Moore) with selected known experimental data (Y, Sn, Xe, Sm).

Use this file to enter default IPs (can be overridden with Cowan data or Colombant and Tonon approximation).

- PMNOSEALL.csv (Ground state configuration)

Default ground state for an isoelectronic sequence using a backwards aufbau principle.

NOTE: This DOES NOT necessarily follow for  $Z > 24$ . Best to use an override file of the form PMNOSE[Z].csv (e.g. PMNOSESn.csv)

The NOSE (Number of outer shell electrons) data is used for Colombant and Tonon (S and A3b) and to determine Saha ground state degeneracy.

NOSEALL doesn't know all.

- PMInElements.csv (x)

Purely descriptive for element name and symbol. PM does use the atomic number in a C&T approx which it gets from here.

- ChisZ.dat (cut .eav file)

This file is the cut Unix .eav file.

After running an "Ionisation potential" Cowan run, cut the .eav file, rename (e.g. ChisSn.dat), and copy into folder.

cut -c113-123 Sn.eav > ChisSn.dat

- CowDef.wo (x)

A blank Cowan file in case there is no .wo data (gf versus lambda) for a particular ion.

- ZNN.wo (Cowan gf file)

The .wo file for a particular ion (e.g. Sn10.wo for Sn 9+ or Sn X).

If the spectrum is plotted, .wo files are needed for each ion stage.

If no file, zeroes are used.

- PMInCXRO.csv

CXRO data (wavelength, percentage, phase) from [http://www-cxro.lbl.gov/optical\\_constants/multi2.html](http://www-cxro.lbl.gov/optical_constants/multi2.html)

(x) No need to change these files.

All input files should be in a PMIn folder under the .exe file.

### 3.0 Output data (PMOut folder)

=====

Various output files can be created. (F10 writes plot to file, F11 writes all plots to file, and F12 prints file to printer.)

Note: F1, F2, and F3 keys magnify/minimise screen plots which is reflected in the output plots.

### 4.0 PlasMod - The program

=====

What does PlasMod do? PlasMod calculates the Colombant and Tonon fraction ion densities in a plasma, from analysis in their 1973 paper, "X-ray emission in laser-produced plasmas."

fz is a function of the incident laser ( $\phi$ ,  $\lambda$ ), the target ( $Z$ ,  $IP$ ,  $NOSE$ ), and electron temperature ( $T_e$ ) and electron density ( $n_e$ ). Various plots and output tables can be plotted (including  $\langle z \rangle$  versus temperature, fz versus  $\langle z \rangle$ , fz versus  $T_e$  and other C&T data.

PlasMod can also weight Cowan theoretical spectra (gf versus  $\lambda$ ) by fz and CXRO reflectivity data (as a function of temperature).

### 5.0 Bugs/Comments

=====

Plasmod is not crash-free. Typically, it may not respond to all inputs as expected, as not all possible uses have been coded. Crashes can occur with repeated interactive use (i.e, multiple z changes, range changes, ...). If it crashes, begin again with the determined range. Comments and suggested output are welcome and encouraged.

### 6.0 Version notes

=====

There is a built-in expiry date. This is only to keep track of who has or is using the program.

john.white@ucd.ie

## Appendix D Medusa

One input file is required to run Medusa (`filename.txt`). To run Medusa in a PC cygwin (UNIX emulator) environment, type

```
Bash-2.02$ ./med<filename.txt>outfile
```

`outfile` is created from which four data files are created using `batchout.txt`.

### Appendix D.1 Running batchout

The gawk script file `batchout` was written by A. Cummings and modified for this thesis for general use. One input file is required to run `batchout` (`outfile`). Note that the `batchout.txt` input file contains the hard-wired name of the input file (`outfile` from Medusa) as `file1`. To run `batchout` in a PC cygwin environment, type

```
Bash-2.02$ ./batchout.txt
```

The `batchout.txt` file for tin is shown below. (Note: for fully stripped ions, as in  $\text{Al}^{13+}$ , `Zlike = stripped`.)

```
file1="SnOut400"
NTS1=401
NTS0=400
NTS=400:
AN=50.00
Zlike=Zn-like
# =====
one=1
two=2
thr=3
fou=4
dat=.dat
p1=$file1$one$dat
p2=$file1$two$dat
p3=$file1$thr$dat
p4=$file1$fou$dat
file2="intermediate"
file3="intermediate*"
# =====
gawk '$10=="$AN",$1=="$NTS1"' $file1 | tr -s " " | cut -d" " -f2-
|gawk {'if($1=="$NTS1') for(i=4;i<=10;++i) $i=0;print'}|cut -d" " -
f2- > $p1
gawk '$1=="nlte",$1=="$NTS"' $file1 |gawk '$1=="1:",$1=="$NTS"'|
gawk {'print;if($1=="$NTS") printf("\n")'}|gawk {'if($1=="")
for(i=1;i<=9;++i) $i=0; print'} | tr -s " "|cut -d" " -f3- > $p2
gawk '$1=="timestep"' $file1 | tr -s " " | cut -d" " -f7 | uniq > $p3
gawk '$3=="$Zlike",$1=="timestep"' $file1 | gawk
'$1=="no",$1=="$NTS0"'|gawk '$1=="1",$1=="$NTS0"'| tr -s " " |
cut -d" " -f4- | split -l$NTS0 - $file2
paste -d" " $file3 > $p4
rm $file3
```

## D.2 LaserPlot

The Matlab GUI program LaserPlot was created to calculate the maximum irradiance,  $P_{max}$ , of a single Gaussian laser pulse (using the Medusa input variables [8]) and from that the time of peak irradiance, and is briefly described below. LaserPlot.m is available for download at [www.ucd.ie/physics/speclab](http://www.ucd.ie/physics/speclab).

The Medusa input variables required to specify the laser pulse are summarised below in Table D.1 (see also Table 4.1). The corresponding math symbol is given for use in the  $P_{max}$  derivation.

variable	unit	meaning	symbol
PLENTH <sup>57</sup>	s	pulse length	$P_l$
PMAX	W/m/rad	peak power	$P_m$
PMULT	--	# of plenth	$P_x$

Table D.1 Medusa laser pulse variables.

Given a total laser energy  $E_{tot}$  (with a focussed spot radius,  $r_{fs}$ , and cylindrical wire radius,  $r_{cyl}$  (for cylindrical geometry)),

$$E_{tot} = \int_0^t P(t)dt \quad (D.1)$$

where, from Medusa,

$$P(t) = P_{max} \exp\left(-\left(\frac{t - P_x P_l}{P_l}\right)^2\right) \quad (D.2)$$

where  $P_l$ ,  $P_m$ , and  $P_x$  are as in Table D.1

For a change of variables, where  $z = t - (P_x P_l)/P_l$ ,  $dz/dt = 1/P_l$  and  $dt = P_l dz$ . Thus, as  $t = 0$ ,  $z = -P_x$  and as  $t = t_{max}$ ,  $z = t_{max} - (P_x P_l)/P_l$ .

Therefore,

$$E_{tot} = P_{max} P_l \int_{-P_x}^{\frac{t - P_x P_l}{P_l}} e^{-z^2} dz \quad (D.3)$$

Now,

$$\int_0^x e^{-z^2} dz = \frac{\sqrt{\pi}}{2} \operatorname{erf}(x), \text{ where } (\operatorname{erf}(-x) = -\operatorname{erf}(x))$$

Thus,

$$E_{tot} = P_{max} P_l \frac{\sqrt{\pi}}{2} \cdot \xi \quad (D.4)$$

and

$$P_{max} = \frac{2E_{tot}}{\sqrt{\pi} P_l} \cdot \frac{1}{\xi} \quad [\text{in J/s}] \quad (D.5)$$

<sup>57</sup> Called PLENTH in Medusa.

where

$$\xi = \operatorname{erf}\left(\frac{t - P_x P_l}{P_l}\right) + \operatorname{erf}(P_x) \tag{D.6}$$

Thus, for planar geometries,

$$\phi_{\max} = \frac{2E_{\text{tot}}}{\sqrt{\pi} P_l} \cdot \frac{1}{\pi r_{fs}^2} \cdot \xi \quad [\text{in W/m}^2] \tag{D.7}$$

And the Medusa input for any geometry (planar, cylindrical, and spherical) is

$$\phi_{\text{equiv}} = \phi_{\max} \cdot f(\text{geometry}) \tag{D.7}$$

where  $f(\text{geometry}) = 1$  (planar),  $1/r_{\text{cyl}}$  (cylindrical) or  $1/r_{\text{sphere}}^2$  (spherical). Here, the spot radius = the cylinder radius.

Thus for a cylindrical aluminium wire,

$$\phi_{\text{equiv}} = \frac{\phi_{\max}}{r_{fs}} \quad [\text{in W/cm}^2] \quad (r \text{ in } \mu\text{m}) \tag{D.8}$$

The LaserPlot output is shown in Figure D.1 for the Medusa variables from Table 4.1.

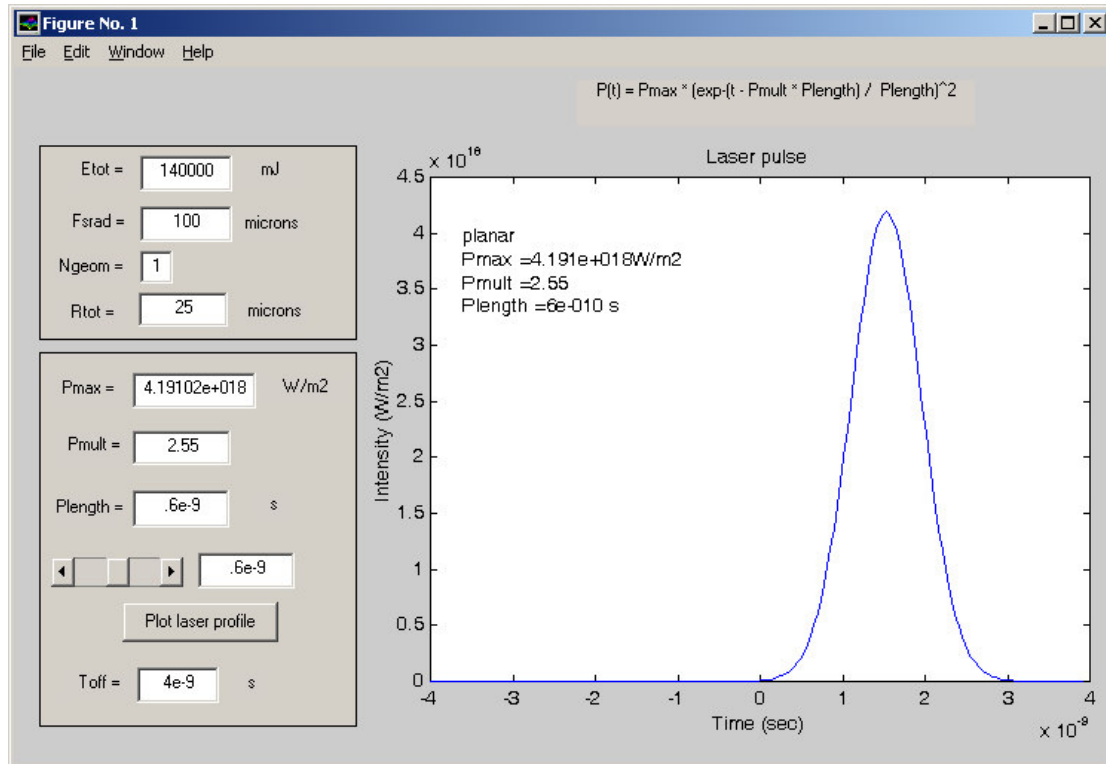


Figure D.1 Input Medusa laser pulse (140 J, 100 μm, 2.55, 0.6 ns)

### Appendix D.3 Medusa code changes and additions

A number of code changes were made to Medusa for this thesis and are outlined below. The page number-line number refers to the printout page (hardcopy) and line number in the original Medusa source code. For multiple changes, only the first page-line is given. For changes, the original line is followed by the change.

- **Change meshsize (max = 998, in current Medusa format)**

page 8-line 579 (and various subroutines)

```
PARAMETER (kk=201
PARAMETER (kk=401
```

- **Add print population energies, temperature**

page 89-line 7085 (in subroutine print)

```
c*****UCD 22/08/05 tstep,cell, nLTE,LTE, te,dens,
c          energy, totenergy (1 is cell)
      rhcons = 118.71 * 1.673e-27 * 1000
      DO 60 l=nst,nfl
c          l=nfl
          rhcalc = rh(l) / rhcons
          engtot = 0.0
          DO 61 i=1,nmax
              engtot = engtot + p(i,l)*eng(i,l)
61      CONTINUE
          IF (te(l)*1.E3.gt.40.and.te(l)*1.E3.lt.60) THEN
              WRITE(8,99901)nstep,l,(p(i,l),i=1,nmax),zstz(l)
              WRITE(8,99901)nstep,l,(pz(i,l),i=1,nmax),zstz(l)
              WRITE(8,99902)te(l)*1.E3,rhcalc,(1.E3*eng(i,l),i=1,nmax),
&          1.E3*engtot
          ENDIF
60      CONTINUE
c*****UCD
```

- **Change non-lte population format**

page 90-line 16532 (in subroutine setup)

```
99004 FORMAT(5x,i3,':',11F10.5)
99004 FORMAT(5x,i3,':',11E18.10)
```

- **Change number of excited states**

page 207-line 16532 (in subroutine setup)

```
nmax = 6
nmax = 10
```

## References

- 1 Meijer, F. G., "The use of gratings in the vacuum ultraviolet," *Optica Applicata*, **17** (3), 255–264, 1987.
- 2 Meijer, F. G., "Construction, adjustment and performance of a 6.600 m grazing incidence vacuum spectograph," *J. Phys. E: Sci. Instrum.*, **12**, 129–135, 1979.
- 3 McGuinness, C., *The XUV Photoabsorption and photoionisation spectra of selected ions: techniques, results, and theory*, Ph.D. thesis, University College Dublin, 1997.
- 4 van Kampen, P., *The outer shell spectra of argon and argon-like ions*, Ph.D. thesis, University College Dublin, 1997.
- 5 Cowan, R. D., *The theory of atomic structure and spectra*, Berkeley, University of California Press, 1981.
- 6 Cowan, R. D., "Programs RCN/RCN2/RCG/RCE," Addendum to *The theory of atomic spectra and structure*, May 1995.
- 7 Colombant, D. and Tonon, G. F., "X-ray emission in laser-produced plasmas," *J. Appl. Phys.*, **44** (8), 3524–3537, 1973.
- 8 Christiansen, J. P., Ashby, D. E. T. F., and Roberts, K. V., "Medusa: a one-dimensional laser fusion code," *Computer Physics Communications*, **7**, 271–287, 1974.

## Acknowledgements

It has been an honour and a privilege to work in the Spectroscopy group at UCD as well as a great adventure. What fun to work on such interesting physics, and in Dublin, where both my parents graduated. Tempus does indeed fugit when you're having fun.

Of course, there are a great many people to thank. Firstly, I would like to thank Professor Gerry O'Sullivan for his guidance and advice throughout my thesis. I would also like to thank Dr. Pdraig Dunne, especially for helping me to get the ball rolling. My thanks to Dr. Anthony Cummings, whose input and suggestions were always invaluable, and to Paddy Hayden for his many helpful contributions along the way. A great debt is owed to both Anthony and Paddy. My thanks also to Gerry, Anthony, and Paddy for their reviews of the thesis.

Throughout my time here, I have enjoyed the company of my colleagues both in 'Spec' and in the School of Physics. My thanks to my office mates Deirdre and Nicola, especially for putting up with my various computer rumblings. Indeed, the computer is always right. Thanks as well to Lynn, Kenneth, Paul, Andy, Mick, Luke, Emma, Eileen, Fergal, Frans, Michael, and Oran for all the craic and for keeping me sane. It was always a joy to come to work and I would especially like to thank Nicola, Paddy, Lynn, Kenneth, Andy, and Paul. My thanks also to Peggy, Bairbre, and Marian, for their constant help. And finally, my thanks to my family, who were never far from my thoughts.

And so, onwards, and ready for what's next.